

AFRL-VA-WP-TR-1999-3053

**DAMAGE TOLERANCE OF RESIN
TRANSFER MOLDED COMPOSITE
SANDWICH CONSTRUCTIONS**

**U.K. Vaidya
H. Mahfuz
S. Jeelani**

**Tuskegee University
Center for Advanced Materials (T-Cam)
Room 100
Chappie James Center
Tuskegee, AL 36088**

MAY 1999



FINAL REPORT FOR 24 APRIL 1996 – 23 APRIL 1999

Approved for public release; distribution is unlimited.

**AIR VEHICLES DIRECTORATE
AIR FORCE RESEARCH LABORATORY
AIR FORCE MATERIEL COMMAND
WRIGHT-PATTERSON AIR FORCE BASE, OH 45433-7542**

20020731 107

NOTICE

USING GOVERNMENT DRAWINGS, SPECIFICATIONS, OR OTHER DATA INCLUDING THIS DOCUMENT FOR ANY PURPOSE OTHER THAN GOVERNMENT PROCUREMENT DOES NOT IN ANY WAY OBLIGATE THE US GOVERNMENT. THE FACT THAT THE GOVERNMENT FORMULATED OR SUPPLIED THE DRAWINGS, SPECIFICATIONS, OR OTHER DATA DOES NOT LICENSE THE HOLDER OR ANY OTHER PERSON OR CORPORATION; OR CONVEY ANY RIGHTS OR PERMISSION TO MANUFACTURE, USE, OR SELL ANY PATENTED INVENTION THAT MAY RELATE TO THEM.

THIS REPORT IS RELEASABLE TO THE NATIONAL TECHNICAL INFORMATION SERVICE (NTIS). AT NTIS, IT WILL BE AVAILABLE TO THE GENERAL PUBLIC, INCLUDING FOREIGN NATIONS.

THIS TECHNICAL REPORT HAS BEEN REVIEWED AND IS APPROVED FOR PUBLICATION.



Forrest Sandow
Project Engineer
Structural Dynamics Branch


Ron Cummins Jr.

Terry Harris, Chief
Structural Dynamics Branch
Structures Division



ERICA ROBERTSON, Maj, USAF
Deputy Chief
Structures Division

Do not return copies of this report unless contractual obligations or notice on a specific document requires its return.

REPORT DOCUMENTATION PAGE

*Form Approved
OMB No. 0704-0188*

The public reporting burden for this collection of information is estimated to average 1 hour per response, including the time for reviewing instructions, searching existing data sources, searching existing data sources, gathering and maintaining the data needed, and completing and reviewing the collection of information. Send comments regarding this burden estimate or any other aspect of this collection of information, including suggestions for reducing this burden, to Department of Defense, Washington Headquarters Services, Directorate for Information Operations and Reports (0704-0188), 1215 Jefferson Davis Highway, Suite 1204, Arlington, VA 22202-4302. Respondents should be aware that notwithstanding any other provision of law, no person shall be subject to any penalty for failing to comply with a collection of information if it does not display a currently valid OMB control number. PLEASE DO NOT RETURN YOUR FORM TO THE ABOVE ADDRESS.

1. REPORT DATE (DD-MM-YY) May 1999			2. REPORT TYPE Final		3. DATES COVERED (From - To) 04/24/1996 – 04/23/1999	
4. TITLE AND SUBTITLE DAMAGE TOLERANCE OF RESIN TRANSFER MOLDED COMPOSITE SANDWICH CONSTRUCTIONS			5a. CONTRACT NUMBER F33615-96-C-3200			
			5b. GRANT NUMBER			
			5c. PROGRAM ELEMENT NUMBER 62201F			
6. AUTHOR(S) U.K. Vaidya H. Mahfuz S. Jeelani			5d. PROJECT NUMBER 2401			
			5e. TASK NUMBER 03			
			5f. WORK UNIT NUMBER 9E			
7. PERFORMING ORGANIZATION NAME(S) AND ADDRESS(ES) Tuskegee University Center for Advanced Materials (T-Cam) Room 100 Chappie James Center Tuskegee, AL 36088			8. PERFORMING ORGANIZATION REPORT NUMBER TCAM-WL-99-02			
			10. SPONSORING/MONITORING AGENCY ACRONYM(S) AFRL/VASM			
9. SPONSORING/MONITORING AGENCY NAME(S) AND ADDRESS(ES) AIR VEHICLES DIRECTORATE AIR FORCE RESEARCH LABORATORY AIR FORCE MATERIEL COMMAND WRIGHT-PATTERSON AIR FORCE BASE, OH 45433-7542			11. SPONSORING/MONITORING AGENCY REPORT NUMBER(S) AFRL-VA-WP-TR-1999-3053			
			12. DISTRIBUTION/AVAILABILITY STATEMENT Approved for public release; distribution is unlimited.			
13. SUPPLEMENTARY NOTES Report has 3 missing figures and several misplaced figures.			14. ABSTRACT (Maximum 200 Words) The objectives of this program were to investigate several innovative sandwich constructions developed by affordable manufacturing process for their impact damage resistance/tolerance. The sandwich composite concepts considered in this study possessed the feasibility to improve the transverse stiffness, provide enhanced damage resistance/tolerance to impact and functionality advantages in comparison to those made from conventional honeycomb and foam cores. The core concepts considered included – traditional foam, titanium, steel and E-glass/epoxy pins-reinforced foam, hollow truss/pin core, foam-filled-honeycomb cores, and honeycomb core with hybrid facesheets. Graphite and glass fabric and prepreg facesheets were considered. A number of low cost manufacturing techniques to produce panels included; resin transfer molding (RTM), vacuum assisted resin infusion/transfer molding (VARTM), co-injection VARTM and vacuum assisted compression molding (VACM). Detailed experimental impact studies were performed under three scenarios – low velocity, intermediate velocity, and high strain rate loading. Supporting analysis and finite element modeling work were conducted. The various tests and analysis conducted revealed that in terms of failure characteristics, the RTM/VARTM processed sandwich composites yielded similar performance as those manufactured from traditional techniques such as vacuum assisted compression molding. The reinforcement of foam core with stiff pins and/or honeycomb cells was found to provide attractive benefits to suppress/contain damage under low velocity, intermediate velocity and due to high strain rate impact scenarios.			
			15. SUBJECT TERMS Z-pin, Truss core, foam core, pin-reinforced form, foam-filled honeycomb, sandwich composites, Low cost Manufacture, Low velocity impact			
16. SECURITY CLASSIFICATION OF:			17. LIMITATION OF ABSTRACT: SAR	18. NUMBER OF PAGES 414	19a. NAME OF RESPONSIBLE PERSON (Monitor) Edward Schopler	
a. REPORT Unclassified	b. ABSTRACT Unclassified	c. THIS PAGE Unclassified			19b. TELEPHONE NUMBER (Include Area Code) (937) 656-5755	

TABLE OF CONTENTS

	Page No.
LIST OF FIGURES	ix
LIST OF TABLES	xxvii
PREFACE	xxviii
Chapter 1. PROGRAM GOALS	
1.1 Program Focus / Air Force Relevance	1
1.2 Program Background and Introduction	4
1.2.1 Sandwich Composite Design Concepts	4
1.2.2 RTM and VARTM : Affordable Manufacturing Alternatives for Air and Space Vehicles	8
1.2.2.1 Resin Transfer Molding (RTM)	10
1.2.2.2 Vacuum Assisted Resin Transfer Infusion / Transfer Molding (VARTM/VARIM)	11
1.2.3 Performance Evaluation	12
1.2.4 Modeling Studies	12
1.3 Stated Technical Objectives in the Original Proposal	12
1.4 Program Accomplishments	12
1.4.1 Research	12
1.4.2 Educational	13
1.4.2.1 Undergraduate and Graduate Students who Worked on the Research Project	14
1.4.3 Pertinent Publications from Research Effort	14
1.5 Organization of the Report	17
1.6 References	17
Chapter 2. SANDWICH CONSTRUCTIONS	
2.1 Concept of a Sandwich Structure	19
2.2 Historical Background	23
2.3 Advantages of Sandwich Construction	24
2.4 Disadvantages of Sandwich Construction	25
2.5 Applications	25
2.6 Motivation	26
2.7 Novel Sandwich Composite Constructions	27
2.8 References	27

Chapter 3	LITERATURE REVIEW	29
3.1 Introduction	29	
3.2 Damage Resistance & Damage Tolerance to Impact on Laminated Composites	29	
3.3 Damage Tolerance & Damage Resistance of Sandwich Composites	32	
3.4 High Strain Rate Impact	33	
3.5 Liquid Molding Processes; RTM, VARTM and Related Processes	35	
3.6 References	36	
Chapter 4	NEED FOR ALTERNATE CORES	39
4.1 Introduction	39	
4.2 Conventional Cores	39	
4.3 New Concepts in Sandwich Core Construction	40	
4.4 References	44	
Chapter 5	MANUFACTURING OF SANDWICH COMPOSITES	45
5.1 Introduction	45	
5.2 Liquid Molding	45	
5.2.1 Resin Transfer Molding (RTM)	45	
5.2.2 Vacuum Assisted Resin Transfer / Infusion Molding (VARTM)	47	
5.2.3 Vacuum Assisted Compression Molding (VACM)	47	
5.3 Manufacturing of Panels in the Current Work	48	
5.3.1 Fabrication of Hollow Z-Pin Truss Core Composites - Preliminary Work	48	
5.3.2 Resin Transfer Molding of Foam and Foam + Pin Core Sandwich Composites	50	
5.3.3 Fabrication of Foam-Filled Honeycomb Core Sandwich Composites with Graphite and S2- Glass Facesheets using Affordable Co- Injection Vacuum Assisted Resin Transfer Molding	51	
5.3.4 Fabrication of Foam, Pin-reinforced Foam & Hollow Z-Pin Truss Core Sandwich Composites using Vacuum Assisted Compression Molding	55	
5.3.5 Fabrication of Foam-Reinforced-Pin Core Sandwich Composites (Vacuum Assisted Compression Molding)	57	
5.3.6 Fabrication of Hollow Pin Core Sandwich		

	Composites (Vacuum Assisted Compression Molding)	57
5.4	References	60
Chapter 6	IMPACT TESTING	61
	6.1 Introduction	61
	6.2 Pendulum Impact Test System	61
	6.3 Drop Weight Impact Test System	61
	6.4 Impact Test Results Analysis	64
	6.5 References	66
Chapter 7	LOW VELOCITY IMPACT STUDIES OF FOAM-FILLED-HONEYCOMB CORE SANDWICH COMPOSITES	67
	7.1 Summary of Work (Chapter 7)	67
	7.2 Materials and Manufacturing	67
	7.3 Introduction	68
	7.4 Low Velocity Impact Testing of Honeycomb-Filled-Foam Core Sandwich Composites with 16-ply Graphite/Vinyl Ester Facesheets	68
	7.5 Low Velocity Impact Testing of Honeycomb-Filled-Foam Core Sandwich Composites with 8-ply S2 Glass/Vinyl Ester Facesheets	78
	7.6 Influence of Facesheet Thickness	88
	7.7 Conclusions	88
	7.8 References	90
Chapter 8	LOW VELOCITY IMPACT STUDIES OF FOAM, Z-PIN REINFORCED FOAM AND HOLLOW Z-PIN SANDWICH COMPOSITES	92
	8.1 Summary of Work (8.0)	92
	8.2 Materials and Manufacturing	92
	8.3 Foam Core Sandwich Composites (FCo)	95
	8.4 Foam-Reinforced-Titanium Pins Core Sandwich (F+PCo-75)	100
	8.5 Hollow Titanium Pin Core Sandwich Composites (TCo)	106
	8.6 Influence of Pin Spacing (F+PCo-150)	111
	8.7 Influence of Facesheet Thickness - FCo-32 and F+PCo-75 (32)	122
	8.8 Frequency Response Tests	127
	8.9 Influence of Manufacturing Technique: FCo (RTM) and F+PCo-75 (RTM)	127

	8.10 Influence of Pin Type: F+PCo-75 (Glass/Epoxy Pins)	133
	8.11 Conclusion	143
	8.12 References	145
	8.13 Low Velocity Impact Response of Honeycomb Composites with Dissimilar Facesheets	147
	8.13.1 Summary	147
	8.13.2 Conclusions	152
	8.13.3 References	153
Chapter 9	COMPRESSION-AFTER-IMPACT AND ACOUSTIC EMISSION STUDIES	154
	9.1 Introduction	154
	9.2 Compression-After-Impact and Acoustic Emission Studies for Foam-Filled-Honeycomb Core Sandwich Composites	154
	9.3 Compression-After-Impact Studies for Foam, Hollow and Z-Pin Reinforced Core Sandwich Composites	157
	9.4 Acoustic Emission Studies for Foam, Hollow and Z-Pin Reinforced Core Sandwich Composites	166
	9.5 References	171
Chapter 10	LOW VELOCITY IMPACT DAMAGE CHARACTERISTICS OF HOLLOW Z-FIBER REINFORCED SANDWICH PANELS WITH GRAPHITE/EPOXY FACESHEETS - AN EXPERIMENTAL STUDY	172
	10.1 Introduction	172
	10.2 Specimen and Method	173
	10.3 Low Velocity Impact Testing	173
	10.3.1 10 Degree Pin Orientation	176
	10.3.2 20 Degree Pin Orientation	181
	10.4 Static Indentation Testing	181
	10.5 Failure Modes	184
	10.6 Ultrasonic C-Scan Testing	184
	10.7 Compression-After-Impact (CAI) Testing	190
	10.8 Acoustic Emission (AE) Testing	192
	10.9 Vibration Testing	192
	10.10 Hollow Steel Pins Truss Core : Conclusions	195
	10.11 References	196

Chapter 11	STATIC TESTING	198
11.1	Introduction	198
11.2	Experimental	198
11.3	Flexural Tests and Acoustic Emission (AE) Nondestructive Evaluation / Monitoring	198
11.3.1	Hollow Truss Core: Flexural Response and Effect of Facesheet Type	198
11.3.2	Flexure Tests: AE Monitoring of Hollow Truss Core	204
11.4	Flexural Testing: Foam, Pin Reinforced Foam and Foam-Filled Honeycomb core Sandwich Composites	210
11.5	WESKOR Foam-Filled-Honeycomb: Effect of Facesheet Material	210
11.6	Flexure: Failure Modes	211
11.7	In-Plane Shear Testing 11.7.1. In-Plane Shear: WESKOR Foam-Filled Honeycomb Reinforced Foam	215 219
11.8	Static Compression Testing 11.8.1 Through-the-Thickness Compression Response of Core & Sandwich Composites	219
	11.8.2 Through-the-Thickness Compression Response of Sandwich Composites	222
	11.8.3 Effect of Geometry and Facesheets	224
	11.8.4 Influence of Cell Spacing	227
11.9	In-Plane Compression Response 11.9.1 Studies on Core (Without Facesheets)	227 227
	11.9.2 Studies on Sandwich Composites	232
11.10	Summary	232
11.11	References	235
Chapter 12	HIGH STRAIN RATE TESTING	236
12.1	Introduction	236
12.2	Experimentation	236
12.3	Comparison of HSR of Sandwich Composites with Different Cores	240
12.4	Influence of Incident-Transmission Bar Diameter	244
12.5	Influence of Momentum Trap Gap	250
12.6	In-Plane vs Through-the-Thickness Loading	256
12.7	High Strain Rate Response of Honeycomb Core Sandwich Composites with Dissimilar Facesheets	257
12.8	Summary	261
12.9	References	262

List of Figures

Chapter 1

- Figure 1.1. a, b and c. Some Application of Composites and Sandwich Constructions in Aircraft Parts
- Figure 1.2. TAFT and FATE Applications of Air Force
- Figure 1.3. Overall Program Plan and Implementation
- Figure 1.4. Foam Filled Honeycomb Core
- Figure 1.5. Concept of Hollow Truss Core Sandwich Composite
- Figure 1.6. Examples of RTM Technology in Aerospace Applications
- Figure 1.7. Cost Comparisons of Various Processing Alternatives for Composites
- Figure 1.8. Schematic of Closed Mold RTM Processing
- Figure 1.9. Vacuum Assisted Resin Infusion/Transfer Molding (VARIM/VARTM)

Chapter 2

- Figure 2.1a and b. Schematic of a Structural Sandwich Composite and Concept of Working of a Sandwich Beam
- Figure 2.2 ~~or~~ ^c. Illustration of the Working of a Sandwich Beam
- Figure 2.3. Use of RTM composite parts in F-22 Aircraft
- Figure 2.4. Use of Laminated and Sandwich Composites in Aircraft
- Figure 2.5. Use of Composites in Aircraft

Chapter 3

- Figure 3.1. Schematic of Z-Fiber Reinforcement of Composites
- Figure 3.2. Schematic of an Interleaved Sandwich Composite

Chapter 4

Figure 4.1. Conventional Honeycomb and Foam Cores

Figure 4.2. Commonly used Honeycomb and Foam Cores and their Sandwich Constructions

Figure 4.3a. Schematic of Foam-Filled Honeycomb Core

Figure 4.3b. Foam-Filled Honeycomb Core

Figure 4.4. Hollow Truss (Z-Pin) Core Sandwich Composite

Figure 4.5. Schematics of Core Types Considered in the Overall Research

Chapter 5

Figure 5.1. Resin Transfer Molding Metering, Mixing and Dispensing Unit

Figure 5.2. a).Schematic of the Resin Transfer Molding process, b) Photograph of the RTM Process

Figure 5.3. Schematic of VARTM process

Figure 5.4. Schematic of Compression Molding Process

Figure 5.5. Layout of Truss Core Pins

Figure 5.6. Foam Core with Pins Prior to Facesheet Placement

Figure 5.7. Finished Truss core panel

Figure 5.8a. Detailed Schematic of Co-Injection Process

Figure 5.8b. Illustration of Co-Injection for Manufacturing Sandwich Composites

Figure 5.9. Typical Vacuum Assisted Resin Transer Molding : Co-Injection of Top and Bottom Facesheets a) Preparing the Foam-Filled-Honeycomb Core, b) and c) Lay-Up and Resin Injection

Figure 5.10a and b. Co-Injection of Sandwich Composite Panels

Figure 5.11a, b, and c. Photographs of Manufacturing of Foam Core Sandwich Composites

Figure 5.12. Pin Spacing and Arrangement of Pins Within the Core

Figure 5.13a,b, c. Photographs of Manufacturing of Pin-Reinforced Foam Core Sandwich Composite Samples

Figure 5.13d and e. Photographs of Manufacturing of Foam and Pin-Reinforced Foam Core Sandwich Composite Samples (Continued).

Chapter 6

Figure 6.1. Schematic of a Dynatup Drop Weight Test system

Figure 6.2. Adjustment of Velocity Detector and flag in the Drop Weight Test System

Figure 6.3. Photograph of Dynatup 8210

Figure 6.4. Schematic of Swing Pendulum

Figure 6.5. Typical Load-Time Energy Histories

Chapter 7

Figure 7.1. Typical Force/Energy-Time Curves for 16-ply Woven Graphite/Vinyl Ester Foam-Filled-Honeycomb Core Sandwich Composite

Figure 7.2. Typical Load/Energy Curves for 16-ply Woven Graphite/Vinyl Ester Foam-Filled-Honeycomb-Core Sandwich Composite

Figure 7.3. Illustration of Localized Foam Core Crushing within Pockets of Honeycomb Cells in Foam-Filled-Honeycomb Core Sandwich Composites

Figure 7.4. Illustration of Core Crushing, Cell Wall Microbuckling and Impact Side Facesheet Damage for Foam-Filled-Honeycomb Core Sandwich Composites

Figure 7.5. Illustration of Core Buckling, Foam Core Crushing, Interfacial Debonding Between Core and Cell and Impact Side Facesheet Damage in Foam-Filled - Honeycomb Core Sandwich Composites impacted at 33 J (Energy Level D)

Figure 7.6. Bottom Facesheet Failure for Impact Level D (16-ply Graphite/Vinyl Ester Facesheets)

Figure 7.7. Ultrasonic C-scans showing Damage Zones at 11, 20, 28.33 and 40J Impact Energy (16-ply Graphite/Vinyl Ester Facesheets)

Figure 7.8. Ultrasonic C-scan showing Distributed Back Skin Damage for Impact Level D (16-ply Graphite/Vinyl Ester Facesheets)

Figure 7.9. Experimental set-up of Vibration Testing

Figure 7.10. Vibration FRF for sample impacted at Energy Level A (16-ply Graphite/Vinyl Ester Facesheets)

Figure 7.11. Vibration FRF for sample impacted at Energy Level E (16-ply Graphite/Vinyl Ester Facesheets)

Figure 7.12. Comparison of FRF of A and E Energy Level Impacted samples (16-ply Graphite/Vinyl Ester Facesheets)

Figure 7.13. Typical Load/Energy-Time Curves for 8-ply S2 Glass Vinyl Ester Honeycomb filled foam core sandwich composite

Figure 7.14. Typical Load-Energy Curves for 8-ply S2 Glass Vinyl Ester Honeycomb filled foam core sandwich composite

Figure 7.15a-b. Top Facesheet and core damage at impact level A (8-ply Glass/Vinyl Ester Facesheets)

Figure 7.16a-b. Top Facesheet and core damage for impact level D (8-ply Glass/Vinyl Ester Facesheets)

Figure 7.17. Vibration FRF for sample Impacted at Energy level A (8-ply Glass/Vinyl Ester Facesheets)

Figure 7.18. Comparison of FRF of A and E Energy level Impacted samples (8-ply Glass/Vinyl Ester Facesheets)

Figure 7.19. Comparison of Force/Energy-time curves of Honeycomb filled foam core, 4-ply, 16-ply Graphite/vinyl ester facesheets, and 8-ply S2 glass/vinyl ester facesheet sandwich composite

Chapter 8

Figure 8.1. Force/Energy-Time curves for the FCo composites (Energy levels A-E)

Figure 8.2. Load-Energy curves for the FCo composites (Energy levels A-E)

Figure 8.3. Load-Deflection curves for the FCo composites (Energy levels A-E)

Figure 8.4a-b. Schematic and Micrograph of Failure Mechanisms for FCo composite:
Interfacial Debond between Facesheet and Core and Core Crushing

Figure 8.5. Force-Time and Energy-Time curves for the F+Pco-75 Composites (energy levels A-E)

Figure 8.6. Load-Energy curves for the F+Pco-75 composites (Energy levels A-E)

Figure 8.7a,b and c. Schematic and Micrograph of Failure Mechanisms for F+PCo-75; a) Schematic showing various damage modes of F+PCo-75, b) Pin-push out, causing upward movement of plies, and creation of shear delaminations joining that join impact location damage to pin location damage, and, c) Interfacial Debonding between Facesheet/Core for F+PCo-75 Composite and Flexural Failure of Top facesheet

Figure 8.8. Load-Deflection curves for the F+Pco-75 composites (energy level A-E)

Figure 8.9. Force-Time and Energy-Time curves for the TCo Composites (energy levels A-E)

Figure 8.10. Load-Energy curves for the TCo composites (Energy levels A-E)

Figure 8.11. Load-Deflection curves for the TCo composites (Energy levels A-E)

Figure 8.12a,b and c. Schematic and Micrograph of Failure Mechanisms for TCo; a) Schematic showing failure modes of TCo, b) Localized Delamination, fiber Breakage & Matrix Cracking; Note the Pin-push out causes plies to move up, while at the impact location, the failure is by flexure. Shear cracks occur between these locations, and c) Pin Buckling

Figure 8.13. Force-Time and Energy-Time curves for the F+PCo-150 Composites (Energy Levels A-E)

Figure 8.14. Load-Energy curves for the F+PCo-150 composites (Energy levels A-E)

Figure 8.15. Load-Deflection curves for the F+PCo-150 composites (energy level A-E)

Figure 8.16. a) Flexural Failure of Top facesheet for the F+PCo-150 composite and, b) Core crushing slightly away from the impact location

Figure 8.17. Comparison of Force-Time curves for FCo, F+PCo-75, TCo and F+PCo-150 samples at energy level A

Figure 8.18. Comparison of Load-Deflection curves for FCo, F+PCo-75, TCo and F+PCo-150 samples at energy level A

Figure 8.19. Comparison of Force-Time curves for FCo, F+PCo-75, TCo and F+PCo-150 samples at energy level E

Figure 8.20. Comparison of Load-Deflection curves for FCo, F+PCo-75, TCo and F+PCo-150 samples at energy level E

Figure 8.21. Load/Energy-Time curves for the FCo-32 composites (Energy levels A-E)

Figure 8.22. Load-Energy curves for the FCo-32 composites (Energy levels A-E)

Figure 8.23a and b. Facesheet to core disbond and core crushing for FCo-32 composite (Energy level E)

Figure 8.24. Load/Energy-Time curves for the F+PCo-75 (32) composites (Energy levels A-E)

Figure 8.25. Load-Energy curves for the F+PCo-75 (32) composites (Energy levels A-E)

Figure 8.26. Facesheet to core disbond and microdelamination around the pin location for F+PCo-75 (32) composite (Energy level E)

Figure 8.27. Comparison of FRF's of FCo, F+PCo-75, F+PCo-150 and TCo composites (energy level A)

Figure 8.28. Comparison of FRF's of FCo and F+PCo-75 composites with 16-ply and 32-ply E-glass facesheets

Figure 8.29. Load/Energy-Time curves for the FCo (RTM) composites (Energy levels D and E)

Figure 8.30. Load-Energy curves for the FCo (RTM) composites (Energy levels D and E)

Figure 8.31. Facesheet to core disbond and core crushing observed for the FCo (RTM) composite (Energy level E)

Figure 8.32. Load/Energy-Time curves for the F+PCo-75 (RTM) composites (Energy levels D and E)

Figure 8.33. Load-Energy curves for the F+PCo-75 (RTM) composites (Energy levels D and E)

Figure 8.34. Core Crushing and Facesheet to core disbond for the F+PCo-75 (RTM) composite (Energy level E)

Figure 8.35. Comparison of Load/Energy-Time curves for the FCo (RTM) and F+PCo-75 (RTM) composites (Energy level D)

Figure 8.36. Comparison of Load-Energy curves for the FCo (RTM) and F+PCo-75 (RTM) composites (Energy level D)

Figure 8.37. Comparison of FRF of the FCo and F+PCo-75 samples manufactured by RTM process (Energy level D)

Figure 8.38. Load/Energy-Time curves for the F+PCo-75 (Glass/Epoxy pins) Composites (Energy levels A, D and E)

Figure 8.39. Load-Energy curves for the F+PCo-75 (Glass/Epoxy pins) composites (Energy levels A, D and E)

Figure 8.40. Facesheet to skin disbond, core crushing and facesheet flexure for the F+PCo-75 (Glass/Epoxy pins) composites (Energy level E)

Figure 8.41. FRF curves for F+PCo-75 (Glass/Epoxy pins) composites (Energy levels D & E)

Figure 8.12.1. Load/Energy-Time curves for sandwich composites subjected to 20J Impact Energy

Figure 8.12.2. Load/Energy-Time curves for sandwich composites subjected to 33J Impact Energy

Figure 8.12.3. Comparison of Load/Energy-Time curves for impact from Glass/Epoxy Facesheet

Figure 8.12.4. Comparison of Load/Energy-Time curves for impact from Graphite/Epoxy Facesheet

Figure 8.12.5 a&b. LVI Failure Modes for Graphite/Epoxy Side Impact, and Glass/Epoxy Side Impact

Chapter 9.

Figure 9.1. SACMA recommended Boeing test fixture for Compression after impact Studies

Figure 9.2a and b. Photograph of the CAI testing using MTS

Figure 9.3. Top view of top facesheet showing CAI failure in the vicinity of the impact Location (Foam-Filled-Honeycomb)

Figure 9.4. CAI failure of top facesheet: Kink-Band formation and shear instability of the Facesheet (Foam-Filled-Honeycomb)

Figure 9.5. Parametric distribution of energy and amplitude of AE activity for the 16 ply facesheet graphite sandwich composite (Foam-Filled-Honeycomb)

Figure 9.6. Load-displacement curve for the FCo, F+PCo-75 and Tco composites with the influence of skin thickness and pin density (Energy level A)

Figure 9.7. CAI curves for FCo samples A and D

Figure 9.8. CAI curves for F+PCo-75 samples A and D

Figure 9.9. CAI curves for F+PCo-150 samples A and D

Figure 9.10. CAI curves for FCo-32 samples A and D

Figure 9.11. CAI curves for F32-PCo-75 samples A and D

Figure 9.12. Parametric distribution for FCo composite sample D

Figure 9.13. Parametric distribution for F+PCo-75 composite sample D

Figure 9.14. Parametric distribution for F+PCo-150 composite sample D

Figure 9.15. Parametric distribution for TCo composite sample D

Figure 9.16. Parametric distribution for FCo-32 composite sample A

Figure 9.17. Parametric distribution for F+PCo-75 (32) composite sample A

Chapter 10

- Figure 10.1a, b and c.
- a) Front View of the truss core sandwich composite
 - b) Top View of the truss core sandwich composite
 - c) Side view schematic of the truss core sandwich composite

Figure 10.2 Schematic of the pendulum test system

Figure 10.3 Force-Time curves for five 10-degree orientation specimens tested at different energy levels

Figure 10.4 Load-Displacement curves for five 10-degree orientation specimens tested at different energy levels

Figure 10.5 Percentage absorbed impact energy vs energy plot

Figure 10.6 Force-Time curves for 20 degree pin orientation specimens tested at different energy levels

Figure 10.7 Load-Displacement curves for 20 degree pin orientation specimens tested at different energy levels

Figure 10.8 Percentage absorbed impact energy vs energy plot

Figure 10.9 Experimental set-up for static indentation testing

Figure 10.10 Static Load-Displacement curves for 10 degree pin orientation specimen

Figure 10.11 Static Load-Displacement curves for 20 degree pin orientation specimen

Figure 10.12. Incipient damage at pin-facesheet interface

Figure 10.13a,b & c. Pin push-out for the top and bottom facesheets

Figure 10.14a&b. Schematic of failure as observed across the top and bottom facesheets

Figure 10.15a&b. SEM photographs showing the shear crack and delamination in the facesheet around the pins

Figure 10.16a&b. SEM photographs showing that the pin penetration into the facesheet is not equal for all pins

Figure 10.17a&b. Pre Impact C-Scans for 10 and 20 degree pin orientation

Figure 10.18a and b. Ultrasonic C-Scans for 10 and 20 degree pin orientation subjected to quasi-static loading

Figure 10.19. CAI Load-Displacement curves (Hollow Z-Pins Steel Core)

Figure 10.20a&b. Ultrasonic C-scans of a specimen subjected to CAI loading

Figure 10.21a&b. Ultrasonic C-Scans for single impact and repeated impact

Figure 10.22. Distribution of amplitude and duration with respect to test time

Figure 10.23. FRF curve for 10 degree pin orientation subjected to a single impact and repeated impact

Figure 10.24. Comparison of FRF of 10 degree pin orientation specimens subjected to a single impact vs that subjected to repeated impact

Figure 10.25 Comparison of FRF for an impact loaded specimen and statically loaded specimen

Chapter 11

Figure 11.1a-c. a) Illustration of static flexural testing of sandwich composites
b) Illustration of static in-plane shear testing of sandwich composites
c) Illustration of static compression testing of sandwich composites

Figure 11.2. Schematic of arrangement of pins in polystyrene foam core in preliminary work

Figure 11.3. Load-Deflection curves for glass/epoxy truss core composites under flexural loading

Figure 11.4. Load-Deflection curves for graphite/epoxy truss core composites under flexural loading

Figure 11.5. AE response in terms of amplitude distribution for glass/epoxy truss core composite

Figure 11.6. AE response in terms of amplitude distribution for graphite/epoxy truss core composite

Figure 11.7. AE response in terms of energy vs time for glass/epoxy truss core composite

Figure 11.8. AE response in terms of energy vs time for graphite/epoxy truss core composite

Figure 11.9. AE response in terms of cumulative AE activity for glass/epoxy truss core composite

Figure 11.10. AE response in terms of cumulative AE activity for graphite/epoxy truss core composite

Figure 11.11. AE response in terms of duration vs amplitude for glass/epoxy truss core composite

Figure 11.12. AE response in terms of duration vs amplitude for graphite/epoxy truss core composite

Figure 11.13. Flexural load-displacement curves for different sandwich composites

Figure 11.14. Flexural load-displacement curves for WESKOR foam filled honeycomb with glass and graphite fiber reinforced facesheets

Figure 11.15. Comparison of flexural strength of the various sandwich composites studied

Figure 11.16. Photographs of flexural failure for different sandwich composites

Figure 11.17. In-plane shear load displacement curves for foam and foam reinforced with glass/epoxy pins

Figure 11.18a-d. Sequence of failure of foam core sandwich composite

Figure 11.19a and b. Photograph of the in-plane failure of foam and foam reinforced with glass/epoxy pins

Figure 11.20. In-plane shear load displacement curve for WESKOR foam-filled - honeycomb

Figure 11.21. Failure characteristics for WESKOR foam filled honeycomb

Figure 11.22. Through-the-thickness load displacement plot for different cores

Figure 11.23a-b. Edge view and top view of honeycomb core cells failed under static compression

Figure 11.24. Through-the-thickness load displacement plot for different sandwich composites

Figure 11.25. Failure of hollow steel pin truss core by simultaneous buckling of pins

Figure 11.26. Load-Displacement plot for through-the-thickness testing of honeycomb core and its sandwich composite

Figure 11.27. Load-Displacement plot for through-the-thickness testing of Rohacell foam core and its sandwich composite

Figure 11.28. Load-Displacement plot for through-the-thickness testing of WESKOR foam -filled-honeycomb core and its sandwich composite

Figure 11.29. Load-Displacement plot for through-the-thickness testing of Rohacell foam reinforced with titanium pin core and its sandwich composite

Figure 11.30. Load-Displacement plot for through thickness testing of WESKOR foam -filled-honeycomb core with different cell spacing

Figure 11.31. Failure of WESKOR foam filled honeycomb core under in-plane loading

Figure 11.32. Load-displacement curve for Rohacell foam reinforced with titanium pins under in-plane loading (From report)

Figure 11.33. Load-displacement curve for WESKOR foam-filled-honeycomb core under in-plane loading (From report)

Figure 11.34. In-plane load-displacement curve for honeycomb core sandwich composite

Figure 11.35. Failure of honeycomb sandwich composite under in-plane loading

Figure 11.36. In-plane load-displacement curve for Rohacell foam reinforced with titanium pins core and its sandwich composite (report)

Figure 11.37. In-plane load-displacement curve for WESKOR foam filled honeycomb core and its sandwich composite (report)

Chapter 12

Figure 12.1a-b. a) Schematic of Split Hopkinson Pressure Bar
b) Split Hopkinson Pressure Bar

Figure 12.2a-b. a) Schematic of Momentum trap gap
b) Momentum trap (Dynamic recovery technique)

Figure 12.3a-c. a) Voltage vs time signal for incident bar (Strain)
b) Voltage vs time signal for transmission bar (Stress)
c) Stress-Strain curve obtained from the above signals for honeycomb core sandwich composite

Figure 12.4a-c. Voltage vs time signal for a) Classical SHPB b) With Momentum trap c) fine tuning with grease coating

Figure 12.5a-d. a) Stress-strain curve for Rohacell foam core sandwich composite with MTG

b) Stress-strain curve for Rohacell foam core sandwich composite without MTG

c) Optical microscopy of foam core sandwich composite

d) Failure schematic of foam core sandwich composite

Figure 12.6a-d. a) Stress-strain curve for honeycomb core sandwich composite with MTG

b) Stress-strain curve for honeycomb core sandwich composite without MTG

c) Catastrophic cell wall buckling of honeycomb core sandwich composite

d) Failure schematic of honeycomb core sandwich composite

Figure 12.7a-f. a) Stress-strain curve for Rohacell foam reinforced with titanium pin core sandwich composite with MTG

b) Stress-strain curve for Rohacell foam reinforced with titanium pin core sandwich composite without MTG

c, d and e) Optical microscopy for Rohacell foam reinforced with titanium pin core sandwich composite

f) Failure schematic of Rohacell foam reinforced with titanium pin core sandwich composite

Figure 12.8a-f. a) Stress-strain curve for rohacell foam reinforced with glass/epoxy pin core sandwich composite with MTG

b) Stress-strain curve for rohacell foam reinforced with glass/epoxy pin core sandwich composite without MTG

c, d and e) optical Microscopy for rohacell foam reinforced with glass/epoxy pin core sandwich composite

f) Failure schematic of Rohacell foam reinforced with titanium pin core sandwich composite

Figure 12.9a-e. a) Stress-strain curve for hollow steel pin truss core sandwich composite with MTG

b) Stress-strain curve for hollow steel pin truss core sandwich composite without MTG

c and d) optical microscopy for hollow steel pin truss core sandwich composite

e) Failure schematic of hollow steel pin truss core sandwich composite

Figure 12.10a-c. a) Stress-strain curve for WESKOR foam-filled-honeycomb core sandwich composite with MTG
b) Stress-strain curve for WESKOR foam-filled-honeycomb core sandwich composite without MTG
c) Failure schematic for WESKOR foam-filled-honeycomb core sandwich composite

Figure 12.11a-b. a) Stress-strain curve for WESKOR foam-filled-honeycomb core sandwich composite tested using 1.5" bar
b) Stress-strain curve for honeycomb core sandwich composite tested using 1.5" bar

Figure 12.12a-c. Optical microscopy for WESKOR foam-filled-honeycomb core sandwich composite tested using 0.75" bar (With MTG)

Figure 12.13a-c. Optical Microscopy for WESKOR foam-filled-honeycomb core sandwich composite tested using 1.5" bar

Figure 12.14a-c. Optical microscopy for 0.5"X0.5" samples subjected to HSR impact at a strain rate of 170/sec using 1.5" bar

Figure 12.15a-f. Optical microscopy for samples subjected to In-plane HSR impact using 1.5" bar

Figure 12.16a-d. a) Stress-strain curve for nomex honeycomb core with hybrid facesheets (with MTG) - glass/epoxy facesheet facing
b) Stress-strain curve for nomex honeycomb core with hybrid facesheets (without MTG) - glass/epoxy facesheet facing
c and d) optical microscopy for nomex honeycomb core with hybrid facesheets - glass/epoxy facesheet facing

Figure 12.17-d. a) Stress-strain curve for Nomex honeycomb core with hybrid facesheets (with MTG) – Graphite/epoxy facesheet facing
b) Stress-strain curve for Nomex honeycomb core with hybrid facesheets (without MTG) – Graphite/Epoxy facesheet facing
c and d) optical Microscopy for Nomex honeycomb core with hybrid facesheets – Graphite/Epoxy facesheet facing

Chapter 13

Figure 13.1 Schematic of Intermediate velocity impact test set-up
a) Details of the fixture b) Specimen mounted on the fixture

Figure 13.2 Intermediate velocity impact damage for Rohacell foam, Rohacell foam reinforced with titanium pin and hollow titanium pin truss core sandwich composites

Figure 13.3 Intermediate velocity impact failure for Rohacell foam and Rohacell foam reinforced with glass/epoxy pin core sandwich composites

Chapter 14

14.1-14.5 *Work Done at Tuskegee University*

Figure 14.1. Unit cell for Z-Pin core

Figure 14.2. Z-pin sandwich core panel

Figure 14.3. Z-Pin sandwich core under CAI loading constraints

Figure 14.4. σ_x distribution for Z-pin sandwich panel under CAI

Figure 14.5. τ_{xy} distribution for Z-pin sandwich panel under CAI

Figure 14.6 Unit cell for honeycomb core

Figure 14.7. Unit cell for honeycomb core under constraints for flexural loading

Figure 14.8. Z-direction displacement for unit cell honeycomb core under flexure

Figure 14.9. σ_z distribution for unit cell honeycomb core under flexure

Figure 14.10. Unit cell honeycomb with facesheets under constraints for flexure

Figure 14.11. σ_z distribution for unit cell honeycomb core with facesheets under flexure

Figure 14.12. Z-direction displacement for unit cell honeycomb with facesheets under flexure

Figure 14.13. Honeycomb core with multiple cells model

Figure 14.14. Honeycomb core sandwich panel model

Figure 14.15. SOLID46 element with eight corner nodes

Figure 14.16. VISCO107 element with eight corner nodes

Figure 14.17. Foam core sandwich panel model

- Figure 14.18. Foam core sandwich panel with constraints
- Figure 14.19. Deformed foam core sandwich panel under transverse compression
- Figure 14.20. Z-direction displacement of foam core sandwich panel under transverse compression
- Figure 14.21. σ_z distribution for foam core sandwich panel under transverse compression
- Figure 14.22. Total strain in the z-direction for the foam core sandwich panel under transverse compression
- Figure 14.23. Distribution of z-direction displacement across the foam core sandwich panel thickness under transverse compression
- Figure 14.24. Distribution of σ_z across the foam core sandwich panel thickness under transverse compression
- Figure 14.25. Distribution of total strain in the z-direction (thickness) of the sandwich Panel under transverse compression
- Figure 14.26. Foam core sandwich panel under flexural loading
- Figure 14.27. Loading and constraints of foam core sandwich panel under flexure
- Figure 14.28. Deformed foam core sandwich panel under flexure
- Figure 14.29. Distribution of z-direction stresses under flexural loading of foam core sandwich panel
- Figure 14.30. σ_z distribution for foam core sandwich panel under flexure
- Figure 14.31. Total strain in z-direction for foam core sandwich panel under flexure
- Figure 14.32. Distribution of z-direction displacement across the foam core sandwich panel thickness under flexure
- Figure 14.33. Distribution of σ_z across the foam core sandwich panel thickness under flexure
- Figure 14.34. Distribution of total strain in the z-direction (thickness) of the foam core sandwich panel under flexure
- Figure 14.35. Foam core sandwich panel model for low velocity impact

Figure 14.36. Constraints and loading for foam core sandwich panel under low velocity impact

Figure 14.37. Deformed foam core sandwich panel under low velocity impact

Figure 14.28. Displacement along z-direction for foam core sandwich panel under low velocity impact

Figure 14.39. σ_z distribution for foam core sandwich panel under low velocity impact

Figure 14.40. σ_x distribution for foam core sandwich panel under low velocity impact

Appendix A :*Work Done under Sub-Contract by Advanced Structural Concepts*

Note : *Figure captions are as per Advanced Structural Concept Report attached along with Appendix A*

Figure 3.1. Sandwich plate model

Figure 4.1. Force-time and energy-time curves

Figure 4.2. Load-deflection curve

Figure 4.3. Sandwich plate model

Figure 4.4. Load position

Figure 4.5. Load-time function

Figure 4.6. Finite element static analysis

Figure 4.7. Load vs. Pin failures

Figure 4.8. Load vs. Pin failures (up to 160 pins)

Figure 4.9. Load vs. Pin failures (up to 10 pins)

Figure 4.10. Vertical displacement of top face sheets, force equals 4.39 kN

Figure 4.11. Vertical displacement of top face sheets, force equals 4.41 kN

Figure 4.12. Vertical displacement of top face sheets, force equals 4.08 kN

Figure 4.13. Vertical displacement of top face sheets, force equals 4.05 kN

Figure 4.14. Vertical displacement of top face sheets, force equals 4.14 kN

Figure 4.15. σ_{yy} at a force equal to 4.39 kN

Figure 4.16. σ_{yy} at a force equal to 4.41 kN

Figure 4.17. σ_{yy} at a force equal to 4.08 kN

Figure 4.18. σ_{yy} at a force equal to 4.05 kN

Figure 4.19. σ_{yy} at a force equal to 4.41 kN

Figure 4.20. σ_{xx} at a force equal to 4.39 kN

Figure 4.21. σ_{xx} at a force equal to 4.41 kN

Figure 4.22. σ_{xx} at a force equal to 4.05 kN

Figure 4.23. σ_{xx} at a force equal to 4.05 kN

Figure 4.24. σ_{xx} at a force equal to 4.41 kN

Figure 4.25. Dynamic analysis results

Figure 4.26. Dynamic analysis results with facesheet failure

Figure 4.27. First mode shape

Figure 4.28. Second mode shape

Figure 4.29. Third mode shape

LIST OF TABLES

Description

Table 1.1 Design Concepts for Innovative Core Constructions

Table 7.1 Nomenclature for Impact Levels

Table 8.1 Details of Constituent Materials and Configurations

Table 8.2 Nomenclature of Samples Tested in Section 8.0

Table 8.3 Sample Details

Table 8.4 Energy Levels at which Samples were Impacted

Table 10.1 Compression-after-Impact Studies on Z-Pin Specimens

Table 11.1 Cores Tested and their Geometry : Static Compression

Table 11.2 Sandwich Composites Tested and their Geometry : Static Compression

Table 11.3 Details of Samples Tested under Flexural Loading

Table 11.4 Summary of Flexural Tests on Four Samples each of Truss Core Composites with Glass/Epoxy and Graphite/Epoxy Facesheets

Table 11.5 Flexural Strength of Various Sandwich Composites

Table 12.1 Sandwich Composites Subjected to High Strain Rate Impact and their Geometry

Table 15.1 Summary : Foam-Filled-Honeycomb Core Sandwich Composites

Table 15.2 Summary : Conventional and Innovative Core Sandwich Composites

Table 15.3 Summary : Other Sandwich Constructions Tested

PREFACE

The work documented in this report was performed at the Center for Advanced Materials, Tuskegee University, Alabama under Contract F33615-96-C-3200 sponsored by Air Force Research Laboratory, WPAFB. The work was performed in the period April 24, 1996 through April 23, 1999. The Air Force Program Monitor was Forrest Sandow to whom we express our profound gratitude for his kind suggestions, assistance and motivation through the effort.

Dr. Uday Vaidya, Center for Advanced Materials (T-CAM), Tuskegee University was the Principal Investigator on the effort. Dr. Hassan Mahfuz and Dr. Shaik Jeelani of T-CAM, Tuskegee University were the co-investigators. A list of students (undergraduate and graduate) who worked on this project is provided in Chapter 1. Notably the authors would like to acknowledge the contribution of the following individuals from T-CAM :

- Pradeep Kumar Mohan, *Graduate Student*
- Dr. Mahesh V. Hosur, *Research Assistant Professor*
- Mohan Kamath, *Graduate Student*
- Hisham Mohamed, *Research Staff*
- Zhenyi Zhang, *Research Staff*

The authors are also particularly grateful to the extensive technical discussions and insights provided by Dr. Anthony Palazatto, Air Force Institute of Technology, WPAFB and Dr. Nagesh Gummadi, Advanced Structural Concepts. The results from this work are presented in a total of fifteen chapters.

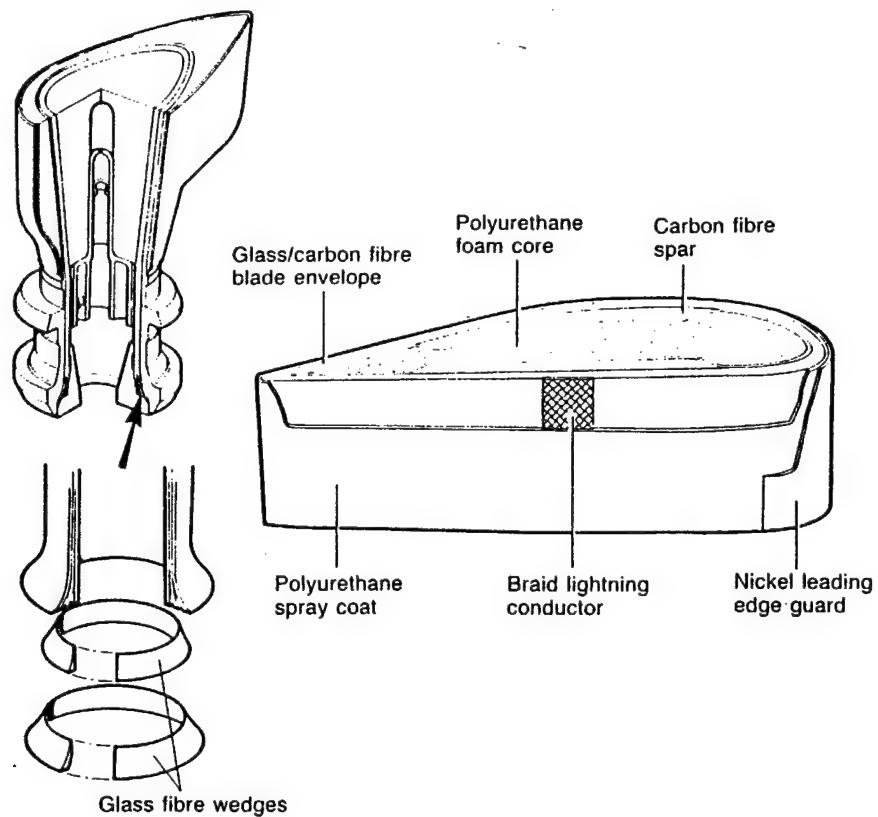
1.1 Program Focus / Air Force Relevance

With new advances in technology, the role of composite materials in air and space vehicles is increasing exponentially. The utilization of composites ranges from composite wing, horizontal stabilizer, composite rudder, scarf nozzles, landing gear door, speed brake, flap segments, aircraft interior panels and seats, to name a few applications. Figures 1.1a-c represent a variety of composites and sandwich constructions used in aircraft structures. Among several technologies identified in the Air Force Initiatives on Todays Aircraft Flying Tomorrow (TAFT) (Fig 1.2a), **survivable aircraft structures and affordability** issues assume prime importance (*Source : Air Vehicles Directorate; Internet Release Information [1]*). Future Aircraft Technology Enhancements (FATE) develop revolutionary technologies that will become the foundation for next generation war fighters. It will be these new systems that will provide the US with air and space superiority into the 21st century. Examples of FATE (Fig 1.2b) technologies include, affordable LO data system, active aeroelastic wing, robust composite sandwich structures, damage tolerant / resistant composite structures, advanced compact inlets, photonic vehicle management systems, self-adaptive flight controls and electric actuation, to mention some.

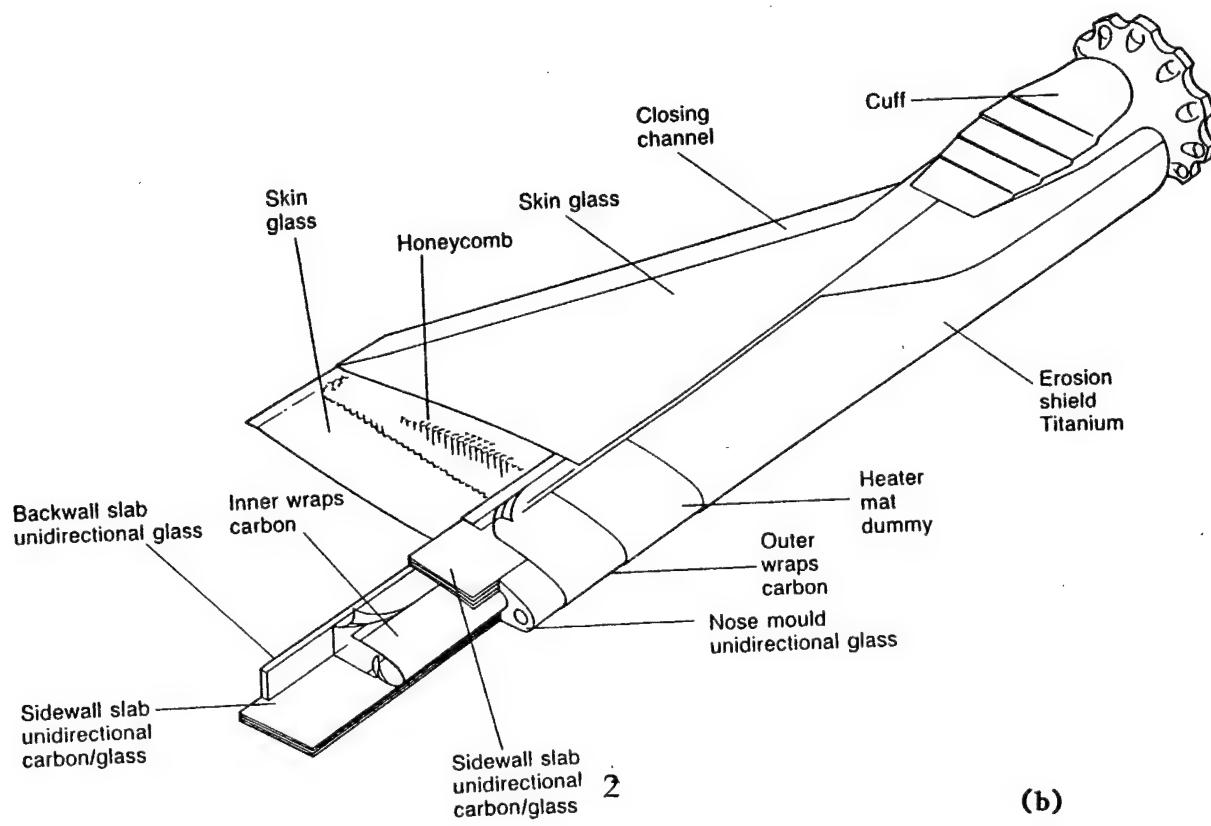
Affordability and **survivability** are key to *air and space vehicles* for higher performance and longer life. **New structural concepts** and design techniques need to be exploited for the latest materials, processes, and manufacturing technologies to produce more durable structures at lower weight and cost [2,3]. **Damage resistance/tolerance** of innovative sandwich composites manufactured by **affordable and other traditional processing techniques** is of high importance in order to justify usage of composites to make them reliable for air and space vehicles applications. The problem of impact under low velocity and high strain rates is of high concern in all aircraft structures. Particularly aerospace structures are subjected to low-velocity and ballistic impact of the kind expected during aircraft maintenance, take-off and landing operations. In most instances, the damage is externally invisible, however, it causes significant reduction of structural stiffness and performance.

Furthermore, the studies on damage resistance / damage tolerance are limited to traditional composites manufactured by well-established expensive techniques, such as autoclave molding for aerospace structures. Such information pertaining to low cost manufacturing techniques, such as resin transfer molding (RTM) and vacuum assisted resin transfer / infusion molding (VARTM / VARIM) processing [4-7], that are affordable and have the potential for primary, secondary and tertiary aircraft structures is much lacking. This research addresses affordable processing / manufacturing of sandwich composite structures and their damage resistance and damage tolerance to low velocity and high strain rate impact.

Section through
blade root and
shank *Dowty*
Rotol Ltd



(a)



(b)

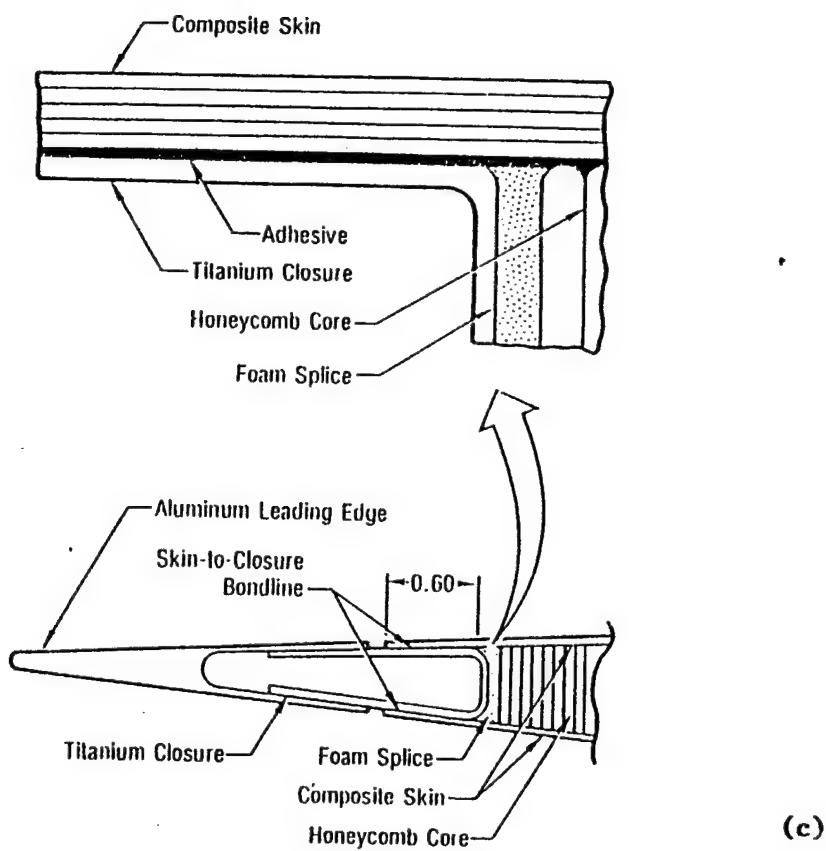


Figure 1.1. a, b and c. Some Application of Composites and Sandwich Constructions in Aircraft Parts

This completed three-year effort addresses pertinent issues pertaining to damage tolerance, functionality and affordability of sandwich constructions with innovative core designs, that have applicability in aircraft and space vehicle technologies and other needs of Air Force structures. The results from the effort will benefit the science base in sandwich constructions, and will benefit the Air Force efforts, for example in the FATE, TAFT and other CAI programs/initiatives. Figure 1.3 represents the overall program plan and implementation. The following sections provide background information and the approach adopted in conducting the present research.

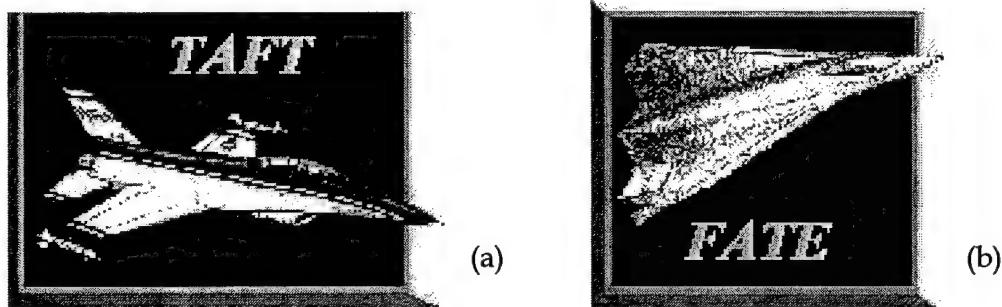


Figure 1.2 a) Today's Aircraft Flying Tomorrow
b) Future Aircraft Technology Enhancements

1.2 Program Background and Introduction

1.2.1 Sandwich Composite Design Concepts

Typically, a sandwich construction stiffens a structure without substantially increasing its weight. Sandwich composite constructions find extensive use as flexural load bearing light weight sub-elements in air and space vehicles due to the versatility and flexibility they offer for design [8-10]. For example, they are utilized in composite wing, horizontal stabilizer, composite rudder, scarf nozzles, landing gear door, speed brake, flap segments, aircraft interior panels and seats [3]. Figures 1.1a, b and c illustrate applications of composite and sandwich structures in aircraft and helicopter sub-components. A typical sandwich structure consists of core material (which provides excellent transverse stiffness) with face sheets/skins (which provide excellent flexural stiffness) bonded to the core on either side by adhesive film. Traditionally polyvinyl chloride (PVC), polymethylmethacrylate (PMMA) or polystyrene (PS) foam and/or nomex or aluminum honeycomb have been used as core materials with studies limited to the use of unidirectional graphite or glass laminates as facesheets/skins. The utilization of fabric facesheets has the potential to provide enhanced damage tolerance. The sandwich constructions with innovative cores (Table 1.1) considered were expected to enhance damage resistance / tolerance as well as functionality.

RTM/VARTM & TRADITIONAL Manufacturing of Sandwich Constructions

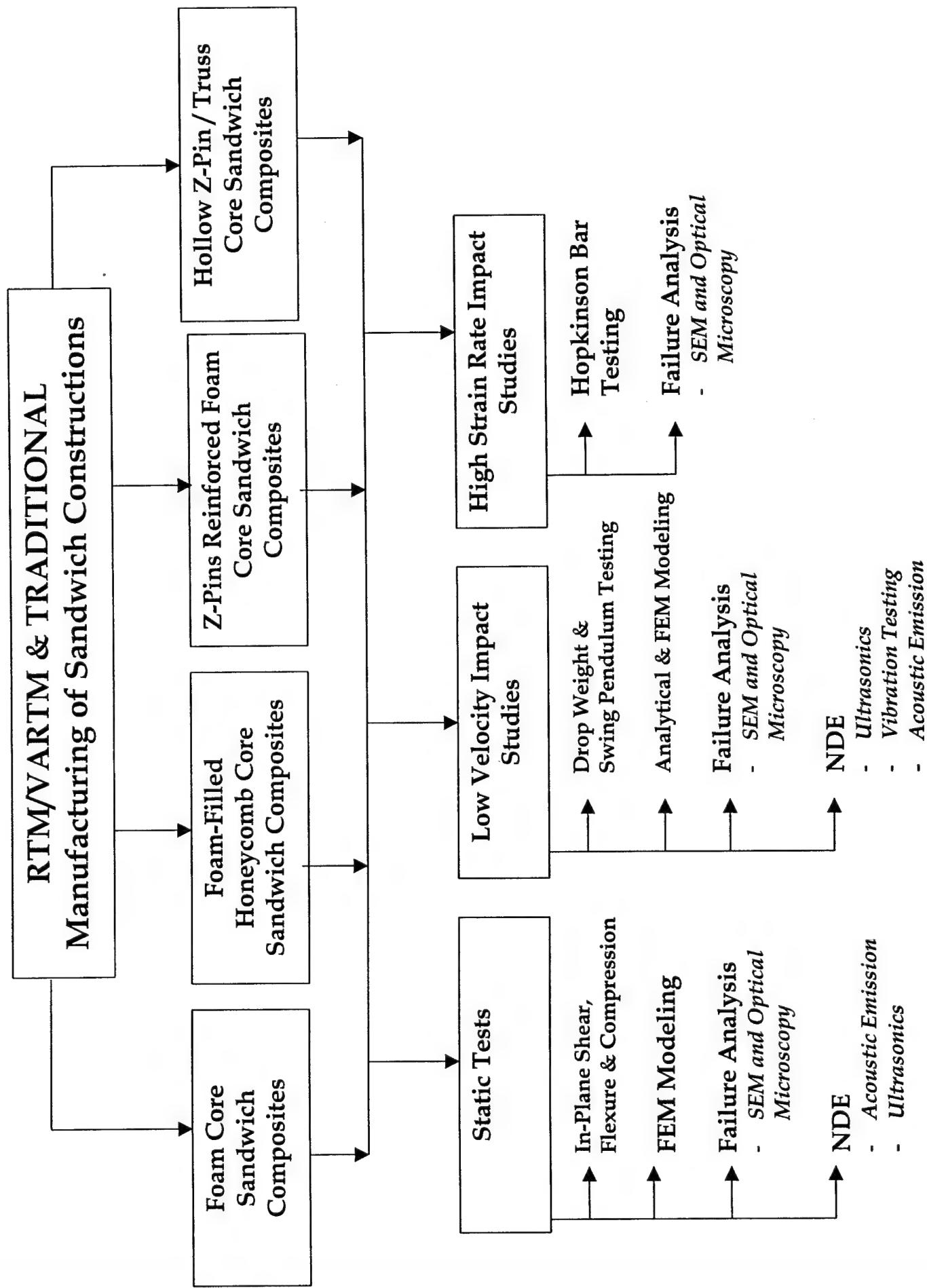


Fig 1.3 Overall Program Plan and Implementation

This Page Left Blank

Table 1.1 Design Concepts for Innovative Core Constructors

Type 1: Glass/Epoxy and Graphite/Epoxy Facesheets with Foam Core

Type 2: Glass/Epoxy and Graphite /Epoxy Facesheets with Foam-Filled Honeycomb Core

Type 3: Glass/Epoxy and Graphite/Epoxy Facesheets with Pin-Reinforced Foam Core

Type 4: Glass/Epoxy and Graphite/Epoxy Facesheets with Hollow Z-Pin Truss Core

The design concepts of the sandwich constructions were expected to provide combined damage tolerance / resistance and functional benefits.

- Type 1 : The foam core was chosen because literature on sandwich structures is concentrated both on honeycomb as well as syntactic foam constructions [5-10].

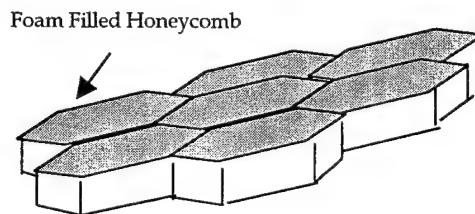


Figure 1.4 Foam-Filled Honeycomb Core

- Type 2 : The foam-filled honeycomb (Fig. 1.4) holds promise for improved energy dissipation deriving advantages from both the constituents, i.e, foam and honeycomb. While honeycomb cells - completely filled with foam, provide the ideal performance characteristics of using both a honeycomb and foam core, it possesses the trade-off of weight addition.
- Types 3 and 4: The hollow (Fig. 1.5) and pin - reinforced sandwich construction possesses the potential to offer space advantages as well as damage resistance /tolerance to the structure. Here metallic (titanium, high strength steel) or carbon pins will be used in a three-dimensional truss entity. The pins are open ended, thereby fuel cells, electronic assemblies and electrical wires can be accommodated to gain space advantages.

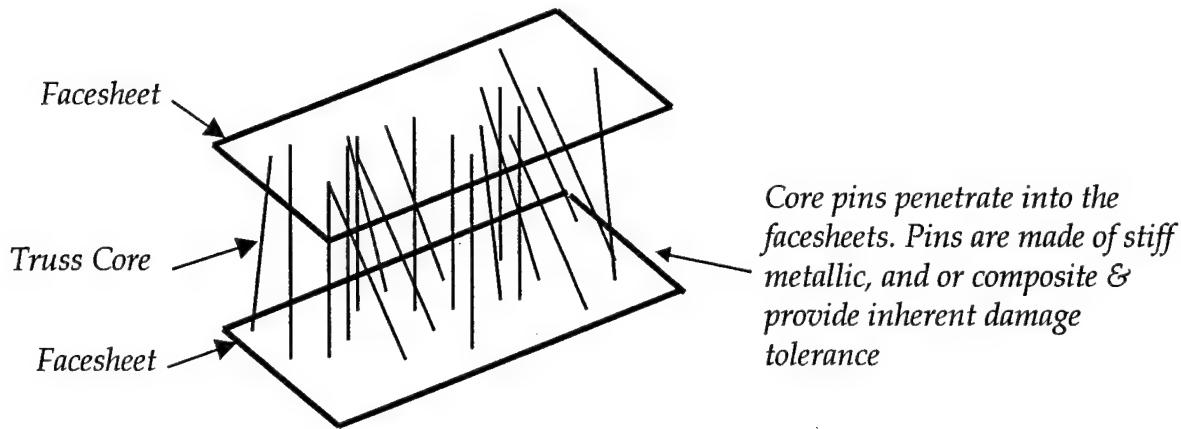


Figure 1.5 Concept of Hollow Truss Core

1.2.2 RTM and VARTM : Affordable Manufacturing Alternatives for Air and Space Vehicles

Liquid molded techniques are finding increasing use in high-performance applications including aircraft components and parts as illustrated in Fig 1.6. Cores, stiffeners, and other materials can be encapsulated in the part with much greater ease than in open molding. Through liquid molding, it is possible to produce affordable load bearing composite parts with complex curvatures and foam, metal or honeycomb cores within the part, thus eliminating the laborious machining operations. Figure 1.7 represents cost comparisons of various manufacturing techniques, and illustrates the

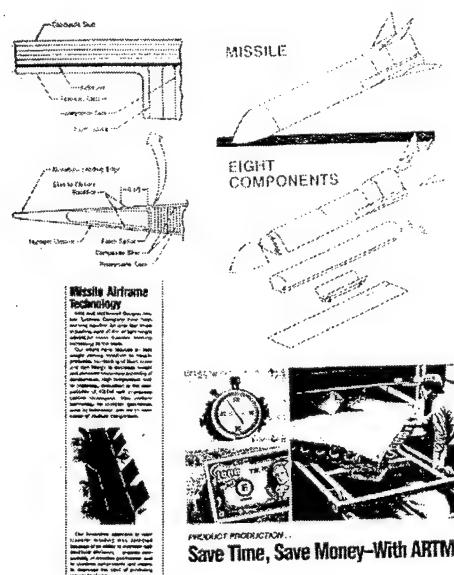


Figure 1.6 Examples of RTM Technology in Aerospace Applications

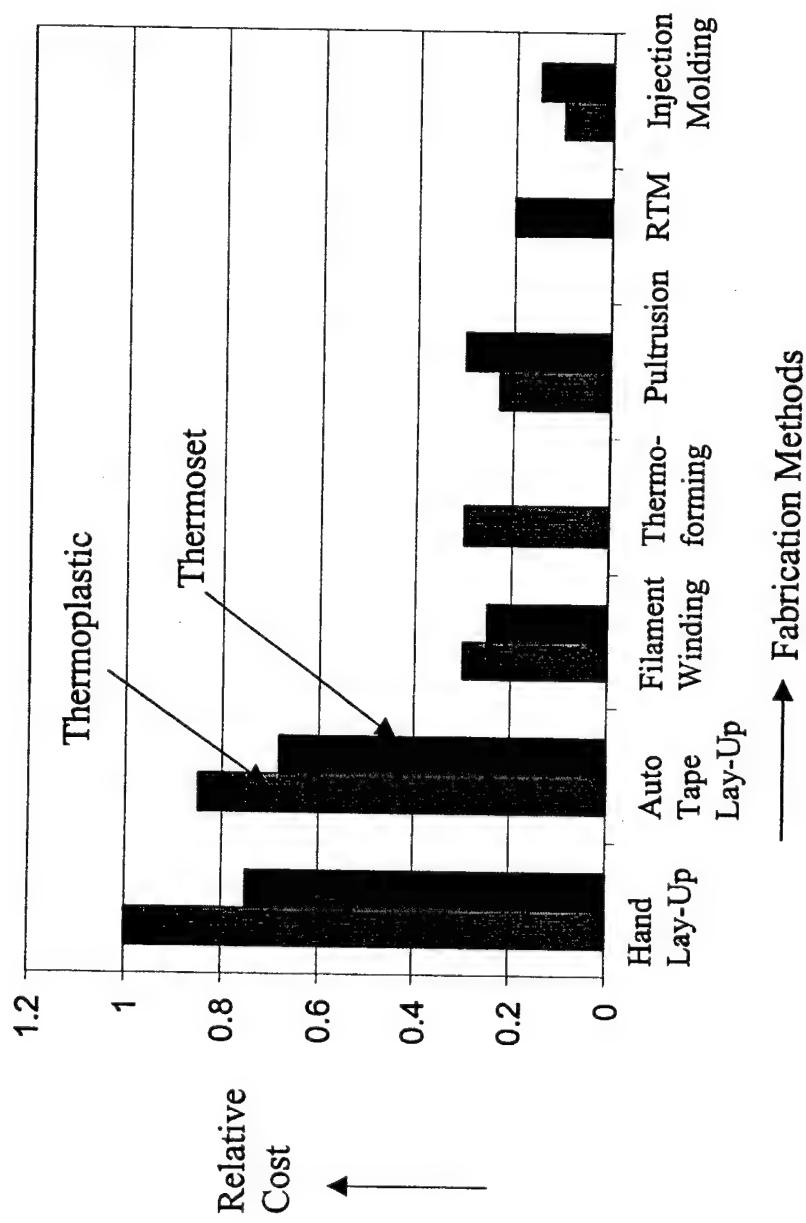


Figure 1.7. Cost Comparisons of Various Processing Alternatives for Composites

cost-effectiveness of the RTM approach. This net-shape manufacturing technique also reduces assembling needs. In traditional autoclave processing, composite parts processed under seemingly similar conditions, can often exhibit significant difference in part quality. Defects such as voids and porosity caused during manufacturing plague composite fabricators resulting in production slow-downs, excessive rework and repair costs. Several variables contributing to formation of defects include: trapped volatiles, variations in chemical composition of resins, resin mixing, pre-pregging procedure and lay-up operations.

RTM and VARTM are the two primary liquid molding processes identified for manufacturing of polymeric monocoque, integrated and sandwich composites. These methods are chosen (but not limited to) particularly because of their potential for manufacturing large-size affordable composites. An understanding of the scientific issues that affect the basics of material processing science can reduce the barrier to the wider usage of RTM and VARTM in the air and space industries.

1.2.2.1 Resin Transfer Molding (RTM)

In the RTM process, dry reinforcement is pre-shaped and oriented into a skeleton of the actual part (i.e., preform) which is then placed into a matched die mold. The mold is closed over the preform and a low viscosity, reactive system is injected into the tool [8] as shown in Fig. 1.8a and b. The air inside the closed mold cavity is displaced by the advancing resin front escapes through vents located at the high points of the tool. During this infiltration process, the resin "wets out" the reinforcement and polymerizes. Once the composite develops sufficient strength, it may be removed from the tool and post-cured (if needed). RTM is an alternative because : a) it is a process in which a relatively high (50-62%) fiber volume content can be achieved, b) the fiber type and orientation can be selected with possibilities of hybridization, c) the process is 'clean' because it uses closed mold techniques, d) there are no storage problems of "B" staged pre-pregs, e) tooling costs are low since injection pressures can be low, f) complex section designs can be accommodated, g) reduced number of molded parts and bonding operations and, h) sandwich construction can be used to optimize the efficiency of composite components.

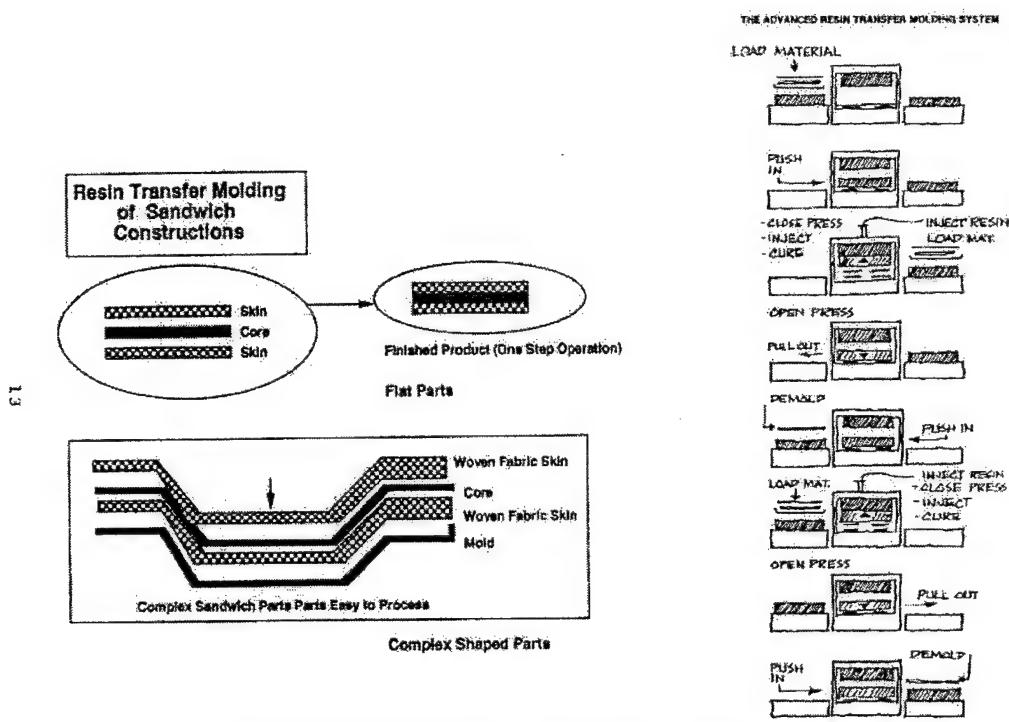


Figure 1.8 Schematic of RTM Processing

1.2.2.2 Vacuum Assisted Resin Infusion/Transfer Molding (VARIM/VARTM)

While RTM is a closed mold process, VARTM is of interest in low cost innovative developments as it uses one-sided tooling and vacuum-bag technology [7-9]. Here resin is infused into dry fabric preform assembled in conventional tooling that is closed with an inexpensive vacuum bag film (Fig 1.9). This process is proving to be a very attractive alternative to spray-up or impregnation methods, and it is far less expensive than conventional manufacturing methods. Other advantages of RTM and VARTM are low process volatile emissions, high fiber to resin ratios and good process repeatability.

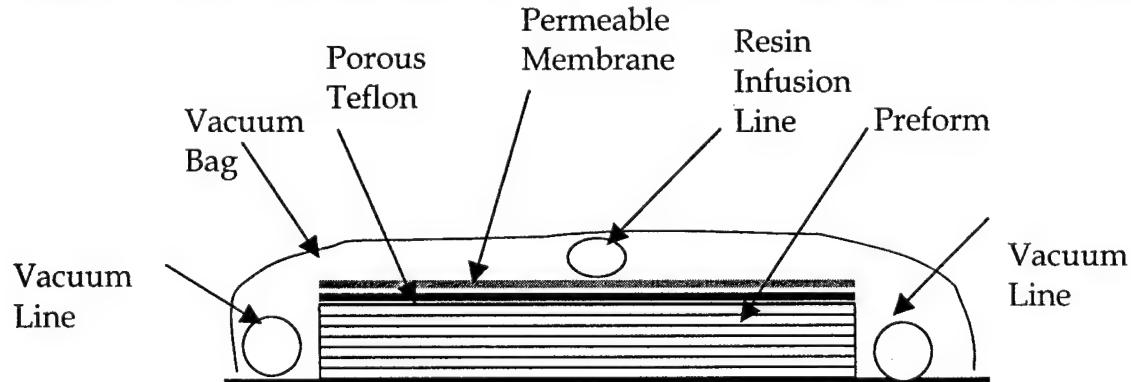


Figure 1.9 Vacuum Assisted Resin Infusion / Transfer Molding (VARIM/VARTM)

1.2.3 Performance Evaluation

The testing program for the sandwich constructions in this study was focussed towards understanding of :

- Performance Evaluation for Static Loading* : In-Plane Shear, Flexure and Compression Response of a variety of Cores and their Sandwich Composites
- Performance Evaluation for Dynamic Loading under Low Velocity and High Strain Rate Impact Scenarios.*
- The low velocity testing was based on instrumented drop weight impact and a few swing pendulum impact studies. The high strain rate impact studies focussed were performed on the compression Split Hopkinson Pressure Bar (SHPB).
- Nondestructive Evaluation* : The NDE studies were based upon vibration, ultrasonic C-scan and acoustic emission for a variety of loading and impact conditions

1.2.4 Modeling Studies

Analytical and finite element modeling (FEM) studies were pursued to understand and predict the low velocity impact response of sandwich constructions. Analytical modeling efforts were directed primarily to understand the hollow truss core sandwich concept. FEM was undertaken for all core configurations considered and various static and low velocity impact conditions.

1.3 Stated Technical Objectives in the Original Proposal

1. To develop and fabricate RTM composite flat sandwich skin / core constructions with an intention of improving impact resistance and thereby damage tolerance
2. To conduct experimental and modeling studies on the low velocity impact performance of sandwich constructions produced in objective one.
3. To perform nondestructive test studies of manufacturing and impact induced damage

1.4 Program Accomplishments (Pertinent to Stated Objectives in the Proposal)

1.4.1 Research

- The research is consistent with Aerospace Sciences Research and Development Program for historical black colleges and universities (HBCUs) to make new advances in aeronautical sciences and technologies, to provide more options and

solutions to Air Force (AF) needs, and to enhance the national research capacity in aeronautical sciences.

- Among several topics of interest to the then Flight Dynamics Directorate (now Air Vehicles Directorate), the completed project is specific to the future vision of AF in light weight/affordable composite sandwich structures with damage resistant and tolerant designs.
- Sandwich constructions are sub-elements of most advanced aircraft and helicopter components. Understanding of low and high-strain rate scenarios and failure mechanisms through experimentation and modeling of sandwich constructions is of critical importance to AF.
- Diversification of Already Existing Significant Activity in Composites Research Into a Continually Strong and Visible Program in Advanced Materials at Tuskegee University – an HBCU institution through Air Force Funding.
- The current work has been extended well beyond what was originally proposed to include studies on high strain rate response of sandwich composites in addition to in addition to Low Velocity Impact as well

1.4.2 Educational

- The project actively involved **African-American** and other graduate and undergraduate students in the sandwich composites research.
- Five graduate students were involved with the research, three of which produced master's thesis, and two as sub-topics within their master's thesis.
- Over fifteen undergraduate students were employed through senior projects, work study or undergraduate researcher programs under the project. They benefited from various aspects of the program including ; manufacturing science, modeling, low velocity impact testing, high strain rate impact testing, specimen preparation, microscopy, data analysis and interpretation, in report writing and presentations.
- One research faculty was appointed half-time through the sponsored effort.
- The activity from the research is now leveraged in the Ph.D. program in Materials Science and Engineering, that started in Fall 1998 at Tuskegee University, and is the only doctoral program in the institution. One Ph.D. student is now pursuing / continuing research in innovative sandwich constructions

1.4.2.1 Under Graduate and Graduate Students Who Worked on the Research Project

Undergraduate Students
1. Ransom Davis (Work Study)
2. Jamal Cherry (Work Study)
3. Bahiy Watson (Senior Project)
4. Olgudiran Solumen (Senior Project)
5. Martin J. Cloyd (Senior Project)
6. Diahann Earl (Senior Project)
7. Aurelia Gardener (Senior Project)
8. Marcian Lloyd (Work Study)
9. Juana Mullins (Senior Project)
10. Tavis Maddox (Senior Project)
11. Michael Lawton (Work Study)
12. Corey Woods (Senior Project)
13. Robert Lee Jr. (Senior Project)
14. Robert Clayton
15. Kemp Kymeski

Graduate Students
1. Mohan Kamath (Master's Thesis)
2. Pradeep Kumar Mohan (Master's Thesis)
3. Girish Basappa (Master's Thesis, currently pursuing)
4. Renee Rodgers (Ph.D. student, Sub-topic in Ph.D. work)
5. David Myers (Master's Thesis, currently pursuing)

1.4.3 Pertinent Publications from Research Effort

1. Manufacturing And Low Velocity Impact Response Of Sandwich Composites With Hollow And Foam Filled Z-Pin Reinforced Core, U.K. Vaidya, M.V. Kamath, M.V. Hosur, H. Mahfuz, and S. Jeelani, **Journal of Composites Technology and Research** (In Press - To appear in April'99 issue).
2. Low Velocity Impact Damage Characteristics Of Z- Fiber Reinforced Sandwich Panels - An Experimental Study, A.N. Palazatto, L.N.B.Gummadi, U.K. Vaidya and E.J. Herup, **Composite Structures**, Vol. 43, Issue : 4, Feb-1999, pp 275-288.

3. Low Velocity Impact Characterization of Foam-Filled Honeycomb Sandwich Composites, U.K.Vaidya et al., **Journal of Reinforced Plastics and Composites**, Vol. 17, No. 9, pp. 819-849, 1998.
4. High Strain Rate Impact Response of Sandwich Composites., U.K. Vaidya and P. Mohan., Submitted to **Journal of Sandwich Structures**, April 1999.
5. Low Velocity Impact Damage Characterization of Z-Fiber Reinforced Sandwich Panels - An Experimental Study, A.Palazotto, L.Gummadi, U.K.Vaidya and E.Herup, **38th AIAA/ASME/ASCE/AHS/ASC Structures, Structural Dynamics and Materials Conference**, April 07-10, 1997.
6. Low Velocity Impact Response of Hybrid Sandwich Composites, U. K. Vaidya et.al **30th International SAMPE Technical Conference**, San Antonio, TX, Oct 20-24, 1998. pp. 96-104, Volume 30, Edited by Brian Wilson, Bob Hunder, R. May and L. Clements.
7. Low Velocity and High Strain Rate Impact of Pin Reinforced Foam Core Sandwich Composites, U. K. Vaidya et al., **Proceedings of the Japan-U.S. Conference on Composite Materials**, Edited by Golan Newaz and Ronald Gibson, Inner Harbor, Baltimore, Sept 24-25, 1998, pp. 721-729.
8. Manufacturing and Low Velocity Impact Response of Innovative Resin Infused Sandwich Composites, U.K.Vaidya, M.V.Kamath, H.Mahfuz and S.Jeelani, **29th International SAMPE Technical Series**, Vol. 29, pp. 713-724, Green, Beckwith and Strong Editors.
10. Low Velocity Impact Response of Unconventional Sandwich Composites, U.K.Vaidya, M.V. Kamath, H.Mahfuz and S.Jeelani, 12th Annual Technical Conference, **Proceedings of American Society for Composites**, pp. 562-571, October 6-8, 1997, Dearborn, Michigan, Edited by Golan Newaz and Ronald Gibson.
11. Low Velocity Impact Response and Nondestructive Evaluation of Sandwich Composite Structures, U.K.Vaidya, A. Palazatto and L.N.B.Gummadi, **ASME International Congress of Mechanical Engineering and Exposition**, pp. 197-202, NCA-Vol. 24, Proceedings of the ASME Noise Control and Acoustics Division, Vibroacoustic Methods in Processing and Characterization of Advanced Materials and Structures, Edited by : V. Dayal, U.K. Vaidya and R. Mantena.
12. Impact Response Of Innovative Sandwich Composites In Low,Intermediate Velocity And High Strain Rate Scenarios, U. K. Vaidya, M.V.Hosur, A. Haque, H. Mahfuz and S. Jeelani, **ICCM-12**, July 06-10, 1999, Paris, France.

13. Effect of Core Density and Facesheet Thickness on the High Strain Rate Impact Response of Foam Core Sandwich Composites., U.K. Vaidya and P.K. Mohan, In Preparation for Submission to the **Journal of Sandwich Structures**.

Student Presentations

1. Mohan Kamath., Manufacturing and Low Velocity Impact of Foam-Filled Honeycomb Core Sandwich Composites, ASME Chattahoochee Section Student Competition, 1997. Won First Place.
2. Mohan Kamath, Compression-After-Impact Response of Sandwich Composites, ASME Chattahoochee Section Student Competition, 1998. Won First Place.
3. Mohan Kamath, Impact Response of Sandwich Composites, Society for Experimental Mechanics, Southeastern Regional Student Meeting, Gainsville, FL, March 1998.
4. Mohan Kamath and U.K. Vaidya, Low Velocity Impact Response of Z-Fiber Reinforced Sandwich Composites, 29th SAMPE International Student Symposium, Anaheim, California, May 1998, Won Second Place.
5. Mohan Kamath, Low Velocity Impact Response of Innovative Sandwich Composites, Sigma Xi Meeting, Tuskegee University, 1998. Won First Place
6. Pradeep Kumar, Static Testing of Innovative Sandwich Composites, Sigma Xi Meeting, Tuskegee University, 1998. Won Third Place.
7. Pradeep Kumar, High Strain Rate Impact Response of Foam Core Sandwich Composites, ASME Chattahoochee Section Student Competition, 1998, Won Third Place.
8. Pradeep Kumar, High Strain Rate Impact Response of Pin-Reinforced Sandwich Composites, Sigma Xi Student Competition, Tuskegee University, 1999. Won Second Place.
9. Pradeep Kumar and U.K.Vaidya, High Strain Rate Impact Response of Sandwich Composites, International SAMPE Technical Conference, Student Symposium, Long Beach, CA May 23-27, 1999.

1.5 Organization of the Report

Chapter 1 provides the broad overview / background introduction to air force interests in the program of the proposed work. This chapter also provides a summary of accomplishments, information on students and personnel that benefited from the funded effort, and the publications resulting from the work. Chapter 2 presents a more detailed introduction to the sandwich structures concept, and presents a literature review on sandwich composites. Chapter 3 reviews some of the existing cores and discusses the need for the development of innovative cores. Chapter 4 discusses the general techniques used for the manufacturing of the sandwich composites, and also some innovative techniques used for manufacturing samples for the current work. Chapter 5 discusses the fundamentals of impact testing as those applied for the testing. Chapter 6 presents the results and discussion for the low velocity response for honeycomb-filled-foam core sandwich composites, while Chapter 7 discusses the same for the foam core, pin reinforced foam core, and hollow / Z-pin truss core sandwich composites. Chapter 7 also discusses the influence of different parameters such as the facesheet thickness, pin density, pin type, and the manufacturing technique. It also presents a brief study of the conventional graphite honeycomb core composite as compared to the cores mentioned earlier. Chapter 8 discusses the compression-after-impact and the acoustic emission studies on the above mentioned samples. Chapter 9 summarizes a series of static tests performed to understand the role of various cores and their composites. These include in-plane shear, flexure, compression (in-plane and through-the-thickness). Chapter 10 is focussed upon the finite element modeling work performed on the foam, honeycomb, pin core composites and analytical aspects. This covers work done at Tuskegee University as well as through a subcontract issued to Advanced Structural Concepts, Ohio in the second year of the project. Chapter 11 deals with the high strain rate impact experiments that were conducted, in addition to the low velocity impact work that was proposed in the original proposal. Chapter 12 briefly presents results on the intermediate velocity experiments, the experimental design and the tests performed. Chapter 13 is a general summary of the work. References are provided at the end of each chapter / section in the interest of better readability.

1.6 References

1. Air Vehicles Directorate Technology Area Plan – FY 98, Internet Release Information, www.wrs.afrl.mil.
2. *Reinforced Plastics*, Dec. 1994, Vol.18, No.11, Elsevier Publishers.
3. Composite Aircraft Structures, R. Glasco, Elsevier Publishers, June 1995.

4. Galli Ed., Resin Transfer Molding : A Cost-Effective Alternative, *Plastics Design Forum*, March/ April 1981, pp.47-51.
5. Rogers . S, SRIM and RTM Sprint Toward High-Volume Uses, *Plastics Technology*, March 1989, pp.50-58.
6. Composites Update - Part I : New Materials and Reinforcements, *Plastics Technology*, April 1991, pp.39-44.
7. *Design Evolution - 4*, Company Literature, Lebanon, Ohio.
8. Honeycomb Sandwich Constructions : *Hexcel Corporation Technical Literature*.
9. Zenkert, D. 1997. *The Handbook of Sandwich Construction*. London, UK: Engineering Materials Advisory Services Ltd., Chameleon Press Ltd.
10. Karlsson, K.F. and B.T. Astrom. 1997. "Manufacturing and Applications of Structural Sandwich Components," *Composites, Part A*, Elsevier Publications, pp. 97-111.

2.0 Sandwich Constructions

2.1 Concept of a Sandwich Structure

One of the most vibrant developments in material science and engineering has been the quest for lighter and stronger materials. Fiber reinforced composites have hence gained extreme importance in critical applications, particularly in aircraft structures. Sandwich composites are further developments of such materials.

A sandwich composite consists of three main parts as illustrated in Fig. 2.1a and 2.1b. Two thin, stiff and strong faces are separated by a thick, light, and weaker core. The faces are adhesively bonded to the core to obtain a load transfer between the components.

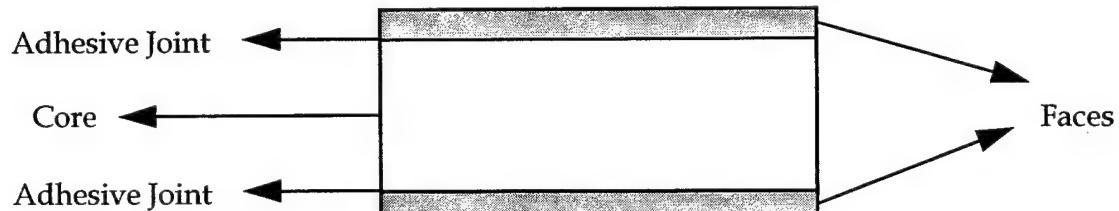


Figure 2.1 Schematic of a Sandwich Construction

The American Society for Testing and Materials (ASTM) defines a sandwich structure as follows:

A structural sandwich is a special form of a laminated composite comprising a combination of different materials that are bonded to each other so as to utilize the properties of each separate component to the structural advantage of the whole assembly.

Bending

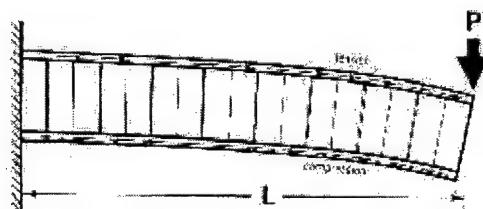
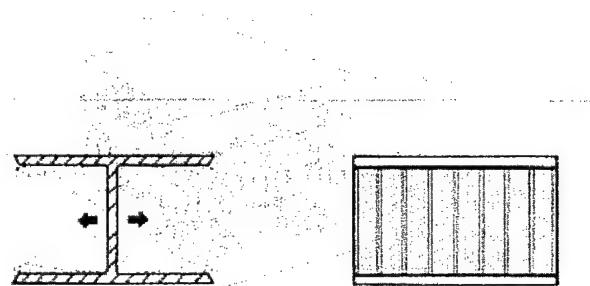
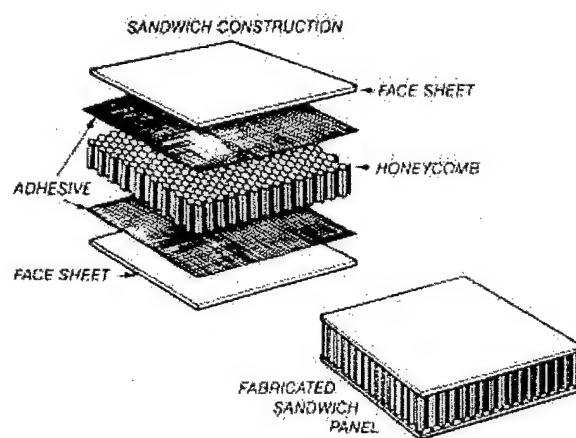


Figure 2.2a. Cantilever Sandwich Beam

Bonded honeycomb sandwich construction has been a basic structure concept in the aerospace industry for the last thirty years. Virtually every aircraft flying today depends upon the integrity and reliability offered by this structural approach. The capability of the concept has been proven and is now widely accepted.

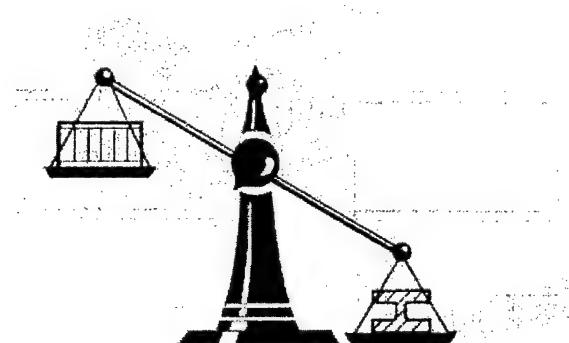
As a result of this history of success, a growing interest has developed in the use of honeycomb sandwich for a broad range of commercial applications

The facings of a sandwich panel used as a beam act similarly to the flanges of an I-beam by taking the bending loads — one facing in compression and the other in tension. Expanding this comparison further, the honeycomb core corresponds to the web of the I-beam. This core resists the shear loads, increases the stiffness of the structure by spreading the facings apart, but unlike the I-beam's web, gives continuous support to the flanges or facings. The core-to-skin adhesive rigidity joins the sandwich components and allows them to act as one unit with a high torsional rigidity.



	Solid Metal Laminate	Sandwich Construction	Thick Skin Sandwich
Relative Stiffness	100	700 7 times more rigid	3700 37 times more rigid!
Relative Strength	100	350 3.5 times as strong	925 9.25 times as strong!
Relative Weight	100	105 5% increase in weight	109 9% increase in weight!

A striking example of how honeycomb stiffens a structure without materially increasing its weight.



Result:

Solid metal or laminates are no match for honeycomb.

Figure 2.1b. How a Sandwich Beam Works

Consider, for example, a cantilever beam one inch wide with a length, L, and a load, P, at its end as shown in Figure 2.2a. This load creates a moment, M, which in this case is equal to $P \times L$ at the fixed end. It also sets up tension and compression stresses within the structure. For the sandwich beam the tensile and compressive force in the facing times the distance between the facing centroids equals the moment. Or the bending stress in the facings is given by

$$\text{Moment } M / \text{Thickness of a Facing} \times \text{Distance Between Facing Centroids}$$

Shear:

The load also imparts a shearing action within the structure. This shear force is taken up by the honeycomb which prevents the top and bottom facings from slipping. The shear force, V, may vary along the beam if a uniform load is applied. The maximum shear force for various load and support conditions. The shear stress in the core is related to V by the distance between the facing centroids.

$$\text{The shear stress in the core} = \text{Shear Load } V / \text{Distance Between Facing Centroids}$$

Deflection

The total deflection of a honeycomb sandwich structure is calculated by adding the deflection caused by the bending reaction and the shear reaction within the structure. Figure 2.2b&c demonstrate the individual deflection and show that the deflection in each case is the result of the basic elastic properties of the stressed materials involved. Thus the bending deflection is related to the modulus of elasticity of the facings, and the shear deflection is related to the core shear modulus.

$$\text{Total deflection} = \text{bending deflection} + \text{shear deflection}$$

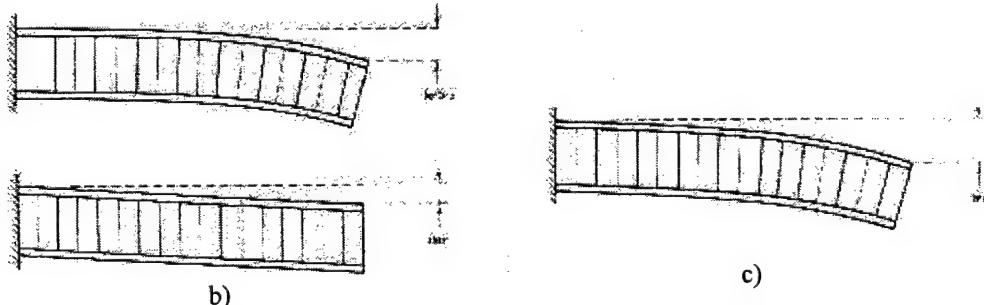


Figure 2.2b & c Illustration of the Working of a Sandwich Beam [1]

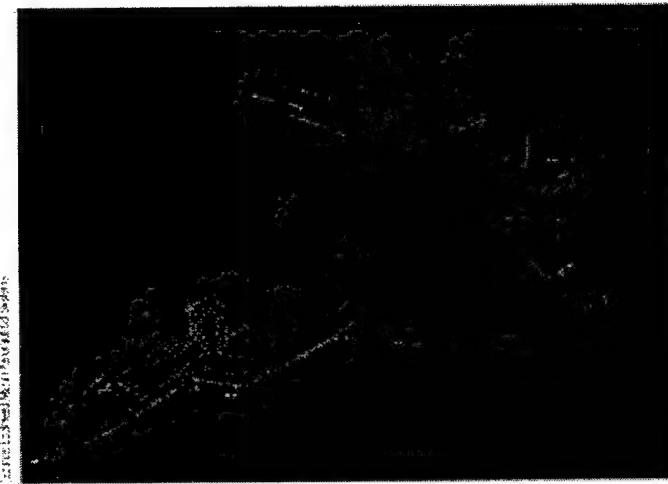


Figure 2.3. Use of RTM composite parts in F-22 Aircraft



Figure 2.4. Use of Laminated and Sandwich Composites in Aircraft

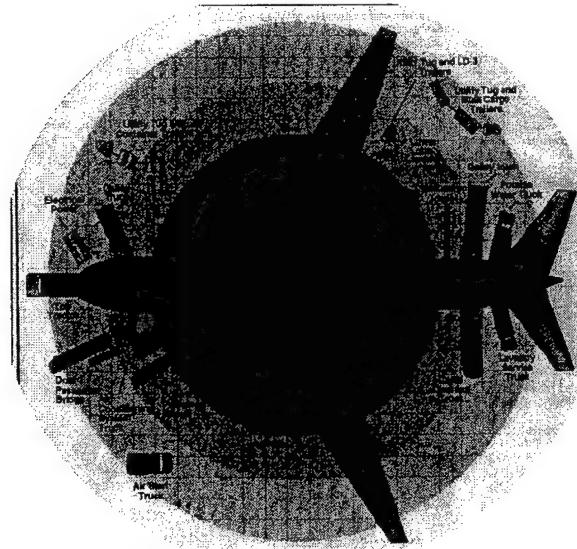


Figure 2.5. Use of Composites in Aircraft

The faces of a sandwich usually consist of a thin but stiff material while the core material is a thick, light but relatively soft material. Figure 2.2 illustrates the working of a sandwich beam. The choice of constituents mostly depends on the specific application and the design criteria set by it. A variety of applications related to sandwich constructions and the core types in aircraft structures, is provided in Figures 2.3-2.5.

2.2 Historical Background

Historically, the advantages of the concept of using two co-operating faces separated by a distance is thought to have been first discussed in [2] Zenkert's handbook which includes a study Frenchman, Duleau, in 1820, and later by Fairburn. Although it was not until 110 years later that the concept was first applied commercially. In World War One, sandwich panels of asbestos faces with a fireboard core were used and prior to World War II, some use was made of sandwich panels in small planes. However it was the invention and widespread acceptance of structural adhesives in England and the United States in the 1930's that allowed the application of bonded sandwich composites. The Mosquito aircraft, produced in England during World War II, saw the mass production of sandwich laminates for the first time, utilizing veneer faces with a balsa core. This was primarily due to a shortage of other materials as opposed to an appreciation of the structural efficiency of the concept. It was towards the end of World War II, in the late 1940's, that some of the first theoretical works on sandwich constructions were published. Since these early days the technology of sandwich laminates has progressed significantly and today far more comprehensive use of the advantages of sandwich laminates is being made.

Development of core materials has continued from the 1940's through today in an effort to reduce the weight of the sandwich laminate. Balsa the first core to be used, is still in use where weight is not critical, such as in cruising yachts and launches. Although heavy, it still generally offers advantages over single facesheet designs. The late 1940's and 1950's saw the advent of honeycomb core materials, developed primarily for the aerospace industry. Honeycomb cores currently offer the greatest shear strength and transverse stiffness-to-weight ratios, but require care in ensuring adequate bonding to the faces. The core materials have been produced in various forms and have been developed for a broad range of applications, generally utilizing a hexagonal cell shape for optimum efficiency. The continued high cost of honeycomb cores has restricted their application predominantly to the aerospace industry.

The late 1950's and early 1960's brought about the advent of the polyvinyl chloride (PVC) and polyurethane (PUR) core materials commonly used today in low and medium cost applications. Although PVC foams were developed in Germany in the early 1940's, they were not utilized commercially until 15 years later due to the softness

of these early cores. In the last twenty years few new cores have been developed with research oriented around facing materials and core bonding techniques. The next generation of core materials under development are cellular thermoplastic cores where properties can be tailored by orienting the cell structure.

In the last twenty years, the emphasis in theoretical research has shifted to optimization of laminates, with finite element analysis used as a design tool for the panel analysis problems. As a result little further work has been conducted into the theoretical analysis of sandwich panels, principally due to the difficulty of obtaining more exact solutions in deriving and solving the differential equations for deflection of sandwich panels. The errors in the current approximations used are often negligible for practical composite laminates but require consideration. Finite element techniques utilizing especially designed sandwich elements also allow accurate analysis of sandwich design problems. These are generally more accurate than many of the existing analytical solutions which require several approximations and the use of finite difference methods to solve the differential equation. Research in sandwich constructions over the last two decades has revolved primarily around the areas of impact resistance, fatigue and fracture analysis since these conditions are of major concern to the aerospace industry. Research is now allowing the introduction of composite materials in aircraft primary structure. The theoretical analysis of sandwich beams and plates has received little attention within the aerospace industry which has primarily adopted finite element analysis for design purposes.

2.3 Advantages of Sandwich Constructions

A sandwich element provides the opportunity through efficient design, to utilize each material component to its ultimate limit [2]. Some obvious advantages of this construction are:

- The sandwich assembly offers a very high stiffness-to-weight ratio and also a high bending strength-to-weight ratio.
- A sandwich enhances the flexural rigidity of a structure without adding substantial weight, hence making it more advantageous as compared to composite materials, which generally offer at least the same or even higher strengths as metals such as aluminum or steel, but have lower moduli and exhibit poor stiffness performance.
- The continuous support of the face sheet, unlike a stiffened structure, implies that surfaces remain flat even under quite high compressive stresses without buckling.
- Sandwich constructions in several applications have exhibited superior fatigue strength, though this needs to be investigated thoroughly.
- Sandwich constructions also exhibit superior acoustical insulation. The absorption of mechanical energy can in some deformation modes be multiplied

compared with monocoque structures due to an imposed shorter mode of buckling waves.

- The sandwich concept has an integrated function as the use of cellular core materials means that no additional thermal insulation needs to be added to the structure, thus ensuring a low structural weight. This is because of the fact that most cellular cores have a very low thermal conductivity.
- Sandwich elements can be manufactured in large sheets, giving large smooth areas without need for connections like rivets and bolts. This means less parts are needed, and hence the assembly is simplified hence reducing costs.
- When using fiber composite faces, even large structures can be manufactured in more or less one piece, thus reducing assembly costs and ensuring smooth and continuous load paths without disturbing stress concentrations.

2.4 Disadvantages of Sandwich Constructions

There are a number of disadvantages associated with the sandwich construction.

- A major obstacle is the lack of general knowledge among designers and engineers in the industry about the concept and the materials used.
- The used manufacturing methods are in infancy, requiring much labor and they are automated to a very small degree.
- Quality control is hence difficult.
- Many materials used are relatively new and there is limited access to their property data. This makes the designer's task tough and often the designs that evolve are heavier, hence defeating the primary aim of saving weight.
- A major area of concern is fatigue life reduction due to damage, either due to manufacture induced flaws or due to in-service. But there is very limited knowledge of the same and there is need for extensive research in this area.

2.5 Applications

Sandwich composites find extensive use in a wide variety of applications. They have been found to be very versatile in their use [2] and the following applications will exhibit the same.

Aerospace Industry: Sandwich composites are increasingly being used in the aerospace industry because of their superior bending-stiffness-to-weight ratio. Floorboards, composite wing, horizontal stabilizer, composite rudder, scarf nozzles, landing gear door, speed brake, flap segments, aircraft interior panels and seats and wingspans are typically made of sandwich composites.

Marine Industry: Sandwich composites are ideally suited for the marine industry's most advanced designs. The kinds of foam cores available meet the critical requirements of strength, buoyancy and low water absorption. Applications include the construction of bulkheads, hulls, decks, transoms and furniture.

Transportation Industry: High strength-to-weight ratios of sandwich composites offers great advantages to the transportation industry. The insulating and sound damping properties of certain foam cores make them the choice materials for the construction of cabs, floors, walls, doors, panels and roofs for vans, trucks, trailers and trains. Construction costs are also reduced.

Architectural Industry: The foam offers excellent thermal insulation and is fire resistant and these properties combined with its strength makes it an ideal choice for the architectural industry. Typical applications include structural columns, portable buildings, office partitions, countertops, and building facades.

Corrosion Industry: With the corrosion resistance, low water absorption, and high strength advantages of certain sandwich composites, they are turning out to be the leading choice for platforms, double containment vessels, tank bottoms and lids, duct work and wherever corrosion is a problem.

2.6 Motivation

The need for strong, stiff lightweight structures in aerospace vehicle components has motivated the design of sandwich plates and shells using composite materials. A principal drawback of laminated composite panels in general and composite sandwiches, in particular, is their susceptibility to low velocity impact as damage is generally spread out, and on a more global level [3,4]. Typical examples of low velocity impacts are those experienced by aircraft structures such as bird hits and runway/taxiway debris hits during landing and take-off operations, tool drops during maintenance operations and the like. In particular, significant loss of stiffness and compressive strength has been found to occur without any visible signs of damage. This is a major concern for both manufacturers and the end-users who need to locate damages and define criteria for acceptance and repair of structural members. There remains considerable room for improvement of damage tolerance of composite sandwich structures. Increasing the damage tolerance of a structure requires understanding of its response to mechanical loads. Furthermore, making composites affordable is vitally important. Although proven for their structural benefits, reduction of manufacturing costs remains a primary concern with advanced composite construction.

Predicting the response of laminated composite plates to mechanical loads is complicated due to effects such as: through-the-thickness property variation, geometric and material non-linearity, transverse shear, and multiple and coupled damage modes. The addition of a low density core in sandwich constructions further complicates the analysis. Closed-form methods are limited to linear solutions for specific geometries, lay-ups, and boundary conditions.

The objective of this research may be summarized as the following. To investigate a) the feasibility of reducing manufacturing costs using innovative resin transfer molding techniques, b) to incorporate innovative material and design schemes in improving the damage tolerance of sandwich constructions, c) to improve the functionality of sandwich constructions, and d) to provide an understanding of, and ultimately predicting the initiation and progression of damage to a composite sandwich plate due to low velocity and high strain rate impact. This study involves manufacturing, low velocity impact, high strain rate impact characterization and modeling of conventional cores such as honeycomb and foam cores and unconventional cores such as foam-filled honeycomb, titanium and glass/epoxy pin reinforced foam, and hollow steel and titanium Z-pin / truss core.

2.7 Novel Sandwich Composite Constructions

With regard to the ongoing research, this research brings forth an extensive experimental and finite element study concentrating on the low velocity and high strain rate impact of conventional and innovative core sandwich composites, which possess a good application potential in both air and space vehicles and other defense industry. Innovative manufacturing techniques have also been discussed to address cost-effectiveness. The results obtained from experimental studies have been correlated to the findings of nondestructive and destructive analysis, to yield a thorough comparison between innovative cores of specific interest. The comparison can serve as a guide for the selection of cores from a given available range for a certain application.

2.8 References

1. Honeycomb Constructions, Hexcel Company Literature, 1998.
2. Zenkert, D. "The Handbook of Sandwich Construction," Engineering Materials Advisory Services Ltd., Chameleon Press Ltd., London, United Kingdom, 1997.
3. Lagace, P.A. and Wolf, E. "Impact Damage Resistance of Several Laminated Material Systems," AIAA Journal, Vol. 33, No. 6, pp 1106-1113, June 1995.

4. Gummadi, L.N.B. "Low Velocity Impact of Sandwich Composite Plates," Technical Proposal submitted to Wright Laboratories, Dayton, Ohio, January 1996.

3.0 LITERATURE REVIEW

3.1 Introduction

A major reason for this study is the paucity of information on research in sandwich constructions. Although several results have been published for impact damage of conventional monolithic composites, the number of publications on sandwich composites were found to be limited. Furthermore, available literature is almost always concentrated on traditional cores like honeycomb and foam core sandwich composites. In the present literature review, references have been made to low-velocity impact and high strain rate impact studies made on conventional monolithic and sandwich composites.

3.2 Damage Resistance and Damage Tolerance to Impact on Laminated Composites

Impacts occur during manufacture, normal operations or maintenance reducing the strength and stability of the composite structure to a significant extent. The presence of damage is particularly critical, as it is generally undetectable to the normal eye. A number of models exist to predict the dynamics of the impact. The state of stress in the vicinity of impact is very complex and requires detailed analysis. Accurate criteria for predicting initial failure are not available and analyses after initiation of damage are grossly inaccurate.

Abbate [1] made a comprehensive review of all literature available till 1989 on impact of laminated composites and concluded that delamination represents a major component of damage and develops according to a definite pattern. Delamination occurs at the interface between plies of different fiber orientation and almost never between plies of similar fiber orientation. The delaminated area always has an oblong shape with the major axis along the direction of fibers in the lower ply at the interface. The projected delaminated area increases linearly as the kinetic energy of the impactor increases. For the same initial kinetic energy level, damage size is larger for a heavier impactor with low initial velocity as compared to a smaller impactor with higher initial velocity. In general, the strength remains unaffected till a certain threshold value of impact velocity is reached. Beyond this value, a rapid drop in residual properties is observed. As the impact velocity is increased, an asymptotic value for the residual strength is reached as the damage type changes from one of extensive delamination and matrix cracking to a clean hole due to shearing of the reinforcing fibers.

Lauder et al [2] reported that the endurance of commercial glass/epoxy composites (ScotchPly 1002 by 3M) is reduced to the same extent by rebound damage zones as it is by a drilled hole of equivalent physical size. However, the compliances differ markedly for impact damage vs. geometrical discontinuity as a result of which

the cyclic stresses that lead to equivalent endurance must also diverge. Elber [3] tested eight-ply quasi-isotropic composite plates of Thorne 300 graphite in Narmco 5208 epoxy resin (T300/5208) and established that static testing can be used for the screening tests of materials as an equivalence was established in the deformation mechanics of low velocity impact tests and static tests in thin composite plates.

Abrate [4] further reviewed over 300 articles that appeared after 1989 to present a comprehensive view of the latest developments in the area of low-velocity impacts of composite materials. He observed that impact induced damage consists of fiber breakage, matrix cracking and delaminations. Delaminations in thick laminates are usually bounded by transverse shear cracks, displacement of the top ply section between cracks causing delaminations at the surface. Damage is introduced when the contact force reaches a certain threshold value which can be determined by static tests. Abrate [4] also concluded that the dynamic response of a composite is elastic upto a given load regardless of the boundary conditions, followed by a definite failure in load. The first failure is due to delamination initiation and local crushing. The process continues with subsequent delaminations until a second major failure occurs, which is strongly influenced by boundary conditions.

Lagace and Wolf [5] studied the damage resistance of several laminated materials systems and reported that force is a key parameter in the assessment of impact damage resistance, particularly the force needed to cause incipient damage. This incipient damage is usually in the form of matrix cracks in laminates followed by delamination at the interface with the cracked ply. This damage mode does not change when the material system is changed, although the force at which this damage occurs is affected.

Abrate [4] reviewed articles referring to the effect of different parameters on impact resistance. He concluded that brittle material systems have lower threshold velocities and higher damage area growth rate than toughened material systems. Improving the strain-to-failure of fibers results in improved impact resistance. Dorey [6] reports that carbon fiber composites are susceptible to impact damage and cause design limits to be set below 0.5% strain, less than one-third of the fiber failure strain. Tougher matrix systems are required to overcome this limitation, but their use opens further avenues for research as their use should not produce degradation of other properties while enhancing some specific properties of concern. Wang et al [7] reports that the addition of glass fibers to laminates with graphite fiber reinforcement improves impact resistance. Work done on the effect of projectile characteristics shows that in the case of projectiles that undergo deformation themselves, less damage is created to the target as compared to a projectile which does not deform itself. The effect of lay-up has minimum effect on the energy for incipient damage but a larger effect on the energy at peak load. Damage is induced at the interface between plies of different fiber orientation. Lay-ups with unidirectional plies generally possess higher impact

resistance as compared to plies with woven reinforcement due to the increased probability of fiber damage during weaving [8]. However stitching has been found to reduce the size of the impact induced delamination area. Ko and Hartman [9] also observed similar trends and reported that a 3-D braided composite tends to limit the damage area more effectively than a 2-D laminated composite. They attributed this to the intensive interlacing in a 3-D braided structure which forms a network of crack arrestors throughout the composite structure providing a higher level of damage tolerance. Lagace and Wolf [5] also report that by its woven nature, fabric naturally inhibits the formation of long cracks and restricts the amount of delamination that occurs. Gandhe and Griffin [10] studied the response of graphite/epoxy composites with and without the presence of a thin thermoplastic film (interleaf) and reported that interleaved laminates exhibit a much lesser delamination as compared to non-interleaved laminates for a given level of impact energy.

A new concept called as Z-fiber reinforcement is now gaining popularity. This reinforcement eliminates the problems of delamination and disbond without significant loss of in-plane strength. Foam preforms containing small diameter composite or metal rods are compacted over an uncured lay-up using a combination of heat and pressure.

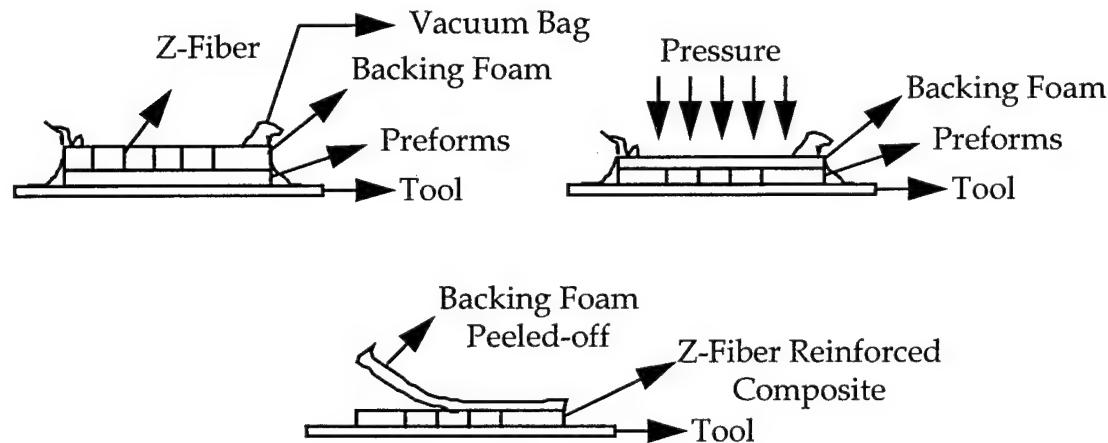


Fig. 3.1 Schematic of Z-Fiber Reinforcement of Composites

The rods are driven through the thickness of the composite like hundreds of tiny nails to reinforce the component. It has been found out that composites reinforced with Z-fibers are 100% more resistant to edge delamination, 55-60% reduction in delamination area due to ice and hail impacts, and have 50% more post impact compression strength [11].

From the review of literature quoted so far, it can be concluded that damage modes are identical for any material system and independent of energy levels. Although accurate prediction of damage is difficult, some approaches are available to quantify impact damage. It can also be concluded that woven fabric increases damage

tolerance in laminated composites. The present study establishes the same trends for sandwich composites. The following pages present a review of the limited relevant literature on the impact tolerance of sandwich composites.

3.3 Damage Tolerance and Damage Resistance of Sandwich Composites

Damage resistance of a sandwich is its ability to sustain the impact event, while damage tolerance is the ability of the sandwich to bear the design loads after the event has occurred and damage has been induced in the structure. Generally for sandwich structures, uniaxial compression is considered to be the design load, as the impact induced damage generally reduces the uniaxial compression strength of the structure [12]. To obtain a clear idea of damage tolerance, it is essential to find out the types of damage that can be induced.

Typically, three types of damages are seen in sandwich composites. In addition to matrix cracking and delamination as seen in monolithic composites, core failure in the form of core crushing is also an important damage mode [13]. Kim and Jun [14] studied the impact resistance of graphite/epoxy facesheets and Nomex honeycomb core and observed that delamination occurs in the fiber direction of the immediate lower ply and a center band is parallel to the fiber direction of the immediate upper ply. They also observed that the delamination size increases rapidly from the impact side to the farthest interply location and is largest at the farthest interply location. Laminates of small relative angular orientation between plies tend to be more damage resistant than those of large relative angular orientation, just as was reported for the case of monolithic composites in the review paper of Abrate [4].

Wu and Sun [15] studied the low velocity impact damage for sandwich beams consisting of graphite/epoxy facesheets and Rohacell foam core, and have also reported that the major modes damage included matrix cracking and delamination in the face laminate and core crushing. They suggest that the maximum principal stress criterion can be used for predicting matrix cracking which, later on induces delamination. The damage mechanisms for the composite facesheets of the sandwich are similar to those of monolithic composites. Because of the additional mode of core yielding or crushing, this factor is an area of extensive research. Hollow honeycomb cells, as core materials, have been an area of research for a very long time. The high transverse Young's modulus and shear modulus of hollow honeycomb cells make them suitable for use as the core in sandwich composites. However, they offer a very small area for bonding to the facesheets and also, the cells crush easily when subjected to concentrated loads. Though the traditional foam core offers a larger surface area for stress dissipation, it is susceptible to high impact and stress situations. The honeycomb-filled-foam combines the advantages of both the foam and honeycomb when acting alone [16]. Wu, et al [15] filled the honeycomb with polyurethane foam and observed that there was a substantial

improvement in the impact resistance properties of the sandwich. There was a notable decrease in facesheet delamination and core crushing.

Just as Gandhe and Griffin [10] reported an improvement in impact resistance in composites with interleaving, Ishai and Hiel [17] have demonstrated that the damage tolerance performance is significantly improved by core interleaving. They tested a composite sandwich system using a syntactic foam having interleaved phases consisting of one ply of glass fabric prepreg oriented at $\pm 45^{\circ}$ to the beam axis embedded between two plies of adhesive film. The interleaved core is as shown in the sketch below.

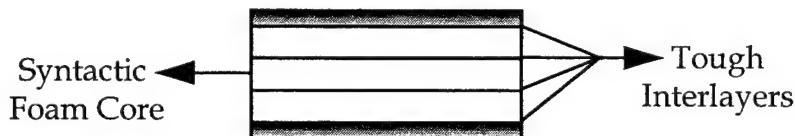


Fig.3.2 Schematic of an Interleaved Sandwich Composite

Weeks and Sun [18] constructed and tested multi-core composite laminates which differ from traditional sandwich composites by the fact that they contain multiple core layers instead of the traditional thick core. They reported that even though the virgin specimens have less flexural stiffness than the traditional composites, the construction does provide improved impact resistance and exhibits less impact damage as compared to the traditional sandwich composites. They also reported that the multi-core construction possesses greater residual compression strength-after-impact than its traditional counterpart.

Herup [12] tested a range of facesheet thicknesses keeping the honeycomb core thickness constant. Hence the bending stiffness essentially became a function of the facesheet thickness. He reported that for any given facesheet thickness, at a threshold impact energy level, a major load drop is seen, which is followed by multiple cycles of loading and partial unloading. He further reported that this major load drop occurs at a load which is independent of the impact energy for any given facesheet thickness. However the load at which this major load drop occurs increases with the facesheet thickness and an increase in the facesheet thickness increases the magnitude of the load drops. The present work validates these observations and establishes these relations for some unconventional cores.

3.4 High Strain Rate Impact

In the area of high strain rate impact response, work is primarily limited to metals, with scanty literature available for composites. Material systems are normally characterized by their mechanical properties such as modulus of elasticity, yield strength and ultimate strength. Testing to determine these properties is usually

performed in accordance with the American Society of Testing and Materials (ASTM) standards, which are typically at low or quasi-static strain rates. The Split Hopkinson Pressure Bar (SHPB) is widely used to conduct high strain rate tension, compression or torsion test at strain rates of around 10,000/s.

The SHPB was first introduced by Bertram Hopkinson, who introduced a single bar configuration as a means of obtaining high strain rate conditions [19]. Kolsky [20] in 1949 introduced a modified version consisting of two bars, an incident bar and a transmission bar. However, various modification of Kolsky's original version has been described by Davies and Hunter [21], Lindholm [22], and Hauser [23] and Choe [24]. At present, many laboratories are using Kolsky's method with only slight variations for a vast number of isotropic materials. Recently high strain rate testing was performed on fiber reinforced composite materials by Harding and Welsh [25], and Saka and Harding [26]. Harding outlined the problems and key tests in high strain rate impact of fiber reinforced composite materials. The influence of strain rate on tensile and compression properties was studied on unidirectional and woven laminated composites. The strain rate dependency of the matrix system was determined to be an important factor in the dynamic performance of the laminate. Nemat-Nasser et. al [27] devised novel techniques to render the classical split Hopkinson bar apparatus suitable for dynamic recovery experiments, where the sample can be subjected to a single pulse for pre-assigned shape and duration. The sample can then be recovered without any additional loading, for post-test characterization; i.e, techniques for fully controlled unloading in Hopkinson bar experiments. For compression dynamic recovery tests, the new design generates a compressive pulse trailed by a tensile pulse (stress reversal), traveling towards the sample. Furthermore, all subsequent pulses which reflect off the free ends of the two bars (incident and transmission) are rendered tensile, so that the sample is subjected to a single compressive pulse whose shape and duration can also be controlled. In the context of sandwich composites, the use of the recovery mechanism is particularly important.

The decrease in strain-to-failure of polymer matrix materials reinforced with glass fibers have been noted by several researchers [28-33]. This observed reduction in ductility has prompted the investigation of the effects of stress concentrations in the matrix resulting from high shear stresses at the fiber/matrix interface during load transfer, from fiber-to-fiber interactions [33], and from strain discontinuities at the fiber ends [35]. Daniel and Liber [36] tested, among other composites, 0° and 90° unidirectional S-glass/epoxy specimens at strain rates of 27/sec. For the 0° specimens they reported no significant changes in strength or modulus but some trend towards higher ultimate strain at higher rates of loading. For the 90° specimens, their results showed a surprising reduction in modulus and some trends towards higher strength and no significant trends in limiting strain with strain rate. Hardly, any literature was found on high strain rate impact of sandwich constructions.

As mentioned earlier, a major motivation of this work is to continue furthering literature on sandwich composites. This work encompasses a broad scope of assessing the damage resistance / tolerance of conventional as well as some unconventional core sandwich composites which possess significant potential in air and space vehicles.

3.5 Liquid Molding Processes ; RTM, VARTM and Related Processes

Resin transfer molding and vacuum assisted resin infusion molding have received considerable attention in recent years, as both are cost-effective manufacturing techniques. RTM was known since the 1940s, but has gained popularity in recent years in the production of commercial products such as computer keyboards, bathtubs, sporting goods, and fertilizer hoppers [37]. Recent developments have taken RTM to new heights, with its use in the F-22 aircraft as illustrated in Fig. 2.3. The cost-effectiveness in using this manufacturing approach was illustrated in Fig. 1.7. The technique is particularly attractive, as it can produce near-net shapes, close tolerances and fast production rates. There is limited information available to the designer in the selection of equipment, material and process variables, but it depends upon prior experience. RTM has many advantages and it offers flexibility to the designer to vary the orientation, type and level of the reinforcement, reduce manufacturing costs, parts integration, local tailoring of reinforcement, and in designing materials for damage containment.

RTM and VARTM belong to a group of processes named liquid molding. The Seeman's Composite Resin Infusion Molding Process (SCRIMP), Structural Reaction Injection Molding (SRIM), High Speed Resin Transfer Molding (HSTRM), and other similar processes are other liquid molding composite processes. One of the significant advantages of RTM is that it allows the use of three-dimensionally stitched fabric preform and textile riveted plies, which enable the designer to make a material that can precisely match a specific requirement, and enhance the impact and compression strength of the composite parts [38,39]. Other advantages of the RTM process include ; low injection pressure, use of different resin systems, capability to make large and complex shaped parts, parts integration, low cost and short cycle time. The operation of the RTM and VARTM process is described in Chapter 1. In the context of sandwich structures, both RTM and VARTM are attractive because simultaneous wet-out of the top and bottom facesheets is possible. In RTM this may be done by using channels / micropores in the core through which resin infiltrates the bottom facesheet preform. In the case of VARTM, the resin may be infused through simultaneous co-injection of the top and bottom facesheets. This has been demonstrated successfully in the current work, in addition to closed mold RTM processing.

3.6 References

1. Abrate, S. "Impact on Laminated Composite Materials," ASME Applied Mechanics Rev. Vol 44, No. 4, pp. 155-190, April 1991.
2. Lauder, A.J., Amateau, M.F., and Queeney, R.A. "Fatigue Resistance of Impact Damaged Specimens vs. Machined Hole Specimens," Composites, Vol. 24, No. 4, pp.443-445, 1993.
3. Elber, W. "Failure Mechanisms in Low-Velocity Impacts on Thin Composite Plates," NASA Technical Paper 2152, May 1983.
4. Abrate, S. "Impact on Laminated Composites: Recent Advances," ASME Applied Mechanics Rev. Vol 47, No. 11, pp. 517-544, Nov. 1994.
5. Lagace, P.A. and Wolf, E. "Impact Damage Resistance of Several Laminated Material Systems," AIAA Journal, Vol 33, No. 6, pp 1106-1113, June 1995.
6. Dorey, G. "Damage Tolerance and Damage Assessment in Advanced Composites," Advanced Composites, Elsevier Applied Science, Chapter 11, pp. 369-398, 1989.
7. Wang, C.J., Jang, B.Z., Panus J., and Valaire B.T. "Impact Behaviour of Hybid-Fiber and Hybrid-Matrix Composites," Journal of Reinforced Plastics and Composites, Vol.10, No. 4, pp 356-378.
8. Dost, E.F., Ilcewicz, L.B., Avery, W.B., and Coxon, B.R. "Effect of Stacking Sequence on Impact Damage Resistance and Residual Strength for Quasi-Isotropic Laminates," Composite Materials:Fatigue and Fracture (Third Volume), ASTM STP 1110, T.K. O'Brien, Ed., American Society for Testing and Materials, Philadelphia, pp. 476-500, 1991.
9. Ko, F.K., and Hartman D. "Impact Behaviuor of 2-D and 3-D Glass/Epoxy Composites," SAMPE Journal, pp. 26-30, July/August 1986.
10. Gandhe, G.V., and Griffin, O.H. "Post-Impact Chararacterization of Interleaved Composite Materials," SAMPE Quarterly Bulletin, Virginia Polytechnic Institute and State University, Blacksburg, VA 24061, pp 55-58.
11. Lagace, AZTEX, Inc. "Z-Fiber - Lighter, Stronger, Tougher Fiber Composites," New Product Announcement Literature, Waltham, MA.
12. Herup, E. "Low-Velocity Impact on Composite Sandwich Plates," Ph.D. Dissertation, Air Force Institute of Technology, Dayton, Ohio, July 1996.

13. Gummadi, L.N.B. "Low Velocity Impact of Sandwich Composite Plates," Technical Proposal submitted to Wright Laboratories, Dayton, Ohio, January 1996.
14. Kim, C., and Jun, E. "Impact Resistance of Composite Laminated Sandwich Plates," Journal of Composite Materials, Vol. 26, No. 15, pp. 2247-2261, 1992.
15. Wu, C.L., Weeks, C.A., and Sun, C.T. "Improving Honeycomb-core Sandwich Structures for Impact Resistance," Journal of Advanced Materials, pp 41-47, May 1995.
16. Westwind Composites, Weskor Foam Filled Honeycomb Literature, Houston, TX.
17. Ishai, O. and Hiel, C. "Damage Tolerance of a Composite Sandwich with Interleaved Foam Core," Journal of Composites Technology and Research, Vol. 14, No. 3, pp. 155-168, Fall 1992.
18. Weeks, C.A., and Sun, C.T. "Multi-Core Composite Laminates," Journal of Advanced Materials," pp 28-37, April 1994.
19. Rinehart, J.S., "Historical Perspective: Metallurgical Effects of High Strain-Rate Deformation and Fabrication," Shock waves and High Strain Rate Phenomena in Metals, Plenum Press, New York, N.Y., 1980.
20. Zukas, J. A., Nicholas, T., Swift, H.F., Greszczuk, L.B., and Gurran, D.R., "Impact Dynamics," John Wiley and Sons, New York 1982, pp. 277-307.
21. Davies, E. D. H., and Hunter, S. C., "The Dynamic Compression Testing of Solids by the Method of the Split Hopkinson Pressure Bar," J.Mech. of the Solids, 11, 1963, pp.155-179.
22. Lindholm, U.S., "Some Experiments with the Split Hopkinson Pressure Bar," J.Mech. and Phys. Of Solids, Vol. 12, 1964, pp. 317-335.
23. Hauser, F.E., "Technique for Measuring Stress-Strain Relations at High Strain rates," Experimental Mechanics, 6,8, 1996, pp. 395-402.
24. Choe, G. H., "Impact Testing of Composite Material at High Strain rates," Master's Thesis, 1989, pp. 1-3.
25. Harding, J. and Welsh, L.M., "Impact Testing of Fiber Reinforced Composite Materials," O.V.E.L. Report No. 1415/82, Presented at the SES Meeting, University of Delaware, August 1983.

26. Saka, K. and Harding, J., "Behavior of Fiber reinforced Composite Materials," O.V.E.L. Report No. 1415/82, Presented at the SES Meeting, University of Oxford, report No. OUEL 1602/1985.
27. Nasser, S. N., Isaacs, J. B. and Starrett, J. E., "Hopkinson Techniques for Dynamic Recovery Experiments", Proc. R. Soc. London, Vol. 435A (1991), pp. 371-387.
28. Bowyer, W.H. and Barder, M.G., Journal of Material Science, Vol. 16, 1972, pp. 1315-1321.
29. Richardson, G.C., Polymer Engineering Science, Vol. 16, 1976, pp. 252-256.
30. Blumentritt, B.F., Vu, B.T and Cooper, S.L., Polymer Engineering Science, Vol. 15, 1975, pp. 428-436.
31. Curtis, P.T., Bader, M.G. and Bailey, J.E., Journal of Material Science, Vol. 13, 1978, pp. 377-390.
32. Lavengood, R.E., Polymer Engineering Science, Vol.12, 1972, pp. 48-52.
33. Lee, L., Polymer Engineering Science, Vol. 9, 1969, pp. 213-224.
34. Chen, P.E., Polymer Engineering Science, Vol. 11, 1971, pp. 51-56.
35. MacLaughlin, T.F and Barker, R.M., Experimental Mechanics, Vol. 1, 1972, pp. 537-543.
36. Daniel, I.M. and Liber, T., "Testing of Fiber Composites at High Strain Rates," Processing, 2nd International Conference on Composite Materials, ICCM/2, Toronto, 1978.
37. Galli Ed., Resin Transfer Molding : A Cost-Effective Alternative, *Plastics Design Forum*, March/ April 1981, pp.47-51.
38. Rogers . S, SRIM and RTM Sprint Toward High-Volume Uses, *Plastics Technology*, March 1989, pp.50-58.
39. Composites Update - Part I : New Materials and Reinforcements, *Plastics Technology*, April 1991, pp.39-44.

4.0 NEED FOR ALTERNATE CORES

4.1 Introduction

We have seen till now that a sandwich construction stiffens the core without materially increasing the weight. The core material provides excellent shear stiffness and the facesheets provide excellent flexural stiffness. A limiting factor to the widespread use of these special composites has been their susceptibility to low velocity impacts, which turn out to be critical due to the extensive loss in the transverse stiffness of the composite due to the impact event. There is potential to improve damage tolerance by incorporation and optimization of facesheets with fabric architectures along with core designs that can dissipate impact energy effectively. Though limited, ongoing work is concentrated on improving the damage resistance of composite facesheets through fabric architecture, there is a strong need to investigate novel and conventional core designs to optimize the sandwich construction on the basis of affordability and viability.

4.2 Conventional Cores

Balsa wood was one of the first cores ever to be used in sandwich construction and is cheap with better mechanical properties. But its use is restricted due to the fact that it is very sensitive to humidity and its properties deteriorate very rapidly with an increase in water content ruling out its applicability in comparatively hostile environments.

The most popular cores presently in use are the honeycomb cores and the foam cores. However, they are restricted in their use. The honeycomb core possesses excellent transverse compressive strength, but shows catastrophic buckling instability at higher energies of impact [1]. Also, the honeycomb offers a very small bonding surface and low in-plane shear properties, the foam offers a greater area for bonding and stress dissipation, but is not suitable for concentrated impacts or stresses. As was learned later on in this research, the initial failure due to low velocity impacts is always in the form of core debonding. The honeycomb core debonds very easily, decreasing the load bearing capacity of the composite. Furthermore, both in honeycomb and foam core sandwich constructions, the space within the core is inaccessible, once the facesheets are bonded to the core. Honeycomb core in a variety of cell sizes and material configurations has been used in structural applications as shown in Figure 4.1 and Figure 4.2. These include - kraft paper cells dipped in phenolic resin, nomex, graphite, thermoplastic and a variety of other honeycomb constructions.

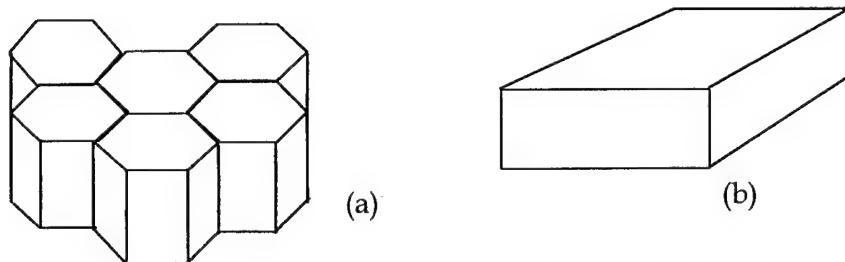


Figure 4.1 Conventional a) Honeycomb and b) Foam Cores

Foam core sandwich constructions are equally popular in a variety of applications. The foam cores are available in various densities of cell spacing – some closed cells and some being reticulated. Some popular foam cores were found to be Rohacell - PMMA, Divinycell, Last-A-Foam and several other core types available in the open market. A particular disadvantage of foam core, is its susceptibility to crushing under low velocity impact loads, and the growth of damage catastrophically, a few core cells below the interface of the facesheets and the foam. In the event of using thicker (32 plies and greater of pre-preg graphite/epoxy) facesheets, the load to create the first damage is substantially increased, however, once crushing initiates in the core, the damage is widespread. The same is true for increasing the core density, with thin (4-16 plies of pre-preg graphite/epoxy) facesheets [2].

4.3 New Concepts in Sandwich Core Construction

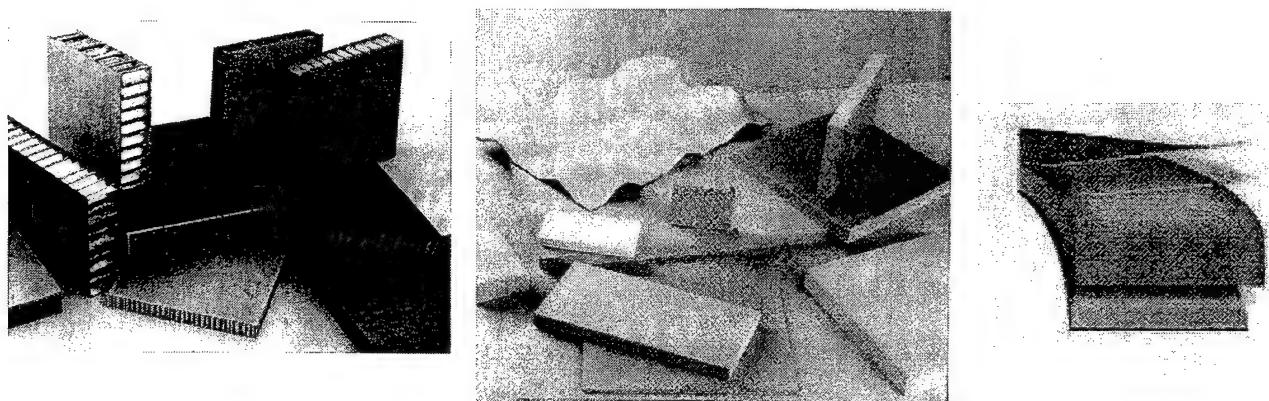


Figure 4.2 Commonly used Honeycomb and Foam Cores and their Sandwich Constructors

Some of the problems outlined in the previous section with conventional cores, are the motivating factors in exploring innovative concepts. The design considerations are based upon improvement of transverse stiffness, damage tolerance, providing delayed damage mechanisms and containment / arrest mechanisms under impact loading. The various innovative concepts studied in this work include :

a) *Honeycomb-Filled-Foam Core :*

A suitable alternative to honeycomb and foam core is the foam-filled honeycomb as a core material [3,4]. This novel concept optimizes the relationship between the honeycomb and the foam (Fig. 4.3a and b), offering the benefits of both the core while

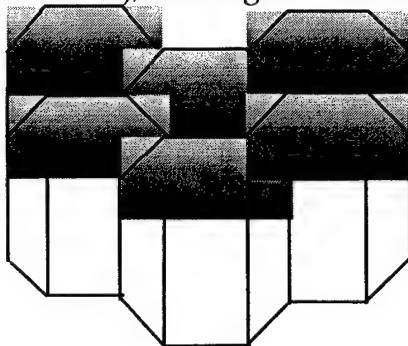


Figure 4.3a Schematic of Honeycomb-Filled-Foam Core

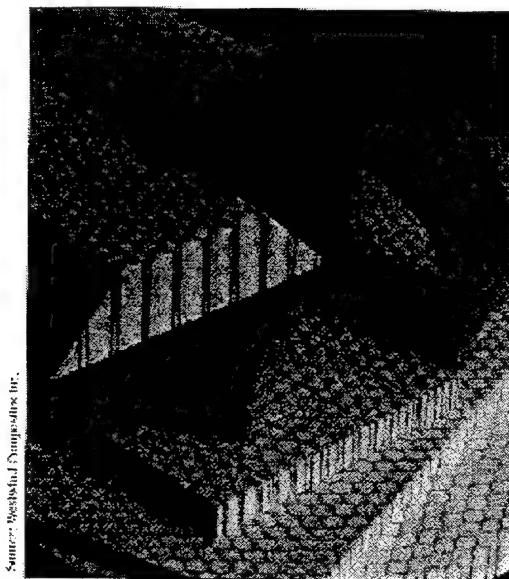


Figure 4.3b. Foam-Filled Honeycomb Core

selectively eliminating the disadvantages of both. The cell walls of the honeycomb are reinforced by the foam. The increased surface area allows stress forces to dissipate over a larger area than that offered by the honeycomb alone. The core absorbs much greater impacts by transmitting forces to the adjacent cells. The effect is greater resistance to the shear force perpendicular to the sandwich (breaking), increased moment resistance (less bending) and better dampening of shock waves along the surface (less vibrations) [3]. As was found through these studies, with the slight weight penalty associated with reinforcing the honeycomb cells with foam, improved impact performance can be obtained through the use of a less expensive honeycomb construction (phenolic dipped kraft paper as compared to Nomex) and a cheaper polyurethane core (compared to PMMA foam core). Both low velocity and high strain rate performance of the foam-filled-honeycomb core were considered.

b) *Pin-Reinforced Foam Core*

A novel core concept called as Z-fiber or truss core or pin core reinforcement has been developed [5]. Truss core or Z-fiber pin core composites provide an alternative sandwich construction, where the core is hollow and comprises of a system of z-fiber pins that penetrate into the facesheets according to a predetermined geometry and configuration. The conventional foam core is reinforced with composite or metallic pins hence increasing the shear stiffness of the core and increasing the resistance of the sandwich construction to impact damage. The foam and pin offer a mutual stabilization to transverse loading, where the foam absorbs the impact energy, while the pins share the transverse load. In the current work, stiff glass/epoxy, steel and titanium pins were used to reinforce the Rohacell foam core.

c) *Hollow Truss Core Sandwich Composites*

The hollow truss core is a derivative of the pin reinforced foam cores. In this case, the foam is washed away with solvents such as MEK or acetone, leaving a network of

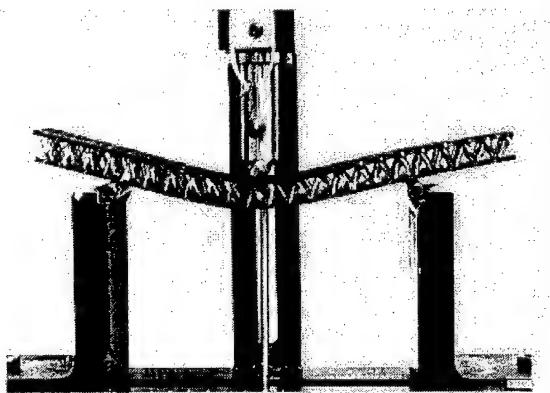


Figure 4.4 Hollow Truss (Z-Pin) Core Sandwich Composite [5]

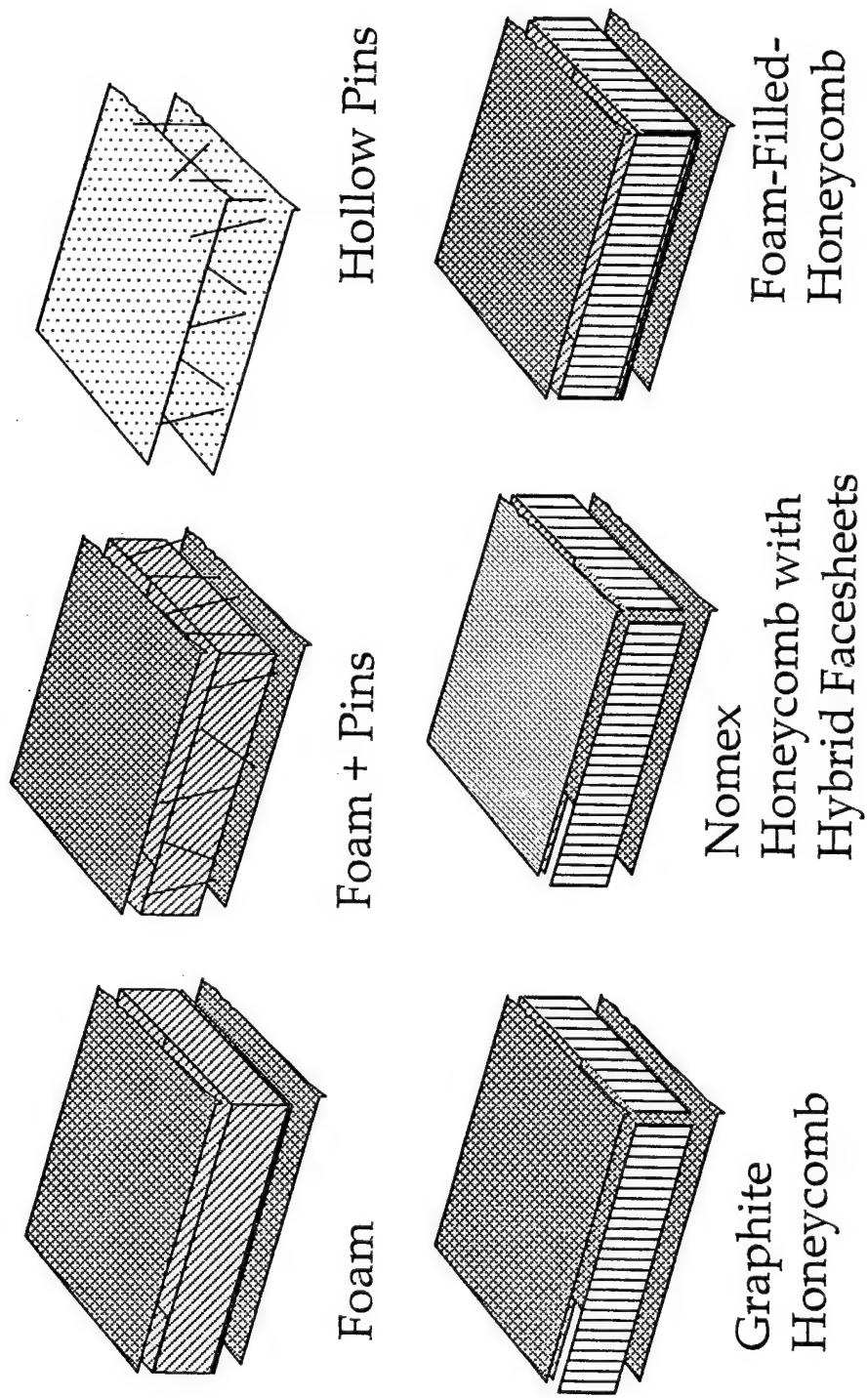


Figure 4.5 Schematics of Core Types Considered in the Overall Research

hollow truss core cells, which are geometrically arranged in a predetermined configuration (Fig. 4.4). These innovative sandwich composites offer space advantages for fuel cells and/or electronic assemblies, besides from high shear and axial stiffness [6]. The functional benefits from this construction are multi-fold. For example, the space could be selectively filled with fire retardant, damping materials, electronic and electrical wires etc. to name a few conceivable advantages. The effects of some parameters in the truss core composites such as a variation in the pin density, effect of facesheet thickness and a variation in the pin type, number of pins per unit area, apart from discussing some innovative manufacturing methods for these special composites are considered in this work.

d) Honeycomb Core with Hybrid Facesheets

A traditional nomex honeycomb core was considered in conjunction with a glass/epoxy facesheet on one side, and a graphite/epoxy on its other. The rationale for hybridizing the facesheets was to obtain enhanced bending stiffness in conjunction with enhanced impact loading benefits. The hybrid facesheets were evaluated for their low as well as high strain rate impact response. Figure 4.5 summarizes the schematics of the various core types considered in this research.

4.4 References

1. Vaidya U.K., and Mohan P.K. "Damage Tolerance of Sandwich Composites," Interim Technical Work Status Report for Research Project, Submitted to Wright Laboratories, Dayton, Ohio, February, 1998.
2. Herup, E. "Low-Velocity Impact on Composite Sandwich Plates," Ph.D. Dissertation, Air Force Institute of Technology, Dayton, Ohio, July 1996.
3. Westwind Composites, Weskor Foam Filled Honeycomb Literature, Houston, TX.
4. Wu, C.L., Weeks, C.A., and Sun, C.T. "Improving Honeycomb-core Sandwich Structures for Impact Resistance," Journal of Advanced Materials, pp 41-47, May 1995.
5. AZTEX, Inc. "Z-Fiber - Lighter, Stronger, Tougher Fiber Composites," New Product Announcement Literature, Waltham, MA.
6. Vaidya, U.K., Palazatto, A.N., and Gummadi, L.N.B. "Low Velocity Impact Response and Nondestructive Evaluation of Sandwich Composite Structures," NCA-Vol. 24, Proceedings of the ASME Noise Control and Acoustics Division, pp. 197-214, 1997.

5.0 MANUFACTURING OF SANDWICH COMPOSITES

5.1 Introduction

Much like the behavior of sandwich composites to mechanical loading, the manufacture of sandwich composites is also a relatively immature field and most of the times, the techniques involved are time consuming and manual to a large extent [1]. The manufacturing of the sandwich composites is complicated by the fact that it has two separate and physically distinct facesheets and thereby, fabricating the two facesheets can be time consuming and uneconomical. Some of the techniques used for the manufacturing of sandwich composites in general as well as the low cost manufacturing techniques adopted in this work are discussed below.

5.2. Liquid Molding

Several related liquid molding processes are feasible for the manufacture of the sandwich composites. The liquid molding process essentially involves the use of a pressure differential to inject resin into the dry fabric preform placed on a female mold or on some special tooling. Two cost-effective liquid molding techniques are : *Resin Transfer Molding (RTM)* and *Vacuum Assisted Resin Transfer / Injection Molding (VARTM)*.

5.2.1 Resin Transfer Molding

RTM is a closed mold low-pressure process that allows the fabrication of composites ranging in complexity from simple, low performance to complex, high-performance articles and in size from small to very large. The process offers low cost

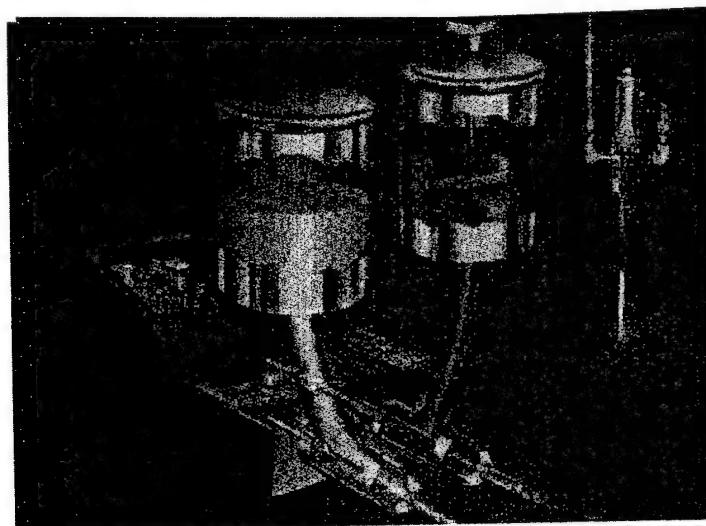


Figure 5.1. Resin Transfer Molding Metering, Mixing and Dispensing Unit

alternative to composite fabrication. It is differentiated from other molding processes in that the dry reinforcement and the resin are combined within the mold to form the composite component. The fiber reinforcement and the core(s), which may be pre-shaped, are placed into a tool cavity, which is then closed. The resin metering, mixing and dispensing unit is then connected to teflon coated hoses which are attached to posimixer head on the tool side as shown in Fig. 5.1. The posimixer head provides a uniform and striated mix of the components of the resin and the catalyst. The resin is then pumped or transferred into the tool to impregnate the reinforcement, which is subsequently cured. Several similar composite fabrication processes fall into the resin transfer molding category, although there are distinct variations. The schematic and photograph of the setup of the RTM process are as shown in Fig. 5.2a and b respectively. The preform is placed in the female mold and the male mold is tightly clamped over the same with the use of pneumatic assistance or by mechanical clamping. The required heating cycle for the resin cure can be used by heating the molds. The resin is then injected into the mold through the duct provided in the male mold. The RTM process offers good quality parts.

Resin Injection

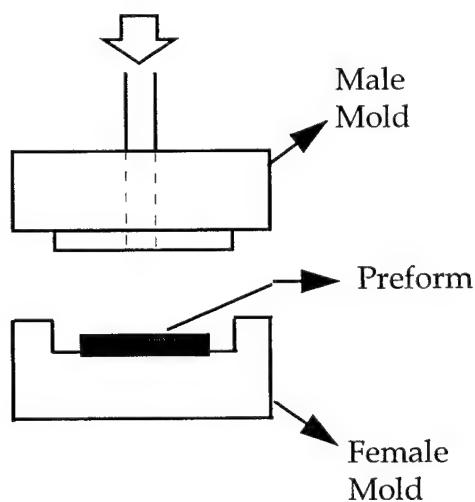


Figure 5.2a Schematic of Resin Transfer Molding

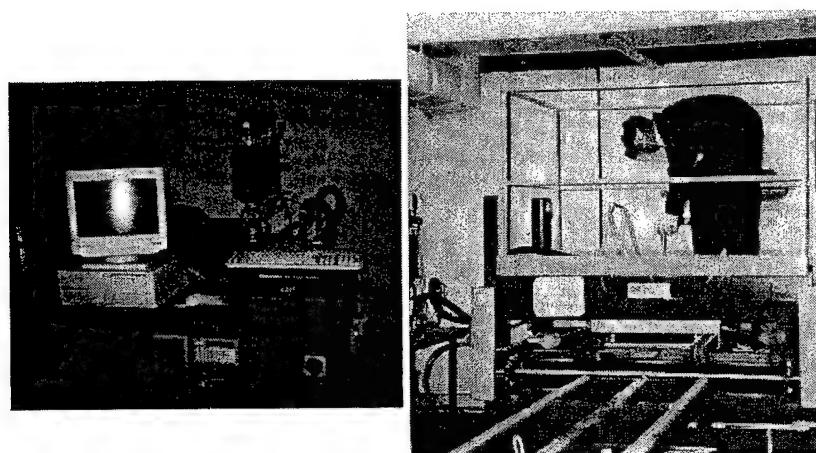


Figure 5.2b Photograph of Resin Transfer Molding

5.2.2 Vacuum Assisted Resin Transfer / Infusion Molding (VARTM)

VARTM is a single sided tooling process that utilizes only the female tool. The preform (facesheet preform and the core) is laid over the tool according to the desired shape and profile. A porous teflon is then placed on the preform over which a highly permeable membrane is positioned. Resin infusion and suction lines are placed at appropriate locations after which the entire part is placed under a vacuum bag. The part is debulked for several hours. Resin is then infused (drawn in) through the infusion lines. The resin flow through the preform is assisted primarily through the vacuum alone. Resin flow takes place both in the plane of the preform as well as in the transverse direction. Uniform wettability is achieved (Fig. 5.3). An innovative co-injection process has been used for the fabrication of the honeycomb-filled-foam core sandwich composites used for this study.

Upon complete part wetting, the infusion lines are blocked. The part is allowed to cure with the vacuum maintained through the entire process. The VARTM process was used effectively in this work to produce sandwich composites. Fiber volume fractions of 50-52% within the facesheets were achieved , void free, in the various panels manufactured.

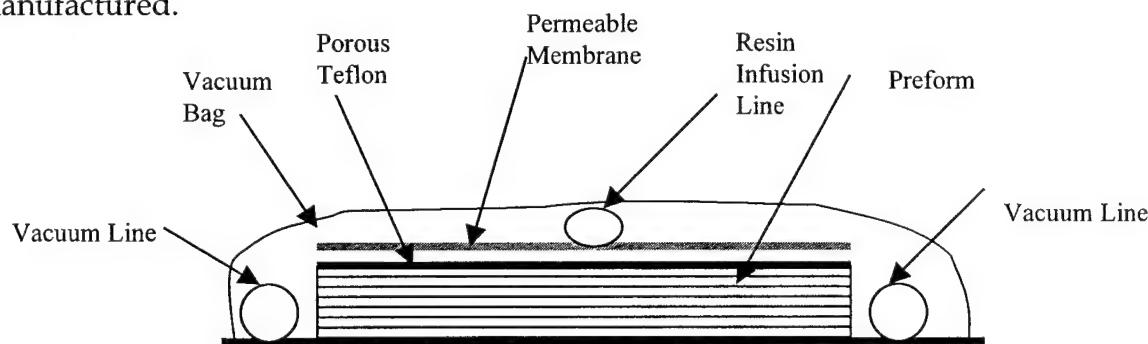


Figure 5.3 Schematic of VARTM process

5.2.3 Vacuum Assisted Compression Molding (VACM)

The vacuum assisted compression molding process is similar to the RTM process except that generally there is no provision for resin injection, and that pressure is applied by the relative movement between the male and the female mold. The mold is closed in such a way that the preform conforms to the shape of the mold and the required temperature and pressure cycles are applied (Fig. 5.4). A very important aspect of the compression molding process is to see whether the core in consideration has the ability to withstand the applied pressure and the temperature required for the resin cure. A schematic is shown below.

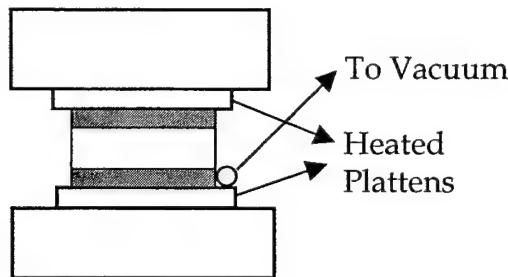


Figure 5.4 Schematic of Compression Molding Process

The compression molding process is also a simple and economical method for the fabrication of sandwich composites. The adhesive bonding technique along with the wet lay-up process can be combined with this process to yield better and economical parts.

5.3 Manufacturing of Panels in the Current Work

The above described processing approaches along with some variations were adopted in manufacturing panels in this current work. The following section describes the manufacturing of various samples adopted in this study. These range from simple hand lay-up, use of co-injection VARTM, RTM/VARTM processing and VACM.

5.3.1 Fabrication of Hollow Z-Pin Truss-Core Composites - Preliminary Work

In the earlier aspect of the work, the feasibility of manufacturing truss core panels was assessed using hand lay-up. The fabrication steps using the hand lay-up process may be broadly divided into the following steps:

a) Machining of Metallic Mold with Pin Inserted at Various Angles

A 0.5" thick aluminum mold with holes located at various angles was machined. The holes have been drilled at +60 and -60 degree angles in the mold to enable the pins to be inserted into the foam at specific angles.

b) Insertion of Pins into the Releasable Foam Core

Polystyrene foam was procured in block of size of 36" x 18" x 12". The block was sliced using an inconel hot wire cutter to 0.5" x 36" x 18" sheet sizes. The mold described in part a, was placed on the foam. Commercially available steel brads of 19-gage diameter steel wire and 5/8" length were inserted through the holes in the mold, so that they were inserted into the foam at an angle of +60 or -60 degrees. The arrangement and

spacing of the pins is shown in Fig. 5.5 (a two-dimensional lay-out of the truss core). Care was taken to ensure that the pins stuck out on both sides of the core, to enable placement of the facesheets as shown in Fig. 5.6.

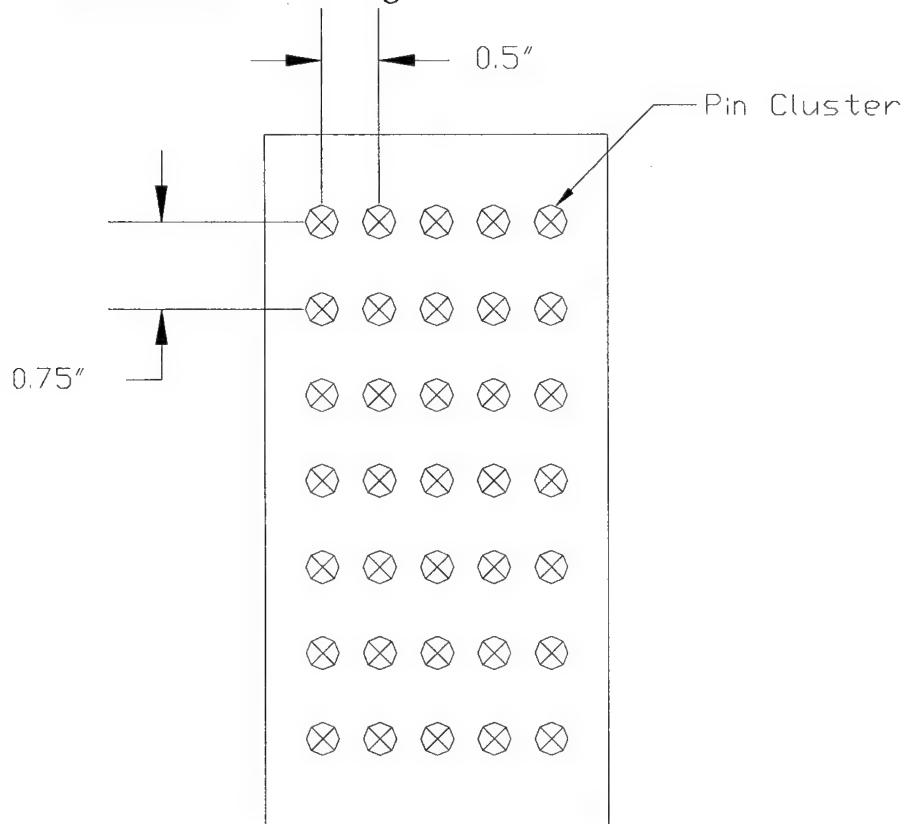


Figure 5.5 Lay-out of Truss Core Pins

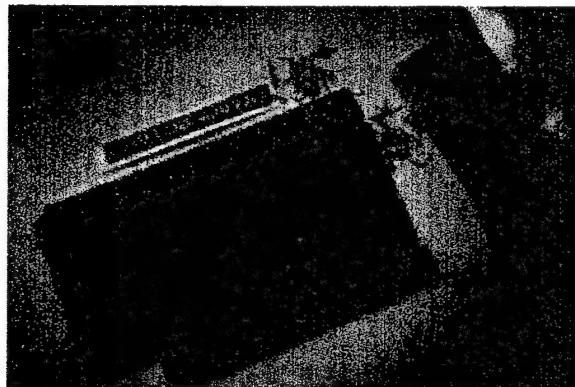


Figure 5.6. Foam Core with Pins Prior to Facesheet Placement.
Preparation of Pin Reinforced Foam Core By Insertion of Pins through a Mold into Polystyrene Foam : Preliminary Work

c) Hand Lay-up of Facesheets

Two categories of facesheets were chosen as a preliminary evaluation step: plain weave E-glass fabric and plain weave graphite fabric. Four layers of plain weave E-glass fabric were wetted with Poly Epoxy (a commercial general purpose) resin. The first two layers of the wetted E-glass fabric were placed on the pin-reinforced foam core and were pressed in using a wooden tongue depressor. Following this, remaining two glass fabric layers were laid on top. The panel was then flipped over gently and a similar procedure was repeated on the other side. A porous teflon layer was placed on either side of the top facesheet, followed by a bleeder to absorb the excess resin. The layup was placed between two aluminum sheets and compression molded at 100° F for eight hours at 60 p.s.i pressure. Figure 5.7 shows the finished panel. Identical fabrication procedure was adopted in making the graphite/epoxy facesheet panels.

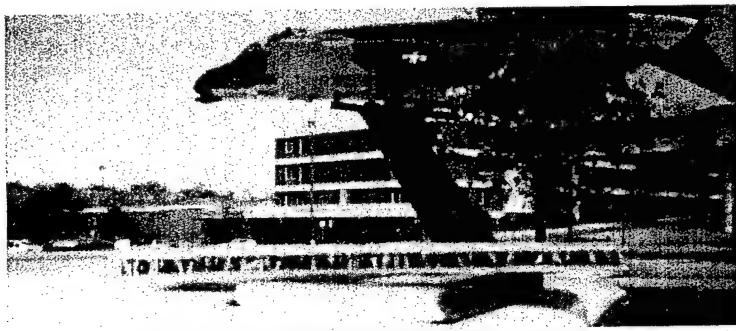


Figure 5.7 Finished Truss Core Panel

d) Releasability of Foam

After curing the composite, the foam was released using Methyl Ethyl Ketone (MEK) as a solvent. The solvent was slowly poured on the polystyrene foam core, which was easily released thereafter exposing the pins. Table 1 shows the details of the panels fabricated using glass and graphite facesheets.

5.3.2 Resin Transfer Molding of Foam and Foam + Pin Core Sandwich Composites

Foam and pin-reinforced foam core composites were fabricated using closed mold resin transfer molding technique. Here the dry preform in conjunction with the core (with and without the pins) was pre-placed into a closed mold, that was pressed in a pneumatic press. The RTM processing is previously shown in Figs 5.4 a and b. Small gaps were left within foam strips to enable wet-out of the top and bottom facesheets simultaneously. A low viscosity vinyl ester epoxy resin (Dow Derakane VE 350) resin in conjunction with appropriate mix ratio of MEKP catalyst, 2,4 Pentadione retarder, DMA (accelerator) was injected into the fabric-core lay-up to wet-out the facesheets. A Liquid Control Corp., resin transfer molding Compact Variable Ratio (CVR) equipment

(Fig. 5.1) with disposable mixing heads was used to meter, mix and inject the resin through the opening within the top mold. The resin flow was radially outward, as the resin entered from the geometric center of the mold. Four vents were present for the excess resin to escape from the mold upon complete wet-out.

5.3.3 Fabrication of Foam-Filled Honeycomb Core Sandwich Composites with Graphite and S2 Glass Facesheets using Affordable Co-Injection Vacuum Assisted Resin Transfer Molding

The foam-filled-honeycomb core sandwich composites used for this study have been fabricated using variation of closed mold RTM that was described in section 5.3.2. The innovative co-injection (Fig. 5.8) offers further cost-benefits even in comparison to closed-mold RTM. The foam-filled-honeycomb used in the current work was polyurethane foam filled in phenolic impregnated kraft paper honeycomb: Style 20, (WESKOR company) graphite fabric was bonded to the core using a microballoon mixed vinyl ester 350 resin system in a compression molding machine (Fig. 5.9). After pre-compression of the single layer of graphite fabric, the lay-up was performed on a single sided aluminum tooling by sandwiching the core between fourteen layers (top and bottom) of plain weave (on each side of the core) graphite fabric preform, a layer of porous teflon and a highly permeable membrane and bagged in a vacuum bag. The resin injection lines were placed at the top as well as the bottom facesheet preforms, so that simultaneous resin infusion of the top and bottom facesheet could be performed as shown in illustrations. (see Figs. 5.8a & b, 5.9a-c and 5.10 a & b).

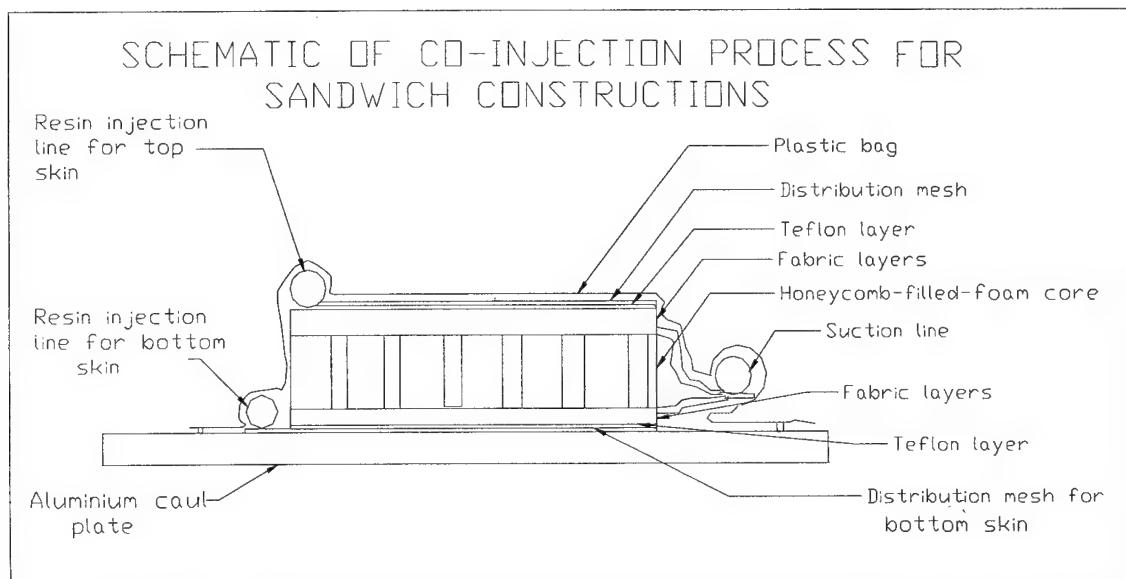


Figure 5.8a. Detailed Schematic of Co-Injection Process

*Aircraft Relevant Sandwich Composites
are being produced by Rapid Co-Injection of
Facesheets for the Foam and Foam Filled
Honeycomb Cores*

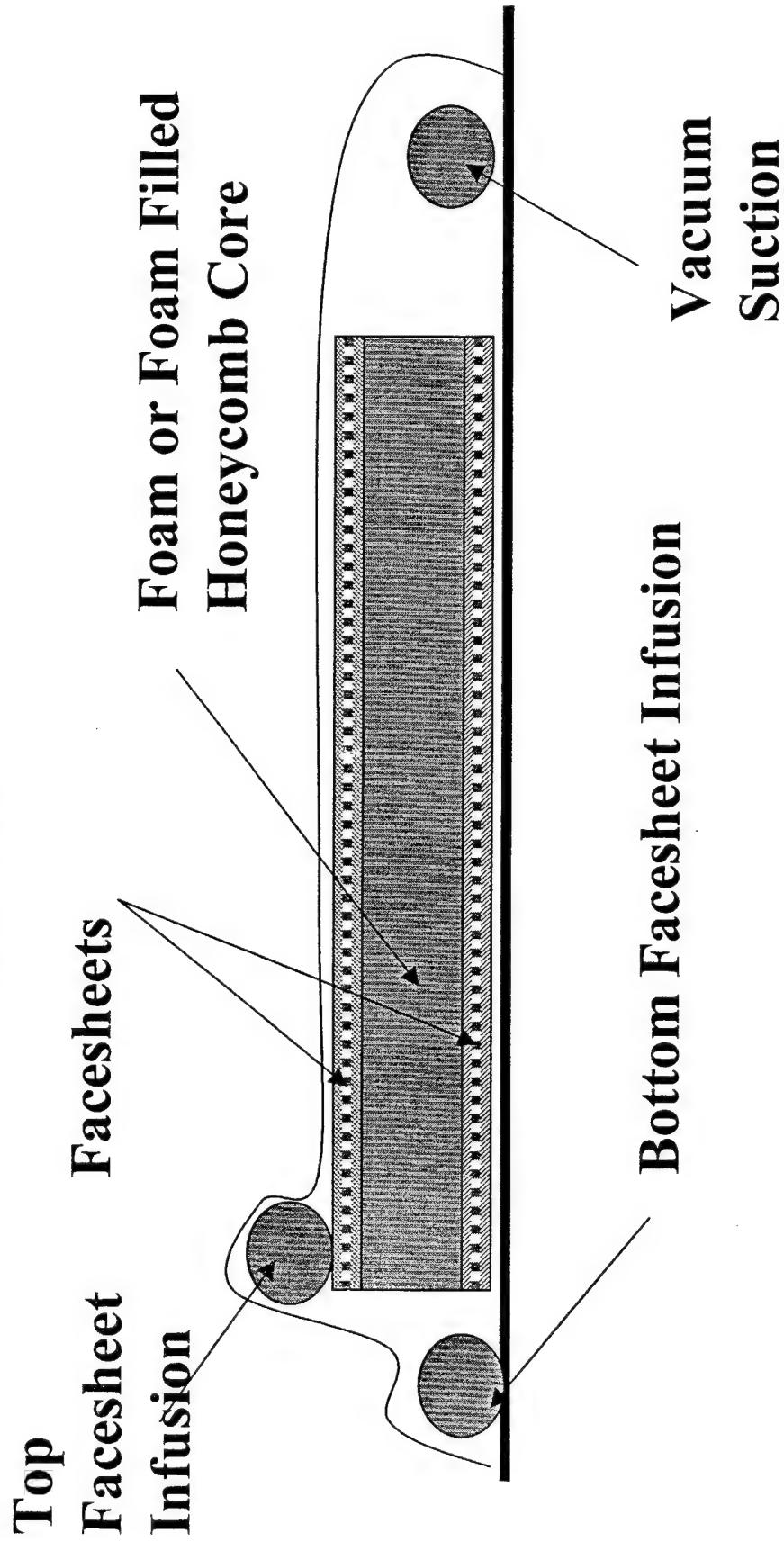
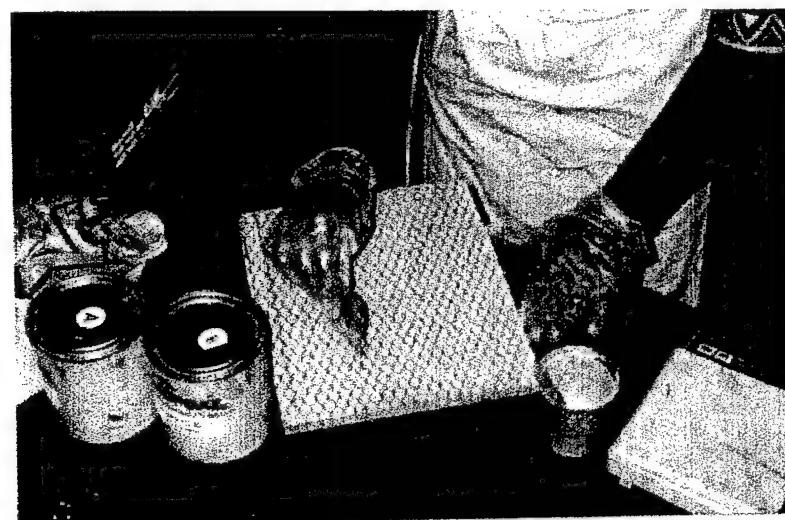


Figure 5.8b. Schematic of Co-Injection Process



a) Preparation
of the Core



(b) Lay-Up and
Begin Resin
Injection

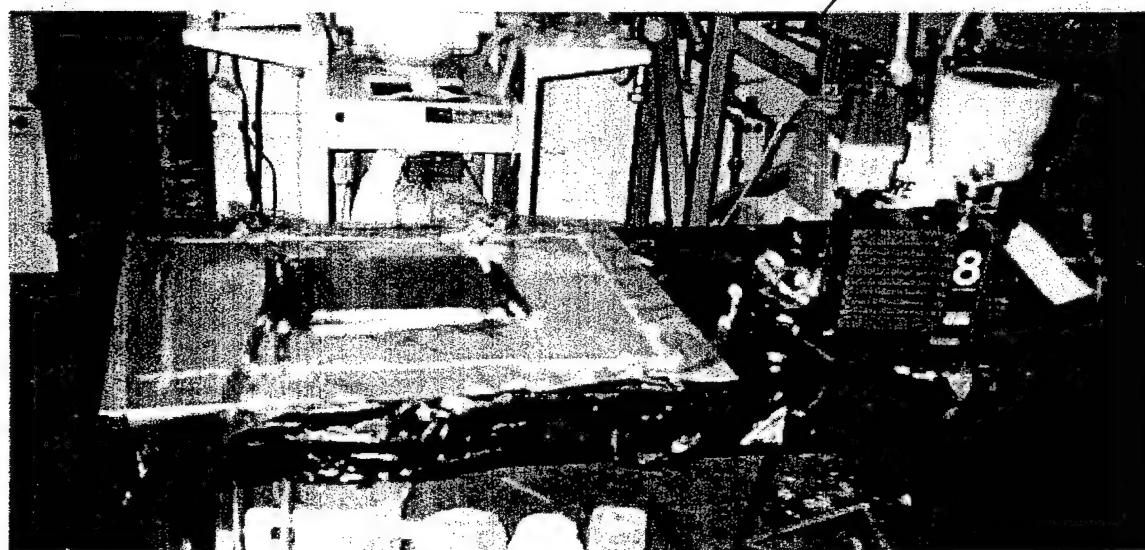


Figure. 5.9 a,b,c . Typical Vacuum Assisted Resin Transfer Molding : Co-Injection of Top and Bottom Facesheets

The part was debulked under vacuum for two hours, prior to the resin injection. Vinyl ester 350 resin with CoNap promoter, MEKP catalyst and DMA accelerator was infused through the top and bottom facesheet preforms through simultaneous co-injection. The in-plane and transverse fill time for the two sides was approximately twelve minutes for a 14" x 14" (355mm X 355mm) panel, as the resin wets the preform. The part was maintained under vacuum until full cure occurred. The resulting panel was trimmed to yield 101.6 x 101.6 mm pieces for low velocity impact testing. Similar procedure was adopted in making sandwich laminates with S2-glass/vinyl ester facesheets as well. The ratio between the facesheet-to-core thickness was maintained at 0.375 for both the



Figure 5.10 a and b. Co-Injection of Sandwich Composite Panels

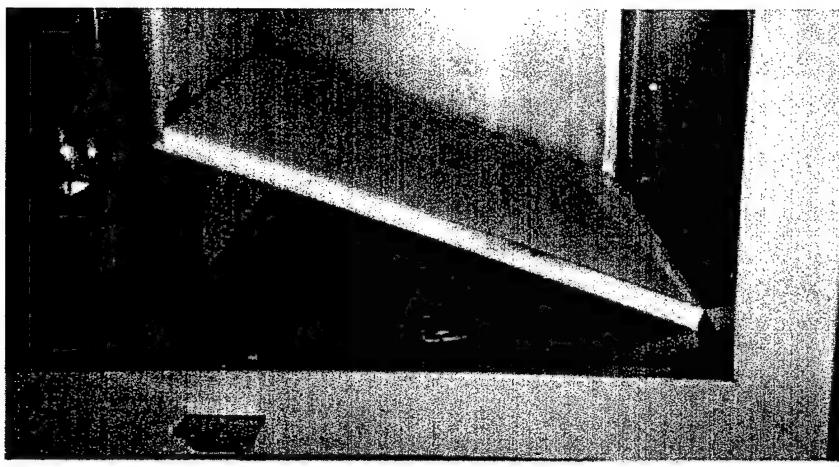
graphite/vinyl ester and glass/vinyl ester facesheet composites. The results of tests from these samples are presented in Chapter 7.

5.3.4 Fabrication of Foam, Pin-reinforced Foam & Hollow Z-Pin Truss Core Sandwich Composites using Vacuum Assisted Compression Molding

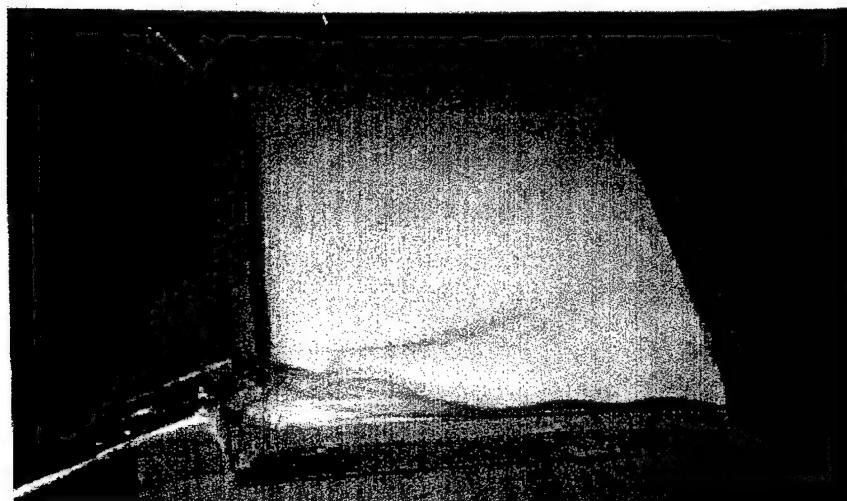
Three identical glass/epoxy facesheet configurations were adopted in manufacturing the foam, pin-reinforced foam and hollow Z-pin truss core sandwich composites. In the absence of any studies with baseline pre-preg based facesheets on z-pin core or pin-reinforced core composites, it was decided to manufacture specimens with the pin concept first using pre-pregs to bond to the core. These were manufactured from the VACM technique described in Section 5.2.3. These results are presented in Chapter 8. Following studies from these specimens, and detailed observations of their impact and static response, RTM and VARTM specimens were manufactured with foam core and pin-reinforced foam cores as described in Section 5.3.2. The results from these specimens are presented in the latter part of Chapter 8.

Manufacturing of Foam Core Sandwich Composites (VACM)

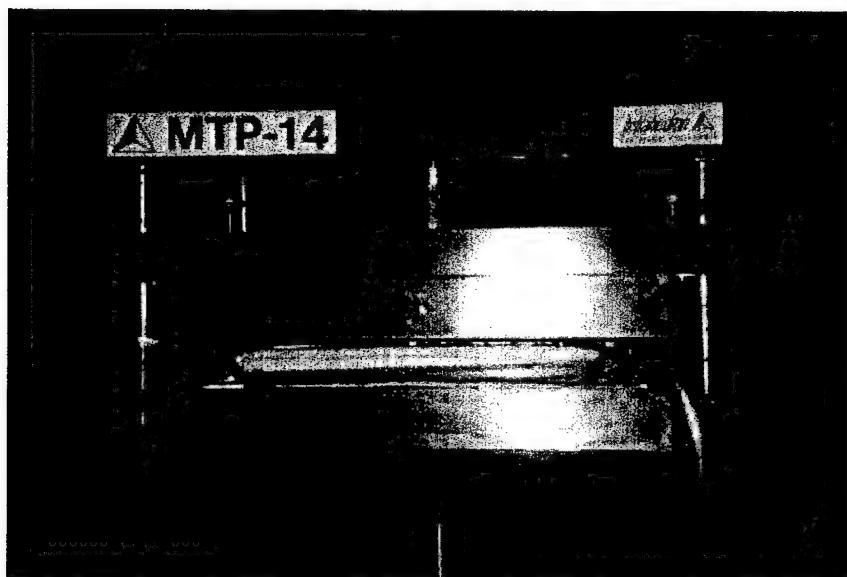
The IG-71 grade Rohacell foam was pretreated (stabilized) according to the manufacturer's recommendation to 250 degree F in an oven for four hours. An adhesive film CYTEC - FM 71 was used between the core and the top facesheet preform as well as the core and bottom facesheet preform. The Rohacell foam was sandwiched between the adhesive layers and sixteen layers of cross-ply E-glass/epoxy scotchply pre-preg tape facesheets on either side. A teflon layer and a thin bleeder were placed on either side of the lay-up, which was then placed on an aluminum caul plate and bagged in a vacuum bag just as in the case of the co-injection process explained earlier. The lay-up was debulked for one hour and subjected to compression molding (under vacuum) as follows. The platens on the compression mold were preheated to 285⁰ F with the specimen and then an average pressure of 35 psi was applied. The details of the fabrication are illustrated in Figs. 5.11a-c. The temperature and pressure were maintained for 100 minutes. The impact test samples were then cut from the finished panel. The areal density of Rohacell foam-core with the E-glass/epoxy facesheet was 1.41 gm/cm².



(a) Stabilization
of Foam



(b) Compression
and Curing



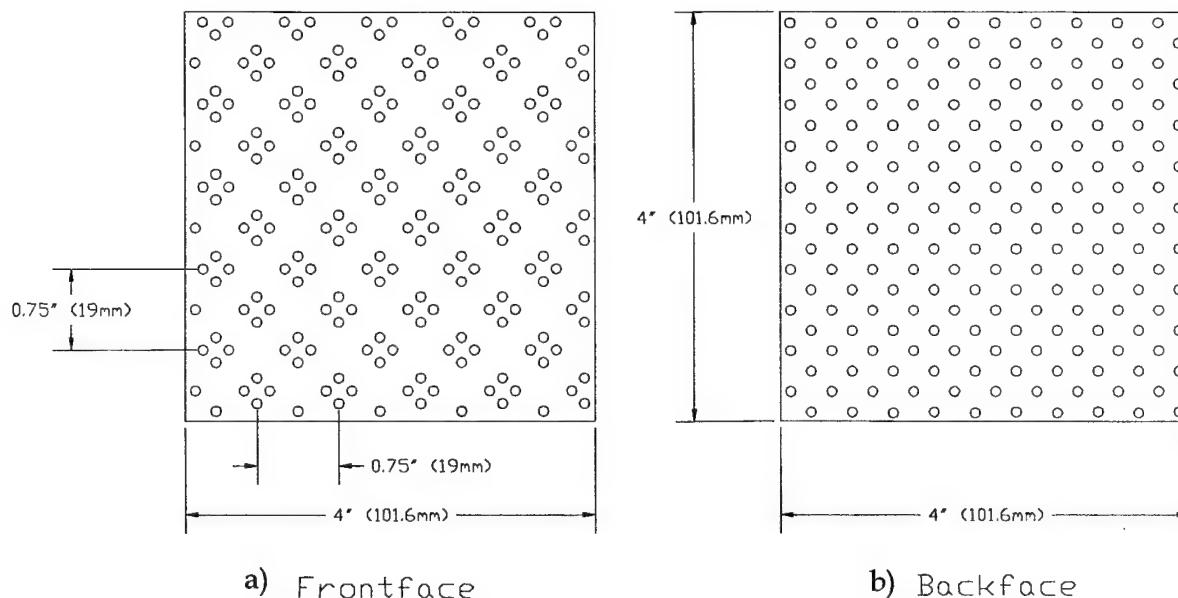
(c) Lay-up

Figure 5.11a, b, and c. Photographs of Manufacturing of Foam Core Sandwich composites

5.3.5 Fabrication of Foam-Reinforced-Pin Core Sandwich Composites (Vacuum Assisted Compression Molding)

The IG-71 Grade Rohacell foam was pretreated as indicated earlier. Titanium, E-glass/epoxy and steel pins were carefully cut from their respective wires to pin sizes. Table 1-3 provides details of the pins. A plexiglass (transparent) template with the exact tolerance to accommodate the pins was used. The pins were precisely placed into the foam core through the plexiglass template. Hence, the angle as well as spacing of the pins was maintained accurately. The orientation of the pins was also kept constant as shown in Fig. 5.12a and b. with respect to the horizontal, by the use of the template. Sufficient tolerance was provided so that the pin length equivalent to the facesheet thickness would protrude out of the foam core. The core with the pins was sandwiched between the facesheet preps. The lay-up was then vacuum bagged and then cured as

Total No of Pins = 200

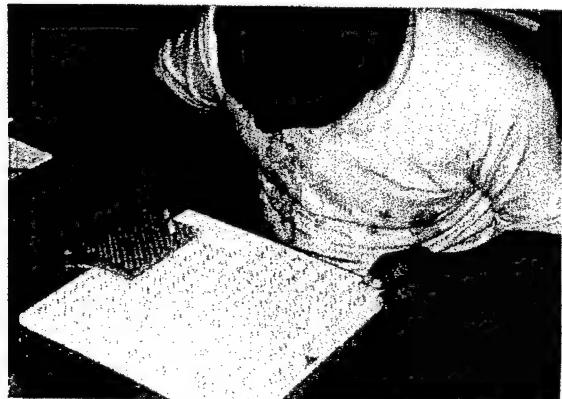


Angle of Inclination $\sim 10^\circ$
Figure 5.12 a and b. Pin Spacing and Arrangement Within Foam Core

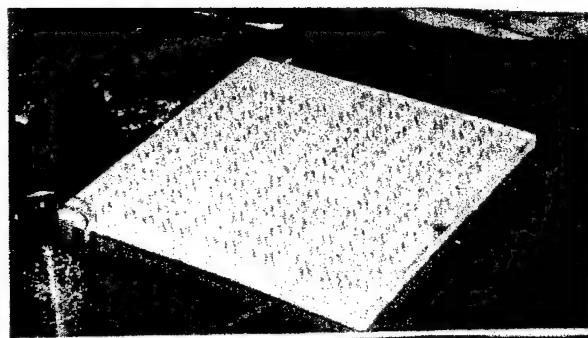
described earlier. The details of the fabrication are illustrated in Figs. 5.13a-e. The areal density of the titanium pin reinforced foam core composite was 1.47 gm/cm^2 .

5.3.6 Fabrication of Hollow Pin Core Sandwich Composites (Vacuum Assisted Compression Molding)

The steps described in the foam core reinforced with pin core were identical to the point of obtaining the cured panel. The Rohacell panel was then released from the core using a combination of mechanical as well as chemical release procedures. Some



a) Preparation of Titanium Pin
Reinforced Rohacell Foam Core. Pins
are guided at specific angles through
Plexiglass Mold

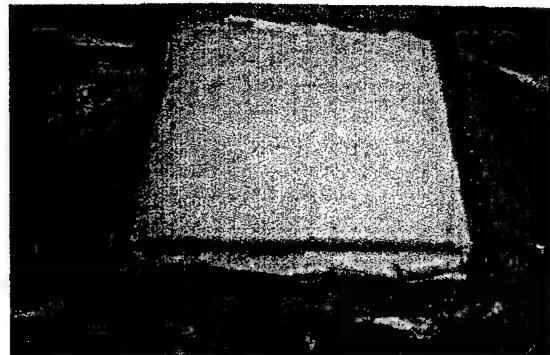


b) Titanium Pin Reinforced Rohacell
Foam Core : Completed Core
Construction

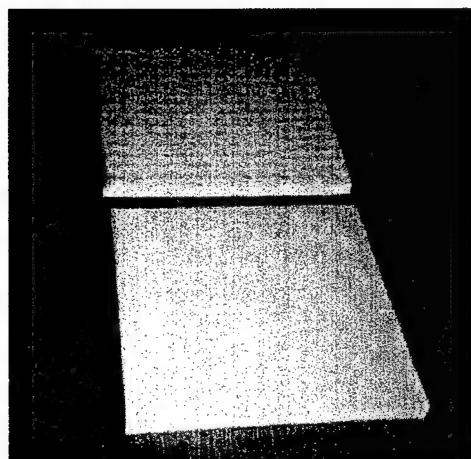


c) Titanium Pin Reinforced Rohacell
Foam Core with Facesheets Bonded to
the Core Through Vacuum Assisted
Compression Molding

Figure 5.13a-e Photographs of Manufacturing of Pin-Reinforced Foam Core Sandwich Composite Samples



a) Lay-Up for Foam and Pin Reinforced Foam Core and Facesheets



b) Foam and Pin Reinforced Foam Core Sandwich Panels

Figure 5.13d and e. Photographs of Manufacturing of Foam and Pin-Reinforced Foam Core Sandwich Composite Samples (Continued).

residue of the foam remained on the pins, however, it was evident that the core would not participate in the load sharing/shedding process during the impact event. The areal density of the hollow core titanium pin reinforced composite was 1.42 gm/cm².

5.4 References

1. Karlsson, K.F., and Astrom, B.T. "Manufacturing and Applications of Structural Sandwich Components," Composites, Part A, Elsevier Publications, pp. 97-111, 1997.
2. Zenkert, D. "The Handbook of Sandwich Construction," Engineering Materials Advisory Services Ltd., Chameleon Press Ltd., London, United Kingdom, 1997.

6.0 IMPACT TESTING

6.1 Introduction

In view of the importance of the low velocity impact phenomenon, it is essential to test the composites for their behavior when they are subjected to the same. Hence the testing procedure becomes extremely important because of the fact that it should give an accurate acquisition of data over the entire time period of the event but at the same time, it should not be too complicated in its utility. Increasing use is being made of instrumented impact testing in conjunction with drop-weight or pendulum type configurations where the supports or striker are instrumented to measure the applied load [1,2]. A representative specimen is then subjected to a typical impact that might be experienced during service.

6.2 Pendulum Impact Test System

The pendulum test system involves a tup which swings at a fulcrum and the specimen is placed at the bottom of the pendulum swing. It is a very accurate method for testing as the impact velocity is measured at the bottom of the pendulum swing (when the tup acceleration is zero) and is hence very accurate. However, control of the pendulum is not automated and to control the energy of impact, the user must calculate the swing length as:

$$\text{swing length} = [\text{drop height} \times (2 \times \text{string vertical length} - \text{drop height})]^{1/2}$$

The pendulum impact tester is particularly of importance for very low energy levels (<1J). In our case, we were interested in energy levels of 10J and onwards. Moreover, the possibility of off-axis motion renders the testing procedure as error-prone and hence, the drop weight was used for the testing of the samples under study.

6.3 Drop Weight Impact Test System

The drop weight impact test system involves a simple procedure of dropping a fixed weight from a pre-determined height. The energy of impact is calculated using the relation,

$$E = mgh, \text{ where } E = \text{Energy of impact}$$

m = mass falling down

g = acceleration due to gravity

h = height through which the weight falls

The velocity at the point of impact can be found by assuming that at the point of impact, all the potential energy is converted to kinetic energy. Hence,

$$E = 0.5 \times m \times v^2, \text{ where } v = \text{velocity of impact}$$

The drop weight impact system has a drawback due to the fact that the impact velocity is not measured when the acceleration is zero. In fact the acceleration is constant throughout the drop. Thus any small variability in the measurement of the location of the velocity detector has a significantly greater effect on the velocity calculations.

Hence, the Dynatup Drop Weight Impact Test System was used to test the samples mentioned in this text [3]. To avoid any variation in the testing parameters, the tup and the mass of the impacting hammer were kept constant throughout the tests and the energy of impact was varied by merely varying the drop height [4].

The Dynatup consists of an instrumented tup mounted on a hammer with variable weight which slides along two stiff guide rails. The specimen to be tested is clamped in a fixture at the base. The tup has a velocity sensor attached to it.

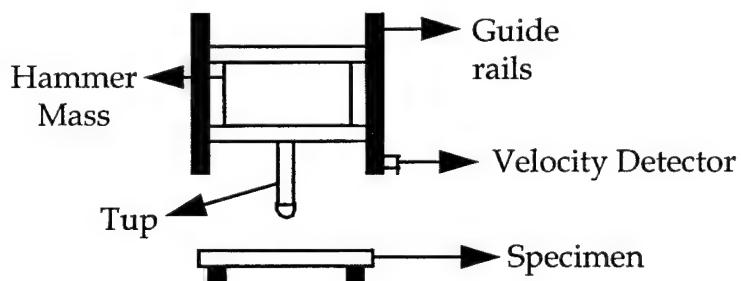


Figure 6.1 Schematic of a Dynatup Drop Weight Test System

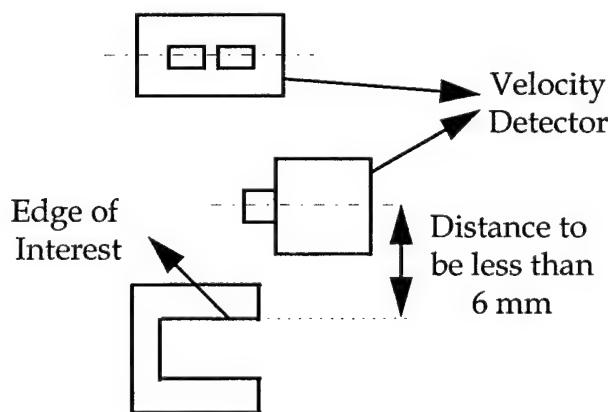


Figure 6.2 Adjustment of Velocity Detector and Flag in the Drop Weight Test System

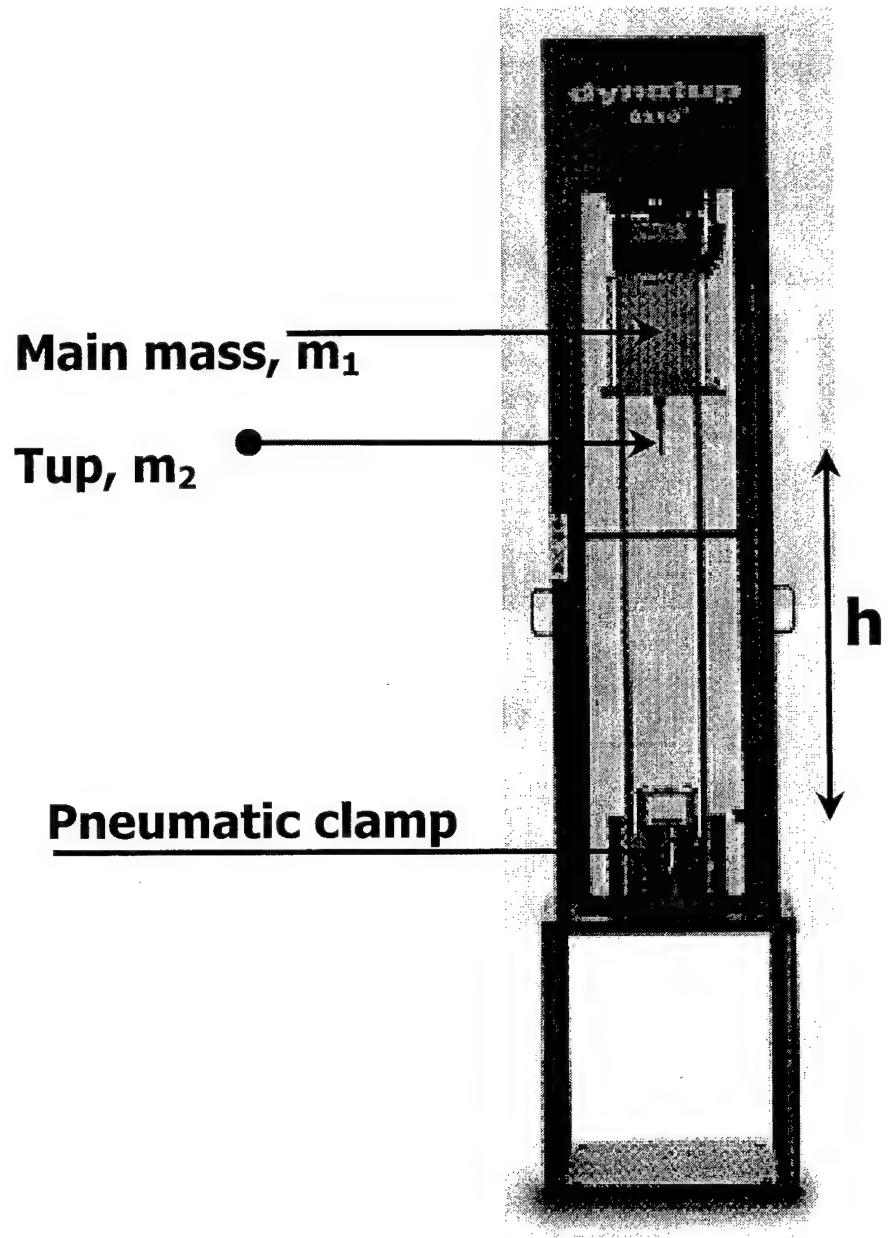


Figure 6.3. Dynatup 8210 Used for Low Velocity Impact Testing

The position of the velocity sensor is very critical and hence extreme care was taken to set the velocity detector as shown. The edge of interest should be about 6mm from the center line of the detector when the tup is just in contact with the specimen.

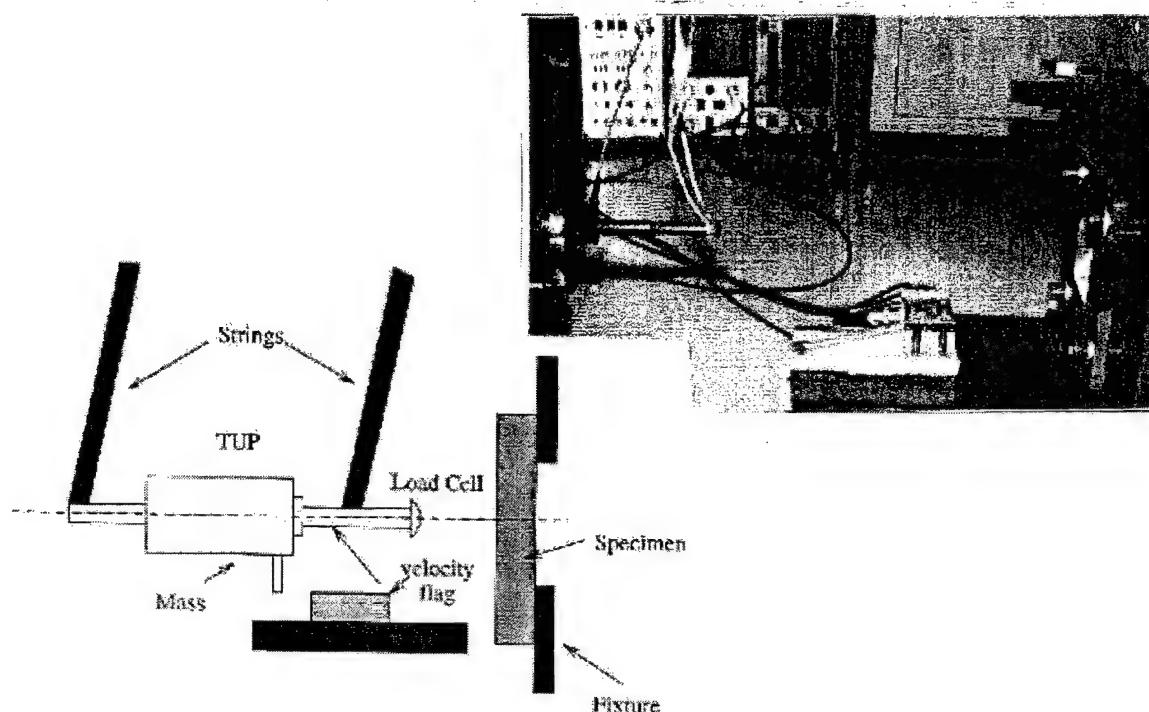


Figure 6.4 Swing Pendulum Setup for LVI of Hollow Steel Pin Core Sandwich Composites

6.4 Impact Test Results Analysis

The machines used for the impact testing have their independent means of finding out the displacement from which the load-time traces are obtained, which are then converted to give the energy-time traces. The Dynatup drop-weight impact testing machine measures the velocity and uses it to calculate the displacement and the acceleration to calculate the load. The features of the load/energy time curves such as peak loads and the absorbed energy can be related to the fracture processes occurring in the material.

Some typical load-time curves are shown in the Fig. 6.5 a & b. The change in the momentum of the projectile is represented by the impulse, that is, the area under the load-time curve. For a perfectly symmetrical curve as shown in Fig. 6.5a, there is no failure in the specimen and the second part of the curve after the peak load corresponds to the rebounding of the projectile. For a flexural failure, the curve drops down suddenly which is indicative of the fact that the projectile does not rebound and is brought to rest, with its energy causing damage to the composite. A change in the stiffness (indicated by the slope of the load-time curves) results from a shear failure and

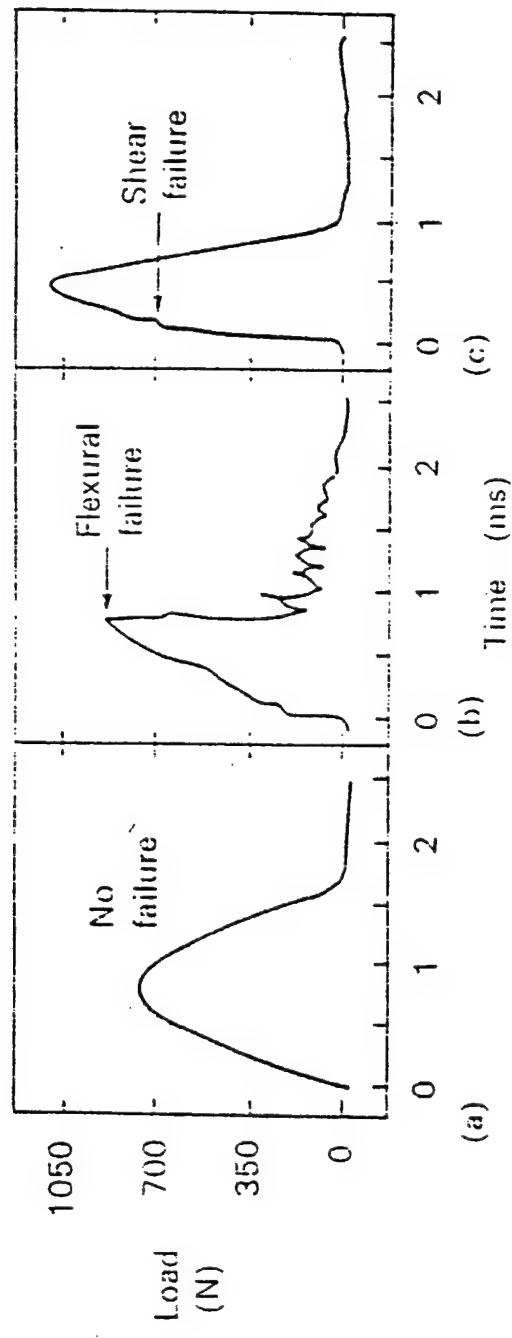


Figure 6.5 Typical Load-Time Energy History Histories

the laminate can still deflect, but the projectile rebounds back with reduced momentum. The failure process can be changed by the geometry of the specimen and the support conditions too.

6.5 References

1. ASTM Special Technical Publication, "Instrumented Impact Testing of Plastics and Composite Materials," Symposium Sponsored by ASTM Committee D-20 on Plastics, Houston, TX, March 11-12, 1985.
2. Lance, D.G., and Nettles, A.T. "Low Velocity Instrumented Impact Testing of Four New Damage Tolerant Carbon/Epoxy Composite Systems," NASA Technical Paper, No. 3029, 1990.
3. GRC International, Inc., Dynatup 8210 Drop Weight Impact Test Machine Manual, GRC Instruments, Santa Barbara, California.
4. Robinson, P., and Davies, G.A.O. "Impactor Mass and Specimen Geometry Effects in Low Velocity Impact of Laminated Composites," International Journal of Impact Engineering, Pergamon Press Ltd., Great Britain, Vol. 12, No. 2, pp. 189-207, 1992.
5. Herup, E. "Low-Velocity Impact on Composite Sandwich Plates," Ph.D. Dissertation, Air Force Institute of Technology, Dayton, Ohio, July 1996.

7.0 LOW VELOCITY IMPACT STUDIES OF FOAM-FILLED-HONEYCOMB CORE SANDWICH COMPOSITES

7.1 Summary of Work (Section 7.0)

In this study the low-velocity impact and post-impact response of low-cost resin infusion molded sandwich composites utilizing a foam filled honeycomb core with graphite and S2-glass fabric facesheets (skins) have been investigated. The foam filled honeycomb core provides combined advantages of the traditional foam core and honeycomb sandwich composites in that it possesses high shear and bending stiffness, and cell wall stability. The low velocity impact response of 101.6 mm x 101.6 mm sandwich plates is studied at five energy levels representative of damage initiation and propagation. The low velocity damage is correlated to ultrasonic C-scan images, vibration resonance frequency and optical microscopy observations. The results indicate that the damage tolerance is enhanced by the foam filled honeycomb core and that load required to initiate damage is independent of the facesheet type for any specific core/ facesheet thickness. The sandwich composites with S2-glass facesheets are found to be possess more damage tolerance as compared to the graphite/epoxy facesheets.

7.2 Materials and Manufacturing

Foam-filled-honeycomb core was used. The details of the core used were : Style 20, 2050R, 8 lbs/ft³, 12 mm thick (Supplier : WESKOR) with phenolic reinforced Kraft paper honeycomb filled with polyurethane foam. The facesheets adopted were a) plain weave graphite fabric, Style 4060-3 (Supplier : FMI), 5 oz.sq.yd, and plain weave S2-glass (Owens Corning, 933 sizing, Style 240SBA-D) reinforced in vinyl ester 350 (Dow Derakane) resin system. The co-injection VARTM process was adopted in manufacturing the foam-filled-honeycomb core sandwich composites. The manufacturing details including the co-injection approach for the specimens studied in this section are provided in Section 5.2.3.

The facesheet thickness in the graphite/vinyl ester, and the S2-glass/vinyl ester was kept constant at 4.5 mm. In order to achieve the 4.5 mm facesheet thickness, sixteen layers of graphite fabric (thickness of each dry fabric layer - 0.3 mm) were comparable to eight layers of S2-glass (thickness of each dry fabric layer - 0.58 mm thick) fabric. Hence, the graphite/ epoxy facesheets were constructed from sixteen plies, while the S2-glass/epoxy facesheets were constructed from eight plies.

7.3 Introduction

A 8210 Dynatup low velocity impact tester equipped with a 1600 kgs load cell was used in conducting the impact tests. The 101.6 mm x 101.6 mm plate sample was placed in the fixture and clamped from all sides using pneumatic actuation. A few dummy tests were run to establish the energy levels at which the samples could be impacted. It was determined that the threshold initiation energy should exceed 8-10 J. The force/energy-time and load-energy curves were obtained using the software accompanying the Dynatup instrument. The samples have been subjected to five impact energy levels as shown below. The energy levels have been selected so as to lead the specimen through the damage initiation to damage progression to just below catastrophic failure.

Nomenclature	Energy of Impact
A	11 J
B	20 J
C	28 J
D	33 J
E	40 J

Table 7.1 Nomenclature for Impact Levels

7.4 Low Velocity Impact Testing of Honeycomb-Filled-Foam Core Sandwich Composites with 16 ply Graphite/Vinyl Ester Facesheets

Table 7.1 represents the nomenclature adopted in identifying the impact energy levels. Typical force/energy-time curves and load-energy curves for the graphite / vinyl ester facesheet composite samples at the indicated energy levels are shown in Figs. 7.1 and 7.2. For the 4.5 mm facesheet thickness graphite samples, the load at which the damage initiation occurs was found to be 5800 N. The damage initiation load is seen to be independent of the energy levels at which the samples were impacted. A

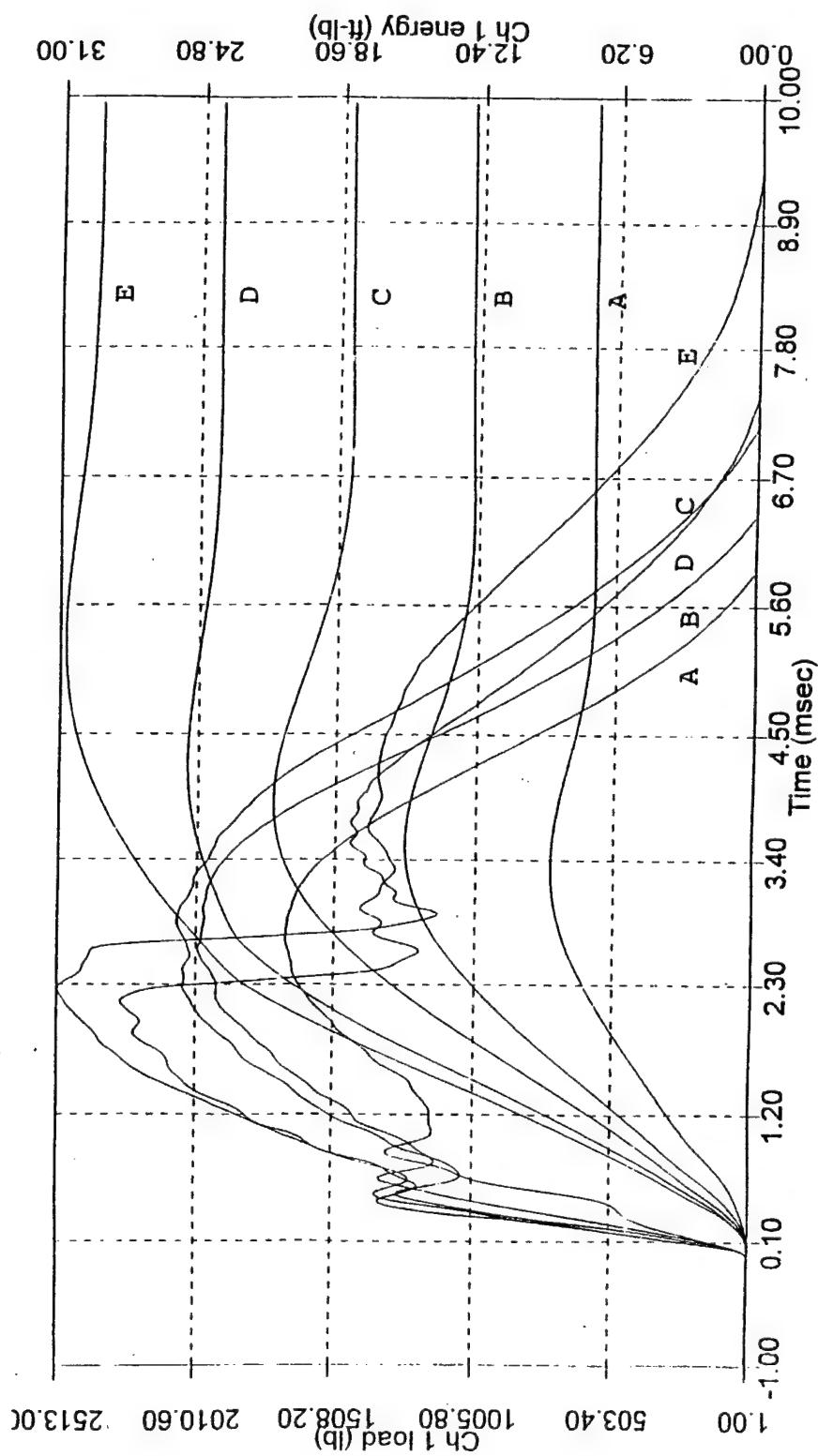


Figure 7.1. Typical Force/Energy-Time Curves for 16-ply Woven Graphite/Vinyl Ester Foam-Filled-Honeycomb Core Sandwich Composite

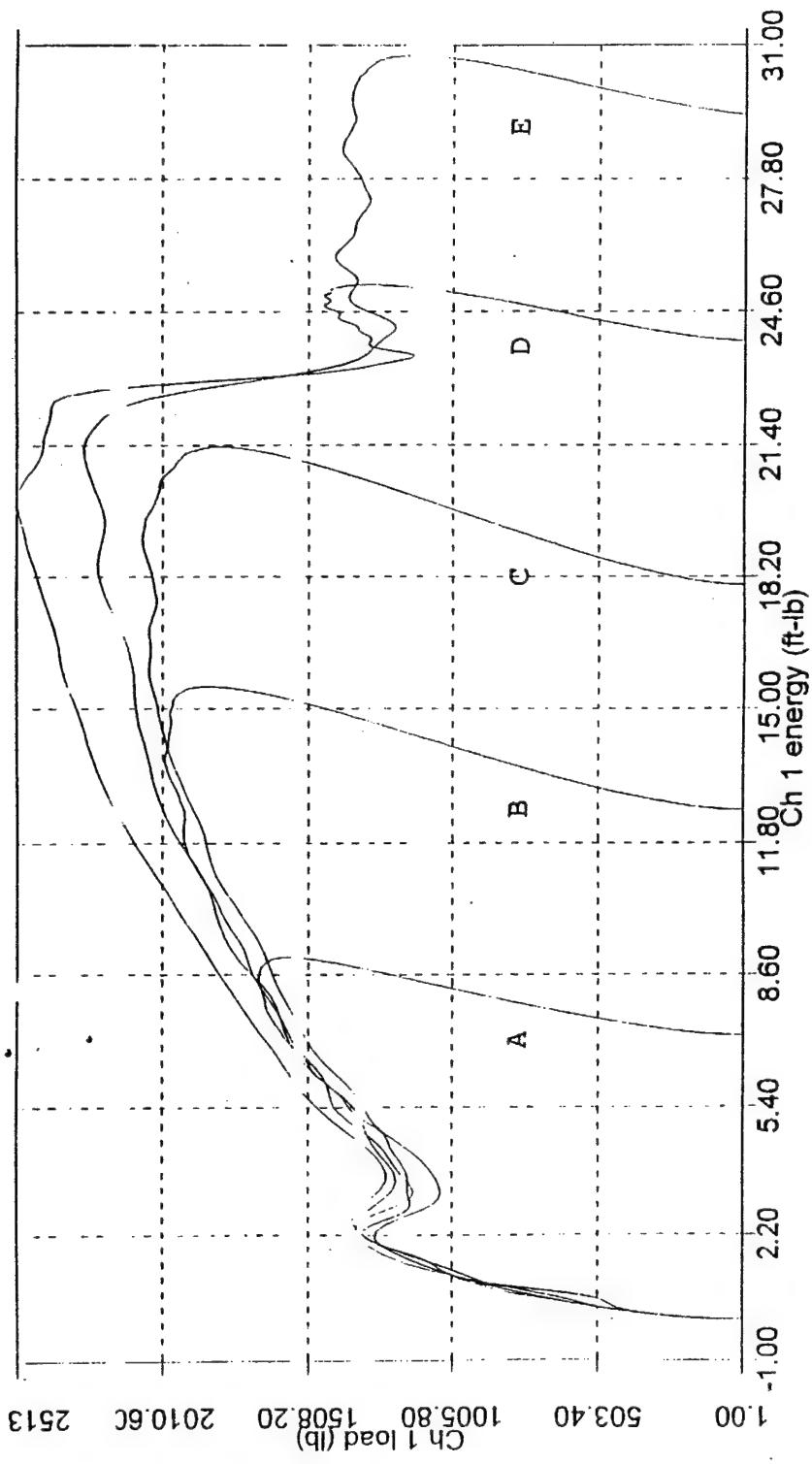


Figure 7.2. Typical Load/Energy Curves for 16-ply Woven Graphite/Vinyl Ester Foam-Filled-Honeycomb-Core Sandwich Composite

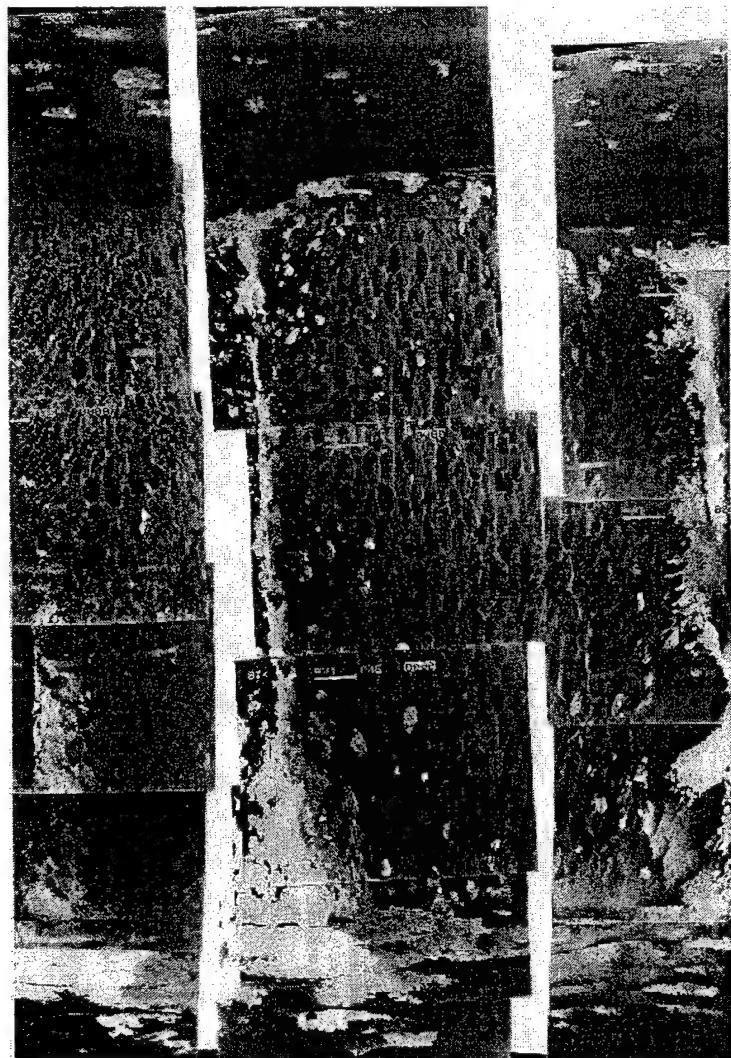


Figure 7.3 Illustration of Localized Foam Core Crushing within Pockets of Honeycomb Cells in Foam Filled Honeycomb Core Sandwich Composites

load drop was obtained at 5800 N, which corresponds to the damage initiated in the top facesheet accompanied by local cell wall crushing and localized debonding of the cell/facesheet, beyond which energy continues to be absorbed by the specimen. At energy level B, it is seen from Fig. 7.3 that damage is highly localized and limited to occurrence of core crushing and core cell wall expansion, within pockets of honeycomb cells. Figures 7.4a-b and 7.5a-b represent two predominant damage mechanisms at the facesheet and the core. Figure 7.3 shows the fiber breakage, localized delamination at the location of the impact in the facesheet and localized wrinkling of a single core cell wall just below the impact point. At lower impact energy levels; A-C these phenomena are limited to the top facesheet and the core crushing behavior only (Fig. 7.3). Figures 7.5 a&b represent the facesheet damage, and that neighboring cells around the impact

At Point of Impact



At Left of Impact



Figure 7.4. Illustration of Core Crushing, Cell Wall Microbuckling and Impact Side Facesheet Damage for Foam Filled Honeycomb Core Sandwich Composites. Note that there is no evidence of Damage in the Bottom Facesheets (Energy level C)



(a)



(b)

Figure 7.5. Illustration of Core Buckling, Foam Core Crushing, Interfacial Debonding Between Core and Cell and Impact Side Facesheet Damage in Foam Filled Honeycomb Core Sandwich Composites impacted at 33 J (Energy Level D)

location undergo cell wall buckling, and core crushing. The foam cells expand in dimension following the impact event and are seen as large black spots in the foam core in Fig.7.3. Additional damage (delamination and matrix cracking) is indicated by further load drops in the force-time curves following the initiation of damage (Figs 7.1 & 7.2). The damage is concentrated around the core and occurs by cell wall buckling, interfacial debonding between the cell wall and the foam and through cell wall expansion due to the impact event. The interfacial debonds between the cell wall and core are observed at higher energies D and E. Herup [2] reported similar observations for conventional honeycomb composites. Although the overall nature of the damage remains similar, in this work, the damage initiation energy is much higher when the cells are reinforced with foam. With reference to Figs. 7.1 and 7.2, as the energy increases from 11-40 J (impact velocity 1.3-2.4 m/s), the pulse width of the force-time curve increases from 5.8 msec to 9.5 msec. The time taken by the striker to rebound is longer as the impact energy increases from energy levels A to E. At energy levels of D and E, in addition to localized delamination in the top facesheet, and fiber breakage in the pockets of the weave, bottom facesheet delamination occurs. The top facesheet delamination is more extensive, and as can be seen in Fig. 7.5, multiple delaminations span through the weave pockets of the facesheet. The bottom facesheet failure does not exhibit delaminations as in the top facesheet, but the failure is primarily by debonding of the core-facesheet, and cracking at the backside of the facesheet as indicated in Fig.7.6. The bottom facesheet failure is identified as a second load step in the force-time history at 2.5 msec (Fig. 7.1 & 7.2), and is only evident for high energy levels of D and E. Samples A, B, and C did not exhibit bottom facesheet damage as evidenced through the force-time, load energy-history and corresponding C-scans. It appears that once the sandwich plate goes into bending under the impact load, the cells at the bottom facesheet debond at distributed locations, hence the damage zone is greater on the bottom facesheet, while it is more concentrated on the top facesheet.

The specimens were subjected to ultrasonic C-scan using a Testech immersion, type pulse-echo system with a Krautkramer USP- 12 ultrasonic pulser-receiver and a 5 MHz transducer. Each specimen was tested for back and front facesheets separately, first for the impact side, and subsequently for the back side. For the pre-impact scans, the process was found to yield uniform and satisfactory quality of the laminate. Figure 7.7 represents the damage zones at 11, 23, 28, 33 and 40 J respectively for the C-scans for the impact side facesheet of the sixteen layer graphite / vinyl ester facesheet composites. The damage zone is observed to follow the energy input into the specimen, for higher energy values, the damage zone is greater. Typically, a four lobed elliptical damage zone develops away from the impact location. The damage is limited to 2-3 cell dimensions. Bottom (opposite side to impact) facesheet scans were repeated at these energy levels as well. Only samples impacted at energy levels of D and E showed bottom facesheet damage, due to flexural failure, away from the impact zone, as shown in Fig. 7.8.

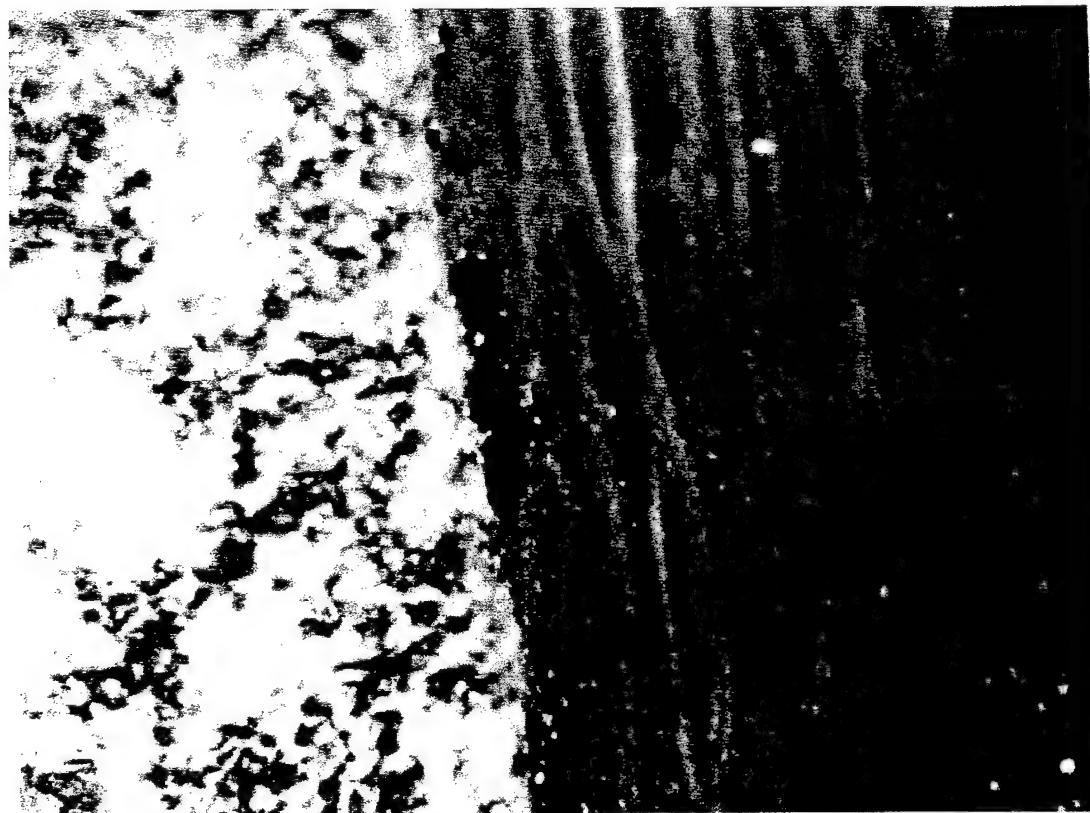


Figure 7.6. Bottom Facesheet Failure for Impact Level D
(16-Ply Graphite/Vinyl Ester Facesheets)

The specimens were also tested to investigate the global stiffness changes using a vibration based nondestructive evaluation (NDE) test following impact and/or static loading. The specimen was mounted in a near free-free boundary condition using bees wax at its geometric center on an impedance head connected to an electrodynamic shaker Brüel & Kjaer 4810 excited using random noise. The input force and output acceleration signals from the impedance head were fed to a dual channel frequency analyzer B&K 2032. The frequency response function (FRF) of the specimens under predominantly bending vibrations were recorded. The vibration based nondestructive evaluation (NDE) testing (Fig. 7.9) was performed on the specimens "before" and "after" impact testing as well. Figure 7.10 represents the frequency response function (FRF) of the sample impacted at the A energy level over a frequency range 0 - 25,000 Hz. The characteristic bending modes may be observed from the figure. It is seen that the first few modes are identical for both the top facesheet vs bottom facesheet facing the impedance head. The higher modes including the fifth, sixth and seventh mode show a higher stiffness loss (lowering of resonance frequencies) for the top facesheet facing the impedance head as compared to the bottom facesheet. This indicates that only certain mode shapes are affected by the presence of the damage. The low density core tends to isolate the two facesheets as separate laminates, and the vibration response is more sensitive to the facesheet mounted on the impedance head. The same

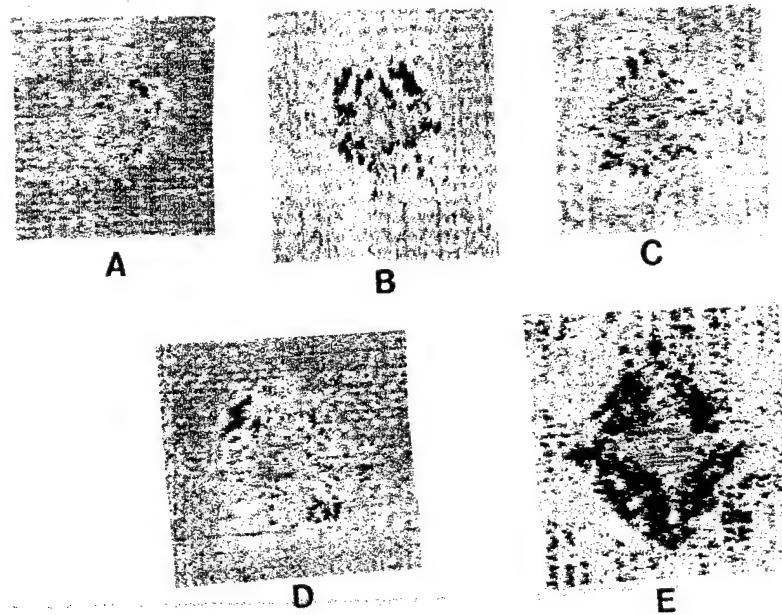


Figure 7.7 Ultrasonic C-scans for Impact Side of Graphite/Epoxy Facesheet and Foam Filled Honeycomb Core Sandwich Composites Impacted at Energy Levels A-E

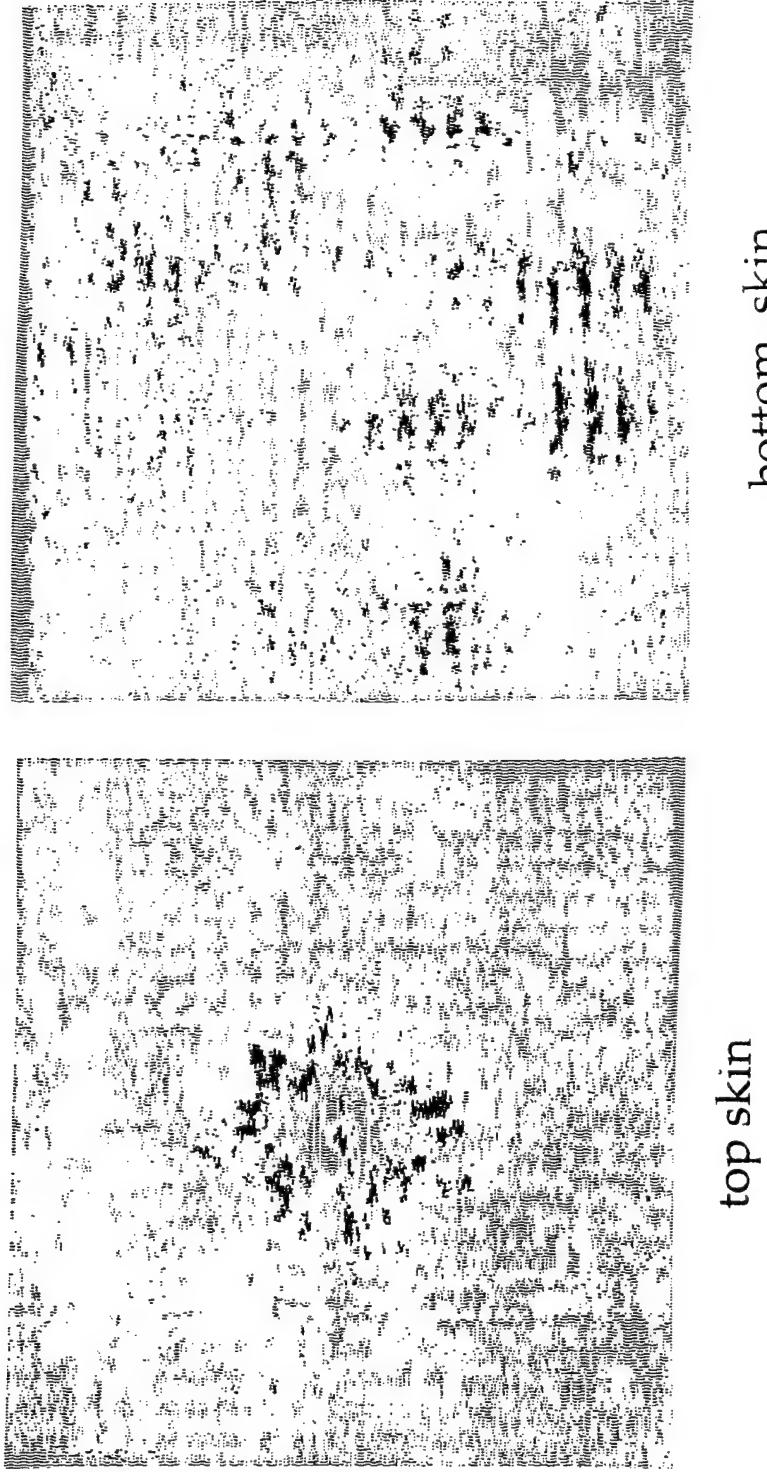


Figure 7.8. Ultrasonic C-scan showing Distributed Back Skin Damage for Impact Level D (16-ply Graphite/Vinyl Ester Facesheets)



Figure 7.9 Photograph of Vibration NDE Setup

trend was observed for all specimen energy levels A through E. Figure 7.11. shows the response of the E energy level. Figure 7.12 represents the comparison of the FRF for an A energy level vs E energy level impacted specimen. As seen in the C-scans, the larger damage zone for the E energy level sample is reflected very well in the vibration FRFs. The resonance frequencies obtained for the E level sample are much lower for all the observed modes, as can be clearly seen from Fig. 7.12.

7.5 Low Velocity Impact Testing of Honeycomb-Filled-Foam Core with 8-ply S2 Glass/Vinyl Ester Facesheets

Figures 7.13 and 7.14 represent the force/energy-time curves for the S2-glass facesheet composites impacted at the same energy levels. Interestingly, the load at which damage initiation occurred in the S2-glass facesheet sandwich composites was also found to be 5800 N (similar to that observed in samples with graphite fabric facesheets), indicating that the first damage is most likely the localized cell wall buckling/ crushing, accompanied by the localized interfacial debond of the core-facesheet wall for the specific ratio of facesheet/core thickness. As stated before, the thickness was maintained at 4.5 mm for both the graphite as well as S2-glass fabric facesheets. Figures 7.15 - a and b represent the micrographs for the A level tested S2-glass fabric composite. The dominant mode of failure is seen to be core crushing, core wall expansion and cracking between core cells. These composites do not show

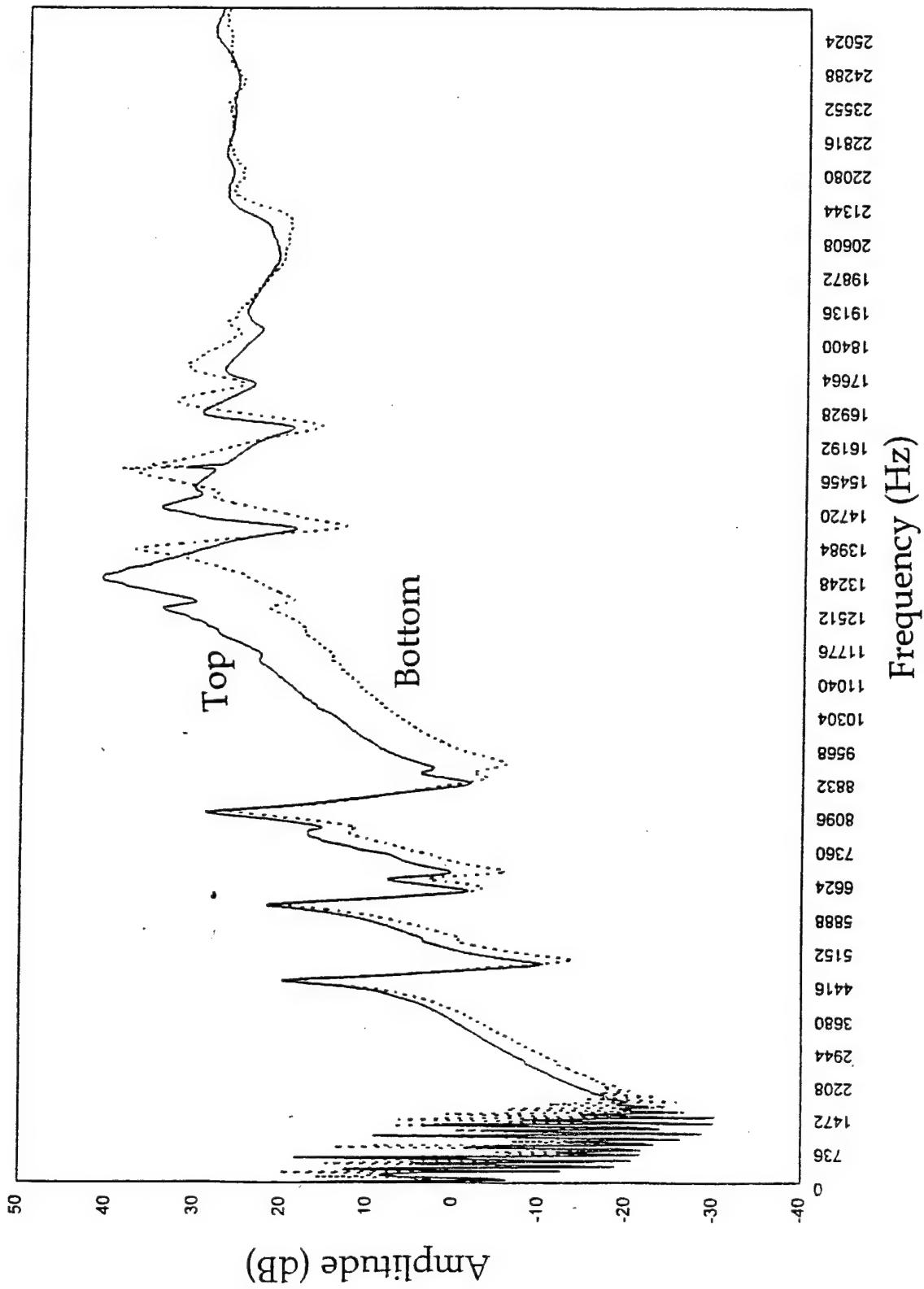


Figure 7.10. Vibration FRF for sample impacted at Energy Level A (16-ply Graphite/Vinyl Ester Facesheets)

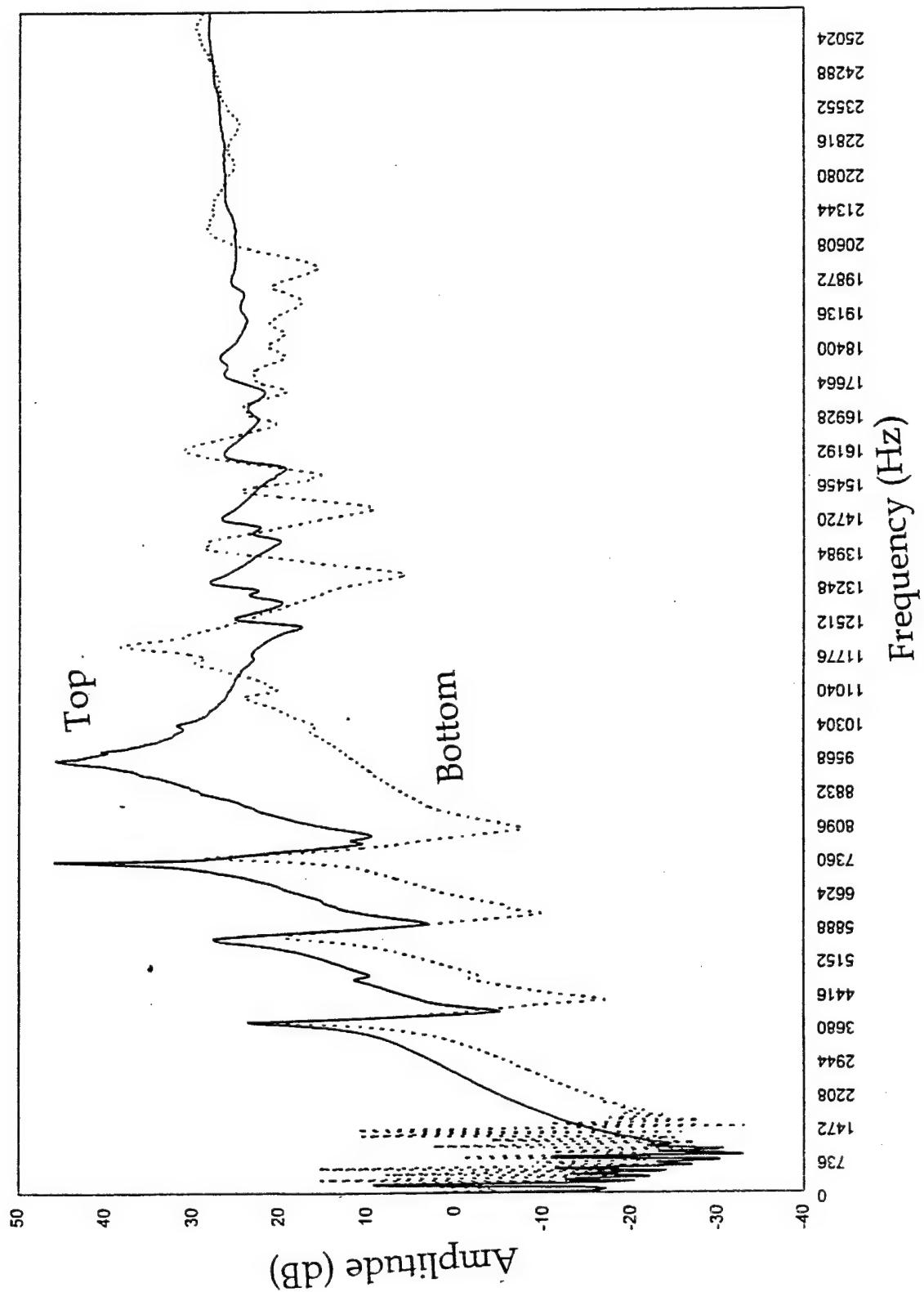


Figure 7.11. Vibration FRF for sample impacted at Energy Level E (16-ply
Graphite/Vinyl Ester Facesheets)

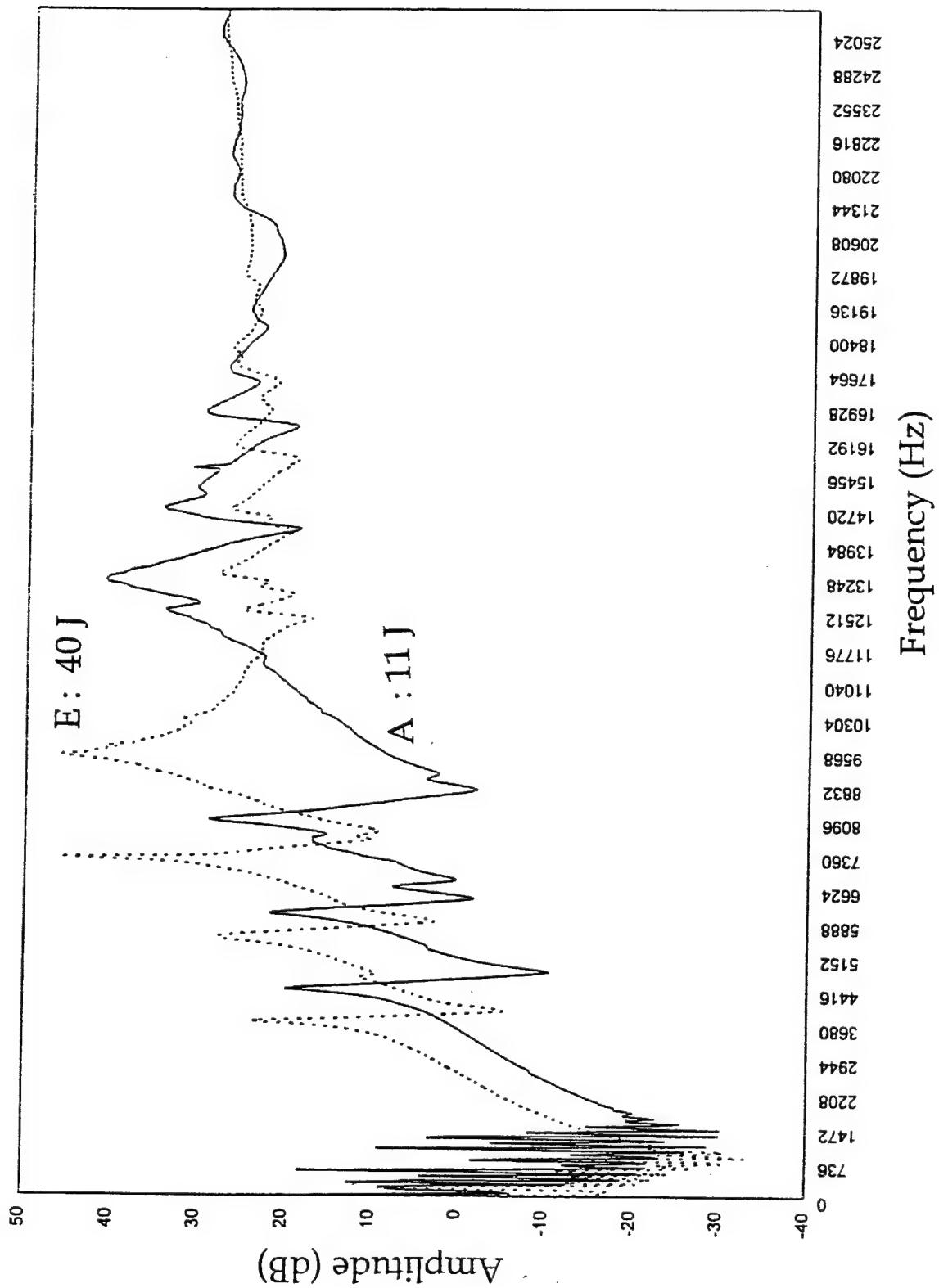


Figure 7.12. Comparison of FRF of A and E Energy Level Impacted samples (16-ply Graphite/Vinyl Ester Facesheets)

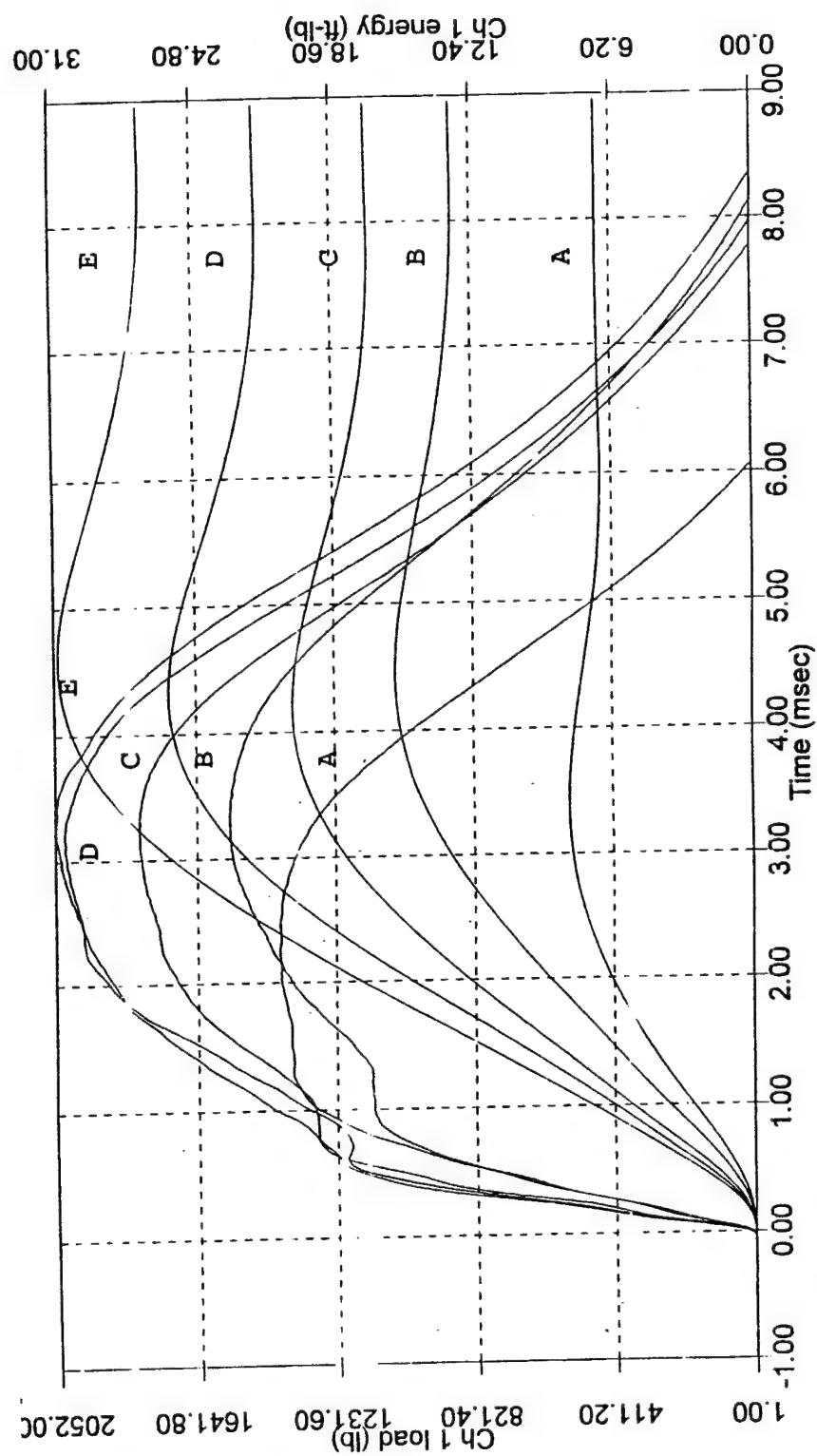


Figure 7.13. Typical Load/Energy-Time Curves for 8-ply S2 Glass Vinyl Ester Honeycomb filled foam core sandwich composite

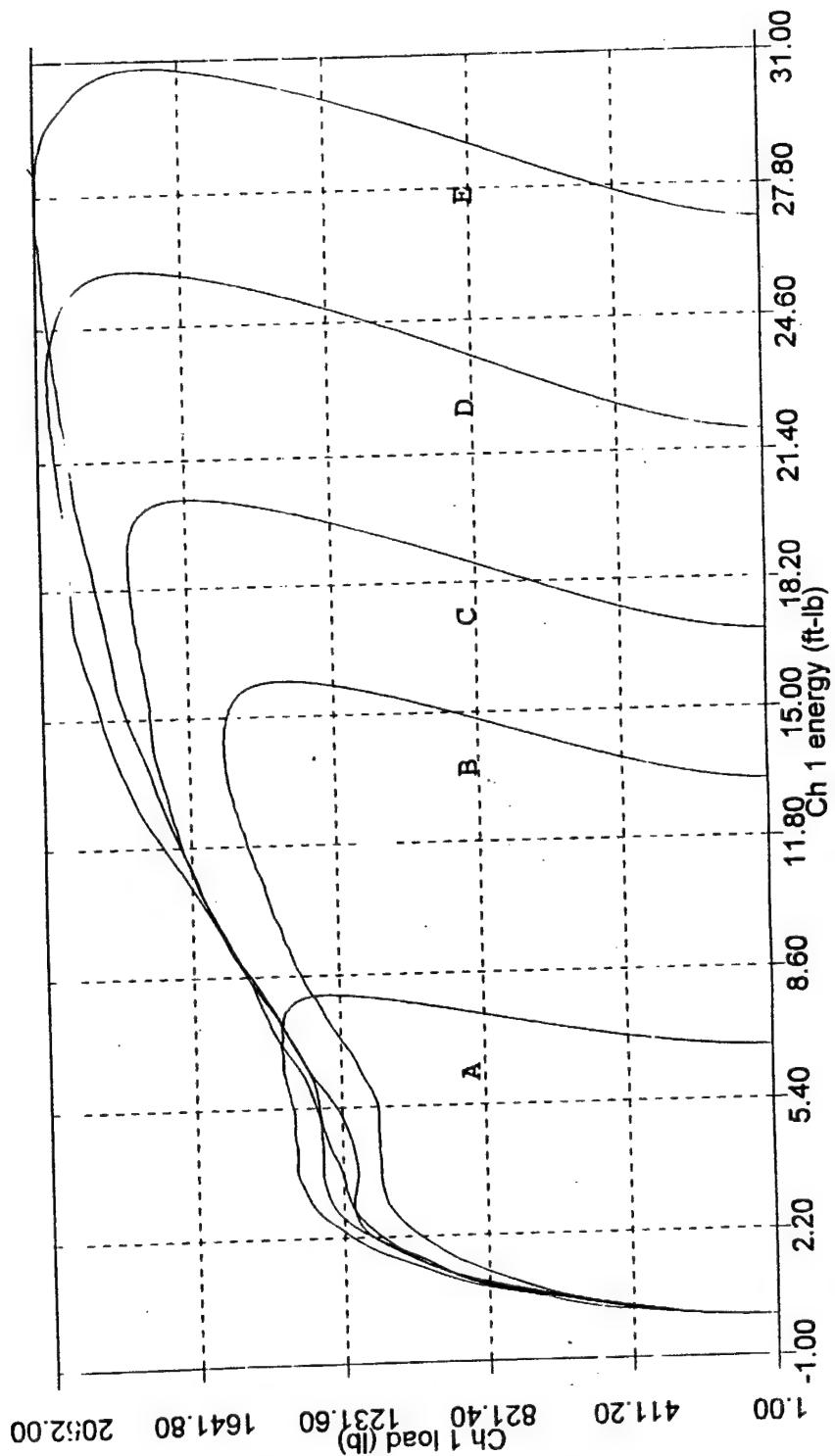
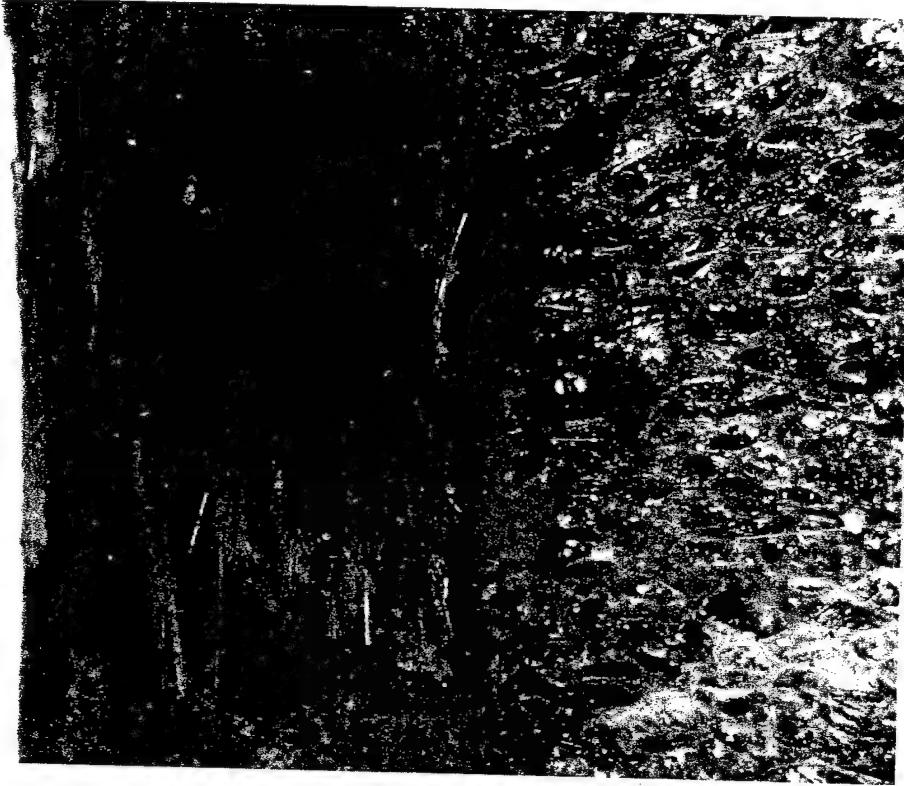


Figure 7.14. Typical Load-Energy Curves for 8-ply S2 Glass Vinyl Ester Honeycomb filled foam core sandwich composite

Figure 7.15a-b. Top Facesheet and core damage at impact level A (8-ply
Glass/Vinyl Ester Facesheets)



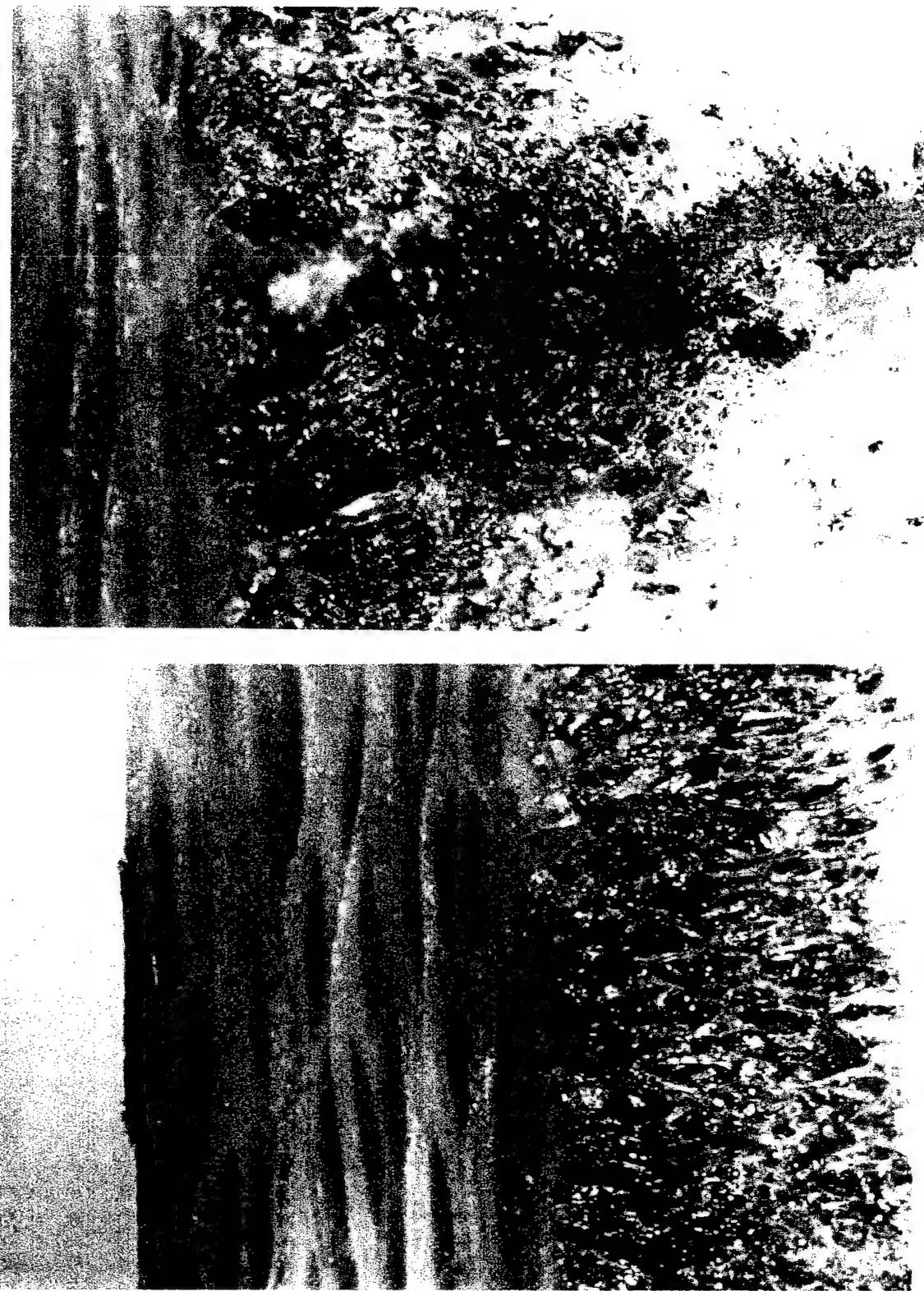


Figure 7.16a-b. Top Facesheet and core damage for impact level D (8-ply Glass/Vinyl Ester Facesheets)

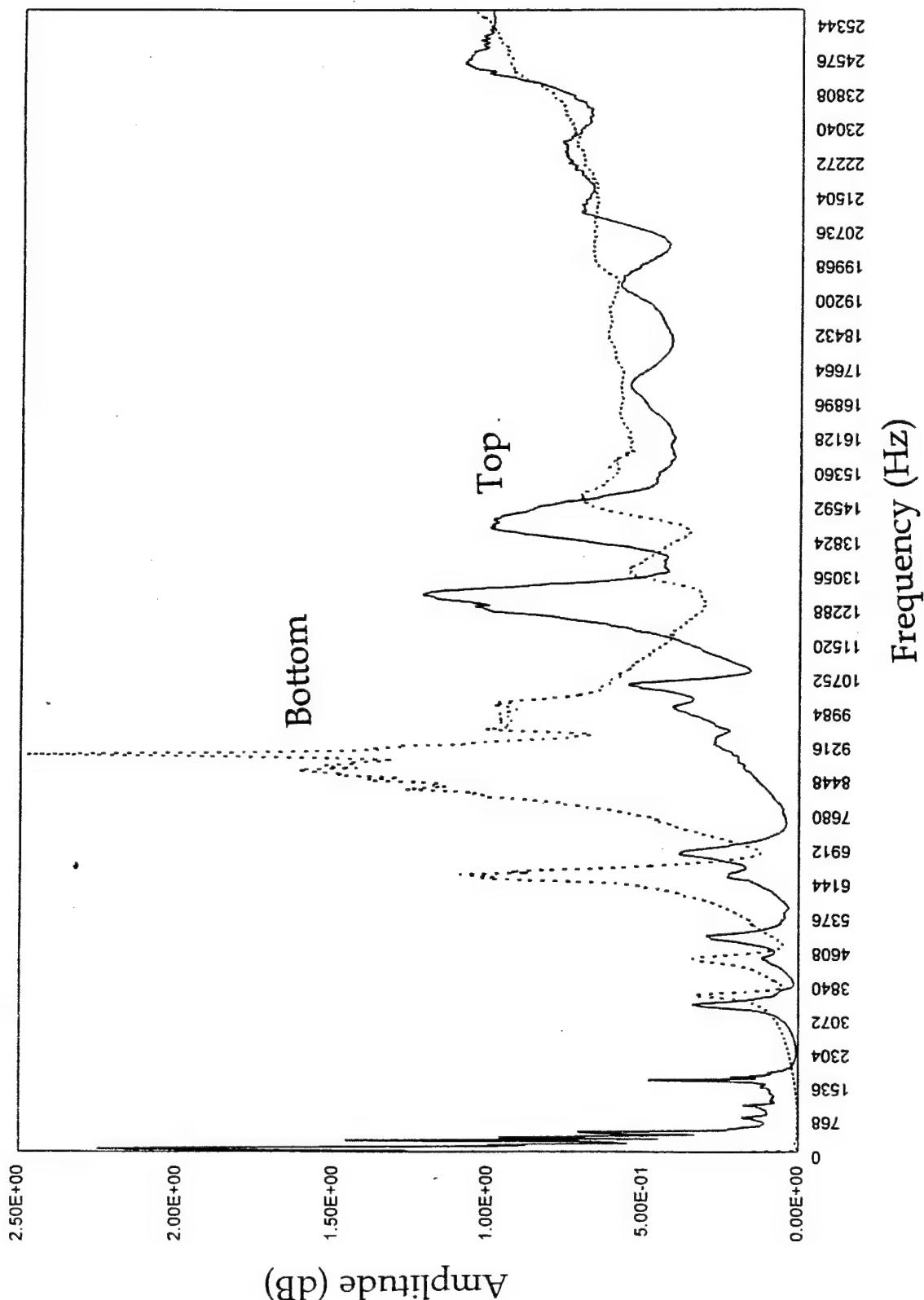


Figure 7.17. Vibration FRF for sample Impacted at Energy level A (8-ply Glass/Vinyl Ester Facesheets)

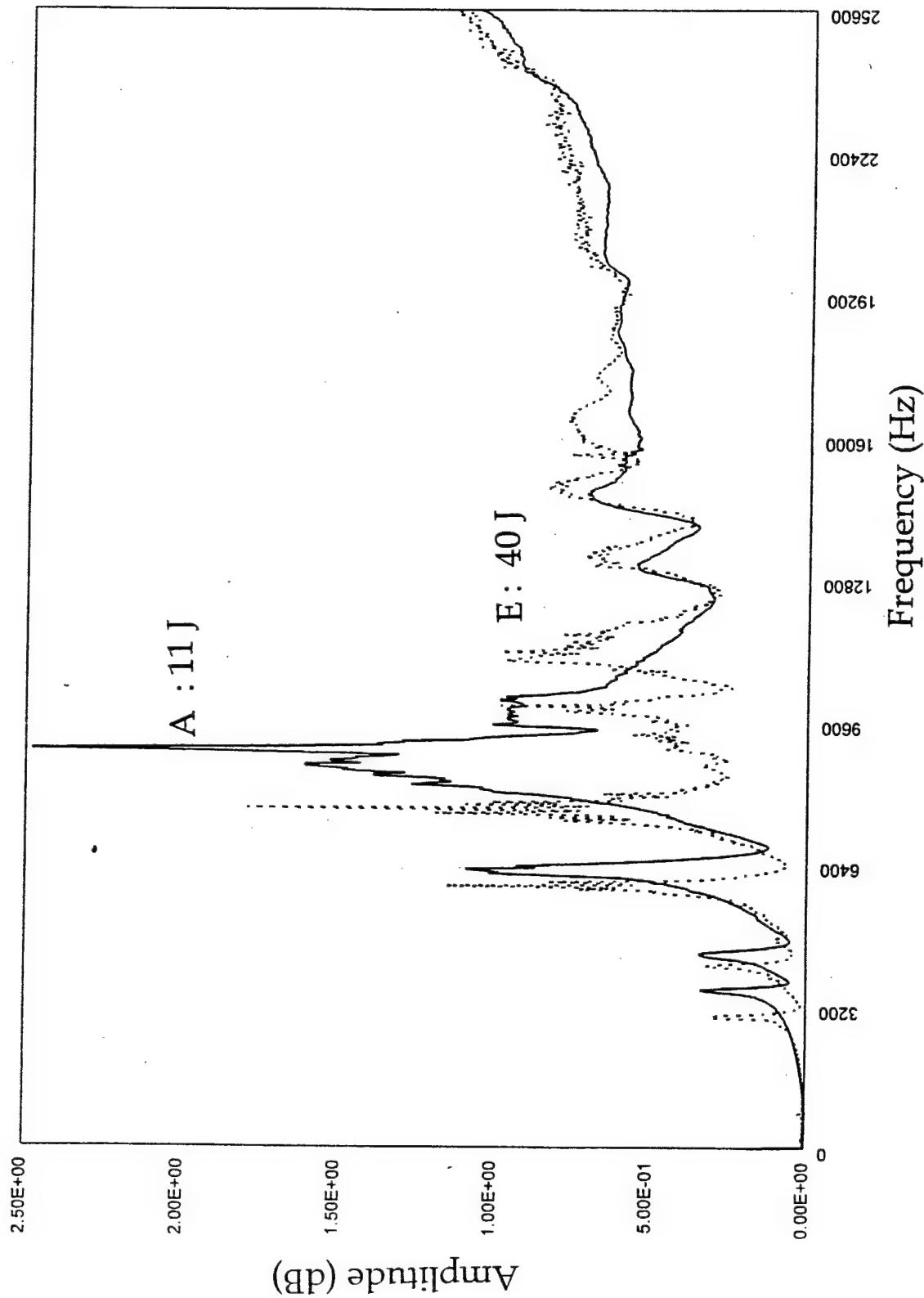


Figure 7.18. Comparison of FRF of A and E Energy level Impacted samples (8-ply Glass/Vinyl Ester Facesheets)

evidence of localized facesheet damage/delamination as observed in the graphite fabric facesheets. Figures 7.16 a&b represent the failure progression for energy level D. Here it may be noted that damage is still contained within the cell walls, however, honeycomb wall buckling is additionally observed. The damage initiation load of 5800 N was independent of the energy levels and facesheet type at which the samples were impacted. As the energy increases from 11-40 J, the pulse width of the force-time curve increases from 6.0 msec to 8.5 msec. This indicates that the time taken by the striker to rebound is longer as the impact energy increases. The S2-glass fabric facesheet composites did not exhibit any bottom facesheet failure, as can be evidenced from both the load - energy curve and force/energy - time curves.

Figure 7.17 represents the FRF obtained from the top and bottom facesheet facing the impedance head. As observed in case of the graphite facesheet composites, the stiffness loss in the vicinity of the top sheet was greater than for the bottom facesheet. In the glass facesheet composites, the damage was primarily at the interface between the facesheet and the core, and this is well represented by higher reduction of frequencies than at the bottom facesheet side. Fig. 7.18 compares the A impact energy level specimens vs the E impact energy level specimens. The E energy level impacted samples show 15-20% reduction of resonance frequencies as a result of the difference in impact damage zones.

7.6 Influence of Facesheet Thickness

The influence of facesheet thickness was studied by comparing the low velocity response of pure core (foam filled honeycomb) and a four layer (as compared to a sixteen layer used earlier) graphite/vinyl ester facesheet composite with the previous set of specimens and is shown in Fig. 7.19. The pure core exhibited a peak failure load of 223 N, and the four layered graphite composite (ratio of facesheet/ core thickness : 0.1016) showed a peak failure load of 1685 N, indicating that the core damage initiates at lower loads for very thin facesheets. Furthermore, the slope of the force-time curve for the four layered graphite facesheet composite is much lower than the 16 layered facesheet, showing the higher stiffness of the latter. It is therefore, seen that the load for damage initiation is sensitive to the ratio of facesheet -to-core thickness.

7.7 CONCLUSIONS (Chapter 7)

A low-cost resin infusion molding process has been effectively adopted in developing foam filled honeycomb core sandwich composites. The damage initiation and containment mechanisms under low velocity impact for these composites are more attractive when compared to either foam or honeycomb core used alone. Within the energy levels tested, the damage in the core did not exceed past two and/or three cell

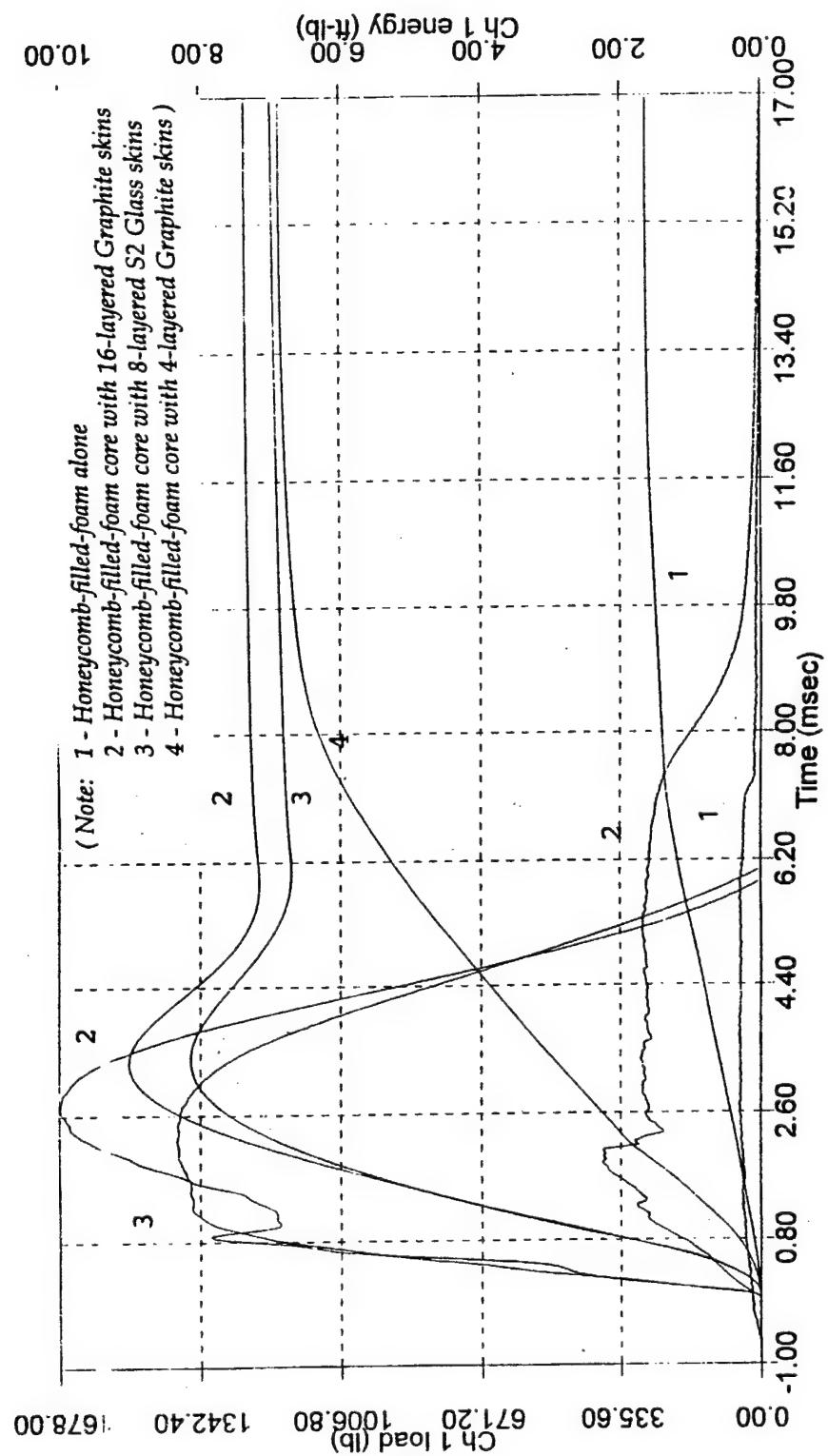


Figure 7.19. Comparison of Force/Energy-time curves of Honeycomb filled foam core, 4-ply, 16-ply Graphite/vinyl ester facesheets, and 8-ply S2 glass/vinyl ester facesheet sandwich composite

dimensions. The damage initiation load is found to depend upon the ratio of facesheet/core thickness and occurs predictably by core related effects such as core crushing, cell wall buckling and localized debonding of the facesheet and the core. Localized top facesheet damage always accompanied the core related damage events. The S2-glass fabric facesheet composites exhibit higher damage tolerance (minimal impact-side facesheet delamination) as compared to the graphite facesheet sandwich composites. The force-time and energy-time histories could accurately predict distinct steps of impact-side facesheet as well as opposite to impact side facesheet failure.

7.8 REFERENCES

1. Abrate, S. 1991. "Impact on Laminated Composite Materials," *Applied Mechanics Review*, Vol.44, No.4, April, 155-190.
2. Herup,E. 1996. "Low Velocity Impact on Composite Sandwich Plates," Ph.D. Dissertation, Air Force Institute of Technology, AFIT/DS/ENY/96-11, Dayton OH, July.
3. *Reinforced Plastics*, Dec. 1994, Vol.38, No.12, Elsevier Publishers.
4. Wu, C.L. and Sun, C.T. 1996. "Low Velocity Impact Damage in Composite Sandwich Beams," *Composite Structures*, 24, 21-27.
5. Sun. C.T and Wu. C.L., "Low Velocity Impact of Composite Sandwich Panels," Proc. 32nd AIAA/ASME/ASCE Structures, Structural Dynamics and Materials Conference, Baltimore, MD, April 1991, pp.1123-1129.
6. Weeks, C.A. and Sun, C.T. 1994. "Multi-Core Composite Laminates," *Journal of Advanced Materials*, April, 28-37.
7. Bernard. M.L., 1987, "Impact Resistance of Composite Sandwich Plates," Proc. ASC, 2nd Technical Conference, Newark, DE Sept.
8. Wu, C.L., Week,C.A and Sun, C.T. 1995. " Improving Honeycomb-Core Sandwich Structures for Impact Resistance," *Journal of Advanced Materials*, 41-47.
9. Honeycomb Sandwich Constructions : *Hexcel Corporation Technical Literature*.
10. *WESKOR Foam Filled Honeycomb*, Westwind Composites Inc., Houston, TX, Company Literature.

11. Vaidya, U.K. 1993. *Nondestructive Evaluation of Graphite Based Composites using Acoustic and Vibration Techniques.*, Ph.D Dissertation, Auburn University.
12. Mallick, P.K. 1995. *Fiber Reinforced Composites*, Marcel Dekker Inc. Second Edition.

8.0 LOW VELOCITY IMPACT STUDIES OF FOAM, Z-PIN REINFORCED FOAM AND HOLLOW Z-PIN SANDWICH COMPOSITES

8.1 Summary of Work (Section 8.0)

In this study, two configurations including a titanium pin / three-dimensional hollow truss core and foam core reinforced with titanium pins have been considered in conjunction with traditional foam core sandwich composites to enhance the impact damage tolerance, provide damage containment mechanisms and space / core accessibility advantages. The top and bottom facesheets in all three types of composites are made from sixteen layers of 3M company E-glass Scotchply prepreg stacked in crossply orientation. The low velocity impact damage tolerance of the composites is studied at five energy levels with an intention of investigating the damage initiation, damage propagation and failure mechanisms. The influence of Z-pin spacing in a foam core has also been studied at the same five energy levels for the foam core sandwich composite. Detailed microscopic inspection has been conducted to determine the impact failure characteristics of the three types of sandwich composites.

8.2 Materials and Manufacturing

The samples from this study were manufactured as described in Section 5.3.2. As stated earlier, due to lack of any previous studies on pin-reinforced samples with traditional manufacturing processes, it was necessary to undertake a series of experiments dealing with investigation of LVI studies on pre-preg based glass/epoxy facesheets with foam core, pin-reinforced foam core and hollow pin-truss core samples. The observed characteristics from these studies were then compared/contrasted with RTM/VARTM manufactured specimens. The constituent materials and configurations are provided in Table 8.1, the specimen nomenclature in Table 8.2, and additional test specimen details in Table 8.3.

The instrumentation used was the same as that used for the honeycomb-filled-foam core sandwich composites. The 8210 Dynatup drop weight impact machine was used and the nomenclature used for energy levels of impact is shown in Table 8.4.

Table 8.1. Details of Constituent Materials and Configuration

Facesheet :	E-glass, 3M Scotchply, Type 1003, 0.28 mm/ply, 16-ply 0/90 orientation
Rohacell Foam :	IG-71, Density : 0.075 gm/cm ³ , Sheet Thickness : 12.8 mm
Adhesive Film :	Metlbond 1113-36"; Amorphous Silica/Epoxy Resin, SS8612-001A, Rev.4, Type I, Class 1, Weight : 0.49 gms/cm, Cytec Engineering
Titanium Pins :	AWS- ERTi-2, Density 5.82 gm/cm ³ , Diameter 1.14 mm, Pin Length : 19.05 mm, Weight of one pin: 0.113 gms
Glass/Epoxy Pins :	NEPTCO, LLI-IC 190, E-glass/epoxy, 85% fiber by weight, 15% resin by weight, 1.9mm diameter, Tensile Strength 1.25 GPa, Modulus of Elasticity, 50 GPa, Flexural Modulus 48 GPa, Elongation at Break 2.5%
Center- to-Center Spacing between Pins for Titanium and Glass/Epoxy :	 F+PCo-75 (19.10 mm [0.75"]) F+PCo-150 (38.10 mm [1.5"])
Pin Orientation for Glass/Epoxy & Titanium:	10 degrees with respect to facesheets,
Average No. of Pins / Unit Area for titanium and glass/epoxy :	0.81 pins / sq.cm
Pin Orientation :	10 degrees with respect to the vertical

Table 8.2. Nomenclature of Samples Tested in Section 8.0

Nomenclature	Description
FCo or FCo-16	Foam Core Sandwich Composite
F+PCo-75	Foam-Reinforced-Pin Core Sandwich Composite using Titanium Pins for the Reinforcement (Center-to-Center distance between adjacent pin clusters being 0.75 in., and 16 Layers of facesheet material)
F+PCo-150	Foam-Reinforced-Pin Core Sandwich Composite using Titanium Pins for the Reinforcement (Center-to-Center distance between adjacent pin clusters being 1.5 in.)
TCo	Hollow Truss Core Sandwich Composites using Titanium Pins as Z-Pins and 16 Layers of Facesheet Material).
FCo-32	Foam Core Sandwich Composites with 32 Layers of Facesheet Material
F+PCo-75 (32)	Foam-Reinforced-Pin Core Sandwich Composite with Titanium Pins for the Reinforcement (Center-to-Center Distance between adjacent pin clusters is 0.75 in., and 32 Layers of Facesheet Material)
F+PCo-75 (Glass Pins)	Foam-Reinforced-Pin Core Sandwich Composite with Glass/Epoxy Pins for the Reinforcement (Distance between adjacent pin clusters being 0.75 in.)
FCo (RTM) and F+PCo-75 (RTM)	Foam Core and Foam-Reinforced-Pin Core Sandwich Composites Manufactured Using the RTM Technique.

Table 8.3. Sample Details

Facesheet & Core Dimensions	
No. of Facesheet Plies	16 (For FCo, F+PCo and TCo)
Facesheet Thickness	3.58 mm
No. of Facesheet Plies	32 (For FCo-32)
Facesheet Thickness	7.03 mm
Core Thickness	12.8 mm
Ratio of Facesheet/ Core Thickness	0.282 (For all three types, 16 ply)

Table 8.4 : Energy Levels at which Samples were Impacted

Impact Energy (J)	Energy Level Identity
11	A
20	B
28	C
35	D
45	E

8.3 Foam Core Sandwich Composites (FCo) :

Typical force/energy-time curves and load-energy curves for the FCo samples at energy levels A through E are shown in Figs. 8.1 and 8.2. For all the five samples, the load at which the damage initiation occurs was found to be ~3000 N as seen in Fig. 8.2. This is indicated by a characteristic drop at this load for all the samples. The sample impacted at energy level A, exhibits this load drop at this load at 3.5 msec, while the samples B through E reach this load within 1 msec. The damage initiation load is seen to be independent of the energy levels at which the samples were impacted. The load drops at ~3000 N corresponded primarily to the localized debonding of the

cell/facesheet just below the point of impact. The energy continues to be absorbed by the specimen well above the damage initiation load because of the residual energy in the tup.

The behavior of the sample at energy level A is somewhat different from that at levels B through E. The time of the event lasted 13.5 msec (the highest). The slope of the force-time curve is much lower than the remaining samples. This suggests that there is a gradual elastic deformation of the foam cells that contribute to the larger time of the impact event (larger response time). At the damage initiation load (~3000 N) onset of local debond between the localized facesheet/core effects release of energy/load (load shedding). This is also observed from the load-deflection curve shown in Fig. 8.3.

For the remaining samples, the slope of the curve increases slightly with increasing impact energies and this occurs within 1 msec suggesting that the foam undergoes instant cell wall closure and thereby stiffening. For impact events B, C and D, the time of the impact event is within close range (10 msec - 11.5 msec). The damage in these samples continue to exhibit the characteristics of the localized debond initiation and small growth of the debond in the vicinity of the impact location. There is little evidence of facesheet damage in these samples, either on the impact side or the backside facesheet. The residual deflection of the sample exhibits an increase with increase in energy levels B through D as seen from Fig. 8.3 (5 mm - 8.8 mm).

For the sample impacted at E, there is a further change in response. First, the slope of the force-time curve is remarkably high in comparison to other impact energy levels. The foam core visibly underwent a reduction in thickness on post-impact observation and significant foam cell closure. This can be clearly observed from the load-deflection curve of Fig. 8.3 that shows stiffening of the foam past the initiation of damage at 3000 N. The residual deflection of the E energy level sample is slightly lower than D indicating that the response time of the sample is reduced at higher impact energies. Further, the E energy level samples, showed considerable core crushing away from the impact location around the top facesheet/core interface. The continued core crushing is seen around ~8000 N both in the Fig. 8.1 and Fig. 8.2. The top facesheet, in addition to localized debonding between the facesheet and the core, exhibited facesheet damage in the form of fiber breakage and matrix cracking. The energy absorbed by the E level samples is ~ 45 J. Fig. 8.2 shows that beyond initiation of first damage, the load-energy curves is smooth, except for the E energy level, where the load shedding process due to additional damage is visible in the load-energy curve. The schematic of the failure mechanisms observed through microscopy is presented in Fig. 8.4 a and 8.4 b, where the facesheet to core disbond and core crushing is clearly illustrated.

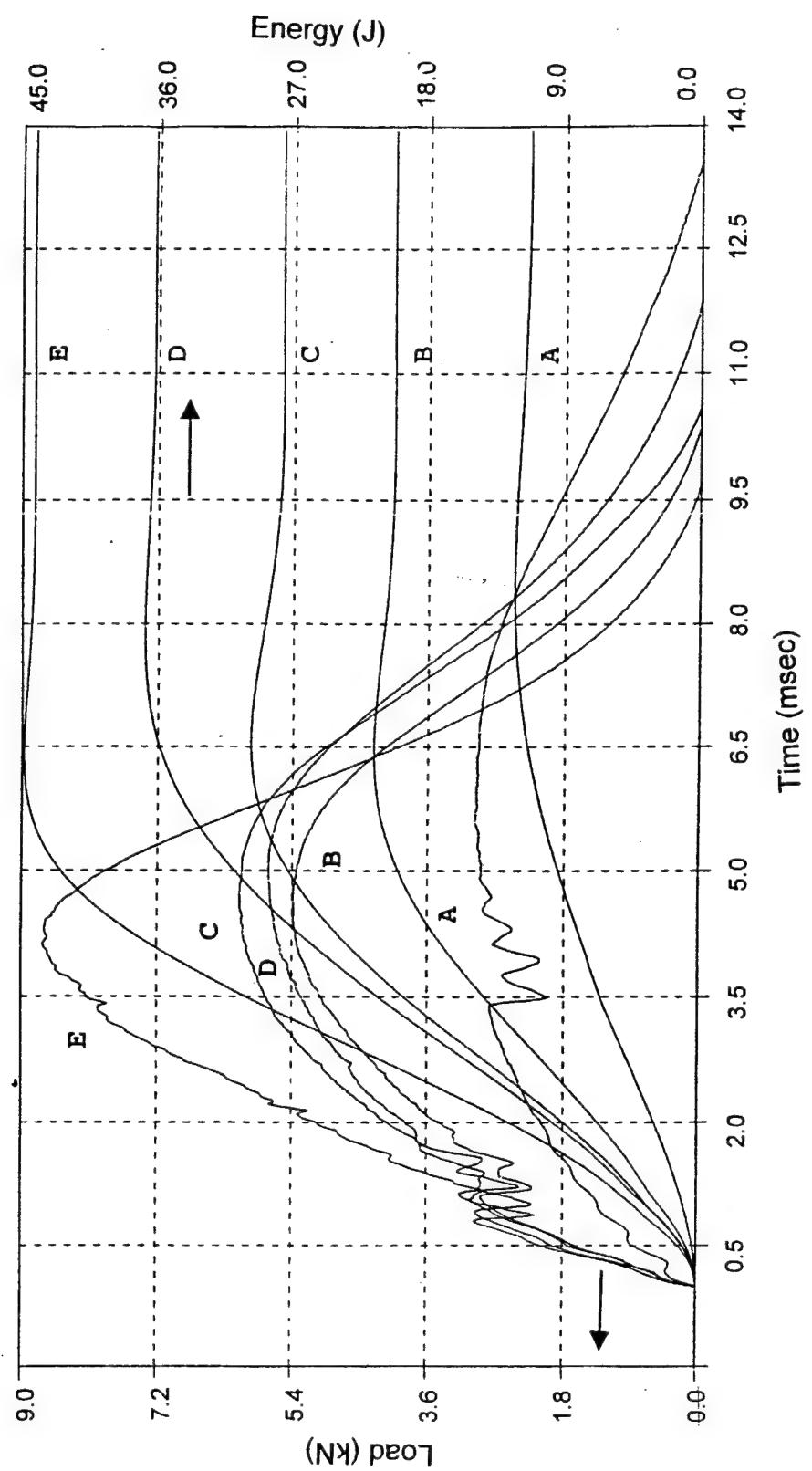


Figure 8.1. Force/Energy-Time curves for the FCo composites (Energy levels A-E)

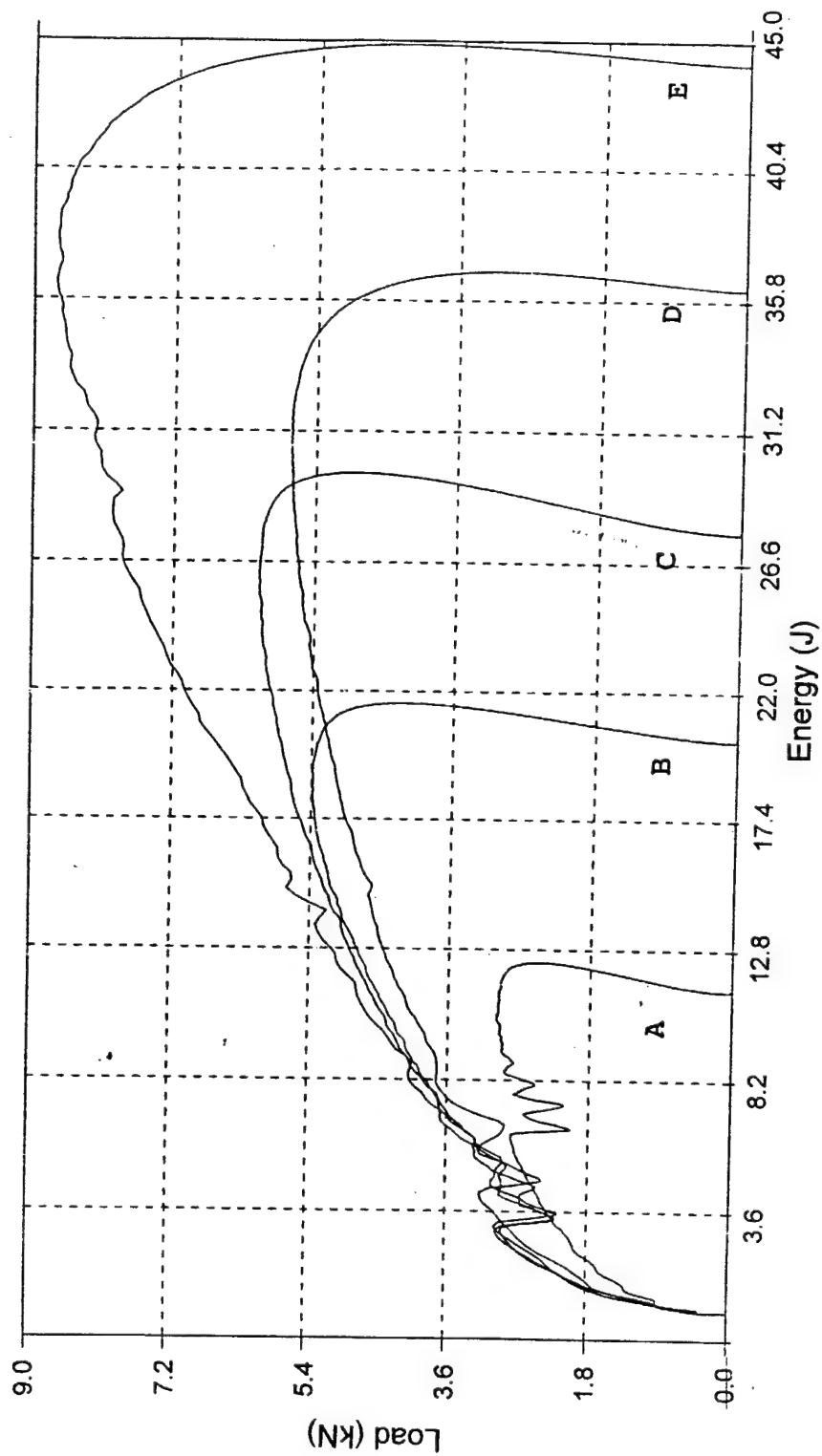


Figure 8.2. Load-Energy curves for the FCo composites (Energy levels A-E)

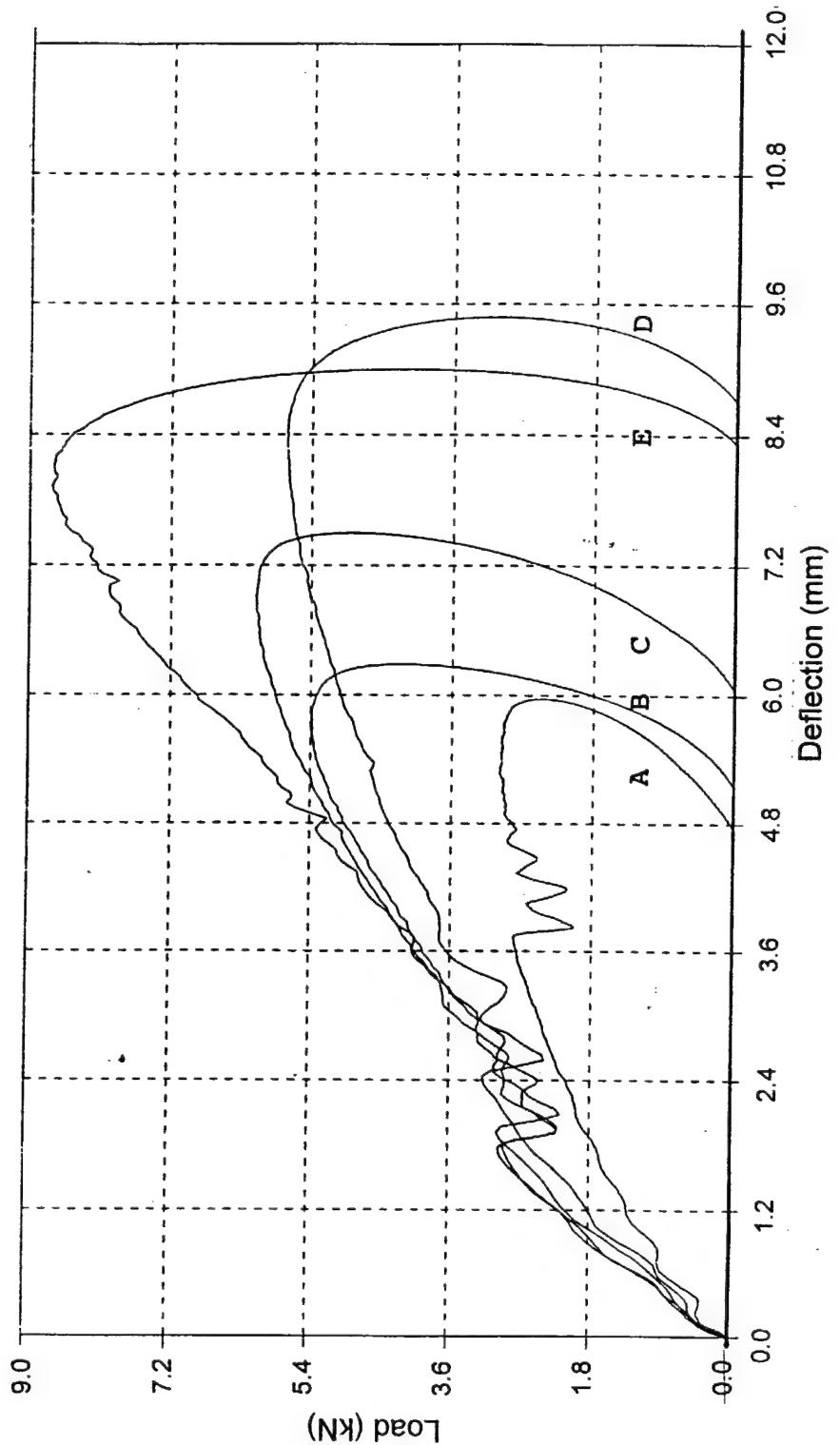


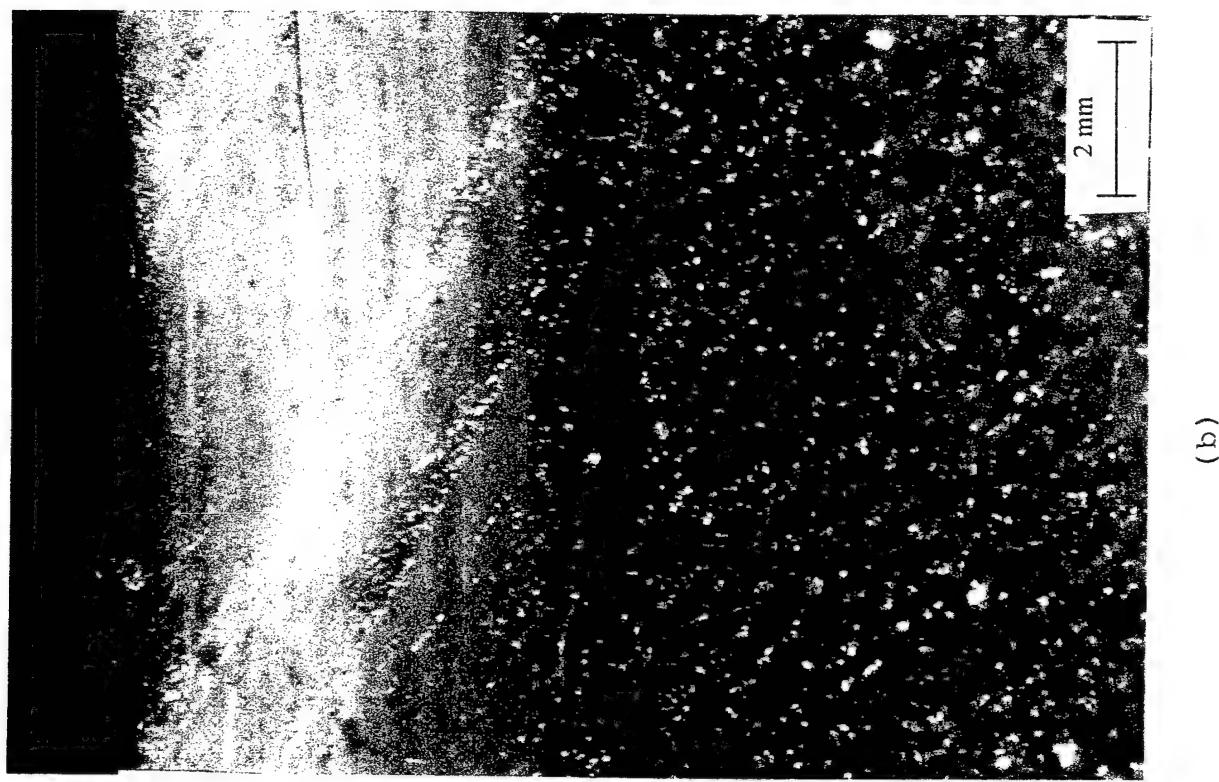
Figure 8.3. Load-Deflection curves for the FCo composites (Energy levels A-E)

8.4 Foam-Reinforced- Titanium Pins Core Sandwich Composites (F+PCo-75)

Figures 8.5 and 8.6 represent the force/energy-time and load-energy curves for the F+PCo-75 samples. The pins are seen to increase the transverse stiffness the panels considerably. For all the energy levels A through E, the slope of the force-time curve of Fig. 8.5 is higher than previously observed. The average load at which the damage initiates in these samples is 2800 N which is 7% lower than the FCo samples. This is to be expected because the pins create microcracks in the facesheet, as they enter the facesheets during manufacturing. The damage initiation load is not identical for all samples because of the position, orientation and extent of penetration of the pins into the facesheet (a manufacturing driven parameter) with respect to the point of impact as seen from both Fig. 8.5 and 8.6. It can also be seen from Fig. 8.5 that damage initiation load is ~ 9% higher at energy level E (higher energy) as compared to A, B C and D. This is likely because the inertial effects of the tup are more pronounced at higher impact velocities. In all experiments, care was taken to ensure that the tup would not impact directly on a point under which a pin entered the facesheet.

The major failure mechanisms as shown in Fig.8.7 a, b and c were observed; a) Localized facesheet delamination (within a span of two pin supports around the impact location) along with associated facesheet wrinkling and fiber breakage, matrix cracking.

The fiber breaks assume the direction of the impact, b) localized debonding between fiber/core interface, c) pin-push out, where fibers follow the pin direction (opposite to the impact direction), and d) shear cracking of plies between push-out location and impact location. The load that causes the first damage among these mechanisms appears to still be localized debonding between fiber / core interface. The pins influence (within a small range) the load at which this mechanism appears. The process of facesheet delamination, fiber breakage and matrix cracking is seen to occur at higher loads. There are several instances of load shedding for all impact energies A through E as is clearly seen in Fig. 8.6 (load-energy curves). The occurrence of these phenomena on the top facesheet, although higher in comparison to the FCo samples, is restricted (or pinned) between adjacent pins around the impact location. This is a localized phenomenon. At the point of impact, the facesheet shows evidence of flexural failure in the direction of loading, while in contrast, the facesheet in the vicinity of the pins surrounding the impact show push-out tendency, thereby the plies tend to displace in the reverse flexure direction. Thus, shearing of several layers occurs between the impact location and the surrounding pin location (due to competing facesheet motions). This causes gradual weakening and multiple load drops along the force-time curve as seen for the E energy level sample from Figs. 8.5, 8.6 and 8.8. Away from these, there is no indication of damage to the specimen to the top facesheet. The bottom facesheet did not exhibit any visible damage through the energy levels A through E. Furthermore,



(b)

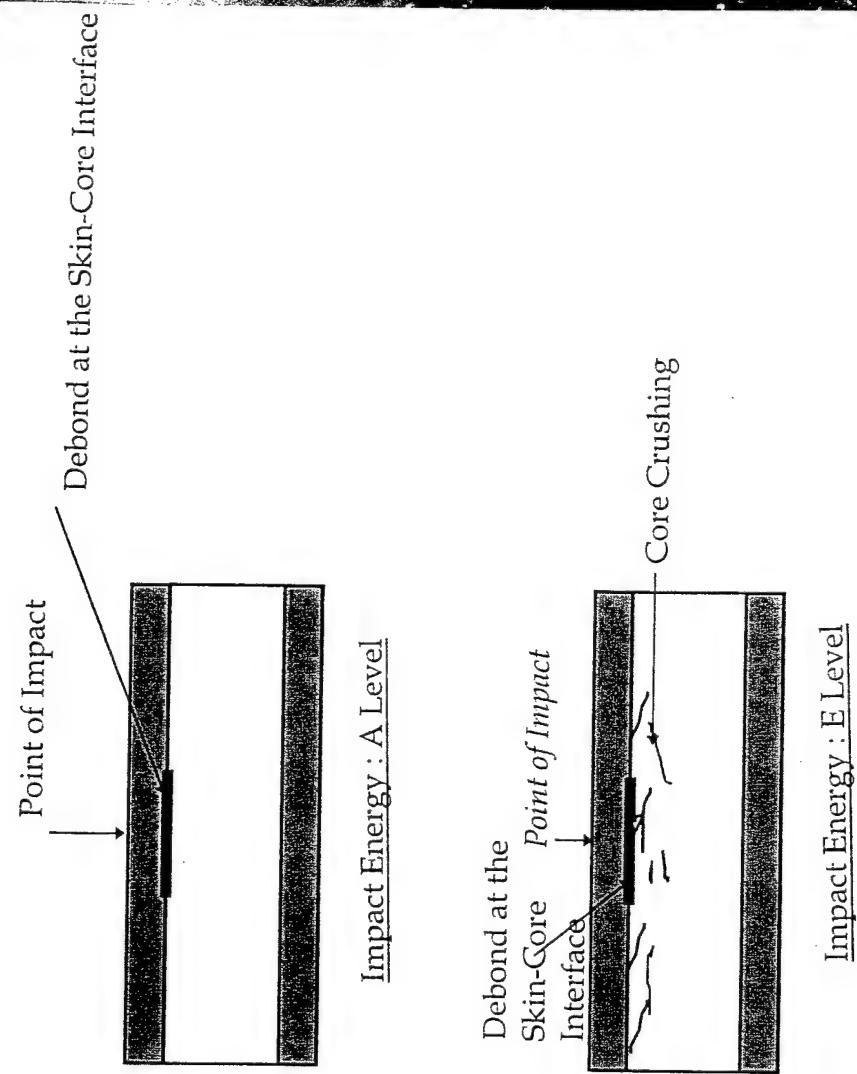


Figure 8.4a-b. Schematic and Micrograph of Failure Mechanisms for FCo composite:
Interfacial Debond between Facesheet and Core and Core Crushing

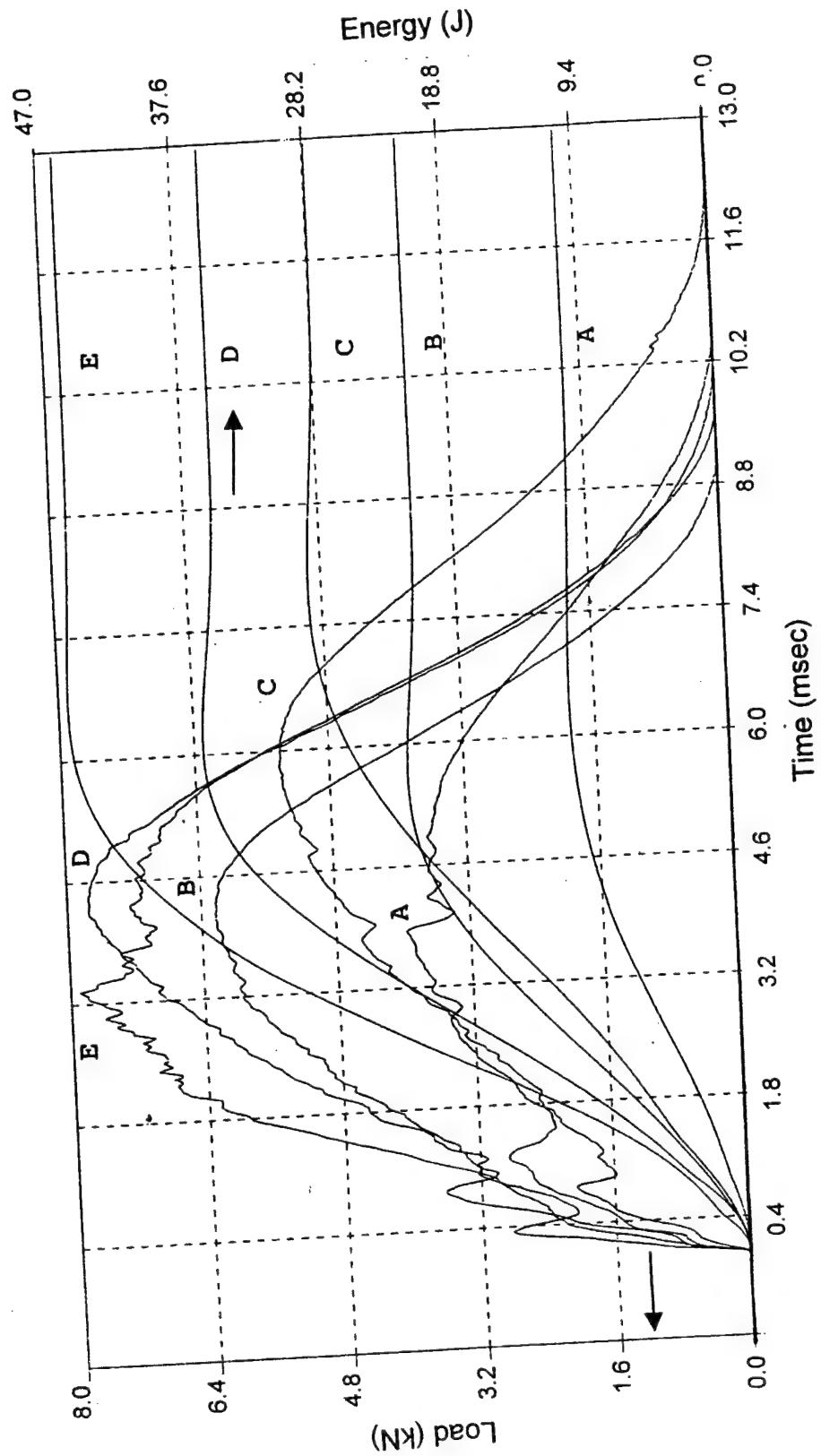


Figure 8.5. Force-Time and Energy-Time curves for the F+Pco-75 Composites (energy levels A-E)

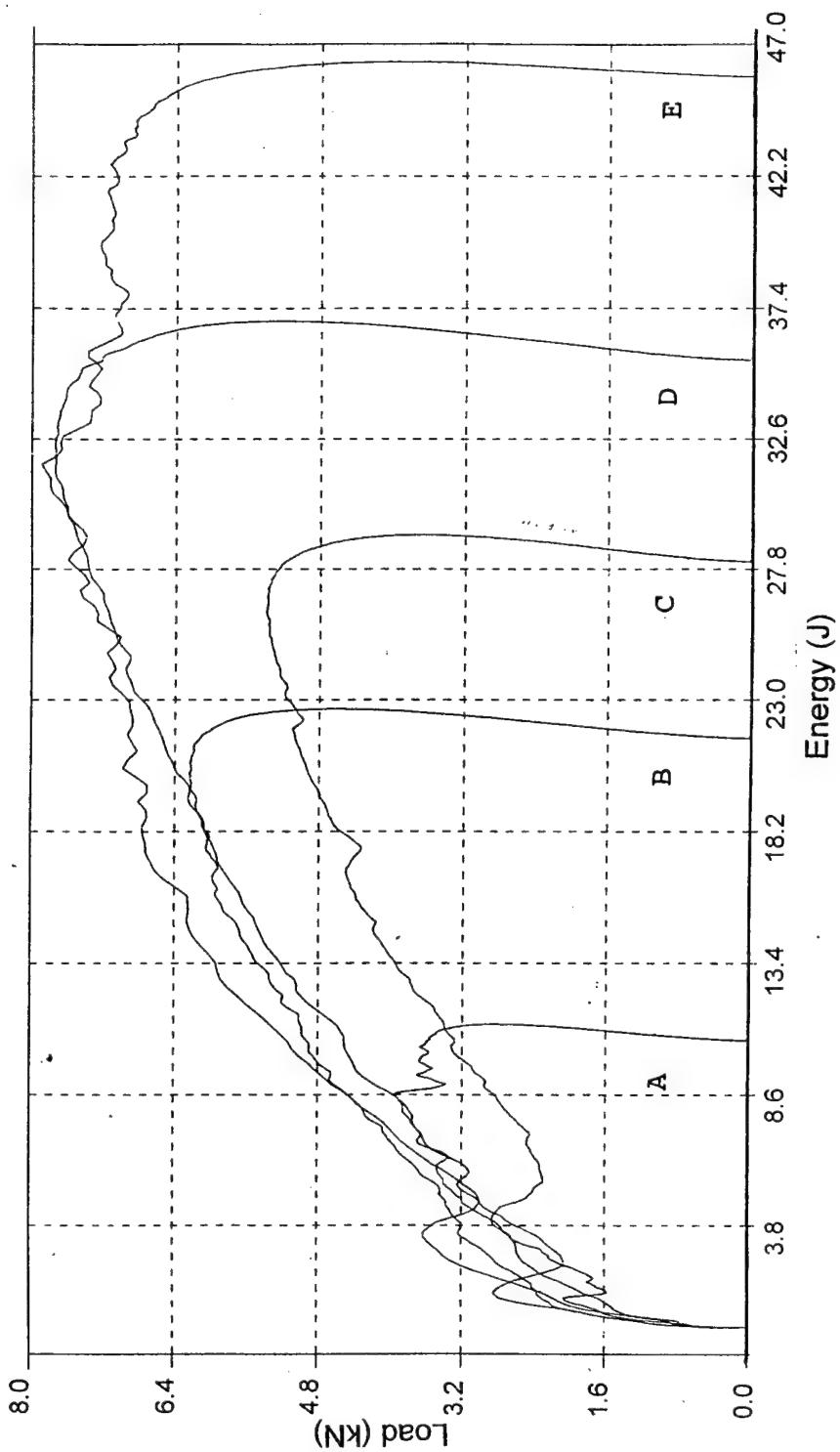


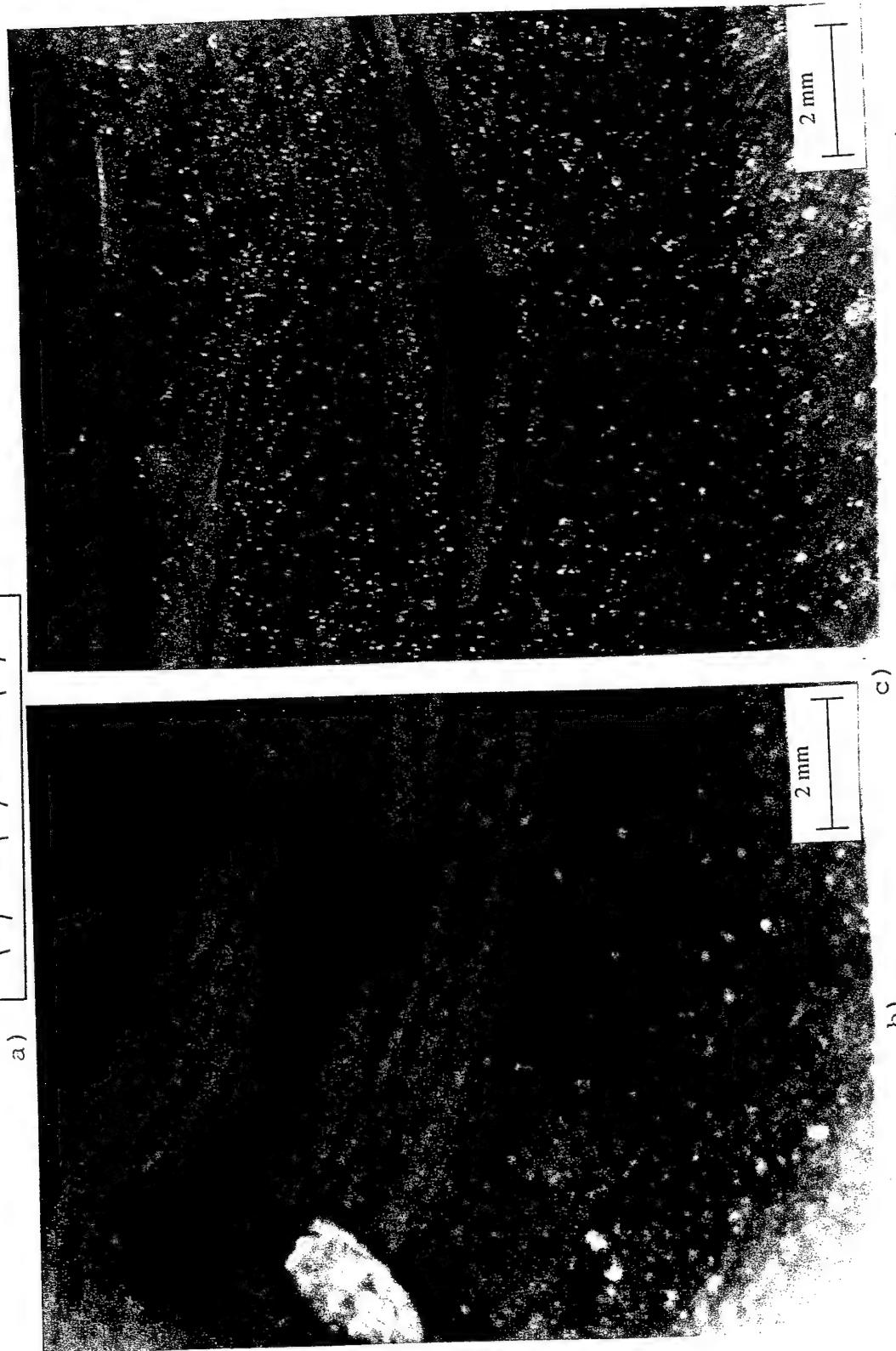
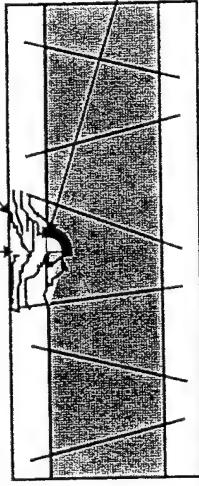
Figure 8.6. Load-Energy curves for the F+Pco-75 composites (Energy levels A-E)

Localized Delamination
Fiber Breakage and Matrix Cracking
(Delaminated plies move in direction of
Impact Event and at the pin locations
the plies move in the reverse direction)

Point of Impact

Core/Facesheet
Debond

a)



b)
Figure 8.7a,b and c. Schematic and Micrograph of Failure Mechanisms for F+PCo-75 ; a) Schematic showing various damage modes of F+PCo-75, b) Pin-push out, causing upward movement of plies, and creation of shear delaminations joining that join impact location damage to pin location damage, and, c) Interfacial Debonding between Facesheet / Core for F+PCo-75 Composite and Flexural Failure of Top Facesheet

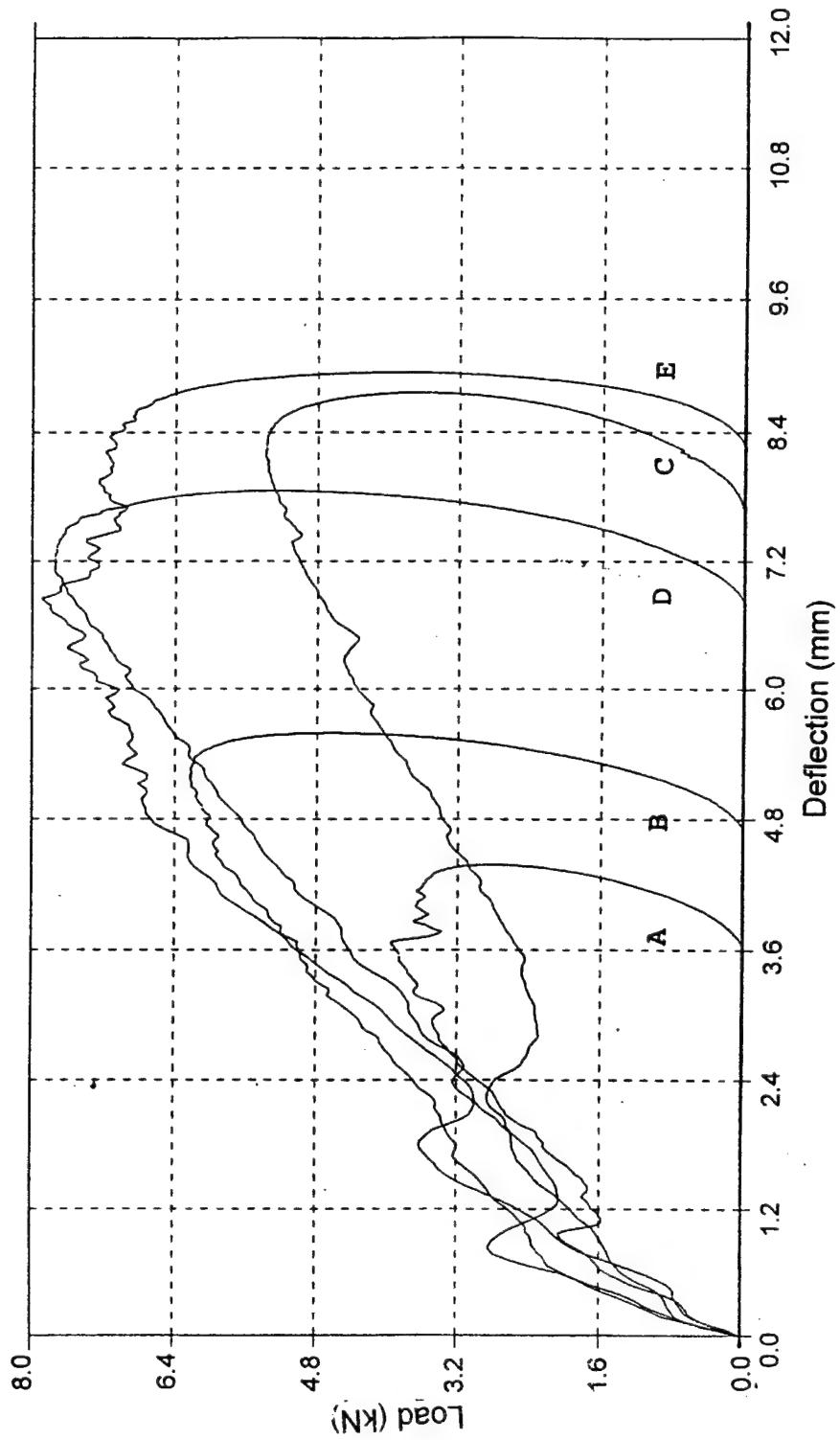


Figure 8.8. Load-Deflection curves for the F+Pco-75 composites (energy level A-E)

the weakening of the core due to crushing at locations around the top facesheet/core interface seen in the FCo samples is completely arrested at the E energy level in this case. Two additional mechanisms contribute to load shedding. First, there is additional fiber breakage and microdelaminations within the top facesheet between the two arresting pins, and secondly, few pin push-outs occur at higher energies. At least two pins were pushed-out of the top facesheet, (not noticed in the A through D samples). This phenomena could not be isolated, but overlaps with the localized facesheet delamination, as seen from Fig. 8.6 between 6400 N to 8000 N region. From the load-deflection curve of Fig. 8.8, it can be seen that pin push out is observed through load sheddings between 6400 N to 8000 N.

8.5 Hollow Titanium Pin Core Sandwich Composites (TCo)

Figures 8.9 and 8.10 represent the force/energy-time and load-energy curves for the TCo samples. The initial slope of the force-time curve of Fig. 8.9, is in between that of the FCo and F+PCo samples. Figure 8.11, which represents the load-deflection history, shows that the damage initiation load is within a small scatter here because pins cause damage initiation and redistribution of the load path. The process of load shedding could vary from sample to sample depending upon the impact event with respect to the pins, and the extent of penetration of the pin into the facesheets during manufacturing. The average damage initiation load is found to be around 2300 N. The impact events lasted within 9.5 msec to 13 msec which were comparable with the FCo and F+PCo samples.

Based on visual and microscopic observation shown in Fig. 8.12 a, b and c, four main failure mechanisms were observed for the TCo samples; a) localized pin buckling was an added failure mechanism that was clearly observed in all the TCo samples. The pin buckling was not evident in the F+PCo specimens, which suggests that the foam may have contributed to supporting and thereby arresting this mode of damage b) pin pull-out which was also a different mechanism. During the relative movement of the facesheet and the pin core, the pins that were seen to have undergone localized buckling around the impact zone also tend to pull out of the facesheet, c) localized facesheet delamination between adjacent pins seen just as in the F+PCo samples. The damage did not grow beyond 2 adjacent pins in the vicinity of the impact location. The delamination was accompanied by fiber breakage and matrix cracking, and the broken fibers deform along the impact direction; and d) pin push-out which was characteristic at high energies. From Fig. 8.9, it is seen that for the sample impacted at energy level E, a significant load drop is seen at 4 msec. This was accompanied by push-out of two pins from the bottom facesheet. The samples impacted at A through D did not exhibit signs of any bottom facesheet damage. The load-deflection curves of Fig. 8.11 show that the process of damage creation due to combined effects of microcracking around the pin-facesheet interface and debonding in the vicinity of the pin occur at several

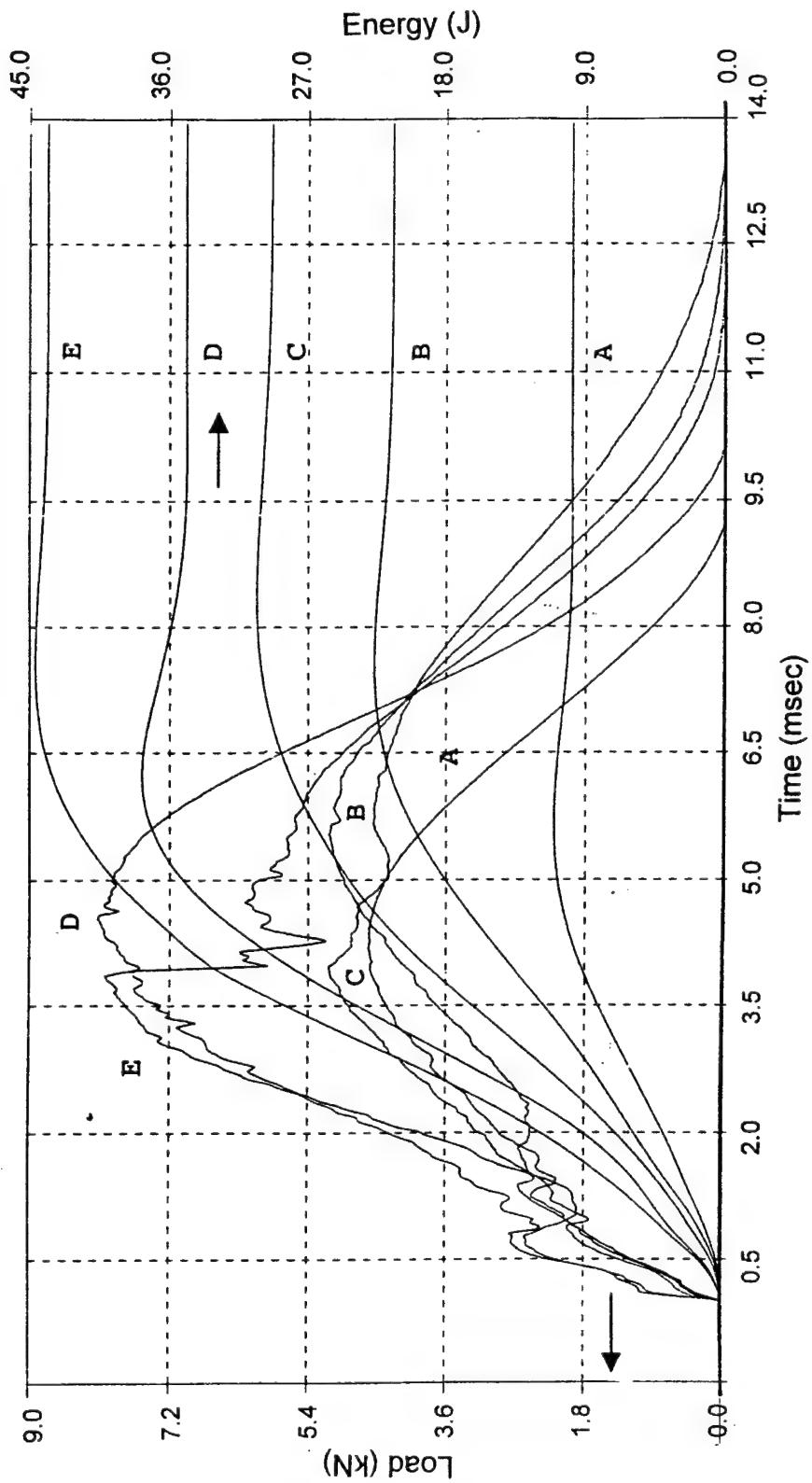


Figure 8.9. Force-Time and Energy-Time curves for the TCo Composites (energy levels A-E)

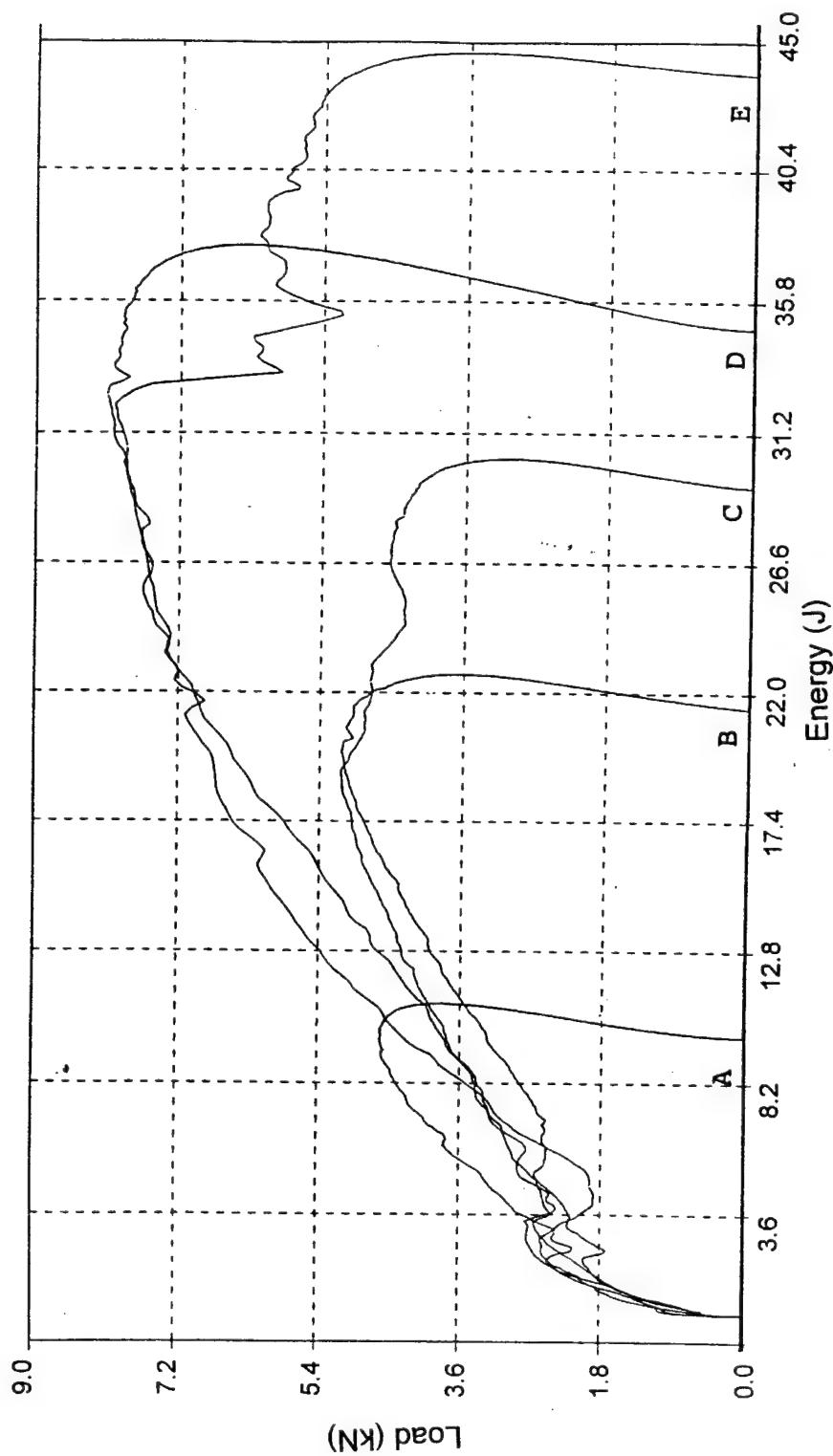


Figure 8.10. Load-Energy curves for the TCo composites (Energy levels A-E)

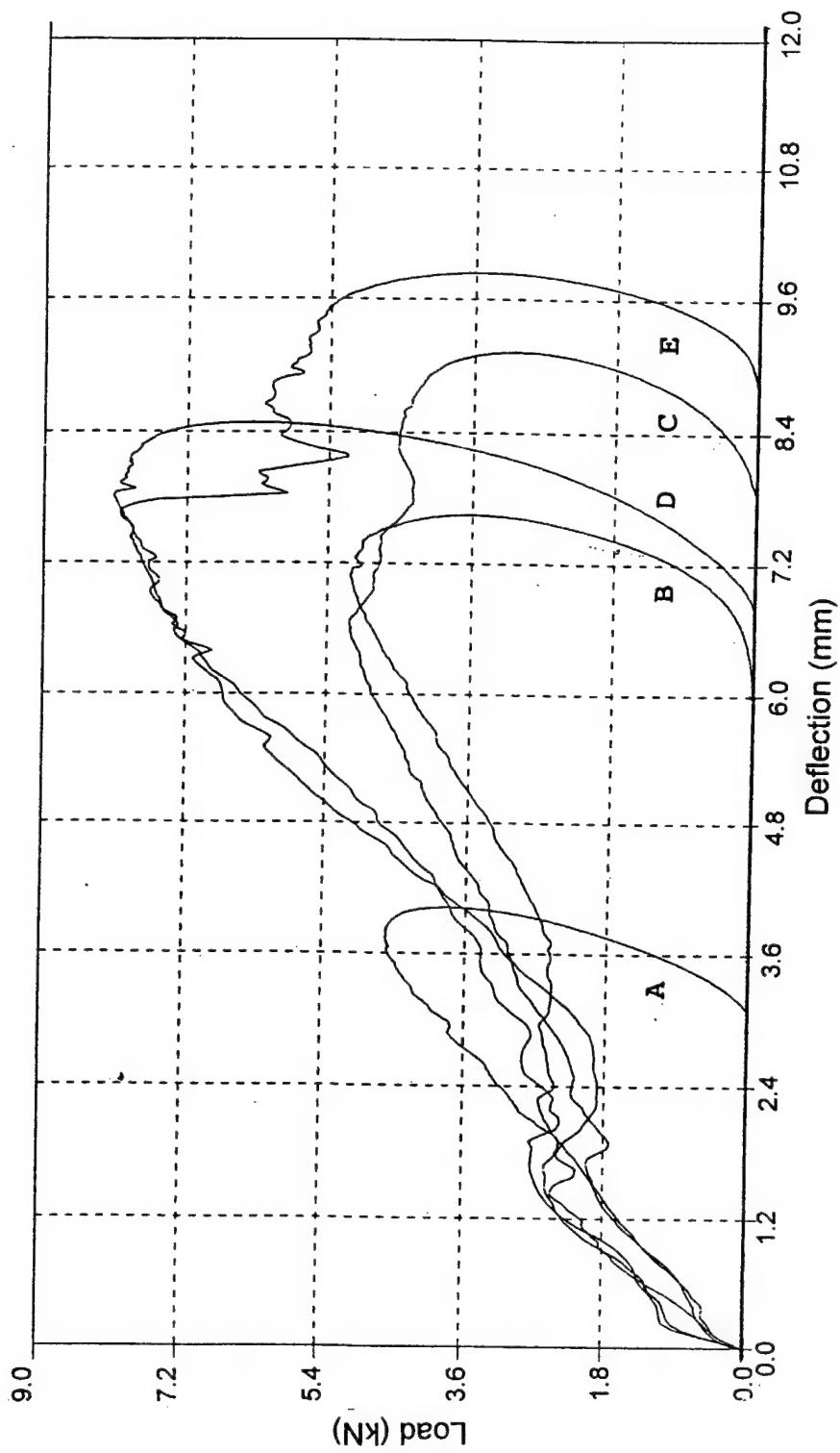


Figure 8.11. Load-Deflection curves for the TCo composites (Energy levels A-E)

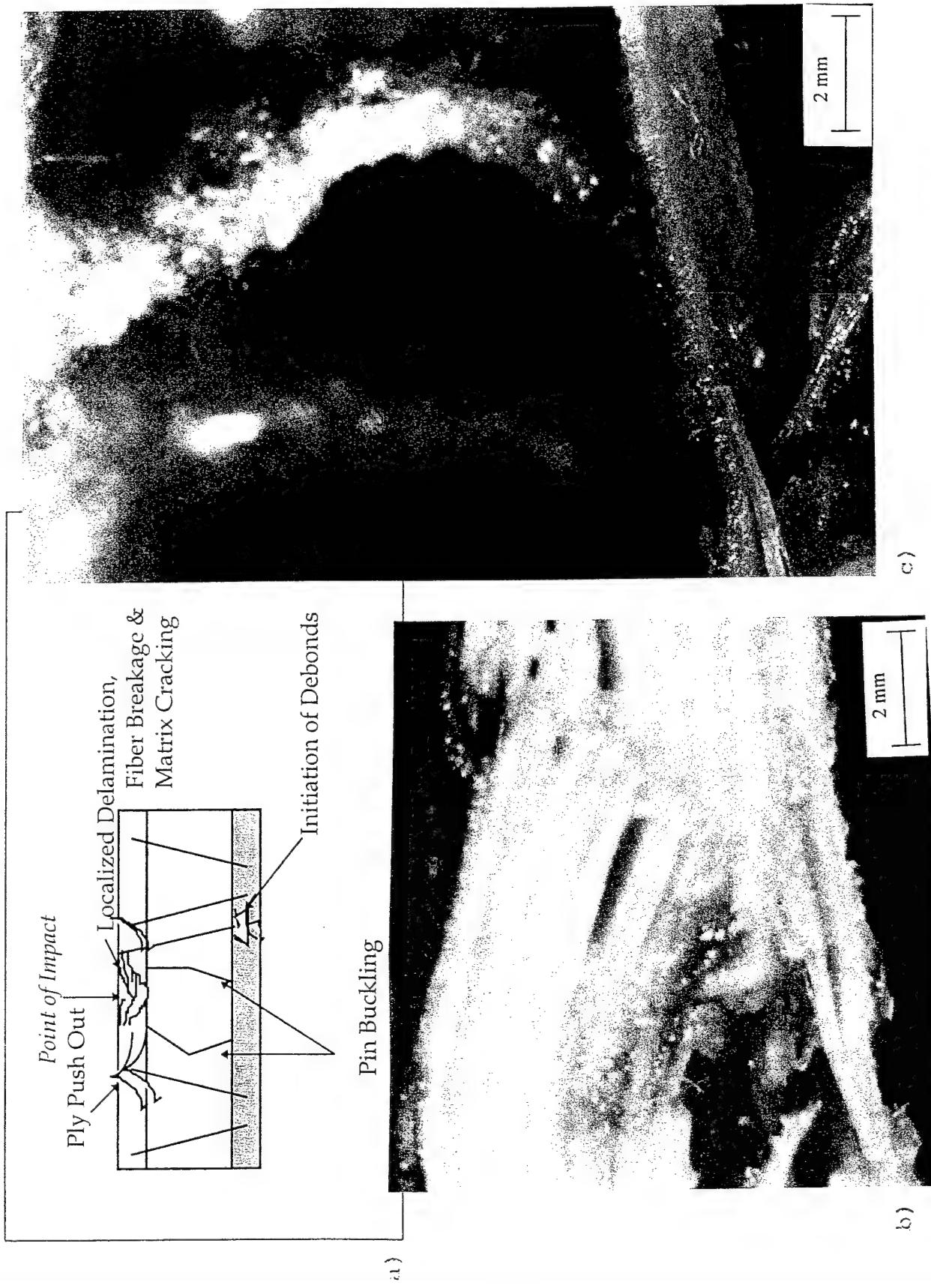


Figure 8.12a,b and c. Schematic and Micrograph of Failure Mechanisms for TCo; a) Schematic showing failure modes of TCo, b) Localized Delamination, fiber Breakage & Matrix Cracking; Note the Pin-push out causes plies to move up, while at the impact location, the failure is by flexure. Shear cracks occur between these locations, and c) Pin Buckling

locations along the loading/unloading phase (several minor load drops). Pin buckling and pin-facesheet debonding are the two competing mechanisms in this case. The TCo samples exhibited similar levels of energy absorbed and peak loads in the FCo and F+PCo-75 samples, as can be seen from Fig. 8.10 (load-energy curves).

8.6 Influence of Pin Spacing (F+PCo-150)

On observing that the pin reinforced foam core provided damage containment, the spacing of the pins was varied in this configuration. For the 16-ply facesheet, the center-to-center distance between the pins was spaced 38.1 mm apart. Impact tests were conducted in an identical manner.

Figures 8.13 and 8.14 represent the force/energy-time and load-energy curves for the pins spaced 38.1 mm apart configuration. In comparison to Fig. 8.5, the initial stiffness of the samples is seen to be slightly lower. By doubling the center-to-center distance between the pins, the transverse stiffness is marginally lowered. The damage initiation load is not as scattered as observed for the F+PCo-75 samples. The pins in the F+PCo-150 samples are further away from the impact location, hence the influence of redistribution of load due to pins in the vicinity of the impact (observed for the F+PCo-75) is not as pronounced. Based on the time of the impact event, the F+PCo-75 samples showed a variation from 8.8 msec to 12 msec, while the time of the impact in the F+PCo-150 samples was repeatable ~9 msec for all energy levels A through E. The impact duration appears to be dominated by the top facesheet and local core stiffness of the foam core. This is consistent within the impact energy range A through E. The stiffness of the samples past damage initiation is also lower as compared to their F+PCo-75 counterparts. From Fig. 8.13, it is observed that apart from indication of minor pin related damage development, the force-time history of samples A, B and C is fairly symmetrical, while for samples D and E, at the peak load, the facesheet flexural failure and pin core debond result in major load drops. This is also observed from the load-energy curves of Fig. 8.14. The peak loads reached by the F+PCo-150 samples is higher (9.8 kN) than the F+PCo-75 (7.8 kN), indicating that state of damage is lower in the F+PCo-150 samples as compared to the F+PCo-75 samples. The proximity of pins in the latter result in higher stiffness, but in comparison the state of microdamage is greater. The load-deflection curves (Fig. 8.15) show that the global deflection of the F+PCo-150 samples is lower in comparison to the F+PCo-75 samples at all energy levels A through E. This is more pronounced at the higher energy levels C, D and E. The overall shape of the load-deflection curves closely resembles that for the FCo samples (foam only). The F+PCo-150 samples hence behave more like the foam core samples, with the exception that damage is contained between the spans of the arresting pins. The deflection of the F+PCo-150 is lower for the same reasons that microdamage (surrounding the pins, pin-facesheet interaction and pin-foam core interaction) is lower than the F+PCo-75 samples. The failure mechanisms of the F+PCo-150 are shown in Figs. 8.16 a and b. In

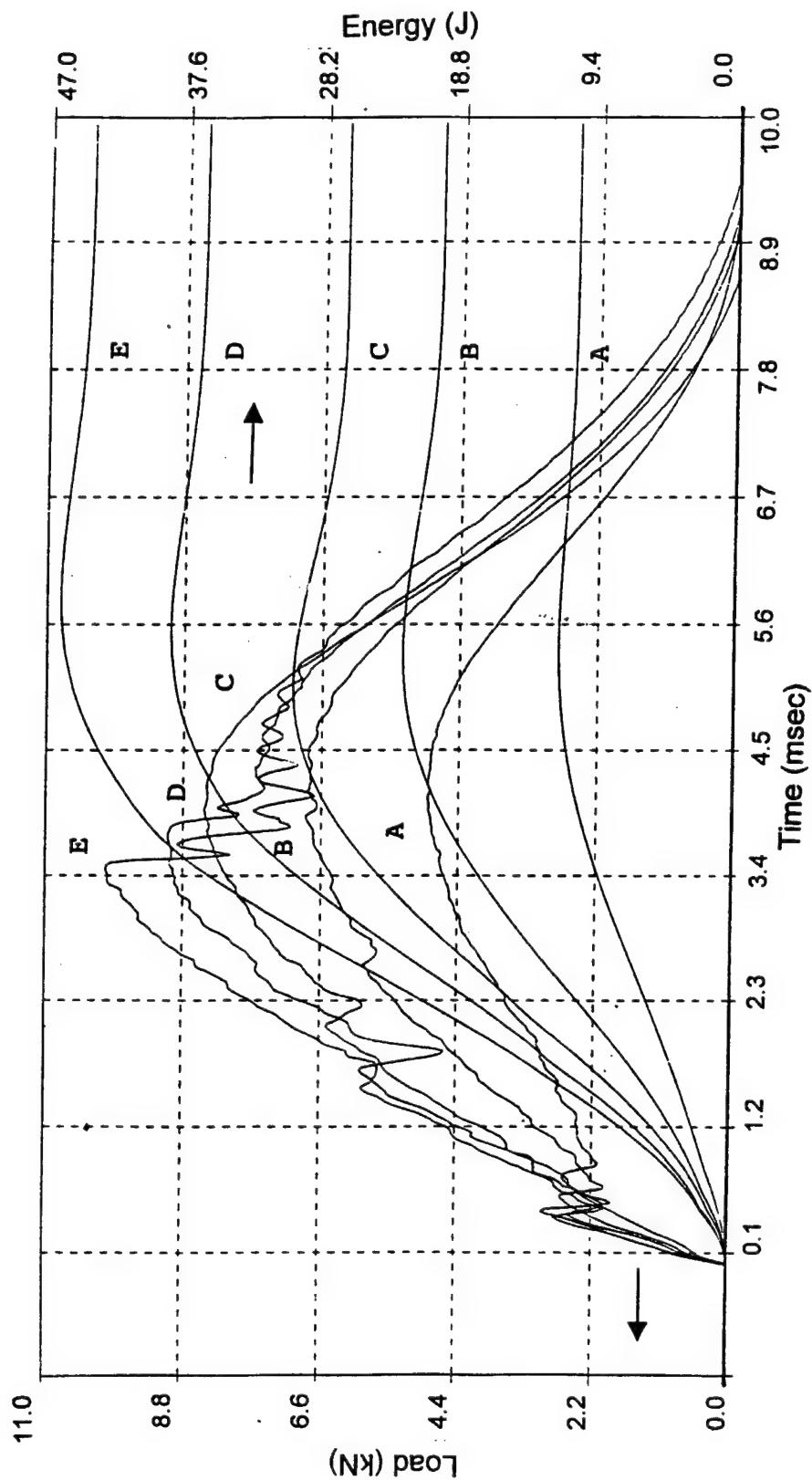


Figure 8.13. Force-Time and Energy-Time curves for the F+PCo-150 Composites
(Energy Levels A-E)

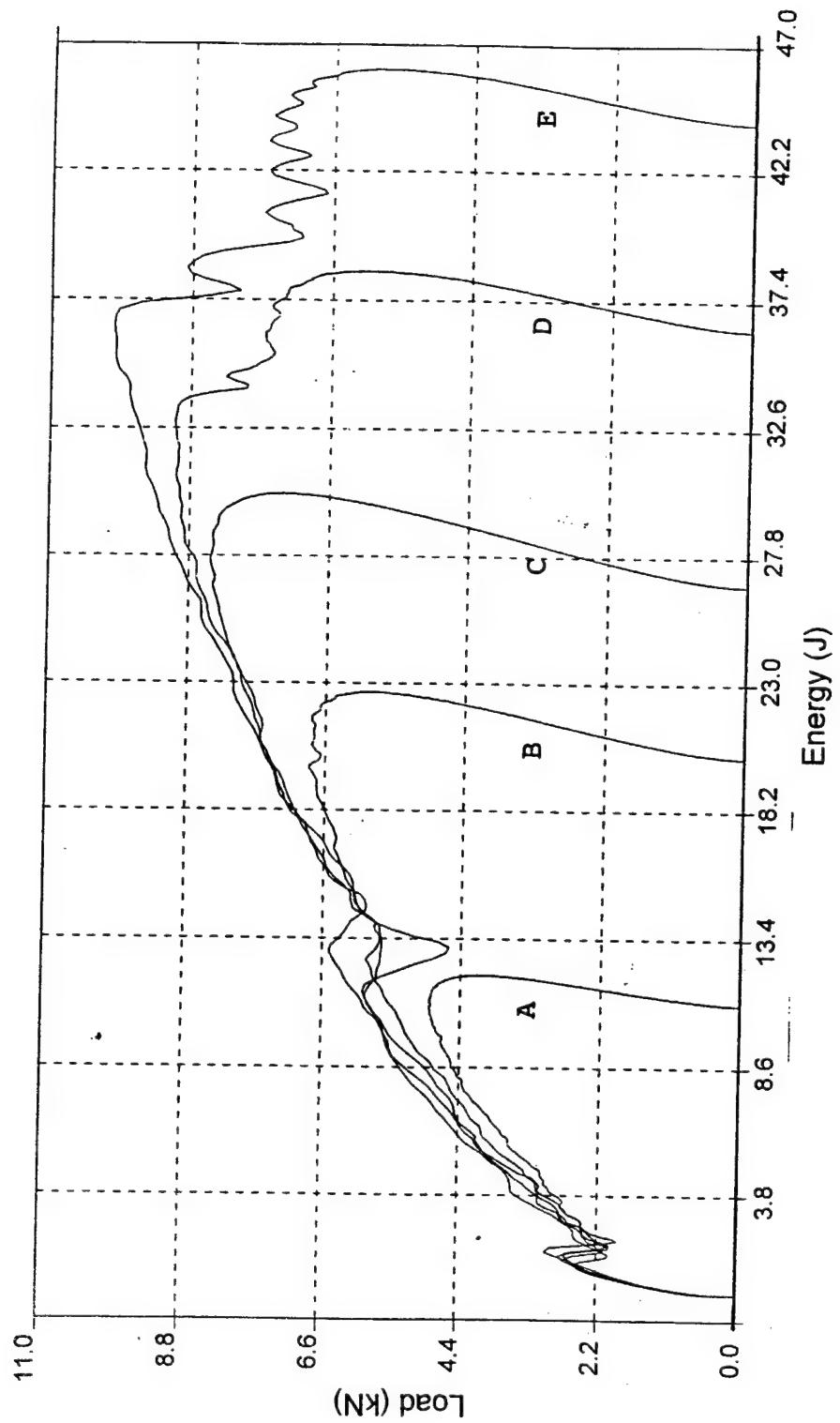


Figure 8.14. Load-Energy curves for the F+PCo-150 composites (Energy levels A-E)

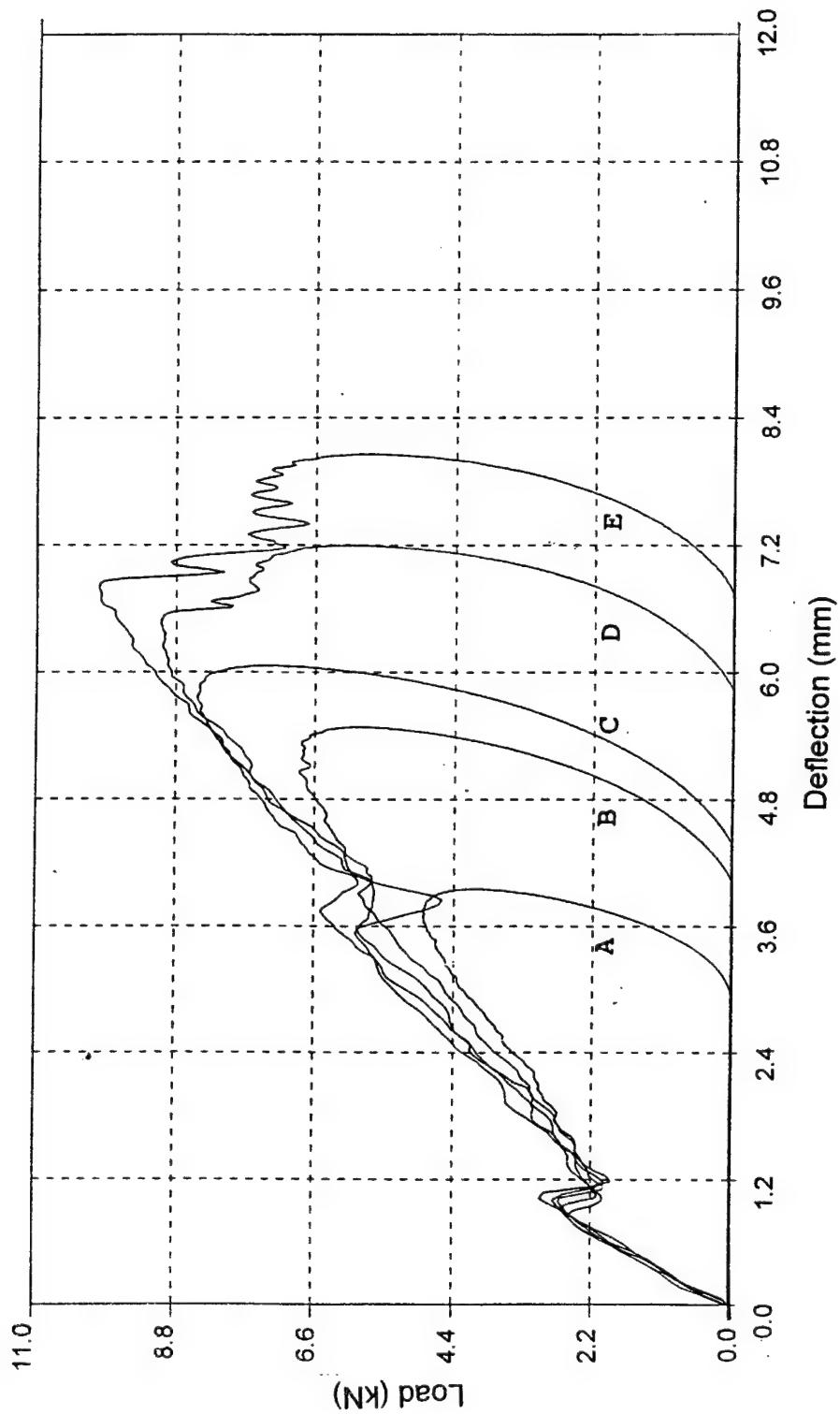
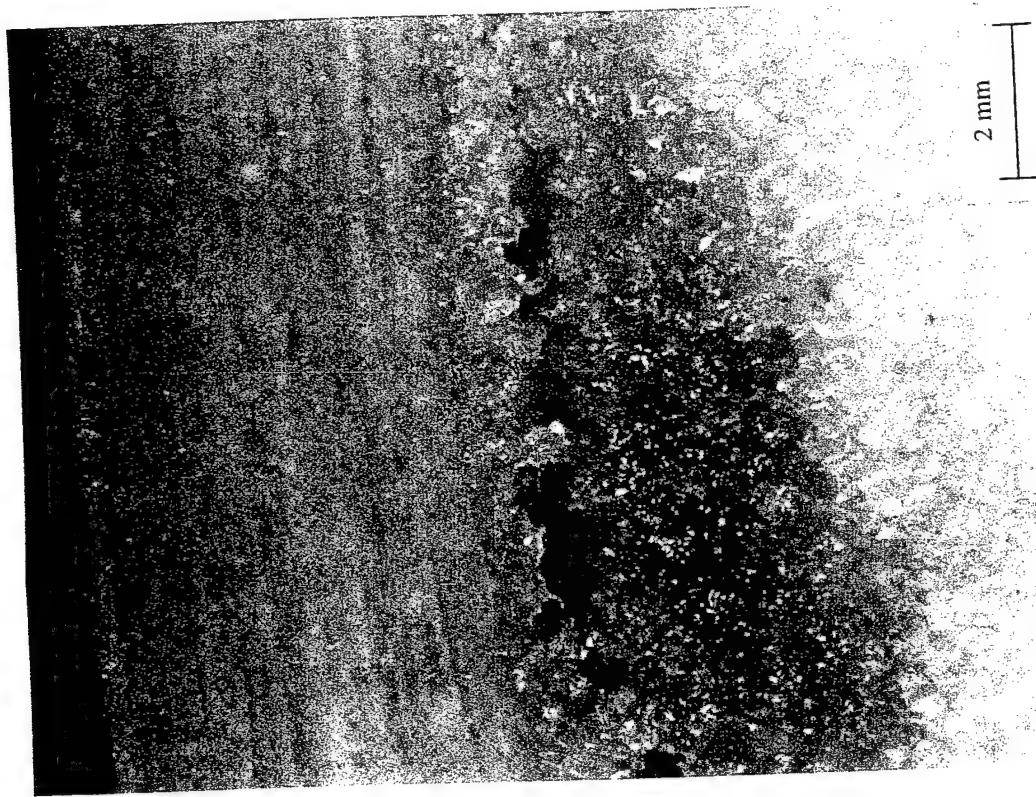


Figure 8.15. Load-Deflection curves for the F+PCo-150 composites (energy level A-E)



b)



a)

Figure 8.16. a) Flexural Failure of Top facesheet for the F+PCo-150 composite and, b)
Core crushing slightly away from the impact location

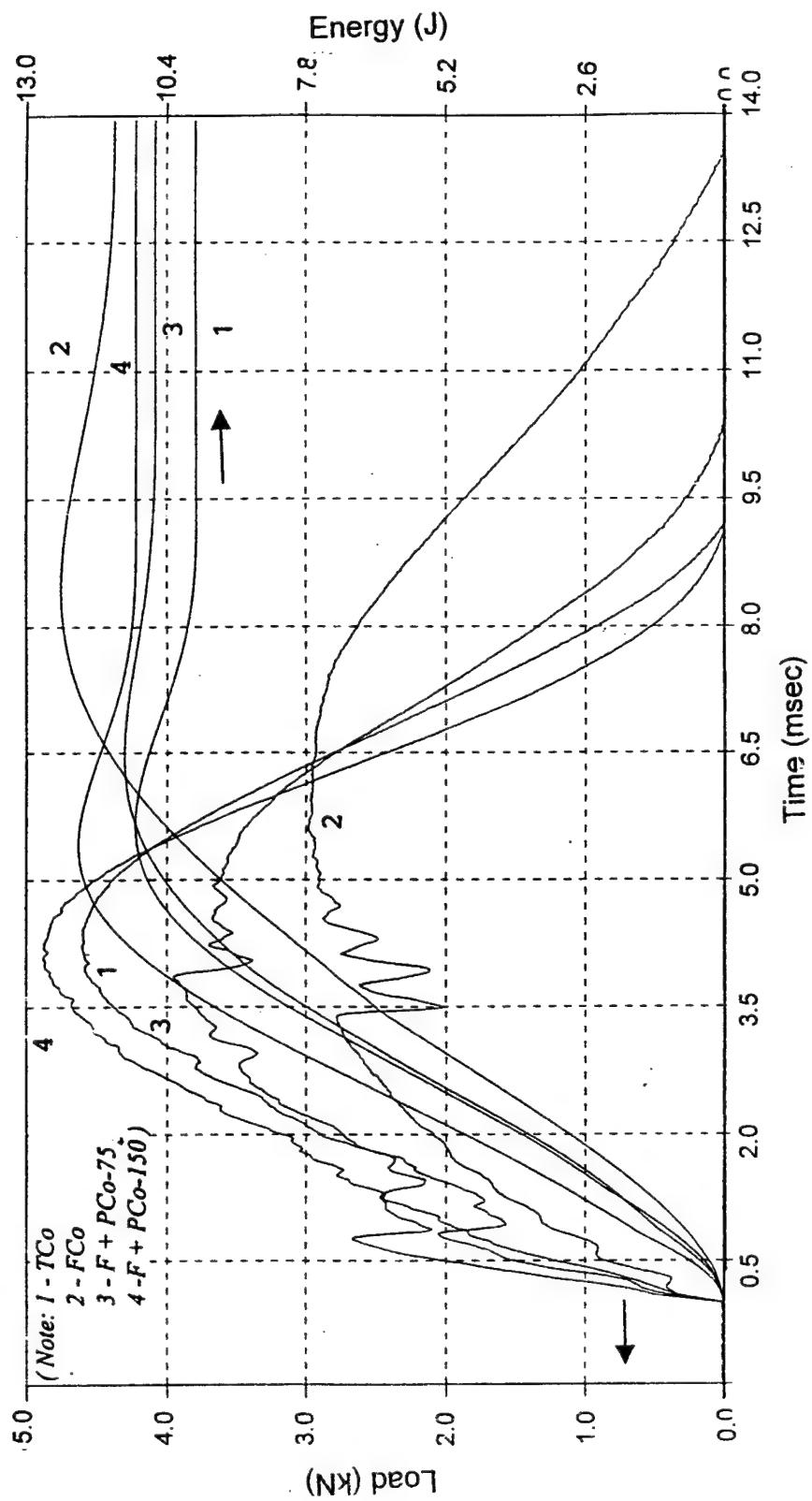


Figure 8.17. Comparison of Force-Time curves for FCo, F+PCo-75, TCo and F+PCo-150 samples at energy level A

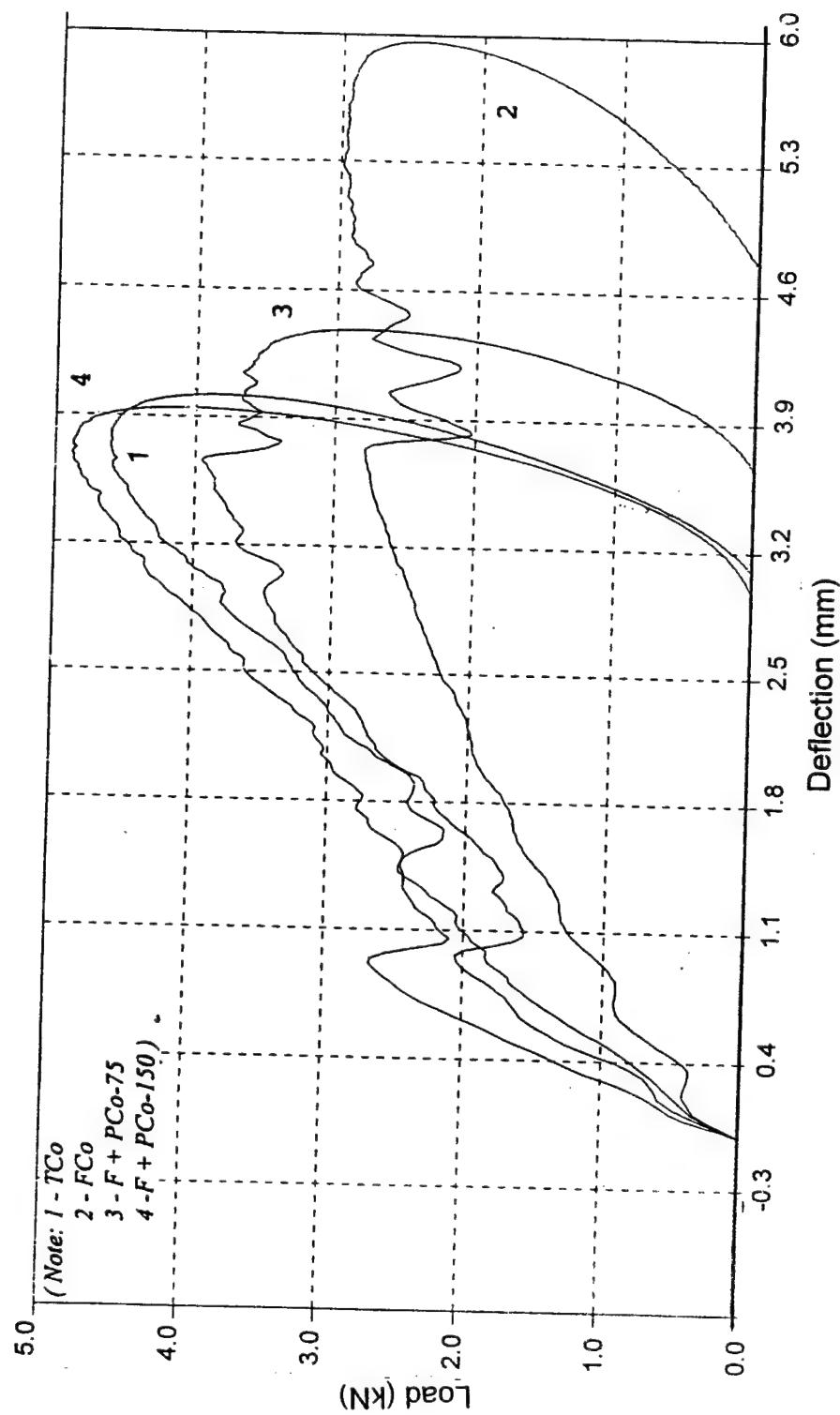


Figure 8.18. Comparison of Load-Deflection curves for FCo, F+PCo-75, TCo and F+PCo-150 samples at energy level A

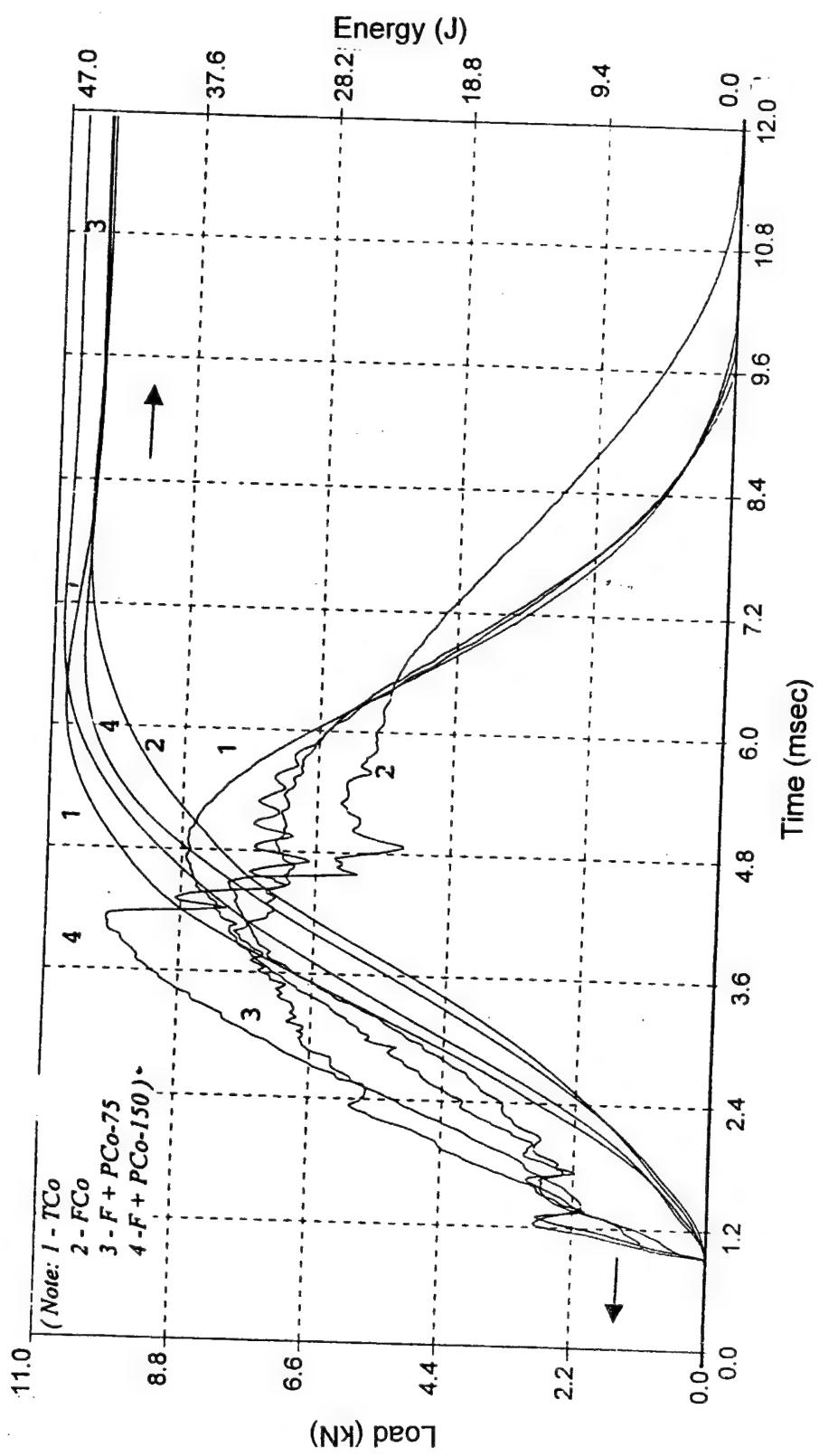


Figure 8.19. Comparison of Force-Time curves for FCo, F+PCo-75, TCo and F+PCo-150 samples at energy level E

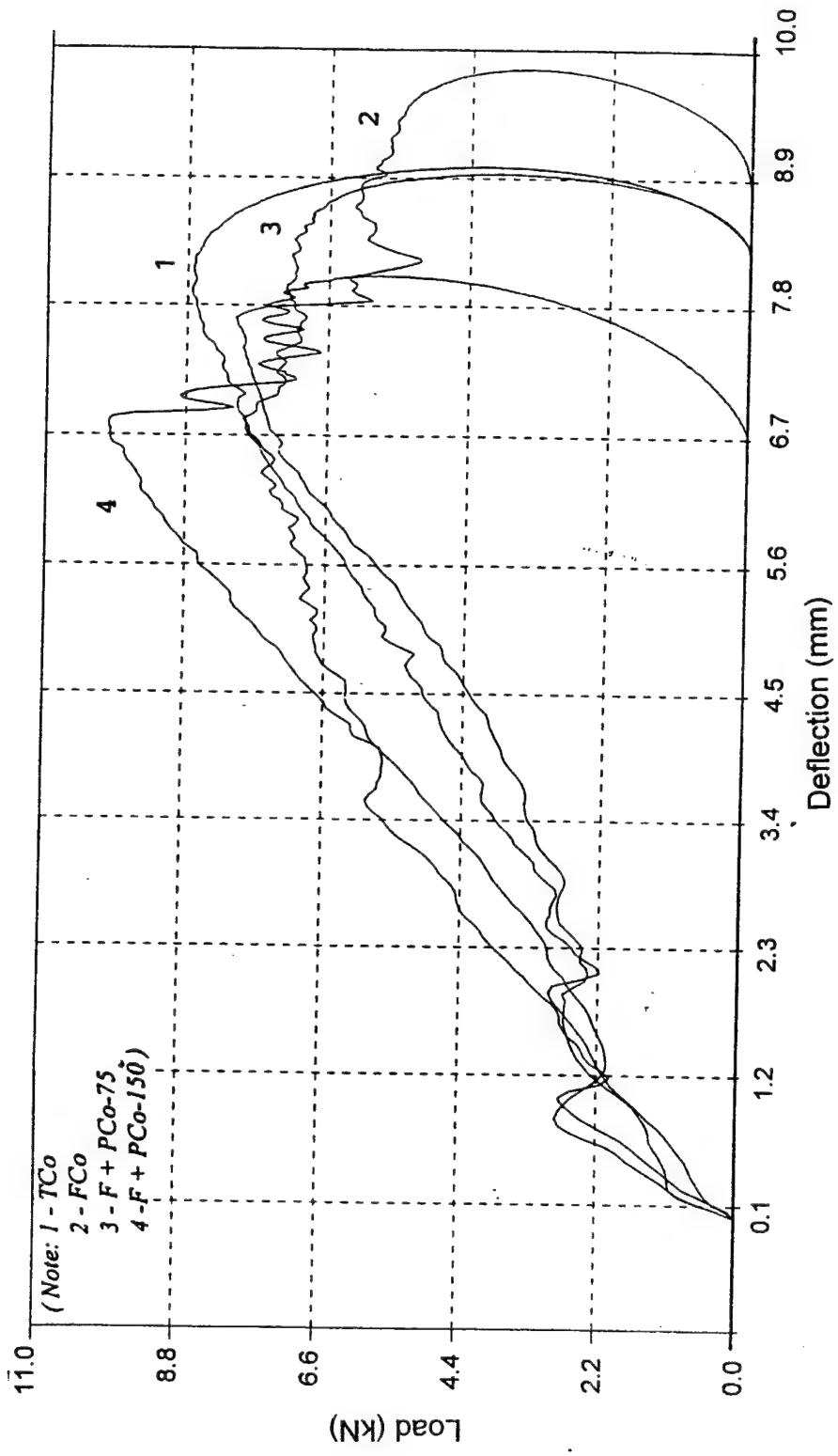


Figure 8.20. Comparison of Load-Deflection curves for FCo, F+PCo-75, TCo and F+PCo-150 samples at energy level E

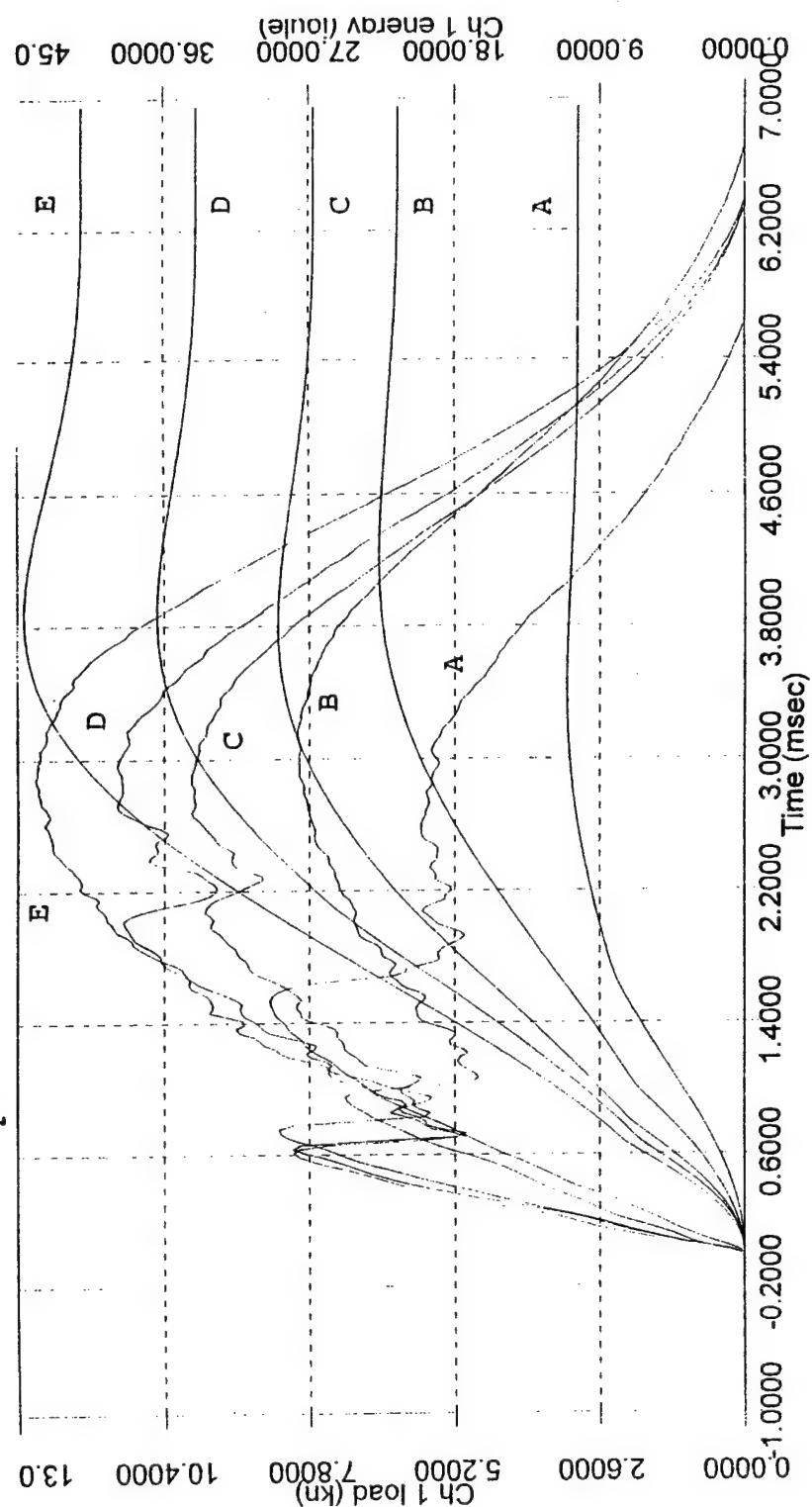


Figure 8.21. Load/Energy-Time curves for the FCo-32 composites (Energy levels A-E)

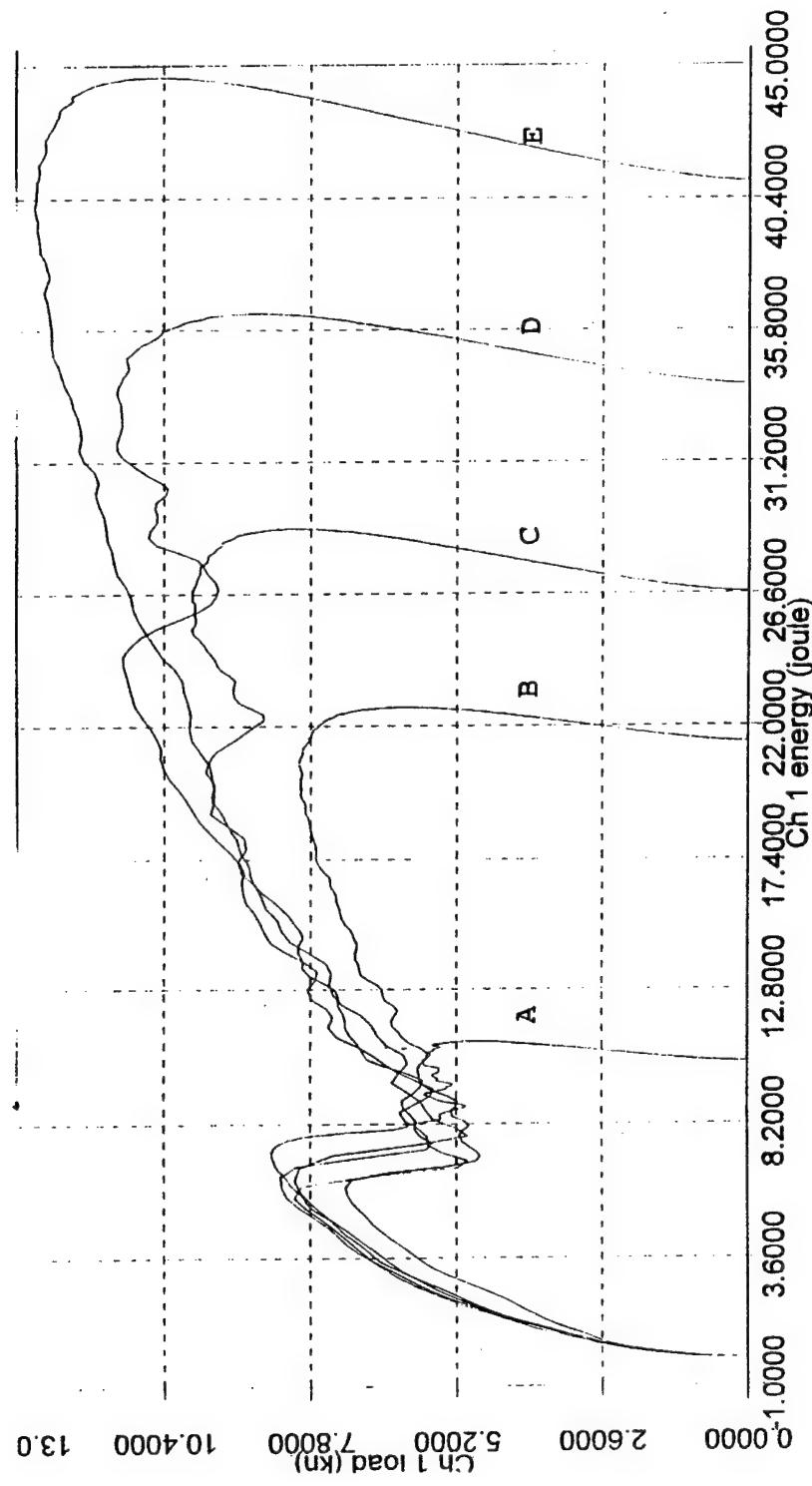


Figure 8.22. Load-Energy curves for the FCo-32 composites (Energy levels A-E)

terms of similarity to F+PCo-75 samples, the damage is confined between the pins to the top facesheet and core only. No bottom facesheet damage is observed. Localized interfacial debonding between the facesheet and the core is observed as before. In contrast to F+PCo-75 samples, the notable difference is that the top facesheet exhibits pure flexural failure at the point of impact (Fig.8.16 a). The competing push-out causing plies to move in the reverse flexure direction (seen in F+PCo-75) is absent here due to the wider spacing between the pins. As a result, the complex failure mode (flexure, reverse flexure and shearing of plies between these and thereby localized facesheet wrinkling) also does not occur. Figures 8.17 through 8.20 present the comparison of the force-time and load-displacement curves between the FCo, F+PCo-75, F+PCo-150 and TCo samples at energy levels A and E.

8.7 Influence of Facesheet Thickness - FCo-32 and F+PCo-75 (32)

The FCo and the F+PCo-75 samples were fabricated using double the number of facesheets, i.e. 32 layers of the prepgs were used on each side of the core as compared to the 16 layers used previously. Figs. 8.21 and 8.22 present the load/energy-time curves and the load-energy curves for the FCo-32 samples at energy levels A through E. For all the samples, the load at which the damage initiation occurs is ~8000 N. Comparing it to its 16-layered facesheet counterpart, and its behavior seen in Figs. 8.1 and 8.2, it is seen that for half the facesheet thickness, the damage initiation load is 38% lower. Hence increasing the facesheet thickness increases the damage initiation load. The initial load shedding as seen in the first load drop can be attributed to the debond of the core/top facesheet interface. Also for energy level A, we see the lower stiffness as compared to that exhibited at higher energy levels. This means that the elastic deformation seen in the FCo-16 for energy level A is a function of the energy of impact and is independent of the facesheet thickness. However, it is more pronounced for lower facesheet thicknesses. For energy level E, the foam undergoes extensive visible core crushing as compared to its corresponding FCo-16 sample. This leads to an increased transverse stiffness due to the closure of the foam cells at higher energy levels and hence for energy level E, a maximum stiffness indicated by the slope of the load-time curve till the first load drop is seen. This effect is more pronounced for the 32-ply facesheet because of the inertia of the thicker facesheet, which causes it to move with the tup, hence leading to minimal facesheet damage and extensive core crushing. This is visible from the greater number of load drops seen in the load/energy-time history and load-energy history of Figs. 8.21 and 8.22 as compared to Figs. 8.1 and 8.2. Figures 8.23 a and b, show the failure modes for the FCo-32 samples. In this case too, the facesheet-to-core disbond and core crushing are clearly seen.

The F+PCo-75 (32) samples show similar trends as their sixteen layer counterparts for the energy levels A through E as indicated in Figs. 8.24 and 8.25. There is a variation in the first load drop due to a variation in the position of the pins.

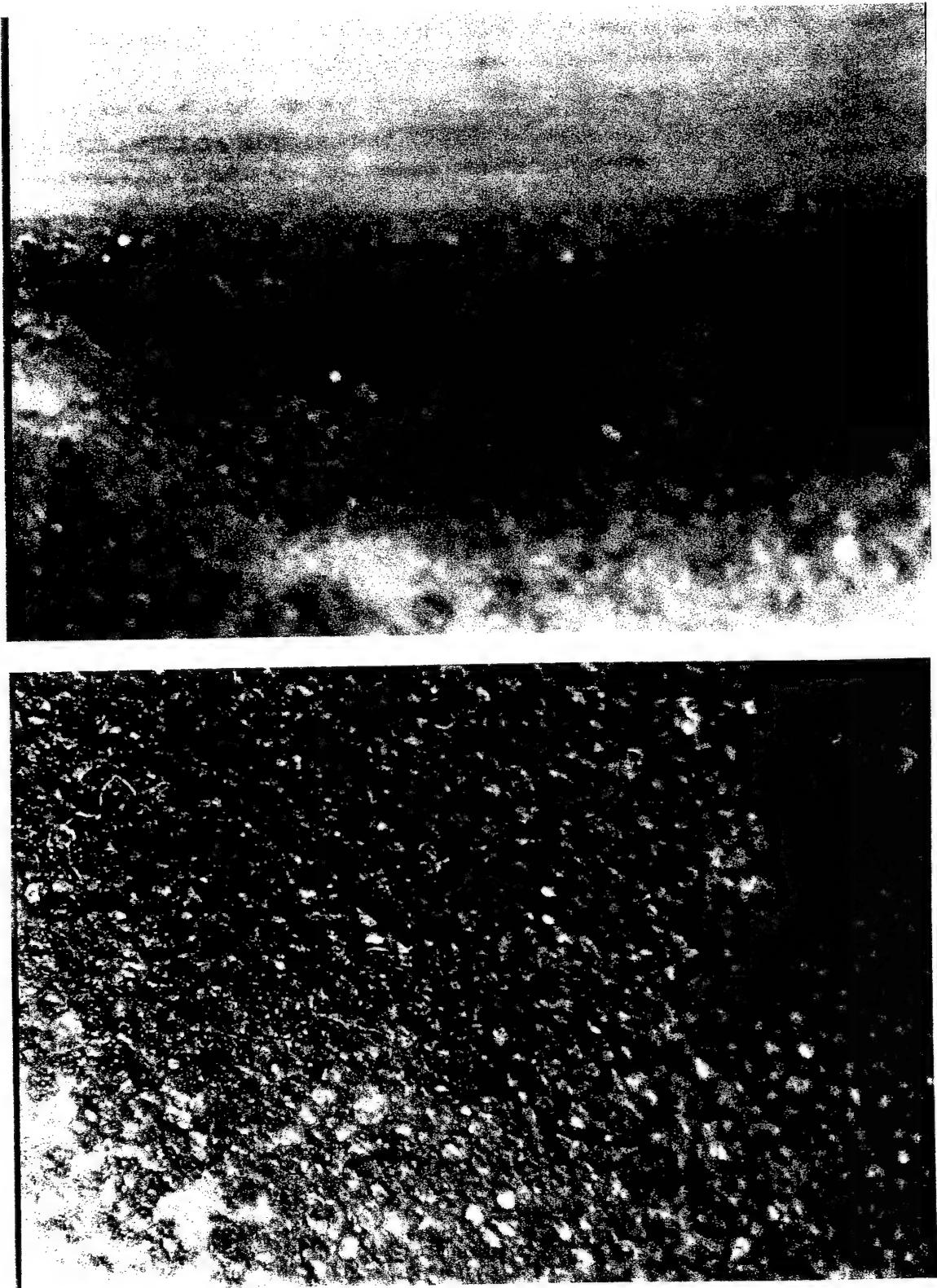


Figure 8.23a and b. Facesheet to core disbond and core crushing for FCo-32 Composite (Energy Level E)

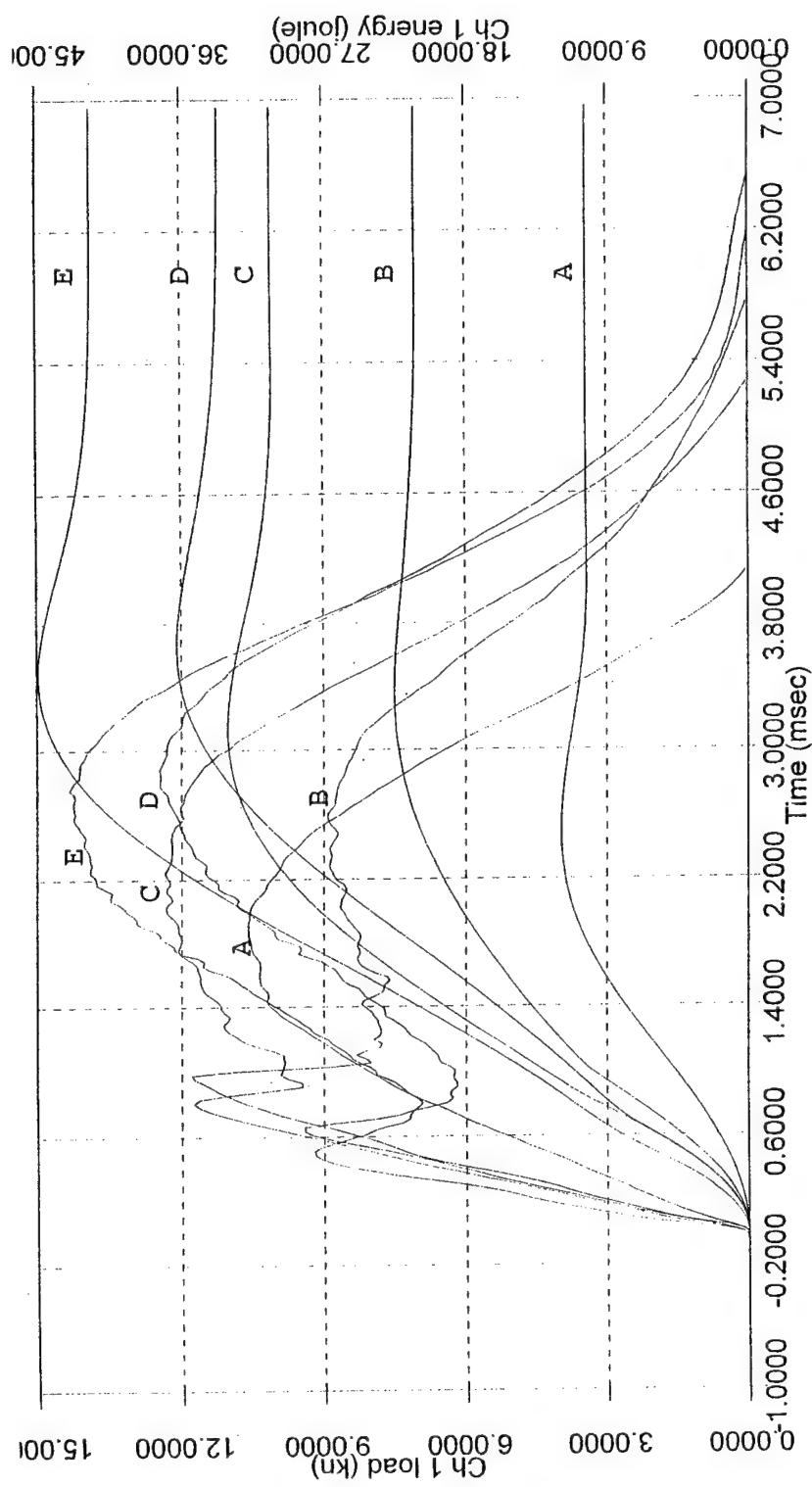


Figure 8.24. Load/Energy-Time curves for the F+PCo-75 (32) composites (Energy levels A-E)

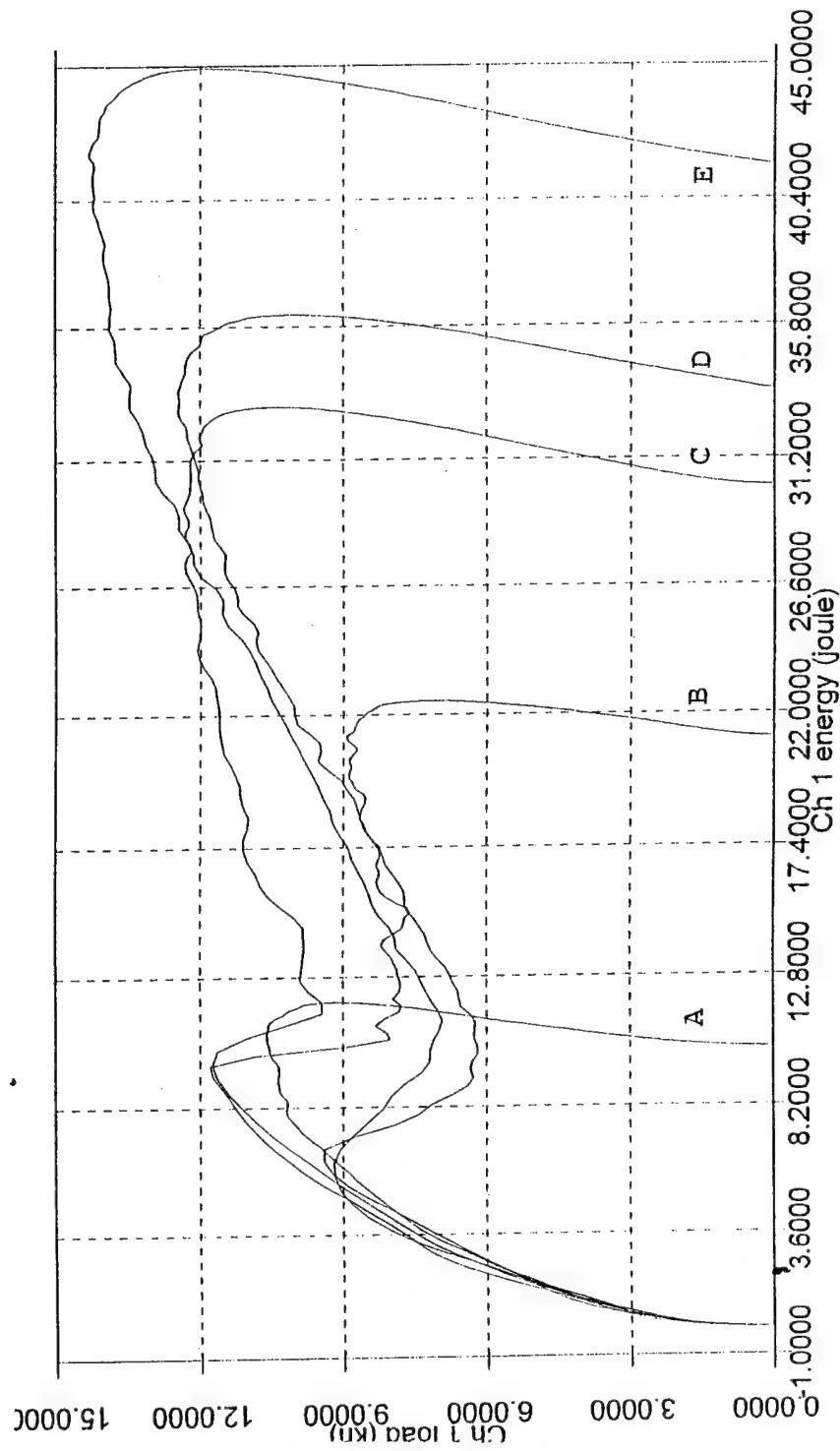


Figure 8.25. Load-Energy curves for the F+PCo-75 (32) composites (Energy levels A-E)

However, there is no characteristic load drop for the energy level A which indicates that damage does not initiate at this energy level. Hence, it is confirmed that increasing the facesheet thickness increases the damage initiation load and reinforcement of the core



Figure 8.26. Failure Mechanism of F+PCo-75 (RTM) Sample

with the pins restricts damage progression. For the F+PCo-75 samples, the average damage initiation load was ~ 2800 N which was 7% lower than that of ~ 3000 N for the FCo samples. However, for the F+PCo-75 (32) samples, the average damage initiation load is ~ 10500 N, which is $\sim 31\%$ higher than the FCo-32 samples. The damage initiation load for the 16-ply specimen was lower for the foam-reinforced-pin core composites as compared to the foam core composites because of the fact that the pins penetrating the facesheets cause a microlevel damage condition, combination of microcracks and fine delaminations (a processing related parameter). For the F+PCo-75 (32) samples, this load is higher than the corresponding FCo-32 samples, because of the fact that the thicker facesheet tends to offset the microdelaminations present because of the pins piercing the facesheets. Also, the curves after the initial load drop are smoother as compared to the FCo-32 samples. This is because, the pins reinforcing the foam restrict the global crushing of the foam and only minor load drops are seen which correspond to pin pushouts and microdelaminations at points where the pin pierces the facesheets. The thickness of the facesheets, however, restricts this mode of damage to a large extent.

The major failure mechanisms as shown in Fig. 8.26, were observed as facesheet to core disbond around the locations where the pins pierce the facesheet. Localized microdelaminations are seen at these points with a major part of the facesheet remaining intact. Evidently, a thicker facesheet restricts this mode of damage progression.

8.8 Frequency Response Tests

Vibration based NDE testing was performed on the specimens after impact testing. Figure 8.27 shows the FRF of the samples impacted at the A energy level over a frequency range 0-25,000 Hz. The characteristic bending modes can be clearly observed. The low density core tends to isolate the two facesheets as separate laminates, and the vibration response is more sensitive to the facesheet mounted on the impedance head. It is clearly seen for the first few modes of vibration that the TCo composites show maximum loss of stiffness, as indicated by the lowest frequency for the first mode of vibration. This is because of the fact that the titanium pin buckles very easily for concentrated impacts in the absence of the supporting foam. The minimum stiffness loss is seen for the F+PCo-75 samples. This may be attributed to the fact that the damage is concentrated between the pin dimensions and hence the stiffness loss is largely local. The second highest loss in stiffness is shown by the FCo composites because of the global crushing of the foam. The F+PCo-150 sample shows a behavior which tends towards that of the FCo sample. This may be attributed to the fact that as the pin spacing increases, the failure mode changes from that shown by a closely spaced pin-reinforced-foam core to a pure foam core.

Figure 8.28 shows the FRF for the samples impacted at energy level A for both the 16 as well as the 32 ply sandwich composite. The maximum stiffness loss is shown by the FCo-16 sample. The minimum stiffness loss is seen for the F+PCo-75 (32) sample. It is evident that for identical facesheet thicknesses, the stiffness loss for the foam-reinforced-pin core composite is lesser than that for the foam core composite. This is because, as discussed earlier, the pins provide damage containment. An important observation to be made here is that doubling the facesheet thickness makes a sandwich exhibit better post-impact stiffness as compared to that exhibited by foam-reinforced-pin core composite.

8.9 Influence of Manufacturing Technique: FCo (RTM) and F+PCo (RTM)

The FCo and the F+PCo-75 samples were also fabricated using the RTM technique as described in the manufacturing section. A direct correlation between the specimens mentioned in Sections 8.2-8.5 cannot be established here because the resin system used in RTM was vinyl ester 350 with the same configuration as that used for

Frequency Response Curves

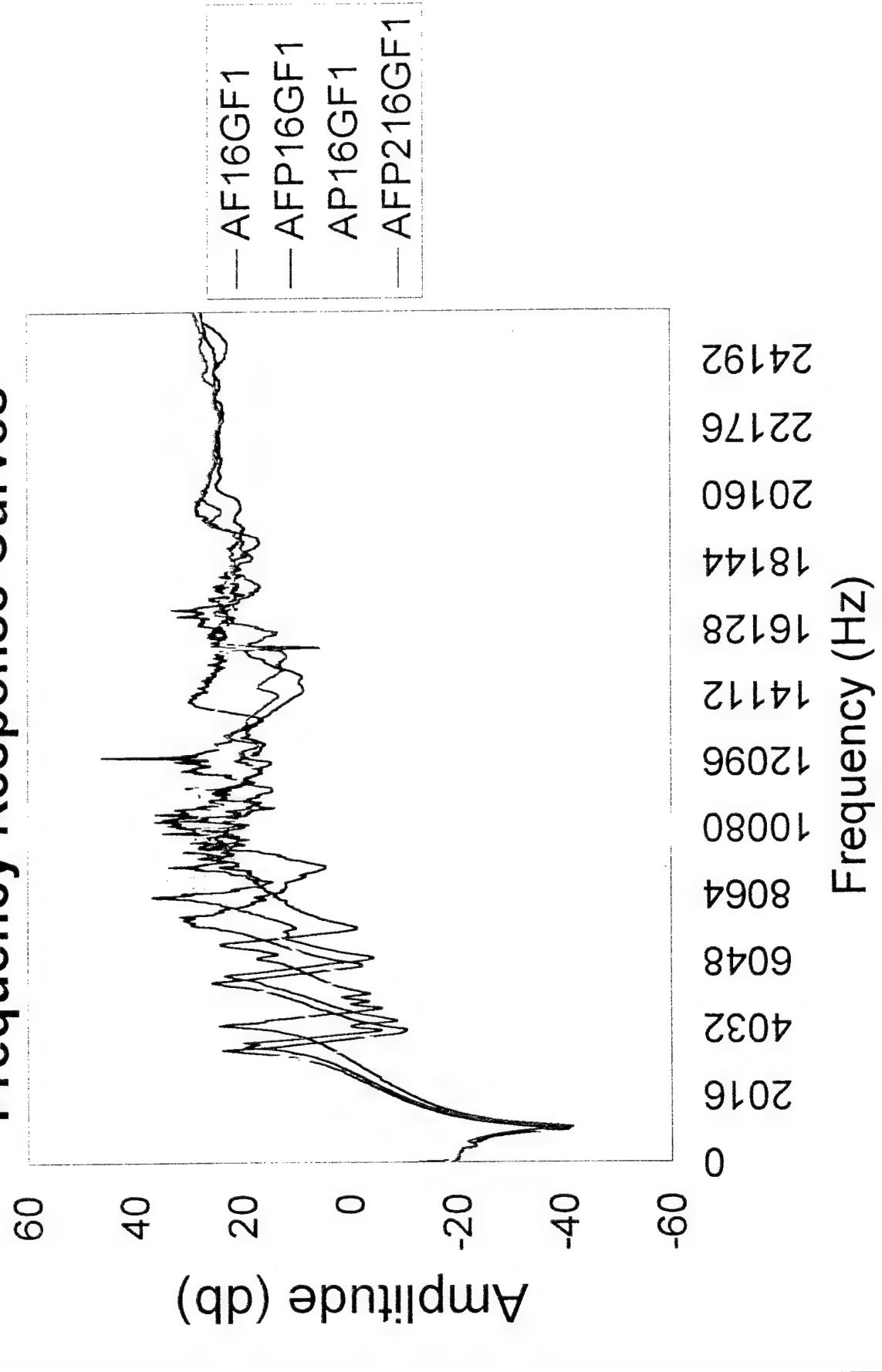


Figure 8.27. Comparison of FRF's of FC₀, F+PCo-75, F+PCo-150, and TCo Composites.(Energy Level A)

FRF Curves

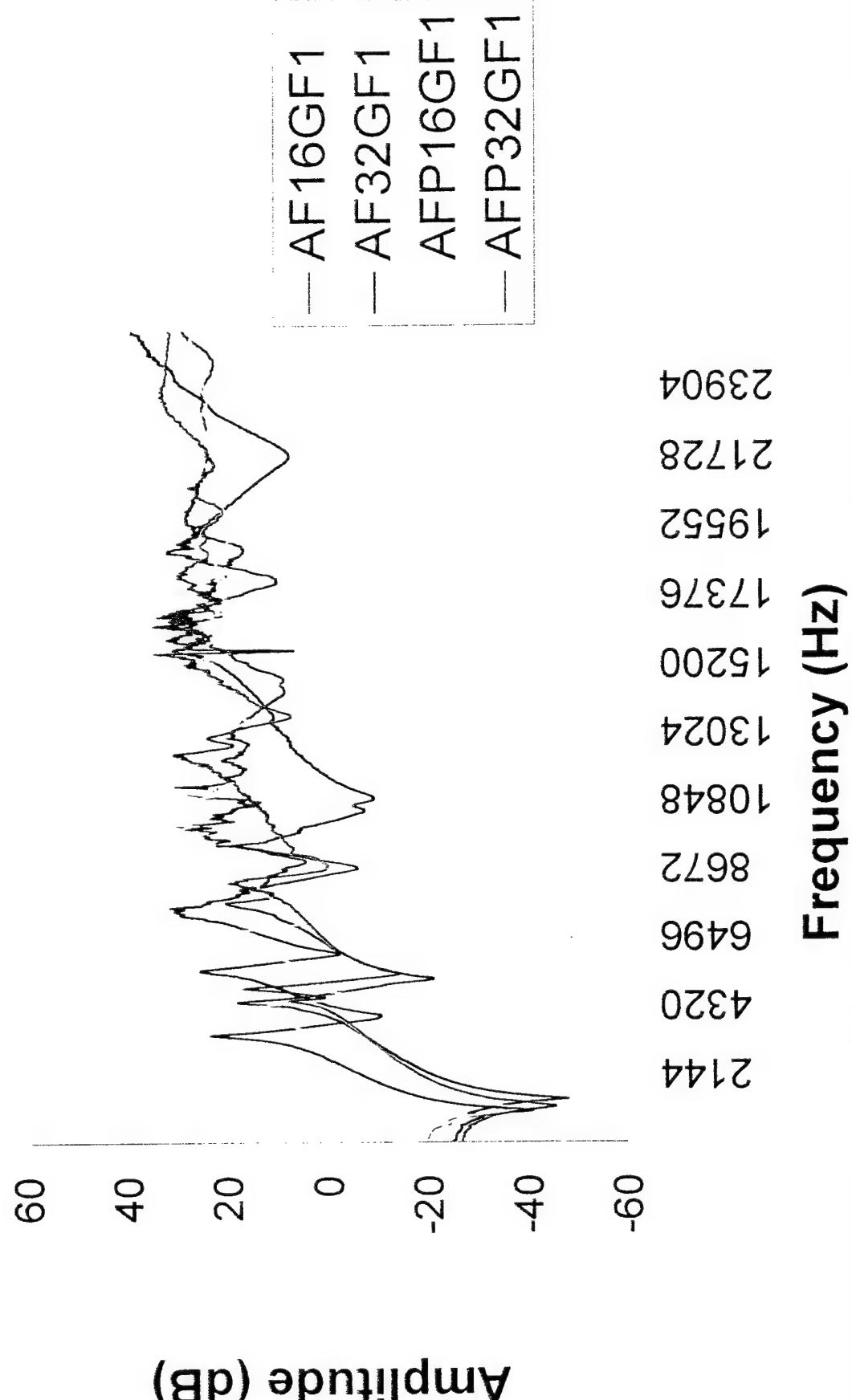


Figure 8.28. Comparison of FRF's of FCo and F+PCo-75 Composites with 16-ply and 32-ply E glass facesheets.

the honeycomb-filled-foam core specimen. Also, the fabric used was woven S2-glass as opposed to the unidirectional E-glass prepreg used earlier. However, this experiment validated various observations and proved them to be truly independent of the manufacturing technique used.

Figures 8.29 and 8.30 show the load/energy-time curves for the FCo composites manufactured by using the RTM technique. The characteristic first load drop is not clearly seen because damage is not extensive at this energy level. Only minor delaminations and fiber breakage with core crushing must be occurring. We also see the same gradual elastic deformation at this energy level and a stiffening effect as the energy level of impact increases due to a closure of foam cells. Apart from the minor undulations in the load/energy-time history, there is minimum damage and a maximum peak load of ~9000N is attained.

Figure 8.31 shows the failure mechanisms for the FCo (RTM) composite. Comparing it with Figure 8.4 a and b, we can see that the failure mechanisms are identical and the disbond between the facesheet and the core is very clear. Also, notable is that the extent of facesheet damage is minimum here, but this can be due to the greater toughness of the woven fabric which was used for the RTM process.

Figures 8.32 and 8.33 show the load/energy-time curves and the load-energy curves for the F+PCo-75 composites manufactured by the RTM technique. The characteristic first load drop is seen here for the energy levels D and E. This is because of our earlier reasoning that the presence of the penetrating pins weakens the facesheet and damage is initiated at ~6000N, about 33% lower than the FCo (RTM) samples. However, as expected, there is a slight variation in the first load drop because of the variation in the position, orientation and penetration of pins within the facesheet. Further load drops are greatly reduced after the first major load drop for the energy level D and the curves are relatively smoother. For energy level E, the pins tend to push out of the facesheets and minor load drops are seen along the load/energy-time history.

Figure 8.34 shows the failure mechanisms for the F+PCo-75 (RTM) samples. The facesheet to core disbond and core crushing is clearly seen here. The orientation of the facesheet fibers indicate flexure of the facesheet though, delamination and fiber fracture is not seen here. A comparison with Fig.8.31 shows that the extent of core damage is minimum for the F+PCo-75 (RTM) composite as compared to the FCo composite. This clearly demonstrates the superior damage containment mechanism of the pin-reinforced-foam core composite.

Figures 8.35 and 8.36 show a comparison between the load/energy-time and load-energy curves for the FCo and F+PCo-75 specimens. The pin reinforcement is seen to increases the transverse stiffness of the specimen and exhibits a higher load for damage initiation as compared to the FCo specimen. The rest of the history is identical

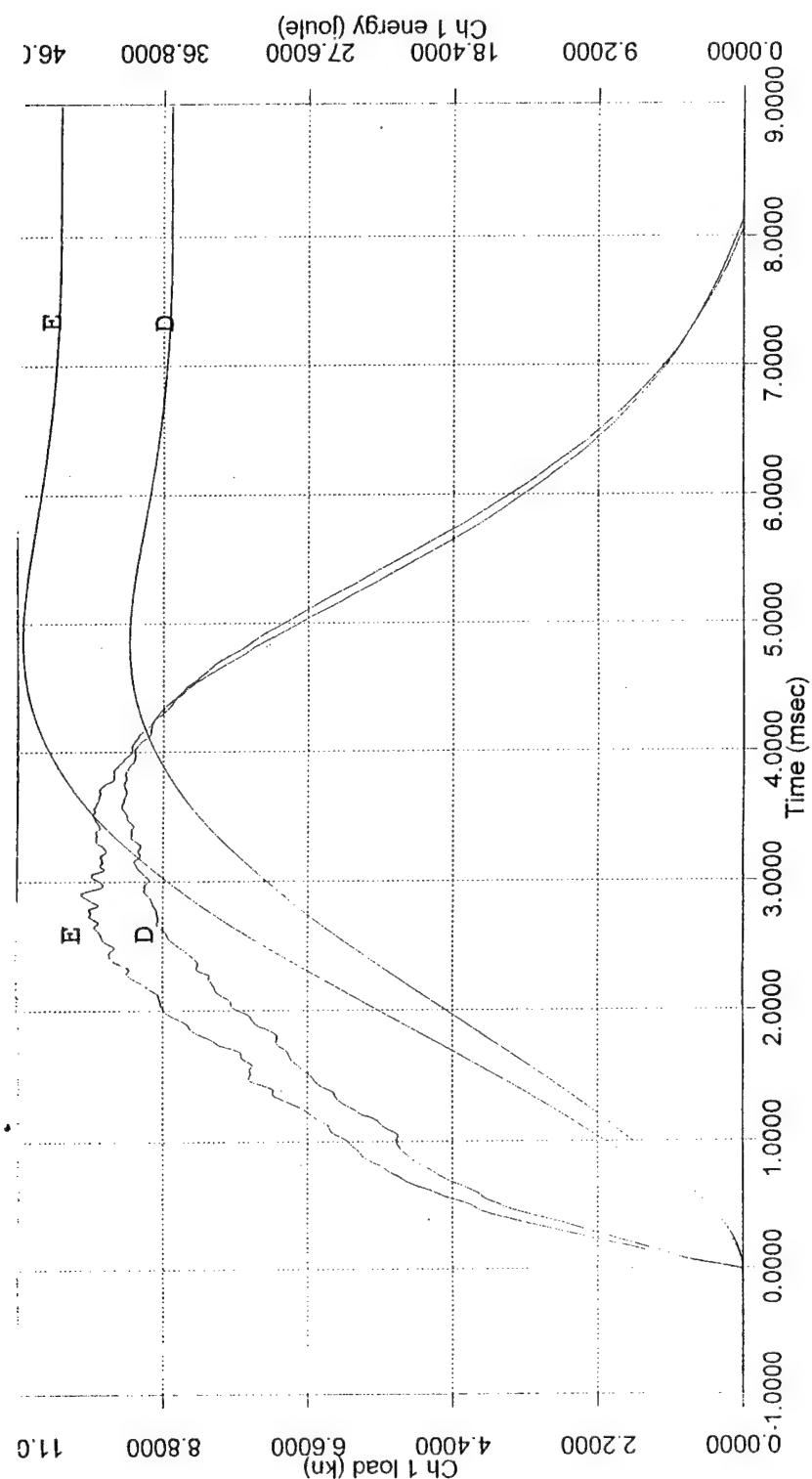


Figure 8.29. Load/Energy-Time curves for the FCo (RTM) composites (Energy levels D and E)

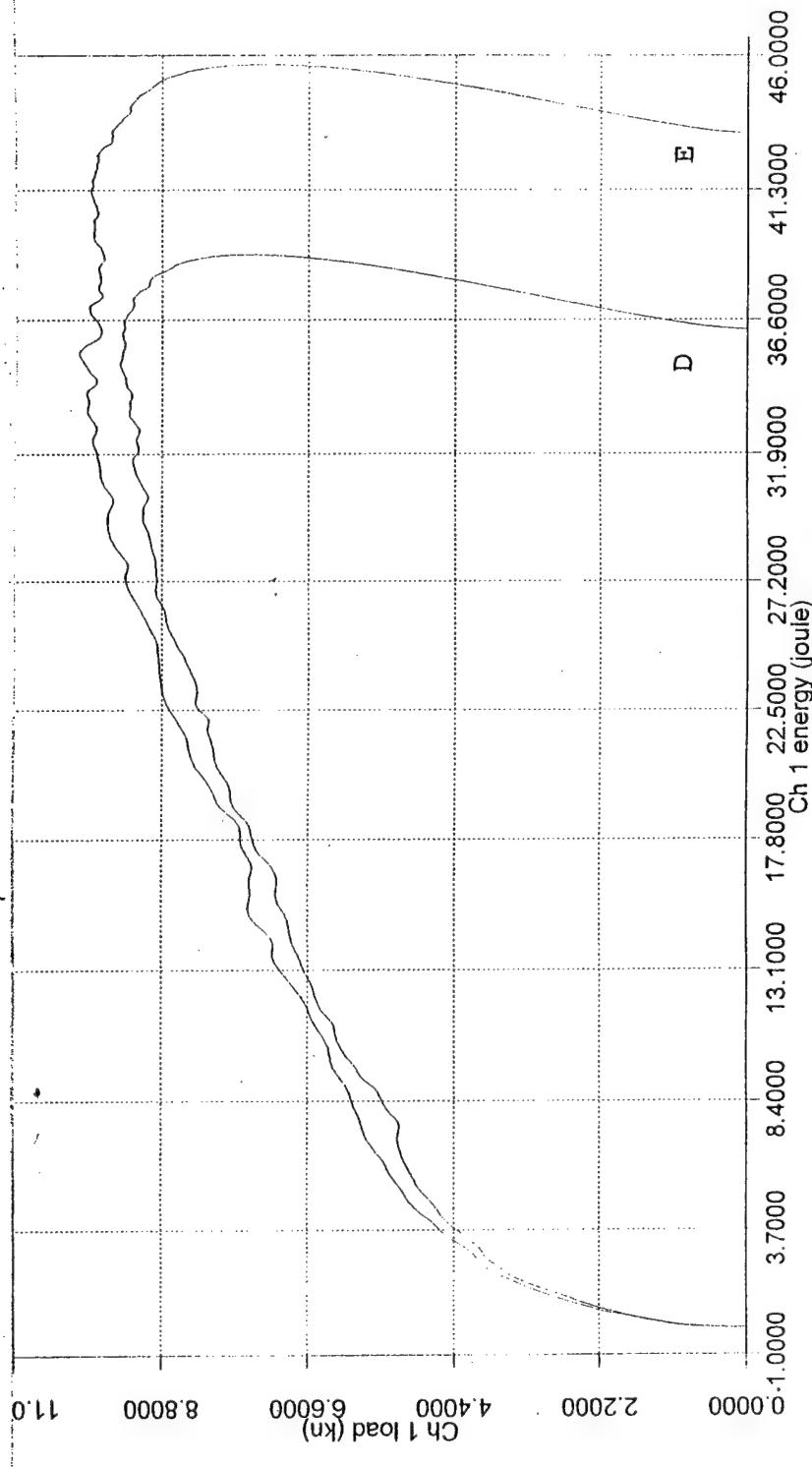


Figure 8.30. Load-Energy curves for the FCo (RTM) composites (Energy levels D and E)

for both the cores. This may be attributed to the greater resistance of the woven fabric in resisting damage progression beyond the damage initiation level as opposed to the unidirectional fibers used for the previously mentioned experimentation.

Figure 8.37 presents a comparison of the FRF curves for the FCo and the F+PCo curves manufactured by the RTM technique and impacted at the energy level D. The FCo composite exhibits a greater loss of stiffness as compared to the F+PCo sample. This proves that the superior damage resistance exhibited by the foam-reinforced-pin core sandwich composite core is independent of the manufacturing technique used.

8.10 Influence of Pin Type : F+PCo-75 (Glass/Epoxy Pins)

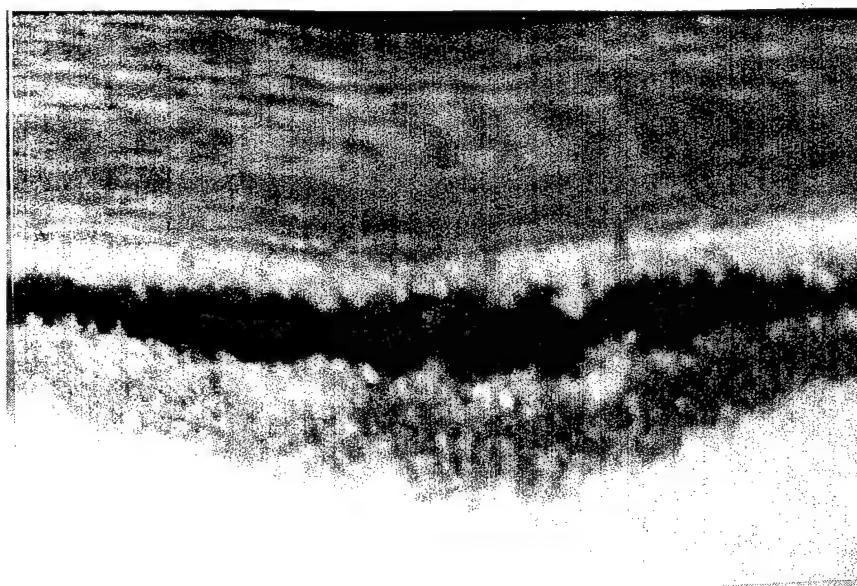


Figure 8.31. Failure of RTM Foam Core Composite. Illustration of Core Crushing Identical to that Observed in the VACM Produced Foam Core Samples

Instead of the titanium pins, E glass/epoxy composite pins produced from pultruded tow rods of diameter 0.075" (1.9 mm) were used for the fabrication of the F+PCo-75 specimen. The specimen was prepared using woven S2-glass fabric and vinyl ester 350 resin system. The wet lay-up technique was used for the fabrication of the same. In this case too, a direct correlation could not be established with the specimen described in Sections 7.2-7.5 as the facesheet and matrix system used were different. The objective was to view the effect of the pin type on damage modes only.

Figures 8.38 and 8.39 represent the load/energy-time and load/energy curves for the F+PCo-75 (glass/epoxy pins) samples impacted at energy levels, A, D and E. As is clear from the picture, damage is not initiated at energy level A. This may again be attributed to the fact that the woven fabric exhibits better impact resistance as compared

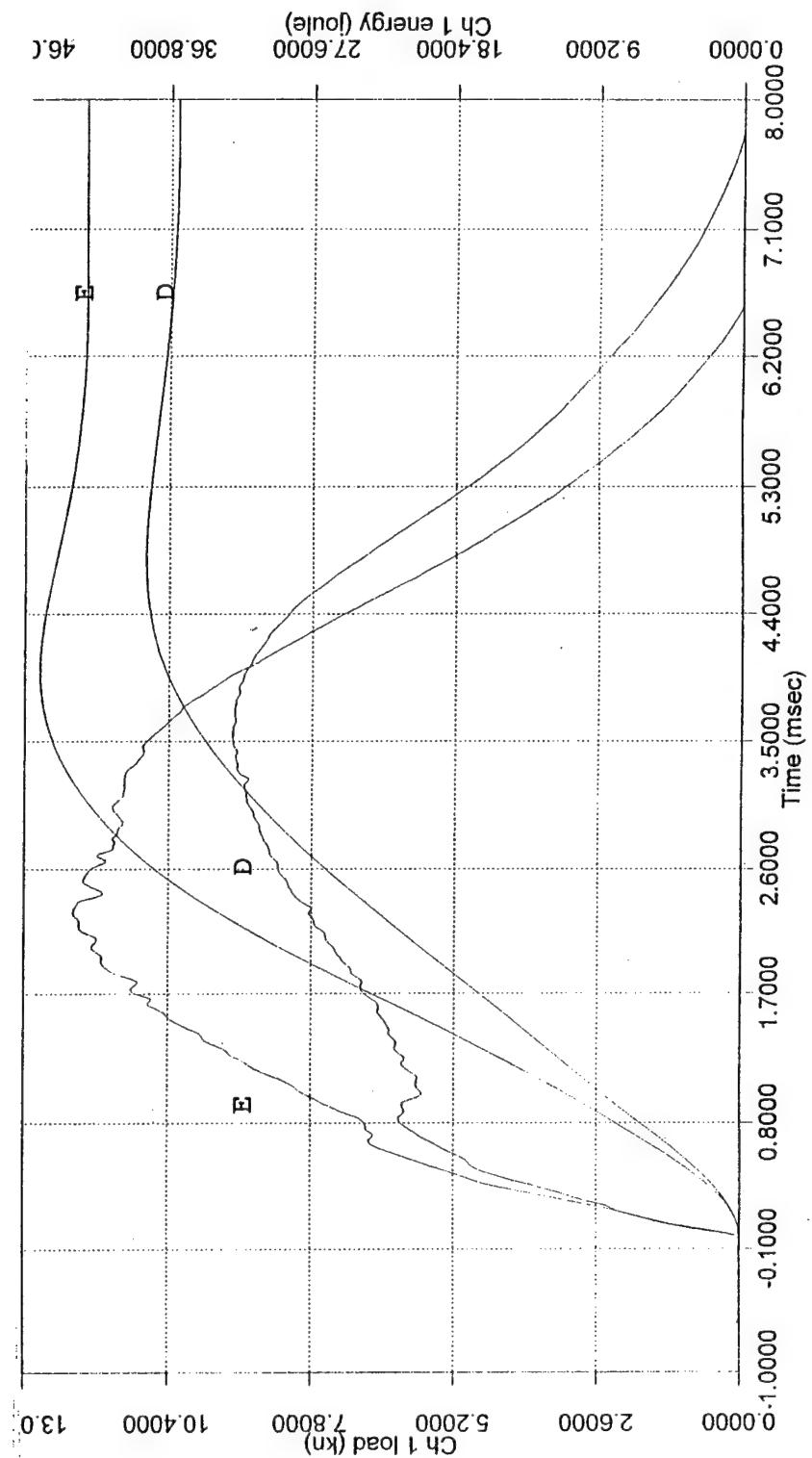


Figure 8.32. Load/Energy-Time curves for the F+PCo-75 (RTM) composites (Energy levels D and E)

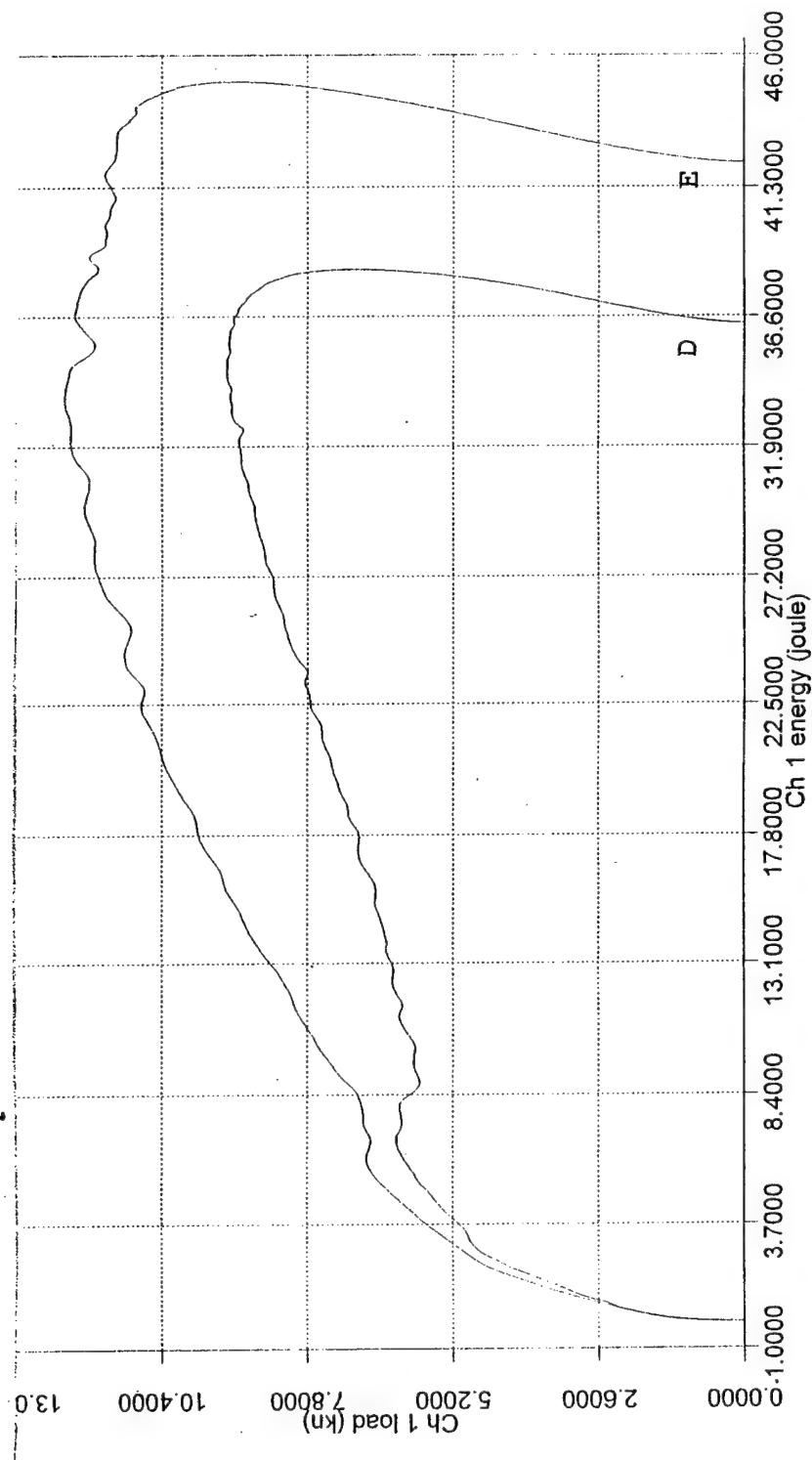


Figure 8.33. Load-Energy curves for the F+PCo-75 (RTM) composites (Energy levels D and E)

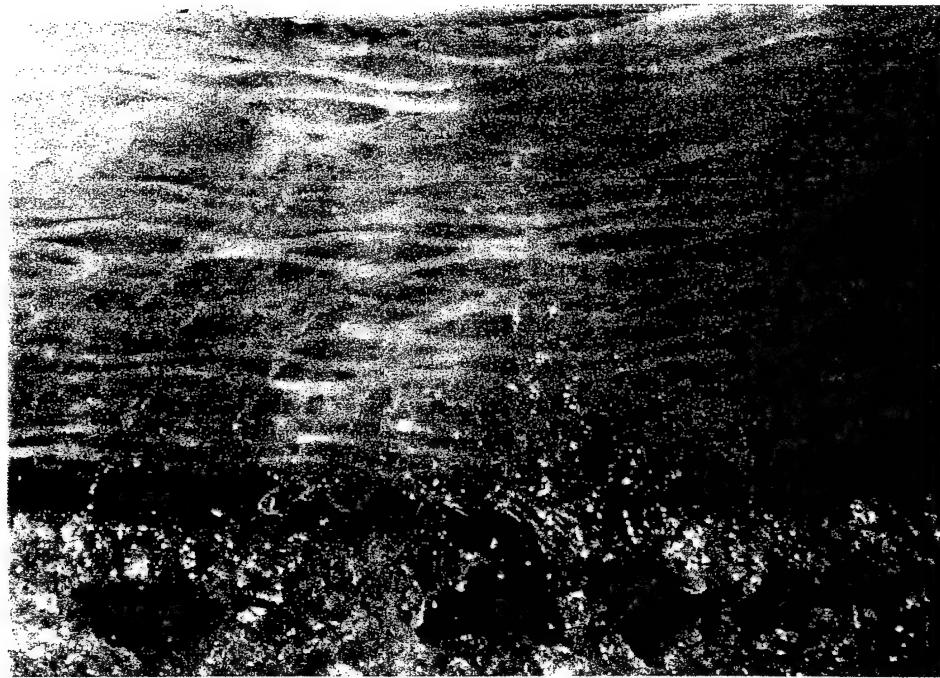


Figure 8.34. Core Crushing and Facesheet to Core Disbond for the F+PCo-75 (RTM) composites (Energy Level E)

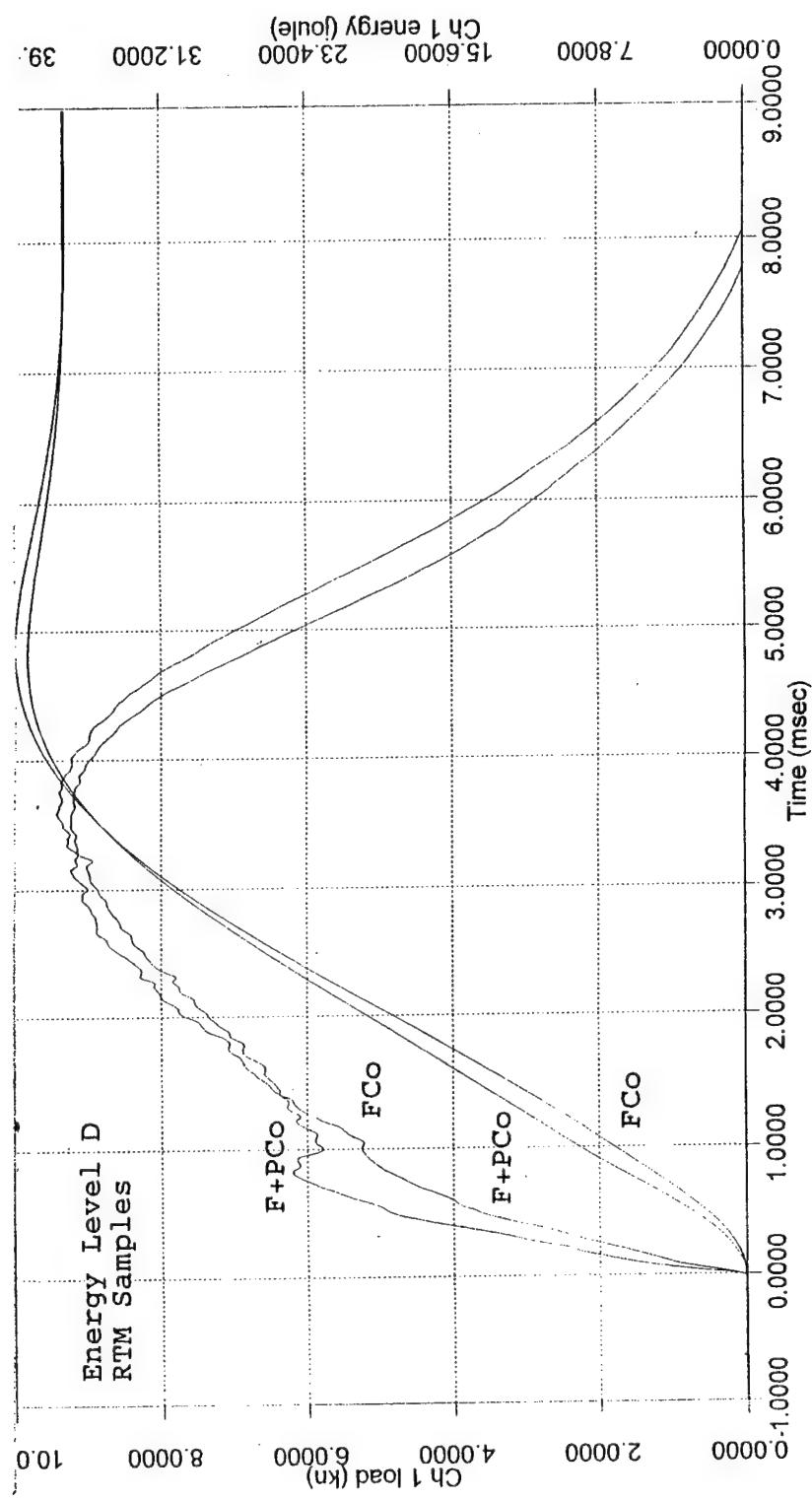


Figure 8.35. Comparison of Load/Energy-Time curves for the FCo (RTM) and F+PCo-75 (RTM) composites (Energy level D)

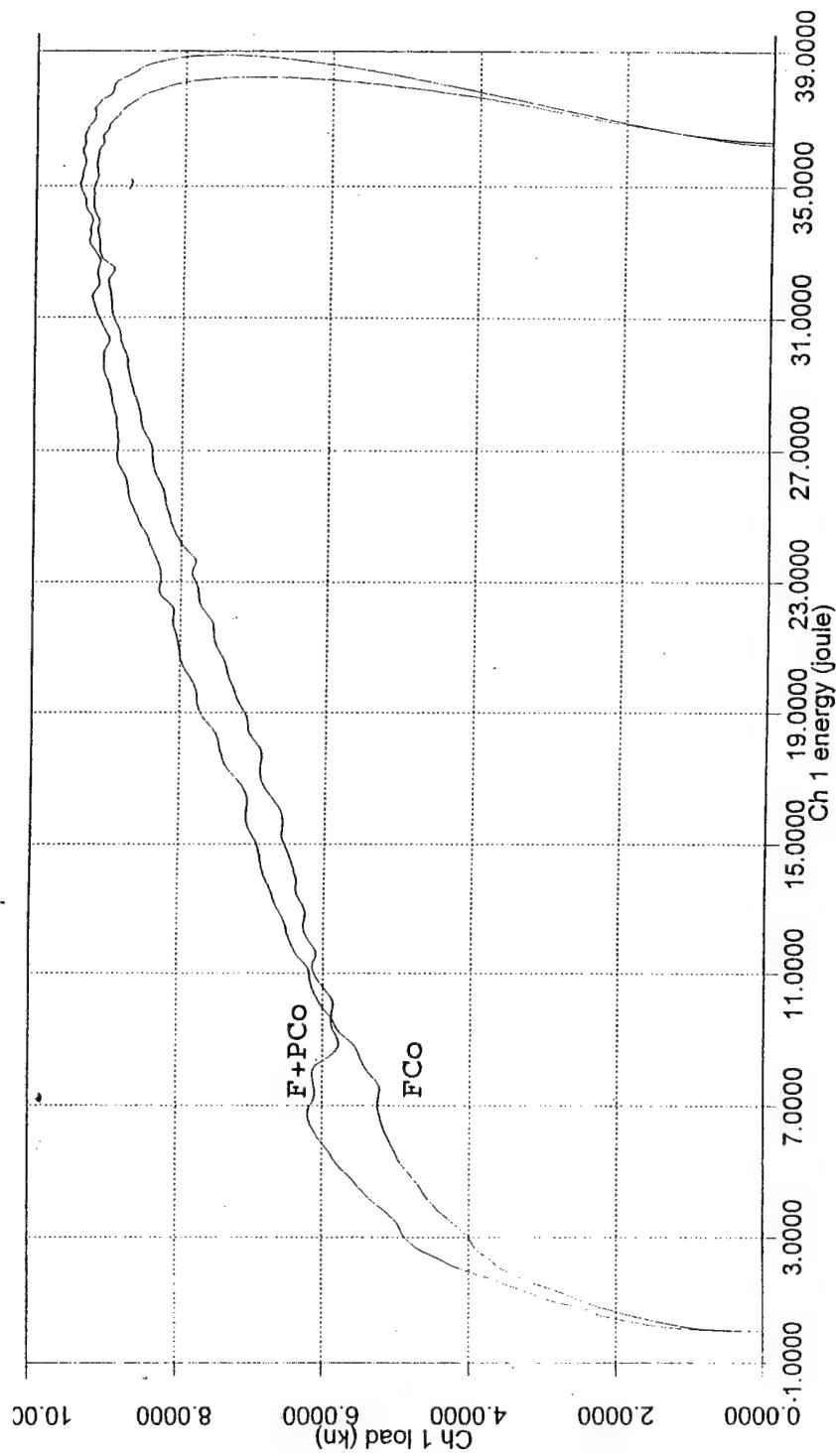


Figure 8.36. Comparison of Load-Energy curves for the FCo (RTM) and F+PCo-75 (RTM) composites (Energy level D)

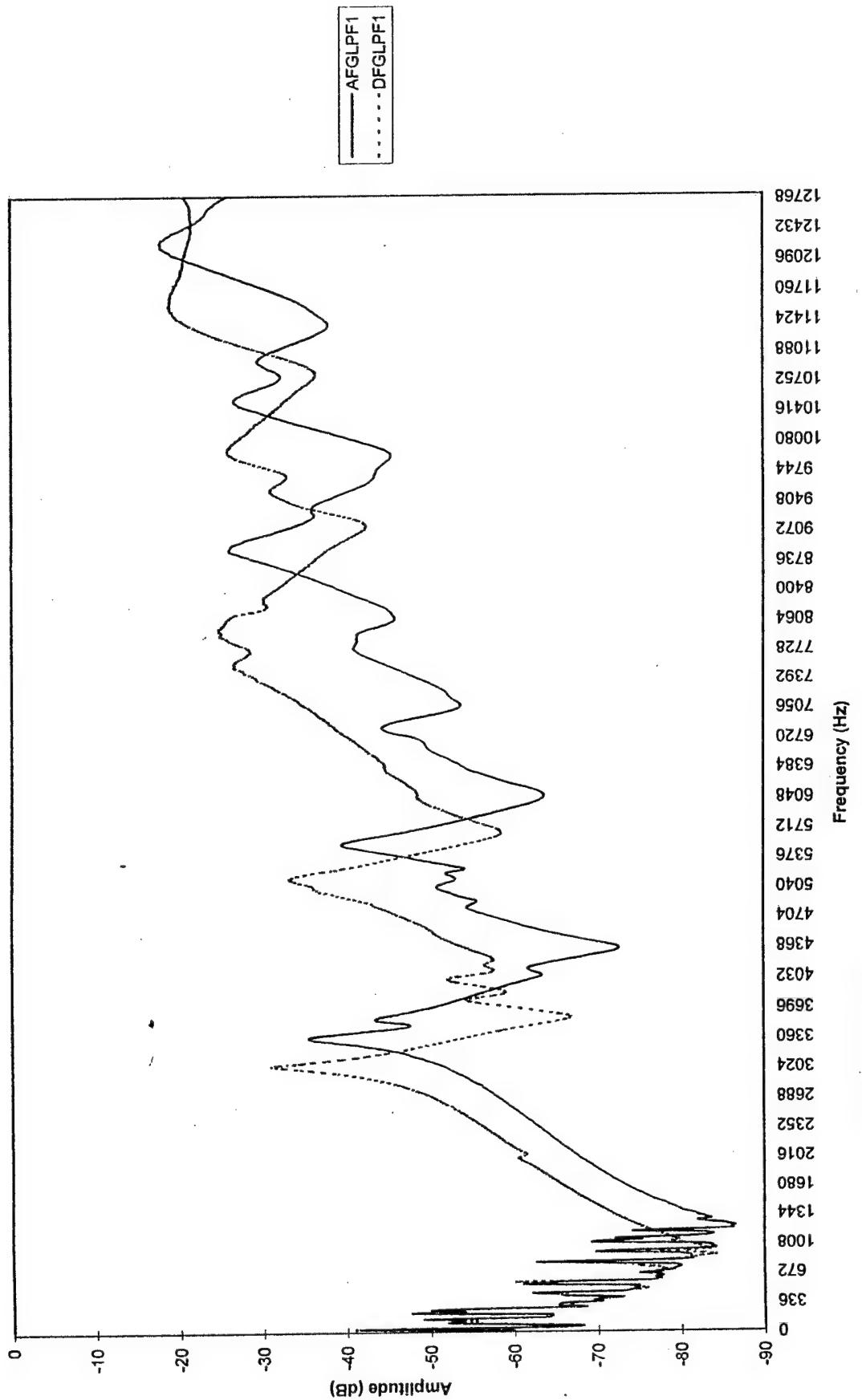


Figure 8.37. Comparison of FRF of the FCC and F+PCo-75 samples manufactured by RTM process (Energy level D)

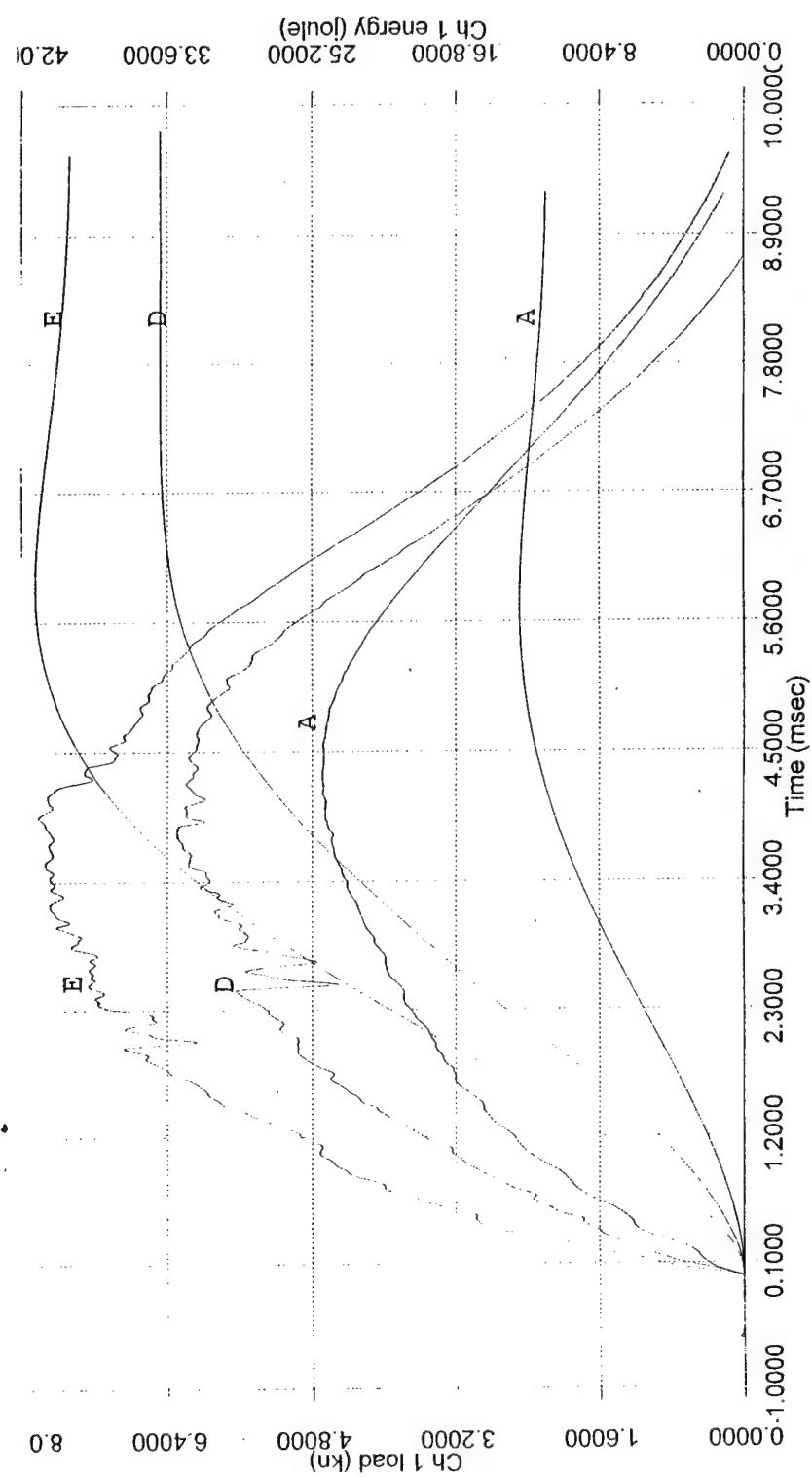


Figure 8.38. Load/Energy-Time curves for the F+PCo-75 (Glass/Epoxy pins) Composites (Energy levels A, D and E)

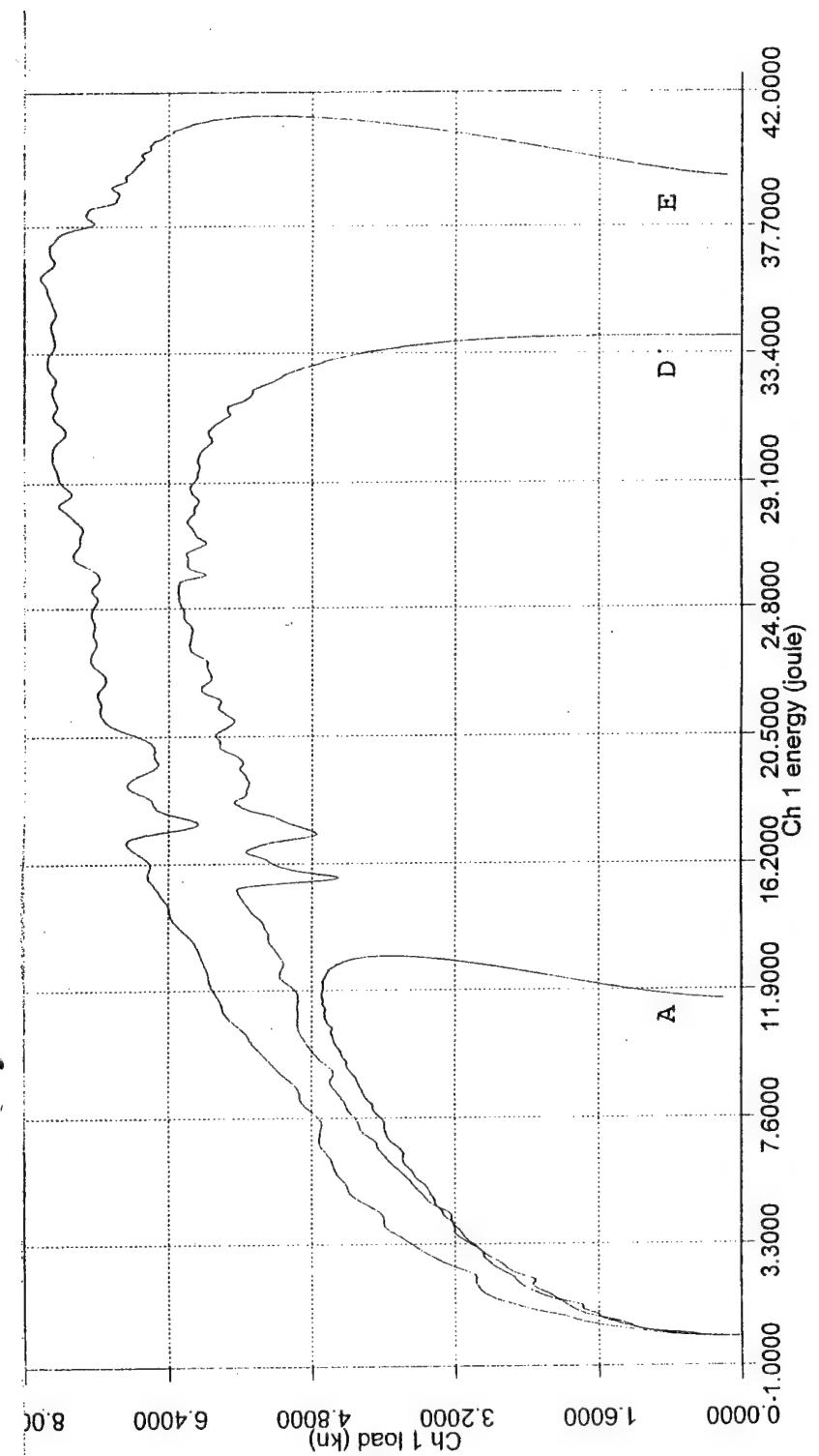


Figure 8.39. Load-Energy curves for the F+PCo-75 (Glass/Epoxy pins) composites
(Energy levels A, D and E)

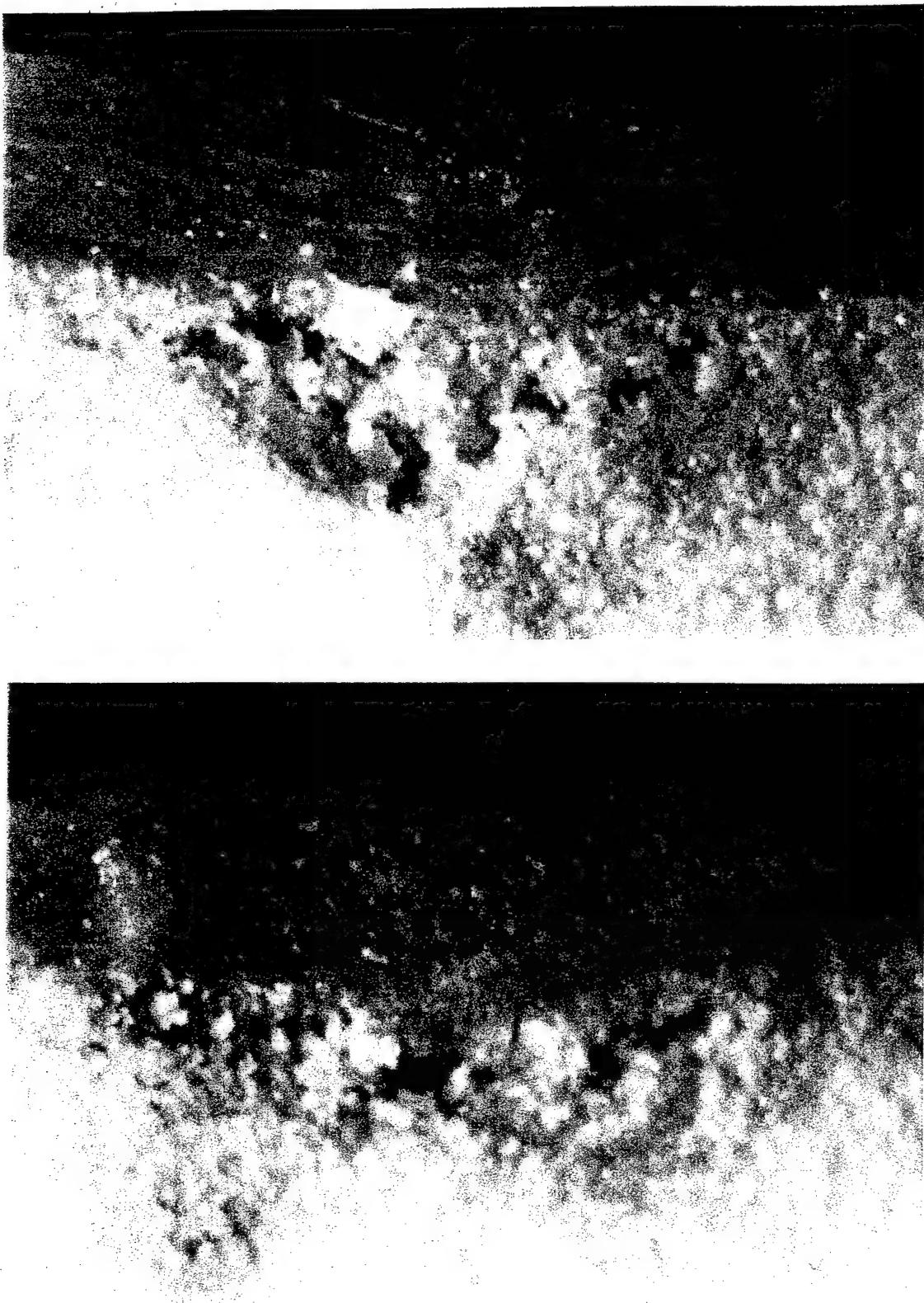


Figure 8.40. Facesheet to Skin Disbond, Core Crushing and Facesheet Flexure for the F+PCo-75 (Glass Pins) Composite (Energy Level E)

to the unidirectional fibers. Damage is being initiated for energy levels D and E as is evident from the load drops. There is some variation as expected because of the fact that there is a variation in the position and orientation of the pins. This condition is identical to that seen for the titanium pin reinforcement. Stiffening effects are evident from the increase of slope of the load-time curve as the energy of impact increases from A to the E level. Some minor load drops are also seen beyond the first major load drop which are indicative of minor fiber breakage and delamination near pin clusters piercing into the facesheets. Figure 8.40 shows the failure mechanisms for the F+PCo-75 (glass/epoxy pins) sample impacted at energy level E. The failure modes are identical to those observed for the corresponding specimen with titanium pins. The core crushing and facesheet-to-core disbond is also evident here. The orientation of the fibers in the direction following flexure of the facesheet is also clear. Delamination and fiber fracture are, however, notable in this case, perhaps because of the fiber architecture and the matrix system used.

The frequency response curves for the F+PCo-75 (glass/epoxy pin) samples shown in Fig. 8.41 indicate that the stiffness loss is proportional to the energy level of impact. The sample impacted at energy level D exhibits a greater loss of stiffness as compared to that impacted at energy level A.

8.11 Conclusions (Chaper 8)

The manufacturing procedure for producing foam core, pin reinforced foam core and hollow pin core sandwich composites by VACM and VARTM was established. While the time to reinforce the foam with pins was the same in both manufacturing techniques, the VARTM sandwich laminates were manufactured at faster processing times, due to the infiltration of the resin through preform, as opposed to the layerwise lay-up required in VACM.

Under low velocity impact, at higher impact energy levels (30 J and greater), damage initiates and propagates catastrophically in the foam core composites, causing extensive facesheet failure that initiates through core crushing and extends across top facesheet/core interface. At similar energy levels, the pin-reinforced foam core composites proved to exhibit superior damage containment and tolerance. Although damage is initiated at ~8% lower loads in the pin-reinforced foam core composite structures, the damage remains confined to the local dimensions of the pins in the vicinity of the impact. The damage initiation and containment mechanisms under low velocity impact for the foam reinforced with pins and the hollow pin core are more attractive than traditional foam core (FCo) composites. Of the three core constructions, the pin-reinforced foam core sandwich construction provided the best damage resistance / tolerance in terms of LVI. Damage was found to be locally confined to the impact side facesheet and the core, within the span of the arresting pins. When center-

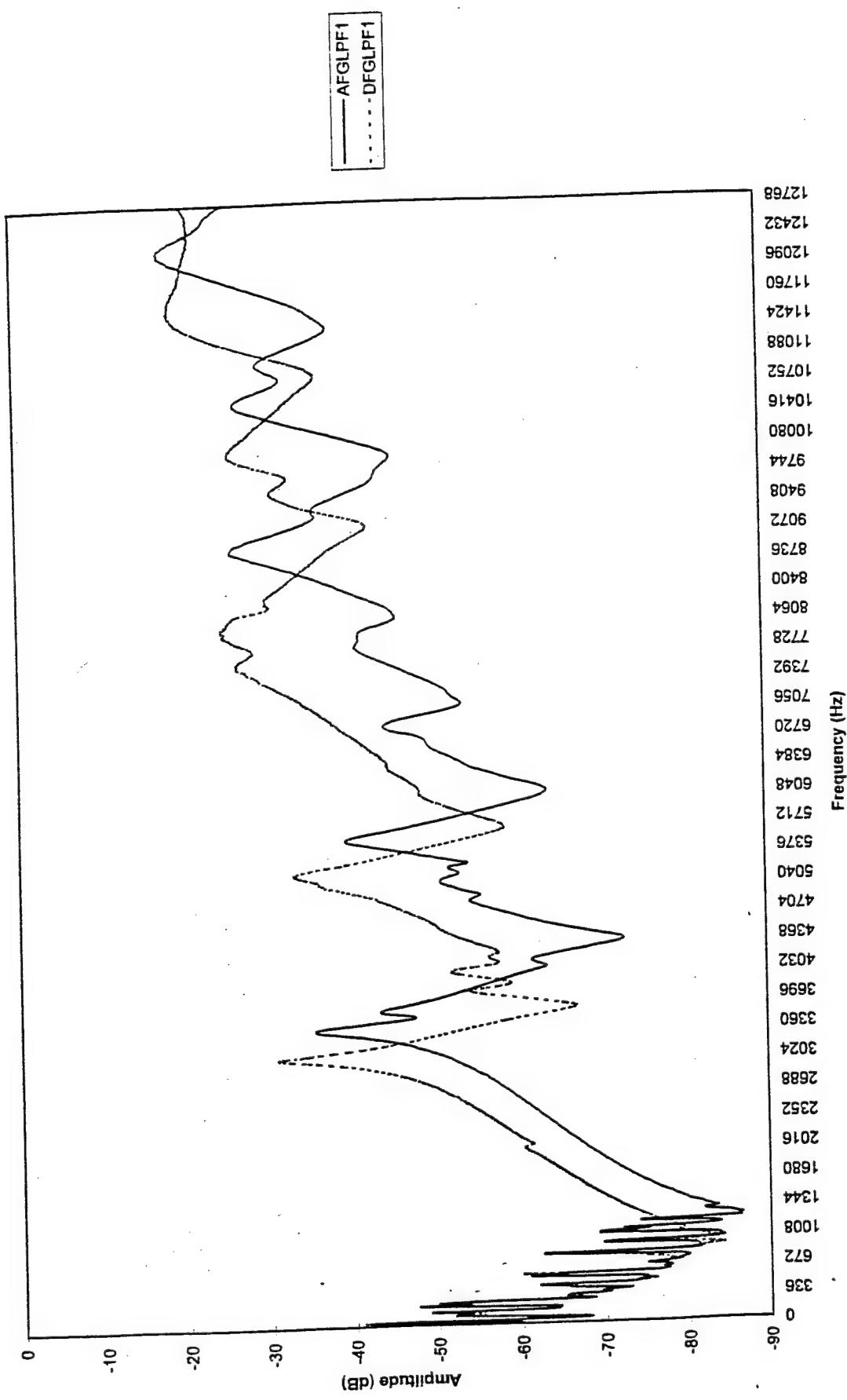


Figure 8.41. FRF curves for F+PCo-75 (Glass Pins) composites

to-center pin spacing was changed from 19.1 mm to 38.1 mm, the failure characteristics of the top facesheet changed from a complex flexure, reverse flexure cum shear failure accompanied by facesheet wrinkling, to a more clean flexure dominated facesheet failure. It appears that from a standpoint of minimizing processing cost and time, and lower core density, the 38.1 mm center-to-center pin spacing performed an adequate function of arresting the damage. Furthermore, when space considerations and weight savings are of interest, studies are underway to investigate several distributed areas of hollow pin core within a foam + pin reinforced core configuration.

The manufacturing process i.e., VARTM or VACM did not have marked influence in the LVI of the pin-reinforced composites in terms of failure initiation and progression. The peak loads attained and absorbed energy under LVI are a function of the facesheet used (whether pre-preg or woven fabric), however the influence of reinforcing the foam with pins has clear damage containment advantages and identical damage evolution mechanisms under both manufacturing techniques.

By doubling the facesheet thickness, the peak load under LVI was almost doubled. However, in the unreinforced foam core, damage was more catastrophic for thicker facesheets (32 vs 16), while in the pin reinforced foam core, damage was limited to the extent of pin penetration within the facesheet. As in thinner facesheets, for the thicker facesheets also, the damage zones were confined to a system of pin cluster. For thicker facesheets, the variations in first load drop (of the force-time curve) did not exhibit variation, because the role of the pin in initiating damage was suppressed due to the layers of the facesheet above the pin penetration. This suggests that pin-reinforced is effective as the facesheet thickness increases.

In terms of pin type, the titanium pin exhibited localized buckling, however, the glass/epoxy pins primarily exhibited localized debonding with respect to the core. At higher energies of impact (>30 J), the glass/epoxy pins exhibited localized fracture (limited to one or two pins surrounding the impact location). Although, in this study the pin diameters between the titanium and glass/epoxy pins were different (because of unavailability of identical diameter pins), the trends observed are expected to remain the same by using smaller diameter glass/epoxy pin, although peak loads attained under LVI may differ.

8.12 References

1. Weeks, C.A. and Sun, C.T., 1994. "Multi-Core Composite Laminates," Journal of Advanced Materials, April, 28-37.
2. Palazatto, A.N., Gummadi, L.N.B., Vaidya, U.K., and Herup, E.J, 1997, "Low Velocity Impact Damage Characteristics of Z-Fiber Reinforced Sandwich Panels

- An Experimental Study," 38th AIAA/ASME/ASCE/AHS SDM Conference, Kissimmee, FL, April.
3. Wu, C.L. and Sun, C.T. 1996. "Low Velocity Impact Damage in Composite Sandwich Beams," Composite Structures, 24, 21-27.
 4. Herup, E.J and Palazatto, A.N., 1996, "Low Velocity Impact Damage Initiation in Graphite/Epoxy Nomex Honeycomb Sandwich Plates," 37th AIAA/ASCE / ASME / AHS SDM Conference, pp.1765-1773.
 5. Abrate, S. 1991. "Impact on Laminated Composite Materials," Applied Mechanics Review, Vol.44, No.4, April, 155-190 (1991).
 6. Bernard. M.L., 1987, "Impact Resistance of Composite Sandwich Plates," Proc. ASC, 2nd Technical Conference, Newark, DE Sept.
 7. Vaidya U.K., Kamath. M.V., Mahfuz. H and Jeelani. S., 1997, "Low Velocity Impact Response of Resin Infusion Molded Foam Filled Honeycomb Sandwich Composites", (Under Review : Journal of Reinforced Plastics and Composites, August).
 8. Freitas, G., Magee, C., Dardzinski, P and Fusco, T., 1994, "Fiber Insertion Process for Improved Damage Tolerance in Aircraft Laminates," Journal of Advanced Materials, Vol.25, No.4, pp.36-43.
 9. Barret. R., Mechanics of Z-Fiber Reinforcement, Composite Structures, 1997.
 10. Vaidya U.K., Palazatto. A., and Gummadi. L.N.B., "Low Velocity Impact Response And Nondestructive Evaluation Of Sandwich Composite Structures," International Mechanical Engineering Congress and Exposition, ASME Winter Annual Meeting, Dallas, TX Nov.17-22, 1997.

8.13. Low Velocity Impact Response of Honeycomb Composites with Dissimilar Facesheets

8.13.1 Summary (9.0)

This section addresses some additional studies conducted on conventional honeycomb core sandwich composites. Honeycomb core with graphite and glass facesheet sandwich constructions are applicable in aerospace structures. In the current work sandwich honeycomb constructions have been considered with a graphite/epoxy facesheet on one side of the honeycomb core, and a glass/epoxy facesheet on the other (hybrid facesheets). Another highlight of the specimen was that the facesheet thickness was slightly offset in that the graphite/epoxy facesheet was 1.25 mm thick and the glass/epoxy facesheet 0.75 mm thick (~40% lower). The rationale behind this offset was to balance the weights of the facesheet. This yielded a stiffer and slightly thicker facesheet (graphite/epoxy) on one side and a facesheet with lower stiffness on the other end. The sandwich plate comprised, Nomex honeycomb core, 2.5 mm cell size, core thickness, 12.5 mm, Specification, 8HS Graphite Fabric/ Epoxy and 8HS Glass Fabric/Epoxy.

The samples were tested at two energy levels of impact; 20 J and 33 J respectively. At both the energies, the samples were tested in two ways : first by placing the graphite/epoxy facesheet facing the impacting head, and second where the glass/epoxy facesheet faced the impacting head. Figures 8.12.1 and 8.12.2 represent the typical force and energy-time response for the two test configurations at 20 J and 33 J, respectively. The difference in contact stiffness due to moduli of the facesheets is clearly seen from the force-time curves. The rising portion of the curves shows a much steeper slope in case of the graphite/epoxy facesheet facing the impactor as compared to the glass/epoxy side facing the impacting head. In case of the glass/epoxy side facing the impacting head, Fig. 8.12.1 indicates minor load drops in the rising portion of the curve that is primarily attributed to (as verified by microscopy) initiation of buckling of the honeycomb cell walls and due to incipient damage in the facesheet. The punch through of the top facesheet causes the major load drop. The retarding portion of the curve shows extended core damage. For any given facesheet thickness, as impact energy increases, eventually a point is reached where the load history shows a major load drop followed by multiple cycles of loading and partial unloading. For the graphite/epoxy side facing the impacting head, the core cell damage is not as evident as for the glass/epoxy side facing the impacting head. This is primarily because the thickness of the graphite side facesheet is ~40% higher than the glass/epoxy facesheet, and hence damage resistant. However, after damage of the facesheet indicated by the major load drop, extensive cell wall crushing is quite evident from the multiple loading/unloading portions beyond the major load drop. The damage or damages that

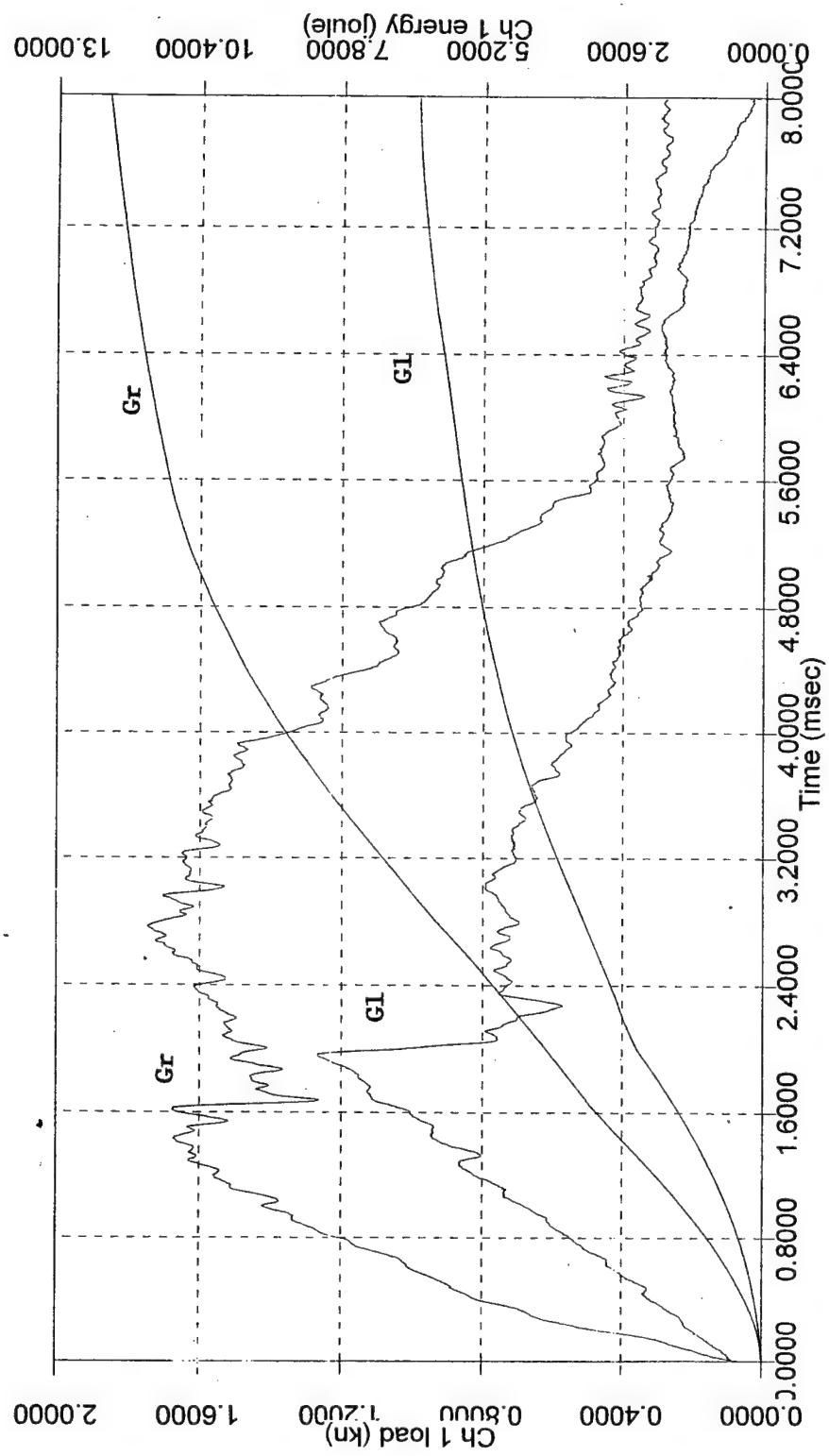


Figure 8.12.1. Load/Energy-Time curves for sandwich composites subjected to 20J Impact Energy

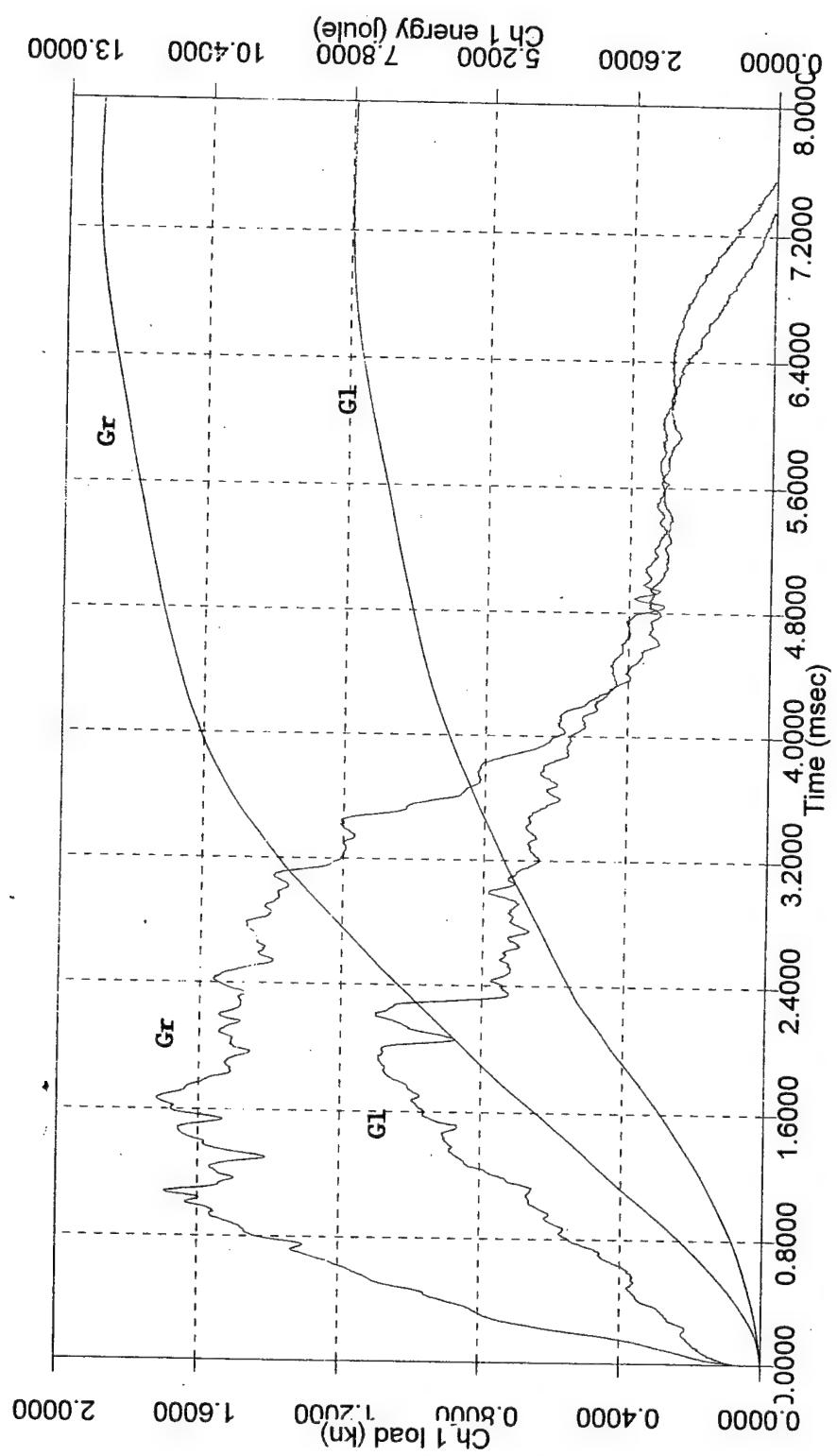


Figure 8.12.2. Load/Energy-Time curves for sandwich composites subjected to 33J Impact Energy

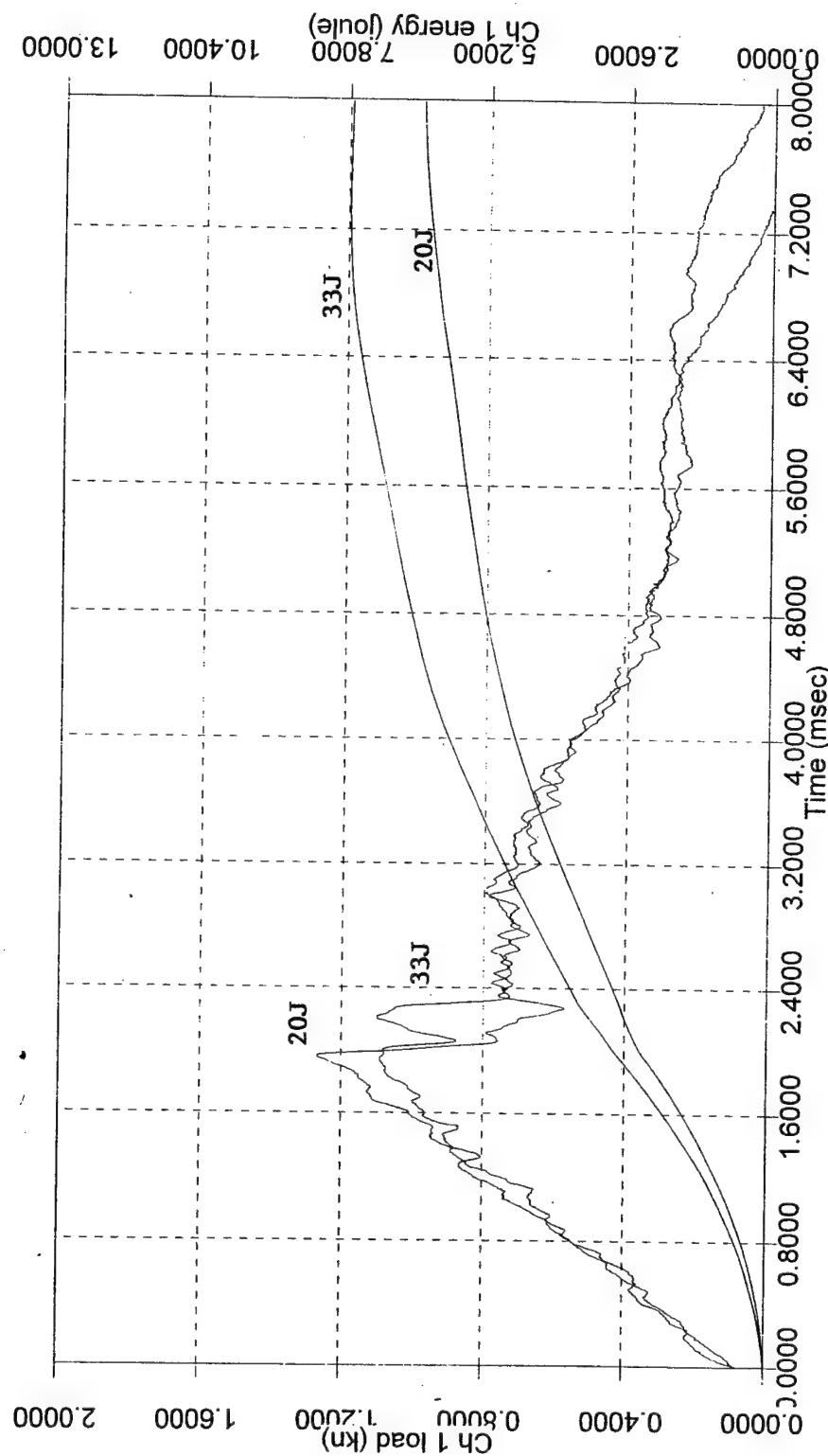


Figure 8.12.3. Comparison of Load/Energy-Time curves for impact from Glass/Epoxy Facesheet

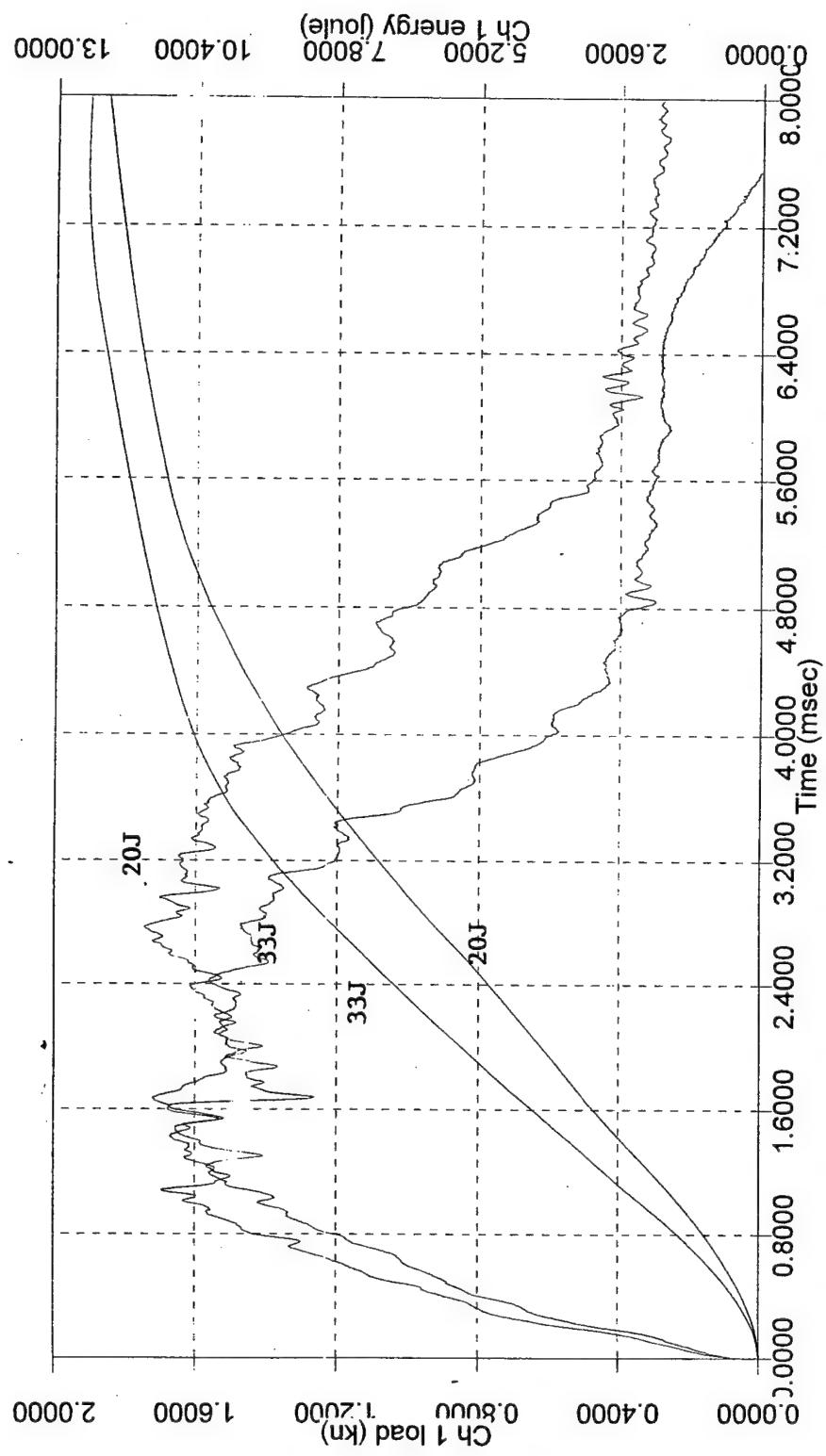


Figure 8.12.4. Comparison of Load/Energy-Time curves for impact from Graphite/Epoxy Facesheet

give rise to the major load drop are of interest. Also for any given facesheet thickness, the load at which the major load drop occurs is independent of impact energy. This is illustrated in Figs. 8.12.3 and 8.12.4. From Fig. 8.12.3, which illustrates the glass side facesheet facing the impacting head, the load drop occurs at ~1.1 kN for energy levels of 20 J and 33 J respectively. Similar response is seen from Fig. 8.12.4, where the graphite/epoxy side faces the impacting head, the load drop occurs at ~1.6 kN for the same energy levels. The initial load drop for a given type of sandwich core is independent of the impact energy it is subjected to. Beyond the first major load drop there are indications of additional load drops. Each load drop corresponds to failure within the sample. As the core material is different, the mechanisms of failure are different. The overall damage was higher in case of samples with graphite/epoxy facesheet facing the impactor. Figure 8.12.5a illustrates the core crushing and severe facesheet indentation and breakage of the graphite/epoxy facesheets. The visible damage in the core extended over three cell wall dimensions surrounding the facesheet. The thinner glass/epoxy facesheet exhibited concentrated facesheet fracture and punch through. The overall buckling of the core cells is lower for this case and so is the gross core damage in comparison to the impact on the graphite/facesheet as illustrated in Fig. 8.12.5b. The glass/epoxy facesheet absorbs significant portion of the energy in addition during the core crushing/buckling phenomenon. In the graphite/epoxy side

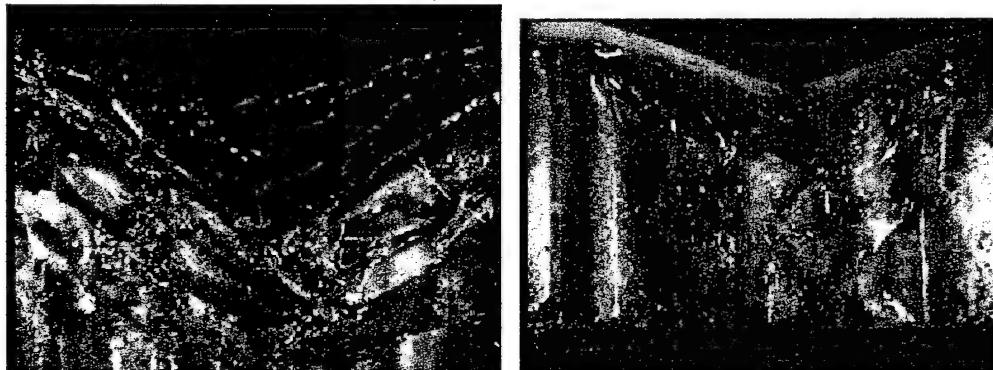


Figure 8.12.5 LVI a) from graphite/epoxy facesheet side, b) from glass/epoxy facesheet side

impacted samples, a major portion of the impact energy goes into crushing of the cells after the punch through of the core.

8.13.2 Conclusions

Under low velocity impact loading from respective sides of the facesheets, the glass/epoxy facesheets although thinner by 40% of the graphite/epoxy facesheets exhibited lesser facesheet and core damage. The glass/epoxy facesheet absorbs significant portion of the impact energy. The graphite/epoxy facesheets are stiffer and exhibit larger facesheet damage and extensive core crushing for similar levels of impact energy as the glass/epoxy laminates.

8.13.3 References

1. Zenkert, D. 1997. *The Handbook of Sandwich Construction*. London, UK: Engineering Materials Advisory Services Ltd., Chameleon Press Ltd.
2. Karlsson, K.F. and B.T. Astrom. 1997. "Manufacturing and Applications of Structural Sandwich Components," *Composites, Part A*, Elsevier Publications, pp. 97-111.
3. Weeks, C.A. and C.T. Sun. 1994. "Multi-Core Composite Laminates," *Journal of Advanced Materials*, pp. 28-37, April.
4. Vaidya, U.K., M.V. Kamath, H. Mahfuz, and S. Jeelani. 1997. "Manufacturing and Low Velocity Impact Response of Innovative Sandwich Composites," 29th International SAMPE Technical Conference, pp. 713-724, Vol. 29, Ed. Green, J.E, Beckwith, S.W and Strong, A.B.
5. Palazatto, A.N., L.N.B. Gummadi, U.K.Vaidya, and E. Herup. 1997. "Low Velocity Impact Response of Z-Fiber Reinforced Sandwich Panel : An Experimental Study, 37th AIAA/AHS/ASCE/ASME SDM Conference, Orlando, Florida, April
6. Herup, E. 1996. *Low-Velocity Impact on Composite Sandwich Plates*. Ph.D. Dissertation, Air Force Institute of Technology, Dayton, Ohio, July.
7. Scarponi, C., G. Briotti, R. Barboni, A. Marcone, M. Iannone. 1996. "Impact Testing on Composite Laminates and Sandwich Panels," *Journal of Composite Materials*, Vol. 30, No. 17, pp. 1873-1911.
8. Wu, C.L. and C.T. Sun. 1996. "Low Velocity Impact Damage in Composite Sandwich Beams," *Composite Structures*, 34, pp. 21-27.
9. Kim, C. and E. Jun. 1992. "Impact Resistance of Composite Laminated Sandwich Plates," *Journal of Composite Materials*, Vol. 26, No. 15, pp. 2247-2261.
10. Nemat-Nasser, S., J.B. Isaacs, and J.E. Starrett. 1991. "Hopkinson Techniques for Dynamic Recovery Experiments," *Proceedings of Royal Society of London*, 435, pp. 371-391.

9.0 COMPRESSION-AFTER-IMPACT AND ACOUSTIC EMISSION NONDESTRUCTIVE EVALUATION

9.1 Introduction

The samples after being subjected to low velocity impact undergo significant loss of stiffness. Damage is seen to initiate in the samples within the energy levels considered, and hence the samples are significantly weakened by the impact event. To obtain a clear idea of the damage tolerance after the impact event, the samples were subjected to compression-after-impact (CAI) and the samples were monitored for acoustic emission (AE). The specimens were subjected to CAI testing in a Suppliers of Advanced Composite Materials Association (SACMA) recommended plate fixture [1] as shown in Fig. 9.1. The specimens were end loaded in a 110 kips MTS load frame as shown in Fig 9.2a and b. A 150 kHz AE sensor was fed to a AE LOCAN AT data acquisition system via a preamplifier [2]. Static compressive load was applied until failure at a crosshead rate of 1.27 mm/min.

9.2 Compression-After-Impact and Acoustic Emission Studies for Foam-Filled Honeycomb Core Sandwich Composites

The failure loads based on impact levels for 16-ply graphite composites tested were: B:14,400 lbs, C:13,920 lbs and E:13,800. For the S2-glass composites, they were: B:14,200 lbs. and C:13,500 lbs. With the exception of two samples, which exhibited end crushing, the remaining samples failed in their gage section. Typically, the failure location coincided with the low velocity impact location as shown in Fig. 9.3. the damage was found to be severe on the low velocity impact side facesheet, and little or no evidence of back facesheet failure due to CAI was evident. The damage state and failure loads were in close accordance with the impact energies that the specimens had suffered. Furthermore, the interface between the core and the facesheets remained intact, except for core shearing and core crushing in the vicinity of the damage location as shown in Fig.9.4 on the impact side facesheet failed by kink-band formation and shear instability of the facesheet, showing a fork in the laminate at the impact location, as is also illustrated in Fig. 9.4. The 8-ply S2-glass facesheet composite, showed higher degree of compliance, and tendency towards end crushing in comparison to the graphite facesheet composites.

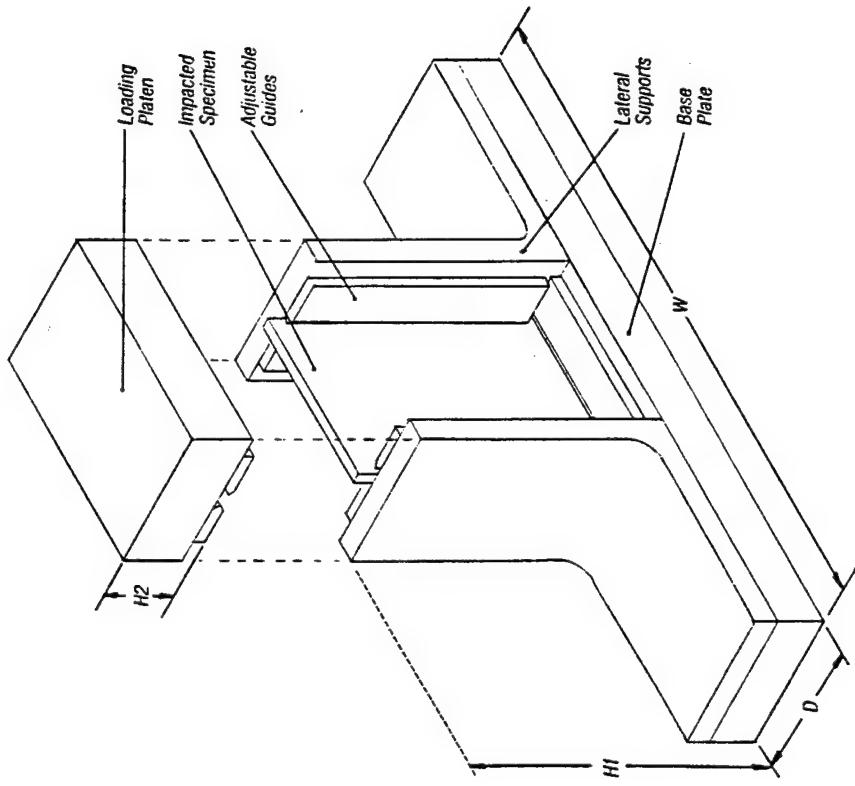


Figure 9.1. SACMA recommended Boeing test fixture for Compression after impact Studies

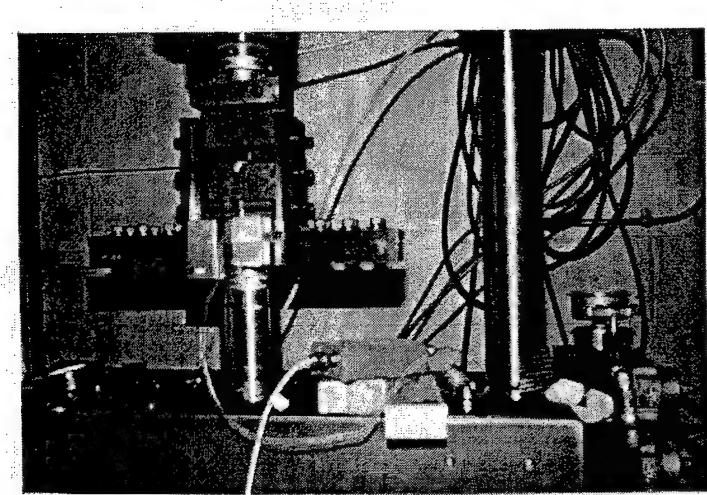
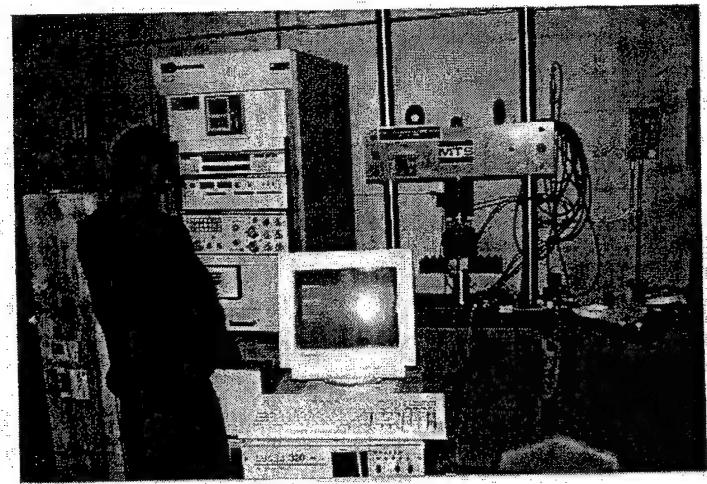


Figure 9.2a,b Photograph of the CAI Testing using MTS



Figure 9.3 Top View of Top Facesheet showing CAI Failure and Failure in the Vicinity of Impact Location



Figure 9.4 CAI Failure of Top Facesheet: Kink-Band Formation and Shear Instability of the Facesheet

Figure 9.5 shows the parametric distribution of energy and amplitude of AE activity for the 16-ply facesheet graphite composites. The high energy events in the initial loading occur during the occurrence of full contact of the loading device to the specimen. With subsequent loading, high energy (>1500) and high amplitude (>80 dB) events occur coinciding with facesheet failure. It is also seen that a stream of low energy events occur throughout the loading period that are characteristic of slow matrix cracking, fiber kinking, kink-band formation and fiber filament level fracture. Beyond 42 seconds of the time axis, three groups of events are seen to occur collectively, small energy (<600), low amplitude (40-60 dB) that are attributed to fast developing kink bands and matrix cracks, medium energy (600-1200), medium amplitude (60-80 dB) that are attributed to frictional energy dissipation due to fiber kinking and matrix facesheet cracking, and high energy (>1500), high amplitude (80-100 dB) events that are due to fiber fracture and delamination around the kink-bands.

9.3 Compression-After-Impact Studies for Foam, Hollow and Z-Pin Reinforced Core Sandwich Composite

The FCo, F+PCo-75 and the TCo samples were also tested in the SACMA recommended test fixture where the plate is free to slide along its edges but is constrained from moving along its bottom edge. The load is applied along its bottom edge. The CAI load-displacement curves represent the failure patterns to follow the facesheet conditions. The ultimate failure loads are seen to depend on the impact history the samples were subjected to. As expected, in the edgewise loading of the samples, the core has minimal participation in the load bearing process.

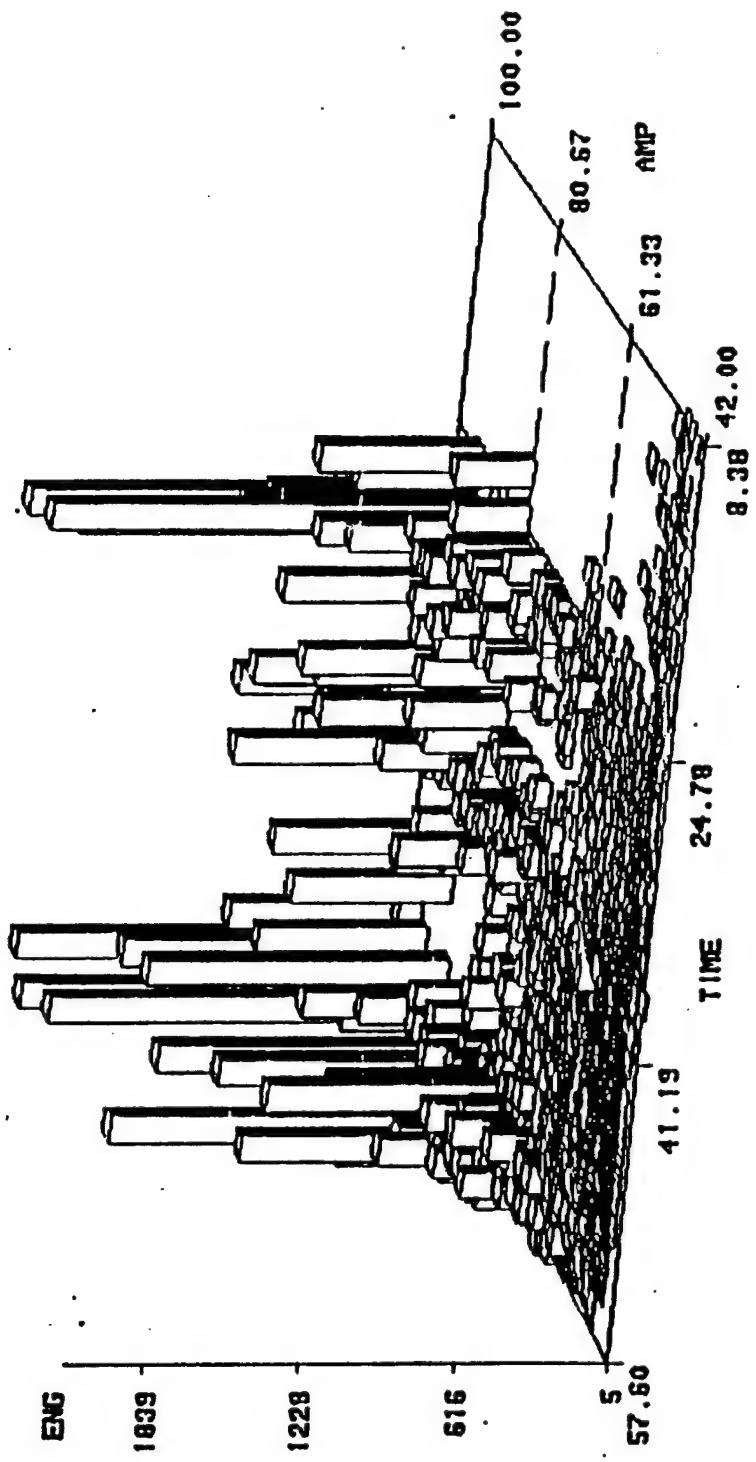


Figure 9.5. Parametric distribution of energy and amplitude of AE activity for the 16 ply facesheet graphite sandwich composite (Foam-Filled-Honeycomb)

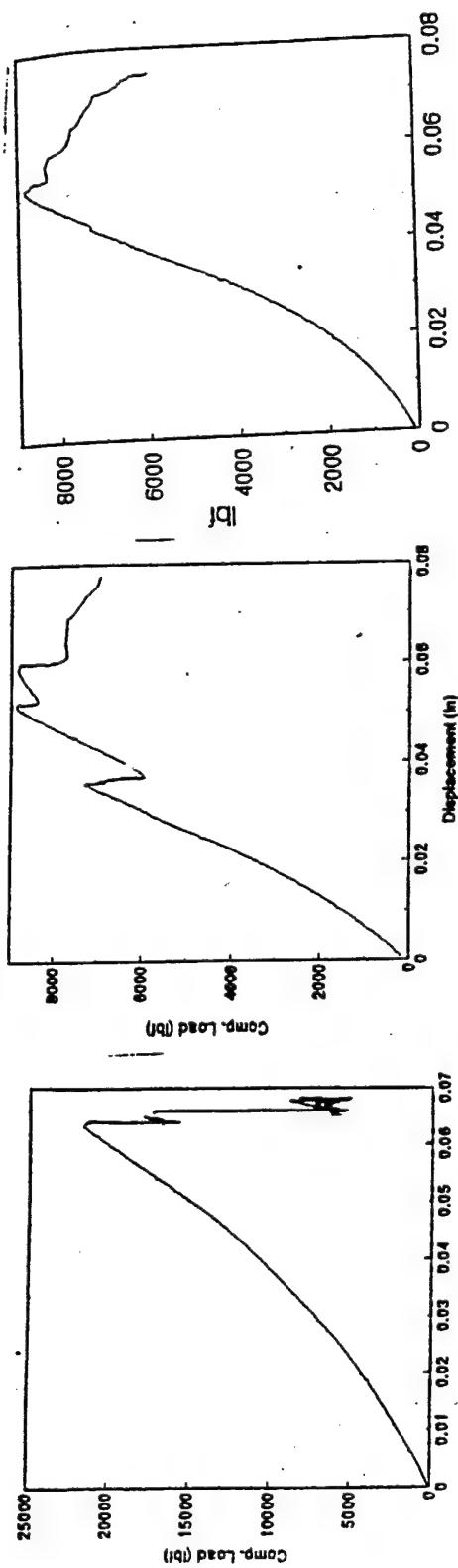
Figure 9.6 shows the compressive load vs displacement curve for the FCo, F+PCo and the TCo samples. It also brings out clearly, the effects of increasing the facesheet thickness and the pin density in the foam reinforcement.

Figure 9.7 shows the load-displacement curves for the FCo composites impacted at the A and D energy level. The FCo samples withstood a load of 22,000 lbs for the A energy level as opposed to 17,000 lbs for the D energy level sample. The initial onset of non-linearity arises during the loading phase of the head with respect to the specimen. The FCo samples indicated that the load carried by the foam was minimal in comparison with the facesheets. The failure was predominantly facesheet related. The damage occurred primarily in the vicinity of the impact damage and spanned across the width of the specimen. The facesheet failed through development of shear cracks.

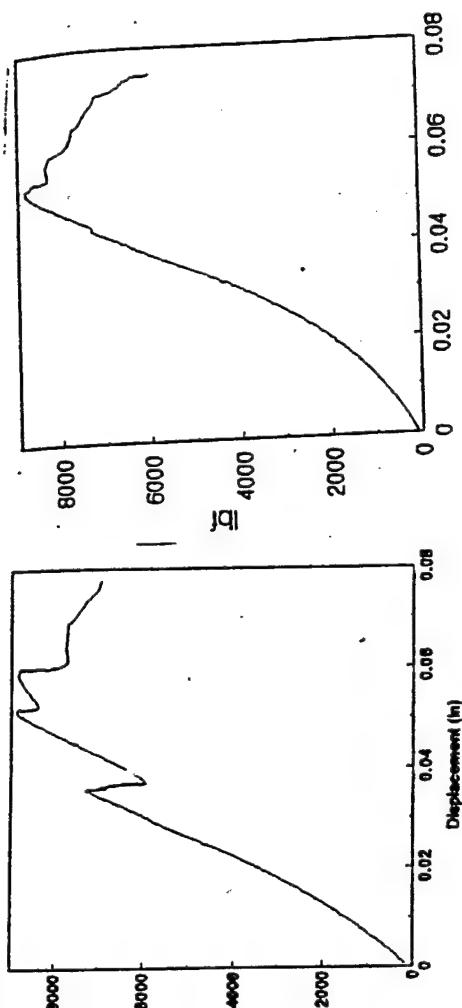
The pin spacing had an influence on the load bearing capacity of the sandwich composites. The F+PCo-75 samples showed a lower CAI load bearing capacity as compared to the F+PCo-150 composite. The closer the pin spacing (0.75"), the lower was the CAI peak load, as the damage appears to progress quickly. For the wider pin spacing (1.5"), the load carried by the facesheet is higher. The load carried by the facesheets was ~8600 lbs for impact energy level A and that for the impact energy level D was 8300 lbs. as shown in Fig. 9.8 for the F+PCo-75 composites. The load carried by the facesheets was ~18000 lbs. for impact energy level A and ~11500 lbs. for the energy level D of the F+PCo-150 composite. This is shown in Fig. 9.9. The higher load bearing capacity of the F+PCo-150 composite as compared to the F+PCo-75 composite may be attributed to the fact that lesser the number of pin clusters, lesser is the inherent damage after the impact event.

The hollow pin/truss core samples fail exhibiting multiple load drops. It appears that as individual pins shear, the subsequent ones assume the load and this process continues till the facesheet weakens considerably. The TCo composite, sample A, withstood a maximum load of ~8900 lbs. as shown in Fig. 9.6. In all the three cases, the impact side facesheet failed finally in a catastrophic manner.

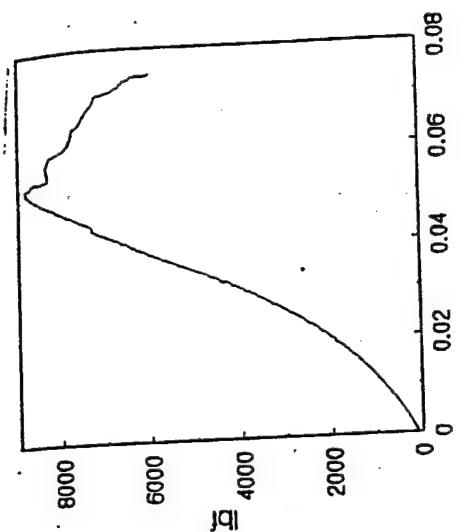
In case of the 32-ply facesheet samples, the load-displacement curves show that the peak load is about 45,000-48,000 both for the foam core and the pin reinforced core samples as shown in Figs. 9.10 and 9.11. This also suggests that the impact damage does not affect the samples with thicker facesheets considerably to cause lower CAI values. This is because the thicker facesheet offsets the pin piercing effects and does not show a marked decrease in properties after impact as compared to the foam core composite. However it does exhibit higher stiffness as is seen from the load-displacement curves.



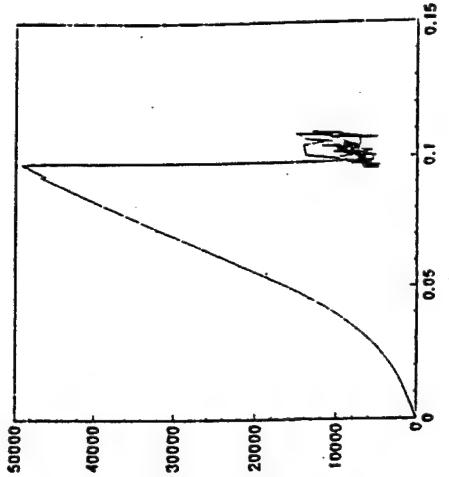
16 - Foam Alone



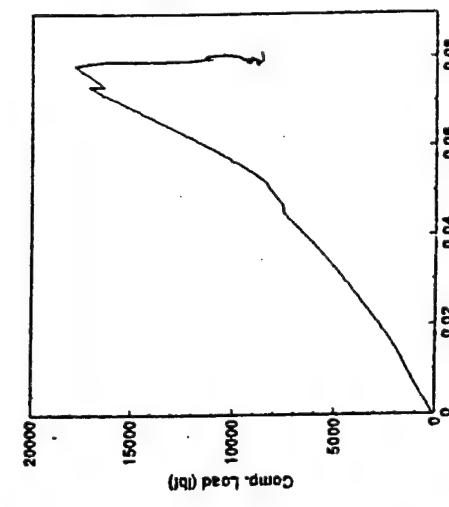
16 - Foam + Pin - 0.75



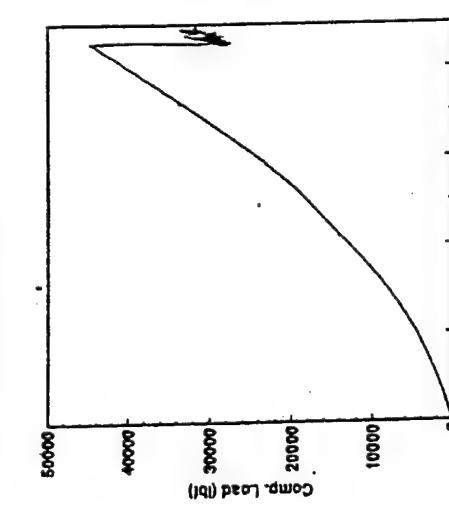
16 - Pin Alone



32 - Foam + Pin - 1.5



16 - Foam + Pin - 1.5



32 - Foam + Pin - 1.5

Figure 9.6. Load-Displacement curve for the FCo, F+PCo-75 and TCo Composites with the Influence of Skin Thickness and Pin Density (Energy Level A)

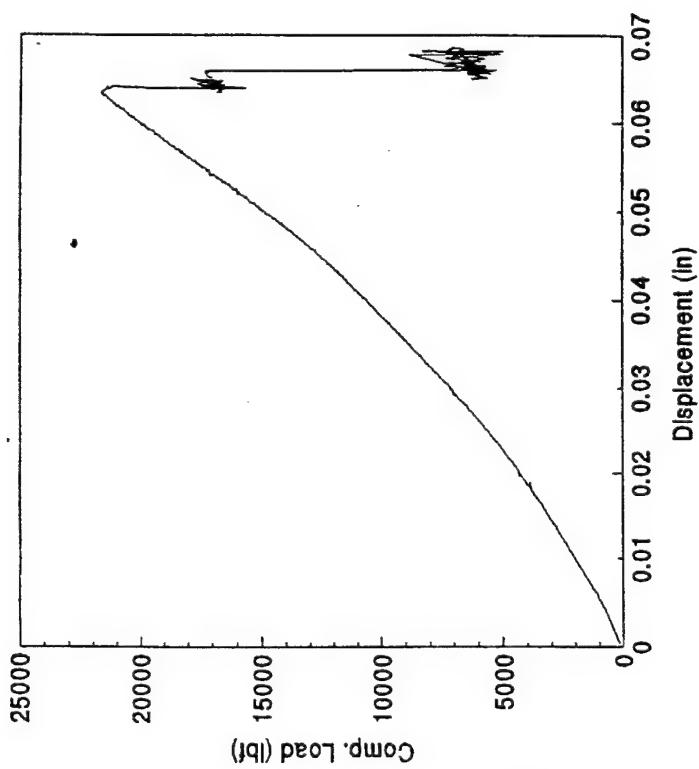
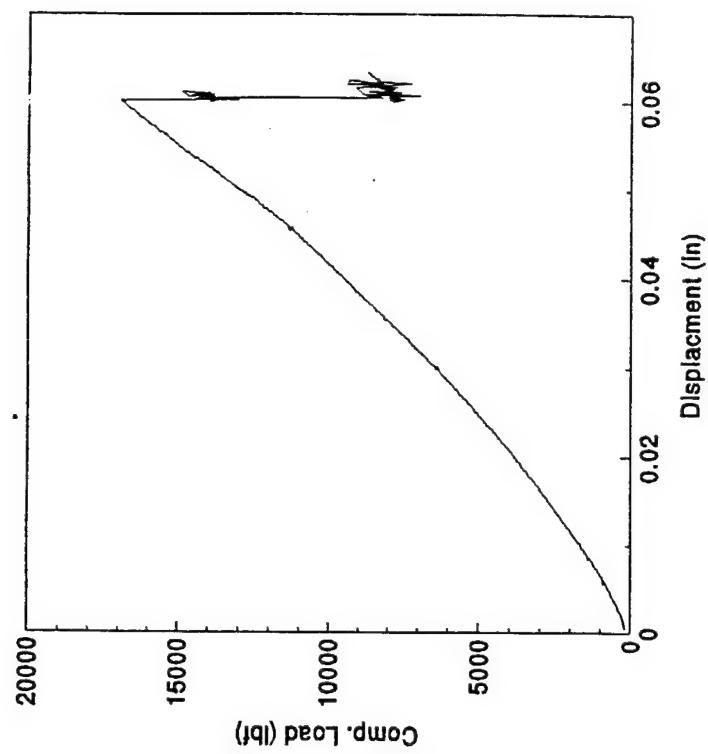


Figure 9.7. CAI curves for FCo samples A and D

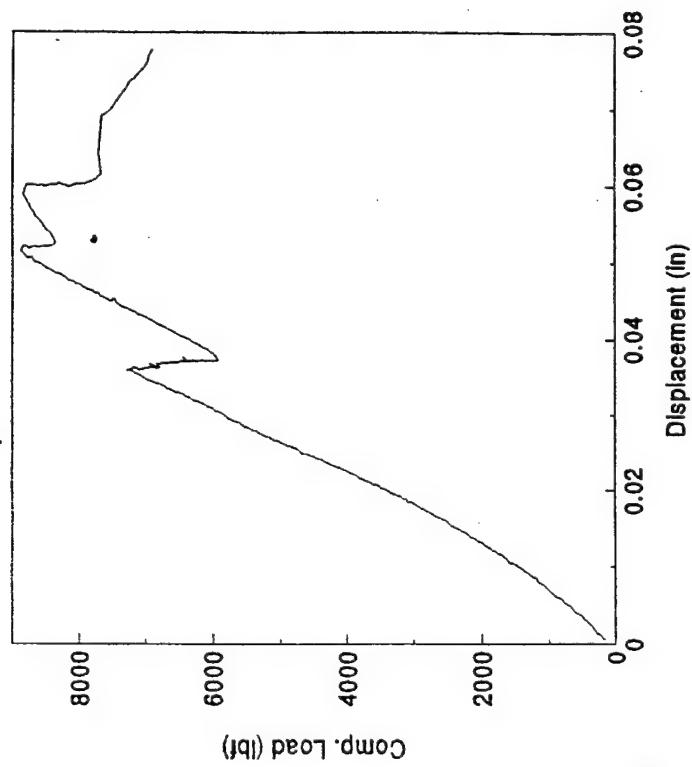
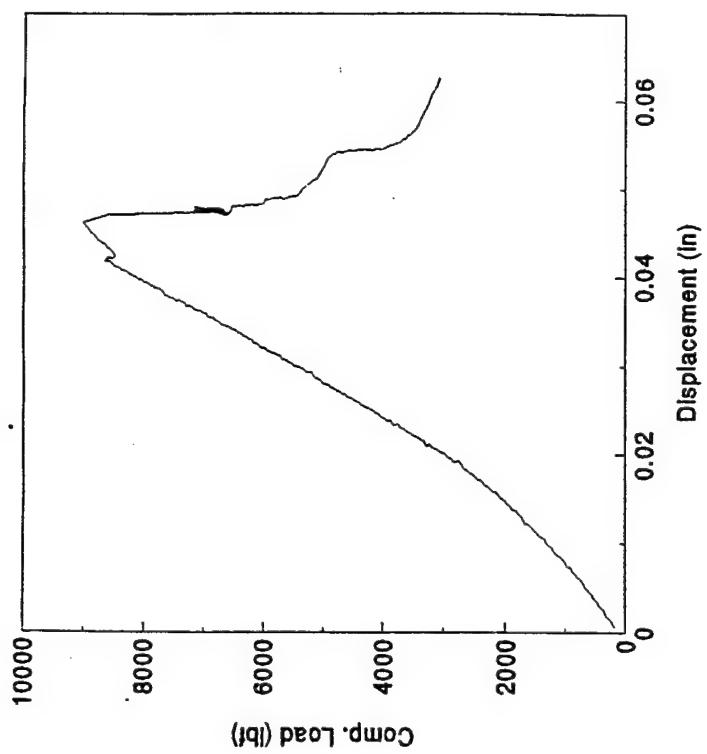


Figure 9.8. CAI curves for F+PCo-75 samples A and D

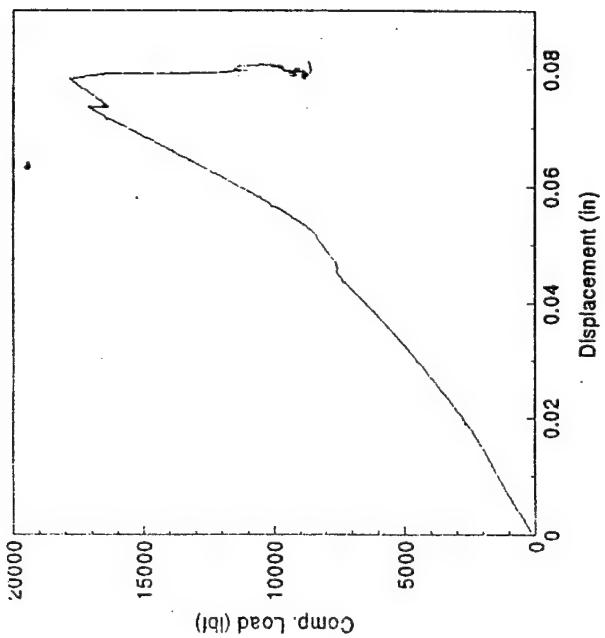
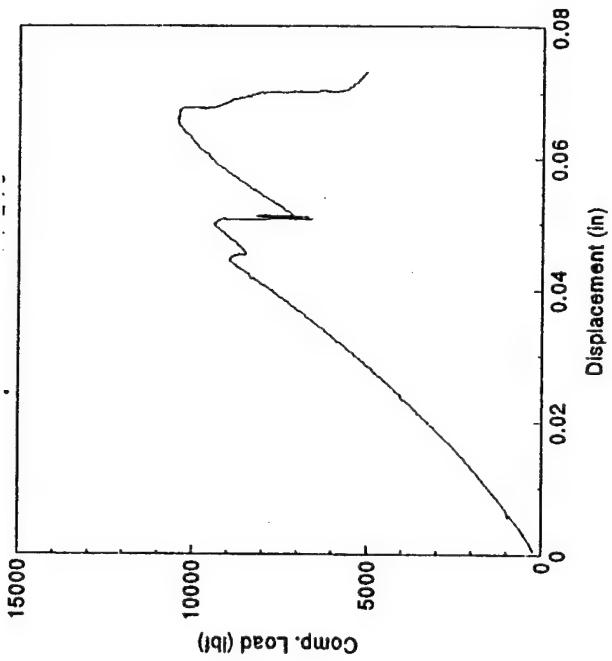


Figure 9.9. Compression - After - Impact curves for F+PCo-150 samples A and D

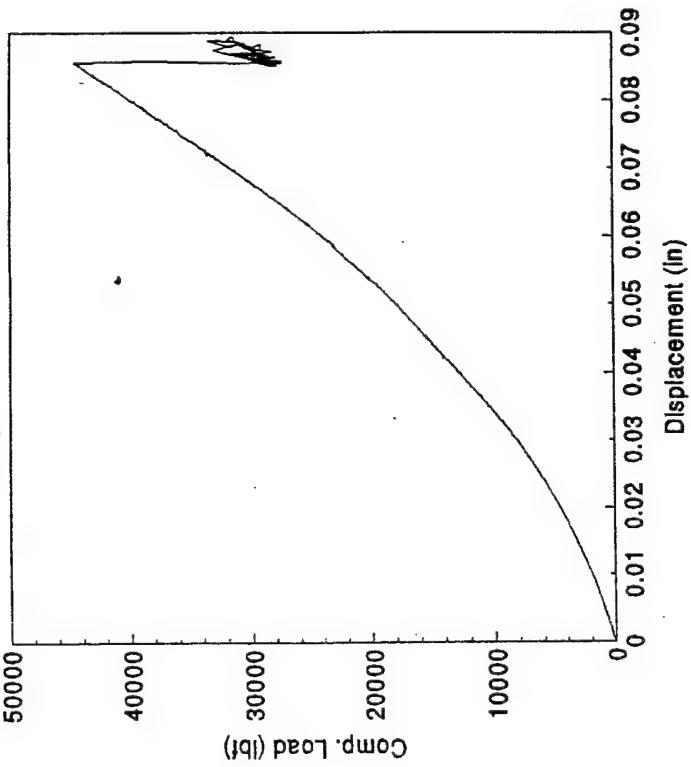
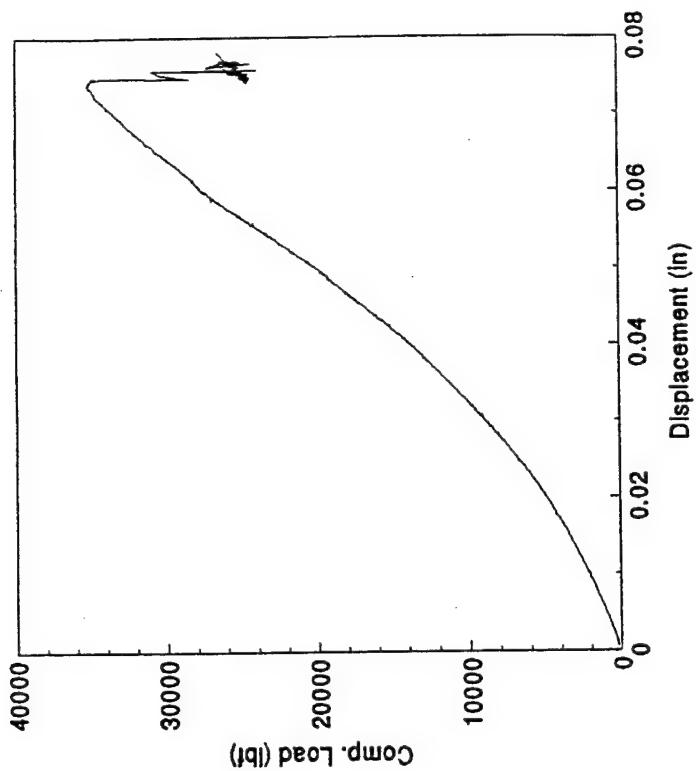


Figure 9.10. CAI curves for FCo-32 samples A and D

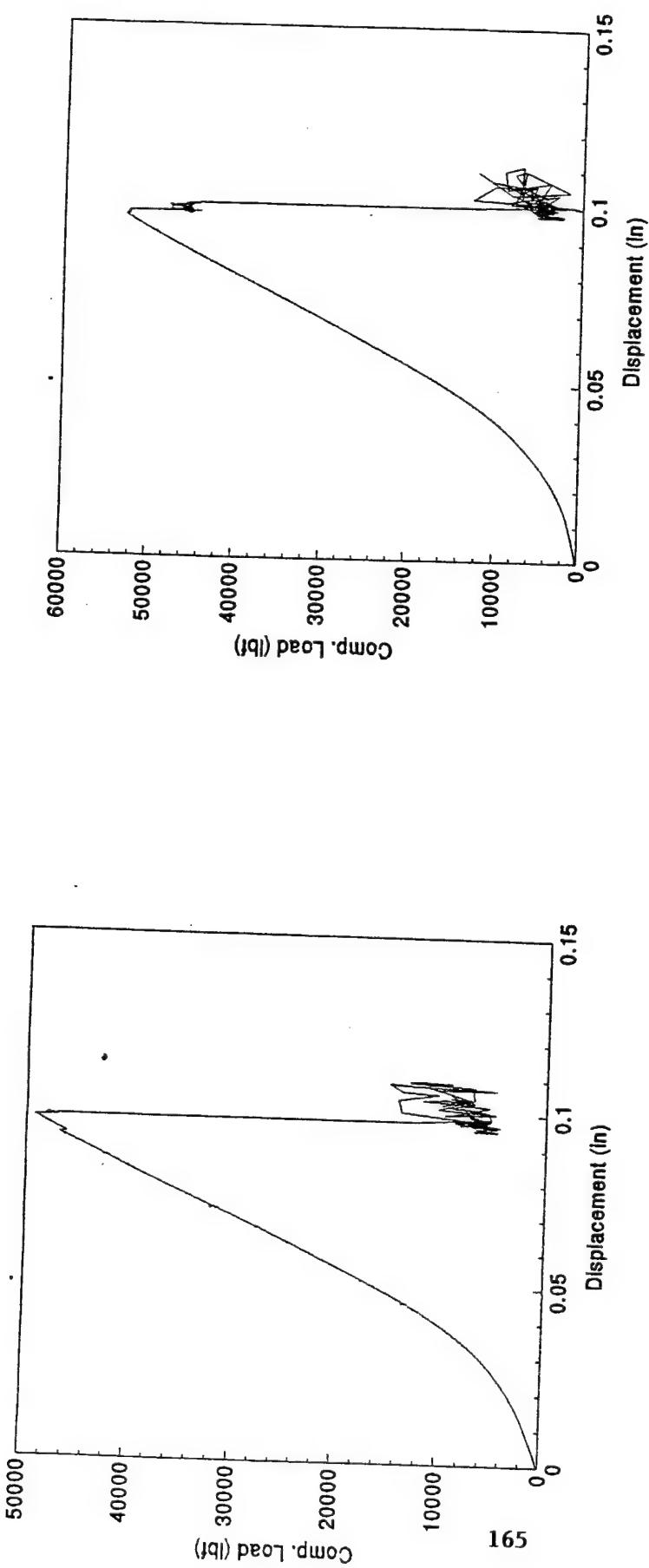


Figure 9.11. CAI curves for F32-PCo-75 samples A and D

9.4 Acoustic Emission Studies for Foam, Hollow and Z-Pin Reinforced Core Sandwich Composites

Figures 9.12 through 9.15 show the parametric distribution of energy and amplitude of AE activity for the 16-ply FCo, F+PCo-75, F+PCo-150, and the TCo composites impacted at energy level D. The facesheet failure coincides with high energy and high amplitude events occurring as seen in all the four curves. A stream of low energy events also occur during the initial loading stage and this may be correlated to the slow matrix cracking, fiber kinking, kink band formation and fiber filament level fracture.

The CAI failure of FCo composite resulted in some medium amplitude (<80 dB) medium energy (<1000) activity after about 40 sec. of the time axis. This is possibly due to the initiation of damage near the impact location. The facesheet possesses some residual strength at this point of time and greater level of activity is seen in Fig. 9.12. The composite fails after 81 secs. with the indication of a shear crack across the entire impacted facesheet.

Figure 9.13 shows the parametric distribution for the F+PCo-75 sample subjected to CAI. In this case too, the medium amplitude (<80 dB), medium energy (<100) activity is seen. However, this activity shows a sudden increase as compared to the FCo sample and the sample fails across the facesheet after 64.72 sec. of the time scale. This may be due to the fact that the penetrating pins weaken the facesheet and the impact has led to a further weakening of these locations. The existing microcracks join together and the sample fails at that instance. This occurs about 17 secs earlier as compared to the FCo sample. Failure in this case occurs by growth of the existing microcracks and the extent of damage is not as severe as compared to the FCo composite. This is verifiable by visual inspection.

Figure 9.14 shows the distribution for the F+PCo-150 composite subjected to CAI. The onset of AE activity is also seen in this case at ~28 secs which indicates that the behavior is grossly identical as compared to the other two cases discussed earlier. Catastrophic failure is seen after 88.72 secs. The extent of AE activity is seen to be much more as compared to both the FCo and the F+PCo-75 composites. This is because in the case of the foam core, the facesheet has little incipient damage from the impact and hence it shows a major crack development at the instance of failure at the weakest point on the composite, i.e. the top facesheet. For the case of the F+PCo-75 composite, microcracks and delaminations exist at locations where the pin clusters pierce the facesheet and these cracks grow and merge together indicating the ultimate failure of the top facesheet. For the F+PCo-150 samples, damage exists at places where the pin clusters pierce the facesheet. However these cracks are spaced further apart due to the lower density of the pins and hence, as these cracks grow, greater activity is seen. They finally merge at a later instance of time and that is when the facesheet shows

DF16

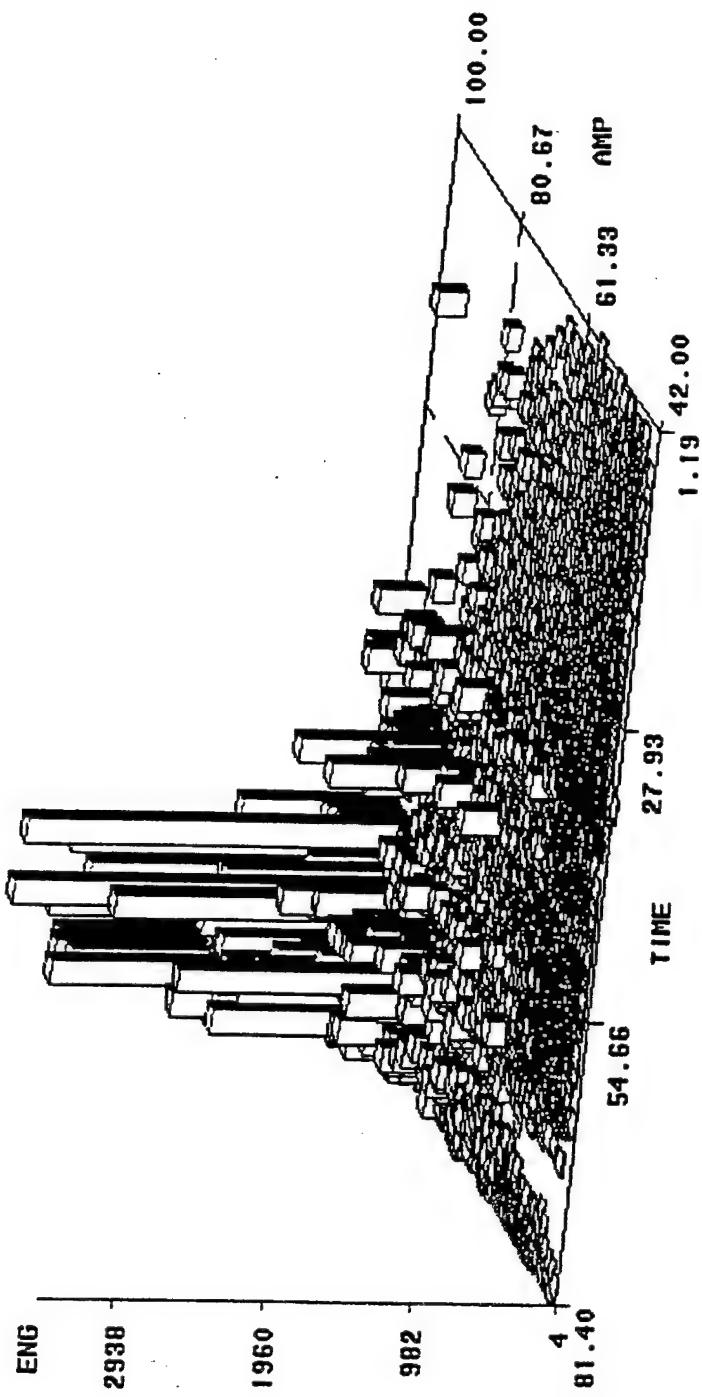


Figure 9.12. Parametric Distribution for FCo composite sample D

DFP16

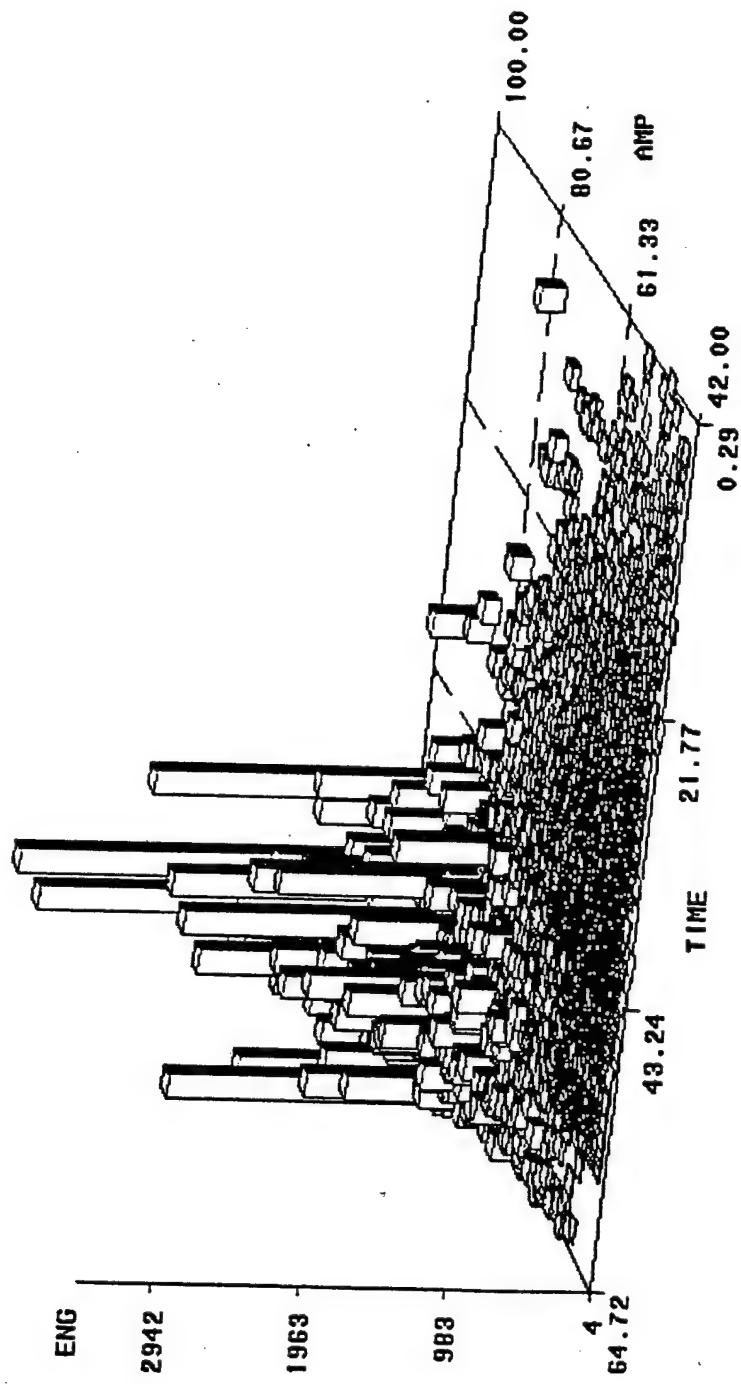


Figure 9.13. Parametric Distribution for the F+PCo-75 composite sample D.

DFP216

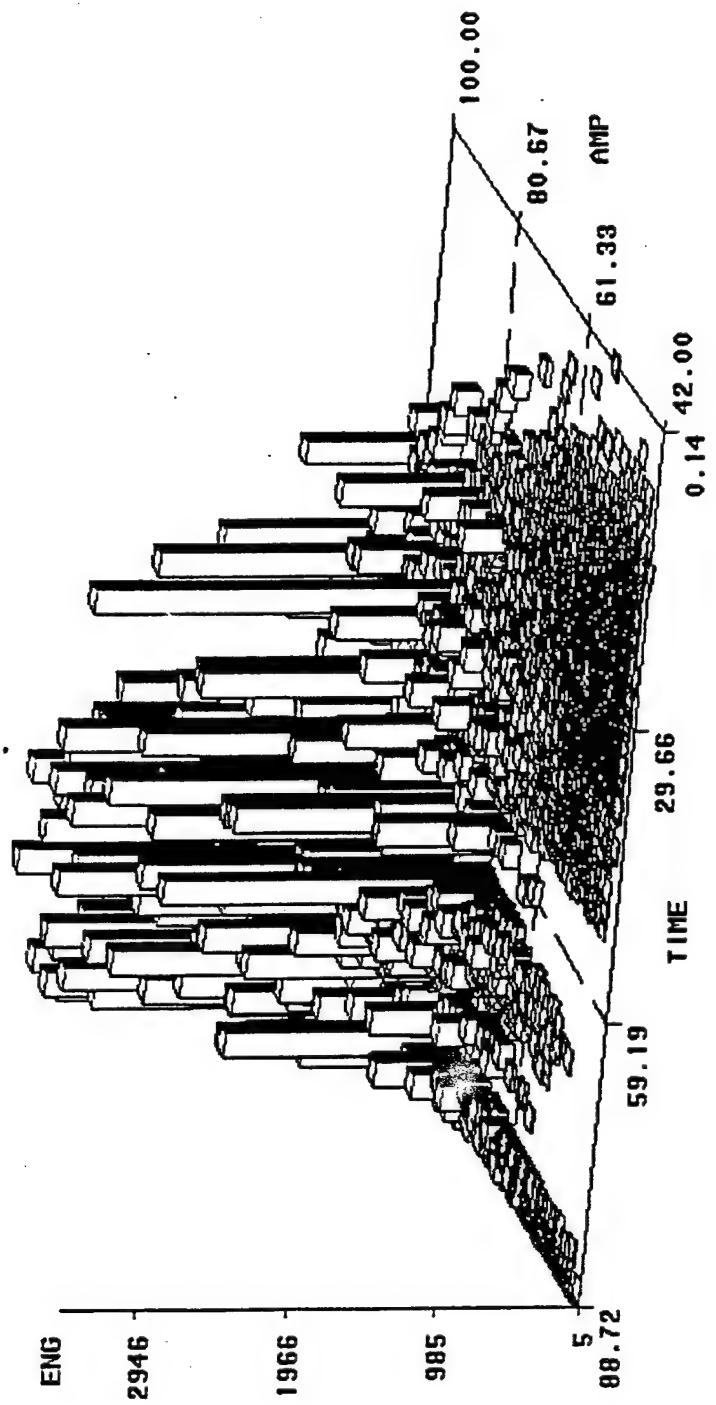


Figure 9.14. Parametric Distribution for the F+PCo-150 composite sample D.

DP16

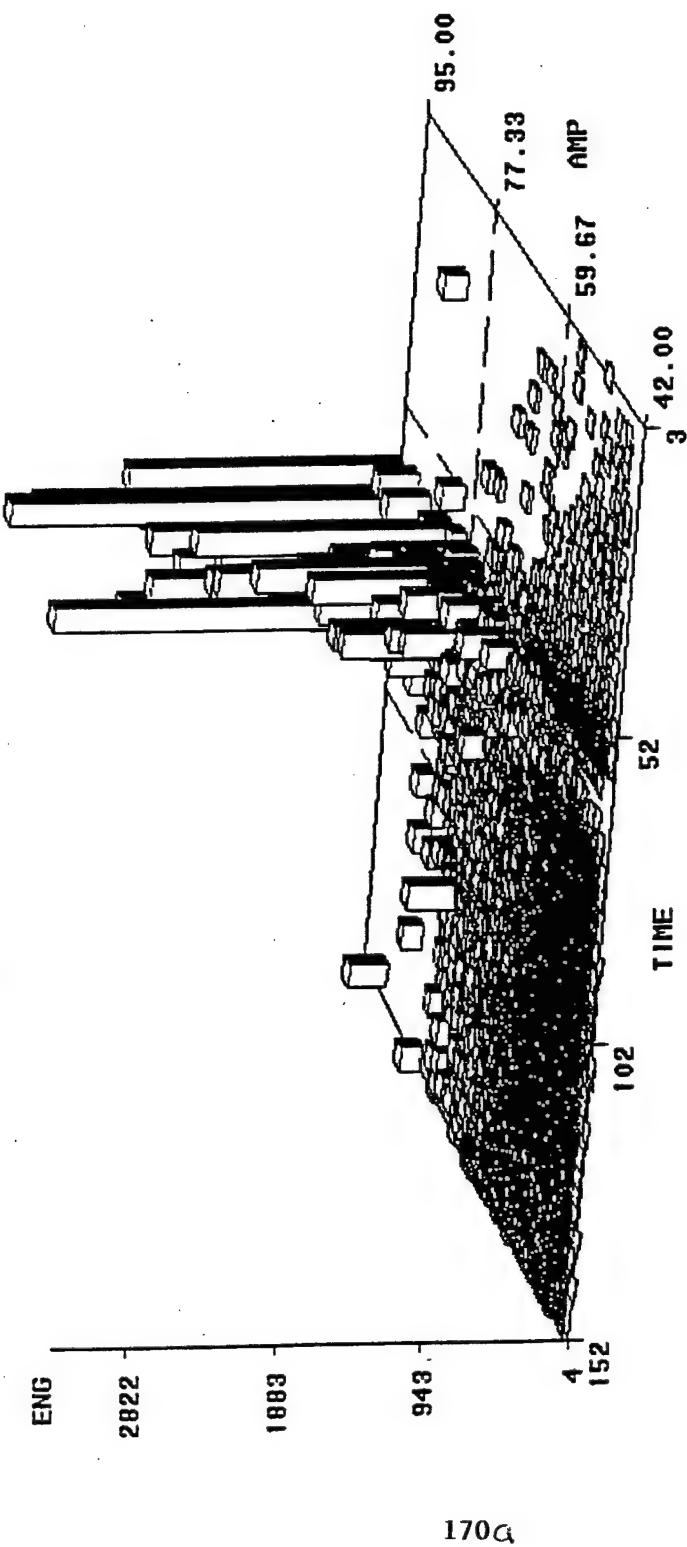


Figure 9.15. Parametric Distribution for the TCo composite sample D.

(FIGURE IS MISSING)

Figure 9.16 - Parametric distribution for FCo-32 composite sample A

(FIGURE IS MISSING)

Figure 9.17 - Parametric distribution for F+PCo-75 (32) composite sample A

catastrophic failure as the shear crack rips across the top facesheet. Visual inspection also validates this point that the extent of damage for the F+PCo-150 composite is more extensive as compared to the FCo and the F+PCo-75 composite.

Figure 9.15 shows the AE distribution for the TCo composite. The TCo composite also fails catastrophically after ~60 secs. It does not exhibit any medium or high amplitude/energy activity before failure due to the fact that the pins hold the facesheets and at the critical load, the facesheet fails at the weakest point i.e., at the impact location on the top facesheet.

Figures 9.16 and 9.17 show the AE parametric distribution for the FCo-32 and the F+PCo-75 (32) composite impacted at energy level A respectively. The distribution validates some of the observations noted above for the 16 layered specimen. The specimen shows a higher load bearing capacity and sustains it for a longer duration of time (105 secs for the FCo composite and 123 secs. for the F+PCo (32) composite). The FCo composite exhibits catastrophic failure towards the end of the loading cycle with little or no activity during the initial phase of the loading. The F+PCo-75 (32) composite shows medium amplitude (~70 dB) medium energy (~600) activity all through the loading phase of the specimen. This, as indicated earlier, is due to the microdelaminations existing within the facesheet during processing and after the impact event. Some activity is seen after failure and for a longer interval of time as compared to the FCo composite. This is clearly seen from the load displacement curve in Figs. 9.10 and 9.11.

9.5 References

1. Mallick, P.K. "Fiber Reinforced Composites," Marcel Dekker Inc., Second Edition, 1995.
2. Vaidya, U.K. "Nondestructive Evaluation of Graphite Based Composites using Acoustic and Vibration Techniques," Ph.D. Dissertation, Auburn University, 1993.

10.0 LOW VELOCITY IMPACT DAMAGE CHARACTERISTICS OF HOLLOW Z - STEEL PIN REINFORCED SANDWICH PANELS WITH GRAPHITE/EPOXY FACESHEETS - AN EXPERIMENTAL STUDY

10.1 Introduction

In this portion of the study hollow steel pins truss core reinforced with graphite/epoxy facesheets were considered. Two different orientations of pin angles are considered. A pendulum type impactor is used to impart very low levels of impact energy. Threshold energy levels at which the observable damage initiation occurs are determined. Nondestructive evaluation studies conducted prior to the impact are compared with the post impact status of the panels for assessing the type and magnitude of the damage. These studies include ultrasonic inspection, microscopic inspection and acoustic emission tests. Damage is also evaluated by carrying out through vibration tests before and after impact. Static indentation tests are carried out to compare with the low velocity impact tests. Effects specific to the impact phenomena are studied by comparing the load displacement characteristics. Also, compression after impact characteristics are evaluated.

In this experimental study, sandwich plates are composed of graphite/epoxy face sheets and steel fiber pins for the core. Two orientations of pin angle (10 and 20 degrees) are considered in which the volume of the pins per unit plate area is kept constant. Face plates consist of 16 layers of symmetric orientation. The sandwich plates are impacted by pendulum type impactors with a hemispherical nose (tup). Contact force is monitored throughout the impact event using an instrumented impactor. Before the impact event, a sampling of the specimens was evaluated using ultrasonic C-scan in order to check for various defects. After impact loading, the specimens are inspected nondestructively for the presence of various damage modes and their extent. Microscopic inspection is also carried out to observe the defects in the face sheets.

Various issues related to the phenomena of low velocity impact events were also studied. These include, the comparison between the responses due to static loading and low velocity impact loading in terms of damage initiation and characteristics of compression after the impact phenomena. Acoustic emission and vibration tests are carried out on the specimens that were subjected to the compression loading after the impact event to study the progression of damage in terms of increased acoustic activity and the reduced natural frequencies.

10.2 Specimen and Method

Specimens used in this experimental investigation consisted of two face sheets each of orientation [0/45/90/-45]_{2S} made up of graphite epoxy material. The pins used in the core are made of steel and are of 0.508 mm in diameter. Foster Miller Inc provided three plates of 10 degree pin orientation and three plates of 20 degree pin orientation, each of size 254 mm X 254 mm. Orientation of the pin angle is measured from the vertical axis as shown in fig 10.1(c) where a schematic of the sandwich side view is shown). Each plate is cut into 4 specimens of 10.16 mm X 10.16 mm dimension. The remaining plate material is used to gain initial insight into the types of damage modes and the energy levels associated. All these specimens are restrained in a 20.32-mm X 20.32 mm fixture providing near simple support on all edges of the 7.62 cm X 7.62 cm effective specimen size.

An instrumented pendulum testing system is used for all the experimentation. Past experience [3-6] with various impact testing systems resulted in the selection of this testing system as it is possible to impart very low impact energies. Impact energies of less than 0.5 Joule are expected to initiate the damage in the specimens. A schematic of the pendulum test system is shown in Fig 10.2. The pendulum consists of a 15 KN load cell with a 1.27 cm radius nose. Impact energy is regulated by means of the swing of the pendulum and resolved by measuring the mass of the pendulum and its velocity just prior to impact. A digital oscilloscope is used to record the force data from the experiment at 5 μ sec intervals. The mass of the pendulum used in the experiments is 3.48 kg. No specimens are impacted more than once. All the specimens are visually and ultrasonically inspected after impact to determine the existence of the damage in the form of crushing failure at the surface under the impactor, inter ply delamination in the top face sheet, buckling or compression failure of the pins, pull out or push up of the pins from the facesheet. Several specimens were sectioned and photo micrographed after C-scanning to reveal the through the thickness distribution of delaminations and matrix cracking.

10.3 Low Velocity Impact Testing

Results obtained from these experimental studies are discussed in two parts. In the first part, results obtained from the low velocity impact experiment, in the form of load deflection curves etc are discussed. The energy levels, at which the damage initiates, are determined. In the second part of this section, specimens are analyzed using nondestructive evaluation techniques.

Newton's second law related to impulse and momentum for the impactor is integrated to calculate velocity as a function of time. The impactor velocity, $V(t)$ is determined from the contact force as

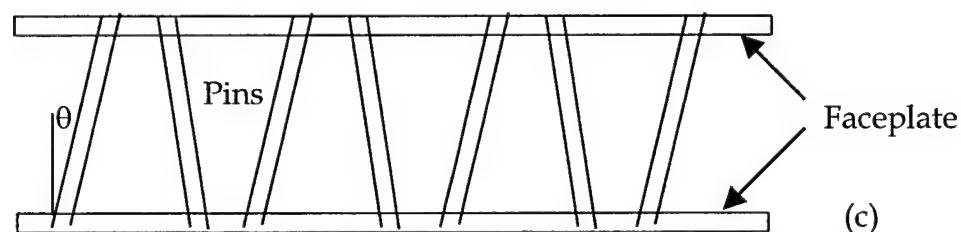
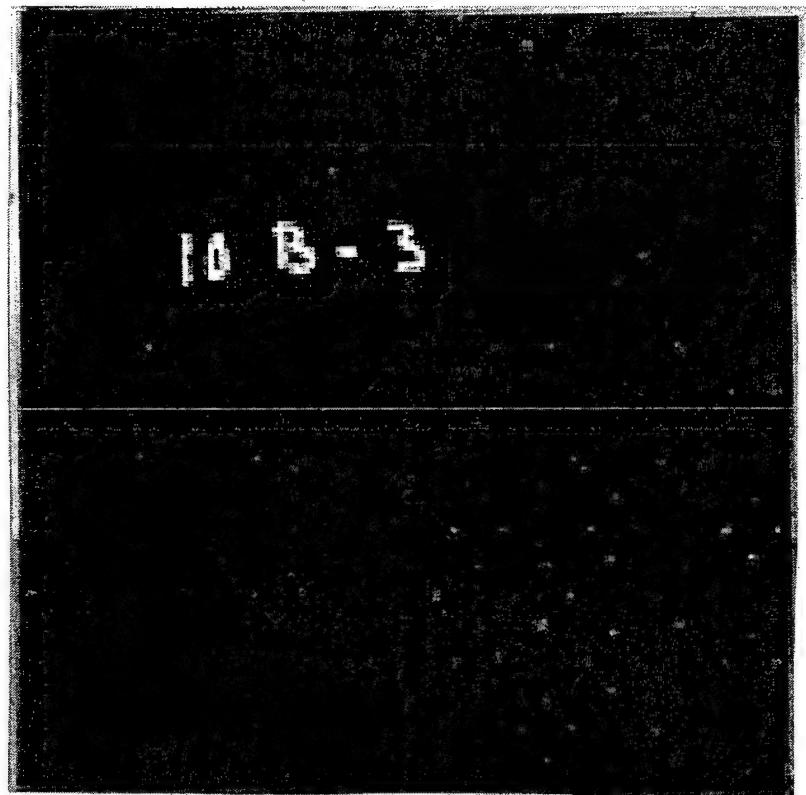


Figure 10.1 a) Front View of the Truss Core Sandwich Composite
b) Top View of the Truss Core Sandwich Composite
c) Side View Schematic of the Truss Core Sandwich

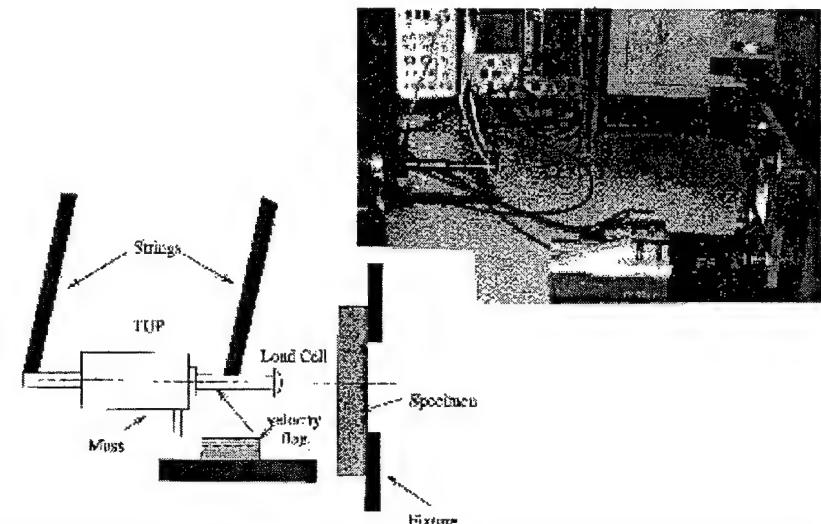


Figure 10.2 Schematic of the Swing Pendulum Test System

$$V(t) = V(0) - \frac{1}{m} \int_0^t F(\tau) d\tau$$

Here $V(0)$ is the initial impact velocity of the impactor which is a measured quantity and m is the mass of the impactor. Based on the velocity calculation, displacement is determined by again numerically integrating with respect to time. The displacement as a function of time $\delta(t)$ can be written as

$$\delta(t) = \int_0^t V(\tau) d\tau + \delta(0)$$

Here $\delta(0)$ is the initial displacement which is taken, equal to zero.

10.3.1 10 degree Pin Orientation

The force-time curves for five 10 degree orientation specimens tested within energy ranges of 0.6984 J to 2.42 J are shown in Fig.10.3. The lower energy force -time histories (for 0.6984J and 1.01J) show symmetrical ascending and descending portions. Even at these energies although no visible indication of load drops existed in the force-time histories, lower end energy absorbing processes including matrix cracking, microdelaminations in the facesheet and pin-facesheet debonds were observed. This fact is further validated from the load - displacement curves of Fig.10.4, where a residual displacement is observed at the low energies. Also, when plotting the ratio of percentage absorbed energy to impact energy against energy in Fig.10.5, approximately 17 percent of the impact energy is not returned to the impactor at energies less than 1 J indicating the various damage modes occurring at very low energy levels. The occurrences of the microdelaminations, matrix cracking and pin debonds are poorly magnified in the force-time histories at the lower energies. For the 1.260 J curve of Fig.10.3, a characteristic load drop at 1400 N corresponding to damage initiation is clearly evident, based on which 1.26 J may be treated as the threshold energy for the 10 degree pin orientation samples. The energy threshold is clearly illustrated in Fig.10.5, where threshold damage approximates a step function , below which the percentage absorbed energy to impact energy shows a linear trend, and beyond the threshold energy step, absorbed energy increases linearly with impact energy. From the microstructural studies, pin push-out appears to be the dominant failure mode at the threshold energy. Beyond this load drop, the load continues to rise depending upon the residual energy in the impactor. At higher energies, i.e. 2.07 J and 2.42 J the load drop corresponding to damage initiation occurs around 1400 N. The small variations in the load depended on whether the impact event occurred on a cluster of pins or between a cluster of pins. The other interesting observation can be made if the force-time history is considered as a half-sine wave over which high frequency sinusoid like signals are seen to be superimposed. These oscillations were attributed to the plate bending vibrations,

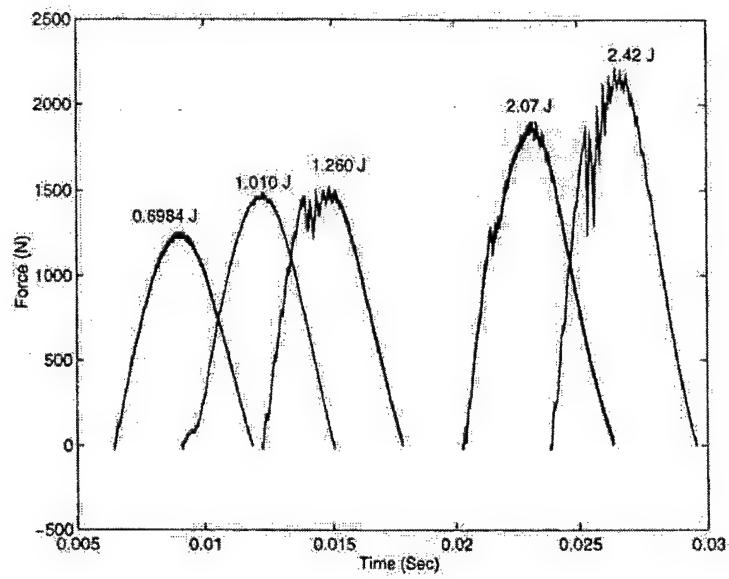


Figure 10.3 Force-Time Curves for five 10 Degree orientation Specimens Tested at Different Energy Levels

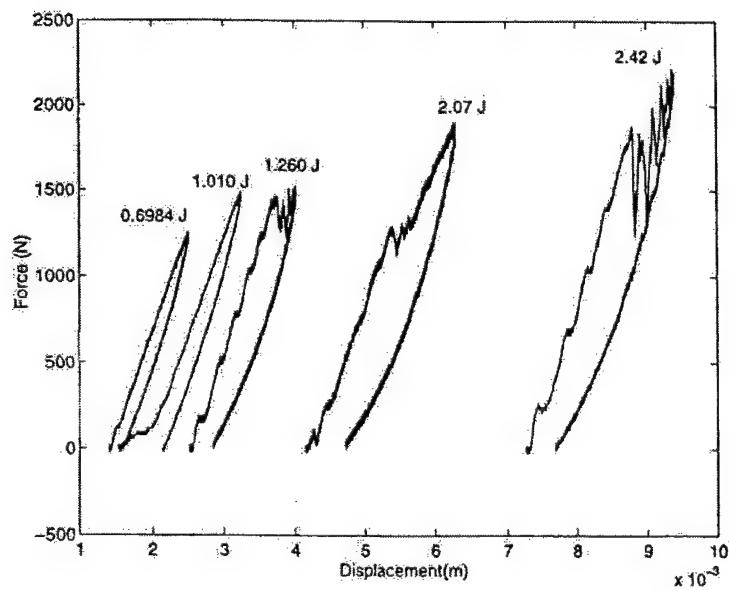


Figure 10.4 Load-Displacement Curves for five 10 Degree orientation Specimens Tested at Different Energy Levels

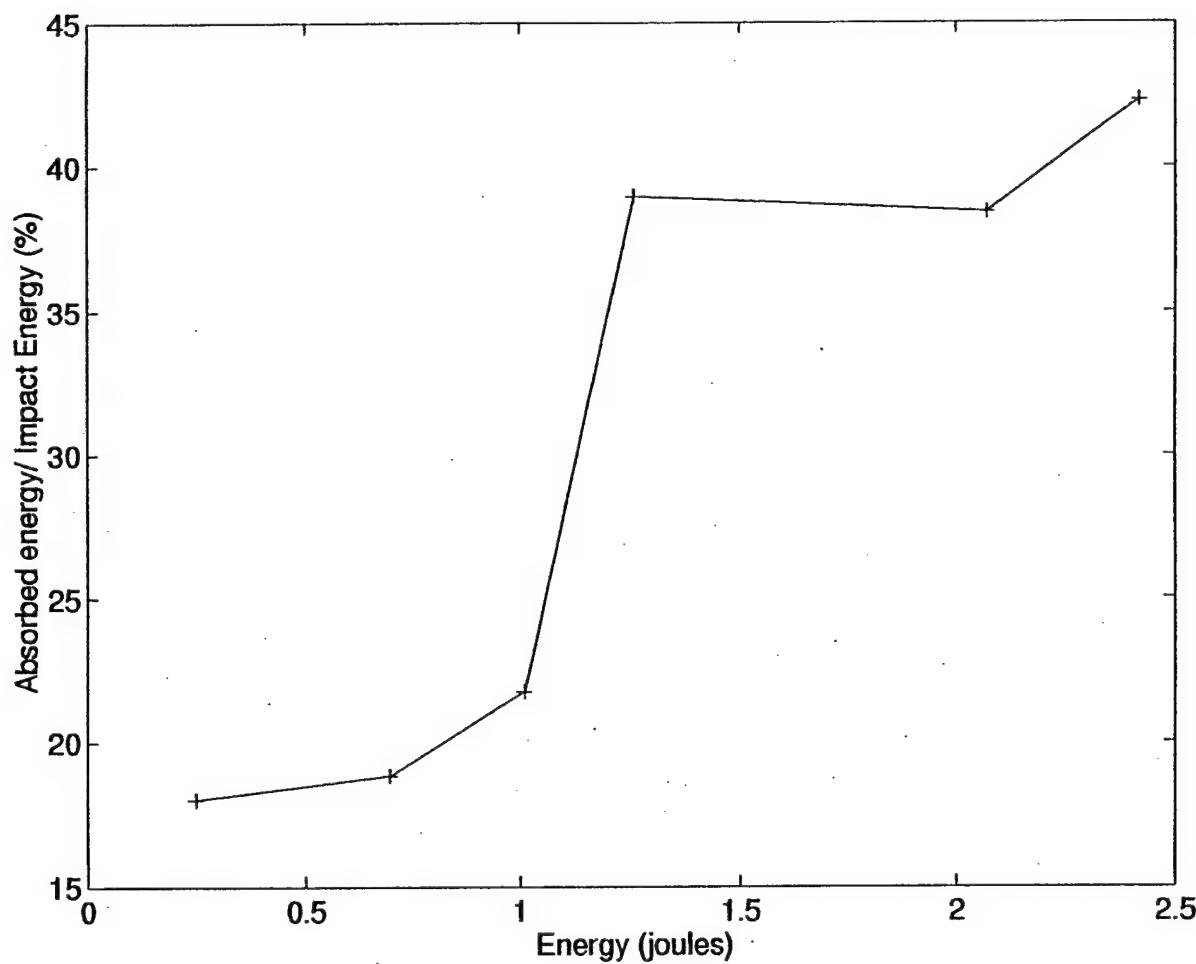


Figure 10.5 Percentage absorbed impact energy vs energy plot

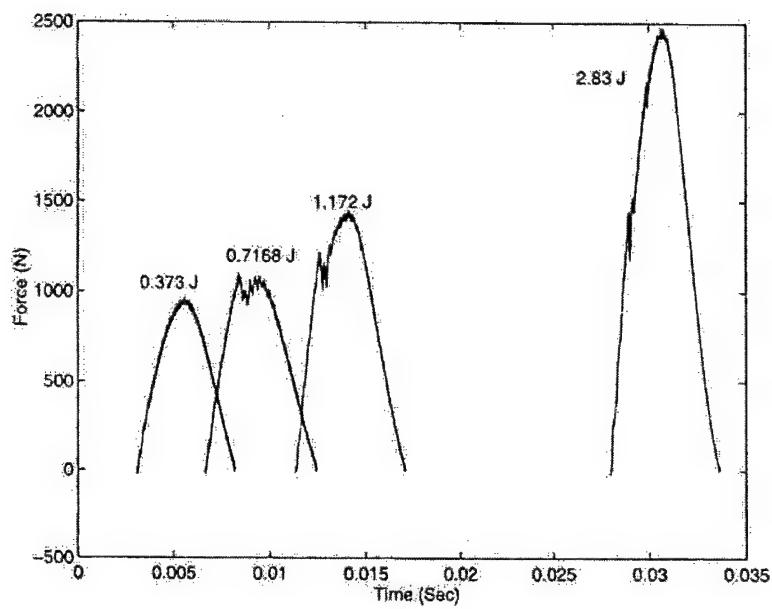


Figure 10.6 Force-Time Curves for five 20 Degree orientation Specimens Tested at Different Energy Levels

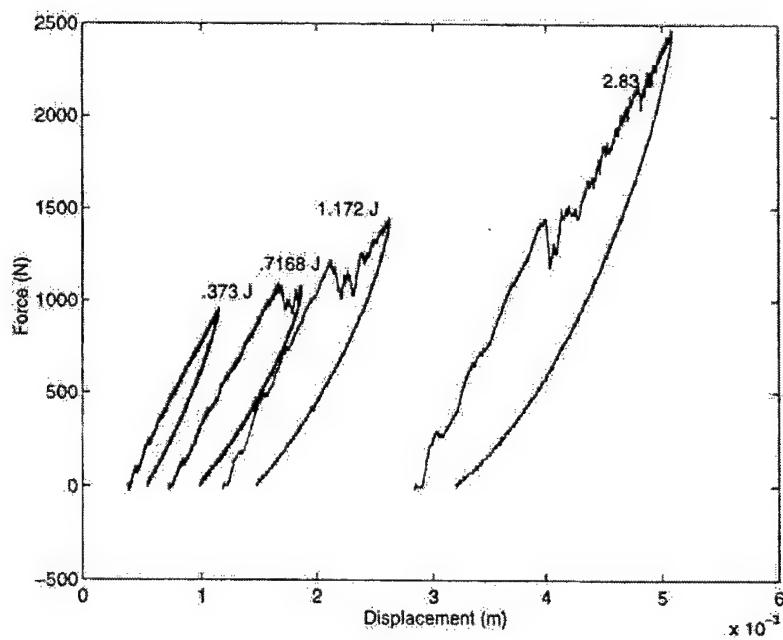


Figure 10.7 Load-Displacement Curves for five 20 Degree orientation Specimens Tested at Different Energy Levels

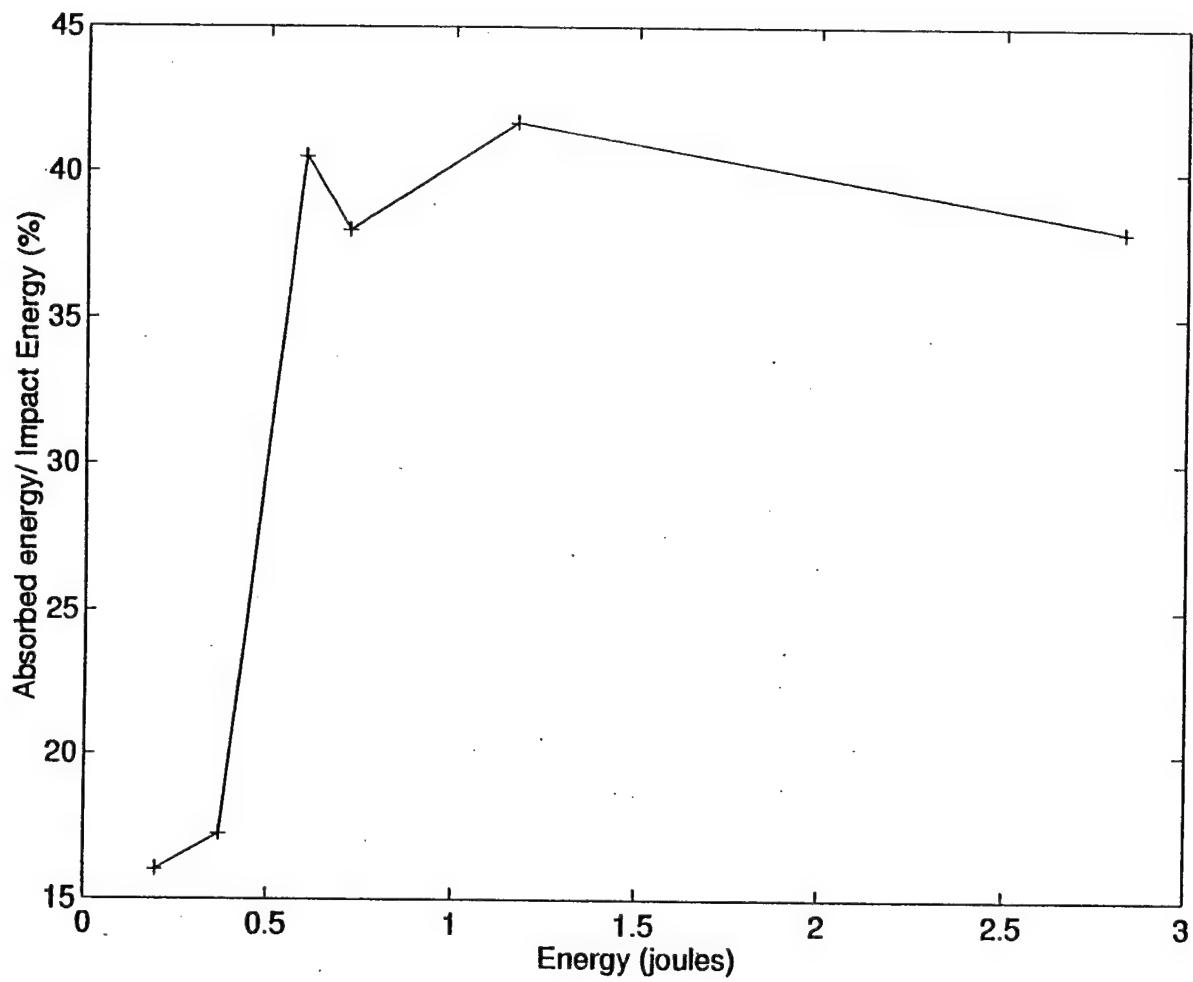


Figure 10.8 Percentage absorbed impact energy vs energy plot

which become more prominent at higher impact energies, as can be seen both from Fig. 10.3 and the load-displacement curves of Fig.10.4.

10.3.2 20 degree Pin Orientation

For the 20 degree pin orientation, as shown in Figs. 10.6 and 10.7, the force-time and load-displacement curves are similar to the 10 degree pin orientations, except that the damage initiation threshold energy is 0.7168 J, occurring at 1000 N as opposed to 1.26 J at 1400 N seen in the 10 degree pin orientation specimens. As seen before, at higher energies, the load continues to rise beyond damage threshold energy due to the residual energy in the impactor. The plate bending modes can be observed from the load-displacement curves of Fig.10.7. The stiffness of the 20 degree pin oriented specimens calculated from the slope of the load-displacement curve is seen to be slightly lower than the 10 degree pin oriented specimens. As before, a energy threshold curve is plotted in Fig.10.8, where the ratio of absorbed energy/impact energy shows the characteristic step at the threshold energy.

10.4 Static Indentation Testing

Static indentation tests were conducted in order to draw analogies between low velocity impact and quasistatic loading. The experimental setup used for conducting these tests is shown in Fig.10.9. Static load-displacement curves are illustrated in Figs. 10.10 and 10.11, where the following observations may be made;

- 1) the failure corresponding to the major load drop is 90 percent lower than their corresponding counterparts of low velocity tests, i.e, it is 1200 N for the 10 degree pin oriented specimens and 900 N for the 20 degree pin oriented specimen
- 2) the slope and therefore the stiffness based on the load-displacement.response is lower when compared to the low velocity impact tests for both 10 and 20 degree pin oriented specimens.

Both these observations can be attributed to the inertial stiffening and contribution of the mass times acceleration term in the dynamic low velocity impact tests, and lack of these in the static tests. This further suggests that low velocity impact testing cannot be substituted for by quasi-static tests.

Screw-type Load Frame

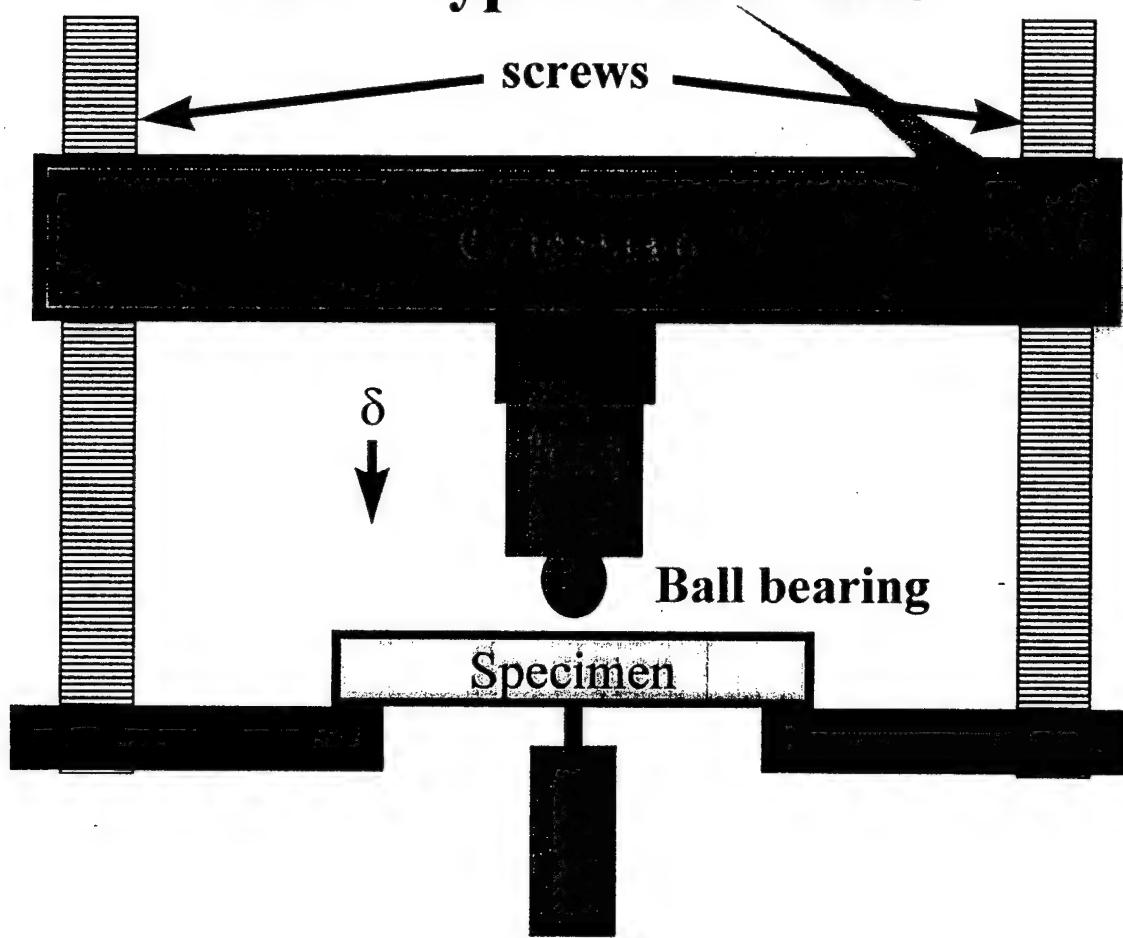
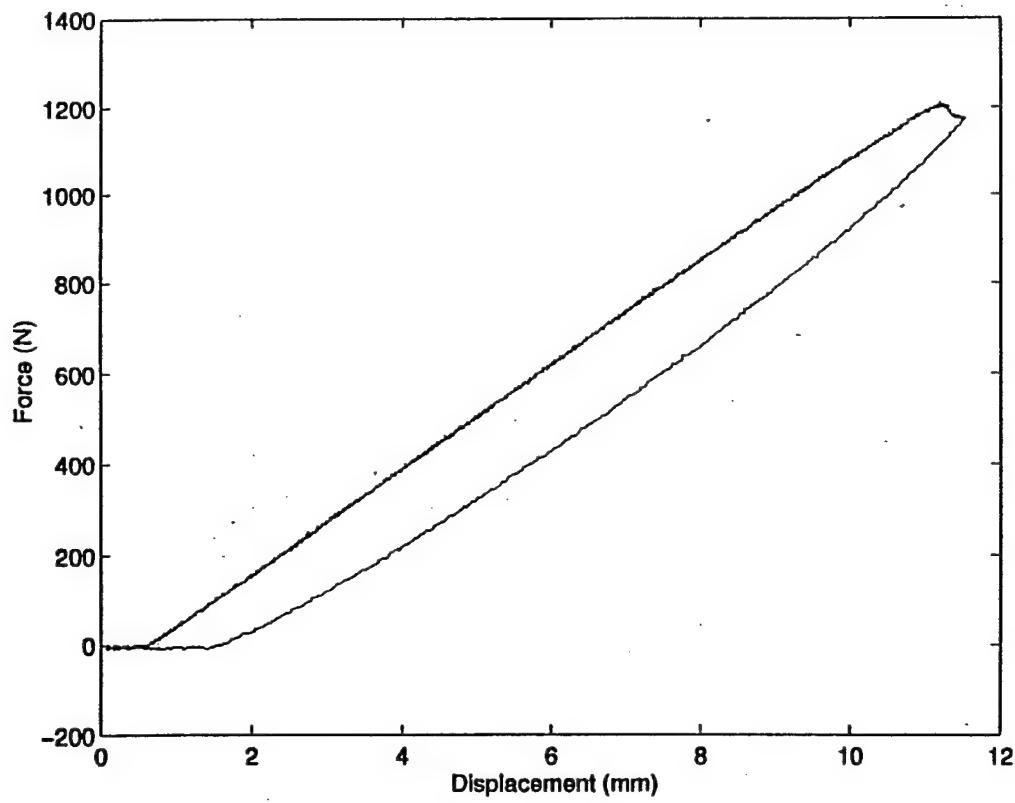
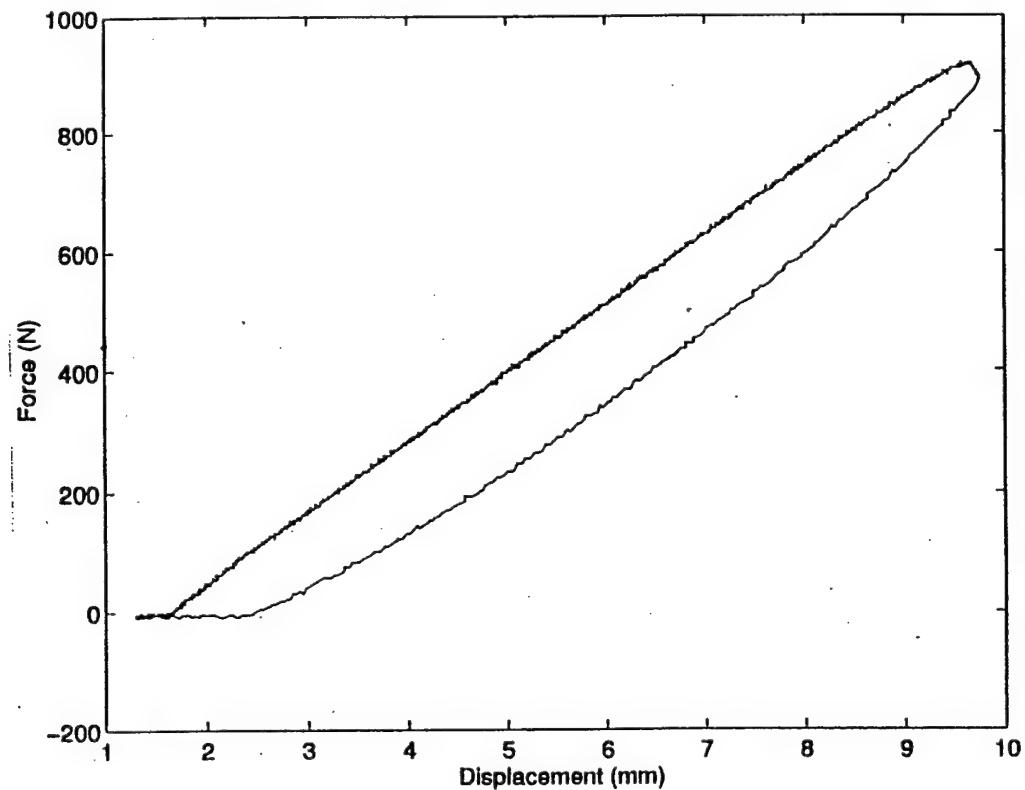


Figure 10.9 Experimental set-up for static indentation testing



10 degree

Figure 10.10 Static Load-Displacement curves for 10 degree pin orientation specimen



20 degree

Figure 10.11 Static Load-Displacement curves for 20 degree pin orientation specimen

10.5 Failure Modes

Typically failure initiation at low impact energies occurred by matrix cracking and microdelaminations in the vicinity of the locations where the pins entered the facesheet. Also, initiation of debond at the pin -facesheet is seen at low impact energies. Similar observations are also made for quasi-static loading. Prior to the pin push-out that occurs at the threshold energy, the facesheet plies around the pin exhibit a tendency to displace along with the pin as shown for the top and bottom facesheets in Figs. 10.12 and 10.13 (a&b). The pin push-through is illustrated in Fig. 10.13c. The process is schematically illustrated in Figs. 10.14a&b. With further displacement, the plies undergo shear cracking and delamination, first at individual pin locations and subsequently coalescence of delaminations occurs between a system of pins. This phenomenon is illustrated in Figs 10.15 (a) and 10.15 (b). The failure is distributed over a system of pins and not limited to a single pin cluster. In addition, it was observed that all the pins do not penetrate to the same extent within the facesheets as shown in Figs 10.16(a) & (b). This is primarily a manufacturing defect, which influences the failure in that the facesheet delaminations are limited to the extent of pin penetration. The schematic of failure as observed across the top and bottom facesheet is illustrated in Fig.10.16 and details around a single pin are shown in Fig.10.12.

10.6 Ultrasonic C-Scan Testing

The specimens were subjected to ultrasonic C-scan using a Testech immersion, type pulse-echo system with a Krautkramer USP- 12 ultrasonic pulser-receiver and a 5 MHz transducer. Each specimen was tested for back and front facesheets separately, first prior to testing and then-for post-damage inspection. The resolution of the C-scan obtained was satisfactory in terms of resolving individual pins and mapping the pin clusters accurately. Figure 10.17 shows typical C-scans for "before testing" of a specimen with 10 degree and 20 degree pin orientations. Figures 10.18(a) and (b) show typical C-scans of a specimen subjected to quasi-static loading. The damage caused by the indentor is clearly observed from Fig. 10.18 (a) on the top (loading side) facesheet. In addition, at several locations on the top as well as bottom (Fig. 10.18(b)) facesheets, a joining of dark lines and enlargement of dark spots indicate locations where pin push-through accompanied by coalescence of delamination between adjacent pins occurs. These observations are in agreement with microstructural studies performed by sectioning the samples in the regions of C-scan indications. These damage conditions are seen to spread out over a large portion of the top (loading side) and bottom (back side) facesheets, and are not localized around the loading region.

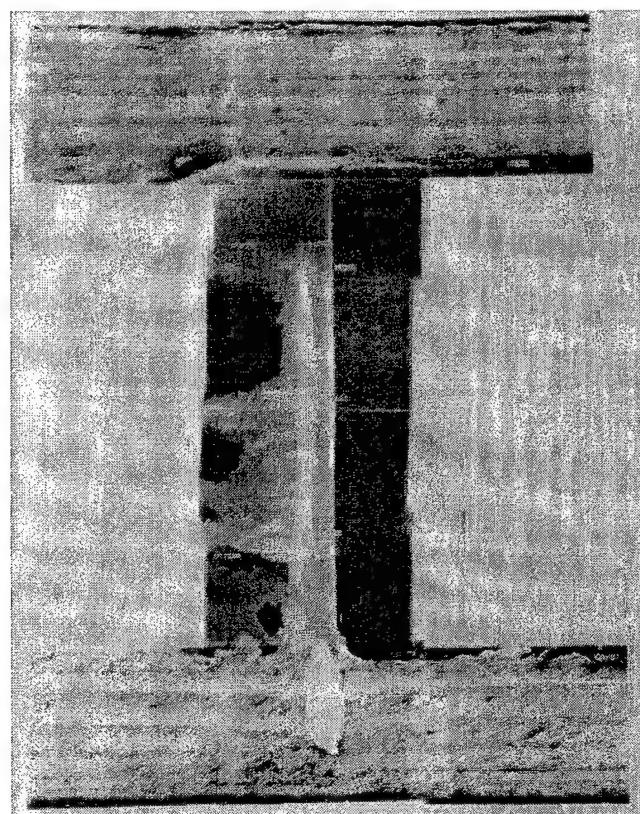


Figure 10.12. Incipient Damage at Pin-Facesheet Interface

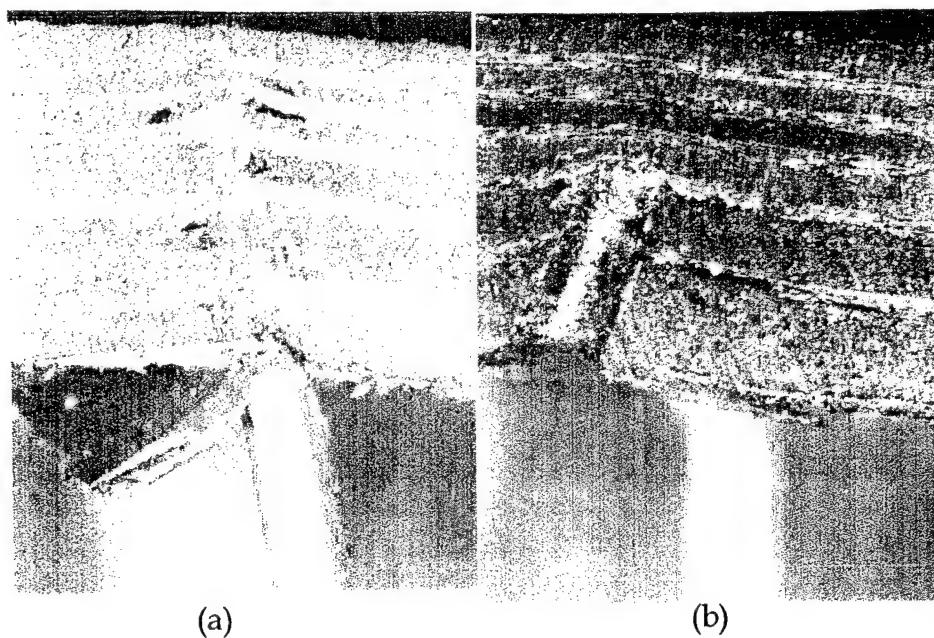


Figure 10.13a,b Pin Push out for the Top and Bottom facesheet



Figure 10.13c Pin Push Through at Higher Energies of Impact

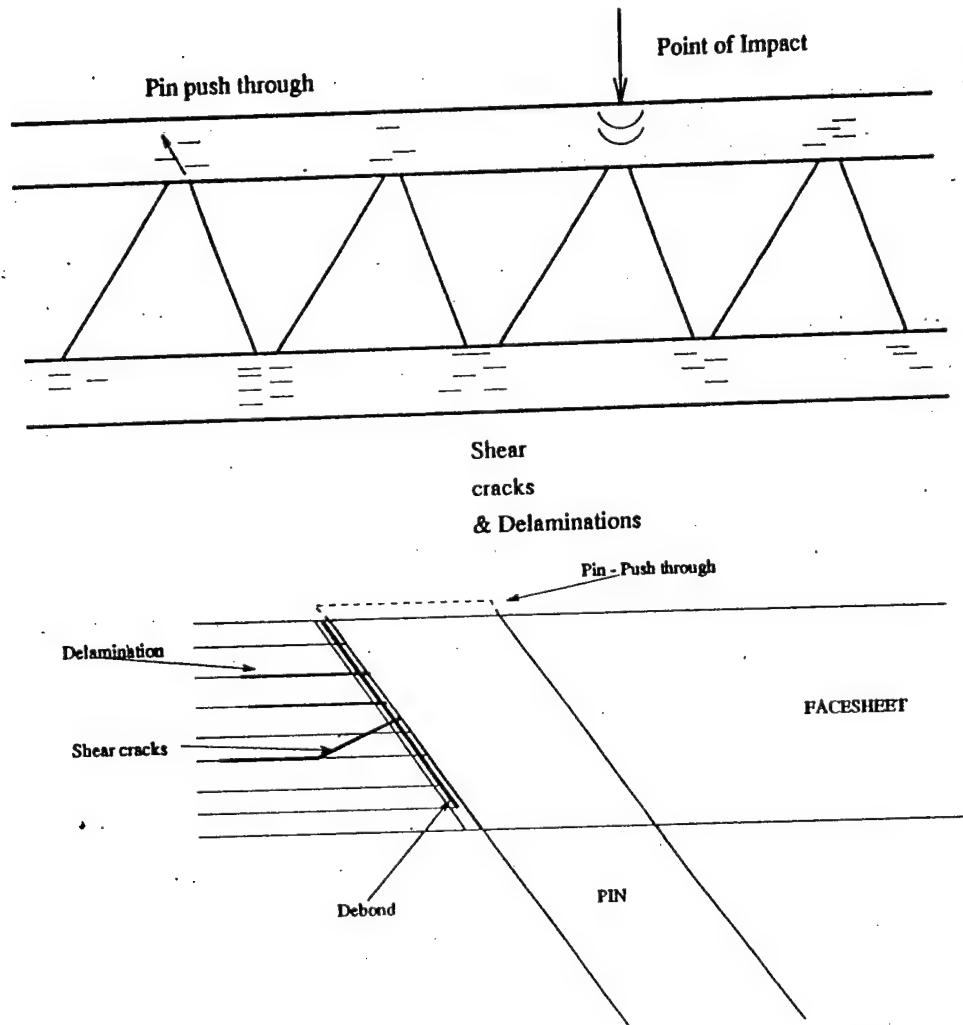
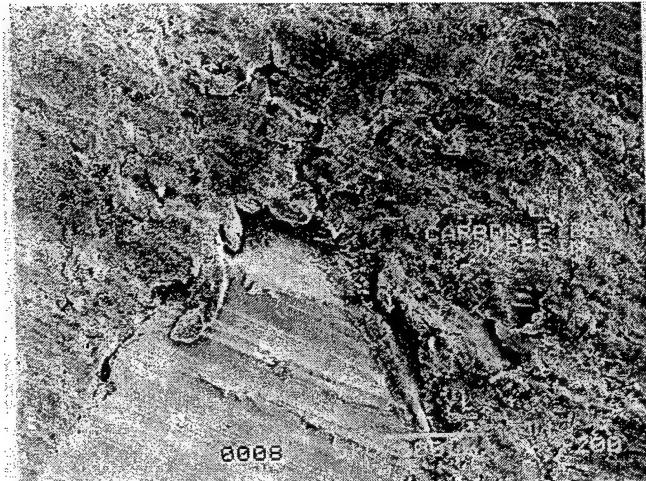
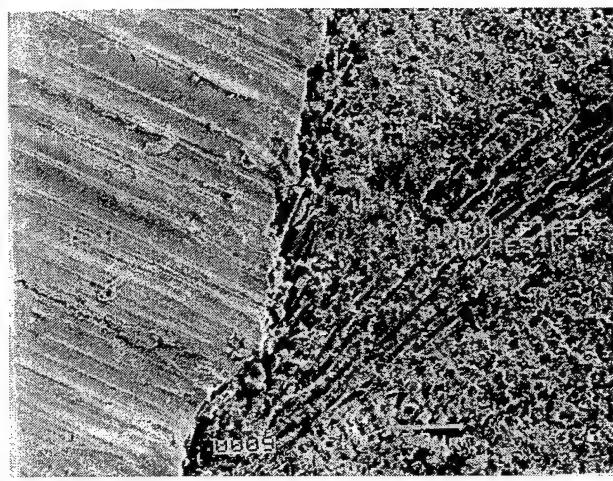


Figure 10.14a&b. Schematic of failure as observed across the top and bottom facesheets

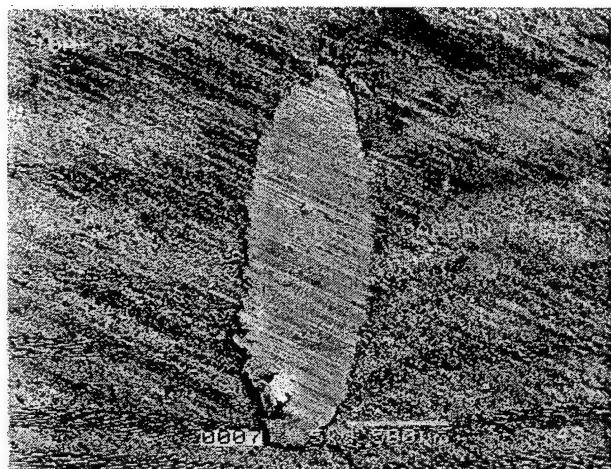


(a)

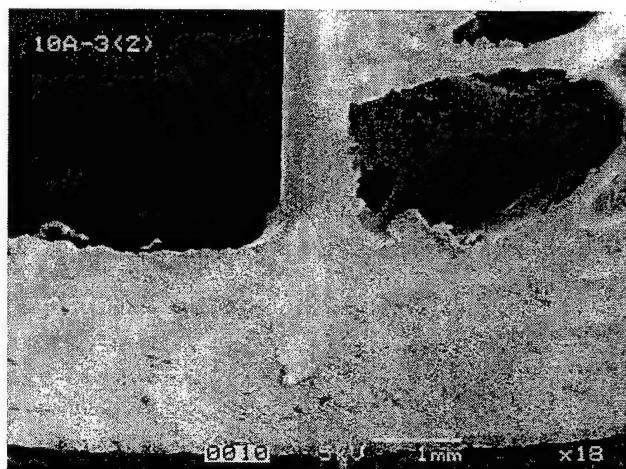


(b)

Figure 10.15a,b SEM Photographs showing the Shear Crack and Delamination in the Facesheet around the Pins

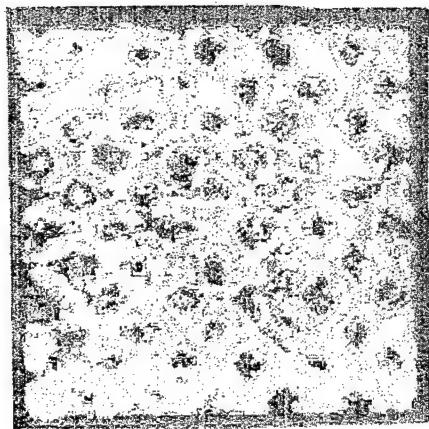


(a)

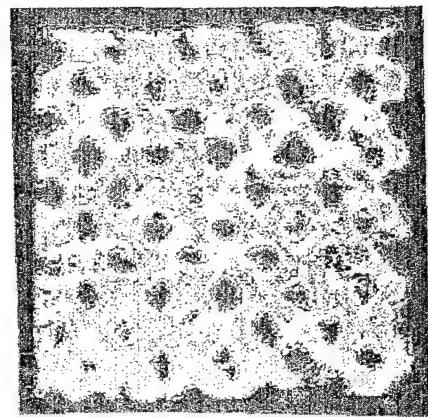


(b)

Figure 10.16a,b SEM Photograph showing that the Pin Penetration into the Facesheet is not Equal for all Pins



10 degree



20 degree

Figure 10.17a,b Pre-Impact C-Scans for 10 and 20 Degree Pin Orientation

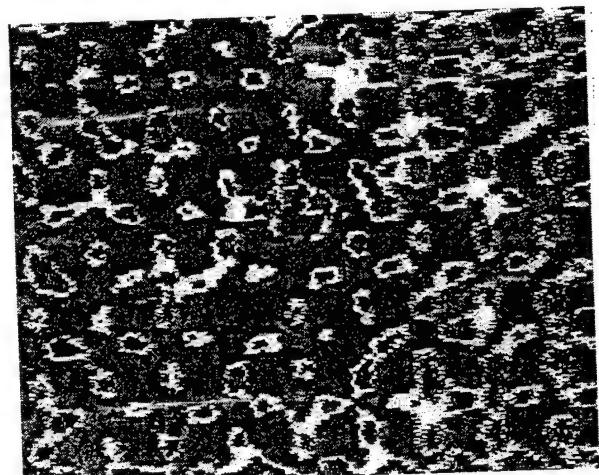
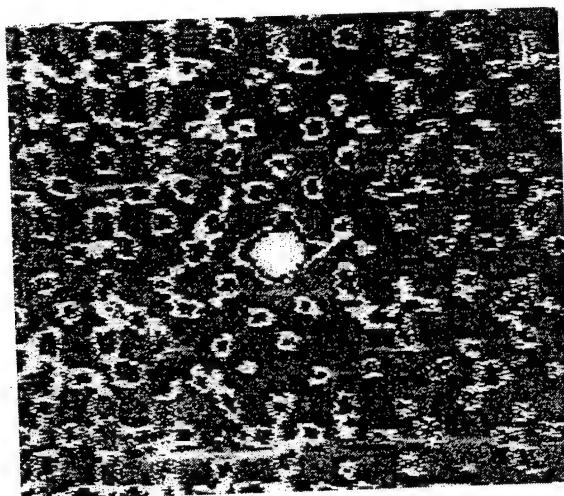
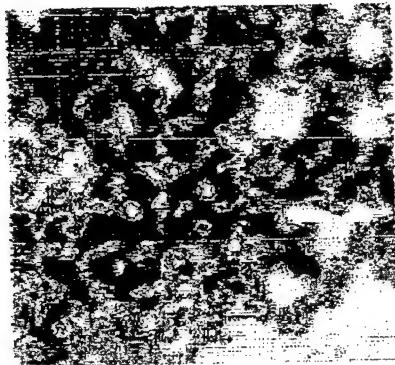
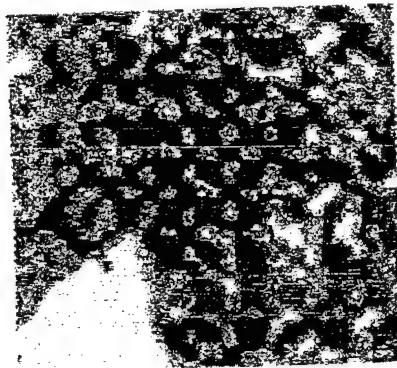


Figure 10.18a,b Ultrasonic C-Scans of a Specimen subjected to Quasi-Static Loading

Figure 10.19 is out of order and is on page 191.

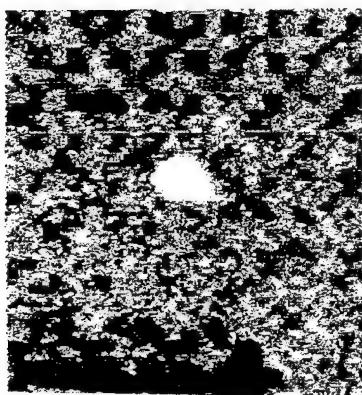


Loading Side Facesheet

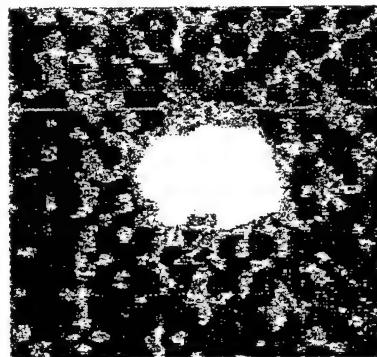


Back Facesheet

Figure 10.20 a,b Ultrasonic C-Scans of a Specimen subjected to CAI Loading



Single Impact



Repeated Impact

Figure 10.21. Ultrasonic C-scans of CAI Loading of Specimens Subjected to Single and

10.7 Compression-After-Impact (CAI) Testing

Four of the samples representative of various impact conditions and pin orientations were subjected to compression-after-impact testing using a SACMA 7 recommended plate compression fixture which attempts to characterize the in-plane compression failure by preventing any out-of-plane buckling. Figures 9.2 (a) & (b) represents a photograph of the CAI testing of the Z-pin sandwich panels. It should be pointed out that the Z - pin core does not support the transverse direction of the face sheets required for the total in-plane failure. A 150 kHz acoustic emission (AE) sensor was attached to the specimen's geometric center using a viscous couplant and electrical tape. A two channel LOCAN-AT Physical Acoustics system was used for AE monitoring. The specimens were loaded at a constant crosshead speed of 0.01"/ min until significant load drop was observed in the load-displacement curve, which was attributed to final failure or buckling. The load-displacement curves are shown in Fig. 10.19. Four specimens were tested under compression-after-impact and the results are summarized in Table 10.1. At several locations along the load-displacement curve, variations in the load corresponding to audible clicking of the pins occurred at which point, the pins tend to debond from the facesheet. Near failure, this phenomenon occurred with more frequency, and an audible facesheet delamination was evident. In the first two rows of Table 10.1, CAI failure load for 10 degree orientation pins shown. In the first case, the specimen was originally impacted only once (to the level of damage initiation) and then tested for compressive failure load. In the second case, the specimen was repeatedly impacted before the compressive failure load was measured. It can be seen from Table 10.1, that the compressive failure load after a single impact is 8687 lb whereas, after multiple impacts, it reduced to 7240 lb (a drop of 16 percent in the compressive failure load). The last two rows Table 10.1 show a comparison of compression after impact (CAI) (failure load) between the 10 degree and 20 degree pin orientations. Both specimens are initially statically loaded below the damage threshold level before the CAI test. It can be observed that the 10 degree orientation (8238 lb) has

Table 10.1 Compression-After-Impact Tests on Specimens

Specimen	Pin Orientation	Load (lbs)
Impact at Threshold Energy	10 deg.	8687
Repeated Impact	10 deg.	7240
Static Under Failure	10 deg.	8238
Static Under Failure	20 deg	7088

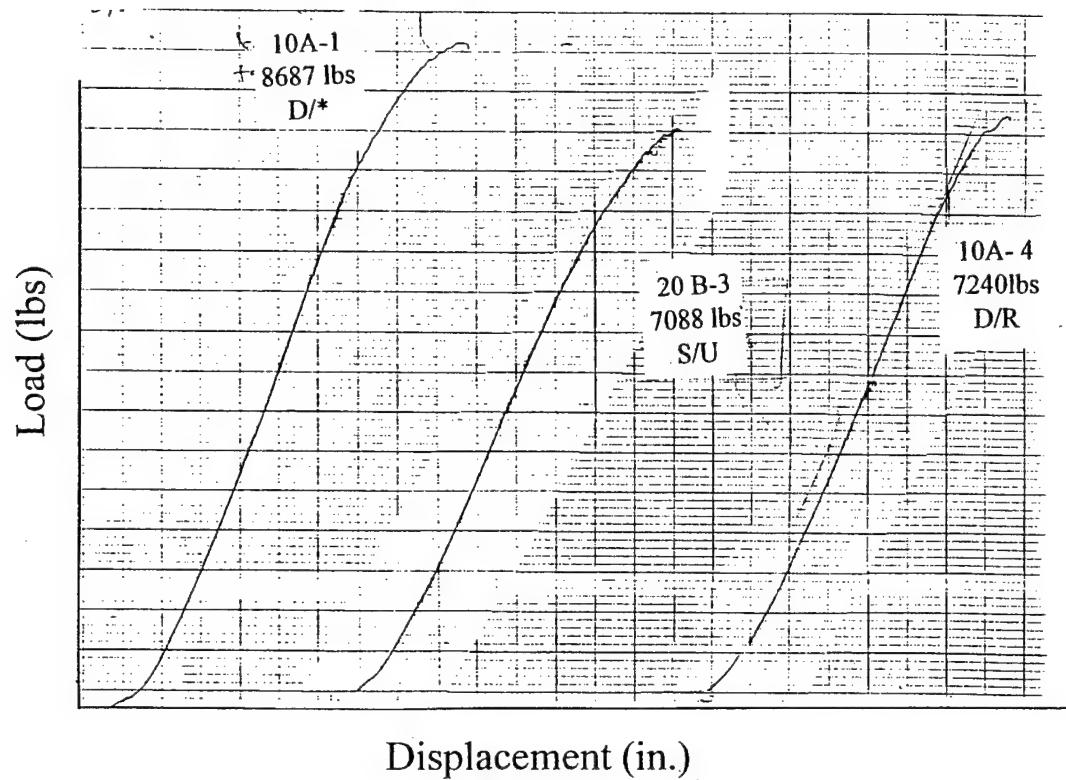


Figure 10.19. CAI Load-Displacement curves (Hollow Z-Pins Steel Core)

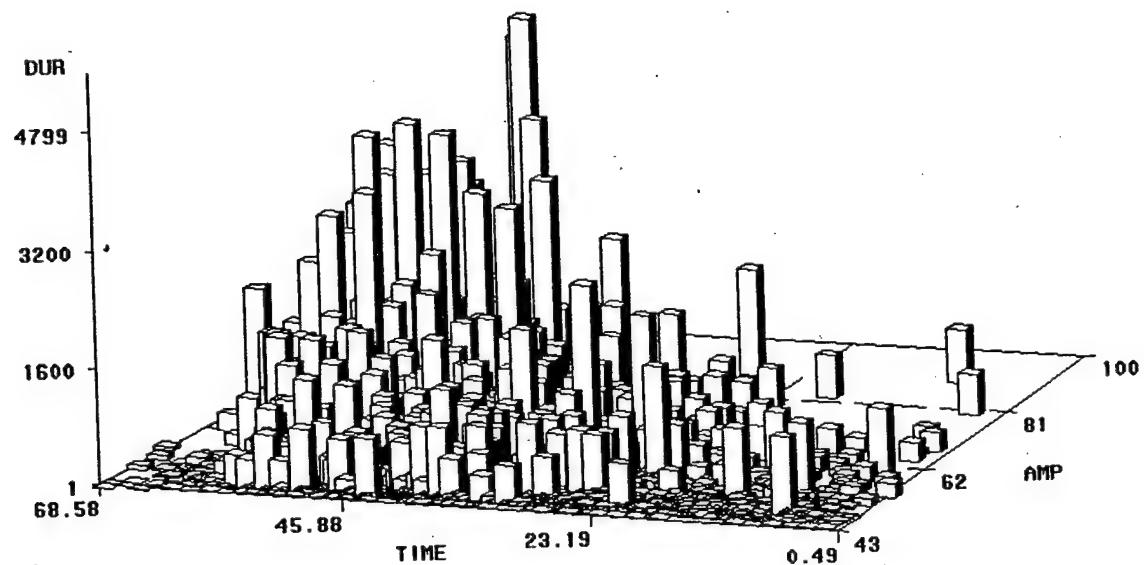


Figure 10.22. Distribution of amplitude and duration with respect to test time

more CAI failure load than the 20 degree orientation (7088 lb). That is, for greater pin orientation angle, the compression after impact failure load is lower. This, in part may be explained by the weaker face sheet support against geometric buckling. Ultrasonic C-scans of the failed specimens are shown in Fig. 10.20.

The coalescence of delaminations across a system of pins is evident for all the specimens tested. The damage area around the centrally located impact is not influenced by the the compression Loading as seen in Fig. 10.20. The failure is initiated primarily by the localized failure of a system of pins. The effect of repeated impacting on the damage area of the upper face sheet can be seen in Fig. 10.21 where C-scans are shown after a single impact and after repeated impacts. A larger damage zone can be observed in the C-scan of the repeatedly impacted specimen.

10.8 Acoustic Emission (AE) Testing

Energy, amplitude and event durations of AE events were monitored during the CAI tests. AE activity was seen to be continuous throughout the loading history of the specimens. Figure 10.22 represents the distributions of amplitude and duration with respect to the test time, while Fig. 10.23 represents the same information using amplitude and energy with respect to test time. The distribution of AE events shown in Fig. 10.21 broadly lies in three groups; first a low duration less than 500 ms, low amplitude 40-55 dB, second, a medium duration 500-2000 ms, medium amplitude 55-70 dB and third, a high duration greater than 2000 ms, high amplitude events. The energy based grouping of these events as shown in Fig. 10.23 show a small energy less than 100 Joules for a majority of type one and type two events described above. Only a few events, are seen to exhibit high amplitude, high energy greater than 750 Joules, corresponding to dominant occurrence of pin pull-out and facesheet delamination. The first set of events occur from the early stage of loading and last until failure and are primarily attributed to matrix microcracking, and events corresponding to the initiation of localized debond between pin-facesheet. The second set of events are primarily due to pins separating and/or sliding within the facesheet plies creating microdelaminations and further debonds. These events also corresponded to audible clicking of the pins, indicating that some pins undergo a pin pull-out phenomenon.

10.9 Vibration Testing

The specimens were tested to investigate the global stiffness changes using a vibration based nondestructive evaluation (NDE) test following impact and/or static loading. The specimen was mounted in a near free-free boundary condition using bees wax at its geometric center on an impedance head connected to an electrodynamic shaker Brüel & Kjaer 4810 excited using random noise. The input force and output acceleration signals from the impedance head were fed to a dual channel frequency

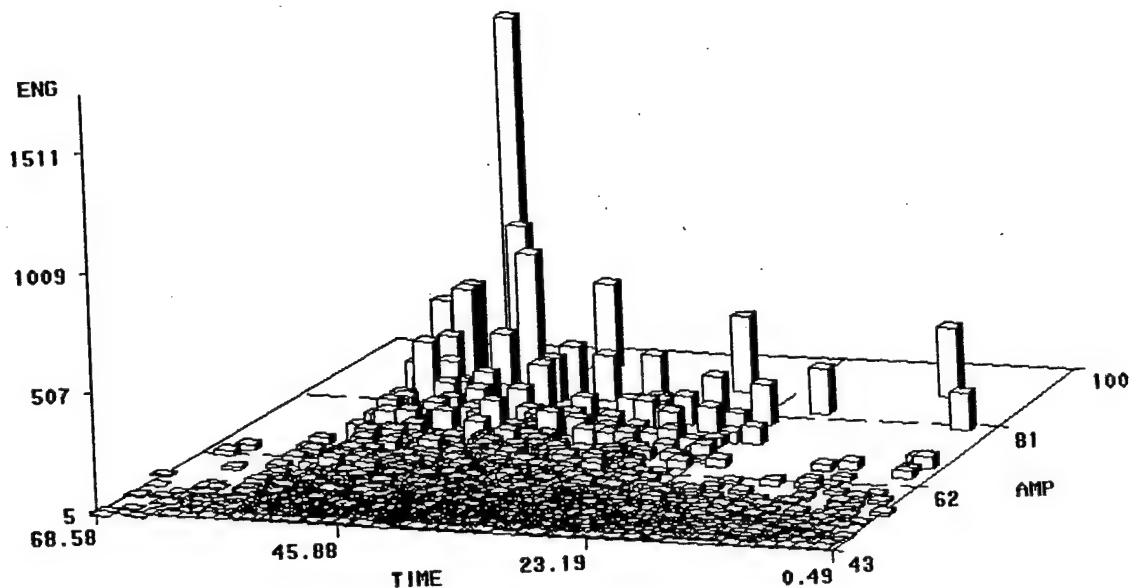


Figure 10.23. FRF curve for 10 degree pin orientation subjected to a single impact and repeated impact

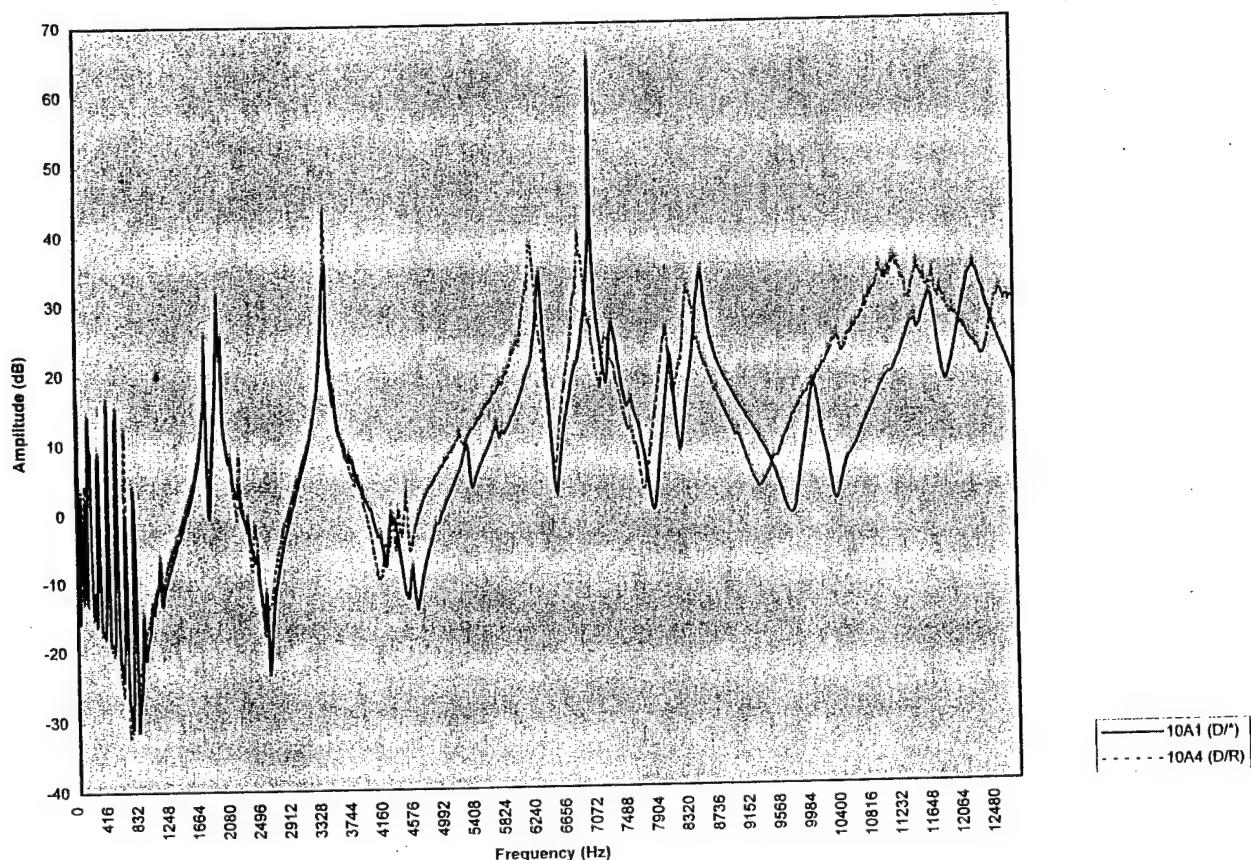


Figure 10.24 Comparison of FRF of 10 degree Pin Orientation Specimens Subjected to a Single Impact vs that Subjected to Repeated Impact

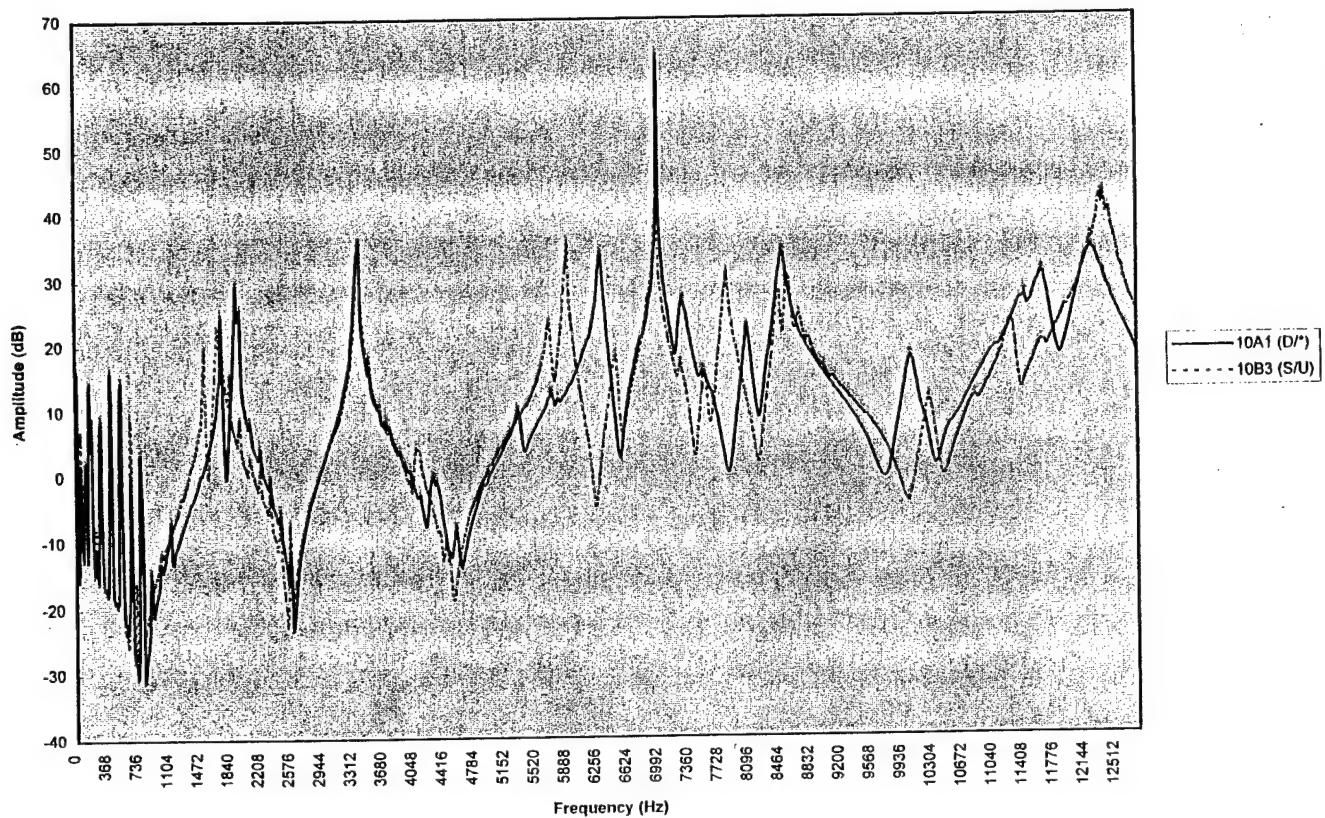


Figure 10.25 Comparison of FRF for an Impact Loaded Specimen and Statically Loaded Specimen

analyzer B&K 2032. The frequency response function (FRF) of the specimens under predominantly bending vibrations were recorded. Figure 10.24 compares the FRF of 10 degree pin orientation specimens subjected to a single impact versus that subjected to repeated impact. Here, the solid line correspond to the FRF curve for the specimen that is single impacted while the dotted line indicates the specimen subjected to multiple impacts. Disregarding the initial noise at low frequency levels, the first three modes are seen to be unaffected by the impact event related condition of the specimens, however, at the higher modes between 4160 Hz - 12,500 Hz within the measurement range, it is seen that the specimen subjected to repeated impact loading exhibits reduction in frequency as compared to the specimen subjected to a single impact at failure load. For example, the 6400 Hz frequency is seen to reduce to 6320 Hz for the specimen subjected to repeated loading (considering an amplitude of 33 db. In Fig. 10.25, the FRF's for an impact loaded specimen at failure load and statically loaded specimen under failure load are compared for the 10 degree pin orientation. The solid line is used to show the FRF of the impacted specimen and the dotted line denotes the statically loaded specimen. In this case, the first two modes and some of the higher modes for the statically loaded specimens show lower frequency values as compared with the impact loaded specimens. This indicates that the stiffness loss for the statically loaded specimen is greater, and hence, the delaminations and pin push-through is more extensive as compared with the impact loaded specimens. Also, based on the vibration tests, it is noticed that some of the modes did not change (between the impact loaded specimen and the static loaded specimen) indicating that all the modes are not sensitive to the presence of damage. This suggests that depending upon the location and proximity of the damage state (which is not at identical locations over the facesheet) for a system of pins, the vibration response of that mode is affected. No correlation has been attempted in this article to investigate the influence of damage position with respect to a mode number.

The damping ratio of the specimens has been measured by performing zoom transform on the peak of the FRF using the half-power points method. The range of damping (ratio) exhibited for the specimens for the modes measured was in the range of 0.0015-0.009. The highest damping ratio was exhibited by the specimen subjected to repeated impact loading (0.009) which was attributed to the large frictional energy dissipated at the larger damage zone, also shown in C-scan of Fig. 10.21.

10.10 Hollow Steel Pins Truss Core : Conclusions

The failure characteristic appears to be pin push-through at the threshold energy level. The surrounding area shows features of delamination and debonding between pins. The 10 degree oriented pins caused threshold energy at a higher level than the 20 degree oriented pins. Damage is significant at 1.2J for 10 degree pin orientation, and 0.53 for the 20 degree pin orientation. The lowest impact energy at

which a significant proportion of the impact energy is absorbed by the specimen is the damage initiation impact energy. The C_{_} scans verify the phenomena of delamination after pin push-through. The natural frequency of the plate was unaffected by the localized failure characteristics for several modes. The compressive failure of the specimen, both 10 and 20 degree is determined by the threshold impact event. It was observed that compressive failure was characterized by pin debond and formation of delaminations. Compressive failure becomes a localized event predicated by local pin debond such as shown by CAI load displacement curves. Acoustic emission parameters indicated the dominant failure modes were pin debonding, matrix cracking and facesheet delamination.

10.11 References

1. Freitas, G., Magee, C., Dardzinski, P and Fusco, T., " Fiber Insertion Process for Improved Damage Tolerance in Aircraft Laminates", Journal of Advanced Materials, Vol. 25, No. 4, pp. 36-43 (1994).
2. Barrett, D.J., " A Micromechanical Model For the Analysis of Z- Fiber Reinforcement", 37 th AIAA/ ASCE/ ASME/ AHS SDM Conference, p. 62-67 (1996).
3. Harrington, T.M., "An Experimental Investigation of Sandwich Panels Under Low Velocity Impact," MS thesis submitted to Air Force Institute of Technology, AFIT/GAE/ENY/94D-22 (1994).
4. Herup, E.J and Palazotto, A.N., " Low Velocity Impact Damage Initiation in Graphite-Epoxy/Nomex Honeycomb Sandwich Plates", 37th AIAA/ ASCE/ ASME/ AHS SDM conference, Salt Lake City, Utah, AIAA-96-1519-CP, pp. 1765-173 (1996).
5. Palazatto, A.N, Herup, E.J and Harrington, T., " An Experimental Investigation of Sandwich Panels Under Low Velocity Impact", ASCE 11th Engineering Mechanics Conference, Fort Lauderdale, Florida, Vol. 1, pp. 402-407 (1996).
6. Herup, E.J., " Low Velocity Impact on Composite Sandwich Plates" A Ph.D Dissertation submitted to Air Force Institute of Technology, Wright Patterson Air Force Base, OH-45433, AFIT/DS/ENY/96-11 (1996).
7. SACMA Recommended Method SRM 2-88. " Compression After Impact Properties of Oriented Fiber - Resin Composites" Suppliers of Advanced Composite Materials Association, Arlington, VA, (1989).

8. Vaidya, U. K., Non Destructive Evaluation of Graphite Fiber Based Composites Using Acoustic and Vibration Techniques", Ph.D Dissertation submitted to Auburn University, AL, (1993).

11.0 Static Testing

11.1 Introduction

The transverse stiffness and strength under flexural loading, in-plane shear and compressive loading are oftentimes of concern in sandwich constructions. In the interest of completeness of the study, several categories of sandwich composites have been considered including hollow truss core, Rohacell foam core, Hexcel graphite honeycomb core, glass/epoxy and titanium pins reinforced Rohacell foam core, WESKOR foam-filled honeycomb core. The cores and their sandwich composites considered are summarized in Tables 11.1 and 11.2. The static tests comprised of flexure, in-plane shear and compression response evaluation of the cores and the sandwich composites made from these cores.

11.2 Experimental

A 22 kips MTS were utilized to test the samples under flexure, in-plane shear and compression according to a typical scheme shown in Fig. 11.1a-c. The test specimens were prepared as per ASTM 393 - 62 for flexure and ASTM 273 - 61 for in-plane shear testing of sandwich composites. For compression testing, the cores and their sandwich composites were loaded between parallel steel plates placed on either side of the specimen. Unless otherwise stated, the samples were subjected to a rate of loading of 0.05" / minute under displacement control mode.

11.3 Flexural Tests and Acoustic Emission (AE) Nondestructive Evaluation / Monitoring

11.3.1 Hollow Truss Core : Flexural Response and Effect of Facesheet Type

Three-point flexural loading of hollow truss core sandwich composite samples was conducted. Two types of hollow truss core (0.5" core thickness) sandwich composites were considered : a) with graphite/epoxy facesheets, and b) with glass/epoxy facesheets. The pins were steel pins of 20 mil diameter arranged according to the configuration of 10 degree samples shown in Fig. 11.2. A l/d ratio of 9: 1 on an MTS 810 servohydraulic MTS machine. The crosshead speed was set at 0.05"/min. Table 11.3 shows the details of the test samples. Table 11.4 summarizes the results obtained from the flexural tests.

An acoustic emission (AE) sensor of 150 kHz resonant frequency was attached to the underside of the sample using constant force spring clamps and

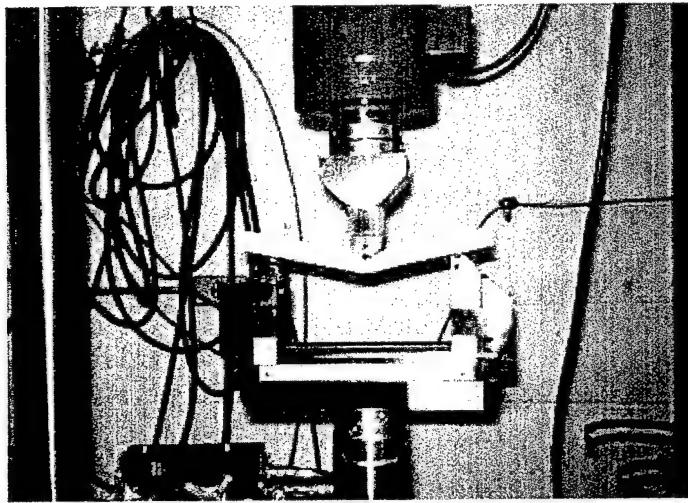


Figure 11.1a Illustration of Static Flexural Testing of Sandwich Composites

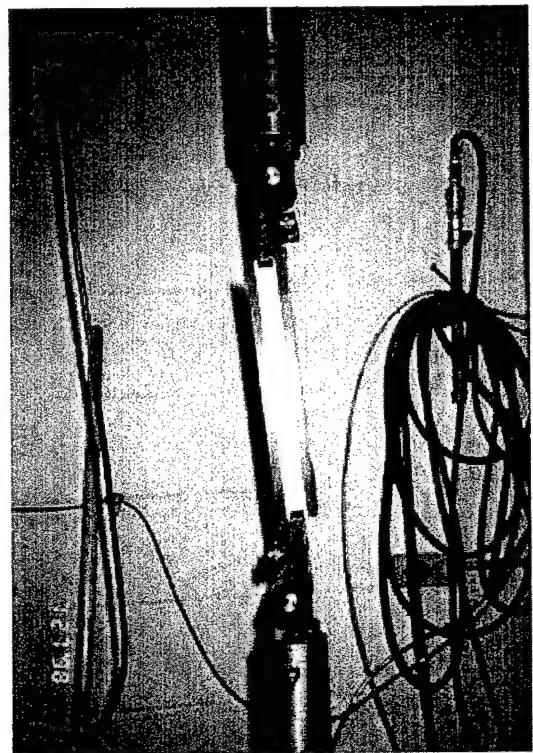


Figure 11.1b Illustration of In-Plane Shear Testing of Sandwich Composites

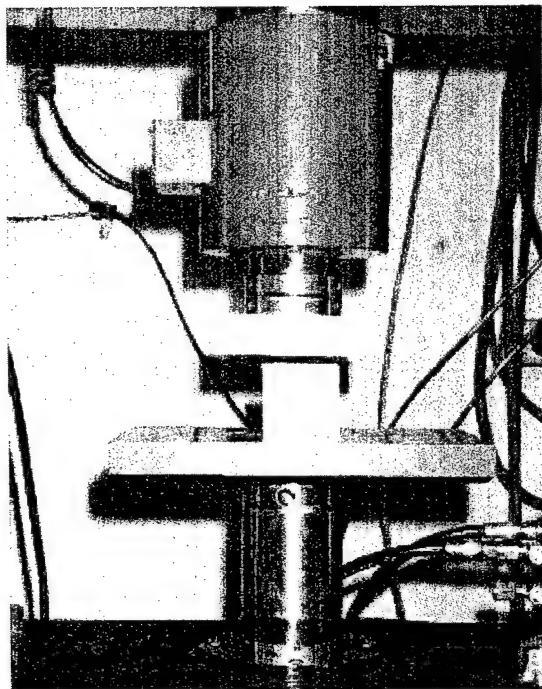


Figure 11.1c Illustration of Static Compression Testing of Sandwich Composites

Table 11.1 Cores Tested and Their Geometry:

Type	Geometry (Set 1)	Geometry (Set 2)
Rohacell Foam	2" X 2" X 0.5"	1" X 1" X 0.5"
Honeycomb	2" X 2" X 0.5" Cell size 0.24"	1" X 1" X 0.5" Cell size 0.24"
Rohacell Foam + Titanium pins	2" X 2" X 0.5"	-
Honeycomb + Foam	2" X 2" X 0.5" Cell size 0.24" & 0.4"	1" X 1" X 0.5"
Rohacell Foam + Glass Pins	2" X 2" X 0.5"	-

Table 11.2 Sandwich Composites Tested and Their Geometry:

Type	Geometry
Rohacell Foam core	1" X 1" X 0.75"
Honeycomb core	1" X 1" X 0.75" Cell size 0.24"
Rohacell Foam + Titanium pins core	1" X 1" X 0.75"
Honeycomb + Foam core	1" X 1" X 0.95" Cell size 0.24"
Rohacell Foam + Glass Pins core	1" X 1" X 0.75"
Truss core	2" X 2" X 0.4"

Table 11.3. Details of Samples Tested under Flexural Loading

Specimen Type	Weigh (gms)*	Length (mm)*	Width (mm)*	Top Skin Thickness (mm)*	Core Thickness (mm)*	Bottom Skin Thickness (mm)*
Graphite/ Epoxy Face Sheet	19	127	26.98	1.36	11.75	1.33
Glass Epoxy Face Sheet	27	127	26.98	2.65	12.04	2.88

* Average of 12 samples

Table 11.4. Summary of Flexural Tests on four samples each of Truss Core Composites
with Glass/Epoxy and Graphite/Epoxy Facesheets

GLASS FABRIC					
SAMPLE ID	SPAN LENGTH (L) (in)	WIDTH (B) (in)	THICKNESS (t) (in)	FAILURE LOAD (P) (lb)	AIRURE DEFLECTIO (in)
GL 4	3.734	1.066	0.704	83.2	0.4518
GL 5	3.734	1.034	0.743	121.6	0.401
GL 6	3.734	1.031	0.761	113.7	0.466
GL 7	3.734	1.044	0.744	132.7	0.522
 GRAPHITE FABRIC					
GR 1	3.734	1.07	0.626	41.9	559.6894898
GR 2	3.734	1.066	0.602	48.1	697.3655058
GR 3	3.734	1.082	0.619	43.1	582.2832321
GR 4	3.734	1.105	0.618	68.6	910.4381763

(FIGURE IS MISSING)

Figure 11.2 - Schematic of arrangement of pins in polystyrene foam core in preliminary work

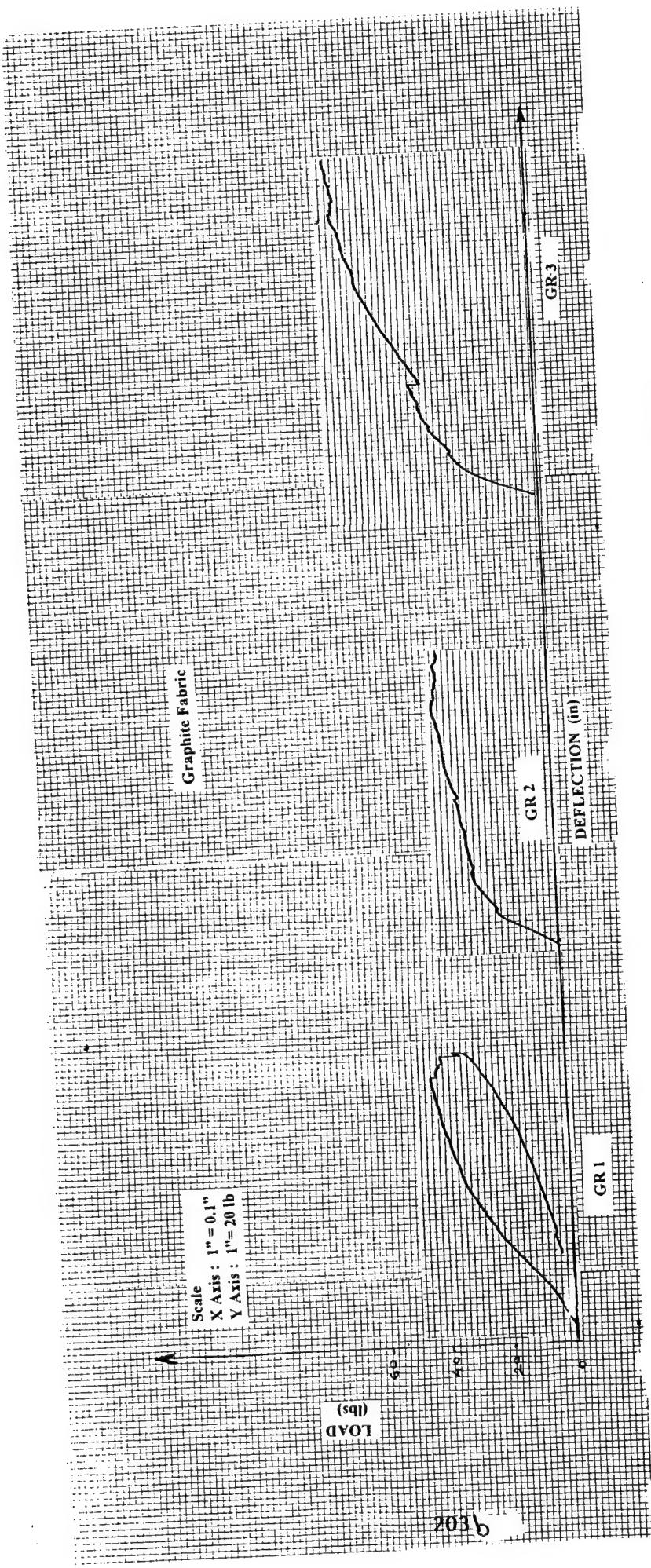


Figure 11.3. Load-Deflection Curves for Graphite/Epoxy Truss Core Composites under Flexural Loading

honey as couplant. A 40 dB gain was set on the preamplifier. The AE data was captured in terms of amplitude, ringdown counts, energy content, event duration and rise time. Cumulative AE events were monitored as well.

The average flexural load withstood by the graphite/epoxy facesheet sandwich composites was 50.83 lbs (flexural strength 687.43 psi), while for the glass/epoxy face sheet sandwich composites, it was 113.7 lbs (flexural strength 1106.98 psi). From the load-deflection curves (Fig. 11.3) of graphite/epoxy face sheet samples, multiple load drops may be observed from about 35% of the ultimate load. From visual observations these load drops were a result of pin pull-outs from the facesheet, originating from the outer edges of the sample. With further loading, the pins start pulling out from "outside-in". Distinct audible creaks accompanied the load drops, and which are attributed to face sheet debonding from the facesheets.

The average load carried by the glass/epoxy composites was 113.7 lbs. The higher load is attributed to thicker face sheets made of glass/ epoxy. The progression of failure was similar in terms of it originating through pin pull-out from the ends and subsequent pin pull-out from the edge of the specimen extending to the inside. Unlike the graphite/epoxy face sheets, the load-deflection curves (Fig. 11.4) do not exhibit multiple load drops, rather there is catastrophic failure at the end. This is primarily attributed to dominant pin-face sheet separation, without notable debonding of the pin-to-face sheet interface. Also, the compression side facesheet completely separated out from the core nearing final failure.

11.3.2 Flexure Tests : AE Monitoring of Hollow Truss Core

AE testing gave an insight into several failure mechanisms including: pin pull-out, friction mechanisms between pin to facesheet, slow facesheet microcracking, face sheet debonding and final pin-pull out from the facesheet. Figures 11.5 and 11.6 compare the amplitude distribution of AE events for the truss core with glass/epoxy and graphite/epoxy face sheets. Primarily, the amplitude distribution of the AE events lies in the 40-80 dB range which is attributed to slow microcrack growth and accompanying frictional mechanisms such as relative movement between the pin and the facesheet. The number of events in the graphite/epoxy facesheet composites are more in comparison with the glass/epoxy face sheet. The AE activity is largely concentrated in the neighborhood of the 50 dB range for both glass/epoxy and graphite/epoxy facesheets. From the energy vs time plots (Figs. 11.7 and 11.8), it is seen that for the glass face sheet composites, the distinct pin pullouts are well characterized by significant increase in energy values (shown in Figs. 11.7 and 11.8). Typically

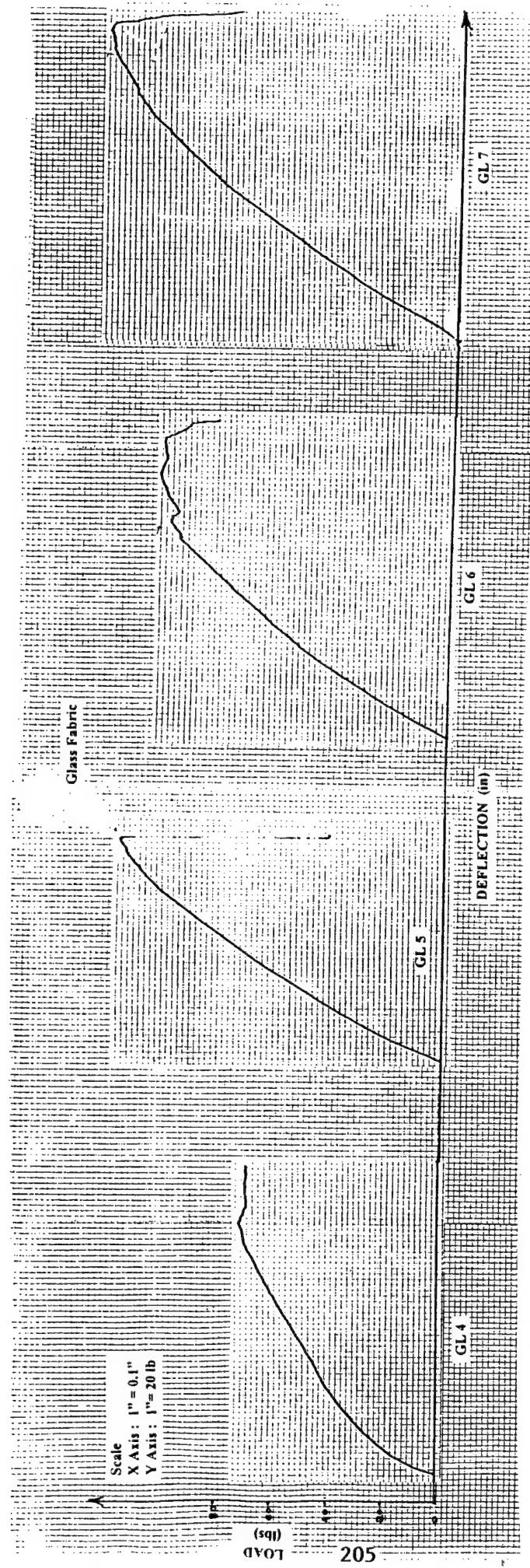


Figure 11.4. Load-Deflection Curves for Glass/Epoxy Truss Core Composites under Flexural Loading

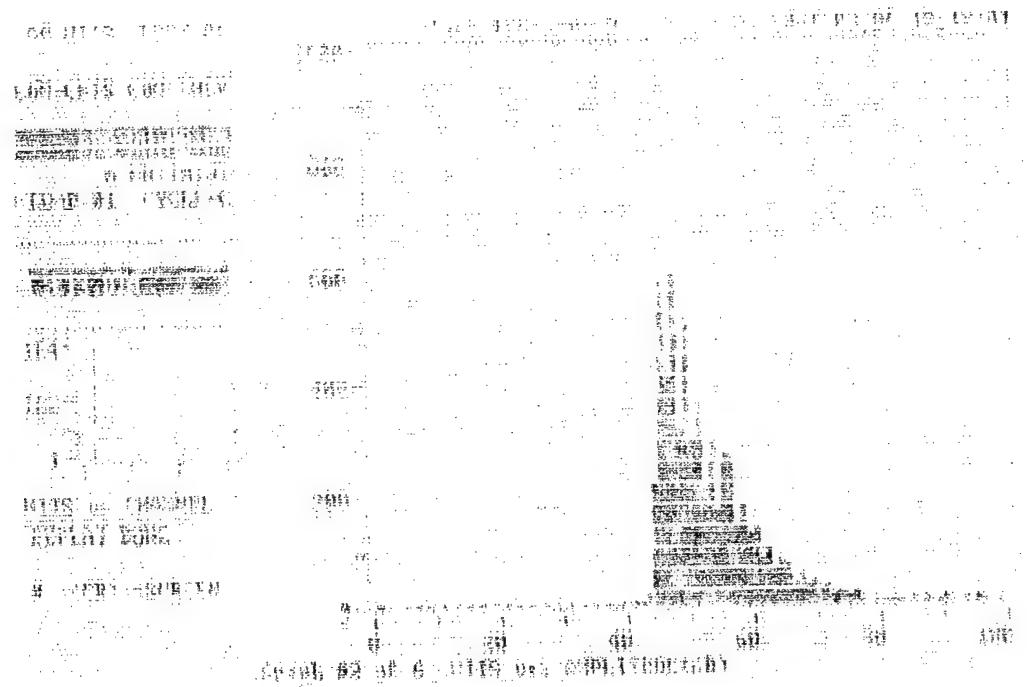


Figure 11.5. AE Response in terms of Amplitude Distribution for Glass/Epoxy Truss Core Composite

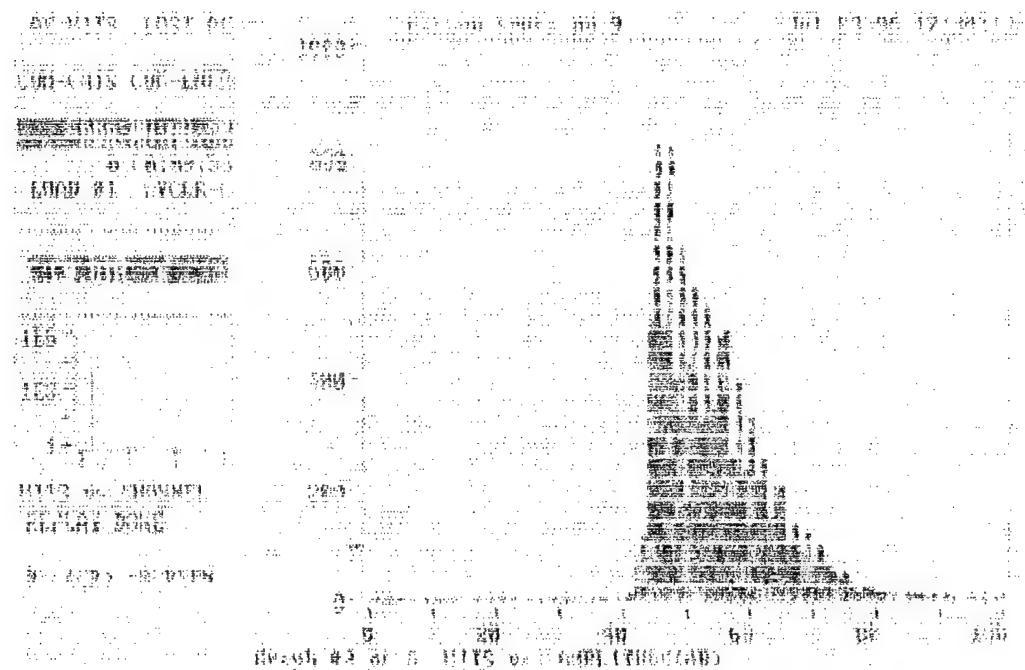


Figure 11.6. AE Response in terms of Amplitude Distribution for Graphite/Epoxy Truss Core Composite

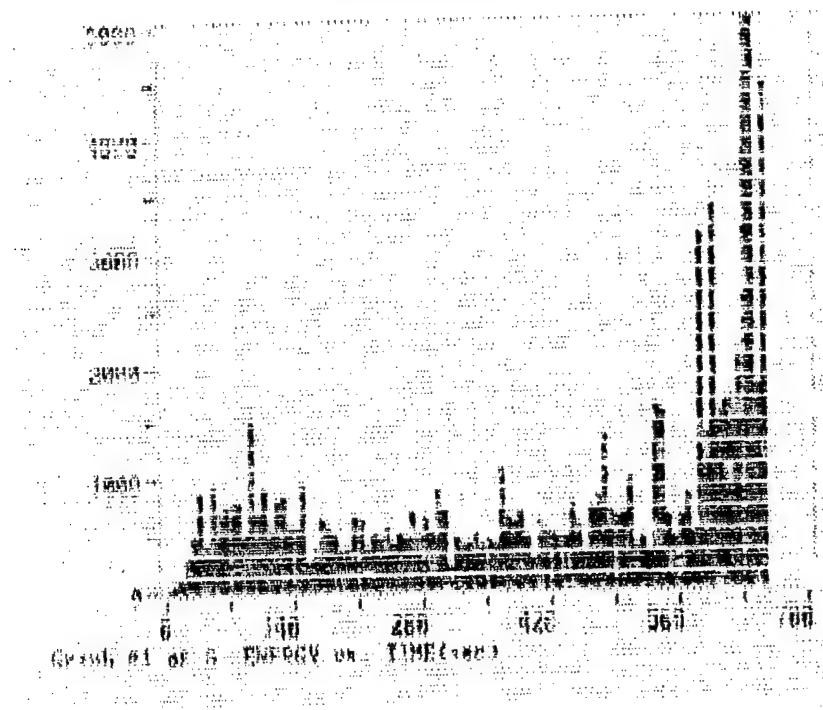


Figure 11.7. AE Response in terms of Energy vs Time for
Glass/Epoxy Truss Core Composite

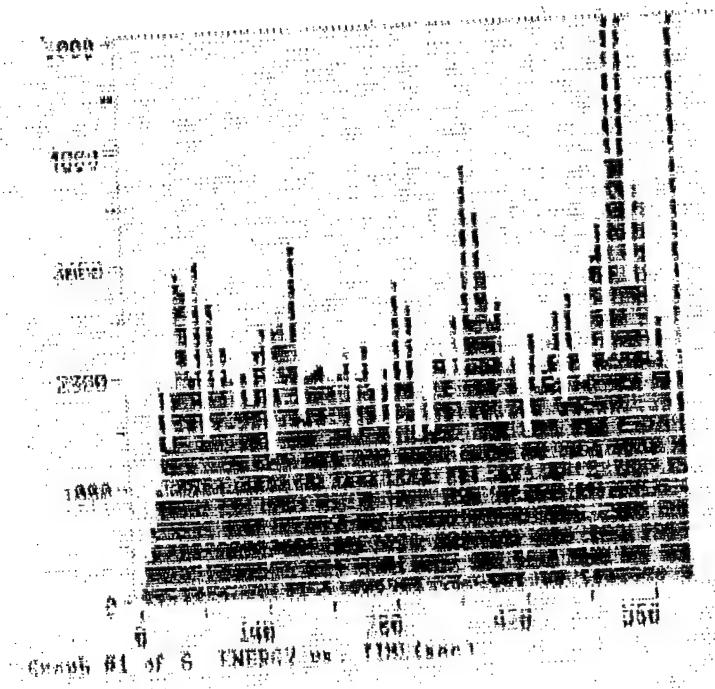


Figure 11.8. AE Response in terms of Energy vs Time for Graphite/Epoxy
Truss Core Composite

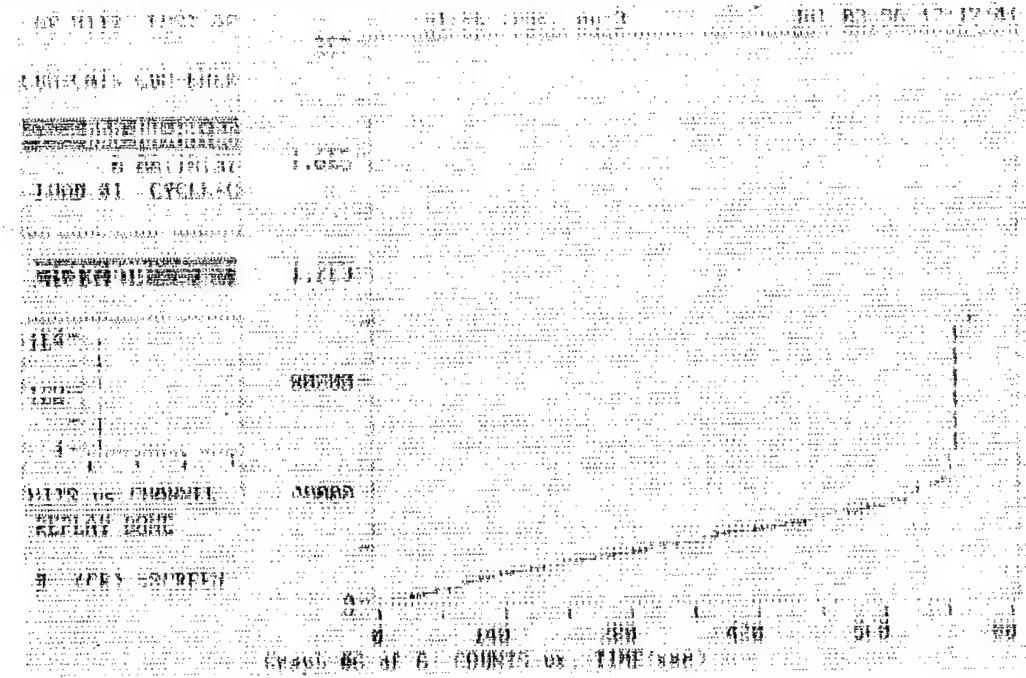


Figure 11.9. AE Response in terms of Cumulative AE Activity for Glass/Epoxy Truss Core Composite

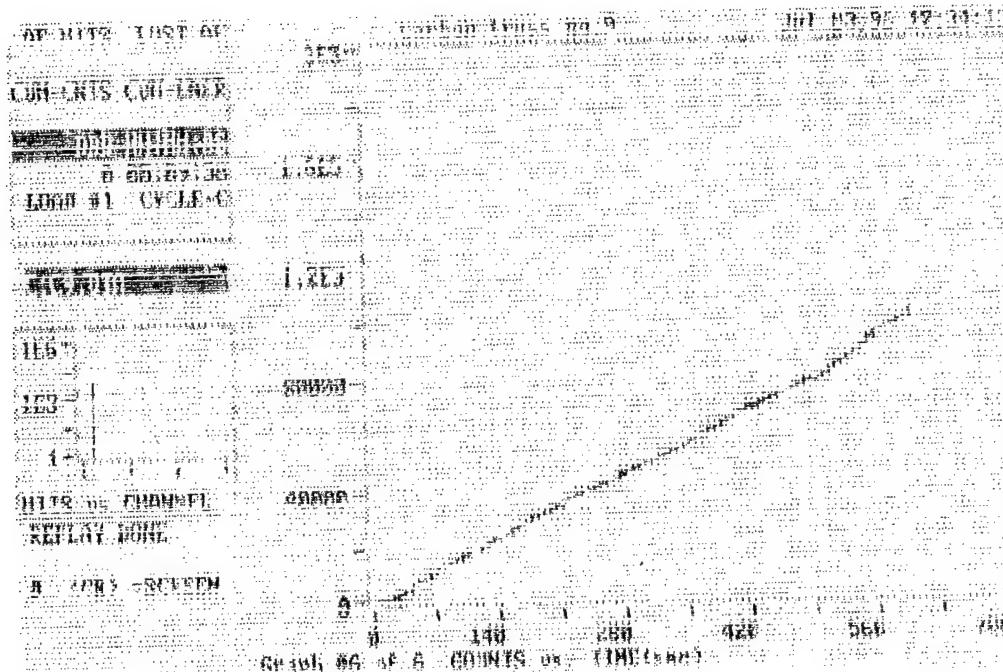


Figure 11.10. AE Response in terms of Cumulative AE Activity for Graphite/Epoxy Truss Core Composite

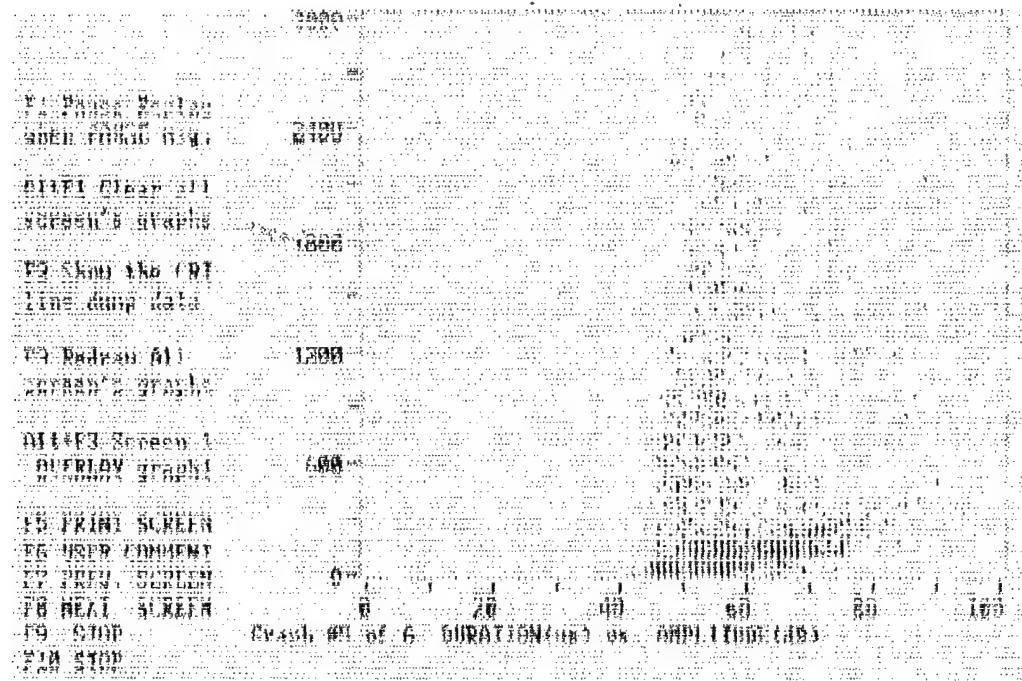


Figure 11.11. AE Response in terms of Duration vs Amplitude for Glass/Epoxy Truss Core Composite

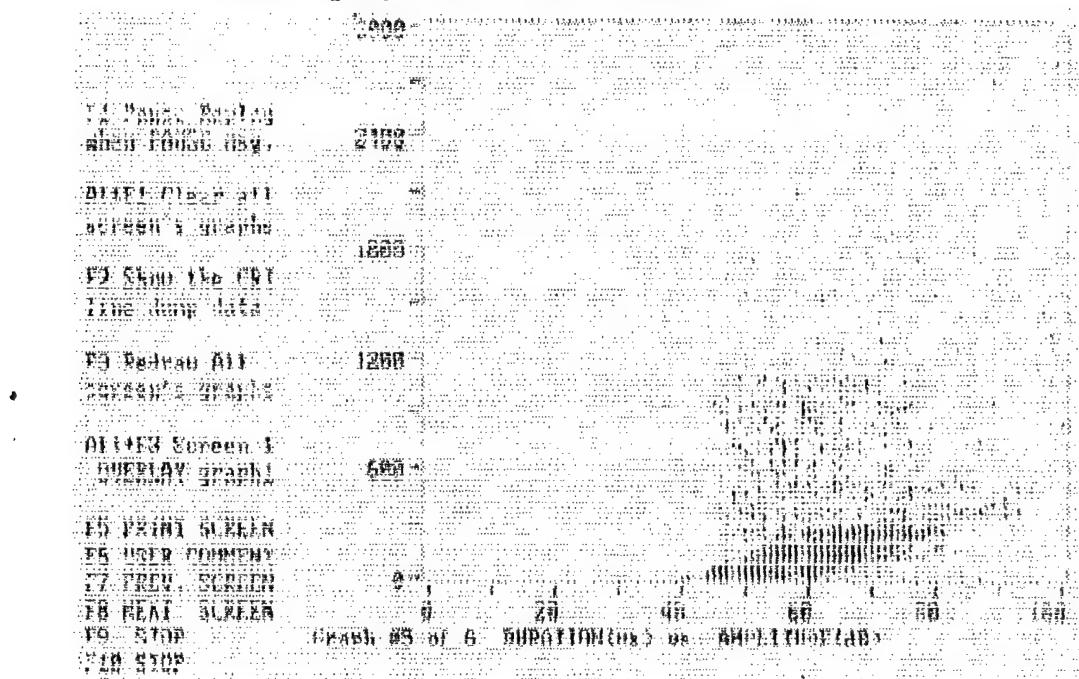


Figure 11.12. AE Response in terms of Duration vs Amplitude for Graphite/Epoxy Truss Core Composite

energy values of 1000-1200 are seen accompanying pin pullout. Nearing final failure, the magnitude of the energy is seen to increase considerably. In contrast for the truss core composites with graphite/epoxy facesheets, the energy is seen to be higher as compared to the specimens with glass/epoxy facesheets. As mentioned earlier, the frictional interaction for the graphite/epoxy facesheets was higher and resulted in multiple load drops, which are well indicated in the larger energy levels as seen from the energy-time curves. The cumulative AE plots show that activity is continuous for both types of samples (Figs. 11.9 and 11.10). The amplitude-duration plots (Figs. 11.11 and 11.12) provide an insight into the frictional events arising from pin contact with the skin. A large number of low duration medium amplitude events are seen to occur in case of the graphite/epoxy facesheets, as opposed to such lower activity in the glass/epoxy facesheet, indicating that the graphite/epoxy facesheets had higher interfacial contact and frictional events. The large duration (>600 us) - medium amplitude (60-80 dB) events primarily correspond to the pin pull-out from the facesheets.

11.4 Flexural Testing : Foam, Pin Reinforced Foam and Foam-Filled Honeycomb Core

Figure 11.13. represents the load-displacement curves for the Rohacell IG-71 foam core, glass/epoxy pins reinforced Rohacell foam and WESKOR foam-filled honeycomb core sandwich composites with average dimensions 9" x 1.5" x 0.8". The peak failure load in case of the Rohacell foam core sandwich composite is noted to be 63.69 lb. The glass/epoxy pin reinforced foam core exhibits significant increase in flexural stiffness and a 54% increase in peak failure load (243.57 lb). The flexural stiffness and peak failure load for the WESKOR foam-filled honeycomb core sample was found to be about 42% higher (111.24 lb) as compared to using only the higher quality, Rohacell foam core (without reinforcement). The stiff glass/epoxy pins in the pin reinforced core, and the honeycomb cell walls in the WESKOR foam, provide attractive benefits in terms of improved flexural stiffness, higher peak loads, and thereby larger damage resistance to flexural loading at a nominal weight penalty.

11.5 WESKOR Foam Reinforced Honeycomb : Effect of Facesheet Material

Figure 11.14 represents the load-displacement curve for the WESKOR foam filled-honeycomb core composite with graphite/epoxy facesheets, and glass/epoxy facesheets of equivalent facesheet thickness (0.112") respectively. Here the flexural stiffness and peak failure loads are higher by ~31% in case of graphite/epoxy facesheets as compared with that of glass/epoxy facesheets. The

high values of flexural stiffness arise because of the stiffness of the graphite/epoxy facesheets in comparison to the glass/epoxy facesheets.

Figure 11.15 compares the flexural strength of the sandwich composites studied. The flexural strength was calculated using the relationship [1]:

$$\text{Facing Stress} = F = P_1 a_1 / 2f (h+c) b$$

$$\text{Flexural Stiffness} = D = E(h^3 - c^3) b / 12 L$$

where P = Maximum failure load,

f = facing thickness, a_1 = span length, c = core thickness,

b = width of the specimen, h = thickness of the sandwich construction

E = young's modulus of the facings, $L = 1 - v^2$, where, v = Poisson's

Ratio, Here the poisson's ratio is taken to be 0.171.

11.6 Flexure : Failure Modes

The failure modes of the sandwich composites were similar in several aspects as shown in Fig. 11.16. The damage progression was predominantly in the core in the neighborhood of the loading location. No catastrophic failure was noted. The failure in the Rohacell foam core was through cell / core crushing around the loading point and matrix cracking (whitening) within the facesheets. In the case of the glass/epoxy pin reinforced Rohacell foam core sandwich, the pins pulled out to some extent, in addition to the core crushing of the foam. Similar pin response was observed for the hollow truss core described earlier. However, the extent of pin pull-out was enhanced for the hollow truss core, while the foam supports the pins and suppresses the pull-out.

For the foam reinforced with honeycomb cells, localized cell wall buckling was observed at the point of loading. Failure progressed by localized core crushing and extension of buckling of the cell walls. No catastrophic failure was observed in any of the systems tested. In all the cases, fiber failure of the facesheet was not observed, mostly matrix cracking was dominant. Failure was represented by a steady drop in the load, past the peak load. Table 11.5 summarizes the flexure experiments.

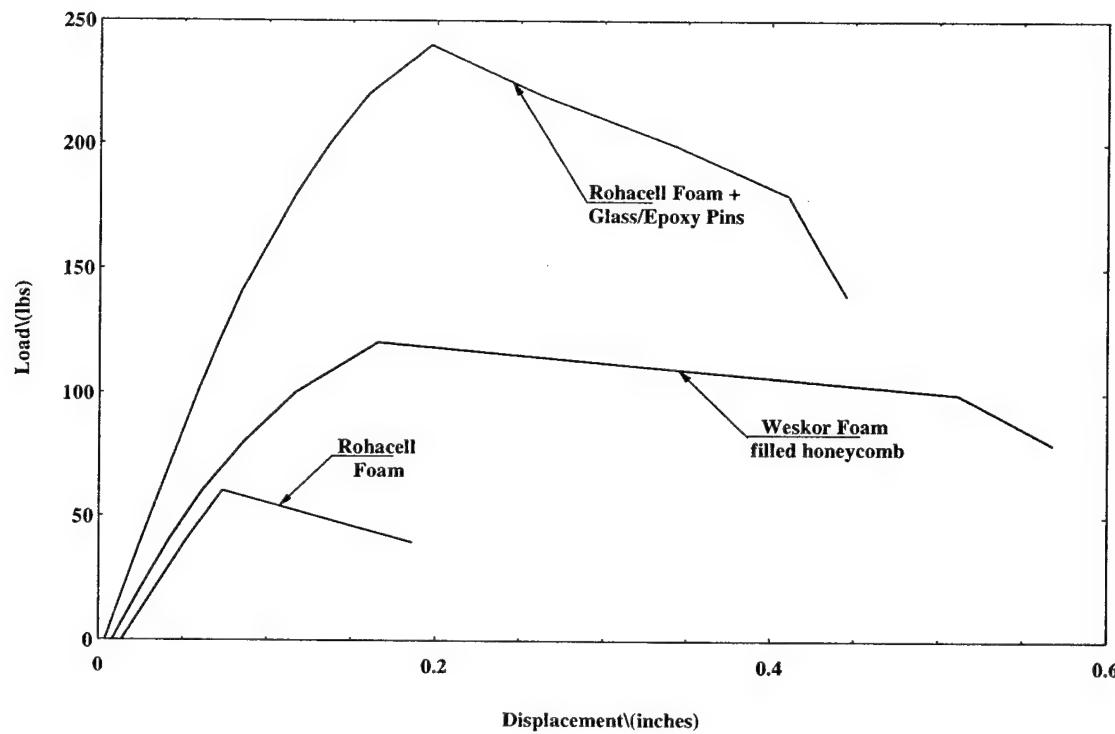


Figure 11.13 Flexural Load-Displacement Curves for Different Sandwich Composites

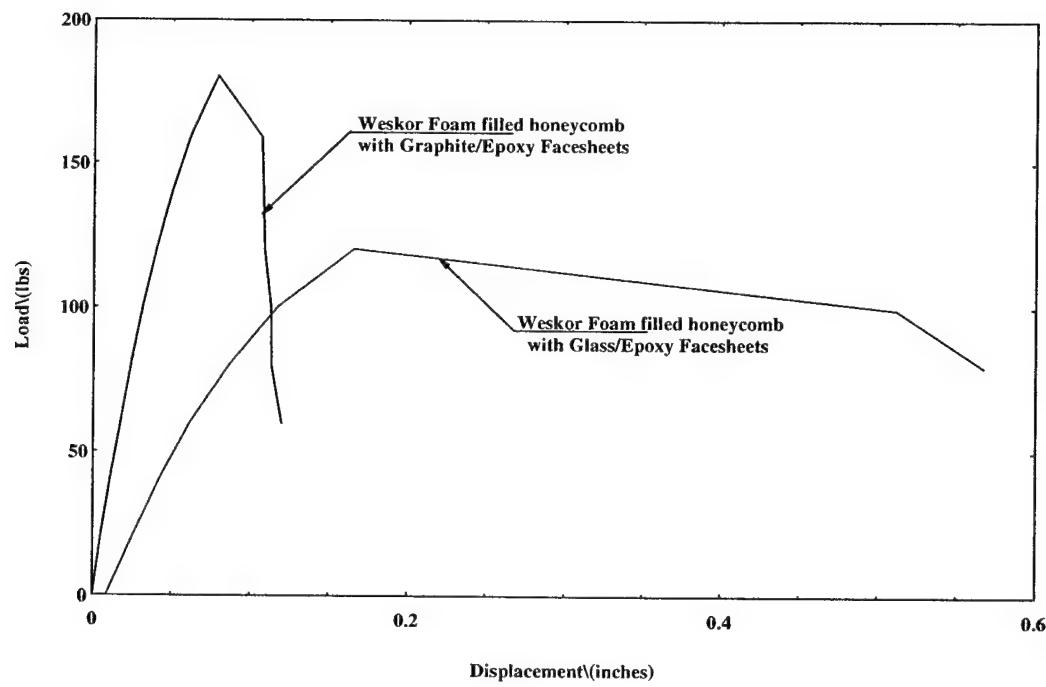


Figure 11.14 Flexural Load-Displacement Curves for WESKOR Foam filled Honeycomb Core with Glass and Graphite Facesheets

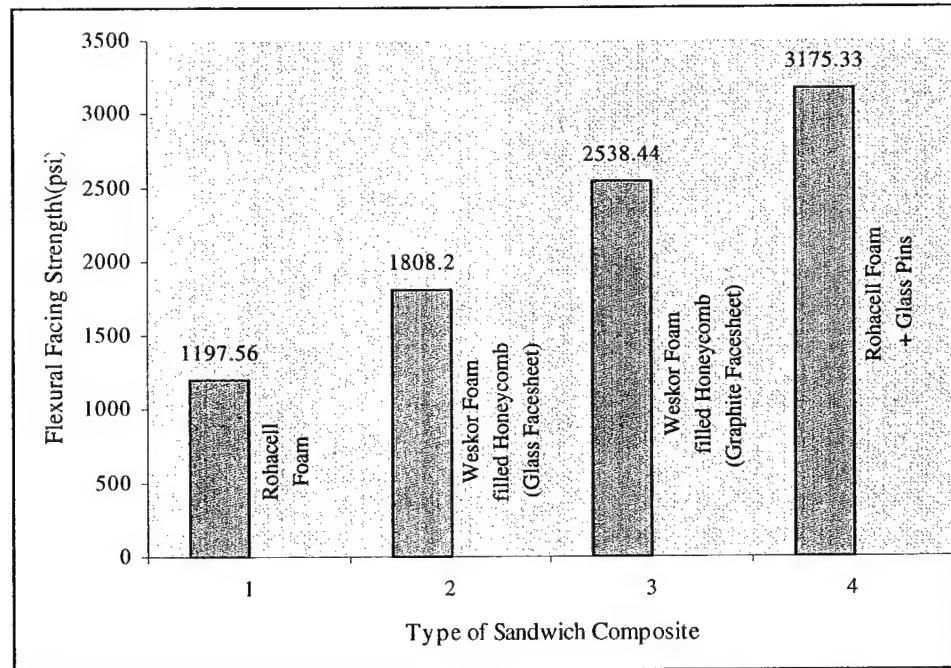


Figure 11.15 Comparison of Flexural Strength for Different Sandwich Composites

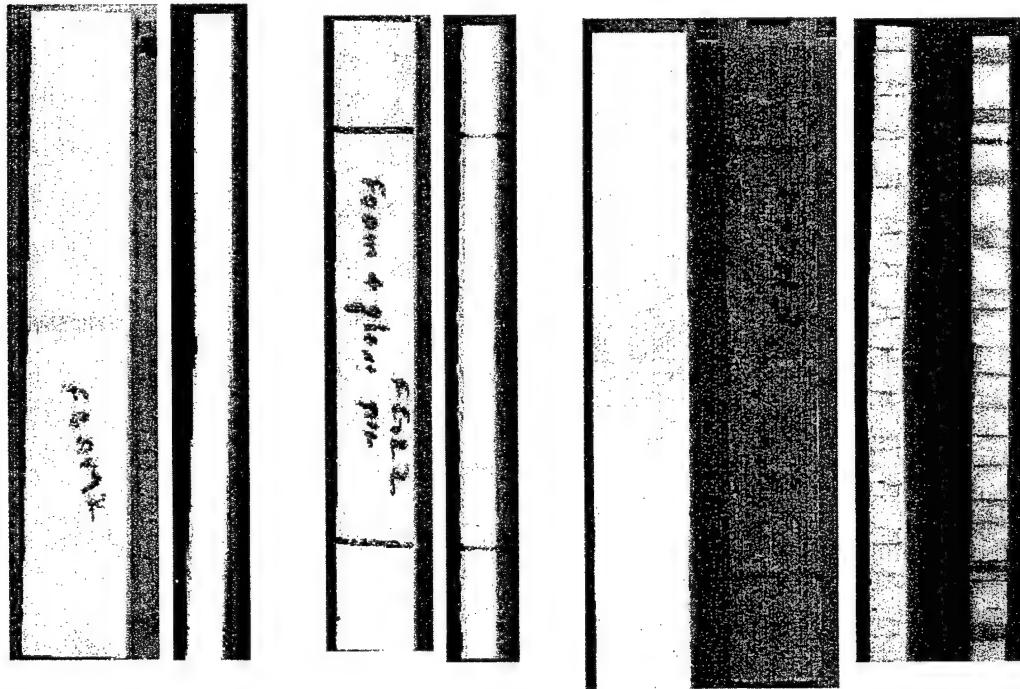


Figure 11.16 Flexural Failure Photographs for Different Sandwich Composites

Table 11.5 Flexural Strength of Various Sandwich Composites

Type	Facing Strength (Psi)	Sandwich Composite Flexural Stiffness
Rohacell Foam (Triaxial Fabric)	1197.56	223.53E3
Weskor-Foam Filled Honeycomb (Glass Facesheets)	1808.2	332.83E3
Weskor-Foam Filled Honeycomb (Graphite Facesheets)	2538.44	376.05E3
Rohacell Foam + Glass/Epoxy Pins (Biaxial Fabric)	3175.33	426.06E3

11.7 In-Plane Shear Testing

The Rohacell foam core, glass/epoxy pin reinforced Rohacell foam core, and the WESKOR foam-filled honeycomb core composites were tested for their in-plane shear response according to ASTM 273-61. For testing the in-plane shear response, samples of average dimension 9" x 2" x 0.6" were bonded to steel plates (as shown in Fig. 11.1b) using Applied Poleramic's SC-15 epoxy resin mixed with microballoons. These plates were pulled in opposing directions initiating shear in the core as per ASTM 273-61.

Figure 11.17 represents the load-displacement curves for foam and glass/epoxy pins reinforced foam core sandwich composites. It may be noted that the glass/epoxy pins reinforced foam core sandwich composite exhibits significantly higher stiffness and ~44% increase in the in-plane failure strength as compared to the unreinforced Rohacell foam core sandwich composite. This is due to the penetration of glass/epoxy pins into the pins, which provides high resistance to shearing of the core, and crushing of the foam. They also stiffen the foam in the in-plane direction, as noted by the higher in-plane shear stiffness. The progression of failure is in two steps : a) coalescence of cracks developed in the foam core in the vicinity of each pin, b) catastrophic pull-out of a system of pins from either facesheet which separates the sandwich construction as seen in Figs. 10.19a and b. This occurrence is noted as an instant load drop in the load-displacement curve. A significant amount of resistance is offered by the pins which is clearly observed on the fracture surface as severe serrations (primarily shear dominated response). On comparing the fracture surface of the pin reinforced core to the unreinforced foam core, the shearing observed on the foam was qualitatively much higher in the reinforced core.

The Rohacell foam core (unreinforced) sandwich sample exhibits lower in-plane stiffness and peak failure loads. Figures 11.18a-d represents the typical sequence of failure of foam core sandwich composite when subjected to in-plane shear. The failure was found to initiate as shear microcracks in the core, (angled cracks). The microcrack(s) propagated along the core, close to the facesheets, but not at the core/facesheet interface. The Rohacell foam core then exhibited extended shearing followed by separation of the core from the facesheet. Patches of foam remained bonded to the facesheet. The fracture surface of the bulk core was represented by several angled serrations, representative of the shear that the core underwent. However, the extent of this was lower, when compared to the pin pull-out that occurred in the reinforced core.

The shear strength of the sandwich composite is calculated using the relationship [2] :

$$f_s = P/Lb$$

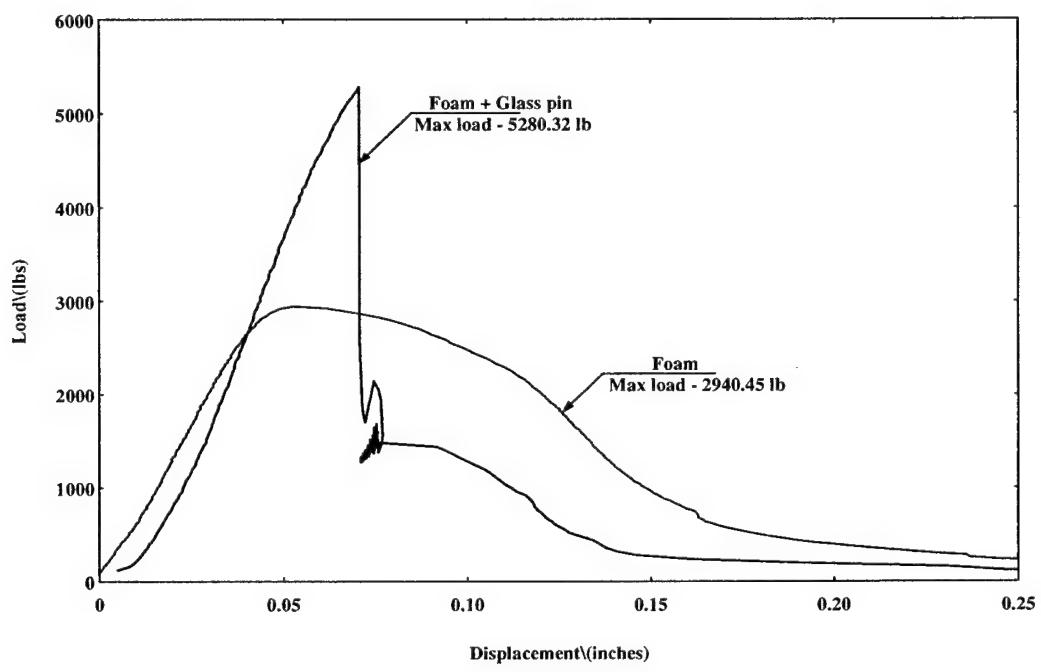


Figure 11.17 In-Plane Shear Load-Displacement Curves for Foam and Foam Reinforced with Glass/Epoxy Pins Core Sandwich Composite

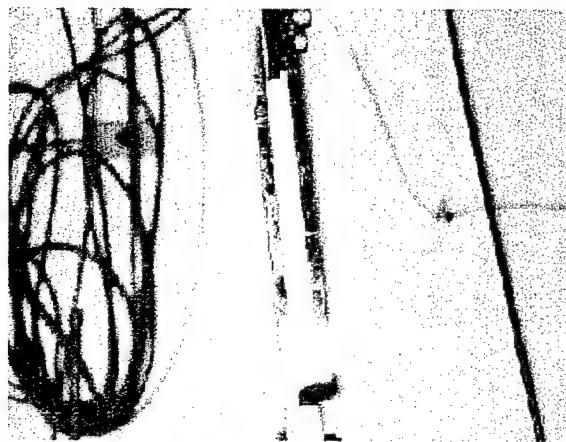


Figure 11.18a Crack Initiation at the Ends

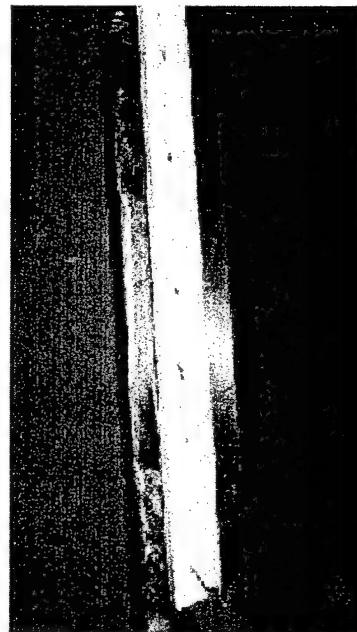


Figure 11.18b Crack Propagation along the Core

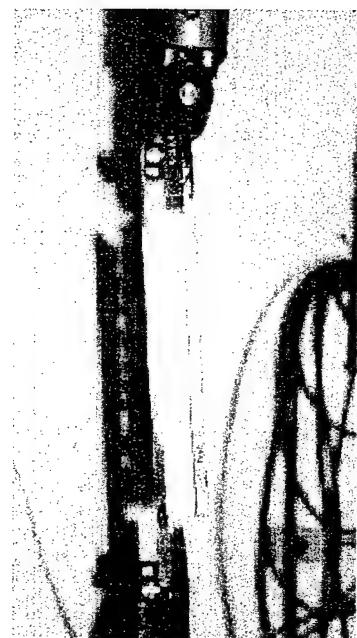


Figure 11.18c Shearing of Rohacell Foam Core



Figure 11.18d Separation of Rohacell Foam Core form the Facesheet

Figure 11.18a-d Sequence of In-plane Shear Failure of Foam Core Sandwich Composite

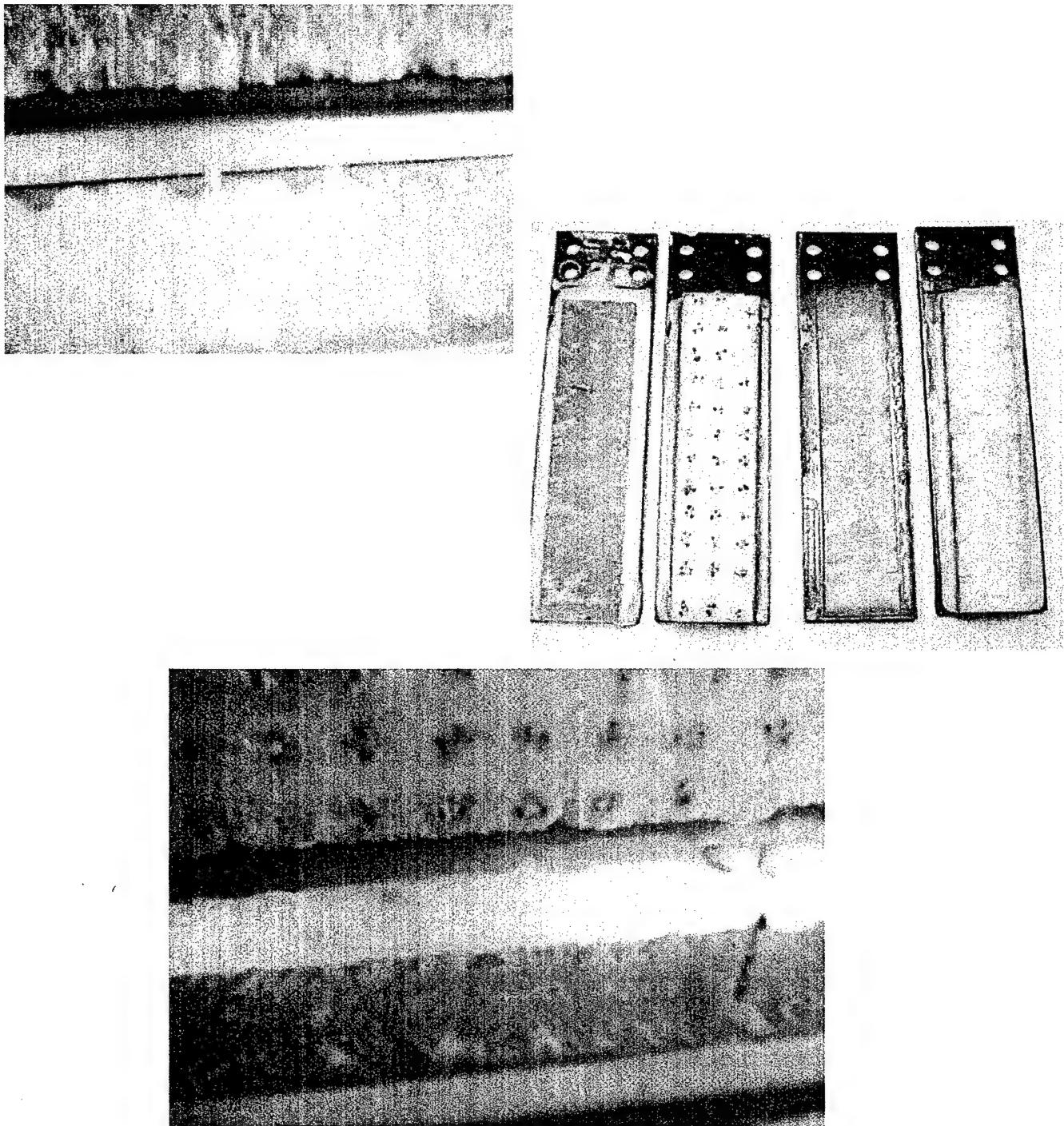


Figure 11.19. Photographs of the In-Plane Shear Failure of Foam and Foam Reinforced with Glass/Epoxy Pins Core Sandwich Composite

Where, f_s = Shear strength of the core

P = maximum load on the specimen

L = length of the specimen

b = width of the specimen

The in-plane shear strength of the foam core sandwich composite is found to be 163.35 psi and that of the foam reinforced with glass/epoxy pins is 293.35 psi.

11.7 In-Plane Shear : WESKOR Foam-Filled Honeycomb Reinforced Foam

The in-plane shear tests were also conducted on the WESKOR foam-filled honeycomb core sandwich samples. The failure was represented by a load sharing process, similar to the pin reinforced foam. In this case, the individual honeycomb cells, were torn apart, before failure proceeded to the next cell level. Figure 11.20 represents typical load-displacement curve obtained from the foam-filled honeycomb core sandwich under in-plane loading. Figure 11.21 represents the failure characteristics of the cell-to-cell in a delayed fashion. Several serrations may be observed on the core surface which represent the pulling apart of the individual honeycomb cells. A maximum load of 3168 lbs and in-plane shear strength of 176psi was attained by these samples. *In general terms, a cheaper WESKOR foam-filled honeycomb reinforced foam provided ~8% improvement in the in-plane shear strength over a more expensive unreinforced Rohacell foam core.*

11.8 Static Compression Testing

A 22 kips MTS was utilized to load the cores and their sandwich composites under transverse static compression. The samples were subjected to a rate of loading of 0.05"/minute under displacement control mode.

11.8.1 *Through-the-Thickness Compression Response of Core Materials*

Figure 11.22 represents the load-displacement curves for graphite honeycomb, Rohacell foam, Rohacell foam reinforced with titanium pins and Rohacell cell foam reinforced with glass/epoxy pin core (core alone - without facesheets) samples of average dimensions 2" x 2" x 0.5". The direction of loading was through-the-thickness of the core material.

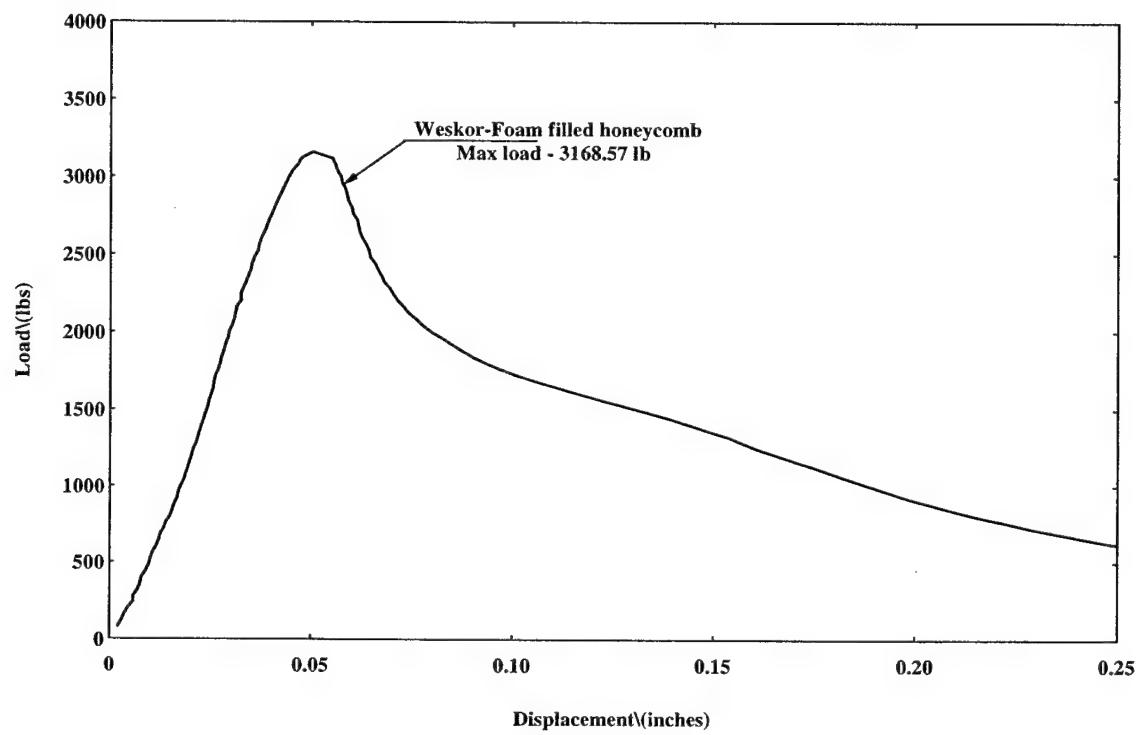


Figure 11.20. In-plane Shear Load-Displacement Curves for WESKOR Foam Filled Honeycomb Core Sandwich Composite

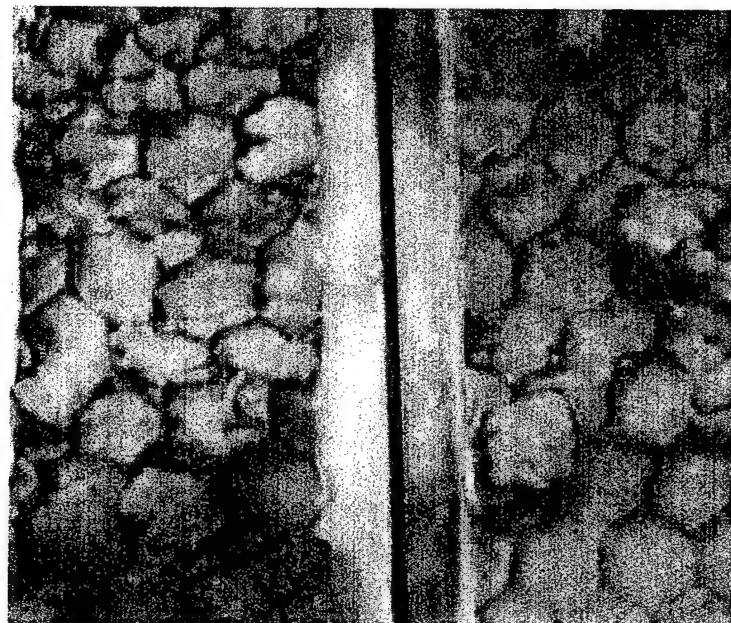
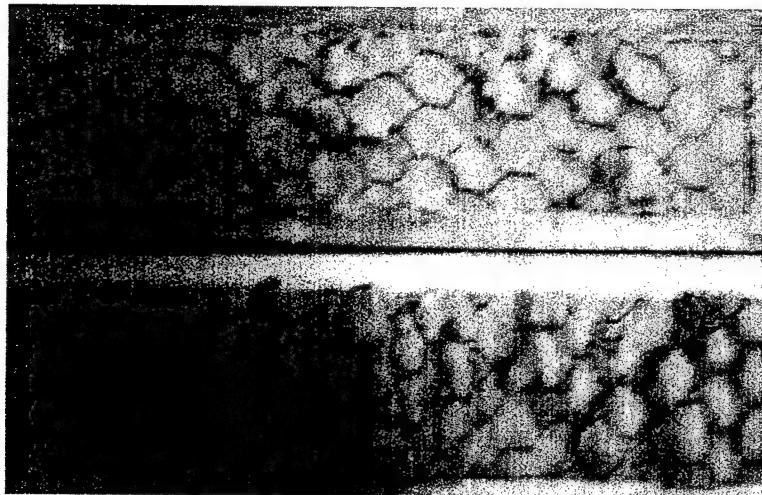


Figure 11.21. Photographs of the In-Plane Shear Failure of WESKOR Foam Filled Honeycomb Core Sandwich Composite

The graphite honeycomb core exhibits the highest transverse stiffness. On reaching peak loads, the core exhibits buckling instability and sudden load drop. Figures 11.23a and 11.23b show the cracking of the honeycomb cells catastrophically at the instance of the load drop. Figure 11.23b represents splitting of the cell wall.

The unreinforced Rohacell foam core exhibits the lowest stiffness. The curve is non-linear and the slight increase in stiffness corresponds to the closing of the foam cells and shear cracking of the core. The curve reaches a plateau when all the cells are closed.

The foam core, with titanium pin and glass/epoxy pin reinforced cores, exhibits initial non-linearity that is similar to pure foam, with increase in load, the stiffness increases, although slightly lower than the honeycomb. There is a stage at which the displacement increases without much increase in load for glass/epoxy pin reinforced foam cores. This is due to the failure at the ends of the pin due to bending and crushing, as the ends of glass pins were machined to a sharp point, to enable easier insertion into the foam. Further, there is a load increase as the pin start bearing the load. In the case of titanium pins, the ends were blunt and due to this reason it can be seen that there is a continuous increase in the load as the pins start bearing the load after the initial stage of core crushing.

11.8.2 *Through-the-Thickness Compression Response of Sandwich Composites*

Figure 11.24 compares the load-displacement curves for the sandwich composites made of hollow steel pin truss core, graphite honeycomb core, titanium pin reinforced Rohacell core, unreinforced Rohacell foam core and glass/epoxy pin reinforced Rohacell foam core with average dimensions 1" x 1 " X 0.75". In general, the core material was found to dominate the stiffness of the sandwich panel. Consistent with the core tests, the glass/epoxy pin reinforced and graphite honeycomb core sandwich composite exhibited high transverse stiffness, while the lowest stiffness was exhibited by the Rohacell foam core sandwich composite. The foam core reinforced with titanium pins sandwich composite exhibited intermediate stiffness values to the foam and the graphite honeycomb core. The failure characteristics were core dominated, and were identical to those observed in the core tests. No damage was evident in the facesheets.

The highest load was carried by the glass/epoxy pin reinforced sample. The drops in the load near the peak load are due to the separation of the pin, which was close to the edge of the sample. The graphite honeycomb core

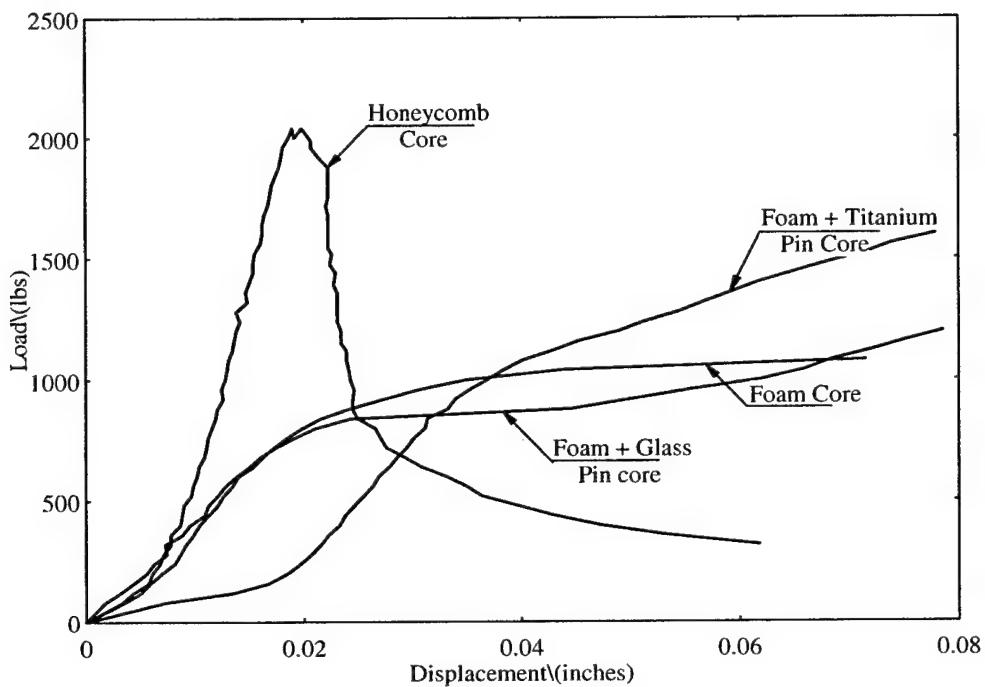


Figure 11.22. Through Thickness Compression Load-Displacement Plot for Different Cores



Figure 11.23a-b. Edge View and Top View of Honeycomb Core Cells Failed Under Static Compression

samples fail by collective cell wall buckling of the honeycomb cells at peak load. The unreinforced Rohacell foam core failed by core crushing following cell compression failure. The foam core continues to take the load through uniform crushing of the foam cells till the facesheet almost comes together. The titanium pin reinforced foam core samples exhibited buckling of the titanium pins, and interfacial debonding between the foam core and the pins.

The hollow steel pin truss core sandwich composite exhibited a transverse stiffness that matched the graphite honeycomb core. Figure 11.25 shows the failure of the hollow truss core sandwich composites as being entirely simultaneous buckling of the steel pins normal to the direction of loading. The buckling pattern is primarily by symmetric failure of the pins. After the peak load is reached all the pins start buckling simultaneously as can be seen from the receding portion of the plot.

11.8.3 Effect of Geometry and Facesheets

A few tests were conducted to investigate the failure loads with increase in surface area of the specimen, and to understand how damage in the core evolves and progresses (with and without the facesheets). For all the samples with facesheets, the facesheet-to-core thickness ratio was 1 : 2. Figure 11.26 compares the response of the graphite honeycomb core with 1" x 1" surface (5 cells), 2" x 2" surface (20 cells) and a 1" x 1" surface honeycomb core with the facesheet. The addition of the facesheet is seen to improve the stiffness considerably, and the peak load by ~ 34%. The 2" x 2" core alone exhibits a peak load of 2000 lbs in comparison to 400 lbs for the 1" x 1" core. The failure in the 1" x 1" and 2" x 2" was through catastrophic buckling and cell wall splitting.

Figure 11.27 compares the response of Rohacell foam core alone for similar geometry. The foam core sandwich composites exhibit marginal improvement from its core response after addition of the facesheets for the 1" x 1" surface. On a core basis, the the 2" x 2" surface exhibited 1100 lbs peak load as opposed to 220 lbs for the 1" x 1" core. The failure was primarily through core crushing, when the cells eventually close and flatten the load-displacement response.

The WESKOR foam-filled honeycomb core as shown in Fig. 11.28 exhibits about 42% increase in peak loads after attaching the facesheets, and higher stiffness for the 1" x 1" surface. For the 1" x 1" surface samples, the response is largely dominated by the foam cells (lower transverse stiffness). However, from the response of the 2" x 2" core samples the transition from the pure foam response to the increase in modulus (indicating load sharing by the honeycomb cells) is well evident. The peak loads attained are 1300 lbs. The failure indicates

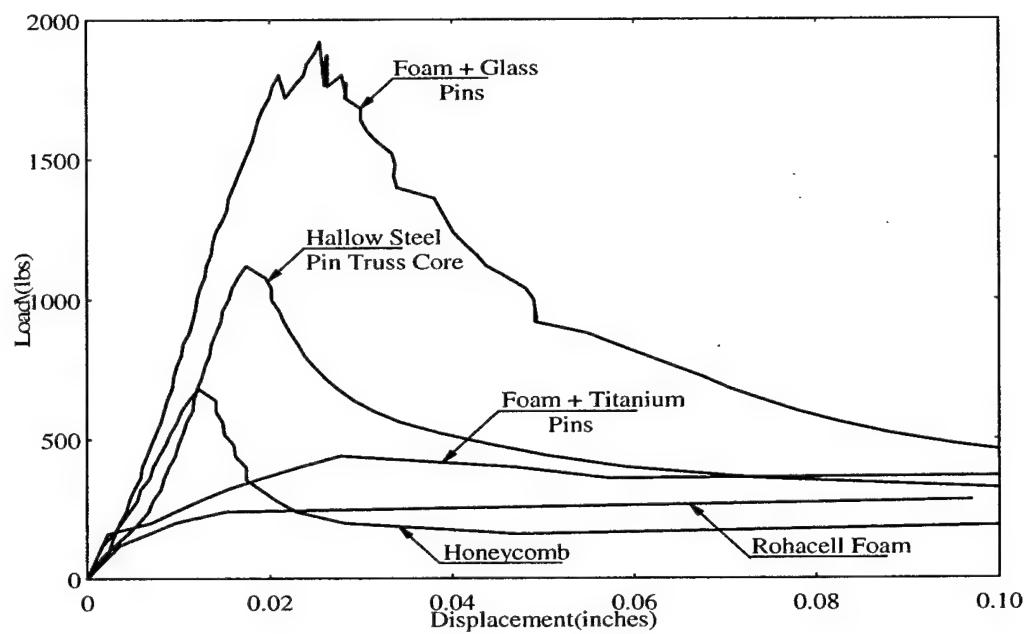


Figure 11.24. Through Thickness Compression Load-Displacement Plot for Different Sandwich Composites

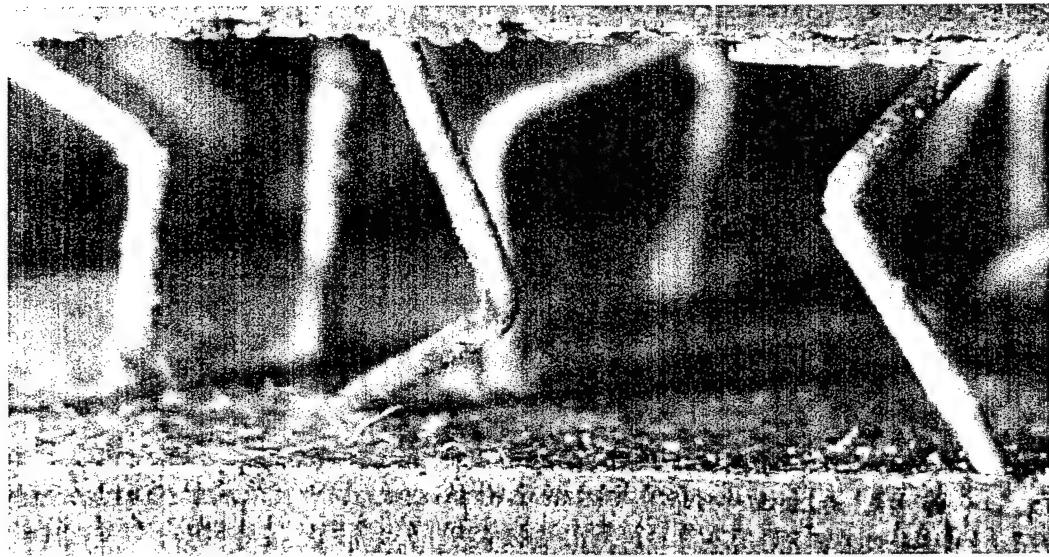


Figure 11.25. Failure of Hollow Steel Pin Truss Core Sandwich Composite

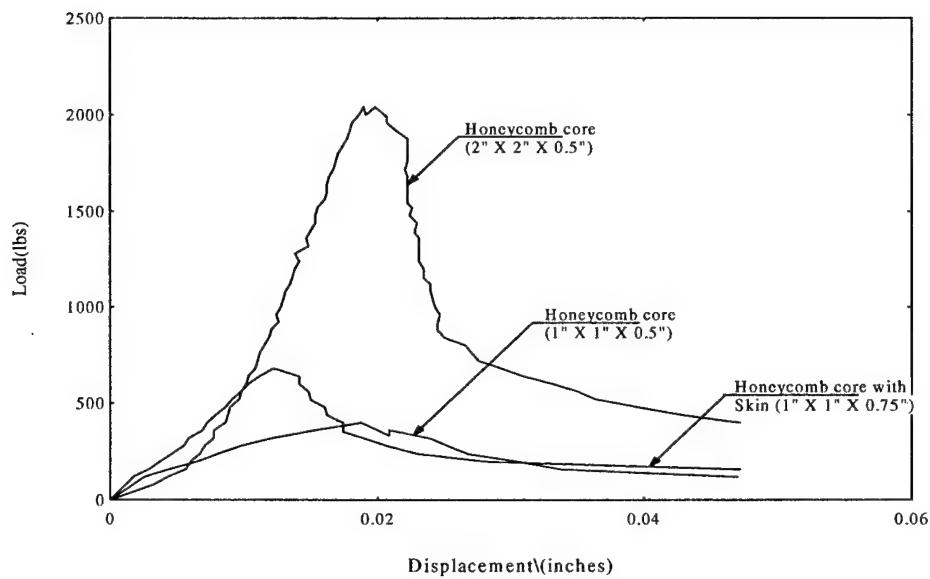


Figure 11.26. Load-Displacement Plot for Through the Thickness Compression Testing of Honeycomb Core and its Sandwich Composite

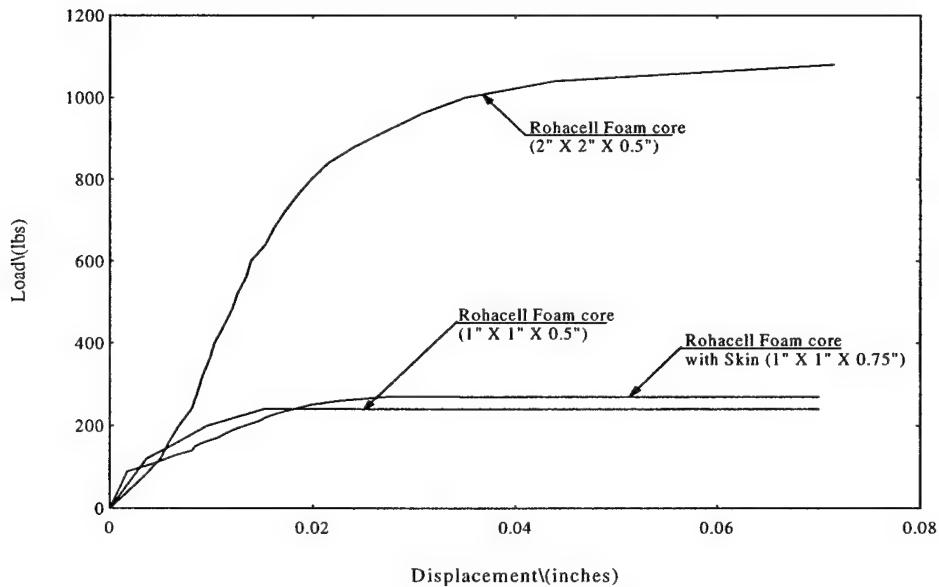


Figure 11.27. Load-Displacement Plot for Through the Thickness Compression Testing of Rohacell Foam Core and its Sandwich Composite

sequential cell wall buckling (unlike collective cell wall buckling observed in the unreinforced graphite honeycomb).

The Rohacell foam reinforced with titanium pins was only tested as a 2" x 2" core and a 1" x .1" sandwich sample due to limitation of testing a 1" x 1" titanium pin reinforced foam core. Figure 11.29 represents the response. The transverse stiffness of the Rohacell foam is considerably enhanced as noted by the initial non-linearity followed by a steep increase in the stiffness. A secondary lower modulus then develops, which corresponds to the buckling of the titanium pins within the core. However, the increased transverse stiffness obtained from reinforcing the foam with titanium pins is equivalent to that obtained from an unreinforced graphite honeycomb core.

11.8.4 Influence of Cell Spacing

For the WESKOR honeycomb filled foam samples, the effect of changing cell wall spacing was studied by considering two cell spacings: 0.24 in. and 0.4 in. respectively as illustrated in Fig. 11.30. The initial loading is seen to be foam dependent, as the stiffness is identical. The 0.24 in. spaced foam-filled honeycomb sample withstood ~11% higher peak loads in comparison to the 0.4 in. spaced foam-filled honeycomb sample. This suggests that the closer spacing of the honeycomb cells offers enhanced transverse stability and strength to the foam core. The secondary stiffness of the 0.4 in. spaced core is found to be marginally higher (however comparable) to that of the 0.24 in. spaced cores, indicating that in that regime the honeycomb response is more dominant.

11.9 In-Plane Compression Response

11.9.1 Studies on Core (Without Facesheets)

The in-plane response of the composites and their cores (wherever possible) was studied. The WESKOR foam-filled honeycomb core exhibited buckling of the cell walls, with the exception that the cell walls are supported laterally by the foam as shown in Fig. 11.31. The in-plane response of the titanium reinforced Rohacell foam core and the WESKOR foam-filled honeycomb core were also evaluated. The titanium pin reinforced Rohacell foam exhibits higher in-plane stiffness (Fig. 11.32) and higher peak loads than the WESKOR foam-filled honeycomb core foam cores (Fig. 11.33). This is thought to be due to the inability of the honeycomb cells to support in-plane loading, while the pins have a localized stiffening effect between the cells.

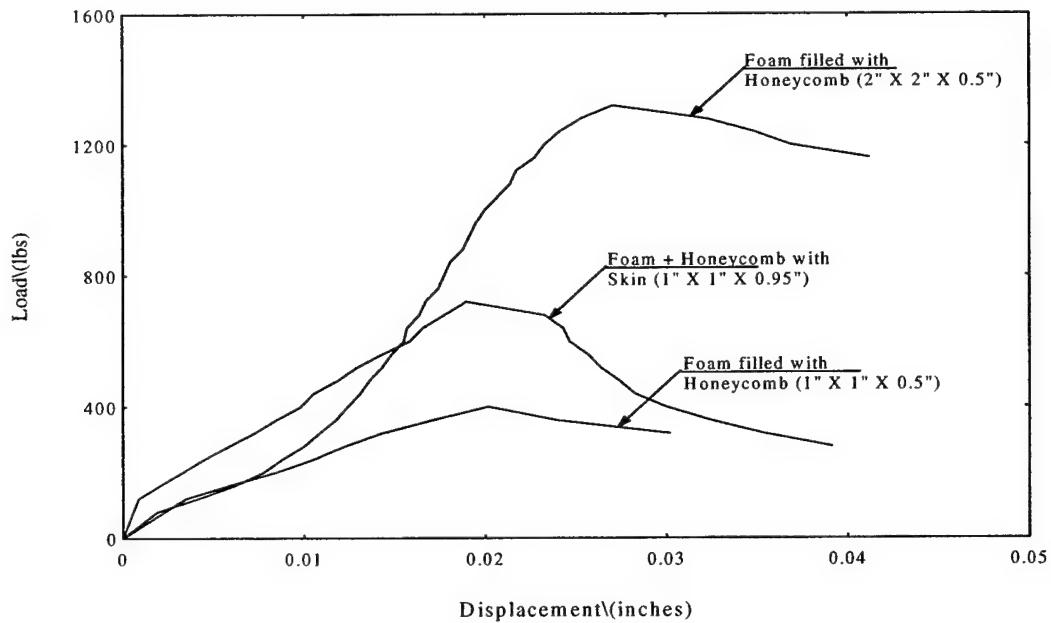


Figure 11.28. Load-Displacement Plot for Through the Thickness Compression Testing of WESKOR Foam Filled Honeycomb Core and its Sandwich Composite

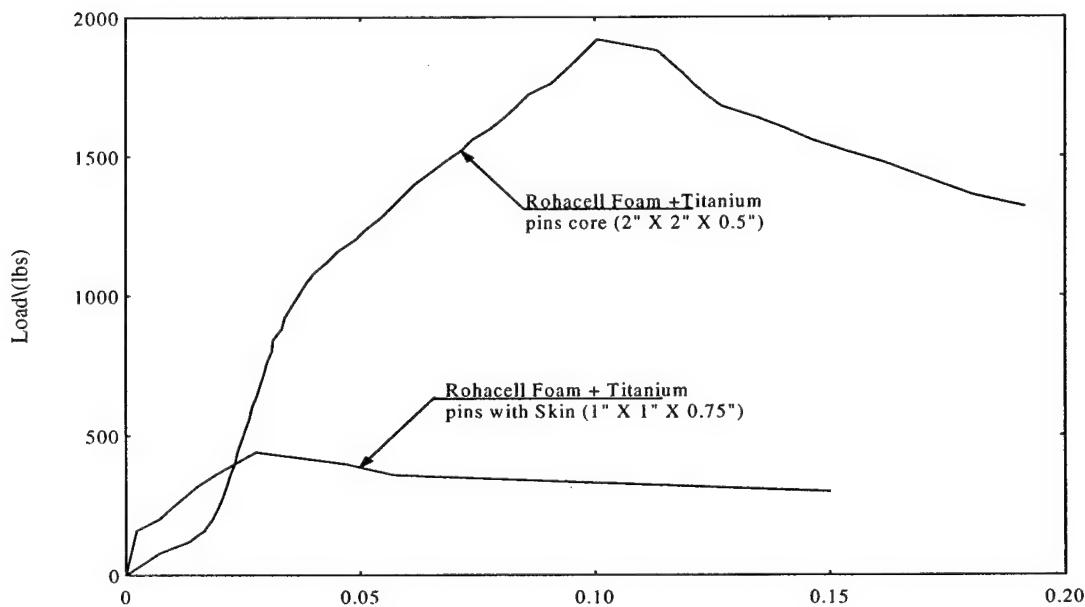


Figure 11.29. Load-Displacement Plot for Through the Thickness Compression Testing of Rohacell Foam Reinforced with Titanium Pin Core and its Sandwich Composite

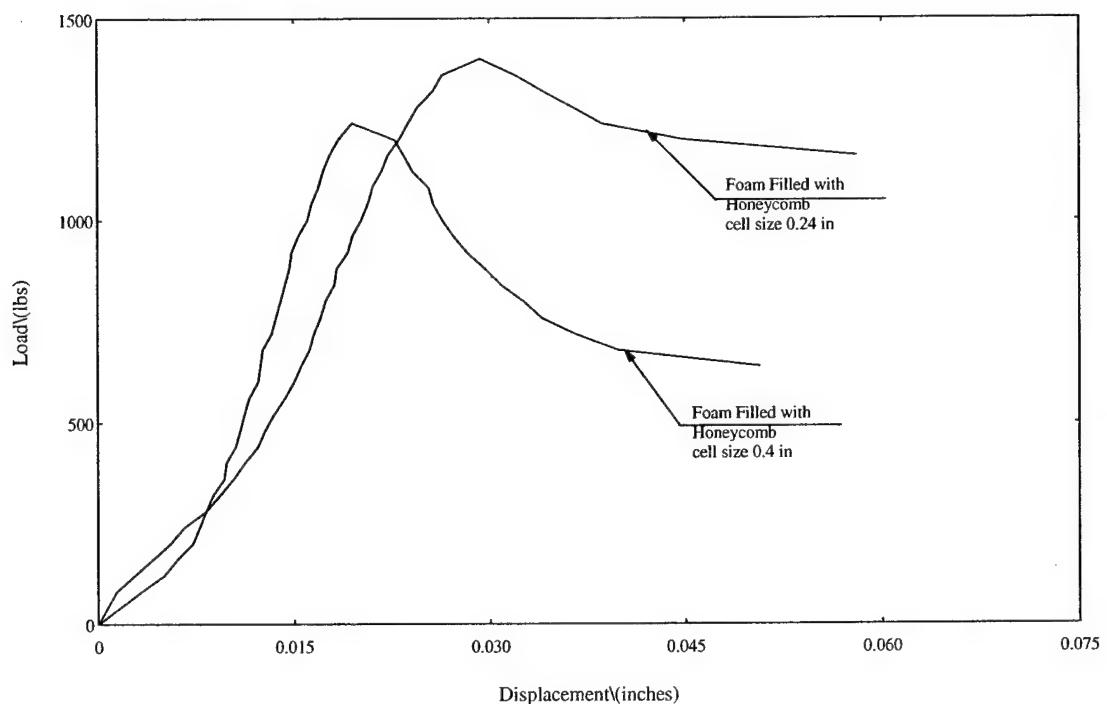


Figure 11.30. Load-Displacement Plot for Through the Thickness Compression Testing of Weskor Foam Filled Honeycomb Core With Different cell Spacing

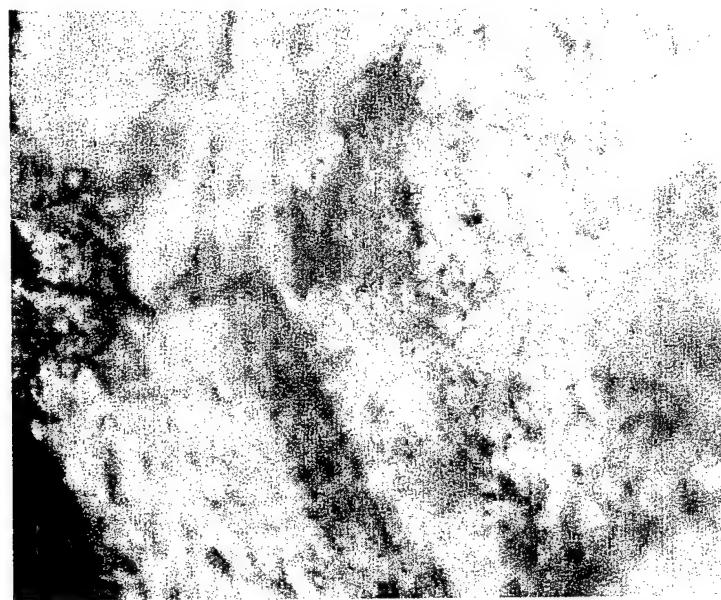


Figure 11.31. Failure Photograph of WESKOR Foam Filled Honeycomb Core under In-Plane Compression Loading

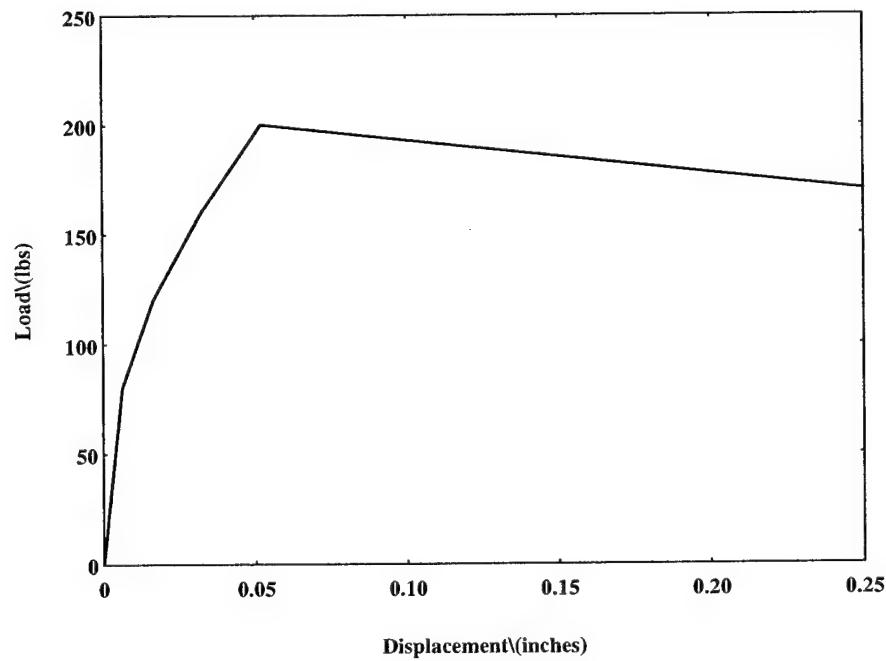


Figure 11.32. Load-Displacement Curve for Rohacell Foam Reinforced with Titanium Pin Core Under In-Plane Compression Loading

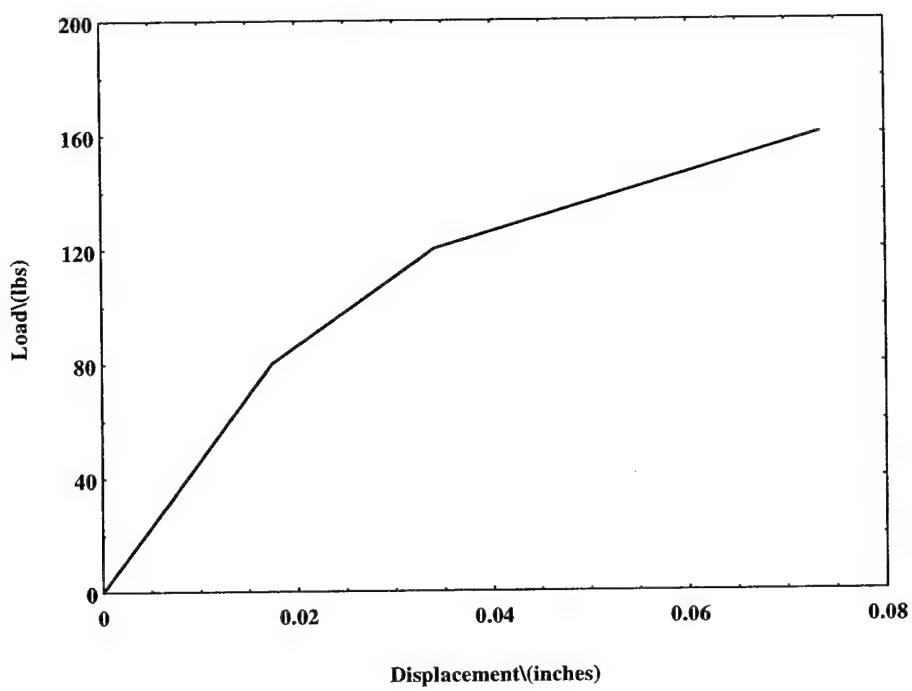


Figure 11.33. Load-Displacement Curve for WESKOR Foam Filled Honeycomb Core Under In-Plane Compression Loading

11.9.2 Studies on Sandwich Composites

Figure 11.34 shows the in-plane loading of the graphite honeycomb core sandwich (as pure honeycomb core did not sustain in-plane loading). The sandwich sample exhibited initial non-linearity (during initial loading), and exhibited linear response followed by buckling instability of the facesheets. The peak load attained was ~12000 lbs. The facesheets failed by extensive and sudden delamination as shown in Fig. 11.35. The sandwich composite of the foam reinforced honeycomb (Fig. 11.37) is also seen to follow similar trends as the honeycomb sandwich composite, the final failure is observed to be due to buckling instability of the facesheets. The in-plane compressive stiffness and peak loads attained were comparable to the honeycomb core sandwich composite (~12000 lbs) as well. The final failure is dominated by the failure of the facesheets due to buckling instability. The titanium pins reinforced foam core sandwich composites exhibit higher peak loads than the honeycomb filled foam core sandwich composite. These tests verified that the reinforcement of pins with the foam (Fig 11.36) did not reduce the in-plane stiffness / strength of the sandwich, being facesheet dominated. The pins assisted in a delayed damage, as the facesheet failure was resisted by pins piercing into the facesheets. In a honeycomb core, failure was catastrophic.

11.10 Summary/Conclusions

Flexural Loading :

The stiff glass/epoxy pins in the pin reinforced core, and the honeycomb cell walls in the WESKOR foam, provide attractive benefits in terms of improved flexural stiffness, higher peak loads, and thereby larger damage resistance to flexural loading at a nominal weight penalty.

In-Plane Shear Loading

A cheaper WESKOR foam-filled honeycomb reinforced foam provided ~8% improvement in the in-plane shear strength over a more expensive unreinforced Rohacell foam core. The glass/epoxy pin reinforced Roahcell foam core provided ~44% improvement in in-plane shear strength and an attractive failure arresting mechanism as compared to unreinforced Rohacell foam core composites.

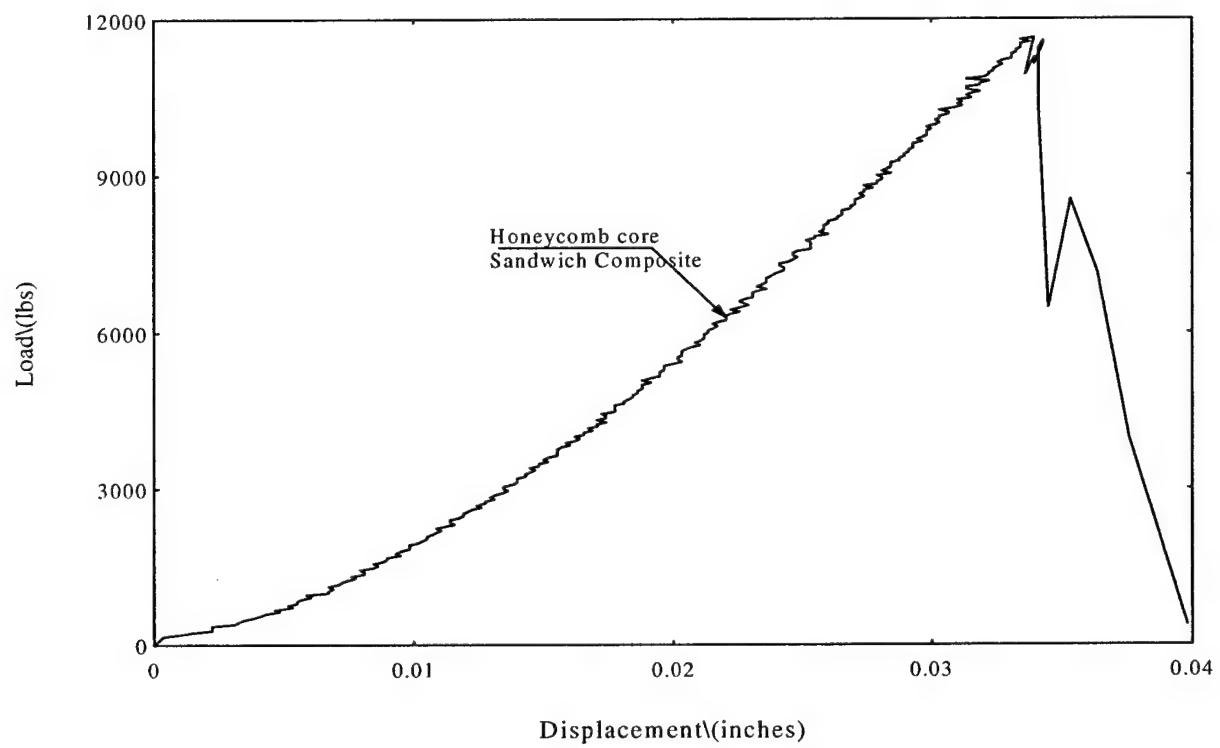


Figure 11.34. In-Plane Compression Load-Displacement Curve for Honeycomb Core Sandwich Composite

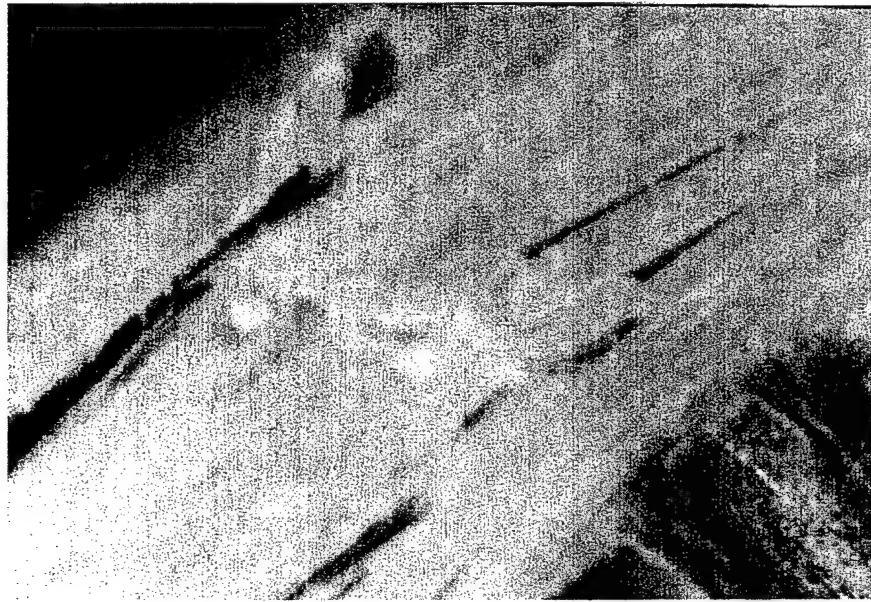


Figure 11.35. In-Plane Compression Failure Photograph of Honeycomb Core Sandwich Composite

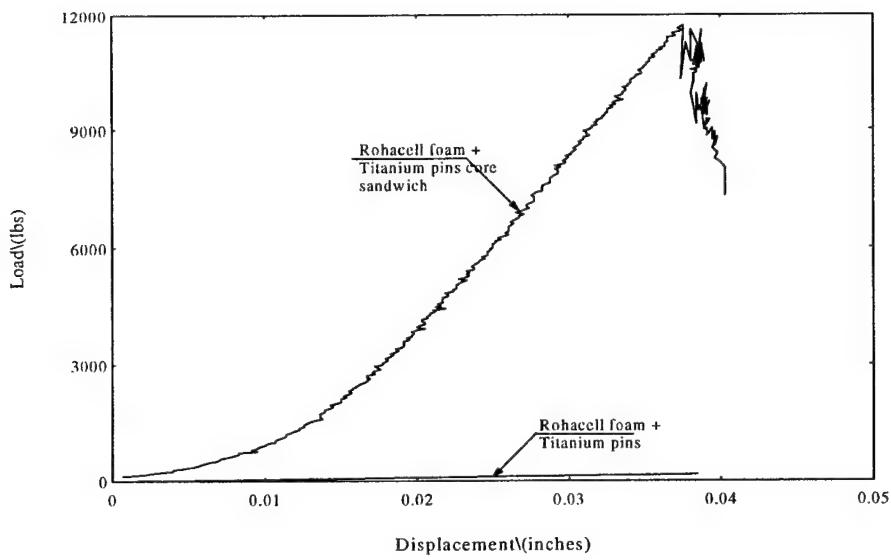


Figure 11.36. In-Plane Compression Load-Displacement Curve for Rohacell Foam Reinforced with Titanium Pin Core and its Sandwich Composite

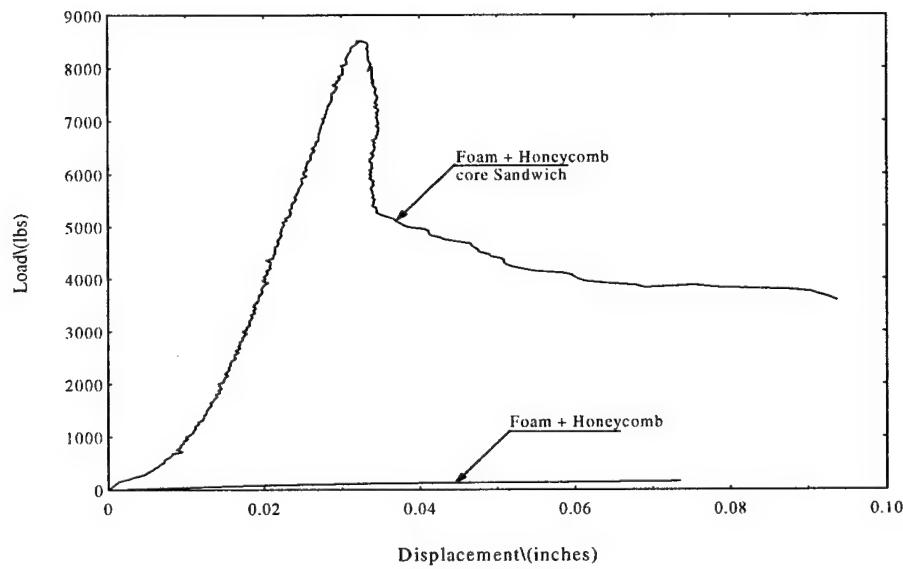


Figure 11.37. In-Plane Compression Load-Displacement Curve for WESKOR Foam Filled Honeycomb Core and its Sandwich Composite

Transverse Compression

Reinforcing the Rohacell foam core with titanium and/or glass/epoxy pins or the using the WESKOR foam-filled honeycomb has the same stiffness benefits as conventional graphite honeycomb core composites, which suffer from catastrophic buckling instability of the honeycomb cells. Furthermore, the reinforced core exhibit a load sharing process which results in a delayed fracture path.

Some additional observations are that the core behavior is reflected in the response of their respective sandwich composites. A steel pin core was found to yield comparative stiffness as that of the honeycomb core composites

- Primary mode of failures may be summarized as follows:
 - ⇒ Buckling of pins in the hollow truss core pin reinforced samples
 - ⇒ Cracking and buckling of the honeycomb cell walls in the pure honeycomb samples
 - ⇒ Core crushing and closing followed by shearing in the case of the unreinforced Rohacell foam
 - ⇒ Buckling and interfacial debonding between the cell walls and the core in the case of the WESKOR foam-filled honeycomb core samples

11.11 References

1. ASTM C393-62, "Standard Test Method for Flexural Properties of Flat Sandwich Constructions", pp 22-24, 1988.
2. ASTM C273-61, "Standard Test Method for Shear Properties in Flatwise Plane of Flat Sandwich Constructions or Sandwich Cores", pp 5-7, 1988.

12.0 High Strain Rate Testing of Sandwich Composites

12.1 Introduction

It is well established that to a greater or lesser extent, most non-metallic composite materials show a significant change in mechanical response under increased rates of straining. An adequate understanding of the rate-dependence of the mechanical properties is required, particularly so for laminated and sandwich composites. Although some literature is available pertaining to high strain rate impact response of laminated composites, such information for sandwich composites is almost lacking. For sandwich composites, there is a complex interaction between the reinforcing fibers and matrix within the facesheets, the interface between the core and facesheet, and within the bulk core material. There exists significant localized strains in the matrix and the fibers, and the core which can affect failure at high strain rates. In the current work, we have considered strain rates ranging from 163/second to 653/second for studying the evolution and progression of damage and in a broad sense, to compare the LVI and static response to high strain rate response.

12.2 Experimentation

For HSR impact testing, a compression Split Hopkinson Pressure Bar (SHPB), as shown in Figs. 12.1a and 12.1b, was used. Samples of typical dimensions of $0.5'' \times 0.5'' \times$ thickness were adopted for testing on a $0.75''$ (19.05 mm) incident-transmission bar pair. The sample dimensions were so chosen to minimize the geometrical effects, and obtain uniform state of strain over the entire sample. Samples were subjected to loading in the through-the-thickness direction at strain rates of 163, 217, 326, 544 and 653 per second respectively. These strain rates were chosen to represent early stages of failure all the way to extended fracture. As pointed out by Nemat-Nasser et.al [1], in a classical Hopkinson bar technique, if the sample does not fail during the passage of the first stress pulse, then it is loaded repeatedly by pulses which reflect off the free ends of the bars. It does not easily allow the recovery of the specimen at various levels of loading for microscopic and related analysis which is necessary for understanding the microstructural evolution associated with loading histories. The problem is further compounded in a sandwich composite, where the core is much softer compared to the facesheets. In this study the experimental setup suggested by Nemat-Nasser et. al [1] was used to achieve dynamic recovery experiments (Fig. 12.2a and 12.2b). This involves imparting a single travelling toward the sample. Furthermore, all subsequent pulses which reflect off the free ends of the two bars (incident and transmission) are rendered tensile, so that the sample is subjected to a single compressive pulse whose shape and duration can also be controlled. This is achieved by incorporating a momentum trap mounted on the incident bar, such that upon reflection from the specimen-incident bar interface, the stress wave is rendered tensile, and the specimen is not subjected to

Table 12.1 Sandwich Composites Subjected to HSR Impact and Their Geometry

Samples Tested	1.5" bar	0.75" Bar	
		With MTG	Without MTG
Foam	0.7"x0.75"x0.75"	0.5"x0.55"x0.75"	0.5"x0.55"x0.75"
Honeycomb	0.75"x0.75"x0.75"	0.55"x0.55"x0.75"	0.55"x0.55"x0.75"
Foam +Titanium Pins	0.75"x0.75"x0.75"	0.55"x0.55"x0.75"	0.55"x0.55"x0.75"
Foam +Glass Pins	0.75"x0.75"x0.75"	0.55"x0.55"x0.75"	0.55"x0.55"x0.75"
Hollow Steel Pin Truss	0.8"x0.8"x0.55"	0.5"x0.5"x0.55"	0.5"x0.5"x0.55"
Foam +Honeycomb	0.75"x0.75"x0.95"	0.55"x0.55"x0.95"	0.55"x0.55"x0.95"
Nomex Honeycomb Core with Hybrid facesheets		0.5"x0.5"x0.55"	0.5"x0.5"x0.55"

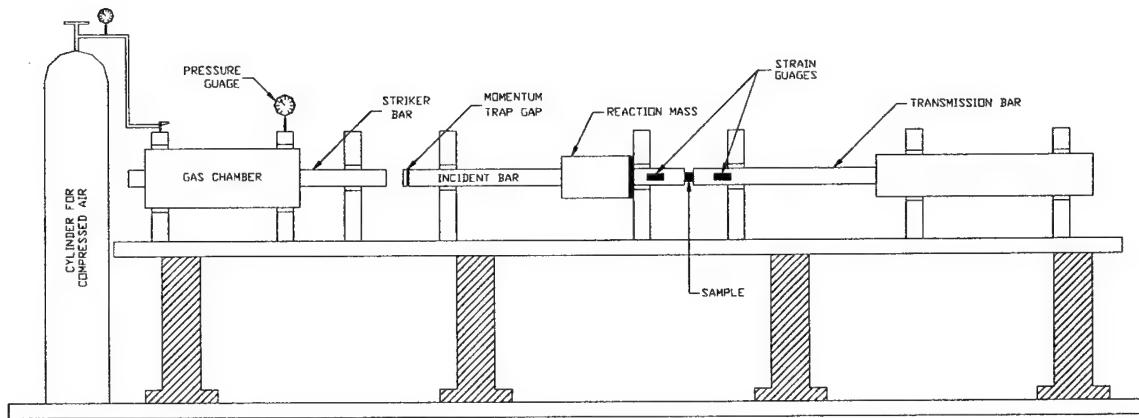


Figure 12.1a. Schematic of Split Hopkinson Pressure Bar

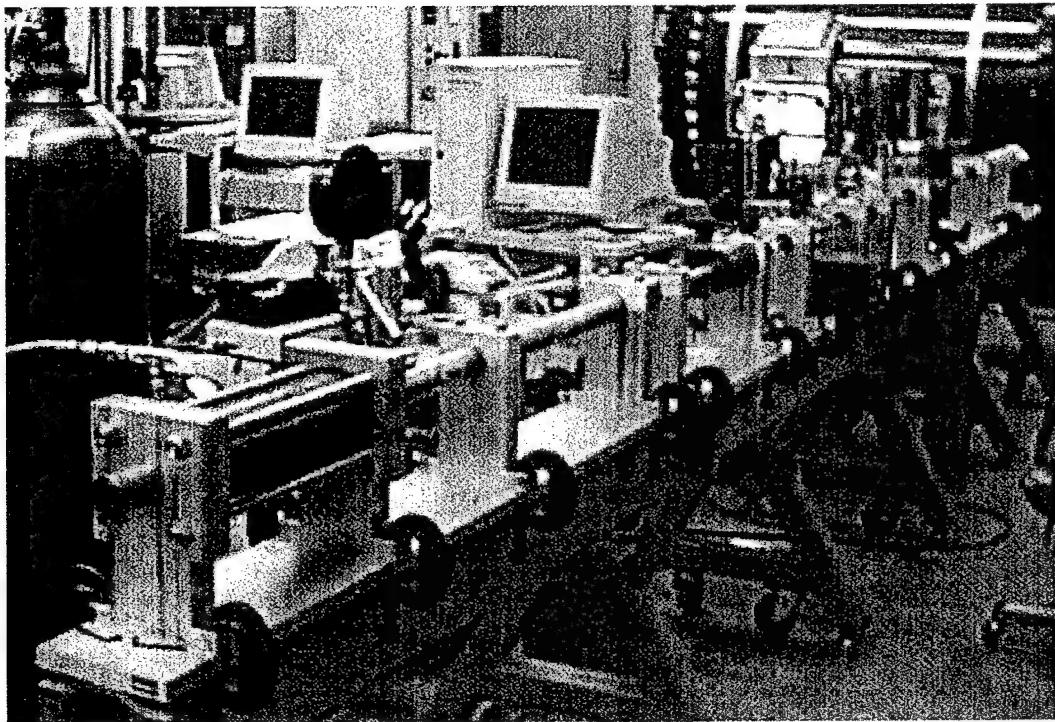


Figure 12.1b. Split Hopkinson Pressure Bar

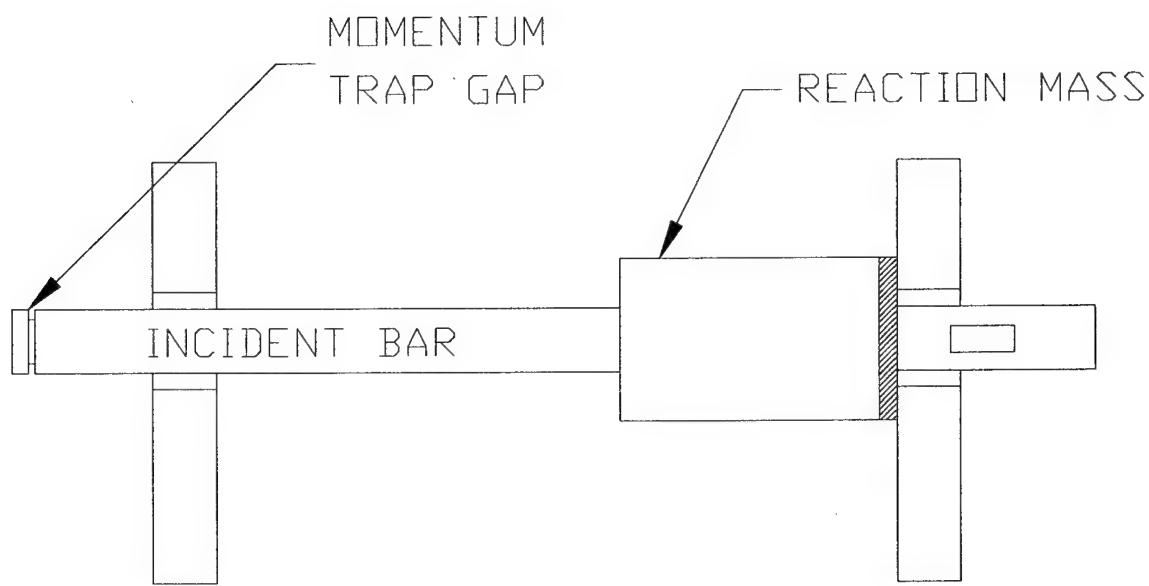


Figure 12.2a. Schematic of Momentum Trap Setup

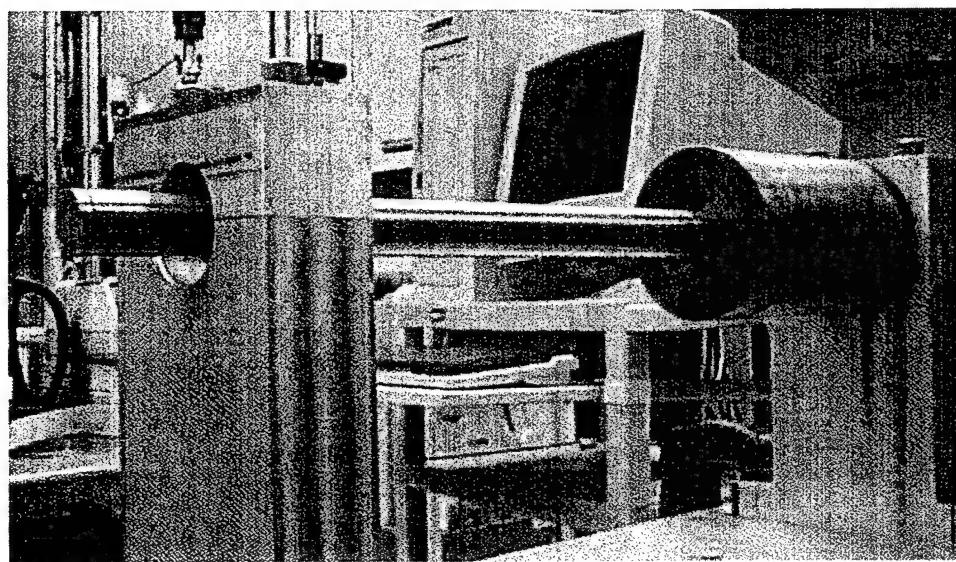


Figure 12.2b. Momentum Trap (Dynamic Recovery Technique)

repeated stress pulse loading. Strain gages are mounted on the incident and transmission bars. The output of the strain gages is obtained as voltage vs time graph. The strain vs time is measured on the incident bar and stress vs time is measured on the transmission bar.

The signals obtained on the transmission bar in case of the sandwich composites were characteristically weak in magnitude, as expected. This is because during passage of the stress pulse through the soft / sometimes discontinuous sandwich core, it undergoes scattering, dispersion and reflection. The signal obtained on the transmission bar is then subjected to filtering techniques, which then is reduced to stress vs strain curves for different strain rates. Typical stress-time and strain-time pulses and the resulting stress-strain curves are illustrated in Fig. 12.3a-c. In the current study the dynamic recovery technique [1] was adopted along with controlled pulse shaping , so that all cores would be subjected to identical impact histories.

Several tests were also conducted to compare the response of the samples, "with" and "without" the momentum trap (the recovery mechanism). The experiment involves adjusting a momentum trap gap (MTG), that in turn controls the shape of the pulse the specimen is subjected to. An illustration of pulse shaping is provided in Fig. 12.4. When the striker bar impacts the transfer flange at some velocity, it imparts a common axial strain to the incident tube and incident bar [1]. The compression pulse in the incident bar travels along this bar toward the specimen. The compression pulse in the incident tube reflects from the reaction mass as compression, and reaches the transfer flange at the same instant that the tension release pulse which is reflected from the free end of the striker, reaches the end in contact with the transfer flange. Since the combined cross section of the incident bar and tube is twice that of the striker bar, having the same material properties, the striker bar begins to bounce back, away from the transfer flange, as the transfer flange is loaded by the compression pulse travelling along the incident tube. This compression pulse then imparts a tensile pulse to the incident bar, which follows the then existing compression, both travelling toward the sample. In the current work, the MTG was maintained constant, to ensure that the various experiments would be comparable. The testing was performed by sandwiching the sandwich core sample between the incident and transmission bar. A 9" striker bar was used to conduct all the tests in the current work.

12.3 Comparison of HSR of Sandwich Composites with Different Cores

Typical stress-strain plot for the different sandwich core materials used in the study are plotted as shown in Figs. 12.5-12.9. Figure 12.5a shows the stress-strain plot for foam core sandwich panel. It can be see that the peak load increases with increase in the strain rate [7]. There are multiple oscillations (loading / unloading) in the stress-



Figure 12.3a. Voltage vs Time Signal for Incident Bar (Strain)

Figure 12.3b. Voltage vs Time Signal for Transmission Bar (Stress)

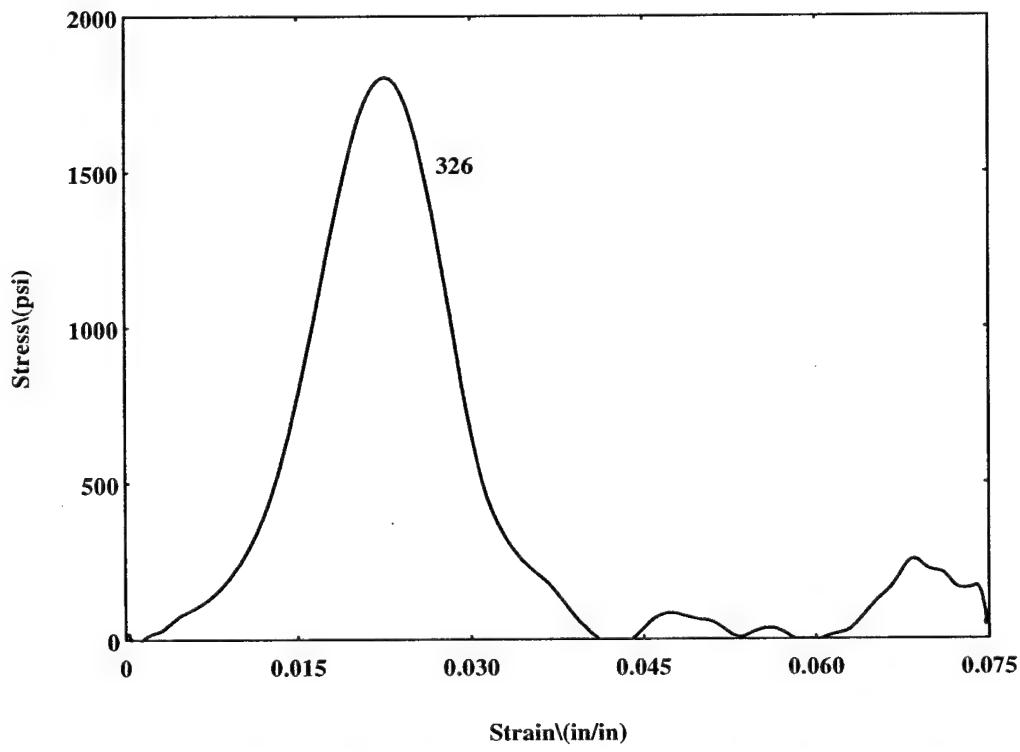
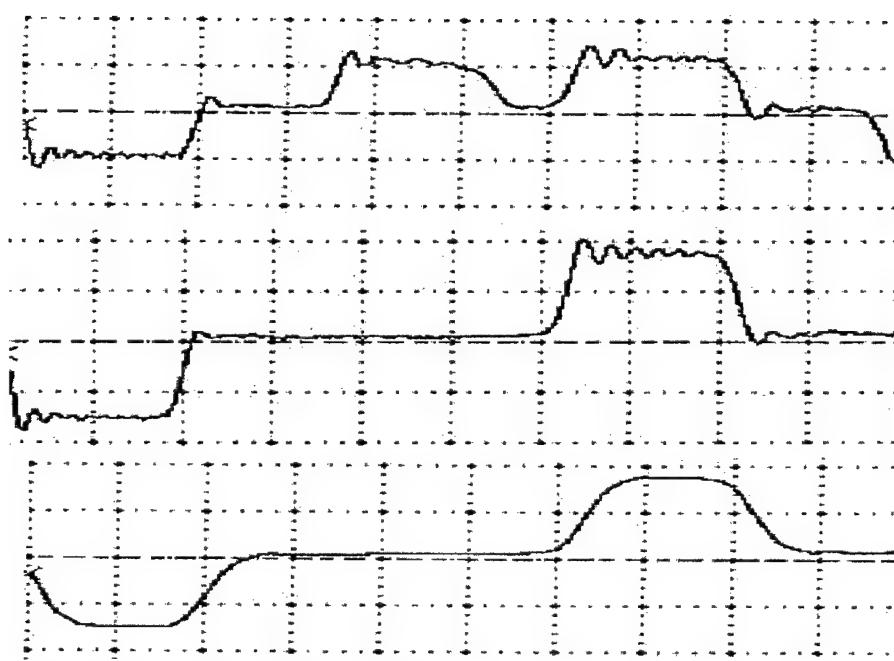


Figure 12.3c. Stress-Strain Curve Obtained from the Above Signal
(Honeycomb Core Sandwich Composite)



Scale: X-Axis: 1 Div = 50 μ sec
Y Axis 1 Div = 200 mV

Figure 12.4. Voltage Vs Time Signal for (a)Classical SPHB (b) With Momentum Trap (c) Fine Tuning with Grease Coating

strain curve. The compression crushing of the foam cells (Fig. 12.5 c,d) within the core was noted to be the dominant mechanism of failure within the core, which contributed to the multiple oscillations seen in the response.

The stress-strain response for the honeycomb core sandwich is shown in Fig. 12.6a. Here the response is quite smooth. The peak load increase with increase in the strain rate. This again follows the expected trend of increase in peak stress with increasing strain rate. The failure is mainly in the cell of the honeycomb core (Fig. 12.6c,d). The failure initiates due to compression failure in the open cell walls and traverses across the closed wall almost horizontally as can be seen from Fig 12.6c. The failure is by crushing in the closed walls.

Figures 12.7-12.9 show typical HSR impact response of foam reinforced with glass pin, titanium pin and hollow steel pin truss core sandwich panels. In panels with foam core reinforced with glass-pins and titanium-pins, the HSR impact stress-strain response was noted to be somewhat in between that of the unreinforced foam and that of high transverse stiffness dominant honeycomb sandwich core.

Figures 12.7a illustrates that for the titanium pins reinforced core, the ascending portions of the curves exhibit very little oscillations / load drops. Instead, the descending portion of the curve exhibits multiple load drops. The interpretation of this response is that the pins are preventing the crushing observed in the unreinforced foam core. The failure is observed to be either between the face sheet and core, where the pin is not present or it is shear failure inside the core adjacent to the pins (Fig 12.7c-f). From Figs. 12.7a and b it can be seen that the expected trend of increase in peak load with increase in the strain rate is not seen. This could be due the fact that the location of the pins with respect to the loading varies from sample to sample. The response depends on the location, orientation and the density of the pin with respect to loading. As the location of the pins within the facesheet is a manufacturing driven parameter, there is a definitive effect on the response.

The glass/epoxy pin reinforced foam core samples exhibited almost four times higher peak stress than its corresponding counterparts (Fig. 12.8a). There was no buckling within the glass pins (due to high compressive strength), rather failure was dominated by the interfacial debonding and debonding between the facesheet and the core (Fig. 12.8c, e & f).

In the case of hollow steel truss core panel, the multiple oscillations in the stress-strain response (Fig. 12.9a) were a byproduct of microbuckling of the unsupported pins. Here again, there was a statistical variation in terms of increasing peak stress with increasing strain rates. It is thought that the failure is promoted by the extent of pin penetration into the facesheets. All the pins present within the bounds of the sample underwent anti-symmetrical buckling. The buckling of the pins was followed by out-

of-plane rotation of the facesheets (Fig. 12.9c,d and e). It is believed that the facesheets undergo rotation following microbuckling of the pins, in order to equilibrate the specimen within the time span of interest.

From the viewpoint of peak stress under dynamic loading, it is seen that the trend seen in static tests is maintained. While the panel with glass pin reinforced foam core panel shows the highest peak stress; the foam core sandwich showed the least. Honeycomb core, titanium pin reinforced foam core, and hollow steel pin core sandwich panels show intermediate value of peak stress in descending order.

12.4 Influence of Incident-Transmission Bar Diameter

Two types of incident-transmission bar diameters were adopted in testing; a 0.75" and 1.5" bar pair. In laminated composites, usually the 1.5" bar pair accommodates larger specimen sizes ($\sim 1'' \times 1''$ surface) while in the 0.75" bar pair, the specimen sizes of $0.5'' \times 0.5''$ are typically used. Furthermore, to obtain a uniform state of strain through the sample, the smaller samples provide for uniform distribution of strain over the specimen. Another consideration was that momentum trap mechanism described above was primarily available on the 0.75" bar diameter pair. For all tests, the 0.75" bar pair along with the MTG (described in the earlier section) were adopted. However, few comparative runs were necessary to investigate the influence of the bar diameters on the specimen and the resulting response. This was done on the foam core, foam filled honeycomb core and graphite honeycomb core samples.

Figure 12.10a represents the dynamic stress-strain response for a foam filled honeycomb core sample that is subjected to HSR impact loading using a 0.75" diameter bar pair, while Fig. 12.11a represents the same for a 1.5" diameter bar pair. While the sample size was $1'' \times 1''$ for the 1.5" bar diameter, it was $0.5'' \times 0.5''$ for the 0.75" pair bars. In the case of the 1.5" diameter bar pair, the sample is seen to exhibit numerous oscillations in the loading and unloading portion of the stress-strain response (Fig. 12.11a). Also the peak stresses attained at a strain rate of 254/second are ~ 800 psi. In contrast, the samples impacted using a 0.75" bar exhibit characteristically smooth ascent in the stress-strain curves (Fig. 12.10a). The sample follows an increasing peak stress with increasing the strain rate from 164/second, to 326/second. The peak stress attained at 326/sec was ~ 1000 psi. The failure was mainly represented in the trailing portions of the stress-strain curve in the form of minor load drops. Figures 12.12a-c and 12.13a-c compare the failure modes of the samples subjected to the 0.75" and 1.5" bar diameters respectively. The 0.75" bar pair indicates localized microbuckling of the honeycomb cells, and foam crushing the extent of which increases with increasing strain rate. No visible failure occurred in the case of the facesheets. In contrast the 1.5" impacted samples, show large amounts of core buckling, interfacial debonding between the foam core and the cells and finally collapse of the cells causing interfacial tearing of

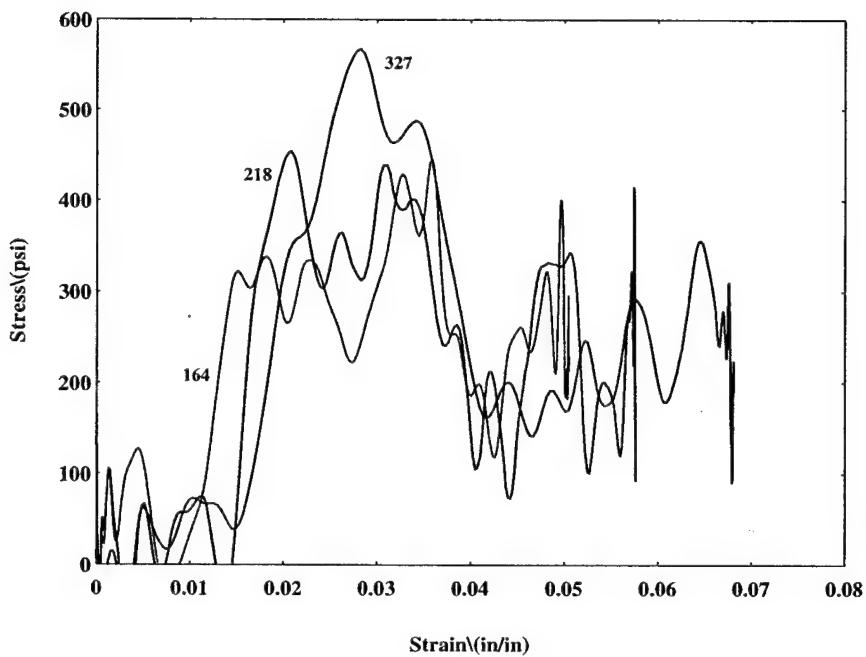


Figure 12.5a. Stress-Strain Curve for Foam Core Sandwich Composite With MTG

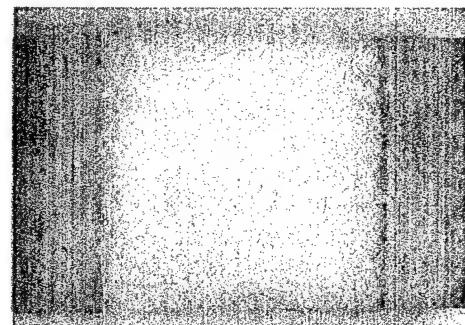


Figure 12.5c. Optical Microscopy of Foam Core Sandwich Composite

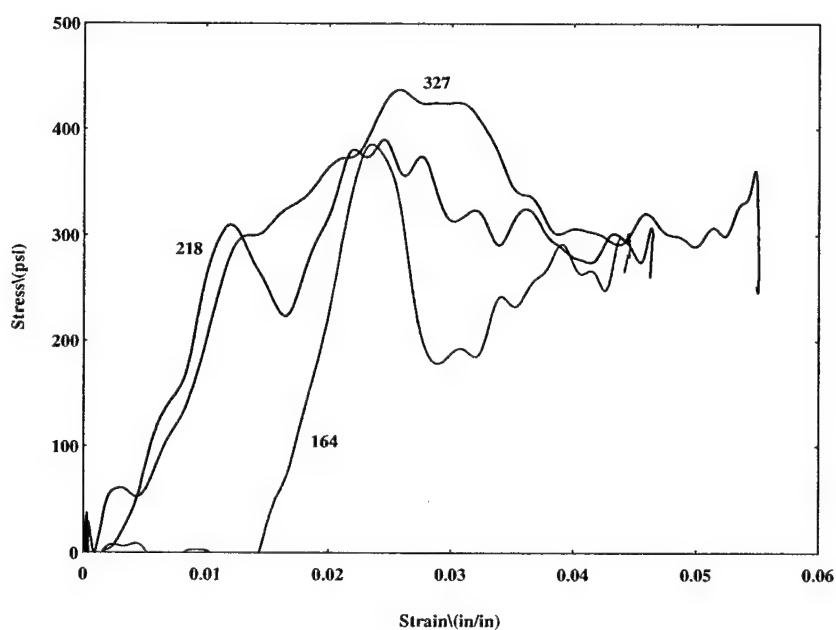


Figure 12.5b. Stress-Strain Curve for Foam Core Sandwich Composite Without MTG



Compressive Core Crushing

Figure 12.5d. Failure Schematic of Foam Core Sandwich Composite

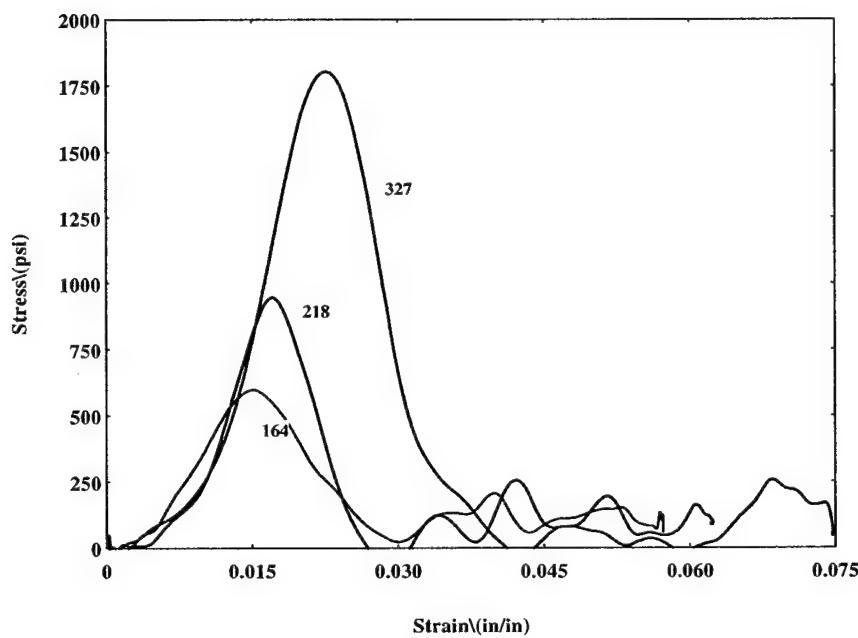


Figure 12.6a. Stress-Strain Curve for Honeycomb Core Sandwich Composite With MTG

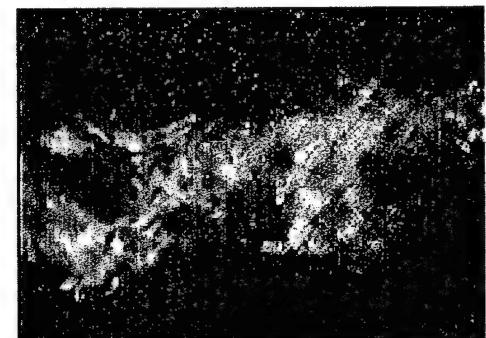


Figure 12.6c. Catastrophic Cell Wall Buckling of Honeycomb Core Sandwich Composite

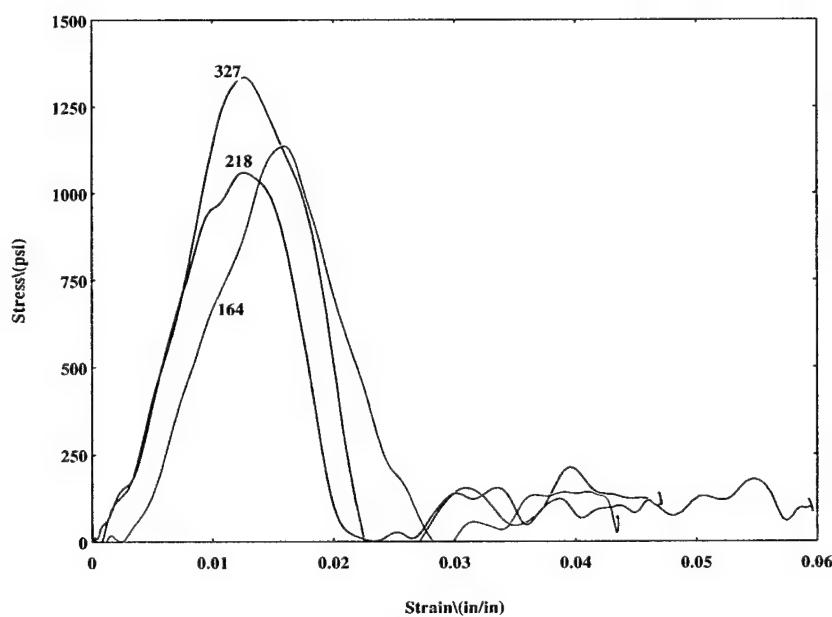


Figure 12.6b. Stress-Strain Curve for Honeycomb Core Sandwich Composite Without MTG

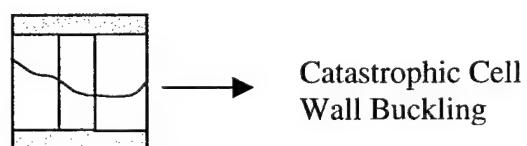


Figure 12.6d. Failure Schematic of Honeycomb Core Sandwich Composite

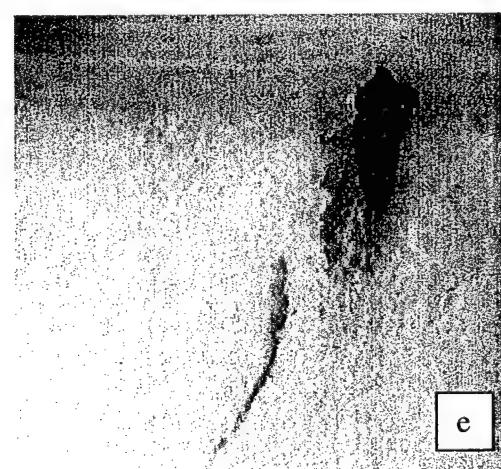
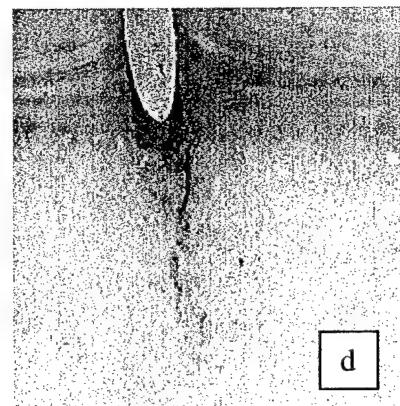
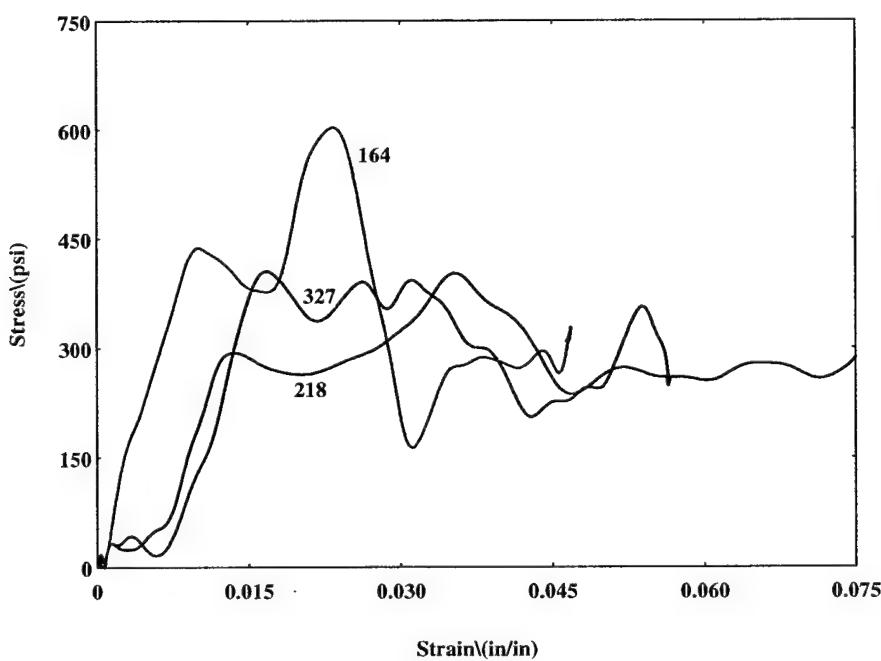
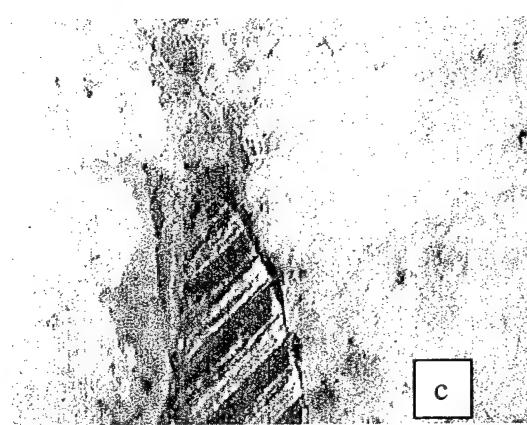
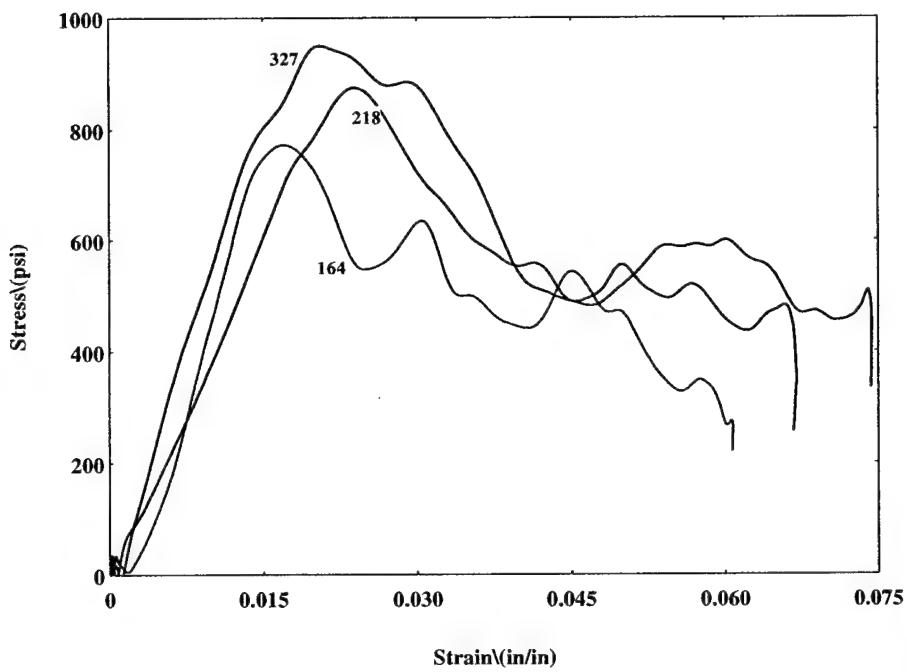
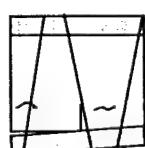


Figure 12.7(c,d,e). Optical Microscopy for Foam + Titanium Pins



Core to Facesheet Disbond and Shear Fracture between the Foam and the Pins

Figure 12.7f. Failure Schematic of Foam + Titanium Pins

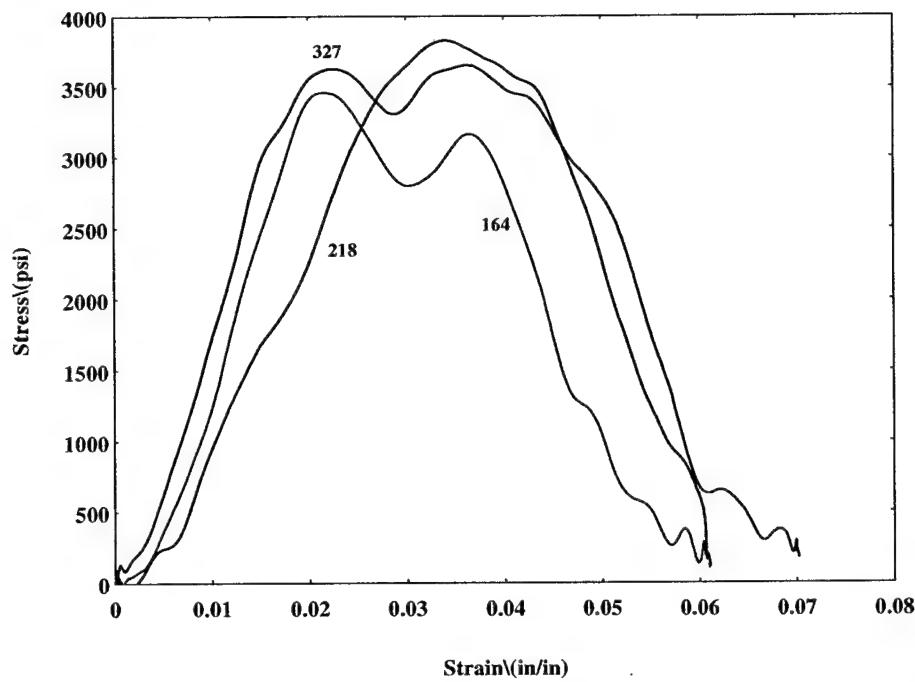


Figure 12.8a. Stress-Strain Curve for Foam + Glass Pins With MTG

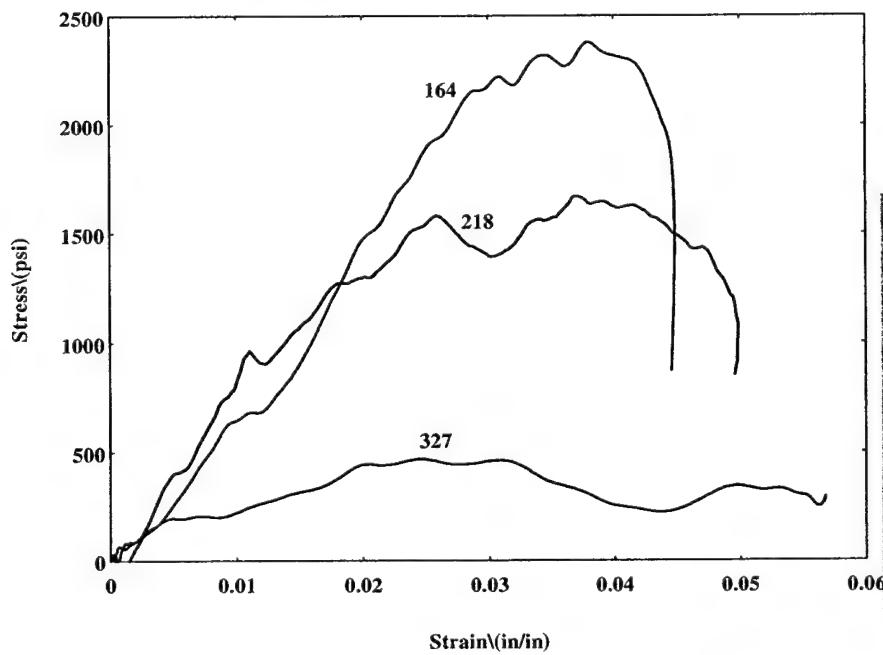


Figure 12.8b. Stress-Strain Curve for Foam + Glass Pins Without MTG

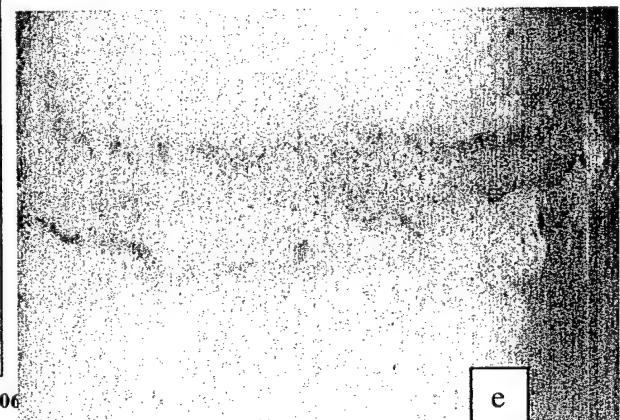
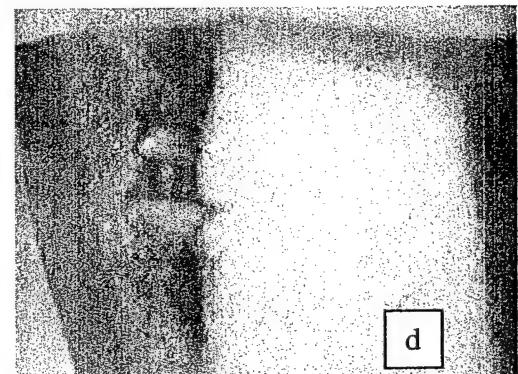
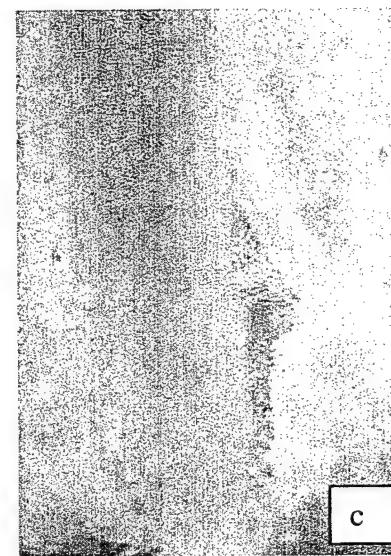
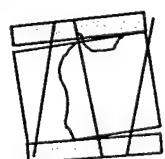


Figure 12.8(c,d,e). Optical Microscopy of Foam + Glass Pins Without MTG



Core to Facesheet Disbond,
Shear Fracture between the
Foam and the Pins and Extensive
Crushing of Foam

Figure 12.8f. Failure Schematic of
Foam + Glass Pins

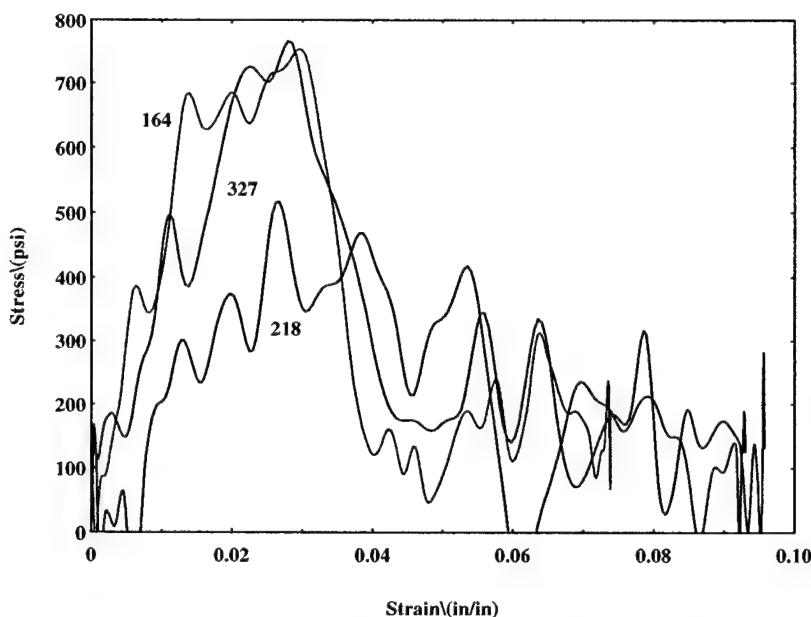
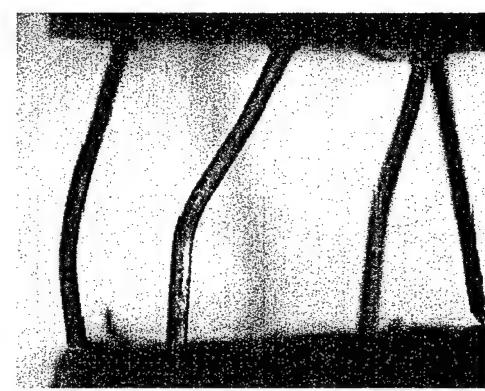


Figure 12.9a. Stress-Strain Curve for Hollow Steel Pin Truss Core Sandwich Composite With MTG



c

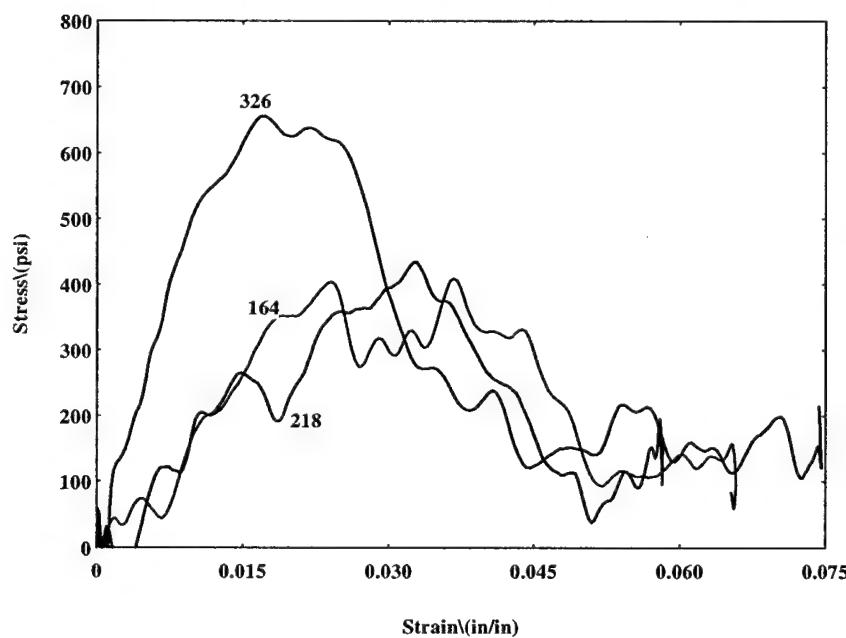
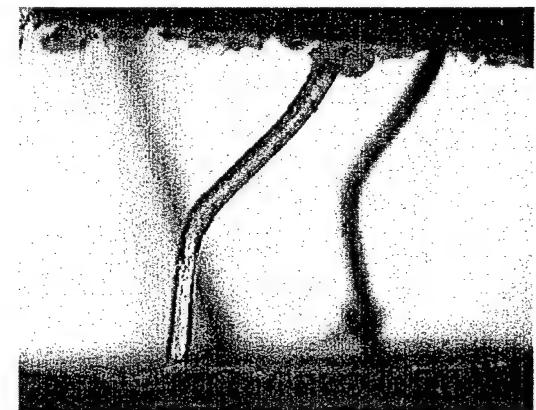
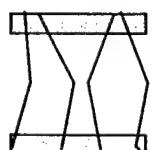


Figure 12.9b. Stress-Strain Curve for Hollow Steel Pin Truss Core Sandwich Composite Without MTG



d

Figure 12.9(c,d). Optical Microscopy for Hollow Steel Pin Truss Core Sandwich Composite



Buckling of Pins
and Rotation of
Facesheets

Figure 12.9e. Failure Schematic for Hollow Steel Pin Truss Core Sandwich Composite

the foam-cell as strain rate is increased. Under identical strain rates, the extent of failure of the samples, hence was significantly influenced using the two bar diameters under this study.

Similar tests were conducted on graphite honeycomb core composites. Figures 12.6b and 12.11b compare the stress-strain response for the two bar diameters. Significant differences were observed in the peak stresses of the 1.5" bar diameter impacted samples. They attained a peak value of only 400 psi at a strain rate of 254/second, while for the 0.75" diameter bar pair, the peak stress attained was 1300 psi, at 327/sec. The several oscillations in the loading and unloading portions of the 1.5" case, were missing in the case of the 0.75" bar impacted samples. The response is smooth till the peak stress is attained, the load drop/oscillations are primarily in the trailing portion, indicative of the microbuckling of the cells observed. The oscillations are mainly attributed to the severe buckling of the honeycomb cells, within the core. It appears that the phenomenon of cell buckling is extensive in the case of the 1.5" bar tests, due to the influence of stress wave travel through a larger diameter bar. Also, several cells are covered in the 1" bar diameter samples. There appears to be a global collapse of the honeycomb cells that results in much lower peak stresses attained. It may be noted that when the 0.5" x 0.5" sample size was used in conjunction with the 1.5" bar, it was not possible to obtain the transmitted signal in the stress bar. However, Fig. 12.14a-c illustrates comparisons of the HSR impact related failure modes for the 0.5" x 0.5" samples used in the 0.75" as well as the 1.5" bars respectively without the use of the MTG (to enable identical comparisons) subjected to a strain rate of 170/sec. It is clear from the illustration of foam core, foam filled honeycomb and honeycomb core sandwich samples, that the extent of failure is much higher in the 1.5" bar for identical strain rates. This is primarily attributed to the multiple stress pulses that the sample is subjected to in the case of the 1.5" bar as opposed to single controlled pulse using the 0.75" bar with the MTG.

12.5 Influence of Momentum Trap Gap

Following testing with the 0.75" and 1.5" bars, it was determined that the most appropriate testing approach would be to use the 0.75" diameter pair, in conjunction with the MTG. As explained earlier, the use of the MTG ensured a single controlled pulse loading of the sample, and an accurate estimation of evolution of damage.

Figures 12.5b-12.10b illustrate the responses of the foam core, foam with pins, hollow pins, honeycomb, honeycomb filled foam core and other types of sandwich composites - "without" the use of MTG. The corresponding Figs. 12.5a-12.10a, are responses discussed in the previous section, which dealt with the response "with" the use of the MTG. From Figs. 12.5b-12.10b, it can be observed that without using the MTG for sandwich composite testing the following observations hold true. First, the

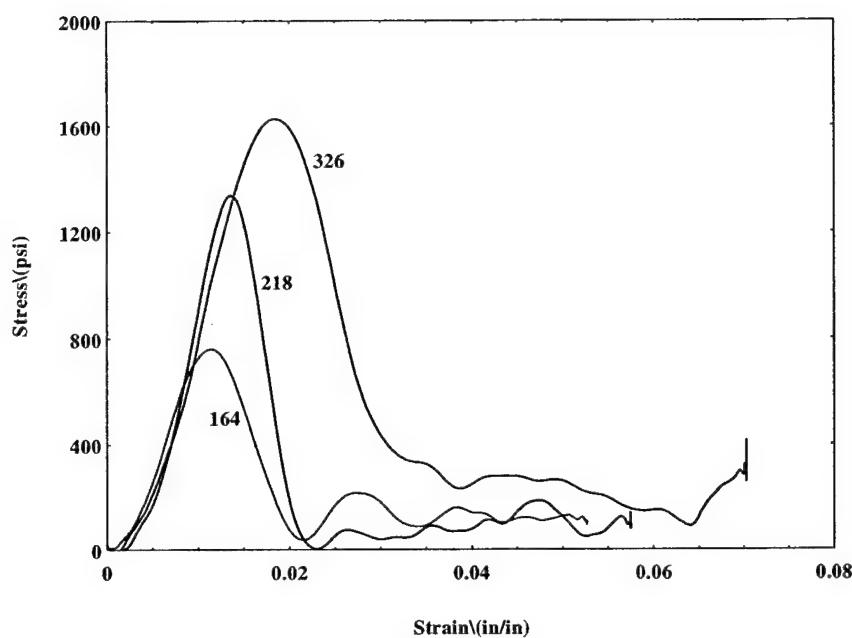


Figure 12.10a. Stress-Strain Curve for Foam+Honeycomb Core Sandwich Composite With MTG

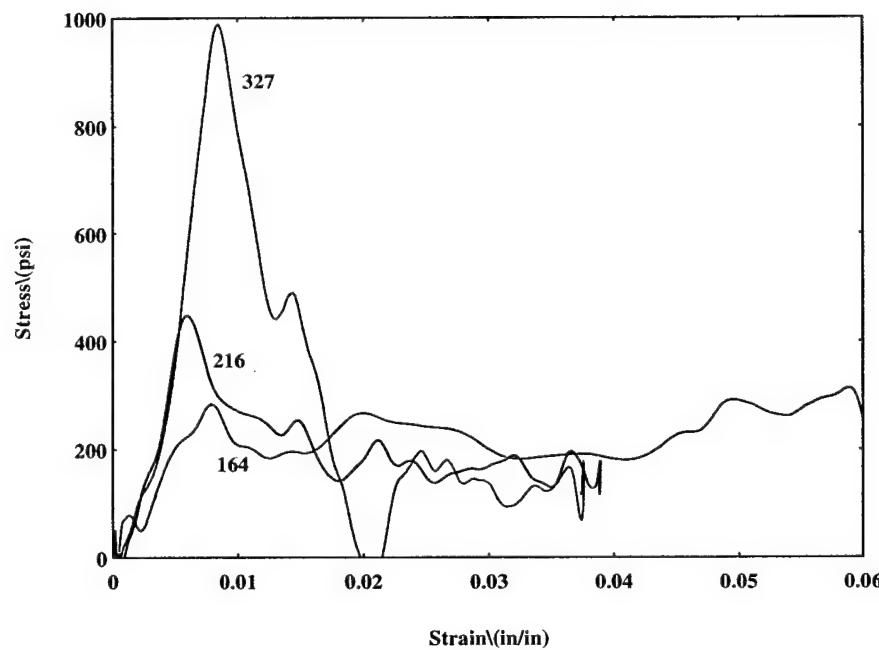
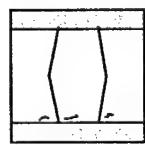


Figure 12.10b. Stress-Strain Curve for Foam+Honeycomb Core Sandwich Composite Without MTG



Cell Wall Buckling
and Compressive
Core Crushing

Figure 12.10c. Failure Schematic for Foam+Honeycomb Core Sandwich Composite

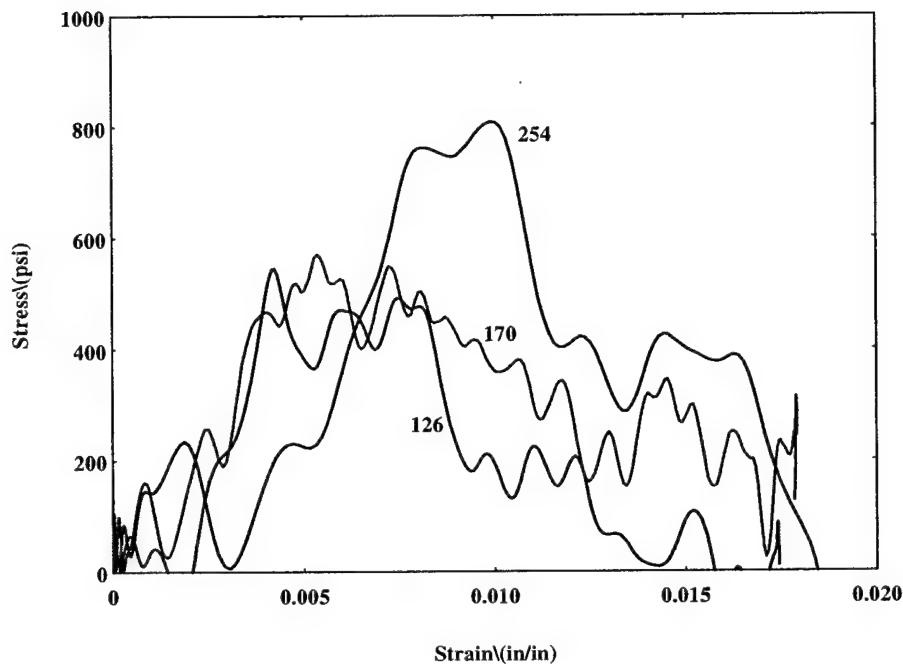


Figure 12.11a. Stress-Strain Curve for Foam+Honeycomb Core Sandwich Composite (1.5" Bar)

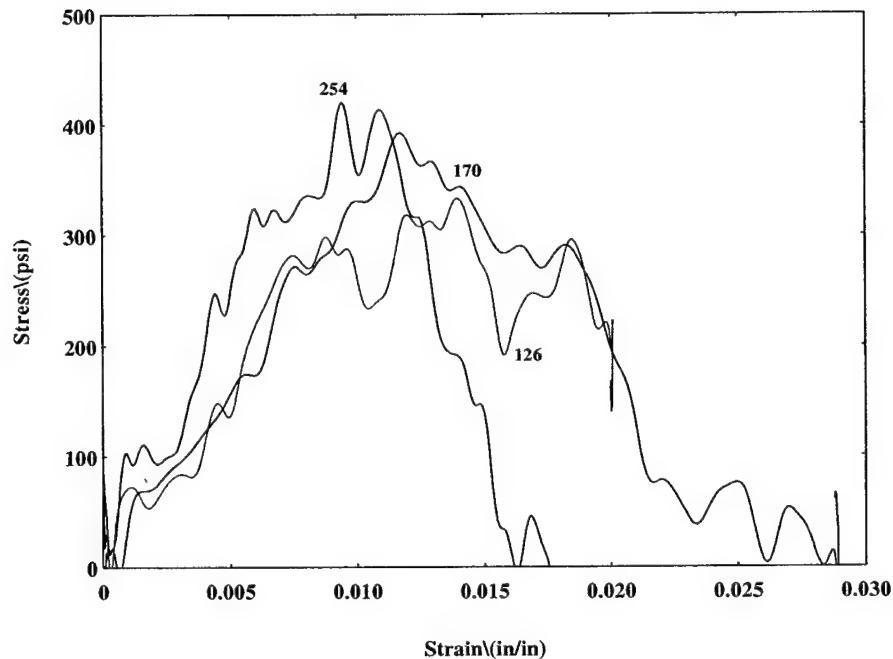
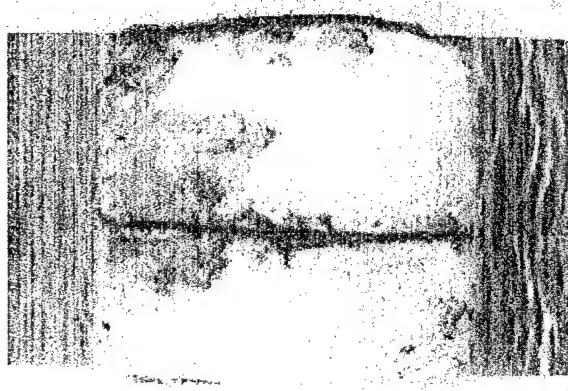
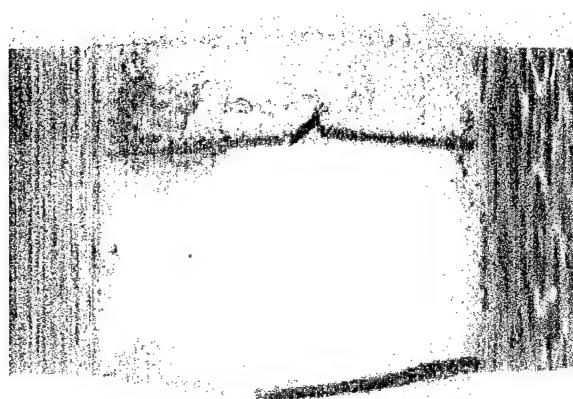


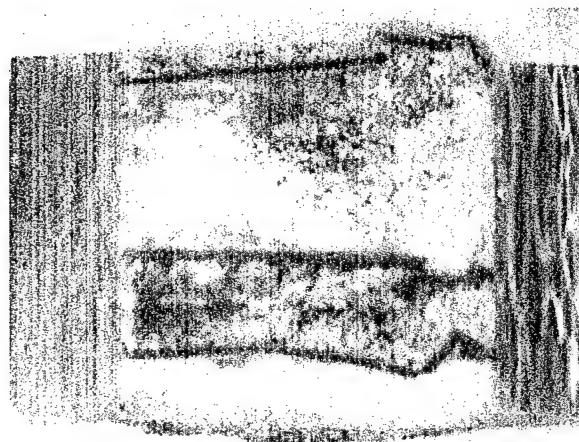
Figure 12.11b. Stress-Strain Curve for Honeycomb Core Sandwich Composite (1.5" Bar)



(a) Strain Rate-164/sec
With MTG



(b) Strain Rate- 218/sec
With MTG



(c) Strain Rate- 316/sec
With MTG

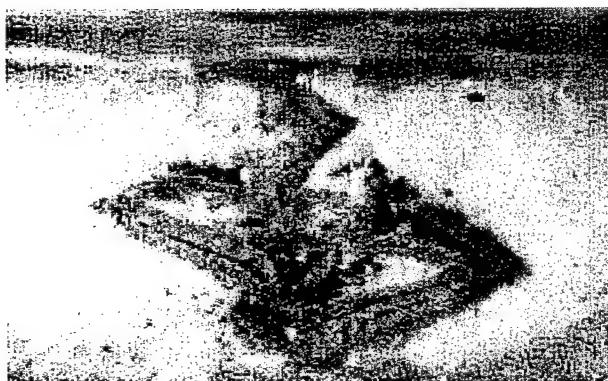
Figure 12.12(a,b,c). Optical Microscopy for WESKOR Foam Filled Honeycomb Core Sandwich Composite Subjected to HSR Testing With MTG (0.75" Bar)



(a) Strain Rate- 126/sec



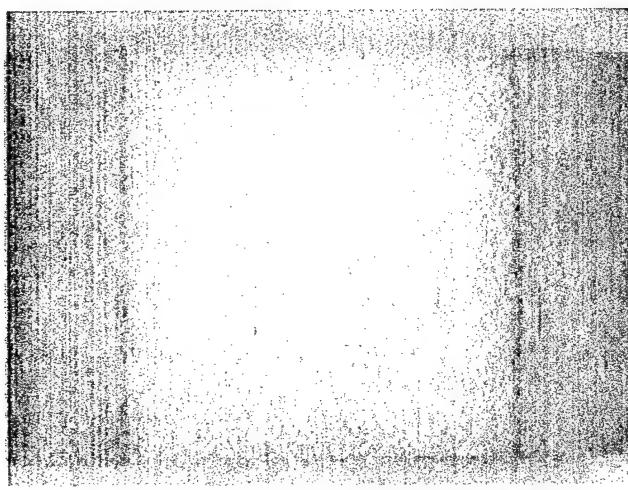
(b) Strain Rate- 170/sec



(c) Strain Rate- 254/sec

Figure 12.13(a, b, c). Optical Microscopy for WESKOR Foam Filled Honeycomb Core Sandwich Composite Subjected to HSR Testing (1.5" Bar)

0.75" Bar



1.5" Bar

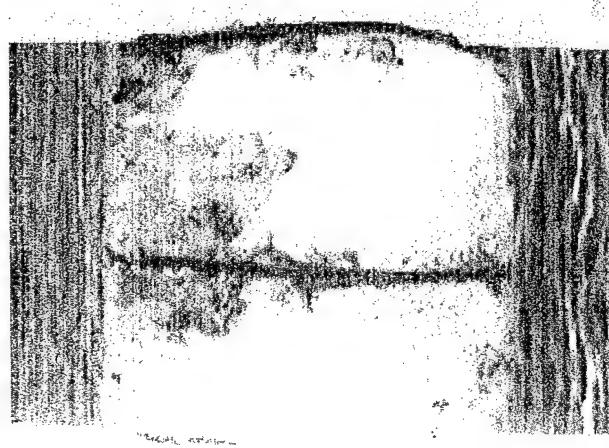
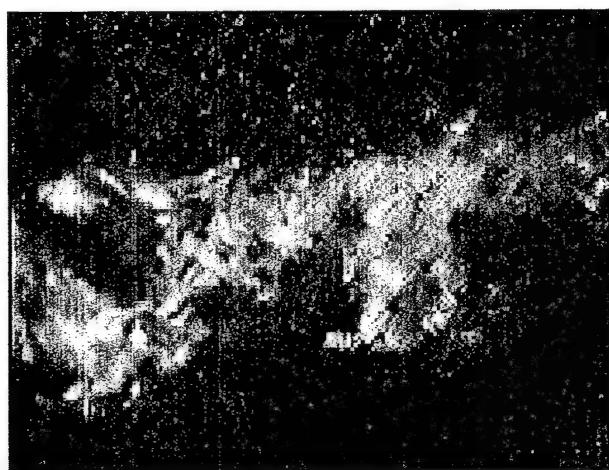
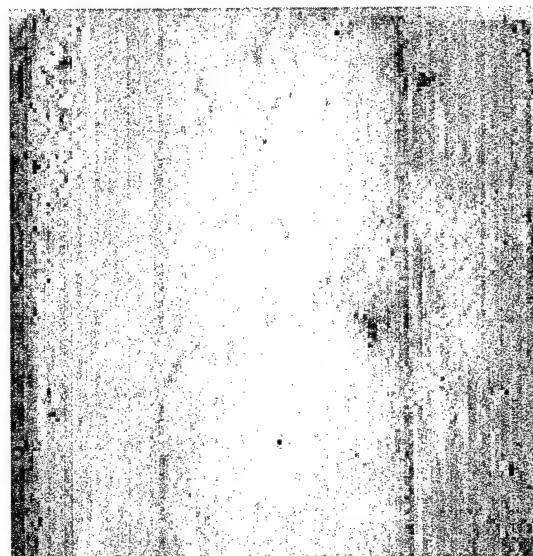


Figure 12.14(a, b, c). Optical Microscopy Comparison for 0.5"X0.5" Samples Subjected to HSR Impact using 0.75" Bar and 1.5" Bar

peak stress for any given strain rate is reduced by 25-40%. The samples undergo premature and extensive failure; so within the strain ranges studied, these samples do not always show increasing peak stress with increase in strain rate. The origin of the damage dictates the progression of the sample to its peak load/stress. There are multiple oscillations/load drops in the stress-strain curves from the samples tested without the MTG both in the ascent and descent portion. This is indicative of the extensive damage state the samples undergo as a result of the multiple compressive and tensile stress-wave reflections the sample is subjected to in the time span of the impact.

Figure 12.5b illustrates the damage in the foam core sandwich composite, when the specimen was subjected to testing without the MTG. For the foam core samples, extensive foam crushing led to "closing-in" of the core resulting in the facesheets almost touching after the impact event. With the use of the MTG, a characteristic foam crushing phenomenon was observed, with the sample integrity still maintained.

For the foam -filled-honeycomb samples, Fig. 12.11b, It is well evident that the foam-filled-honeycomb undergoes extensive cell wall buckling and interfacial debonding, followed by core crushing failure without the use of the MTG (Fig. 12.13). In contrast, with the use of the MTG, Fig. 12.12 illustrates a much lower damage state, showing the origin of failure as cell wall buckling, which leads to interfacial failure and then foam core crushing.

For the pin-reinforced foam core sandwich samples (Figures 12.7b), without the use of MTG, a characteristic reduction in dynamic modulus and lowering of the peak stress is observed. Furthermore, the samples do not follow the modulus trends seen with the use of the MTG. The origin of failure appears to be at the pin-to-core interface both in the "with" and "without MTG", however, failure propagates rapidly in the presence of the multiple stress waves the sample is subjected to without the use of MTG. Similar observations were noted in the case of the hollow truss core samples (12.9b).

12.6 In-Plane vs Through-the-Thickness Loading

The influence of impacting the samples through-the-thickness vs in-plane was investigated to a limited extent as well. It was not possible to obtain the stress-strain curves for the in-plane loading conditions, however, failure modes are compared for identical test configurations (in terms of strain rate and samples used). The in-plane response of the samples, as expected, was primarily dominated by the facesheet properties. For all the through-the-thickness tests, damage within facesheets was either non-existent or very limited to early stages of matrix microcracking. The in-plane tests demonstrated high levels of compressive microdelaminations in the facesheets. The facesheets exhibited microbuckling of the fibers, matrix shearing (whitening),

progression of delaminations (in some instances, separation) limited debonding between the core and the facesheets. In these samples, the core did not exhibit the damage states noted in case of the thickness direction loading. Fig. 12.15 a-f represents the damage condition of the honeycomb core, foam filled honeycomb, glass pin reinforced foam core, titanium pin reinforced foam core and hollow steel truss core respectively. In all these cases it may be noted that the damage is dominated within the facesheets. The most aggravated damage condition is noted in the hollow core (Fig. 12.15e) where the pin pull-out and in some instances "shearing-off" of the pin from the facesheet were observed.

12.7 High Strain Rate Response of Honeycomb Core Sandwich Composites with Dissimilar Facesheets

The specimen description was provided earlier in the Section 8.13 of Chapter 8. In the current work, the specimen was sandwiched in the incident-transmission bar of the high strain rate setup in two ways; first with the graphite/epoxy facesheet facing the incident bar, and second with the glass/epoxy facesheet facing the incident bar. Typical stress-strain curves for the core materials used in the study are plotted in Figs. 12.16-12.17.

Tests Conducted Without Momentum Trap :

Figures 12.16b and 12.17b compare the stress-strain plot for the case without the momentum trap (multiple compressive pulses). It can be seen that peak stress ranges from 800 psi to 900 psi for the strain rates of 163 to 326 per second for both specimen types (i.e., graphite/epoxy facing incident bar and glass/epoxy facing incident bar), indicating mainly that the peak stress was dominated by the failure of the core. The failure of samples was primarily by core failure - compression core crushing and buckling. For the graphite/epoxy side facing the incident bar (Fig. 12.17b), the peak stress increases with increase in strain rate (within the 800 - 900 psi range), which is attributed to the thicker graphite/epoxy facesheet. The load transferred to the core results in core damage as can be seen through multiple oscillations in the rising portion of the curve. However, for the thinner glass/epoxy facesheets (Fig. 12.16b), the number of minor load drops are more in number as compared to the graphite/epoxy facesheet facing the incident bar. This is because the core is subjected to the stress wave earlier than in the graphite/epoxy facesheet facing the incident bar. Hence, core damage in terms of buckling and core compression is more. It is thought that the load gets transferred to the core in lesser time, and hence the peak stress is influenced by the instance of core failure. As such, in this case the peak stress reduces (within the 800 psi - 900 psi) range with increase in strain rate.

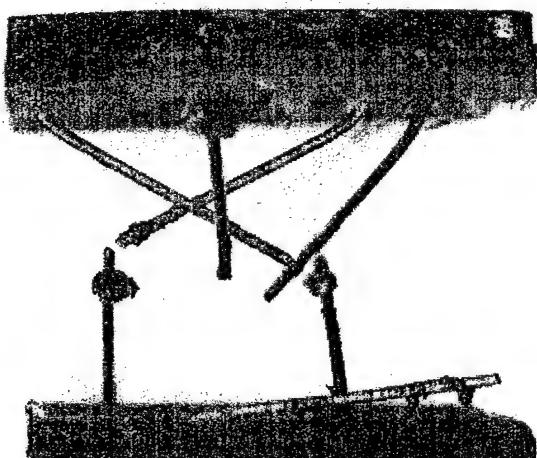
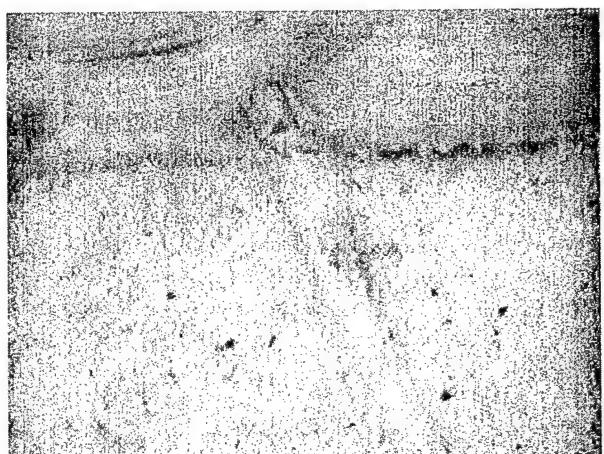
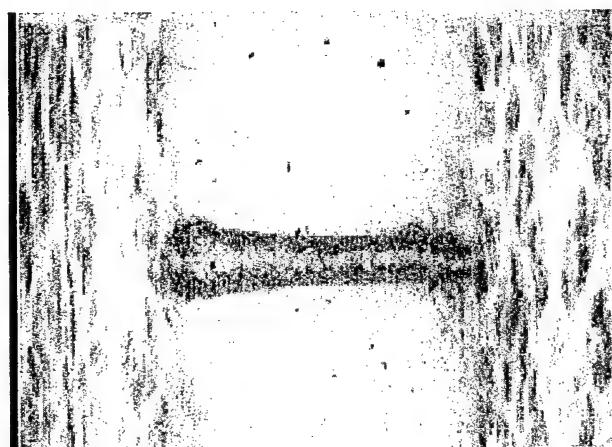
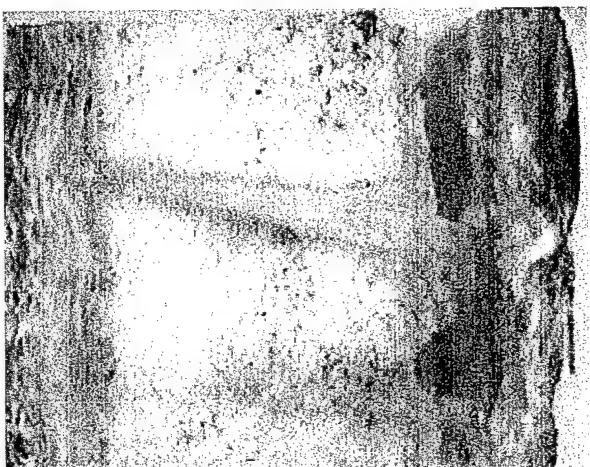
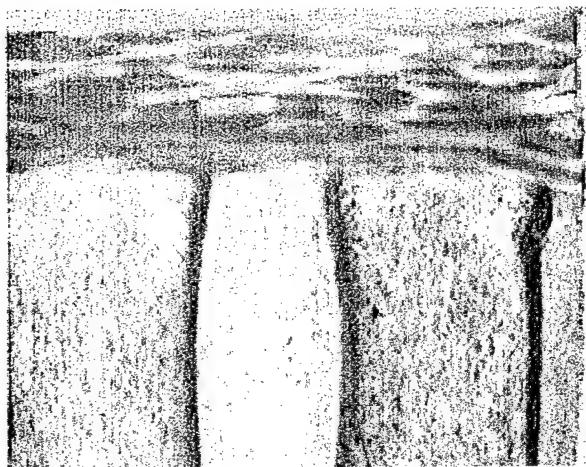


Figure 12.15(a, b, c ,d, e and f). Optical Microscopy for Samples Subjected to In-Plane HSR Impact Testing using 1.5" bar

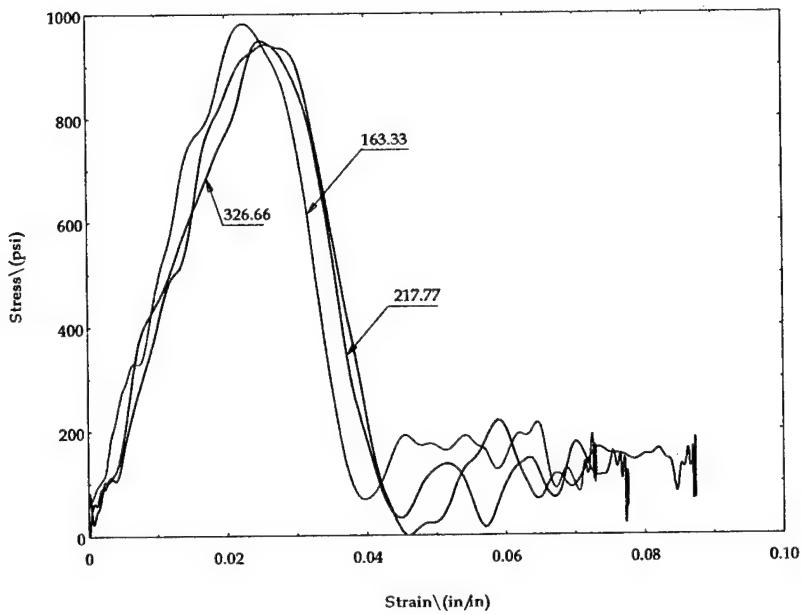
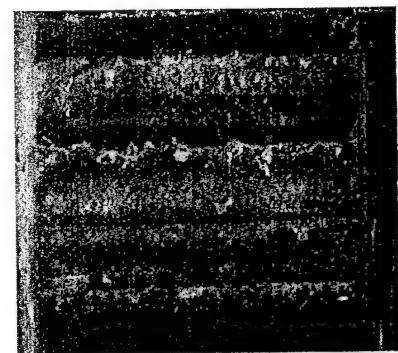


Figure 12.16a. Stress-Strain Curve for Nomex Honeycomb Core With Hybrid Facesheets (With MTG)
– Glass/Epoxy Facesheet Facing



(c)

Figure 12.16c. Photograph of Nomex Honeycomb Core With Hybrid Facesheets Glass/Epoxy and Graphite/Epoxy

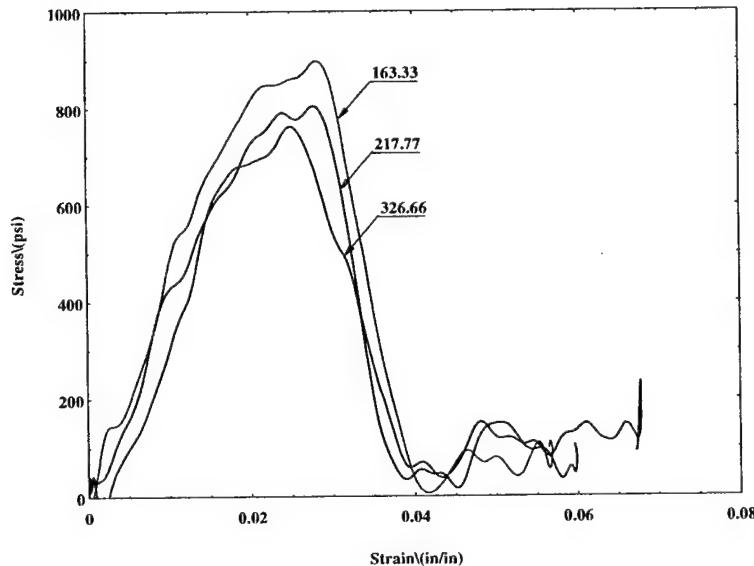
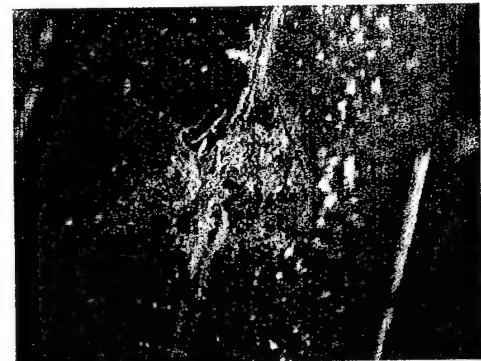


Figure 12.16b. Stress-Strain Curve for Nomex Honeycomb Core With Hybrid Facesheets (Without MTG) – Glass/Epoxy Facesheet Facing



(d)

Figure 12.16d. Optical Microscopy for Nomex Honeycomb Core With Hybrid facesheets -Glass/Epoxy Facing the Incident Bar side; Without Momentum Trap

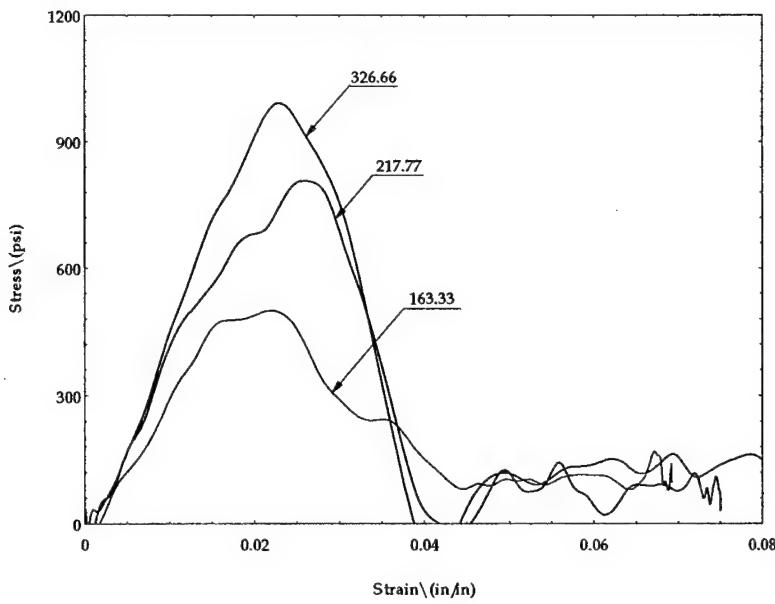
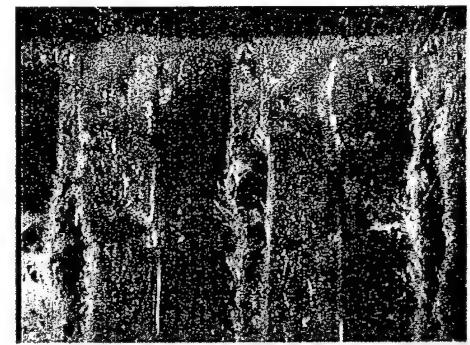


Figure 12.17a. Stress-Strain Curve for Nomex Honeycomb Core With Hybrid Facesheets (With MTG)
– Graphite/Epoxy Facesheet Facing



(c)

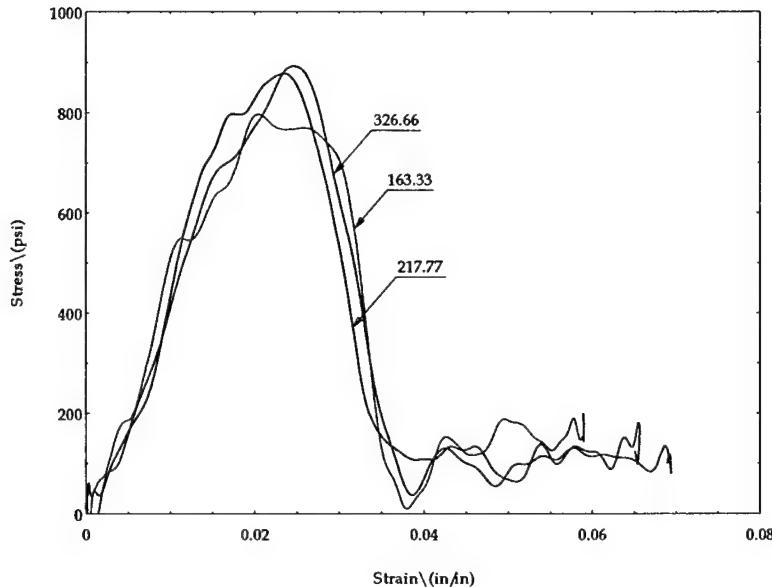


Figure 12.17b. Stress-Strain Curve for Nomex Honeycomb Core With Hybrid Facesheets (Without MTG) – Graphite/Epoxy Facesheet Facing



(d)

Figure 12.17c,d. Optical Microscopy for Nomex Honeycomb Core With Hybrid facesheets -Graphite/Epoxy Facing the Incident Bar side; Without Momentum Trap

Tests Conducted With Momentum Trap : The trends observed for the sample without the momentum trap gap are in general repeated here. The samples were now subjected to a single compressive pulse unlike in the those described in the prior section, where they were subjected to multiple compressive pulse. Figure 12.17a represents the stress-strain response for the graphite/epoxy facesheet facing the incident bar. The influence of facesheet stiffness is more pronounced here, as the peak stress attained is proportional to the strain rate the samples are subjected to. The range of peak stresses for strain rates of 163, 217 and 326 per second are 500 psi to 1000 psi. Also, a stiffening effect is noted with increase in strain rate, which is typical of high strain response of laminated composites [4, 5, 6]. This also means that core integrity is retained more than when the sample is repeatedly loaded by multiple reflections of the compressive pulse. For the glass/epoxy facesheet facing the incident bar, as seen in Fig. 12.16a, the peak stresses are similar to what was observed for repeated compressive pulse loading. They range from 780 psi to 900 psi in for strain rates of 163, 217 and 326 per second respectively. This validates that the facesheet being thinner, has a minimal role in the strain rate response. Hence what is observed is primarily the core response. Figures 12.16d and Figs 12.17c,d show the optical microscopy of the failed specimens.

12.8 Summary/Conclusions

A comparative study between the traditional core and innovative cores is presented here. Traditional core configurations considered are foam core and honeycomb core. Innovative core configurations considered include hollow pin truss core, foam core reinforced with titanium pins and glass pins.

The primary dominant modes of failure under HSR loading may be summarized as follows:

1. Buckling of pins in the hollow truss core sandwich samples , followed by rotation of the facesheets out-of-plane.
2. Cracking and collective buckling of the honeycomb cell walls in the pure honeycomb core sandwich samples.
3. Core crushing and cell wall closure followed by shear crack propagation in the case of the Rohacell foam core sandwich samples.
4. Titanium pin reinforced foam core samples failed either by debonding at the face sheet, microbuckling of the pins and/or interfacial separation between the core and pins.
5. In the case of glass pin reinforced panels the failure was due more to debonding between the face sheet and the core and by shear cracks in the foam with very little evidence of pin fracture/buckling.

6. In all the cases considered, for the through-the-thickness direction loading, the facesheets did not exhibit any notable evidence of damage accumulation. Failure was in all the cases, within the domain of the core(s).
7. Under high strain rate loading, the core crushing behavior primarily dominates the strain rate sensitivity. No significant differences were noted in the stress-strain curves from impacting the samples either from the glass/epoxy side or the graphite/epoxy side, except that the thinner glass/epoxy side exhibited more core damage. The use of a momentum trap is justified in the sandwich composite samples, as the pure response to a single compressive pulse and hence, damage evolution could be ascertained.
8. For the in-plane loading, the facesheet dominated failure was noted, where fiber microbuckling, compression delamination within the facesheet and interfacial debonding between facesheet-to-core were noted. The core damage was not prominent.
9. No significant differences were noted in the stress-strain curves from impacting the samples with dissimilar facesheets either from the glass/epoxy side or the graphite/epoxy side, except that the thinner glass/epoxy side exhibited more core damage.

12.9 References

1. Nemat-Nasser, S., J.B. Isaacs, and J.E. Starrett. 1991. "Hopkinson Techniques for Dynamic Recovery Experiments," *Proceedings of Royal Society of London*, 435, pp. 371-391.
2. Zenkert, D. 1997. *The Handbook of Sandwich Construction*. London, UK: Engineering Materials Advisory Services Ltd., Chameleon Press Ltd.
3. Karlsson, K.F. and B.T. Astrom. 1997. "Manufacturing and Applications of Structural Sandwich Components," *Composites, Part A*, Elsevier Publications, pp. 97-111.
4. Kim, C. and E. Jun. 1992. "Impact Resistance of Composite Laminated Sandwich Plates," *Journal of Composite Materials*, Vol. 26, No. 15, pp. 2247-2261.
5. Vaidya, U.K., M.V. Kamath, H. Mahfuz, and S. Jeelani. 1997. "Manufacturing and Low Velocity Impact Response of Innovative Sandwich Composites," 29th International SAMPE Technical Conference, pp. 713-724, Vol. 29, Ed. Green, J.E, Beckwith, S.W and Strong, A.B.
6. Weeks, C.A. and C.T. Sun. 1994. "Multi-Core Composite Laminates," *Journal of Advanced Materials*, pp. 28-37, April.

7. Kim, C. and E. Jun. 1992. "Impact Resistance of Composite Laminated Sandwich Plates," *Journal of Composite Materials*, Vol. 26, No. 15, pp. 2247-2261.

13.0 Intermediate Velocity Tests : Dynamic Flexure

13.1 Introduction and Test Results

In several practical situations, the sandwich constructions are subjected to a impact phenomena which represents an intermediate velocity range (between a low velocity impact (<5 m/s), and a high velocity / ballistic impact (>100 m/s). While the influence of such impacts has hardly been addresses, they may cause extensive damage, that evolves through a combination of quasi-static loading situations, such as encountered in LVI, and some time dependency, due to the speed of the impact. This scenario is referred to as intermediate velocity impact in the current research. The range of velocity here is in the neighborhood of 20-40 m/s.

To conduct such intermediate velocity tests, the Split Hopkinson Pressure Bar (SHPB) setup was improvised to obtain intermediate projectile velocities up to 30 m/s. The rationale here was to use to the specimens of identical sizes used in the low velocity impact experiments, however to subject the samples to velocities, higher by an order of magnitude. Furthermore, the samples would be subjected to dynamic flexure because of the impact loading.

A striker bar with 0.5" hemispherical end launched from the SHPB's [1] pressurized gas chamber. The specimen was simply supported (using light adhesive tape) on stiffened bars bolted within a hollow box fixture shown in Fig. 13.1. The incident and transmission bars of the SHPB were not used in these tests. The velocity of the striker was measured, just prior to impact. Knowing the mass of the striker, and the velocity of the striker, and therefore the kinetic energy of impact was determined. The experimental setup provided a means of rapid comparison of various sandwich cores to impact.

In the current study, the pin reinforced Rohacell foam, hollow titanium truss core, and the unreinforced Rohacell foam core sandwich composite samples were subjected to intermediate velocity impacts. A breech pressure of 35 psi was adopted which launched the striker at a velocity of 31.96 m/sec (1258.27 in./sec). The mass of striker adopted was 356 gms (0.78 lbs) and bar length 6 in. (152.4 mm) resulting in an impact energy of 181.81 J on the sandwich panels.

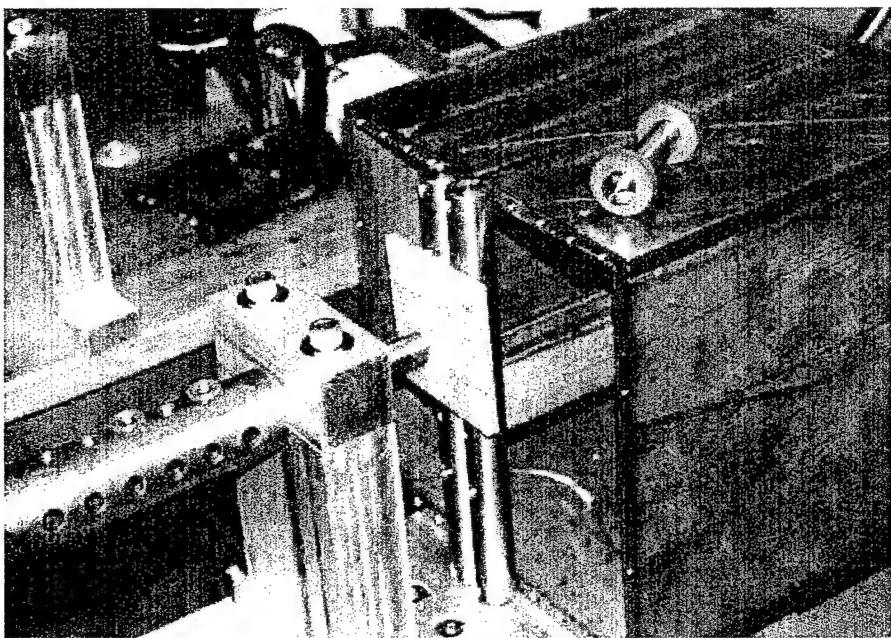
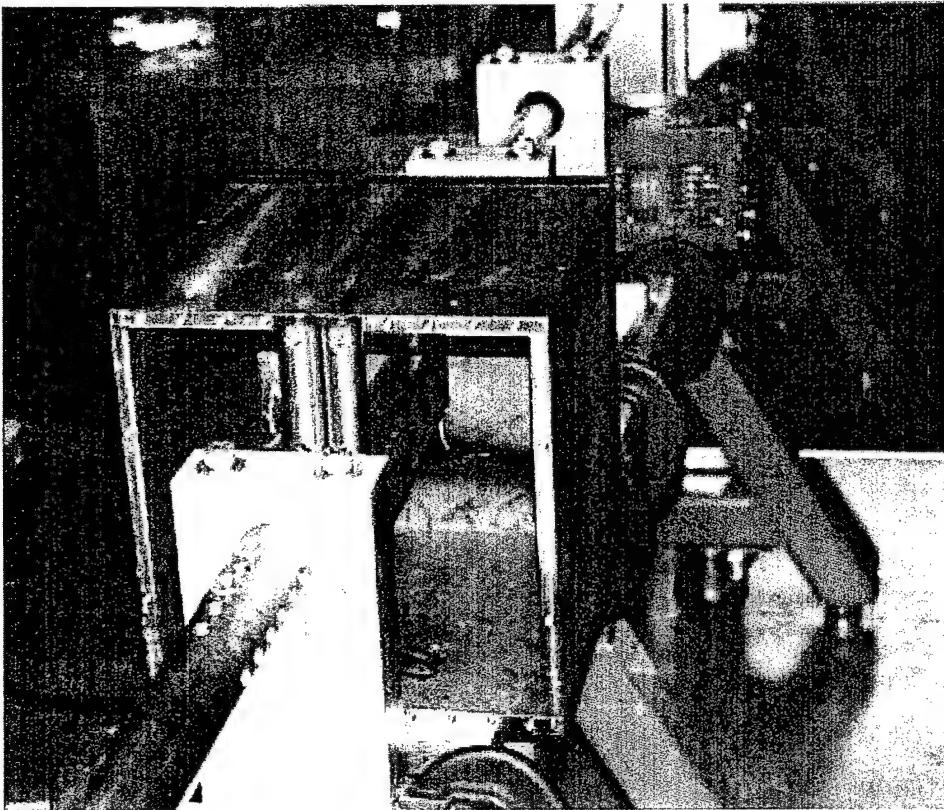


Figure 13.1. Schematic of Intermediate Velocity Impact Test Set-Up
The instrument is a modified version of the Split Hopkinson Pressure Bar
used in high strain rate testing experiments.
a) Details of the Fixture, b) Specimen Mounted on the Fixture

Figure 13.2 a, b and c illustrate intermediate velocity impact damage for the unreinforced foam core, the pin reinforced foam core and the hollow titanium truss core sandwich composites, respectively. The unreinforced foam exhibited higher flexural deformation and damage state due to the impact. The facesheet on the impact side

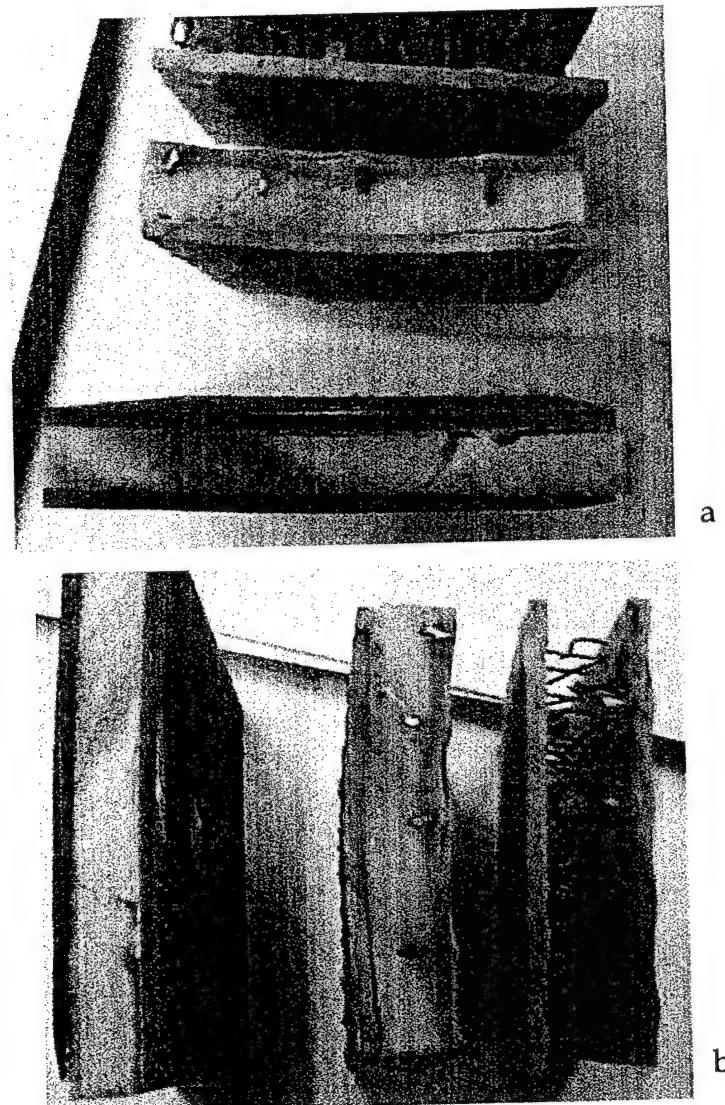


Fig 13.2.. continued on next page

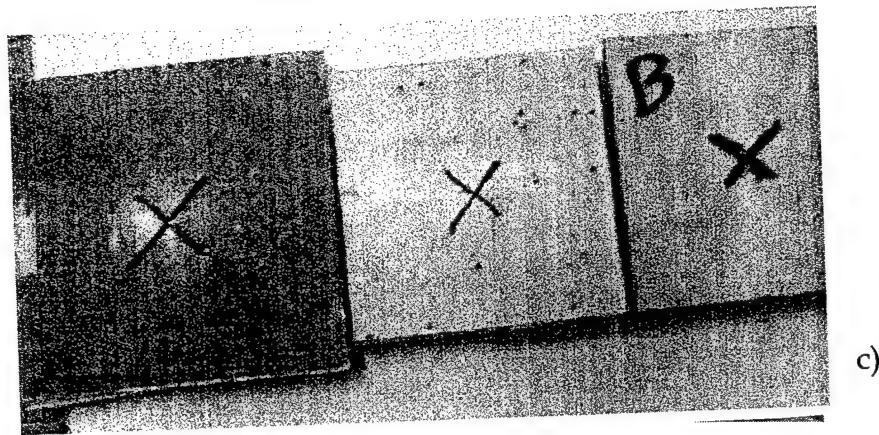


Figure 13.2 . Intermediate Velocity Impact Failure of Foam, Titanium Pins Reinforced Foam and Hollow Titanium Z-Pins Reinforced Core
a) and b) represent different details for the same samples.
c) Top View of the samples

underwent localized whitening due to the deformation of the matrix, and extended damage across the facesheet-core interface, as well as shear dominated fracture of the foam. In contrast, the pin reinforced foam, showed a much contained flexural deformation. The core damage was minimal, while the major damage appeared to be at the impact side facesheet, by foam crushing, and thereby debonding of the foam/facesheet across the pins. The pins themselves underwent buckling in the localized area of the impact, and pull-out away from the impact, at the tensile side. The failure was similar to that observed for static flexural loading of the core.

The hollow truss core shows the primary mode of failure to be dominated by collective buckling of the titanium pins in a symmetrical fashion, much like that observed in the case of the static flexure experiments. In addition, whitening of the matrix in the vicinity of the facesheets is observed as well.



Figure 13.3. Intermediate velocity impact failure of a) glass/epoxy pins reinforced foam and b) foam core. Figures represent top view of samples.

Under intermediate velocity, flexural deformation and growth of damage was much contained when the foam core was reinforced with the pins. Further experiments on the intermediate velocity response are underway.

13.2 References

1. Nemat-Nasser, S., J.B. Isaacs, and J.E. Starrett. 1991. "Hopkinson Techniques for Dynamic Recovery Experiments," *Proceedings of Royal Society of London*, 435, pp. 371-391.

14.0 Finite Element Modeling and Analytical Studies

Some aspects of the finite element modeling were performed at Tuskegee University, and a portion of the work and the analytical studies were performed through a sub-contract to Advanced Structural Concepts (ASC), Inc., Ohio. Chapter 14.0 is divided into two sections. In the sections 14.1-14.3, work done at Tuskegee is outlined. The work performed at ASC is provided as Appendix A. (Please note that the page nos., figure nos. etc. for the ASC part of the work have not been changed).

14.1 Work Done at Tuskegee University

14.1.1 Finite Element Modeling (FEM) of Hollow Truss Core Composites

The truss core composites as described before have a three-dimensional core identity, where steel or light weight metallic pins penetrate into the top and bottom facesheets. The core is an open core which provides the space advantages as well as high shear stiffness as opposed to traditional closed cell core configurations. Finite element work on the sandwich composites was done using the ANSYS - finite element analysis / modeling (FEA/FEM) [1] software. A building block approach is taken for FEM of the sandwich composites [2]. First, a model is created to represent a three-dimensional unit cell configuration, where one unit cell consists of three pins oriented at 10 degree angles with respect to the facesheets as shown in Fig. 14.1. The unit cell is then repeated along the x and y directions to simulate the truss core sandwich plate as shown in Fig. 14.2 to obtain the sandwich composite with hollow truss core.

A solid modeling approach is adopted by defining keypoints, and areas. Automatic mesh generation is used to mesh the areas. In the solid model, the load is applied on the facesheet and the model is constrained along the edges of the facesheet in a cantilever manner. The stress concentration around the pin-facesheet interfaces can be clearly observed. BEAM4, a three-dimensional beam element is used to model the truss pins as a three-dimensional entity. The facesheets are modeled using SHELL99, which is a layered-shell element. The material properties of graphite/epoxy are provided to the facesheets. The material properties of steel are provided to the truss pins. The unit cell and the the 3D model are generated by solid modeling, sharing the keypoints between the facesheets and the pins, and meshing of four areas on each facesheet. The boundary and loading conditions for a plate compression test have been used to check for working of the model. The boundary conditions to test the model have been applied to simulate a static loading compression-after-impact test in a SACMA recommended test fixture, as shown in Fig. 14.3. The distribution of stresses σ_x along the loading axis are represented in Fig. 14.4. The stresses of largest magnitudes are present at the pin-to-facesheet boundaries indicating the most likely locations of damage initiation. Figure 14.5. represents the distribution of the τ_{xy} stresses. Here

again, the maximum stresses are seen to occur in the periphery of the pins-to-facesheets. As noted in the CAI experiments for the hollow steel pin sandwich composites with graphite/epoxy core, the failure was largely unaffected by the impact location, but was dominated by the pin-to-facesheet shearing, which resulted in an accumulation of microcracks from various pins to cause final failure. The FEM studies support the experimental observations accurately. Although exact correlations between microstructure - impact energy levels - ultrasonic inspection have yet to be determined, the damage observed around the pin locations observed through microscopy and ultrasonic inspection, is well represented by the finite element model.

14.1.2 Finite Element Modeling (FEM) of Honeycomb Core Composites

In the modeling of the honeycomb, the core and facesheets have modeled using the SHELL99 elements. A unit cell approach has been adopted in representing the geometry of a single honeycomb cell as shown in Fig. 14.6. The unit cell has been constrained at its bottom edge, and been tested for transverse loading as shown in Fig. 14.7. The resulting displacement and stresses σ_z are shown in Figs. 14.8 and 14.9 respectively. The displacements based on the simplified model do not capture the buckling of the cell walls, however, the stress distributions indicate that at each intersection of the honeycomb cell wall, the stresses are higher. In the experimental test, this translates to cell wall buckling and tearing failure at the intersections. Subsequently, facesheets have been added to the model, and the nodes at the extreme ends of the unit cell have been constrained, as shown in Fig. 14.10. The unit cell has then been loaded at the free end, with a single concentrated point load. In simplistic terms, this quasi-static loading condition may be analogous to a low velocity impact load, at a cell wall transition point on a honeycomb core composite. The resulting stress distribution in the z direction, as shown in Fig. 14.11 indicates high stresses at the interface, and at the center of the honeycomb cell wall. In experimental testing, these stresses lead to the buckling of the cell wall, accompanied by interfacial debonding of the core from the facesheet. Figure 14.12 represents the deformation of the unit cell under the loading condition just described. The model is extended in three-dimensions to obtain the entire geometry of the cells and the sandwich construction as shown in Figs. 14.13 and 14.14.

14.1.3 Finite Element Modeling (FEM) of Foam Core Sandwich Composites

Rohacell foam core sandwich composite geometry has been modeled using ANSYS 5.3. This model has been tested under static compression, flexure and Low velocity impact. A solid modeling approach is adopted by defining keypoints and volumes. Automatic mesh generation is used to mesh the volumes.

A 3-D layered structural solid element - SOLID46, is used to model the facesheets. The geometry, node locations, and the co-ordinate system for this element

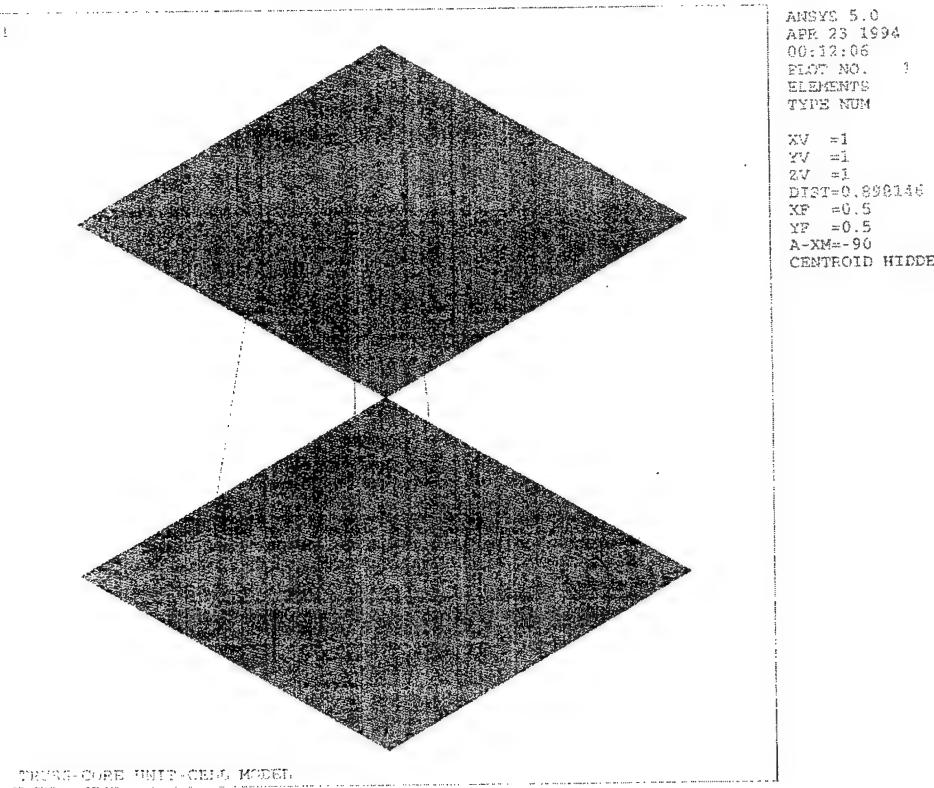


Figure 14.1. Unit Cell for Z-Pin Core

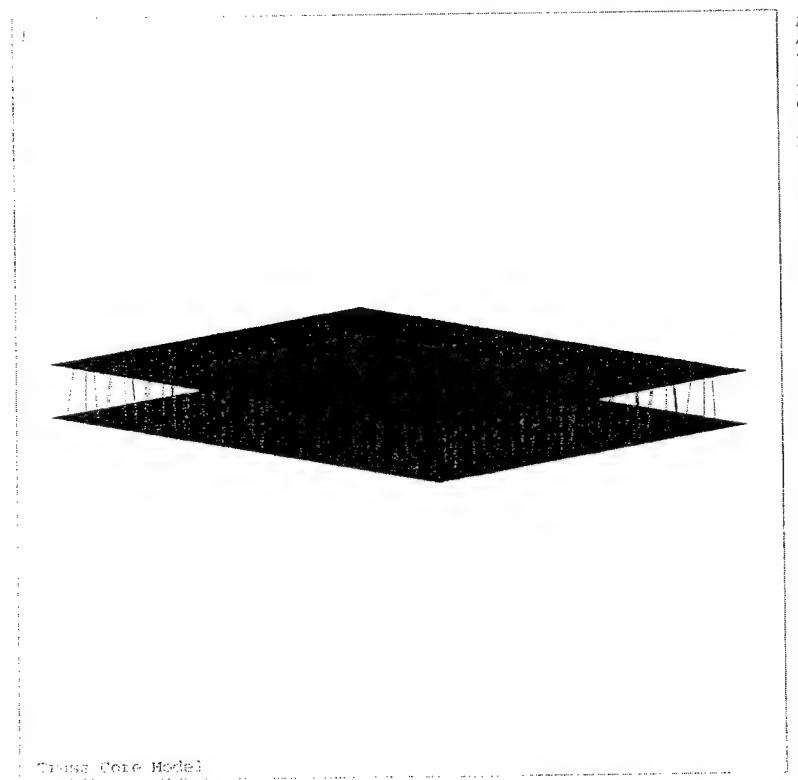


Figure 14.2. Z Pin Sandwich Core Panel

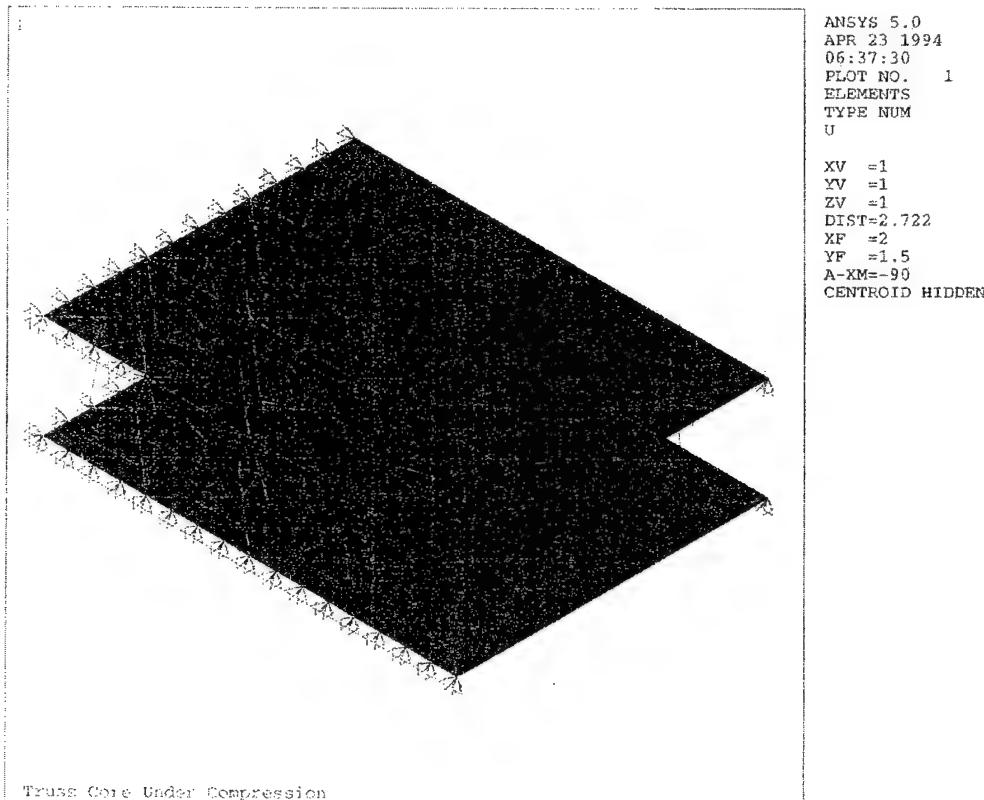


Figure 14.3. Z-Pin Sandwich Core Under CAI Loading Constraints

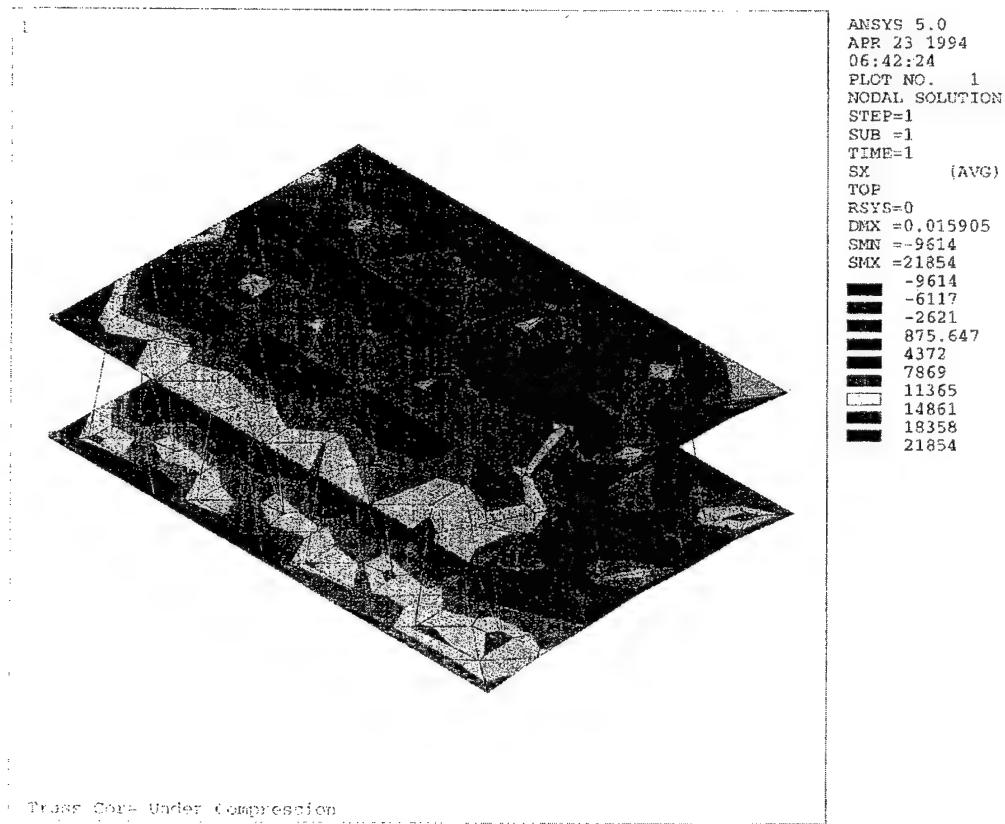


Figure 14.4. σ_x Distribution for Z-Pin Sandwich Panel Under CAI

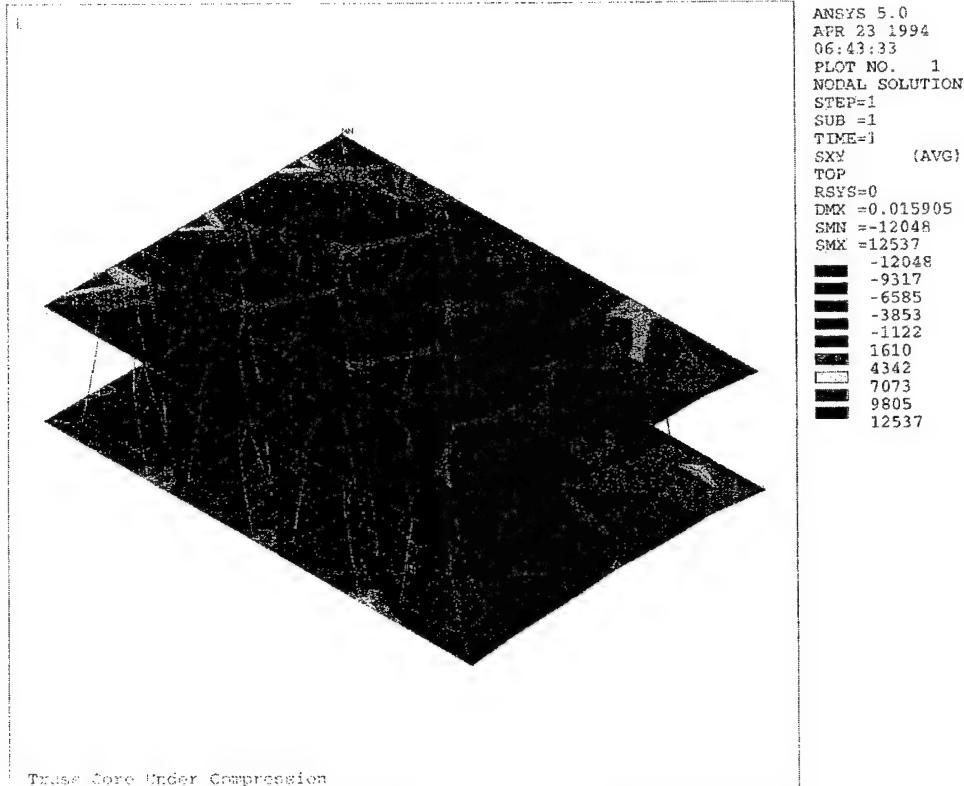


Figure 14.5. τ_{xy} Distribution for Z-Pin Sandwich Panel Under CAI

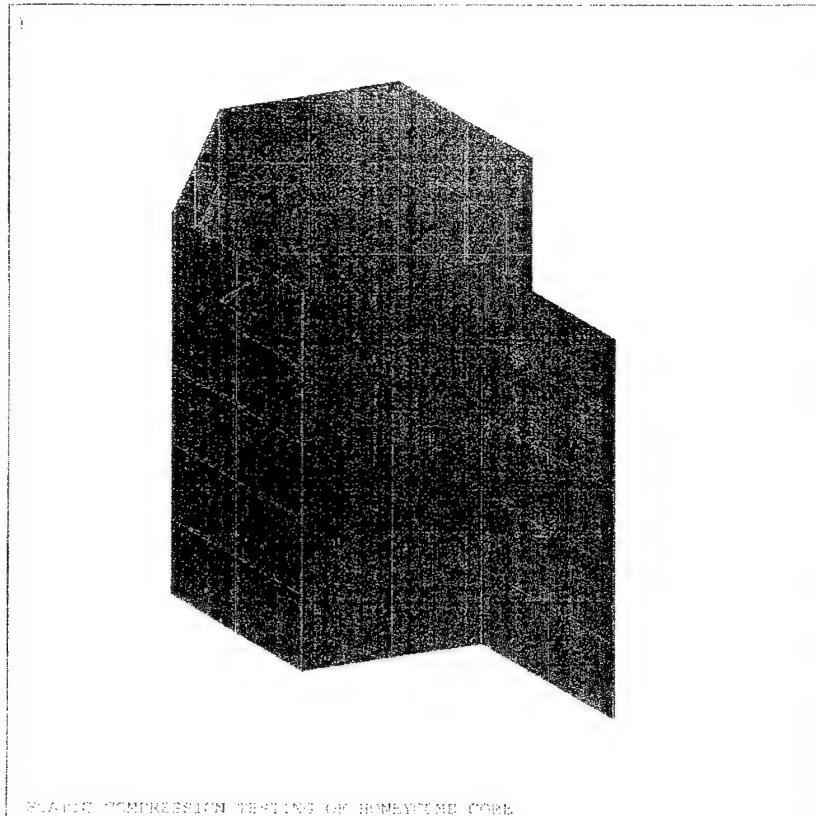


Figure 14.6. Unit Cell for Honeycomb Core

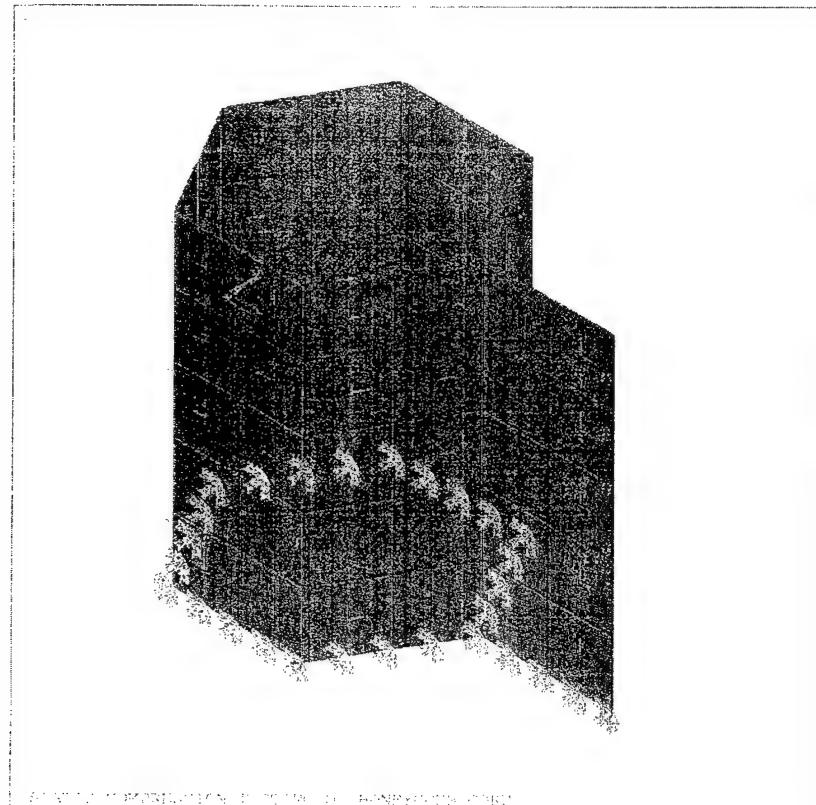


Figure 14.7. Unit Cell for Honeycomb Core Under constraints for Compression Loading

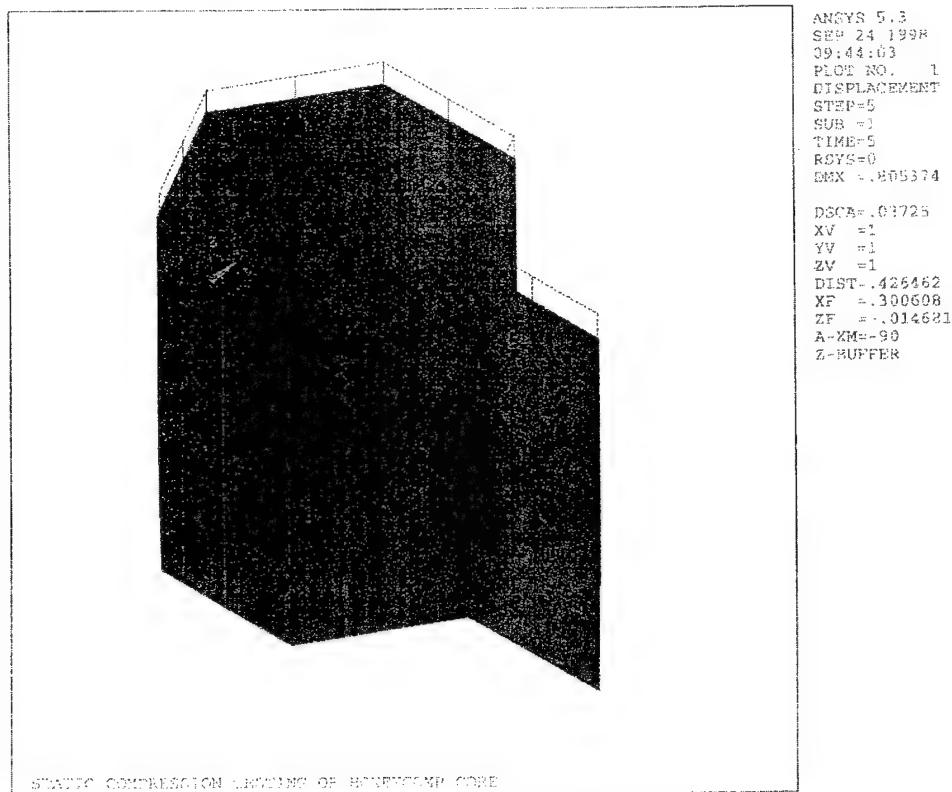


Figure 14.8. Z-Direction Displacement for Unit Cell Honeycomb Core under Compression

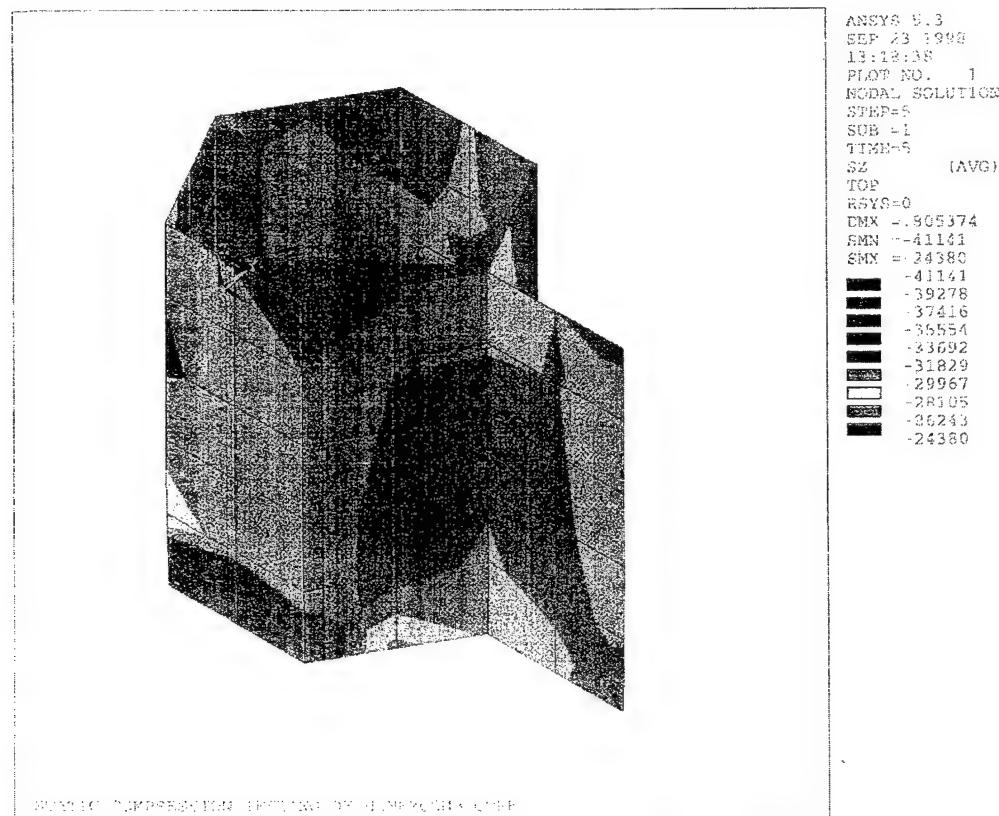
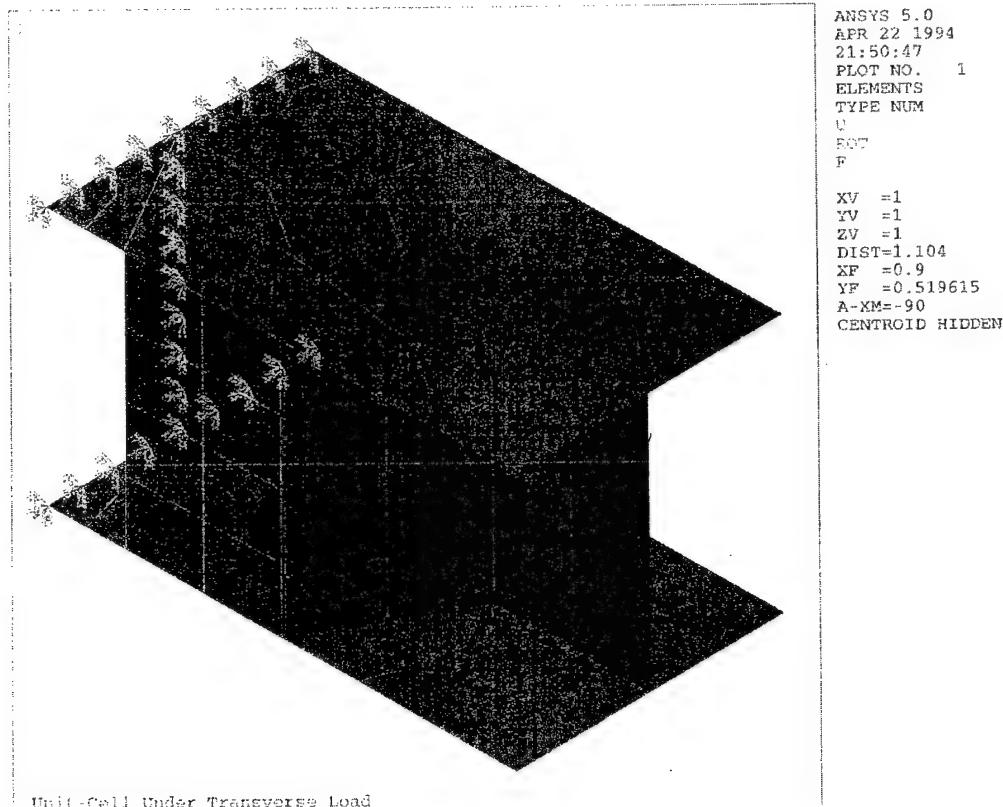
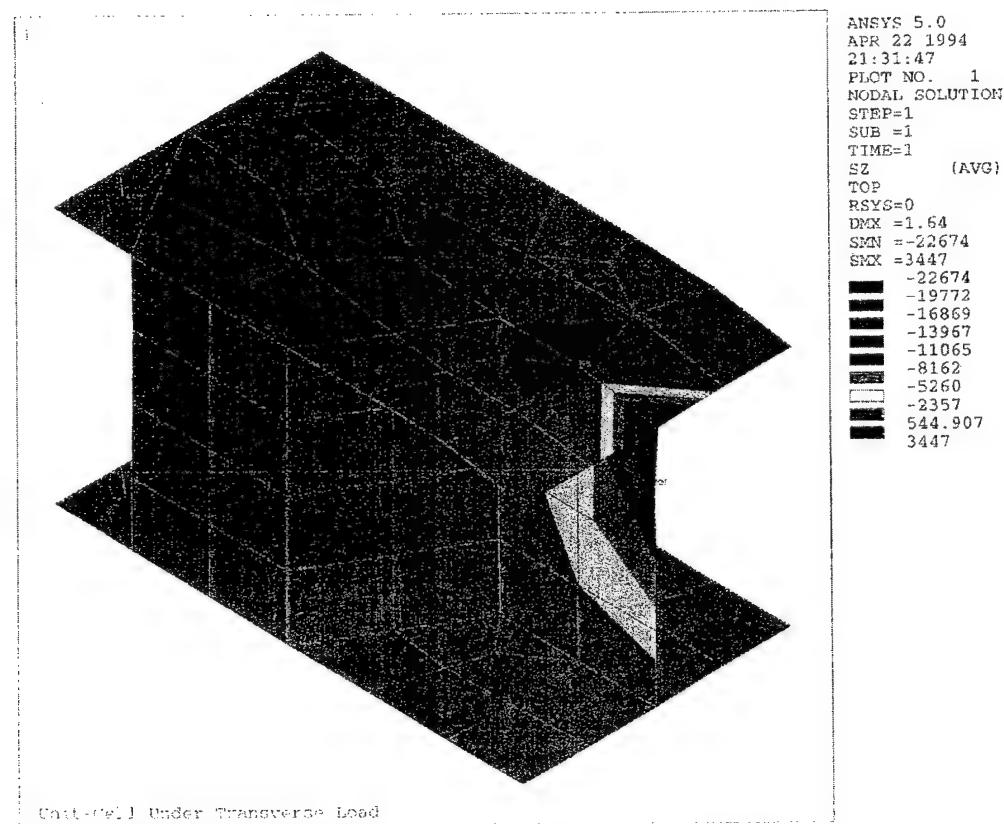


Figure 14.9. σ_z Distribution for Unit Cell Honeycomb Core under Compression



Unit-Cell Under Transverse Load

Figure 14.10. Unit Cell Honeycomb with Facesheets Under Constraints for Compression



Unit-Cell Under Transverse Load

Figure 14.11. σ_z Distribution for Unit Cell Honeycomb Core With Facesheets Under Compression

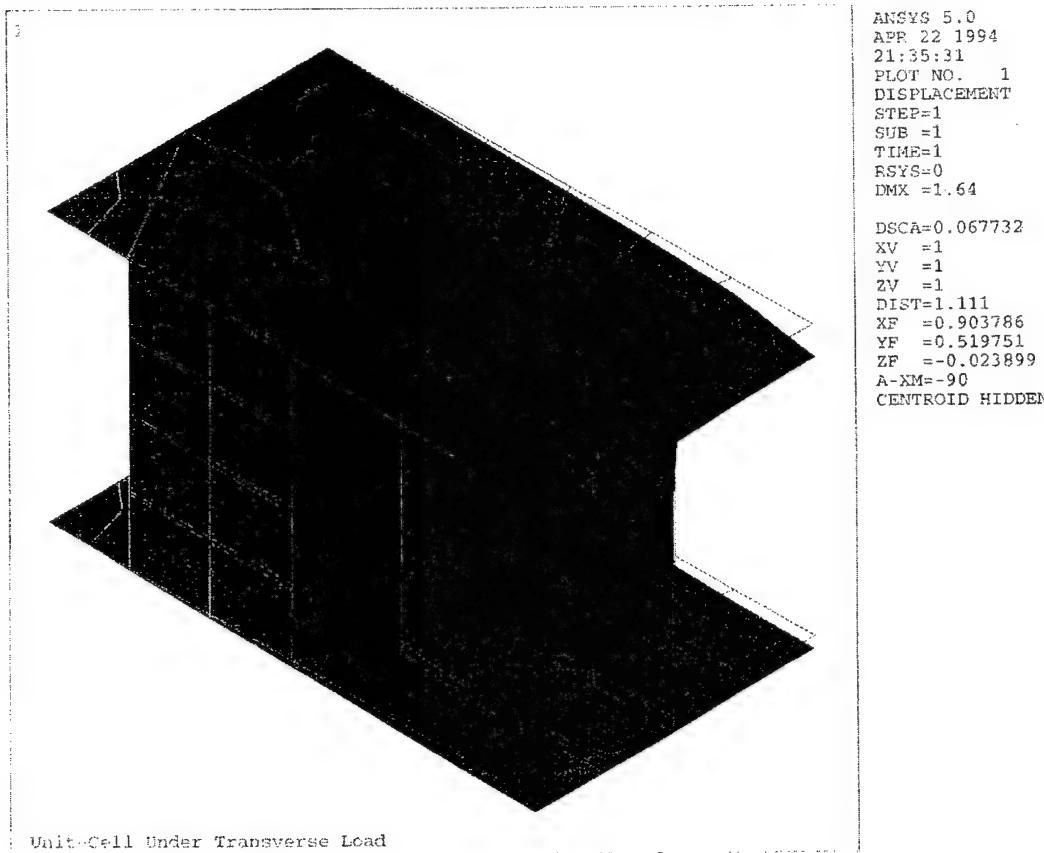


Figure 14.12. Z-Direction Displacement for Unit Cell Honeycomb With Facesheets Under Compression

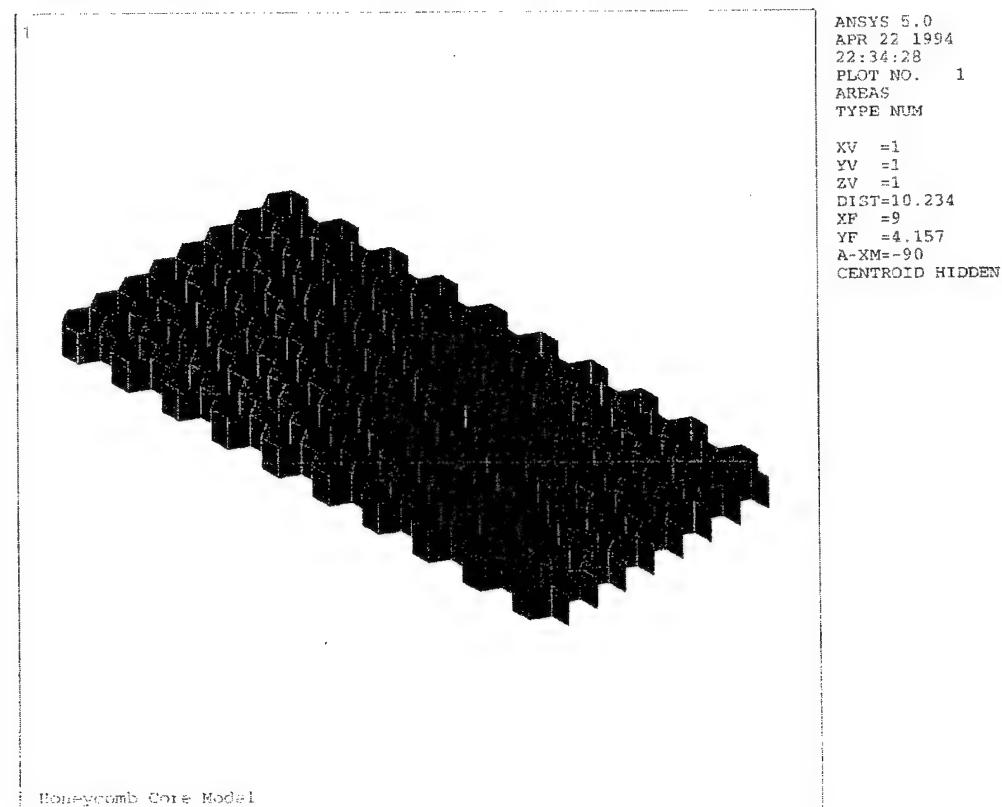


Figure 14.13. Honeycomb Core With Multiple Cell Model

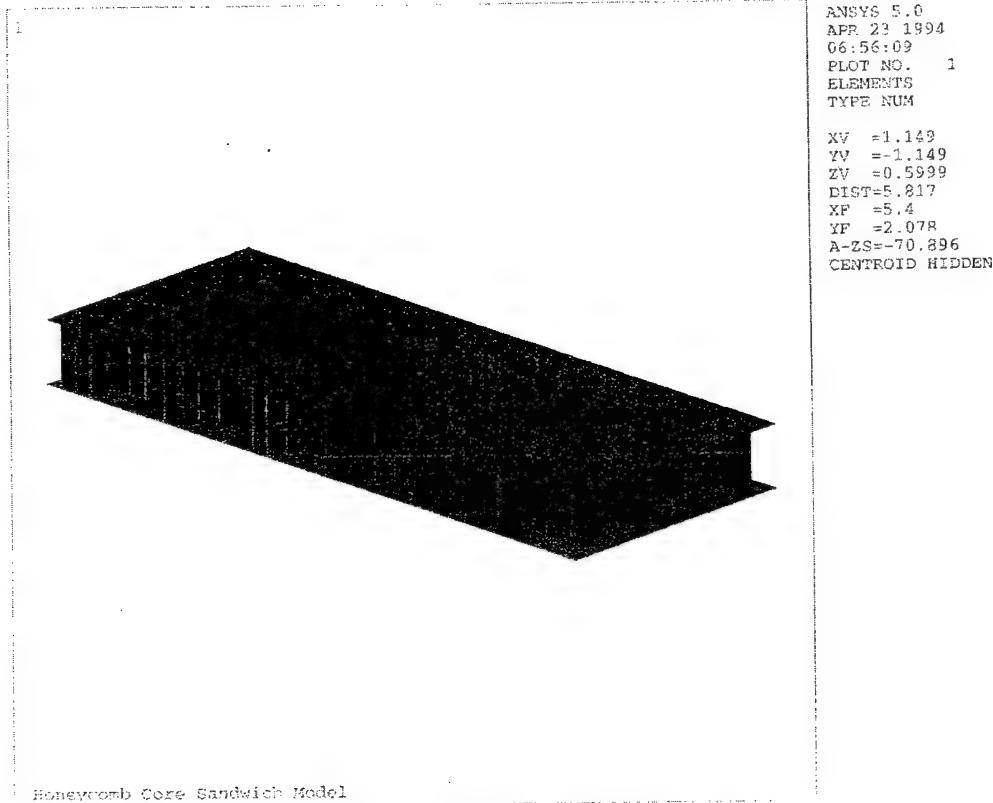


Figure 14.14. Honeycomb Core Sandwich Panel Model

are shown in Figure 14.15. It is a layered version of the 8-node structural solid (SOLID45) designed to model layered thick shells or solids. The element allows up to 100 different material layers. If more than 100 layers are required, a user input constitutive matrix option is available.

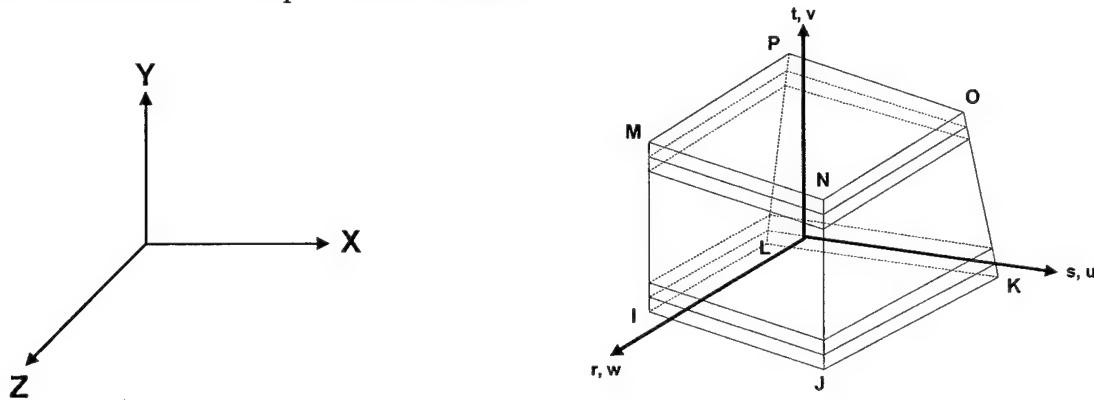


Figure 14.15 SOLID46 element with eight corner nodes (I-J-K-L-M-N-O-P)

The element may also be stacked as an alternative approach. The element is defined by eight nodes having three degrees of freedom at each node (translation in x, y and z directions), layer thicknesses, layer material direction angles, and orthotropic material properties. The material properties of each layer may be orthotropic in the plane of the element. The real constant MAT is used to define the layer material number instead of the element material number applied with the MAT command. The total number of layers is specified with the NL real constant.

The material properties of glass/epoxy were used to represent the facesheets. These were obtained from published literature. The material properties used in the present study are: $E_x = 3.618E6$ psi, $E_y = 1.399E6$ psi, $E_z = 0.957E6$ psi, $\nu_{xy} = 0.3$, $\nu_{yz} = 0.3$, $\nu_{xz} = 0.3$, $G_{xy} = 1.16E6$ psi, $G_{yz} = 0.53E6$ psi, $G_{xz} = 0.368E6$ psi, $\rho = 2.14E-03$ kg/cc. A 3-D large strain solid element - VISCO 107, was used to model the foam core. The element is designed to solve both isochoric (volume preserving) rate-independent and rate-dependent large strain plasticity problems. Iterative solution procedures are used with VISCO107, since it is used to represent highly non-linear behavior. The geometry, node locations, and the co-ordinate system for this element are shown in Figure 14.16. The element input data includes eight nodes having three degrees of freedom at each node (translation in x, y and z directions) and linear and non-linear material properties. The material properties of Rohacell foam grade IG-71 were used to model the foam core. The material properties used in the present study are: $E_x = 15.22E3$ psi and $\nu_{xy} = 0.0$.

The 3-D model is generated by solid modeling, sharing the keypoints between the facesheets and the foam core and thus maintaining the continuity between the nodes for different materials.

14.1.3.1 Transverse Compression Loading

Figure 14.17 represents the finite element model of the Rohacell foam core sandwich composite. The foam core is sandwiched between four layers of glass/epoxy facesheet on either side. Figure 14.18 represents the loading and constraints on the

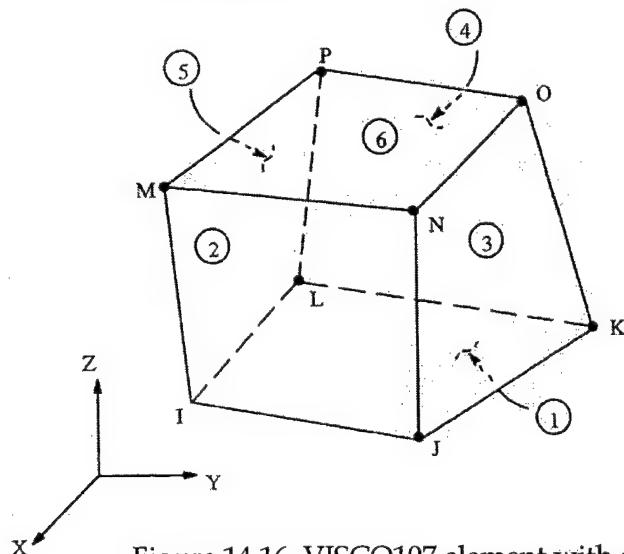
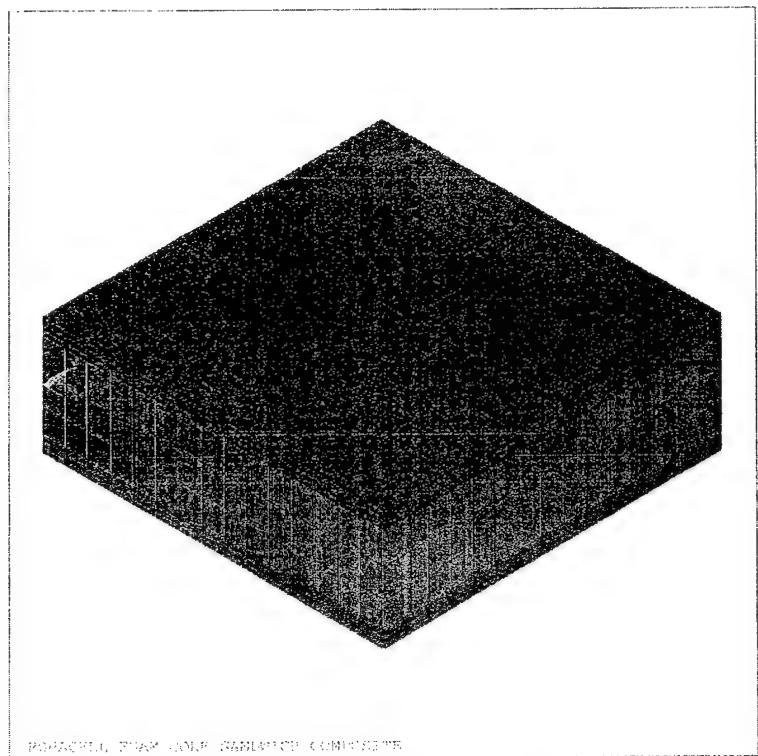


Figure 14.16 VISCO107 element with eight corner nodes (I-J-K-L-M-N-O-P)

model. The bottom facesheet is constrained and the top face sheet is loaded in time steps to simulate the experimental condition. Figure 14.19 represents the deformed finite element model. The facesheets are not affected notably, under the applied loading, whereas the foam core compresses linearly and substantially. The magnitude of core compression was found to be similar in the experimental and finite element studies. Figure 14.20 represents the total displacement in Z-direction (direction of loading), the colors on the right hand side indicate the corresponding magnitude of the displacement. Figures 14.21 and 14.22 represent the stress distribution in Z-direction and total strain in z-direction respectively. Figures 14.20-14.22 have been graphically represented in the Figures 14.23-14.25. Figure 14.23 indicates the deformation in Z-direction vs the thickness of the sandwich construction. Here the distance corresponds to the thickness of the sandwich composite. There is zero deformation at the bottom facesheets as it is constrained. Beyond the facesheet thickness, i.e., (after 0.1") at the location of the foam core, the deformation of the core is linear until 0.6" (the thickness of the core). The top facesheet is now located, and the deformation is seen to fall off to zero. This was found to be similar in the experimental work, where the damage was



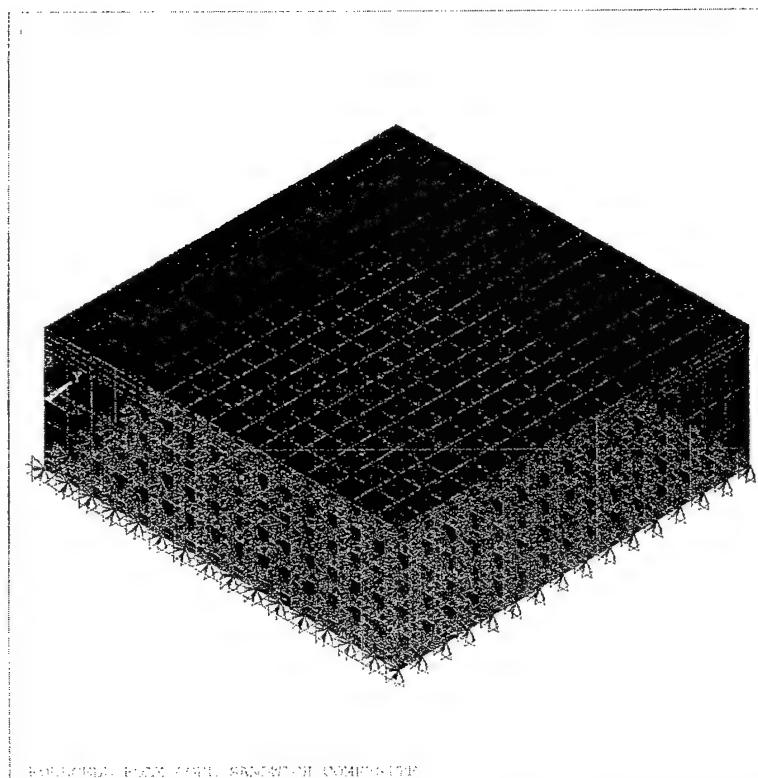
```

ANSYS 5.3
MAR 31 1999
17:11:03
PLOT NO.: 1
ELEMENTS
TYPE NUM

XV =1
YV =1
ZV =1
DIST=1.556
XF =1
YF =1
A-XM=-90
Z-BUFFER

```

Figure 14.17. Foam Core Sandwich Panel Model



```

ANSYS 5.3
MAR 31 1999
15:30:23
PLOT NO.: 1
ELEMENTS
FLUENCES
ETMNN:0
ETMX:0
U
PRES
1000

XV =1
YV =1
ZV =1
DIST=1.556
XF =1
YF =1
A-XM=-90
Z-BUFFER

```

Figure 14.18. Foam Core Sandwich Panel With Constraints.

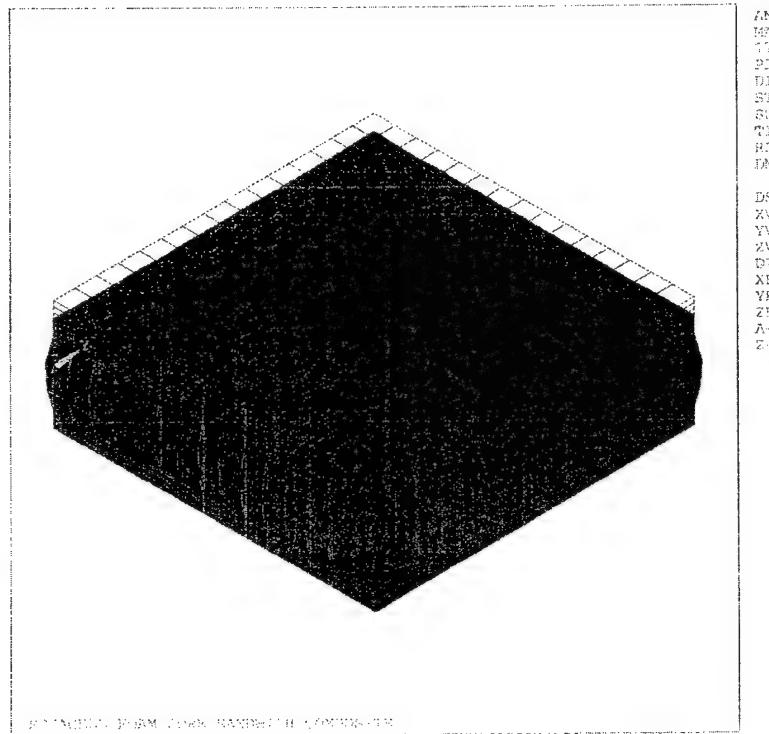


Figure 14.19. Deformed Foam Core Sandwich Panel Under Transverse Compression.

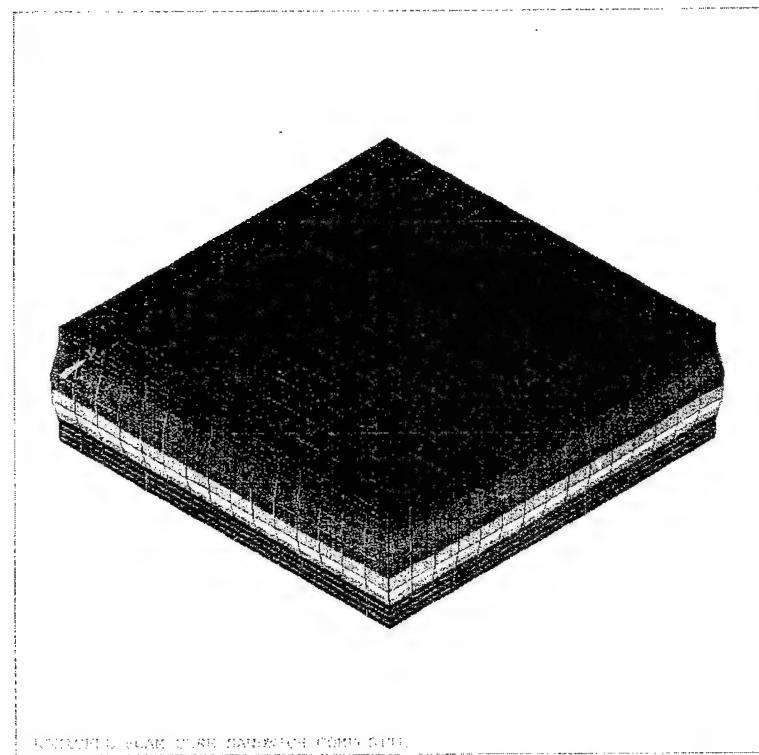


Figure 14.20. Z-Direction Displacement of Foam Core Sandwich Panel Under Transverse Compression.

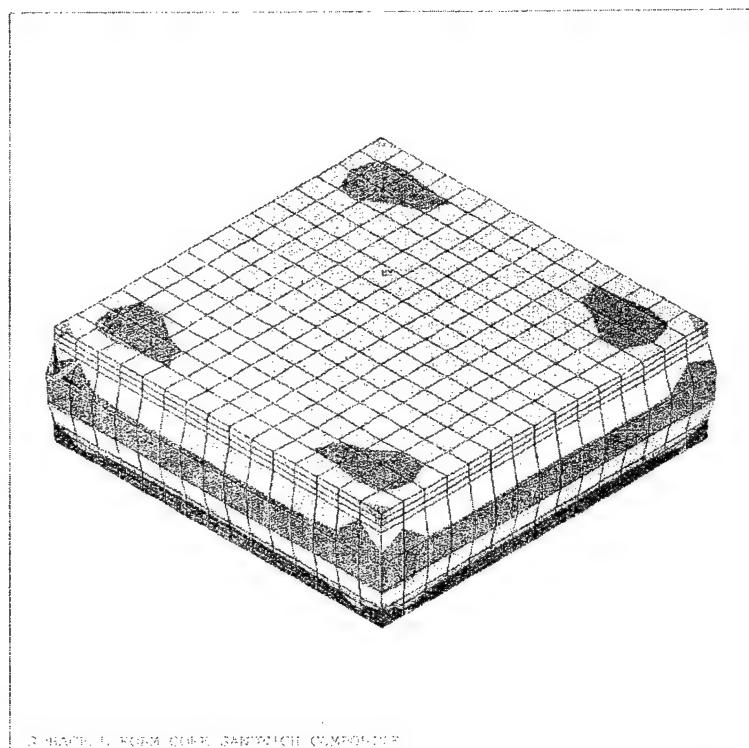


Figure 14.21. σ_z Distribution for Foam Core Sandwich Panel Under Transverse Compression.

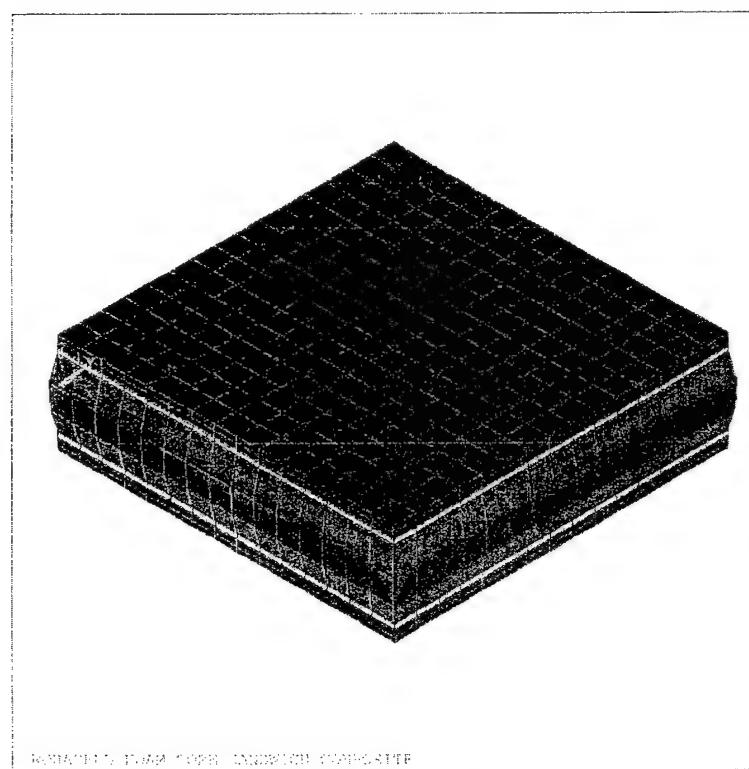
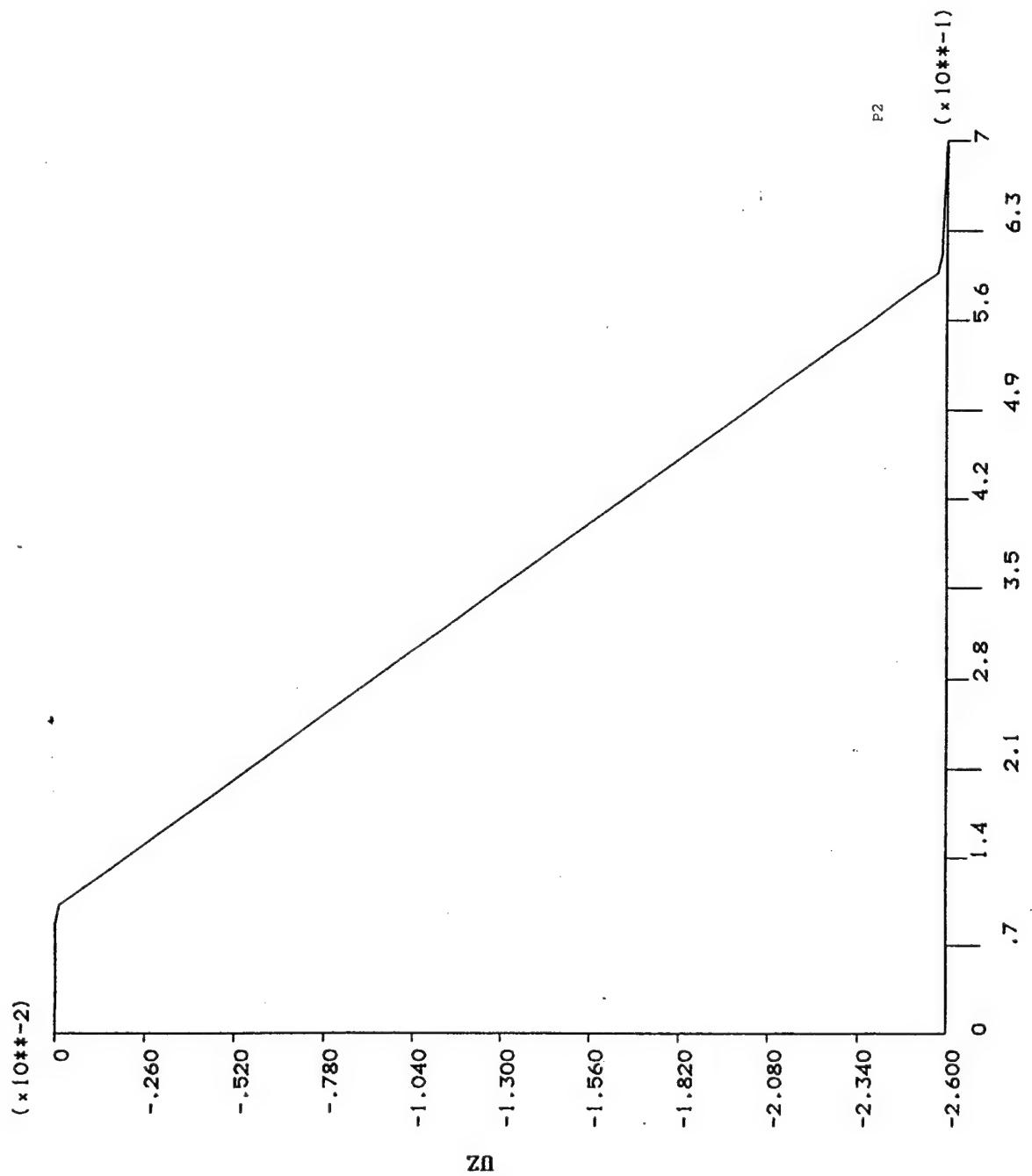


Figure 14.22. Total Strain in the z-Direction for the foam Core Sandwich Panel Under Transverse Compression.

ANSYS 5.3
SEP 23 1998
09:34:52
PLOT NO.
1
POST1
STEP=5
SUB =1
TIME=5
PATH PLOT
NOD1=81
NOD2=444

ZV =1.732
DIST=.75
XF =.5
YF =.5
ZF =.5
Z-BUFFER



DIST

Figure 14.23. Distribution of Z-Direction Displacement across the Foam Core Sandwich Panel thickness Under Transverse Compression.

ANSYS 5.3
SEP 23 1998
09:33:53
PLOT NO. 1

POST1
STEP=5
SUB =1
TIME=5
PATH PLOT
NOD1=81
NOD2=444

ZV =1.732
DIST=.75
XF =.5
YF =.5
ZF =.5
Z-BUFFER

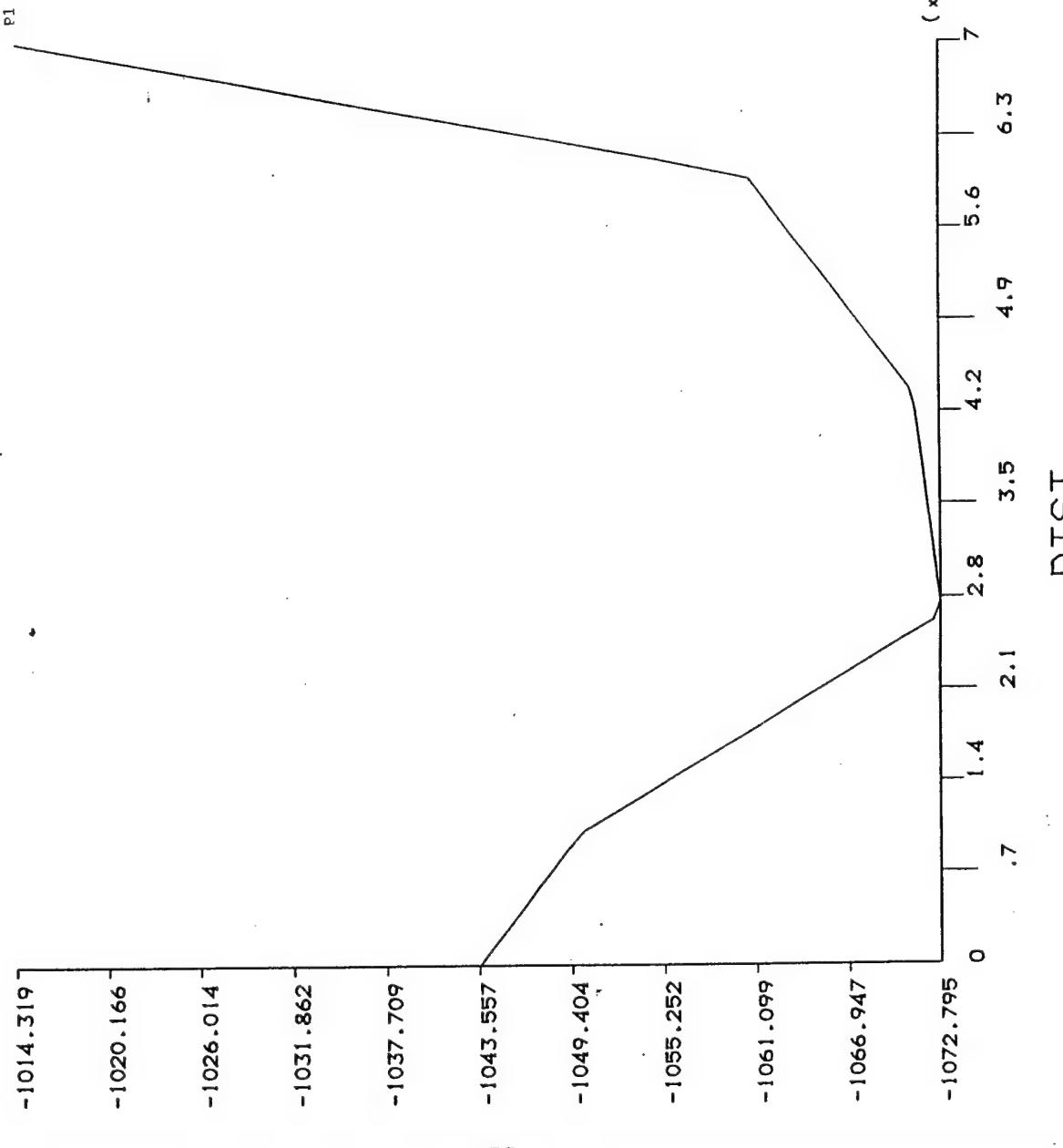


Figure 14.24. Distribution of σ_z across the Foam Core Sandwich Panel thickness Under Transverse Compression.

This Page Left Blank

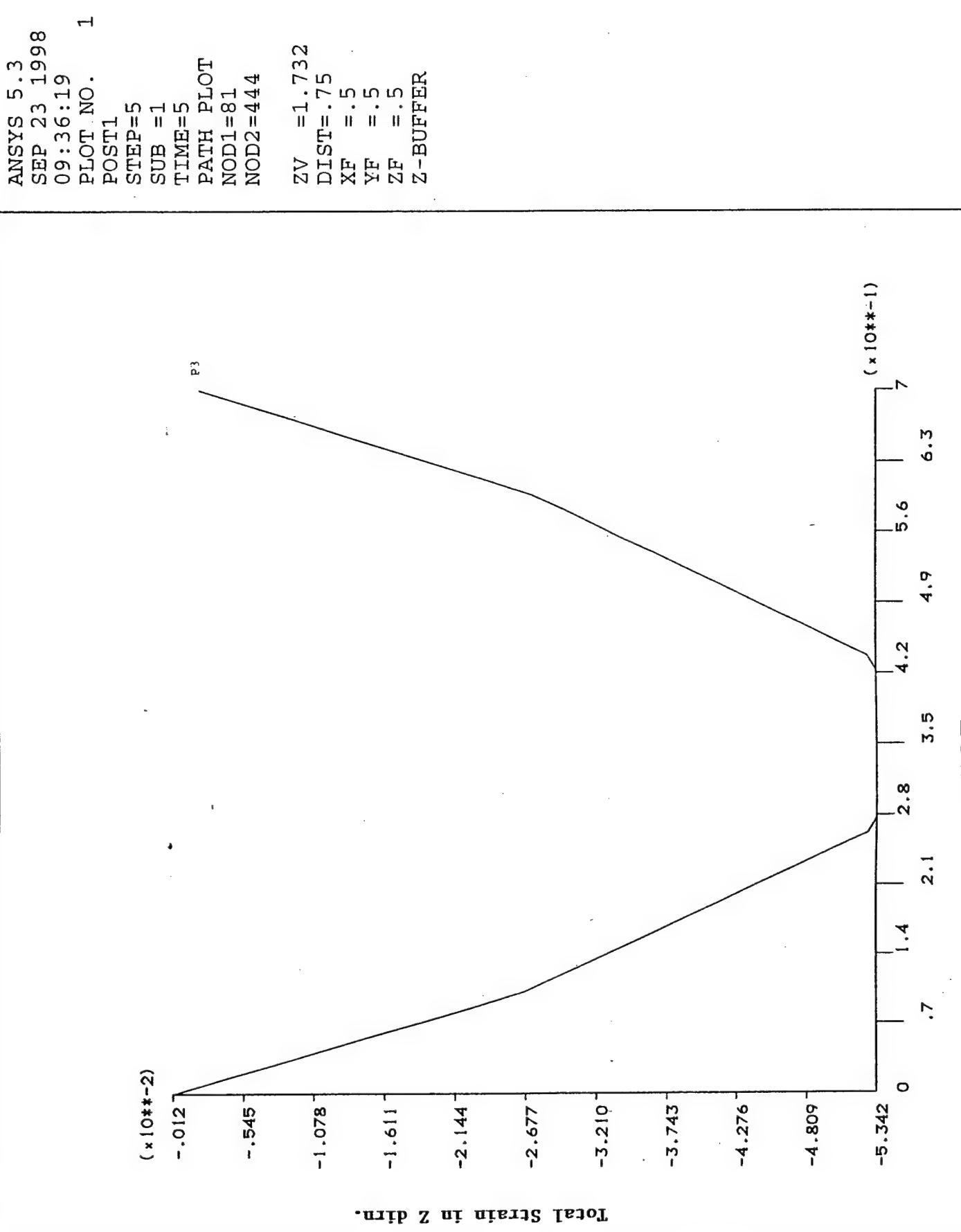


Figure 14.25. Distribution of Total Strain in the Z-Direction (Thickness) for the Sandwich Panel Under Transverse Compression.

primarily concentrated in the core. Figure 14.24 represents the stress in Z-direction vs the thickness of the sandwich construction. From the figure it is clear that the maximum stress is in the foam area which corresponds from 0.1 to 0.6 (thickness of foam core = 0.5) on the X-axis. Figure 14.25 indicates the total strain in Z-direction vs the thickness of the sandwich composite. The same explanation follows for this graph also.

14.1.3.2 Flexural Loading

Figure 14.26 represents the finite element model of the Rohacell foam core sandwich composite under static flexural loading. The specimen geometry was 9"X1.5", as adopted in the experimental tests. The foam core is sandwiched between 4 layers of glass/epoxy facesheet on either side. Figure 14.27 represents the loading and constraints on the FE model. A span length of 6" was chosen according to the experimental condition as well. All the nodes in the bottom facesheet at 1.5" from each end were constrained and the load was applied on the geometric center of the top facesheet. Figure 14.28 represents the deformed finite element model. The deformation was similar to that observed in the experimental setup. Figure 14.29 represents the total displacement in Z-direction (direction of loading). The maximum displacement was observed at the point of loading as expected. Figures 14.30 and 14.31 represent the stress distribution in Z-direction and total strain in z-direction respectively. From Fig. 14.30 it can be observed that the stress concentration is at the point of loading and at the support points (bottom facesheet). Also localized stress concentration was observed in the foam core below the loading points, and in the facesheet around the vicinity of loading. Figure 14.31 validates this fact, as we can see maximum strain occurring on the top facesheet and near the supports. Figures 14.29-14.31 have been graphically represented in the figures 14.32-14.34. Figure 14.32 indicates the deformation in Z-direction vs the thickness of the sandwich construction. Here the distance corresponds to the thickness of the sandwich composite. A slight deformation in the facesheets, although the foam core deformation is more predominant is noted. This was found to be the same in experimental work. Figure 14.33 indicates the stress in Z-direction i.e., thickness direction vs distance, taken at the point of loading. Here the distance corresponds to the thickness of the sandwich composite. From the figure it is clear that the maximum stress is in the location of the foam which corresponds from 0.1 to 0.6 (thickness of foam core = 0.5) on the X-axis. Figure 14.34 indicates the total strain in Z-direction vs the thickness of the sandwich composite. The same explanation follows for this graph also.

14.1.3.3 Low Velocity Impact

Figure 14.35 represents the FE model of the Rohacell foam core sandwich composite under low velocity impact. The specimen geometry was 4"X4"X0.7". The foam core was sandwiched between four layers of glass/epoxy facesheet on either side.

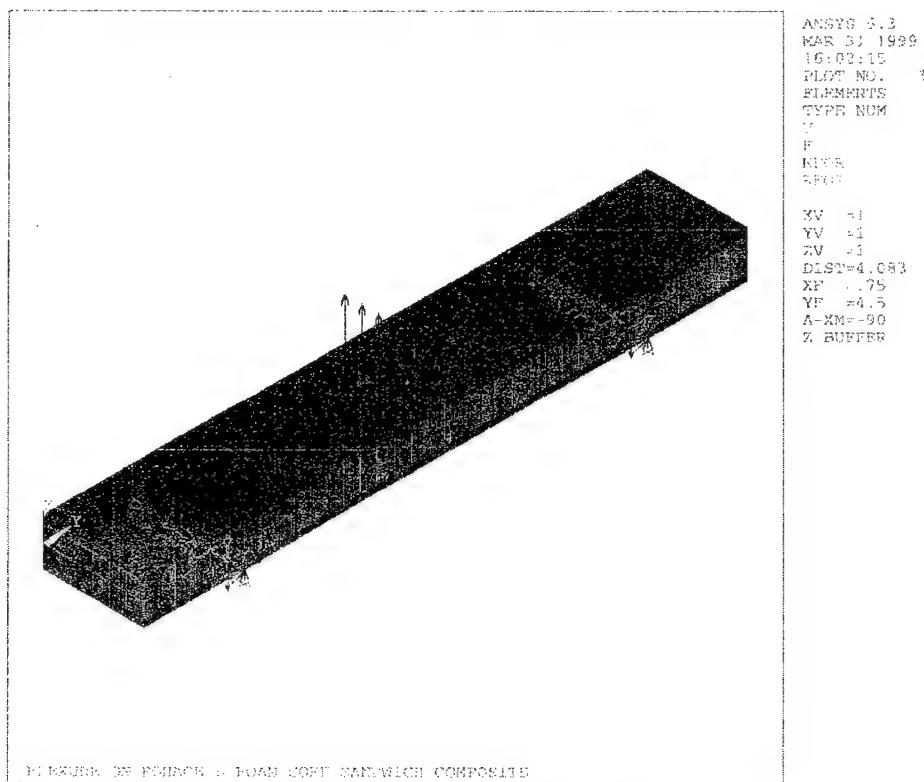


Figure 14.26. Foam Core Sandwich Panel Under Flexural Loading

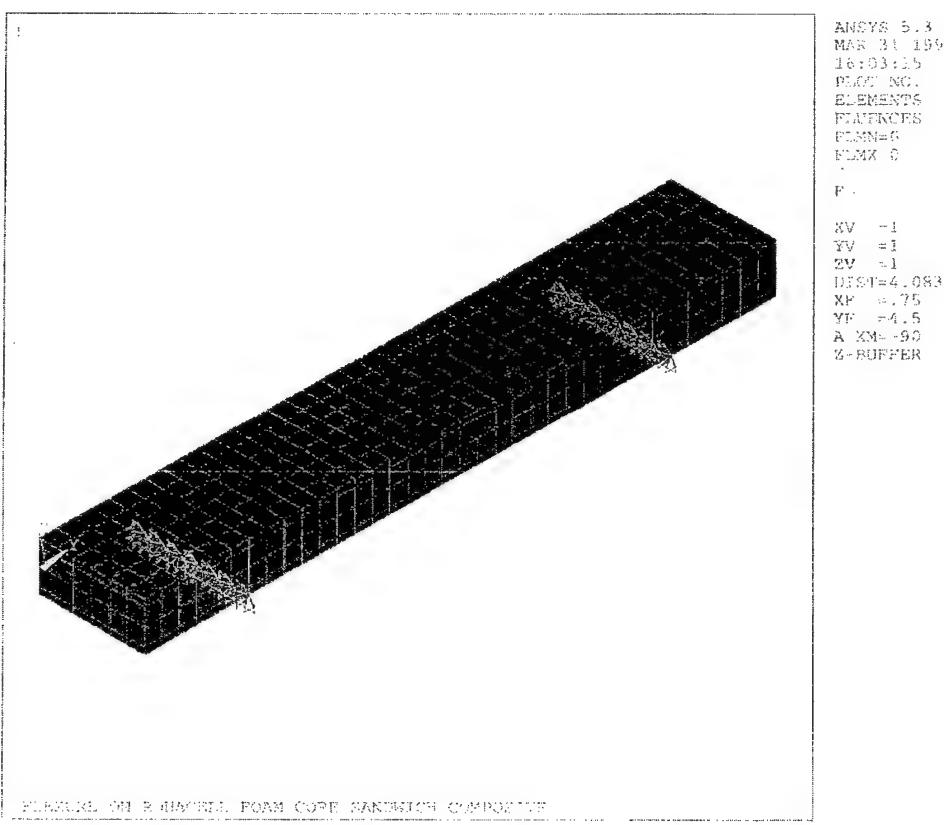


Figure 14.27. Loading and Constraints of Foam Core Sandwich Panel Under Flexure

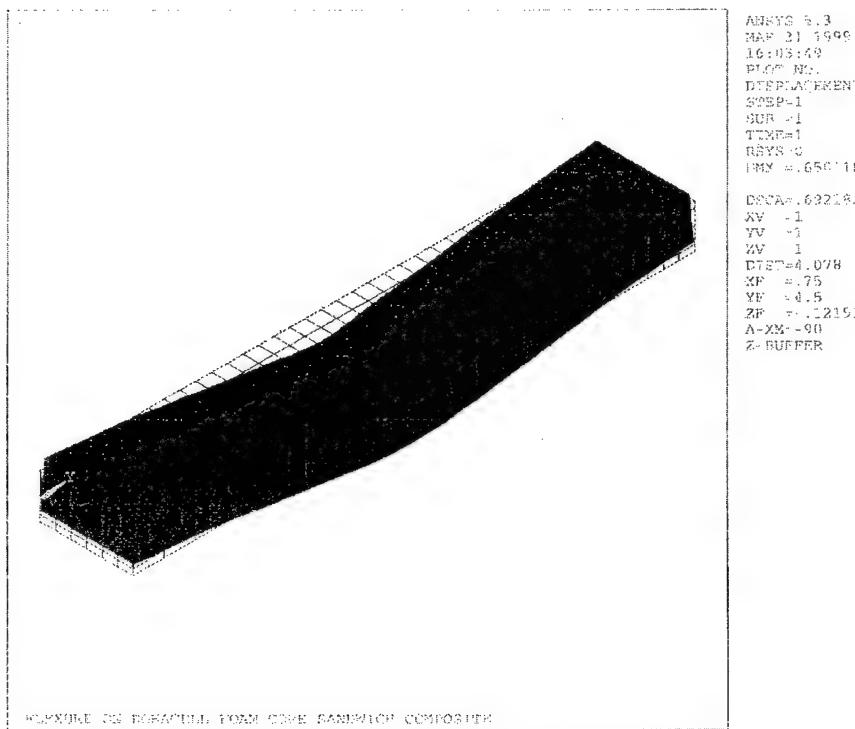


Figure 14.28. Deformed Foam Core Sandwich Panel Under Flexure

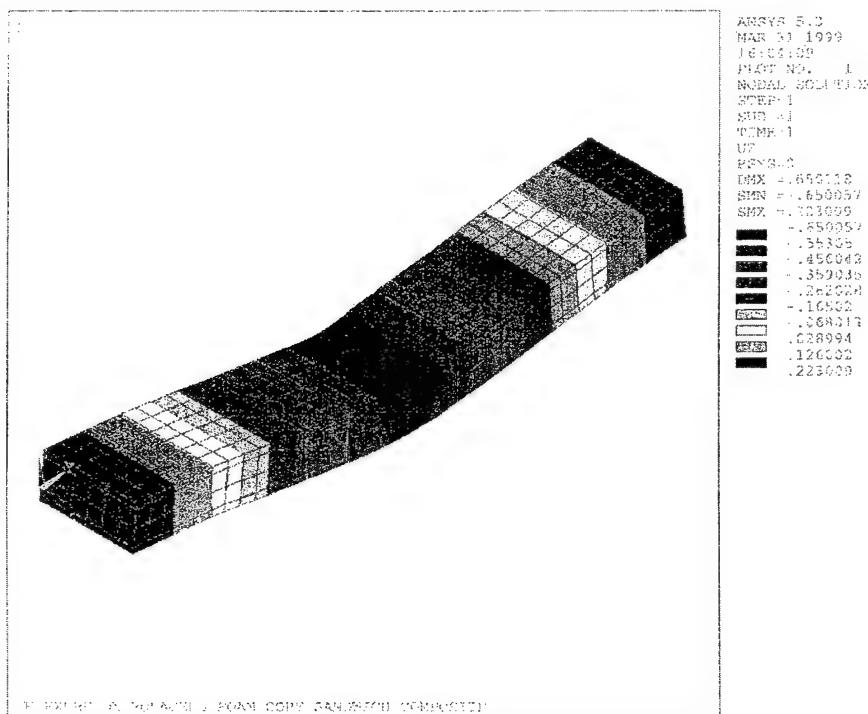


Figure 14.29. Distribution of Z- Direction Stress Under Flexure Loading of Foam Core Sandwich Panel

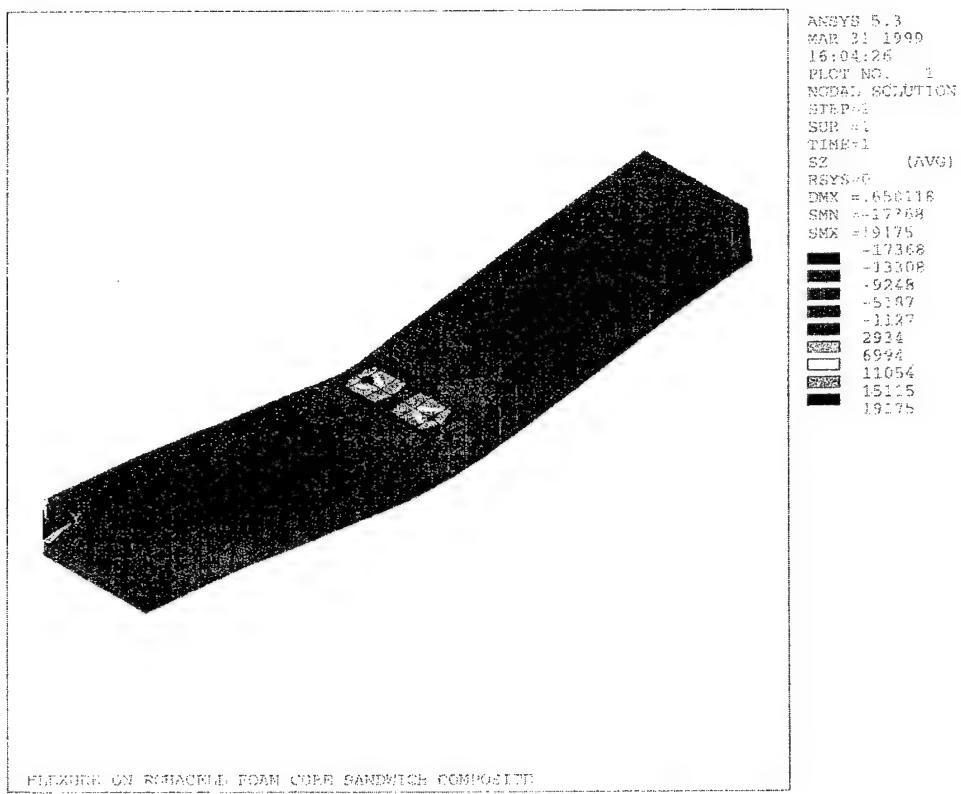


Figure 14.30. σ_z Distribution for Foam Core Sandwich Panel Under Flexure

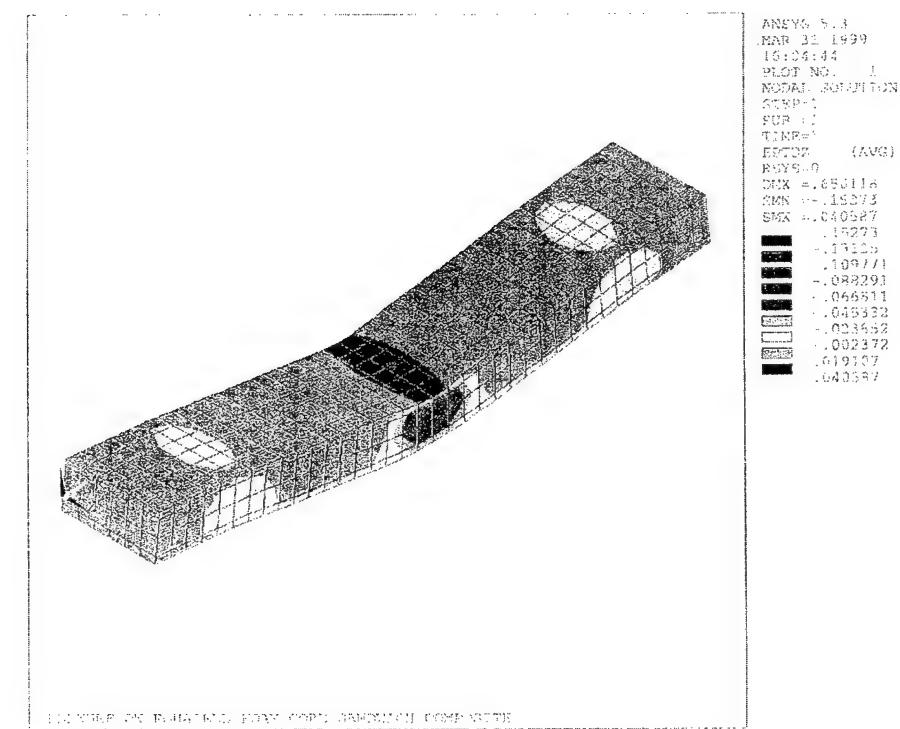


Figure 14.31. Total Strain in Z- Direction for Foam Core Sandwich Panel Under Flexure

```

1
ANSYS 5.3
SEP 25 1998
13:19:50
PLOT NO. 1
POST1
STEP=1
SUB =1
TIME=1
PATH PLOT
NOD1=114
NOD2=716
ZV =1.732
DIST=.75
XF =.5
YF =.5
ZF =.5
Z-BUFFER

```

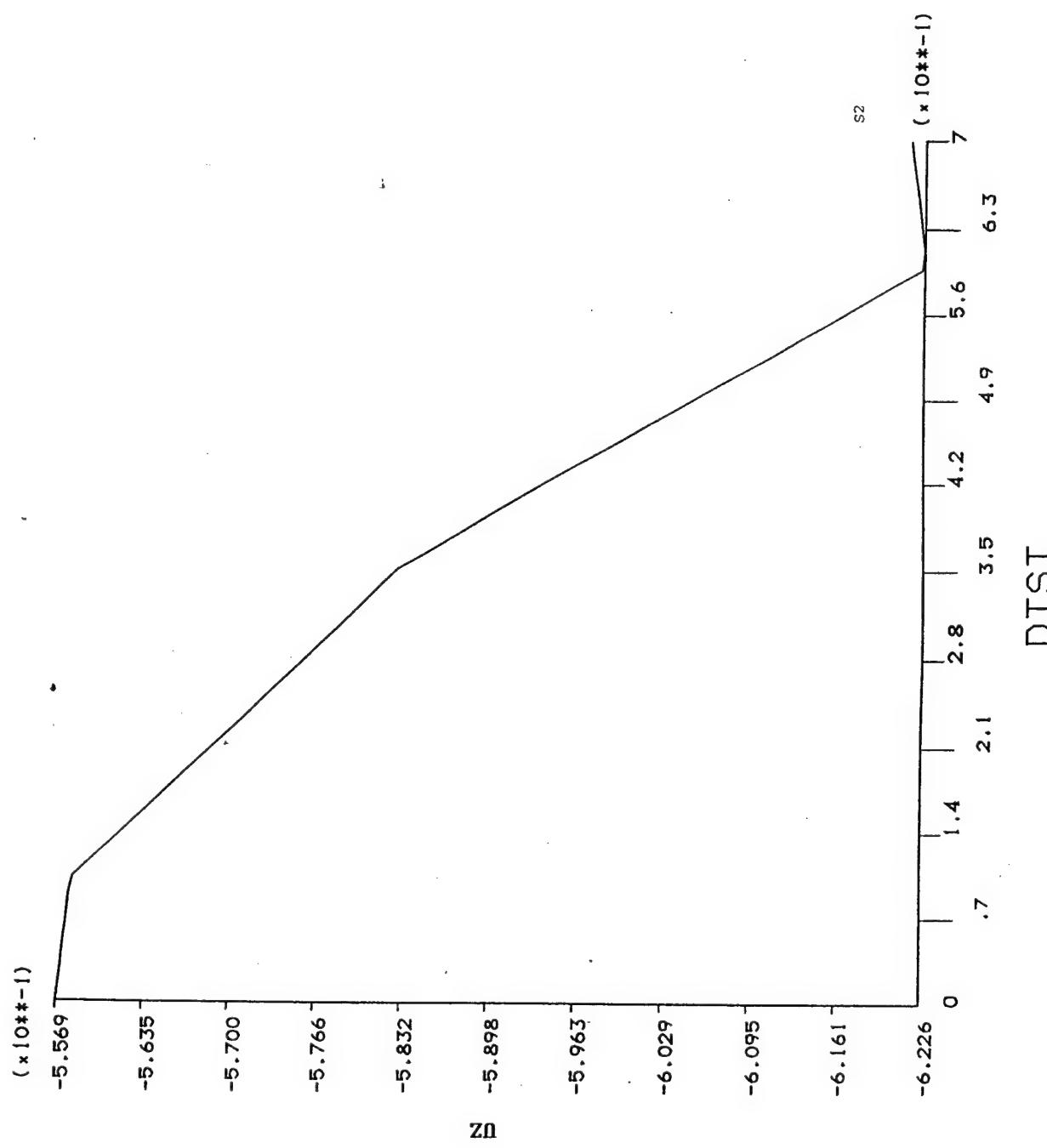


Figure 14.32. Distribution of Z-Direction Displacement across the Foam Core Sandwich Panel thickness Under Flexure

1
 ANSYS 5.3
 SEP 25 1998
 13:19:23
 PLOT NO. 1
 POST1
 STEP=1
 SUB =1
 TIME=1
 PATH PLOT
 NOD1=114
 NOD2=716

ZV =1.732
 DIST=.75
 XF =.5
 YF =.5
 ZF =.5
 Z-BUFFER

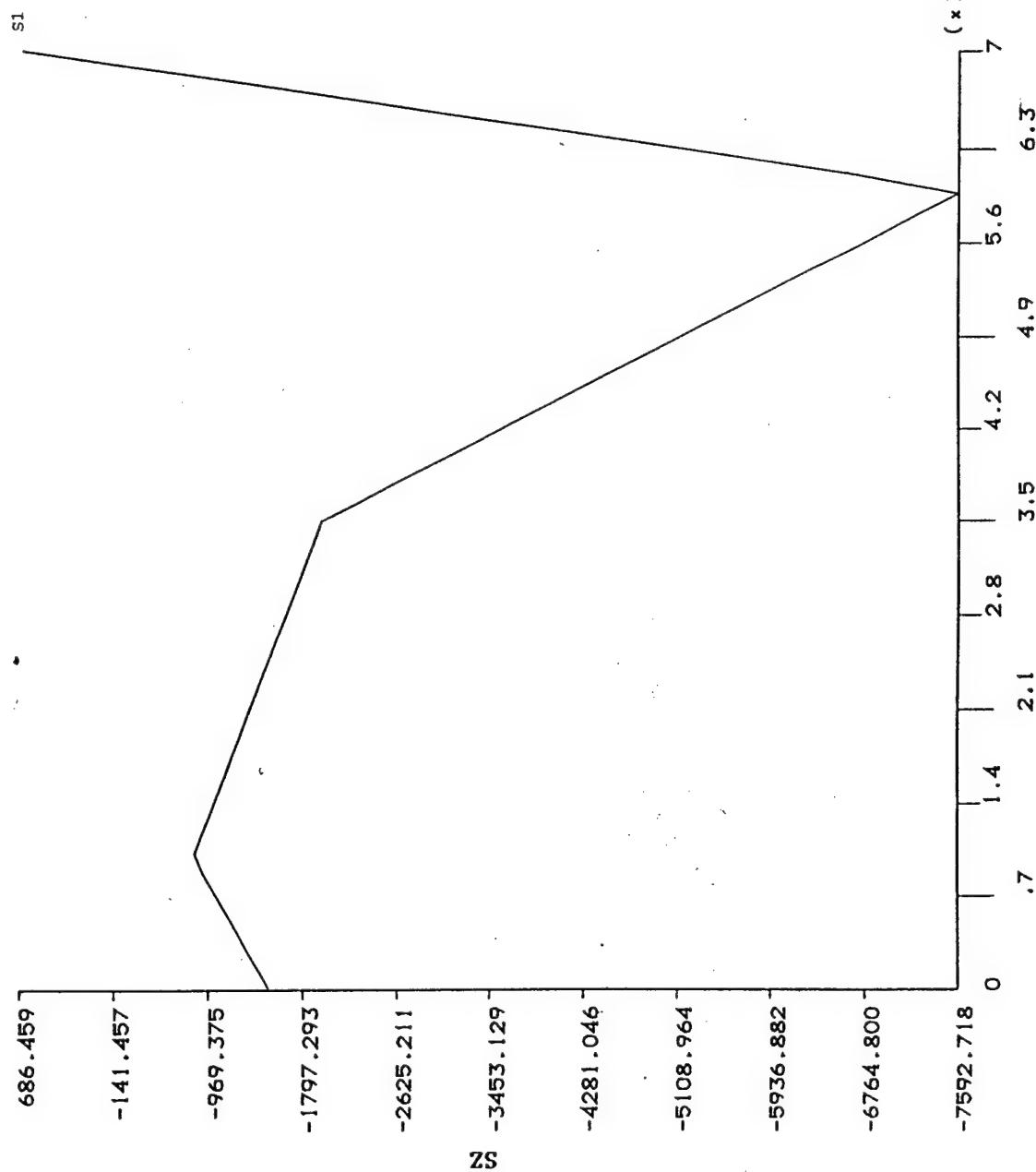


Figure 14.33. Distribution of σ_z across the Foam Core Sandwich Panel thickness Under Flexure

ANSYS 5.3
 SEP 25 1998
 13:20:23
 PLOT NO. 1
 POST1
 STEP=1
 SUB =1
 TIME=1
 PATH PLOT
 NOD1=114
 NOD2=716

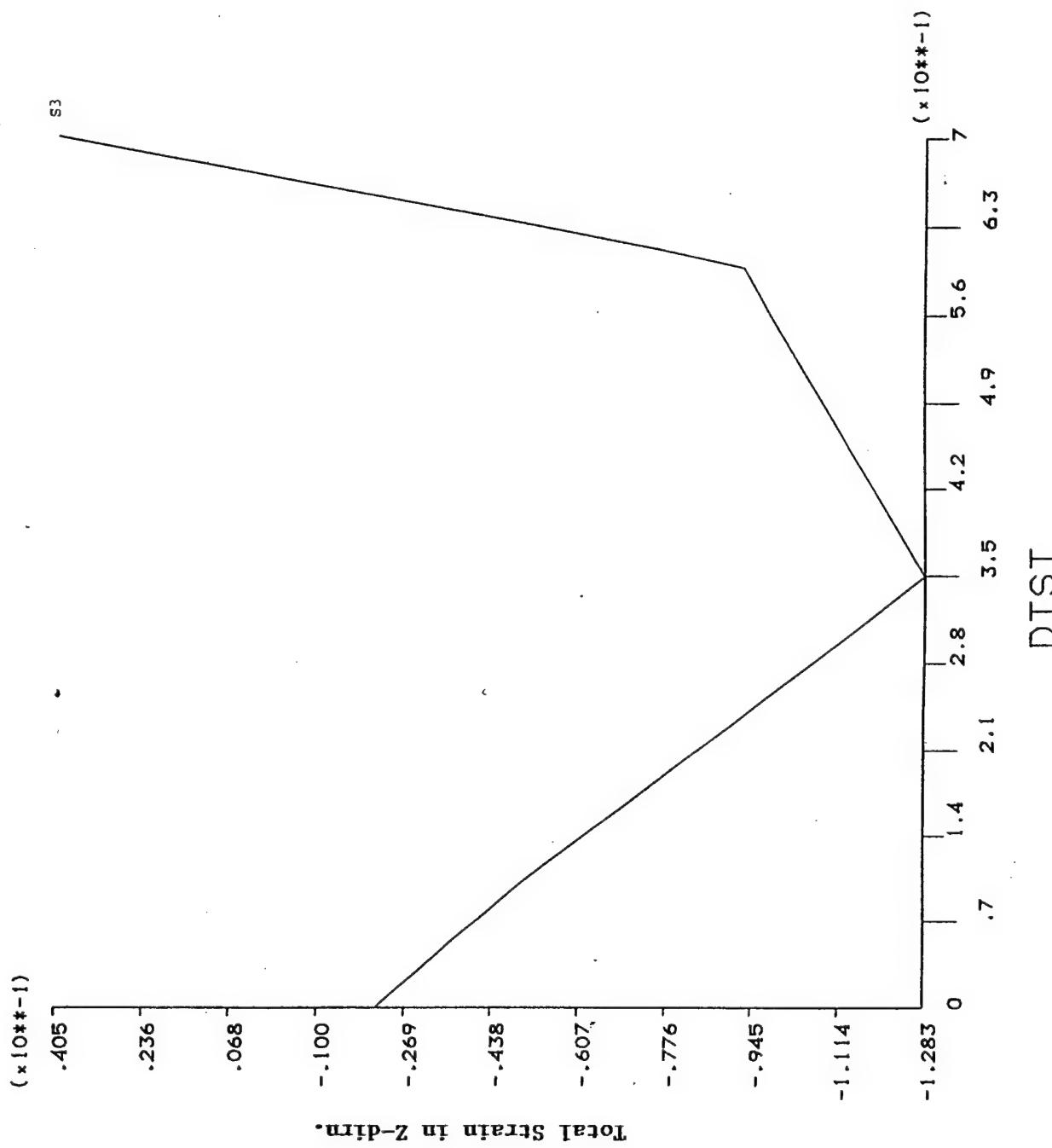


Figure 14.34. Distribution of Total Strain in the Z-Direction (Thickness) for the Sandwich Panel Under Flexure

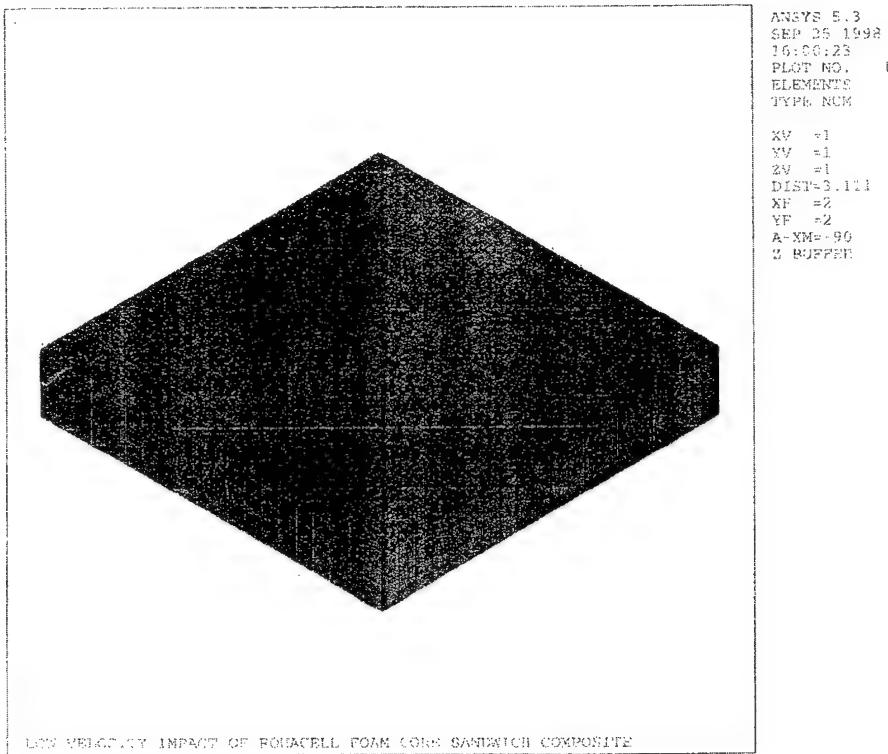


Figure 14.35. Foam Core Sandwich Panel Model for Low Velocity Impact

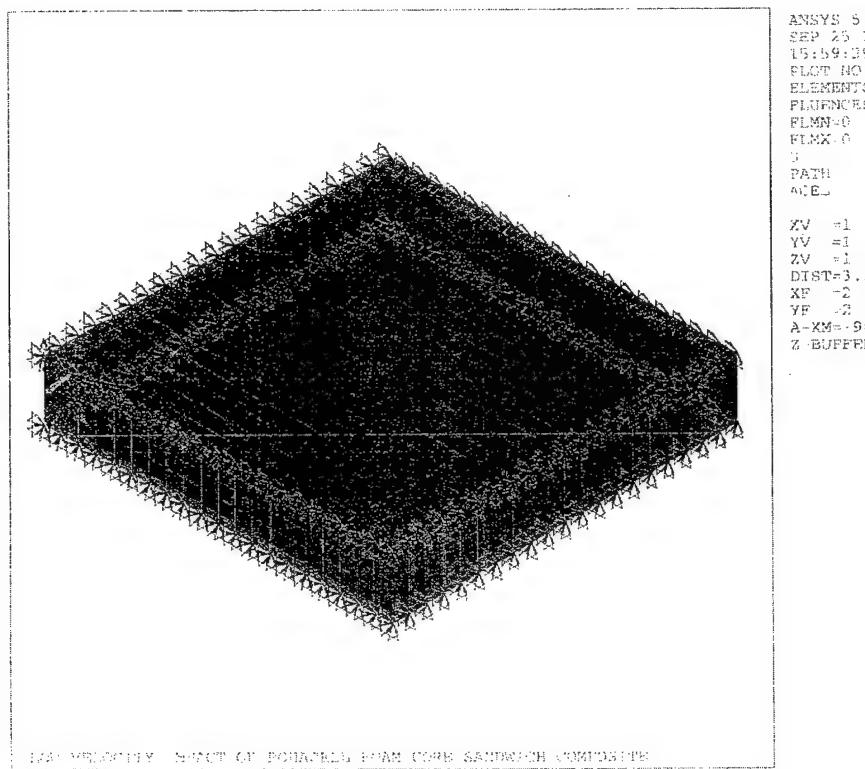


Figure 14.36. Constraints and Loading for Foam Core Sandwich Panel Under Low Velocity Impact

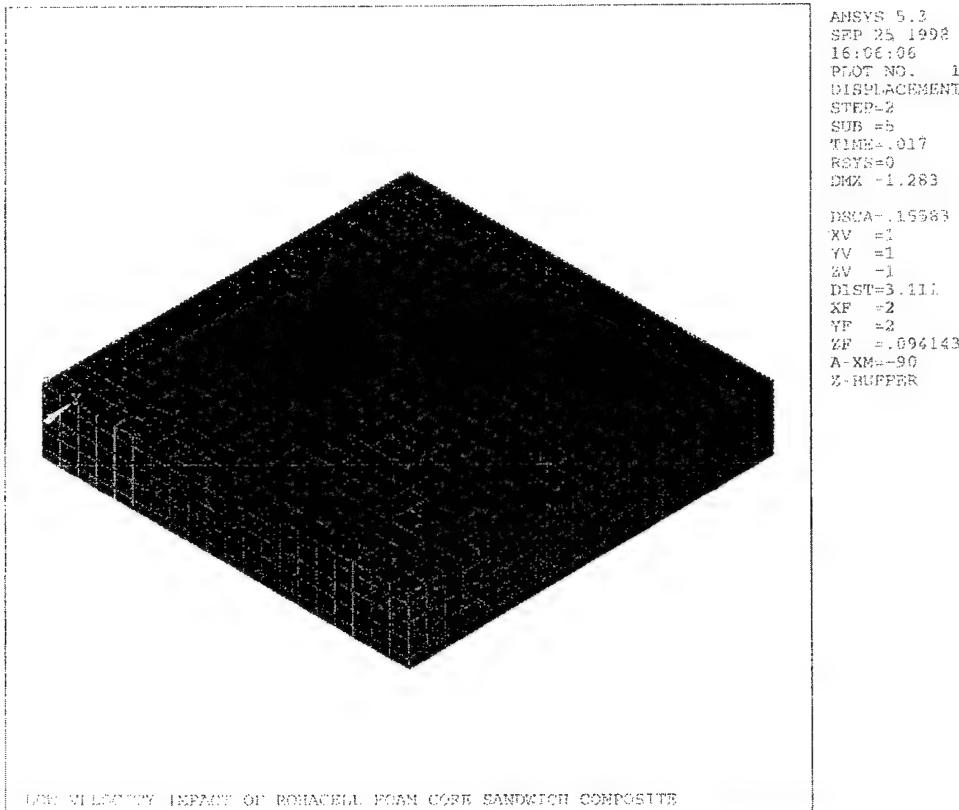


Figure 14.37. Deformed Foam Core Sandwich Panel Under Low Velocity Impact

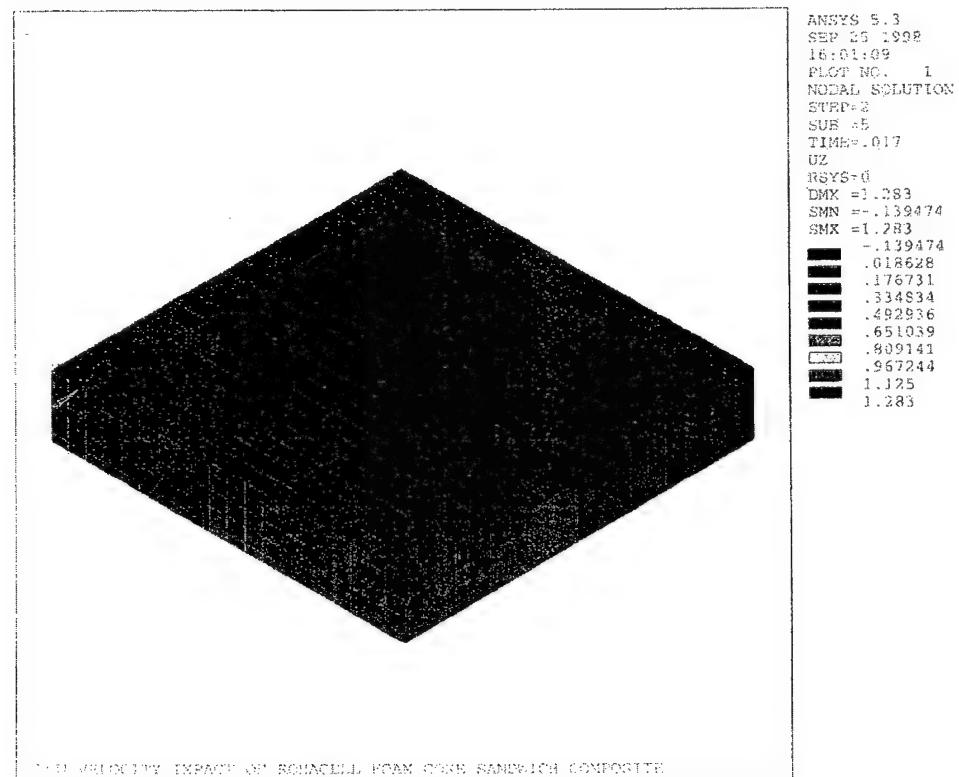


Figure 14.38. Displacement along Z-Direction for Foam Core Sandwich Panel Under Low Velocity Impact

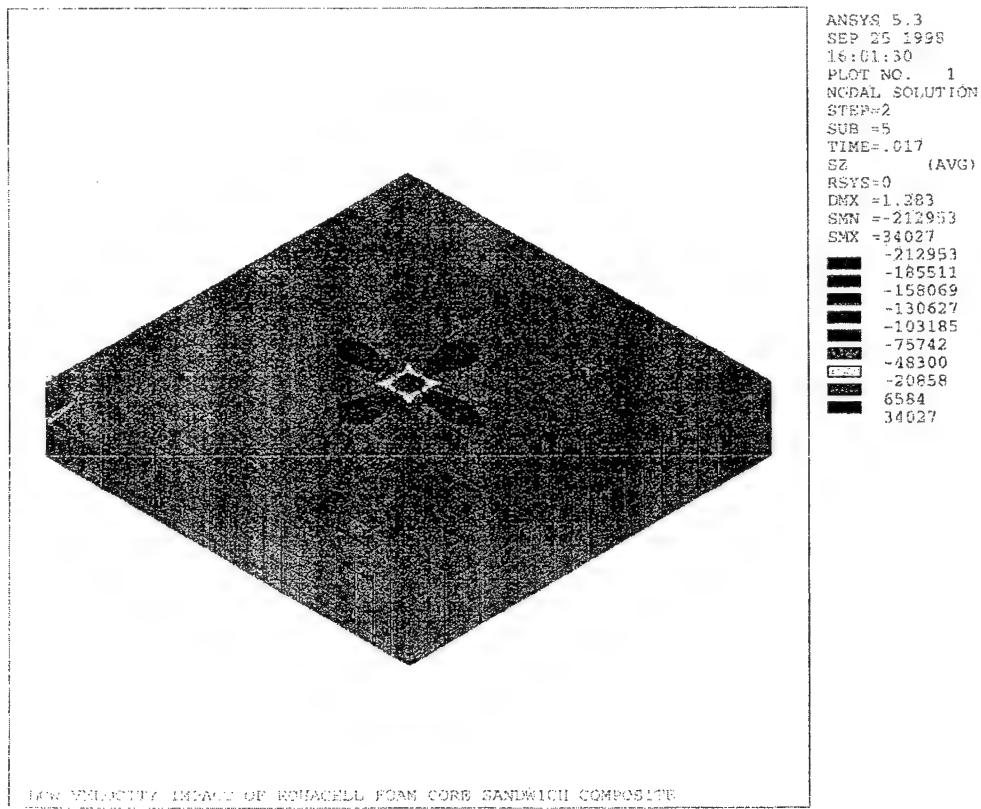


Figure 14.39. σ_z Distribution for Foam Core Sandwich Panel Under Low Velocity Impact.

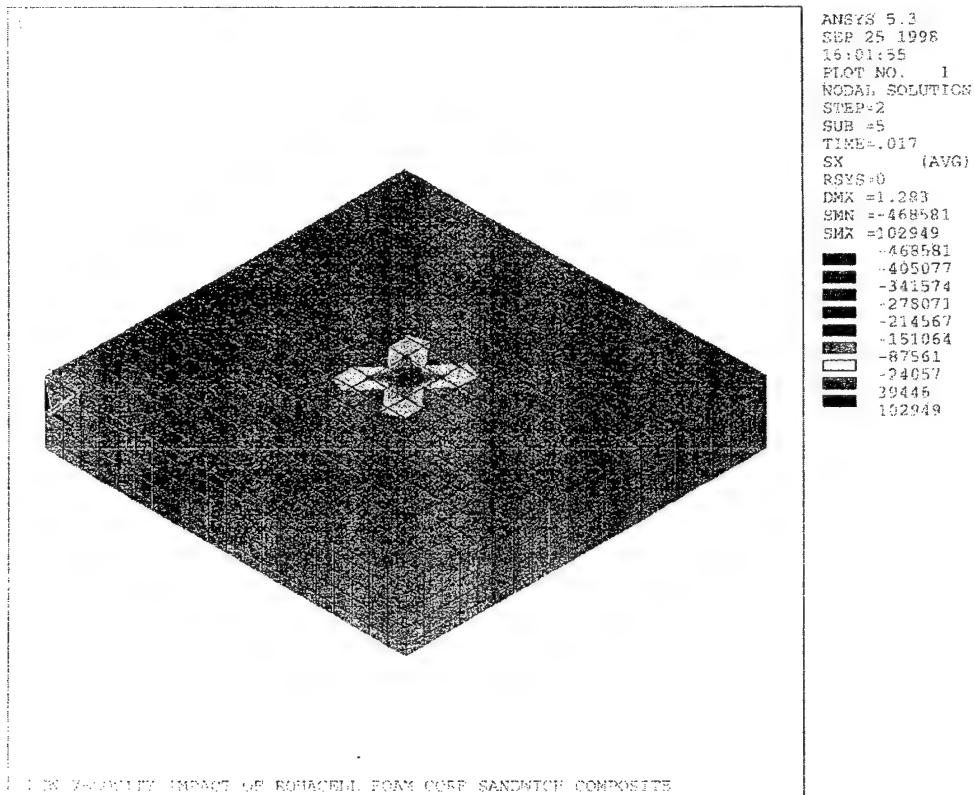


Figure 14.40. σ_x Distribution for Foam Core Sandwich Panel Under Low Velocity Impact

The element type of MASS21 was used to model the hemispherical tup. MASS21 in ANSYS is a point element having up to six degrees of freedom: translations in the nodal x, y and z directions and rotations about the nodal x, y and z axes. A different mass and rotary inertia may be assigned to each co-ordinate direction. The mass element is defined by a single node and concentrated mass components in the element co-ordinate directions. If the element requires only one mass input, it is assumed to act in all appropriate coordinate directions. Figure 14.36 represents the loading and constraints on the FE model. All the trailing edges were constrained and a velocity was given to the mass element to simulate the impact. The constraints were different in the experimental setup where we had the specimen pneumatically clamped in a circular support. Figure 14.37 represents the deformed finite element model. The deformation was similar to that observed in the experimental setup. At low velocities a micro-deformation in the facesheet and the core at the point of impact was noted. Figure 14.38 represents the total displacement in Z-direction (direction of loading). Figures 14.39 and 14.40 represent the stress distribution in Z-direction and X-direction respectively. In both the figures we can see stress concentration at the point of impact and in the vicinity around the point of impact. This was similar to that observed in the actual experiment. At the early stage of loading, the deformation of the facesheets, and subsequent stress concentration, was seen to develop the core crushing, pertaining to the foam core composites.

14.2 Summary/Conclusions

Simplistic FEM based models were developed to verify the loading conditions on foam, hollow-truss core and honeycomb core sandwich composites under transverse compression, compression-after-impact, flexure and low velocity impact. The results from the FEM studies agreed qualitatively to the observations in detailed experimental studies. Further work may be necessary to quantify the damage areas, stress magnitudes and other parameters of interest.

14.3 References

1. ANSYS Reference Manual, Version 5.3, Swanson Analysis, Inc. 1998.
2. Herup, E and Palazotto, A, " Low Velocity Impact Damage Initiation in Graphite/Epoxy/Nomex Honeycomb Sandwich Plates, Composites Science and Technology, Vol. 57, pp.1581-1598, 1997.

15. Overall Summary And Conclusions

This completed three-year effort addressed issues pertaining to damage tolerance, functionality and affordability of sandwich constructions with innovative core designs, that have applicability in aircraft and space vehicle technologies and other needs of Air Force structures. The results from the effort will benefit the science base in sandwich construction, and will benefit the Air Force efforts, for example in the FATE, TAFT, and other CAI programs/initiatives. The outcome of the program benefits both the research (science base in sandwich constructions) and educational (research training of African-American and other students) objectives.

Various sandwich cores were investigated in the program for enhanced damage resistance and affordable manufacturing. These included; foam, foam-filled-honeycomb, honeycomb, pin-reinforced foams, hybrid facesheet sandwich structures among others. Several innovative techniques for the manufacturing of the foam-reinforced pin core and truss core sandwich composites were developed in conjunction with traditional sandwich manufacturing techniques. Some of these included; vacuum assisted resin transfer molding (VARTM), closed-mold resin transfer molding, co-injection VARTM (economical and time-saving), vacuum assisted compression molding in producing the sandwich composites.

Detailed low velocity, static, high strain rate and intermediate velocity impact scenarios were considered in assessing these materials for their damage resistance/tolerance. Several advances were made in the evaluation of different cores and a vast gamut of data and information was generated for the evaluation. The important conclusions are summed below:

15.1 Low Velocity Impact Testing

Foam Core (Rohacell IG 71 Grade, 12.8 mm thick) Sandwich Composites

- The *Foam Core* sandwich composites show the first load drop at ~3000 N.
- The sample impacted at energy level A exhibits this load drop at 3.5 msec as compared to the other samples impacted at higher energy levels. This is because of the gradual elastic deformation of the foam cells at lower energy levels of impact.
- Damage initiated as core crushing across the facesheet/core interface.
- Facesheet damage was minimum. The core underwent a reduction in post-impact thickness due to significant foam cell closure.
- Increasing the facesheet thickness, increases the peak load sustained by the composite. However, the core crushing is much more severe as the inertial effects of a thicker facesheet are predominant.

The foam core composites exhibit lowest stiffness at lower energies of impact. This is because of a gradual elastic deformation of the foam cells at lower energies. At higher energies, the foam cells remain closed hence making the foam dense due to the impact event and the sandwich exhibits higher stiffness.

Innovative Core Sandwich Composites

Honeycomb-Filled-Foam Core (Kraft Paper Honeycomb Filled With Polyurethane Foam) Sandwich Composites

- The *Honeycomb-Filled-Foam Core* sandwich composites showed the first load drop at 5800 N for both the graphite as well as the S-2 glass facesheets confirming core damage as the initial failure mode.
- Damage initiated as facesheet/core disbond and was top facesheet dominated. However, bottom facesheet failure was initiated at higher energy levels of impact for the graphite facesheet composite (at 33J energy of impact).
- Core crushing and cell wall buckling were seen to be major modes of failure.

Impact damage is always top facesheet dominated, though at higher energy levels of impact, bottom facesheet damage is initiated. The bottom facesheet damage was initiated for the graphite facesheet specimen for the energy level D (33J). But the same was not seen for the S2-glass facesheet sandwich composite. Also, damage was more extensive for the graphite facesheet sandwich composite as compared to its S-2 glass facesheet counterpart. The most important observation was that for the same facesheet thickness, the glass facesheet composite exhibits greater damage resistance as compared to the graphite facesheet composite.

The first load drop occurs predictably at the same load for a given facesheet/core thickness. This is because damage initiation is a core related phenomenon and not a facesheet related phenomenon. In other words, damage initiation always occurs as core crushing and this was validated by optical microscopy. The load-time history also gives a good idea of the damage modes. A second major load drop can be directly related to bottom facesheet damage initiation or to pin-push-out, depending on the type of core being considered.

Foam-Reinforced-Pin Core (IG 71 Grade Rohacell Foam Reinforced With Titanium and E-glass/Epoxy Sandwich Composites

- The *Foam-Reinforced-Pin Core* sandwich composites showed the first load drop at ~2800 N which was about 7% lower than the *Foam Core* sandwich composites. This is because of the fact that the titanium pins piercing the facesheet initiate damage at a lower load as compared to the *Foam Core* sandwich composites.
- There was also some variation in the first load drop due to a variation in the position and orientation of the pins within the facesheet.
- The pins restricted damage progression and hence damage was found to be concentrated within the pin clusters.
- Core crushing and pin push-out were seen to be major modes of failure.
- A variation in the type of pin used for reinforcement (E-Glass pins of 1.9 mm. diameter were used) may vary the incipient load but the damage mode remains largely unaffected.
- An increase in the distance between the pin clusters changes the mode of failure from a shear dominated one for closer spacing of pins to a flexure dominated one for wider spacing of pins.

Truss Core (Titanium Pins Of Diameter 1.14 mm.) Sandwich Composites

- The first load drop for the *Truss Core* sandwich composites was seen at ~ 2300 N.
- There is some variation in the first load drop because of the variation in the position and the orientation of the pins.
- Also, the absence of foam in the core affects the damage modes and pin buckling is an additional mode of failure seen in these composites.
- Damage in the facesheet and core was seen to be more extensive as compared to the other composites and the samples displayed the lowest post-impact properties.

There is a slight variation in the first load drop for the foam-reinforced-pin core and truss core sandwich composites. This is due to a variation in the position and orientation of the pins within the core and the facesheet. However, this variation is within a small load range and can be further minimised by increasing the pin spacing and/or increasing the facesheet thickness or by changing the fiber architecture. The increase in pin spacing increases the maximum load for the foam-reinforced-pin core sandwich composite. This is because the pin reinforcement stiffens the sandwich composite, while an increase in the distance between the pin clusters within the foam decreases the facesheet damage due to pin piercing in the virgin samples. The honeycomb core show maximum loads much higher than the innovative cores because of the highest transverse compressive strength that it possesses. However, it is not a viable core option as it poses fabrication challenges due to resin pooling in the hollow cells. Also the honeycomb core shows catastrophic buckling instability at higher impact levels which is not seen for the other innovative cores.

The above mentioned behavior of the force/energy-time history is definitely a characteristic of the respective cores. The behavior was found to be independent of the manufacturing technique and the pin type used. Though these factors may influence the overall strength of the composite and subsequently, the extent of damage, the force/energy - time histories follow similar trends.

The C-scan technique validated that the damage area increases with the energy level of impact. A literature review of relevant material showed that this increase of damage area was proportional to the energy of impact.

The facesheet damage was in the form of localized fiber breakage and flexural cum shear failure at the location of the impact. Core crushing, accompanied by cell wall crushing and buckling was observed to be a major mode of failure for the honeycomb-filled-foam core sandwich composite. Facesheet damage is minimum for the foam core composites as damage occurs as core crushing extending across the top facesheet/core interface. The pin reinforcement restricts damage progression beyond the pin dimensions. Though facesheet damage for the foam-reinforced-pin core composite is more extensive as compared to the foam core composite at identical impact levels, this damage is highly localised between pin clusters. The same is observed for the truss core composites. At higher energy levels, pin pushout is a major mode of failure, but this also depends on the location of impact at or near a pin cluster. This may be minimised by increasing the facesheet thickness or by toughening the facesheet. Pin buckling is a special and major mode of failure seen in the truss core composite. This occurs due to the fact that the foam and pins offer stability to each other. The absence of either element can lead to either extensive foam crushing or pin buckling due to concentrated impact or compressive force.

The influence of the manufacturing technique and the pin type does influence the strength and extent of damage due to the impact event, but the composite as such follows similar trends. There is a loss of stiffness in the sandwich composites due to the impact event. The frequency response curves verify that the damage is restricted to the impact side of the facesheet and it affected only certain modes of frequency. The impacted facesheet exhibits a lower post-impact stiffness as compared to the bottom facesheet. The loss of stiffness for the top facesheet was found to be maximum as compared to the bottom facesheet for the graphite facesheet composite. This is because of the more extensive damage in the graphite facesheet composite as compared to the glass facesheet composite. Also, the loss of stiffness of the impacted facesheet as compared to the bottom facesheet increases as the energy of impact increases. The difference in the stiffness of the two facesheets can be minimised by either increasing the facesheet thickness or by reinforcing the core by pins.

Also, the for identical facesheet and core thicknesses, the foam-reinforced-pins core sandwich composite exhibits the highest post-impact stiffness for a given energy level of impact. This is because of the superior damage containment mechanism of the

composite. The lowest post-impact stiffness is indicated by the truss core composite due to the tendency of the pins to buckle under impact. The foam core composite shows intermediate behaviour. As the spacing between the pin clusters increases, the post-impact stiffness tends to decrease and tends towards the foam core composite. This is because of the larger area of the damage between the pin clusters within the core.

The Compression-After-Impact (CAI) behaviour follows the impact histories that the samples were subjected to. The load bearing capacity decreases with an increase in the energy level of impact. An increase in the facesheet thickness increases the load bearing capacity of the sandwich composite because of the lesser extent of damage in thicker facesheet composites (It is important to note here that as the samples were subjected to in-plane compression, the facesheets were the main load bearing elements and the core had little or no contribution in the failure process). The damage containment mechanism of the foam-reinforced-pin core composite is very evident as these composites show maximum load bearing capacity as compared to the other sandwich composites with identical facesheet and core thicknesses. The truss core composites exhibit the lowest load bearing capacity after impact due to a greater extent of damage. The failure always occurs across the facesheet which has suffered impact and failure occurs due to the shear instability of the facesheet.

Acoustic Emission was used successfully to capture the matrix cracking, localized fiber breakage and delamination of the impact side facesheet under the CAI loading scenario. For a given facesheet and core thickness, the foam-reinforced-pin core sandwich composite has the best damage containment mechanism and exhibits the best post-impact properties.

Facesheet Type	First Load Drop	Failure Modes	Bottom Facesheet Damage	Load Taken By Sample During Compression-After-Impact
Plain Weave Graphite Fabric and Vinyl Ester 350	5800 N	Core crushing, cell wall buckling and extensive facesheet damage.	Initiated for sample D (33 J impact energy)	B: 14,400 lbs C: 13,920 lbs.
Twill Weave S-2 Glass and Vinyl Ester 350	5800 N	Core crushing, cell wall buckling and minimal facesheet damage	Not initiated at all five energy levels of impact (11 J - 40 J)	B: 14,200 lbs. C: 13,500 lbs.

Table 15.1 Honeycomb-Filled-Foam Core (Kraft Paper Honeycomb Filled With Polyurethane Foam) Sandwich Composites

Type Of Sandwich Composite	First Load Drop	Failure Modes	Failure Loads Of Samples During Compression-After-Impact
FCo	3000 N	Core crushing across facesheet/core interface	A: 22,000 lbs. D: 17,000 lbs.
F+PCo-75	2800 N	Core crushing, localized delamination, shear failure of facesheet plies	A: 8600 lbs. D: 8300 lbs.
F+PCo-150	3000 N	Core crushing, , flexural failure of facesheet plies.	A: 18,000 lbs. D: 11,500 lbs.
TCo	2300 N	Fiber breakage, pin push-out, pin buckling	A: 8900 lbs.

Table 15.2 Conventional and Innovative Core Sandwich Composites

Type Of Sandwich Composite	First Load Drop	Failure Modes	Failure Loads Of Samples During Compression-After-Impact
FCo-32	8000 N	Extensive visible core crushing	A: 45,000 lbs. D: 35,000 lbs.
F+PCo-75 (32)	10,500 N	Facesheet to core disbond and delaminations near the pin clusters	A: 49,000 lbs. D: 52,000 lbs.
GHCo	7800 N	Global cell crushing	-----

Table 15.2(Cont.) Conventional and Innovative Core Sandwich Composites

Type of Sandwich Composite	First Load Drop	Failure Modes
F+PCo-75 (Glass Pins)	5200 N	Facesheet to core disbond, core crushing, and facesheet flexure
FCo (RTM)	5200 N	Facesheet to core disbond, core crushing and facesheet flexure
F+PCo-75 (RTM)	6100 N	Facesheet to core disbond, core crushing and facesheet flexure

Table 15.3 Other Sandwich Constructions Tested

(Note: These results are not directly comparable to the other results as the facesheet as well as the resin systems used were different)

Hollow Steel Pins Truss Core Sandwich Composites

For hollow sandwich panel with steel pin cores, the failure characteristic appears to be pin push-through at the threshold energy level. The surrounding area shows features of delamination and debonding between pins. The 10 degree oriented pins caused threshold energy at a higher level than the 20 degree oriented pins. Damage is significant at 1.2J for 10 degree pin orientation, and 0.53 for the 20 degree pin orientation. The lowest impact energy at which a significant proportion of the impact energy is absorbed by the specimen is the damage initiation impact energy. The C-scans verify the phenomena of delamination after pin push-through. The natural frequency of the plate was unaffected by the localized failure characteristics for several modes. The compressive failure of the specimen, both 10 and 20 degree is determined by the threshold impact event. It was observed that compressive failure was characterized by pin debond and formation of delaminations. Compressive failure

becomes a localized event predicated by local pin debond such as shown by CAI load displacement curves. Acoustic emission parameters indicated the dominant failure modes were pin debonding, matrix cracking and facesheet delamination.

15.2 Static Testing of Sandwich Composites

Flexural Loading :

The stiff glass/epoxy pins in the pin reinforced core, and the honeycomb cell walls in the WESKOR foam, provide attractive benefits in terms of improved flexural stiffness, higher peak loads, and thereby larger damage resistance to flexural loading at a nominal weight penalty.

In-Plane Shear Loading

A cheaper WESKOR foam-filled honeycomb reinforced foam provided ~8% improvement in the in-plane shear strength over a more expensive unreinforced Rohacell foam core. The glass/epoxy pin reinforced Rohacell foam core provided ~44% improvement in in-plane shear strength and an attractive failure arresting mechanism as compared to unreinforced Rohacell foam core composites.

Transverse Compression

Reinforcing the Rohacell foam core with titanium and/or glass/epoxy pins or the using the WESKOR foam-filled honeycomb has the same stiffness benefits as conventional graphite honeycomb core composites, which suffer from catastrophic buckling instability of the honeycomb cells. Furthermore, the reinforced core exhibit a load sharing process which results in a delayed fracture path.

Some additional observations are that the core behavior is reflected in the response of their respective sandwich composites. A steel pin core was found to yield comparative stiffness as that of the honeycomb core composites

- Primary mode of failures may be summarized as follows:

- ⇒ Buckling of pins in the hollow truss core pin reinforced samples
- ⇒ Cracking and buckling of the honeycomb cell walls in the pure honeycomb samples
- ⇒ Core crushing and closing followed by shearing in the case of the unreinforced Rohacell foam

⇒ Buckling and interfacial debonding between the cell walls and the core in the case of the WESKOR foam-filled honeycomb core samples

15.3 Intermediate Velocity Tests

Intermediate velocity experiments (10-30 m/s) performed in a modified Split Hopkinson Pressure Bar (SHPB) yielded information pertaining to damage evolution in the three composite types ; foam core, pin-reinforced foam, and hollow pin core. Buckling was the predominant failure in the hollow pins, while the crack propagation took place circumventing the pins, in the case of the pin-reinforced foam core sample. The overall deformation was lower, when the foam was reinforced with the pins. In the case of the foam core, the foam developed catastrophic failure below, within the core, a few microns below the facesheet.

15.4 High Strain Rate Impact Studies

A comparative study between the traditional core and innovative cores is presented here. Traditional core configurations considered are foam core and honeycomb core. Innovative core configurations considered include hollow pin truss core, foam core reinforced with titanium pins and glass pins.

The primary dominant modes of failure under HSR loading may be summarized as follows:

1. Buckling of pins in the hollow truss core sandwich samples , followed by rotation of the facesheets out-of-plane.
2. Cracking and collective buckling of the honeycomb cell walls in the pure honeycomb core sandwich samples.
3. Core crushing and cell wall closure followed by shear crack propagation in the case of the Rohacell foam core sandwich samples.
4. Titanium pin reinforced foam core samples failed either by debonding at the face sheet, microbuckling of the pins and/or interfacial separation between the core and pins.
5. In the case of glass pin reinforced panels the failure was due more to debonding between the face sheet and the core and by shear cracks in the foam with very little evidence of pin fracture/buckling.
6. In all the cases considered, for the through-the-thickness direction loading, the facesheets did not exhibit any notable evidence of damage accumulation. Failure was in all the cases, within the domain of the core(s).
7. Under high strain rate loading, the core crushing behavior primarily dominates the strain rate sensitivity. No significant differences were noted in the stress-strain curves from impacting the samples either from the glass/epoxy side or the graphite/epoxy side, except that the thinner glass/epoxy side exhibited more core

- damage. The use of a momentum trap is justified in the sandwich composite samples, as the pure response to a single compressive pulse and hence, damage evolution could be ascertained.
8. For the in-plane loading, the facesheet dominated failure was noted, where fiber microbuckling, compression delamination within the facesheet and interfacial debonding between facesheet-to-core were noted. The core damage was not prominent.
 9. No significant differences were noted in the stress-strain curves from impacting the samples with dissimilar facesheets either from the glass/epoxy side or the graphite/epoxy side, except that the thinner glass/epoxy side exhibited more core damage.

Considering all studies, it appears that isolated hollow-pin composites may be better utilized as opposed to large areas of hollow-pin cores. The pin-reinforced and honeycomb reinforcement of pin provide superior properties in terms of static, low velocity and high strain rate impact loading scenarios.

Analysis of Pin Core Sandwich Plates

By

**L.N.B.Gummadi, Ph.D.
Principal Investigator
Advanced Structural Concepts Inc.
West Chester, OH**

Table of Content

Acknowledgment	iii
Figure Captions	iv
Chapter 1: Introduction	1
Chapter 2: Optimization	4
Chapter 3: Modeling	16
Chapter 4: Results	23
Chapter 5: Conclusions	66

Acknowledgment

The author appreciates all the help offered to him by Dr. Uday Vaidya of Tuskegee University, and also appreciates the confidence shown by Dr. Shaik Jeelani.

Figure Caption

- Figure 3.1 Sandwich plate model
Figure 4.1 Force-time and energy-time curves
Figure 4.2 Land-deflection curves
Figure 4.3 Sandwich plate model
Figure 4.4 Load position
Figure 4.5 Load-time function
Figure 4.6 Finite element static analysis
Figure 4.7 Load vs. Pin failures
Figure 4.8 Load vs. Pin failures (up to 160 pins)
Figure 4.9 Load vs. Pin failures (up to 10 pins)
Figure 4.10 Vertical displacement of top face sheets, force equals 4.39 kN
Figure 4.11 Vertical displacement of top face sheets, force equals 4.41 kN
Figure 4.12 Vertical displacement of top face sheets, force equals 4.08 kN
Figure 4.13 Vertical displacement of top face sheets, force equals 4.05 kN
Figure 4.14 Vertical displacement of top face sheets, force equals 4.14 kN
Figure 4.15 σ_{yy} at a force equal to 4.39 kN
Figure 4.16 σ_{yy} at a force equal to 4.41 kN
Figure 4.17 σ_{yy} at a force equal to 4.08 kN
Figure 4.18 σ_{yy} at a force equal to 4.05 kN
Figure 4.19 σ_{yy} at a force equal to 4.41 kN
Figure 4.20 σ_{xx} at a force equal to 4.39 kN
Figure 4.21 σ_{xx} at a force equal to 4.41 kN
Figure 4.22 σ_{xx} at a force equal to 4.05 kN
Figure 4.23 σ_{xx} at a force equal to 4.05 kN
Figure 4.24 σ_{xx} at a force equal to 4.41 kN
Figure 4.25 Dynamic analysis results
Figure 4.26 Dynamic analysis results with face sheet failure
Figure 4.27 First mode shape
Figure 4.28 Second mode shape
Figure 4.29 Third mode shape

Chapter 1 Introduction

Sandwich plates made from composite materials are being increasingly used in various aerospace applications. Some of the advantages of using sandwich materials when compared to the conventional materials include high specific modulus, high specific strength and the ability to tailor the design to the requirements. Typically, a composite sandwich plate consists of stiff face sheets, primarily for resisting flexural bending and a core for transferring the shear and transverse compression loads. In general, the material used for the core is light weight and of low flexural stiffness but provides significant shear stiffness. Conventional materials used for the core include honeycomb and foam and they have been investigated extensively.

A newly developed concept of a truss reinforced core has entered the market place in recent years. This concept involves the replacement of a conventional foam core with either a truss reinforced core or truss reinforced hollow core. Details of the construction of the core can be found in Ref. [1]. The general idea is based on inserting high strength and stiffness pins into a sandwich panel, either to replace or supplement the existing core. These pins act as trusses transmitting forces throughout the sandwich and provide the required structural integrity. If the space between the pins is filled with foam, the filler material will provide a higher pin stability. On the other hand, if the core space between the pins is left empty, one can provide space for; among other things, fuel storage. Both types of sandwich constructions offer better

delamination growth control when compared with other sandwich type constructions. These pin core structures, though, are prone to many defects such as pin compression failure, pin buckling, pin pullout from the face sheets, delaminations, debonding, etc. All or some of these damage modes can be severe under low velocity impact conditions, which is a most common occurrence in the life span of the material. An experimental study of various damage modes due to low velocity impact has been extensively studied by researchers Refs. [2-6]. Analytical modeling of the performance of these pins is the primary objective of this report.

The first aspect that was studied in this report is the development of simple analytical models to represent the sandwich material, and use these analytical models for determining the optimum pin angle that is suitable for use in low velocity impact. As a next step, a progressive failure analysis methodology was developed in conjunction with commercially available nonlinear finite element software "ABAQUS". A user defined subroutine was developed to interact with ABAQUS for establishing the failure progression due to pin buckling. Using this algorithm, static and dynamic loading conditions were applied to study the progression of damage. Results were compared with experiments conducted at Tuskegee University. Also included in the report is the effect of pin failure on the natural frequencies. Finally, concluding remarks are provided.

References:

- [1] Freitas, G., Magee, C., Dardzinski, P., and Fusco, T., "Fiber Insertion Process for Improved Damage Tolerance in Aircraft Laminates," *Journal of Advanced Materials*, Vol. 25 (4), pp. 36-43 (1994)
- [2] Vaidya, U.K., Palazotto, A.N., and Gummadi, L.N.B., "Low Velocity Impact Response and Nondestructive Evaluation of Sandwich Composite Structures," *ASME Winter Annual Meeting*, Dallas, TX (1997)
- [3] Palazotto, A.N., Gummadi, L.M.B., Vaidya, U.K., and Herup, E.J., "Low Velocity Impact Damage Characteristics of Z-Fiber Reinforced Sandwich Panels - An Experimental Study," *38th AIAA/ASME/ASCE/AHS SDM Conferences* (1997)
- [4] Palazotto, A.N., Gummadi, L.N.B., Vaidya, U.K., and Herup, E.J., "Low Velocity Impact Damage Characteristics of Z-fiber Reinforced Sandwich Panels - An Experimental Study," Accepted for publication in *Composite Structures* (1998)
- [5] Palazotto, A.N., and Gummadi, L.N.B., "Failure Characteristics of Sandwich Plates Under Static and Dynamic Loading," *AFIT/ENY/TR-97-03*
- [6] Kamath, Mohan, J., "Damage Tolerance of Sandwich Composites," Masters Thesis, Tuskegee University, Tuskegee, Alabama, 1998

Chapter 2 Optimization of a Truss Core

The present chapter characterizes certain optimization parameters for a sandwich panel. The primary objective of the optimization of the core is to determine the orientation of the truss member under a critical load such that the total weight of the sandwich panel is reduced. It should be noted that the sandwich plate is configured as intersecting trusses at right angles to each other. In this analysis, the intersecting truss arrangement is simplified to the consideration of a truss running in one direction. Furthermore, the optimization design of a truss subjected to static load assumes that the global bending of the truss does not affect the forces in the diagonal elements. This assumption is applicable only if the truss length is significantly larger than its depth, as is the case for the truss used in the core of the sandwich panel. In this situation, the gradient of the global bending deflection along the length of the truss must be kept small to avoid excessive deformations. By this assumption, the pins in the sandwich panel can be analyzed using the truss model. Also, the pin members are assumed to be solid circular cross sections. Thus, the objective is to reduce the weight of the sandwich panel. However, the weight and the volume are linearly dependent. Hence, one can optimize either the weight or the volume. In this report, the volume of a truss is chosen to be optimized. Also, the failure criterion of the truss becomes a constraint criterion in the development of the optimization modeling. The failure criteria considered are the axial buckling strength and compressive strength. Furthermore, considering a truss element of

a unit length subjected to a load P, the volume V of the diagonal element is given by

$$V = \left(1 / (2h \cotan \alpha) \right) 2h A \operatorname{Cosec} \alpha = 2h N A \operatorname{Cosec} \alpha = A / \operatorname{Cosec} \alpha \quad (1)$$

Where $(1/2h \cotan \alpha)$ is the number of "bays" along the unit length, $h \operatorname{Cosec} \alpha$ is the length of two diagonal elements that form one bay, A is a cross sectional area of a diagonal element, h is the thickness height, N is the number of pins which could be assumed constant or variable, and α is the angle the pin direction makes with the horizontal axis. Note that Equation (1) is applicable only if there is a large number of bays within a unit length. The development of the optimization modeling will be present for both N constant and variable.

Optimization Based On Axial Buckling Load With Variable Number Of Pins:

The force in a diagonal element is the compressive force P is

$$P = P_a / 2 \operatorname{Sin} \alpha \quad (2)$$

Where P_a is the perpendicular load applied at the sandwich panel. This force can not exceed the critical buckling force P_{cr} where P_{cr} is

$$P_{cr} = (\pi / L)^2 EI \quad (3)$$

where EI is the bending stiffness of the element (i.e., E is the elastic modulus and I is the moment of inertia) and L is the unsupported length of the pin considered for buckling and is equal to

$$L = h \operatorname{Cosec} \alpha \quad (4)$$

Using Equations (3) and (4), the load reduces to

$$P_{cr} = 2(\pi / h)^2 EI \sin^3 \alpha \quad (5)$$

where the parameter L is substituted in terms of h and α using Equation (4). The area A for a solid circular cross section is

$$A = \pi r^2 \quad (6)$$

where r is the radius of the cross section. Also, the moment of inertia for a solid circular cross section is

$$I = (\pi / 4) r^4 = A^2 / 4\pi \quad (7)$$

Using Equations (6) and (7), the load reduces to

$$P_{cr} = \frac{1}{2} (\pi / h)^2 E A r^2 \sin^3 \alpha \quad (8)$$

Thus, for an applied force P_{cr} under the condition that the forces in the pins are equal to the critical buckling load, the applied force P_{cr} is related to the cross sectional area A as shown in Equation (8). One can use Equation (8) to compute the area of the cross section A . That is the cross-sectional area become equal to

$$A = P_{cr} / \frac{1}{2} [(\pi / h)^2 E r^2 \sin^3 \alpha] \quad (9)$$

or, it can be written as

$$A = C / \sin^3 \alpha \quad (10)$$

where C is a constant. Note that even though the constant C includes the force P , the magnitude of the force is assumed that it does not affect the optimization process and all other quantities are constant. Hence, once the area is computed, the optimization problem reduces to determining the values of the angle α which leads to the volume that will give the lightest diagonal element of

the truss, i.e. the smallest value of V. In another words, the volume V in Equation (1) can be written in terms of α by substituting the value of the cross sectional area A which is given in Equation (8). The volume V become

$$V = C / \sin^3 \alpha \cos \alpha \quad (11)$$

From the extremum requirement, it implies that the partial derivative of the volume V with respect to the angle α is zero (i.e. minimizing V with respect to α). That is, using Equation (11), one obtains

$$dV / d\alpha = -C [d / d\alpha (\sin^3 \alpha \cos \alpha)] / [\sin^6 \alpha \cos^2 \alpha] \quad (12)$$

Note that the angle α can vary between zero and $\pi/2$, since the denominator in Equation (12) can not be equal to zero. Thus,

$$d / d\alpha [\sin^3(\alpha) \cos(\alpha)] = \sin^2(\alpha) (3 \cos^2 \alpha - \sin^2 \alpha) = 0 \quad (13)$$

From Equation (13), one can also deduce

$$\tan^2 \alpha = 3 \quad (14)$$

Which implies that

$$\alpha = 60^\circ$$

(15)

Finally, to insure that the extremum is a minimum in the above calculation which yields the lightest weight of the sandwich panel rather than the heaviest, the second derivative of the volume V with respect to the angle α must be positive. That is, taking the partial derivative of Equation (12) with respect to the angle α gives

$$\frac{d^2 V}{d \alpha^2} = C [8 \cos \alpha \sin \alpha (\sin^4 \alpha \cos^2 \alpha) - (1-4 \cos^2 \alpha) d/d\alpha (\sin^4 \alpha \cos^2 \alpha)] / (\sin^8 \alpha \cos^4 \alpha) \quad (16)$$

Since the constant C and the denominator are positive, the condition of the minimum, i.e. the condition that the second derivative of the volume is positive, implies

$$[(8 \sin^5 \alpha \cos^3 \alpha) - (1-4 \cos^2 \alpha) d/d\alpha (\sin^4 \alpha \cos^2 \alpha)] > 0 \quad (17)$$

Substituting the value of ($\alpha = 60^\circ$) in Equation (17) yields a positive value. Hence, the optimum value of the angle α of a circular diagonal element of a truss should equal

$$\alpha = 60^\circ \quad (18)$$

The cross sectional area A and the volume V of the element can be computed from Equation (10) and (11), respectively, which gives the lightest weight for the sandwich panel.

Optimization Based on Axial Buckling Load with Constant Number of Pins:

When the number of pins are held constant, the volume of the pins are equal to

$$V = 2h \operatorname{Cosec} \alpha A N \quad (19)$$

The force in a diagonal element under a compressive force P is calculated as

$$P = P_a / 2 \operatorname{Sin} \alpha \quad (20)$$

Where P_a is the perpendicular load applied at the sandwich panel. As before, the force in the pin should not exceed the critical buckling force.

$$P = P_{cr} = \pi^2 EI / L^2 \quad (21)$$

Where EI is the bending stiffness of the element (i.e. E is the elastic modulus and I is the moment of inertia) and L is the pin length, and it is equal to

$$L = h \operatorname{Cosec} \alpha \quad (22)$$

Using Equations (21) and (22), the load reduces to

$$P_a = 2 (\pi / h)^2 E I \sin^3 \alpha \quad (23)$$

where the parameter L is substituted in term of h and α using Equation (22). The area A for a solid circular cross section is

$$A = \pi r^2 \quad (24)$$

where r is the radius of the cross section. Also, the moment of inertia for a solid circular cross section is

$$I = (\pi / 4) r^4 = A^2 / 4 \pi \quad (25)$$

Using Equations (24) and (25), the load reduces to

$$P_a = 2 \pi^2 E J \sin^3 \alpha / h^2 \quad (26)$$

Considering the optimization of the sandwich panel, the problem can be posed as minimizing a functional J which consist of the volume V to be minimized

subjected to constraint of the load given in Equation (26) through a parameter λ .

That is the minimization becomes

$$J = V + \lambda (P_a - 2 \pi^2 E I \sin^3 \alpha / h) \quad (27)$$

which gives

$$J = 2h N A / \sin \alpha + \lambda (P_a - 2 \pi^2 E I \sin^3 \alpha / h) \quad (28)$$

$$\partial J / \partial \lambda = 0, P_a = 2 \pi^2 E I \sin^3 \alpha / h^2 \quad (29)$$

From Equation (29), the area can be written as

$$A = P_a h^2 / 2 \pi^2 E R^2 \sin^3 \alpha \quad (30)$$

Thus, the volume can be written as

$$V = (2h / \sin \alpha) P_a h^2 / 2 \pi^2 E r^2 \sin^3 \alpha = C / \sin^4 \alpha \quad (31)$$

Finally, the minimization of the functional J with respect to the angle α gives

$$\partial J / \partial \alpha = -4 C \sin^3 \alpha \cos \alpha / \sin^8 \alpha \quad (32)$$

Since the denominator can not be zero (i.e. $\alpha \neq 0$), one obtains

$$\sin^3 \alpha \cos \alpha = 0 \quad (33)$$

Which leads to either $\alpha = 0^\circ$ or 90° . But since $\alpha \neq 0^\circ$, then $\alpha = 90^\circ$. That is to minimize the weight of the sandwich panel, the angle of the constant number of pins equals 90° or in a vertical direction based on minimization of the volume. This obviously is not practical since the pin orientation must be at an angle conducive to, through the thickness shear resistance. For it to occur, the pin must be connected to the upper and lower face plate, in the sandwich construction, as a restraint connection.

Optimization Based on Compressive Strength

A third optimization restraining parameter is considered. This is the pins crushing or material compressive strength. One first must calculate the pin's compressive resistance force. The compressive force in the diagonal element under an applied force P_a perpendicular to the sandwich panel is equal to

$$P = P_a / (2 \sin \alpha) \quad (34)$$

From Equation (34), the cross sectional area A becomes equal to

$$A = P / J \sigma = P_a / (2\sigma \sin \alpha) \quad (35)$$

where σ is the compressive yield strength of the pin. Using Equation (35) and Equation (1), the total volume of the element reduces to

$$V = C / \sin \alpha \cos \alpha \quad (36)$$

Optimizing the volume of the element to obtain the lightest weight, i.e. minimize the volume with respect to the angle α in a fashion similar to Equation (12), one obtains

$$\sin^2 \alpha - \cos^2 \alpha = 0 \quad (37)$$

From Equation (37), the angle α is equal to 45° . That is, an angle of 45° will lead to the minimum weight for the sandwich panel using the compressive strength criterion.

Conclusions:

Optimization for minimizing the total weight of the sandwich panel is carried out with different constraints on the strength of the core component. These include axial buckling and compressive strength. It was found that an angle α could be chosen at either 45° or 60° with the horizontal axis to reduce

the lightest sandwich construction. Previous investigation, [1] has shown that the orientation of 60° is the most practical.

Reference:

- [1] Palazotto, A. N., and Gummadi, L. N. B., "Failure Characteristics of Sandwich Plates Under Static and Dynamic Loads," AFIT/ENY TR 97-07.

Chapter 3 Modeling

A reinforced sandwich plate with a Z-pin core (see Figure 3.1) is modeled numerically using the commercial code ABAQUS. The model will be used to investigate the response of a sandwich plate under low velocity impact. The sandwich plate consists of two face plates with the Z-pins bridging the two face plates at an angle. This high stiffness titanium Z-pin provides a way to connect the two plates and transfer the loads. The use of the Z-pins provides a lighter and stiffer plate structure making it attractive for aerospace applications.

Note that the Z-pins and the two face sheets are discrete in that they are two separate structures brought together by a constraint condition where the pin ends are embedded into the two face sheets, and a change in any part of the structure leads to a different global response of the structure. For example, the stiffness of the Z-pin core is a function of the orientation of the pins. In addition, the weight of the structure is a function of the Z-pin's spacing. An optimization study has been performed and discussed in Chapter 2 to determine the orientation of the Z-pin using ASTROS, where the spacings between the Z-pins are taken equal to that value determined by a 60 degree angle with respect to the horizontal axis.

The major failure mode observed through experimentation of a sandwich plate under low velocity impact is dominated by Z-pin buckling according to Ref. [1]. Considering this observation, the numerical model characterizes failure to

the Z-pins using a buckling criterion. That is, the finite element analysis computes the axial forces acting on the Z-pin. If the force exceeds the critical buckling force then the Z-pin is assumed to buckle. The post-buckling mode of the Z-pin is assumed to carry very little load, and its stiffness is reduced to 1% of its original stiffness within the global stiffness matrix. The buckling equation for a pin simply supported at its ends is referred to as the Euler buckling equation.

It can be written as

$$P_{cr} = \pi^2 E I / L^2 \quad (1)$$

where: P_{cr} equals the buckling or failure load in a pin; E is the pin's modulus of elasticity equal to 16.8×10^3 ksi; I is the moment of inertia (all pins are taken to be circular with a radius of 0.02 in.); and L is the unsupported length of the pin taking into account the inclined dimension of the pin between the face sheet surfaces.

The Z-pin reinforced sandwich plate is modeled both statically and dynamically. The problem is analyzed statically to develop an insight to the buckling characteristics of the Z-pins, and their effect on the global response of the sandwich plate. In the static case, all the energy supplied by the external load is carried by the plate, which leads to the buckling failure of the Z-pins. Thus, incorporating the finite element equilibrium equation (which is obtained by minimizing the stationary potential energy obtained from the virtual work formulation) one has

$$[K] \{U\} = \{F\} \quad (2)$$

where $[K]$ is the stiffness matrix, $\{U\}$ is the displacement degree of freedom (DOF) vector representing kinematic movement at each node within the finite element model, and $\{F\}$ is the applied force vector. Note that the stiffness matrix changes due to the buckled Z-pin. This idea will subsequently be elaborated upon. For the static case, both the small displacement and large displacement (i.e., geometric nonlinearity) formulations, which are available in ABAQUS, are used to investigate the response of the sandwich plate. The large displacement causes a stiffer plate response to loading due to an increase in the membrane forces within the face plate and thus the potential of larger forces in the pins. The extent of stiffening the plate response depends on the application which will be shown later for the Z-pin sandwich in the Result chapter.

The dynamic analysis results are more representative of the experimentation; since the impact problem is a dynamic problem where the mass at the point of impact transfers its mechanical energy as well as causing an initial velocity in the sandwich plate equal to the impacting mass velocity. The process of transferring the energy to the plate is modeled by using the experiment's measured force time function as an input concentrated force located at the mid-center of the sandwich plate. The finite element dynamic analysis is different from the static analysis due to the inertia forces. The equation of motion of the finite element model is:

$$[M] \{ \ddot{U} \} + [C] \{ \dot{U} \} + [K] \{ U \} = \{ F(t) \} \quad (3)$$

where

$[M]$ is the mass matrix

$[C]$ is the damping matrix

$\{ \ddot{U} \}$ represents the acceleration. A dot over a function represents

the derivative of that function with respect to time.

$\{ \dot{U} \}$ represents the velocity DOF

and $\{ F \}$ is the forcing function.

The present analysis ignores the damping effect within the plate ($[C] = [0]$).

ABAQUS incorporates the Newmark technique to integrate the equation of motion (Equation (3)) numerically.

The equation of motion changes to:

$$[\hat{K}] \{ U \}_{t+\Delta t} = \{ P \}_{t+\Delta t} + [M] (a_0 \{ U \}_t + a_2 \{ \dot{U} \}_t + a_3 \{ \ddot{U} \}_t) \quad (3)$$

where

$$[\hat{K}] = 1/\beta \Delta t^2 [M] + [K] \quad (4)$$

$$a_0 = 1/\beta \Delta t^2 ; a_2 = 1/\beta \Delta t ; a_3 = 1/2\beta - 1 \quad (5)$$

Solve in this order

$$\{\bar{U}\}_{t+\Delta t} \quad \text{in Equation (3)} \quad (6)$$

$$\{\bar{U}\}_{t+\Delta t} = a_0 (\{U\}_{t+\Delta t} - \{U\}) - a_2 \{\dot{U}\}_t - a_3 \{\ddot{U}\}_t \quad (7)$$

$$\{\dot{U}\}_{t+\Delta t} = \{\dot{U}\}_t + a_6 \{\ddot{U}\}_t + a_7 \{\ddot{U}\}_{t+\Delta t} \quad (8)$$

$$a_6 = \Delta t (1 - \gamma) ; a_7 = \gamma \Delta t \quad (9)$$

$$\gamma = \frac{1}{2} ; \beta = \frac{1}{4}$$

also $t + \Delta t$ is the time at evaluation over an increment Δt and $\{U\}$ is once again the DOF.

The reader should note that in Equation (3) the matrix $[\hat{k}]$ contains the stiffness matrix $[K]$. This is where the failure of the pins have their effect. The $[K]$ matrix includes the buckled pin stiffness reduction, and thus the state of equilibrium must be achieved through a numerical scheme which uses the Riks method.

Details of this method can be found in the user's manual of ABAQUS.

The finite element model for both the static and dynamic analyses can be stated as follows: The model consists of two face sheets connected by the Z-pin (see Figure 3.1). The face sheets are modeled with a four nodded shell element (i.e., ABAQUS S4R shell element). The Z-pin is modeled as a bar (i.e., ABAQUS T3D2 truss element). The load on the sandwich plate is modeled by

applying a concentrated force at the mid-center of the sandwich plate. For the dynamic case, the concentrated load is applied as a function of time which is obtained from the experiment. The boundary condition used is a simple support at the mid-thickness of the bottom face plate. The experimental device for holding the sandwich plate prevents the upper face sheet from moving in the upward direction but allows the upper face sheet to deform in the normal direction toward the bottom face sheet. That is, under an impact force, the distance between the two face sheets could not increase beyond the initial value, but could decrease due to deformation of the pins caused by the impact force. The modeled boundary condition is a reasonable compromise to the actual condition.

The buckling failure is implemented in ABAQUS using the USDFLD subroutine provided by ABAQUS. This subroutine allows the user to access the material properties at the beginning of the incremental process of the load for the static analysis or time increments for a dynamic problem where the force is time dependent. However, one of the drawbacks of this subroutine is that the routine provides access to the material point quantities only at the start of the increment. The solution dependence introduced in this way is explicit. Thus, the material properties for a given increment are not influenced by the results obtained during the increment (e.g. in the static analysis once the material property of a truss element is reduced due to buckling, ABAQUS does not recompute the equilibrium state for the model after the change in the stiffness, but the change is carried on to the next increment where the equilibrium state is

satisfied). Hence, the accuracy of the results depends on the size of the time increment, and the user should use a reasonable time increment to avoid large accumulative errors in the process. The present analysis used the USD-FLD subroutine as follow. At every time integration point, the stresses in the pins are checked against the buckling stress (i.e., buckling force divided by the Z-pin cross sectional area). If the stresses in the Z-pin are larger than the buckling stress, the elastic modulus of the Z-pin is reduced to one percent of its original value which means that the buckled Z-pin carries a very small load after buckling. If the stress in the element is below the buckling value, the elastic modulus of the Z-pin remains the same.

The modeling of failure in the Z-pin sandwich plate assumes that the buckling of the Z-pin is the dominant failure mode compared to a Z-pin push through failure, crushing failure of face sheets, especially the upper face sheet due to impact,....etc. The validity of such an assumption will be investigated next in the Results chapter where the analysis and experimental results are compared. Note that the experimental results are only available for the dynamic case. Based on this comparison, one can assess how much the bucklings of the Z-pins are dominant considering the actual failure response of the Z-pin sandwich plate.

References:

- [1] Kamath, Mohan, V., "Damage Tolerance of Sandwich Composites," Masters Thesis, Tuskegee University, Tuskegee, Alabama, 1998.

Figure 3.1 is out of order and is on page A-37.

Chapter 4 Results

This chapter will present the results of the Z-pin reinforced sandwich plate analyzed using the finite element method with buckling failure as discussed in Chapter 3. The verification of the results is done by a comparison with experimentation obtained from Ref. [1]. A description of the experiment and its results will be presented for clarity sake. It will be followed by the static and dynamic analyses of the Z-pin reinforced sandwich plate. Finally, a comparison between the experimentation and the numerical results will be presented, and a discussion of the validity of the modeling process will be given.

The low velocity impact experiment [1], which was performed on the Z-pin reinforced sandwich plate, uses the drop weight impact test system. The test system involves the procedure of dropping a fixed weight from a pre-determined height. The energy at impact is calculated using the potential energy relation,

$$E_p = mgh \quad (1)$$

where m = mass; g = acceleration due to gravity; h = height above impact point. The velocity at the point of impact can be found by assuming that all the potential energy is converted into kinetic energy, which is equal to

$$E_k = \frac{1}{2} m v^2 \quad (2)$$

where v = velocity. For better control over the drop weight, a Dynatup impact test system was used in the experiment. The Dynatup consists of an instrumented tup tip mounted on a weight that can be varied which slides along two stiff guide rails. The specimen to be tested was placed in a fixture at the base of the rails. The velocity is measured, as a check to Equation 2, using sensors. To avoid variations in the testing parameters, the tup and the mass of the impacting hammer was kept constant throughout the test, and the energy of impact was varied by merely varying the drop height. Five different energy levels of impact were performed where the drop height varied to produce 11J, (Joules), 20J, 28J, 33J, and 40J impact energies. Note that the verification of the analysis will be done against an impact energy of 33J. The load-time function is obtained as follows. The Dynatup drop-weight impact testing machine measures the velocity between two set points. This velocity value is referred to as the initial velocity at the point of impact. The tup tip of the mass system is connected to a load cell. The impulse and linear momentum equation are then used to determine the changing velocity, and thus the energy convergence between the dropped mass and the object (plate).

In Ref. [1] different configurations and compositions of the Z-pin reinforced sandwich plate were tested. This report will focus on one case to verify the analyses. The case that will be considered is a hollow titanium pin core sandwich composite. That is a core made up of titanium Z-pins with no foam between the two face sheets. For this condition, the two face sheet materials used are weave graphite fabric which are bonded to the Z-pin core

using a vinyl ester 350 resin system in a compression molding machine. The face sheets consisted of sixteen plies (for both the top and bottom face sheets), where each ply has a 0.0118 in. thickness. The face sheets total thickness is equal to 0.177 in., or 0.0885 in. for each face sheet. The ratio between the face sheets to core thickness is maintained at 0.375 which means that the core thickness (i.e., the distance between the two face sheets) is 0.472 in. The Z-pin reinforced sandwich plate dimensions are 4.0 in. X 4.0 in. where the actual unsupported dimensions equal 3.0 in. X 3.0 in. The impactor weighs 15.1 Kgs and was dropped from a height of 0.44 m. Thus, the impact velocity computed from Equation (2) is 82.30 in/sec (6.86 ft/sec).

The results of the experimentation for the specimen described above are shown in Figures 4.1 and 4.2, where only the case label D (i.e., 33J) will be used to verify the analysis. Figure 4.1 shows the time versus load, and Figure 4.2 shows the displacement versus load. From Figure 4.1, the average damage initiation load is at 2300 N. Note that the feature of the load/energy time curves is such that the peak loads and absorbed energy can be related to the fracture process occurring in the material. That is, a change in the stiffness (indicated by the slope of the load-displacement curve, Figure 4.2) results from failure within the face sheets while a sudden drop signifies a dramatic failure of the system such as multi pin buckling.

Based on the above data, the finite element model uses a 3.0 in. X 3.0 in. dimension which is shown in Figure 4.3. The core thickness (i.e., the distance between the top and bottom face sheets) is modeled as 0.48 in. The top and

bottom face sheet thicknesses is 0.085 in., where eight plies are used for each face sheet with a 0° fiber orientation. The material for the face sheets used in the model is graphite/epoxy with the following material coefficients:

$$E_1 = 20 \times 10^6 \text{ psi}, E_2 = 1.5 \times 10^6 \text{ psi}, v_{12} = 0.27 \text{ and } G_{12} = 1.04 \times 10^6 \text{ psi.}$$

The mass density used for the face sheet is 7.200×10^{-5} (slug/in³). For the titanium Z-pins, the material coefficients are:

$$E = 16.8 \times 10^6 \text{ psi, } v = 0.3.$$

The mass density used for the titanium Z-pin is 6.53×10^{-3} (slug/in³). The titanium Z-pin radius is 0.02in. The Z-pins are modeled using an ABAQUS truss element T3D2 (i.e. a bar element), and for the face sheets a shell element S4R is used. The boundary condition used to model the fixture support of the sandwich plate is a hinge (i.e., the displacements are fixed, but the rotations are free) for all edges. For the static case, the displacement control option in ABAQUS is used, and a 0.157 in. is applied at the mid-center of the Z-fiber reinforced sandwich plate (see Figure 4.4). For the dynamic case, the load applied is a function of time which is shown in Figure 4.5. Note that the load versus time is obtained from the experimental data given in Figure 4.1 for case D. Furthermore, the initial velocity at the time of impact is 82.30 in/sec as indicated previously.

The static analysis of the Z-pin reinforced sandwich plate is performed, and the results are the following. The load versus displacement for the static case is shown in Figure 4.6, which shows results for an analysis with buckling failure and without buckling failure. It is shown that the buckling failure changes

the stiffness response of the sandwich plate as the plate continue to deformed indicating a damage response of the sandwich plate. The first change in the stiffness response due to pin buckling is at a load of approximately 900 N., and continues to change until it reaches 4500 N. At 4500 N., the number of Z-pins that buckled was large enough such that the sandwich plate is no longer capable of carrying further loading. The damage became so extensive that any additional externally applied energy could not be supported, and it transferred into additional buckling damage of the Z-pins. The experimental results shown in Figure 4.1 indicate the first stiffness change (i.e., slope change) is at 1000 N. However, the average damage initiation load for the experiment is at 2300 N., Ref. [1]. This is bounded between the analysis damage load of the first stiffness change equal to 900 N., and the maximum static damage load is equal to 4500 N. Note that, the test in Ref. [1] is done for a dynamic weight drop experiment, and no static test has been carried out (i.e., loading the Z-pin reinforced sandwich plate at a very slow rate such as 0.05 in/sec.) In Ref. [2], both the static and dynamic tests are carried out where the results show a variation of 10%-20% depending on the configuration and composition of the sample specimen. A full discussion on the static versus dynamic test can be found in Ref. [2].

The progressive buckling failure is monitored in the analysis for the static case, where the first buckled Z-pin occurred when the force applied at the mid-center of the sandwich plate was at a value of 841 N. However, the number of Z-pin failures increased as the deformation continued. The number of buckled

Z-pins versus the load is shown in Figures 4.7 through 4.9. The total number of Z-pins in the model is 2400. The load as a function of the buckled Z-pin is traced more closely in Figures 4.8 and 4.9. The nonlinear accumulation of damage during the plate's deformation can be observed. Figure 4.9 also shows that it took between four to five Z-pins to buckle before the load reached the average damage initiation load for the experiment which is 2300 N., Ref. [1].

The displacement of the plate was also investigated. The maximum displacement occurred is at the point of contact where the mass (i.e., the point of loading at the mid-center) first impacted the sandwich plate. Figure 4.4 implies that the upper and lower face sheets move relative to each other. Experimental observation does prove this out. The phenomena is very local. Ref. [2] also observed the same features. It can be said that during the analysis the two face sheets never came in contact, and the maximum vertical displacement at the applied force position reached 0.157 in. The displacement for the top face sheet is presented as contour plots in Figures 4.10 through 4.14 at different load levels considering pin failure. The results in those figures show the vertical displacement of the upper face sheet at its mid-height. Figure 4.10 indicates what is occurring at a force level of 4394 N., where 200 pins have failed (see Figure 4.7). One can observe a displacement region under the load that is significantly different than other areas within the model. Figures 4.11 through 4.13 characterize the increase pin collapse but with a slight load change. The maximum displaced region increases significantly. Figure 4.14 displays a region of vertical displacement in which over 1600 pins have collapsed. It becomes

obvious that the failure is creating displacement areas of significant proportion for the same loading (compare Figures 4.11 and 4.14 both are at a force of 4.41 kN). The reader should also observe the shape of the contours are going from circular, at the lower pin collapse number to elliptic as the failure characteristics come more into play. The nature of the local phenomena is reflected in the stress field.

The stresses at the mid-surface of the upper face sheet are presented for the y directed stresses (transverse to the 0° oriented composite fibers) in Figures 4.15 through 4.19. The stress distribution is consistent with the displacement results, which indicates that the maximum stress level is at the point of impact and increases with increasing amounts of pin collapse. The reader should observe the stresses adjacent to the load are tension but become compression near the boundary. A tension stress implies that a greater amount of membrane stretching is occurring due to the local behavior characteristics as compared to a plate bending phenomena indicative of compression in the top face sheet. This feature is also evident for the X directed stress shown in Figures 4.20 through 4.24. The contour stress distributions reflects the X orientation of the fiber.

For static analysis, in addition to modeling the loading process (i.e., transfer of energy to the Z-pin reinforced sandwich plate) as a displacement control, a load control analysis (which governs the solution based on load incrementation) using the RIKS technique was also performed. The results are consistent with those using the displacement control. Hence, the results for the

RIKS load control case were not shown, since they do not add any new insight to the problem. Furthermore, the effect of the nonlinear geometry (i.e., including the large displacement features for the top and bottom face sheets) on the buckling failure of the Z-pin was investigated. The option of NLGEOM in ABAQUS is used, and the results did not show any variation from the linear displacement control analysis. Hence, the results are also not shown to eliminate repetition.

The dynamic analysis of the impact problem was also examined. In this case, the load control option in ABAQUS was used where the load input in the analysis was taken to be the same as the one given by Figure 4.5. Note that only a portion of the experimental load was carried out into the analysis due to the computational time required. The load versus displacement is shown in Figure 4.25 for both the analytic dynamic results and the experimental data given in Ref. [1]. The comparison between the analysis and the experimental results show that the response of the Z-fiber reinforced sandwich plate from the dynamic analysis is stiffer compared with their experimental counter parts (i.e., the slope of the curve for the analysis is larger than the slope for the experimental curve). Yet, the observation of a close approximation to the initial significant failure load is apparent (1000 N.). Note this load is larger than the static value of 841 N., due to the inertia effects within the dynamic solution.

The difference between the experiment and analysis is postulated to be due to the failure within the top face sheet brought about by the impact of the dropped weight e.g., delamination, matrix cracking and fiber debonding. This

damage results in a lower material stiffness. Since the face sheet failure was not included in the analysis, a discrepancy between the experiment and the numerical modeling can be observed. In order to include the apparent face sheet damage effects, a phenomenological technique is developed in this report. Since the face sheet damage does not create a reduction in failure load, it becomes necessary, using the method of pin buckling to describe damage, to increase the number of buckled pins for an increase in flexibility due to face sheet damage. Thus, face sheet damage is indicated by an additional buckling failure in the Z-pins at the first significant failure load. In other words to achieve the same response the experiment shows for the Z-fiber reinforced sandwich plate, one should include a larger number of buckled pins on top of the number of Z-pins predicted by the analysis. The number of Z-pins required to buckle in order to obtain the same amount of experimental damage corresponding with the first significant failure load (1000 N.) is determined based on the initial slope (i.e., stiffness) of the experimental results. This decrease of slope is taken to be linearly related to the number of buckled pins. Thus, if we go back to Figure 4.9 (even though it relates to a static condition) it is observed that at 1000 N., there is one pin failing. In order to decrease the slope to correspond initially to the experiment, one would expect five pins to fail using this technique which is not unreasonable. After which, by adjusting the initial response of the model to account for the face sheet damage, one can continue to evaluate further plate response by including the analytical stiffness over the remaining time as shown

in Figure 4.26. The method produces reasonable results compared to experimentation.

In addition to the equation of motion study as related to a force-time function, the author studied the natural frequencies and mode shapes of the Z-pin sandwich panel with and without failure. The commercial software NASTRAN was used for the analysis. The same simply supported boundary conditions along all the free edges of the lower face sheets previously indicated was used as the boundary conditions. A total of 7202 elements and 5000 nodes were used in the model. Of these, 4802 are QUAD4 elements (to represent the face sheet) and 2400 are CROD elements (for pins). Overall effective dimensions of the panel are 3. In X 3. in. The finite element model to represent the panel is shown in Figure 4.3. The first three natural mode shapes for this panel without any pin failures are shown in Figures 4.27-4.29. The natural frequencies corresponding to this panel are shown in the second column of Table 4.1.

As a next step in order to study the effect of the failure of the pins on the natural frequencies, 8 central pins are assumed to have failed. To model this pin failure, the Young's modulus of the failed pins was reduced to one percent of their original value as before (without modifying the density or the connection of the pins). A normal mode analysis was carried out using NASTRAN, and the natural frequencies along with mode shapes were determined. From the natural frequencies and mode shapes, it was observed that there is no noticeable change in the first three mode shapes. Changes in the natural frequencies

corresponding to these pin failures are listed in the third column of Table 4.1. The next two failure configurations considered were 32 pin failures and 48 pin failures. Again, while there is no significant change in the mode shapes, the changes in the natural frequencies are listed in Table 4.1. Also shown in the table is the percent change in the natural frequencies corresponding to each failure. It can be observed, as one would expect, that as the number of pins fail the natural frequency reduces. The reduction is less significant as the mode number increased.

References:

- [1] Kamath, Mohan, J., "Damage Tolerance of Sandwich Composites" Masters Thesis, Tuskegee University, Tuskegee, Alabama, 1998.
- [2] Herup, Eric, and Palazotto, Anthony, "Low Velocity Impact Damage Initiation Graphite/Epoxy/Nomex Honeycomb Sandwich Plates," Composite Science and Technology, Vol. 57, pp. 1581-1598, 1997.

Table 4.1: Natural Frequencies of Z-pin Panel

Mode Number	Panel without failure	8 pins failure	32 pins failure	48 pins failure
1 st mode	2621.02 Hz	2569.73 Hz (-1.95%)	2484.9 Hz (-5.19%)	2466.49 Hz (-5.9%)
2 nd mode	3008.01 Hz	2995.7 Hz (-0.43%)	2937.8 Hz (-2.33%)	2912.1 Hz (-3.19%)
3 rd mode	3676.82 Hz	3674.15 Hz (-0.07%)	3664.12 Hz (-0.35%)	3659.34 Hz (-0.48%)

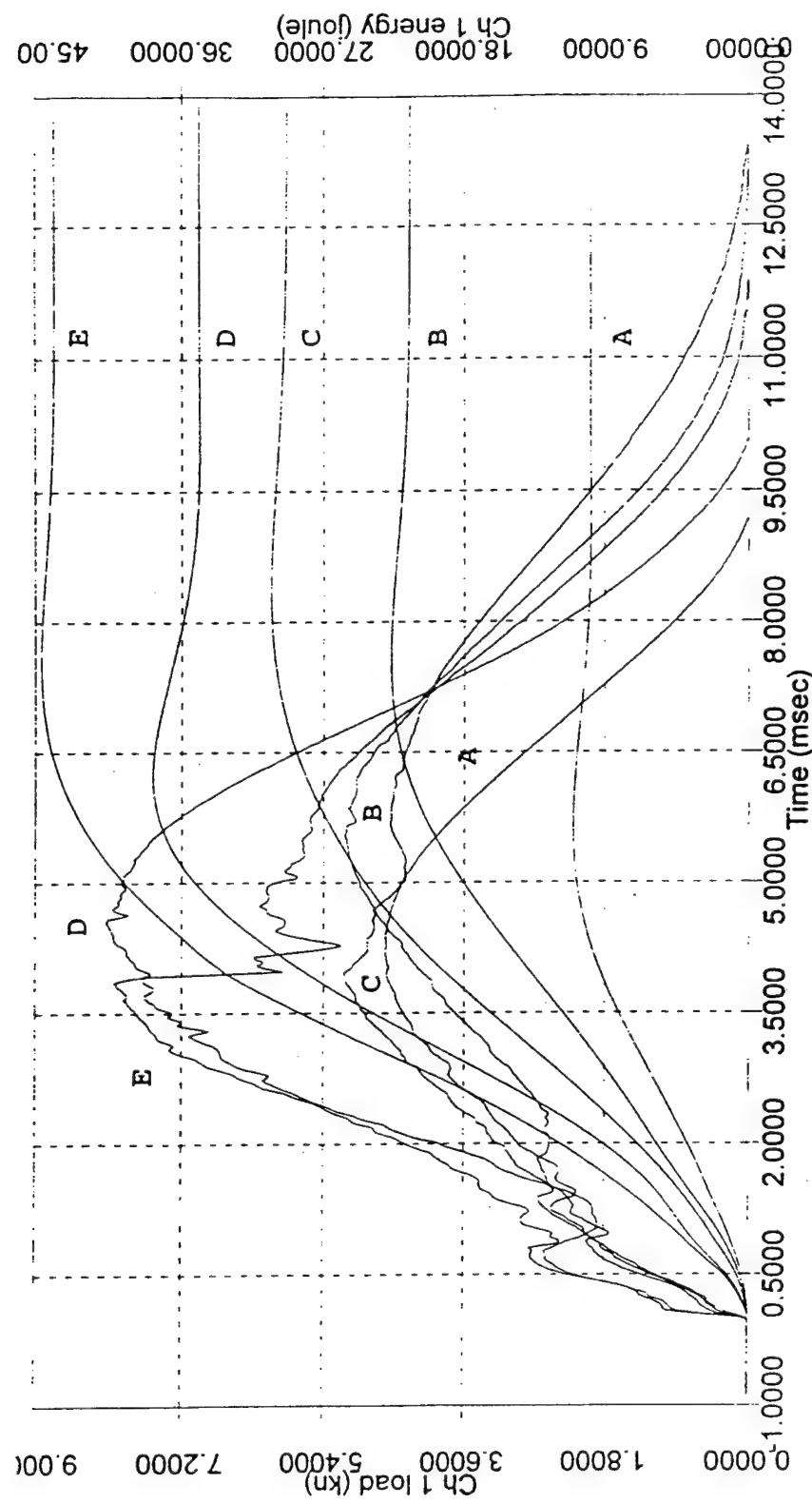


Figure 4.1 Force-time and energy-time curves

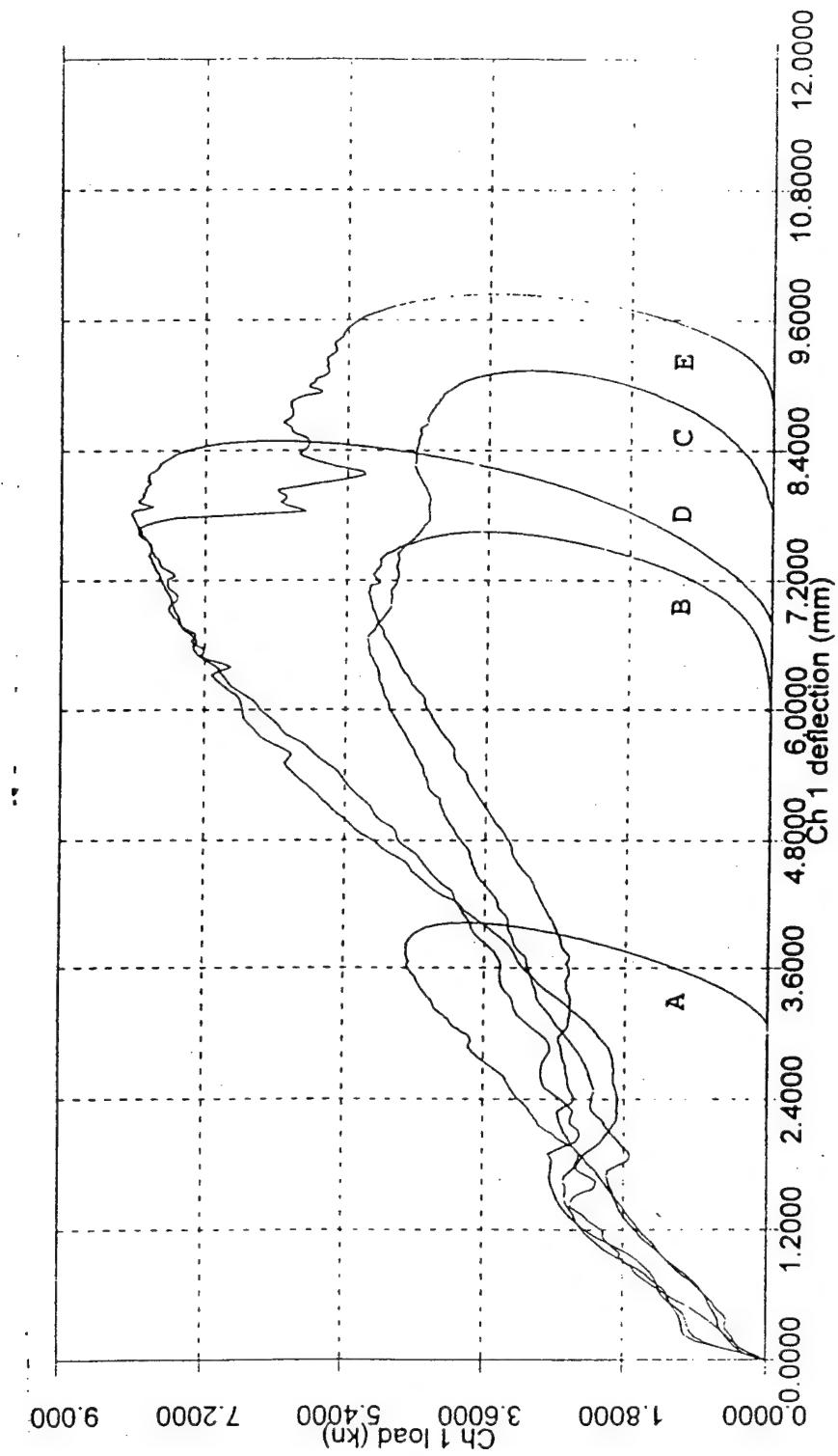
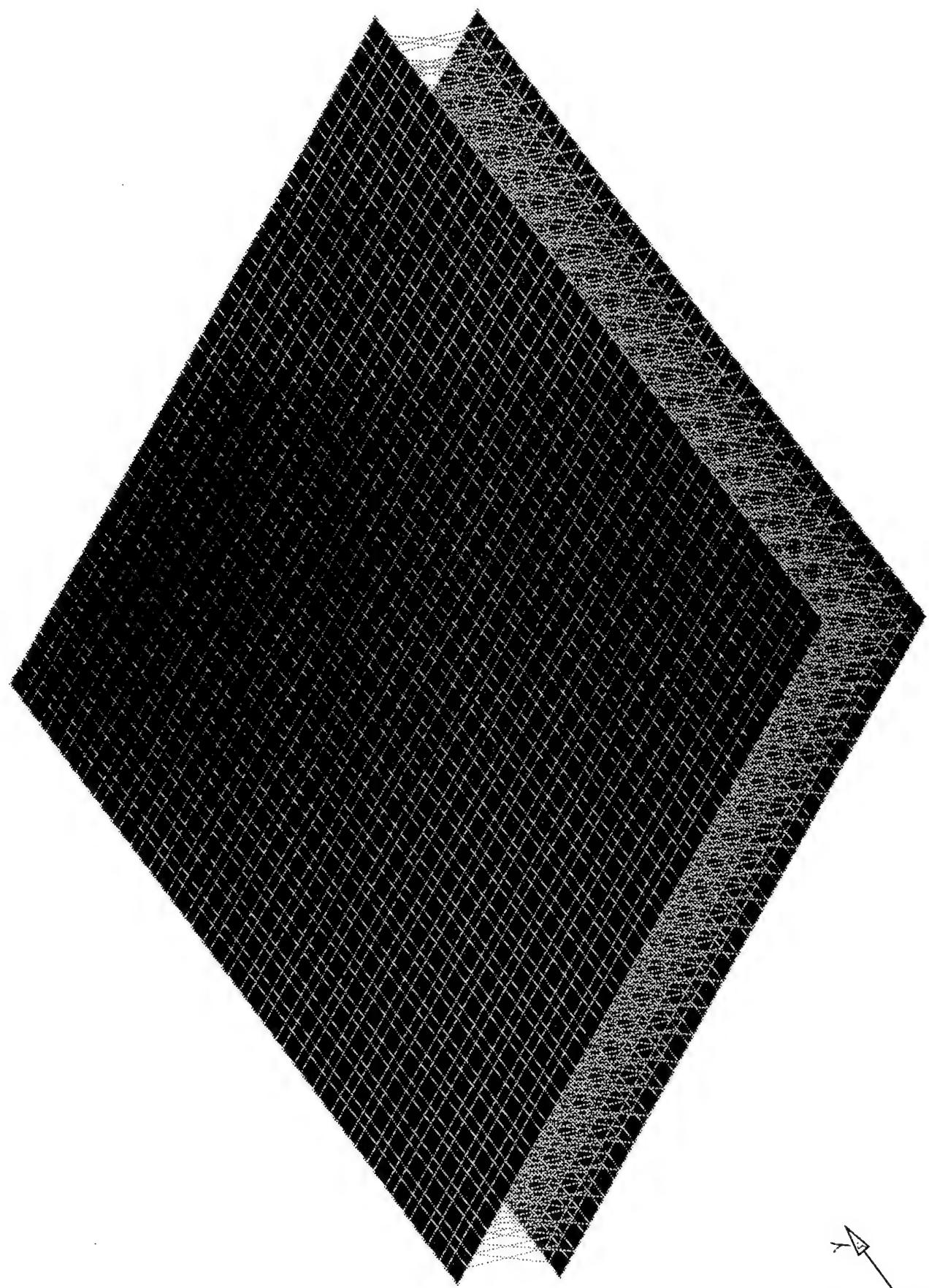


Figure 4.2 Land-deflection curves



A - 37

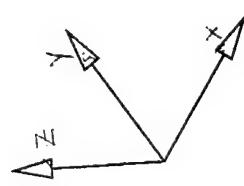


Figure 3.1 Sandwich plate model

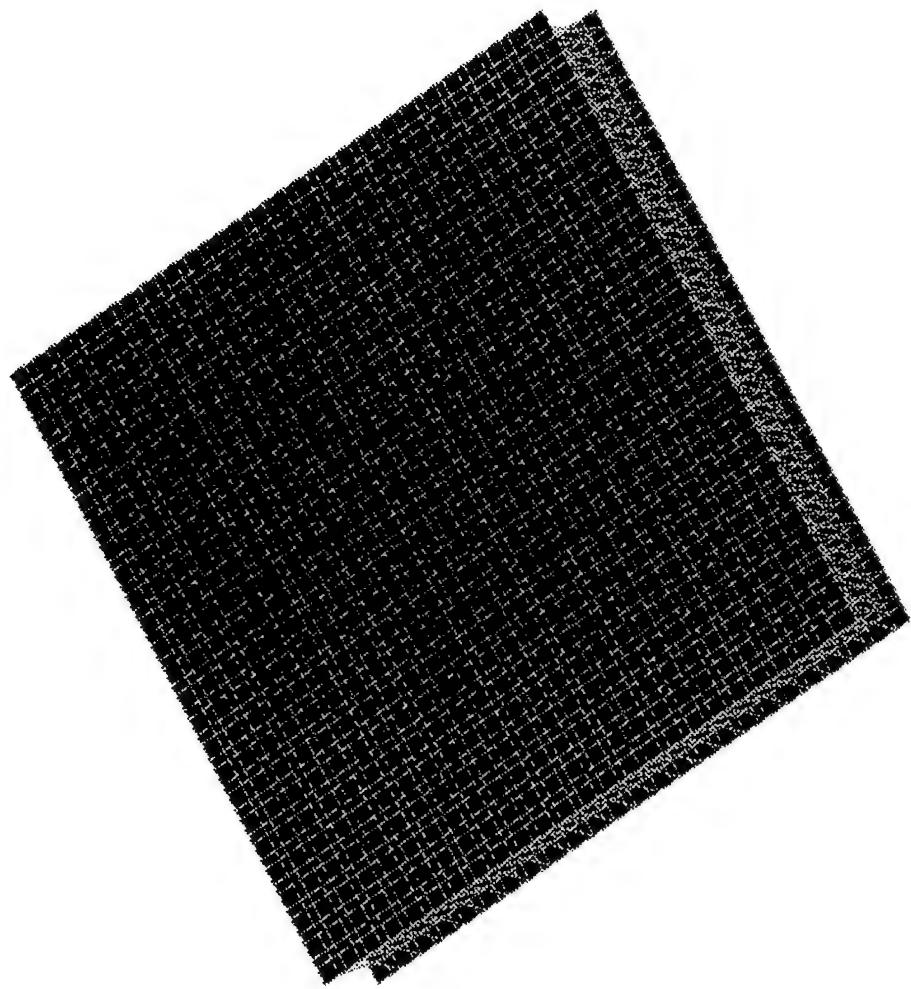
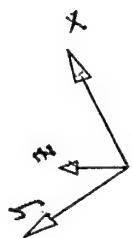


Figure 4.3 Sandwich plate model



step inc 5, t=2.50e-02
Displacements

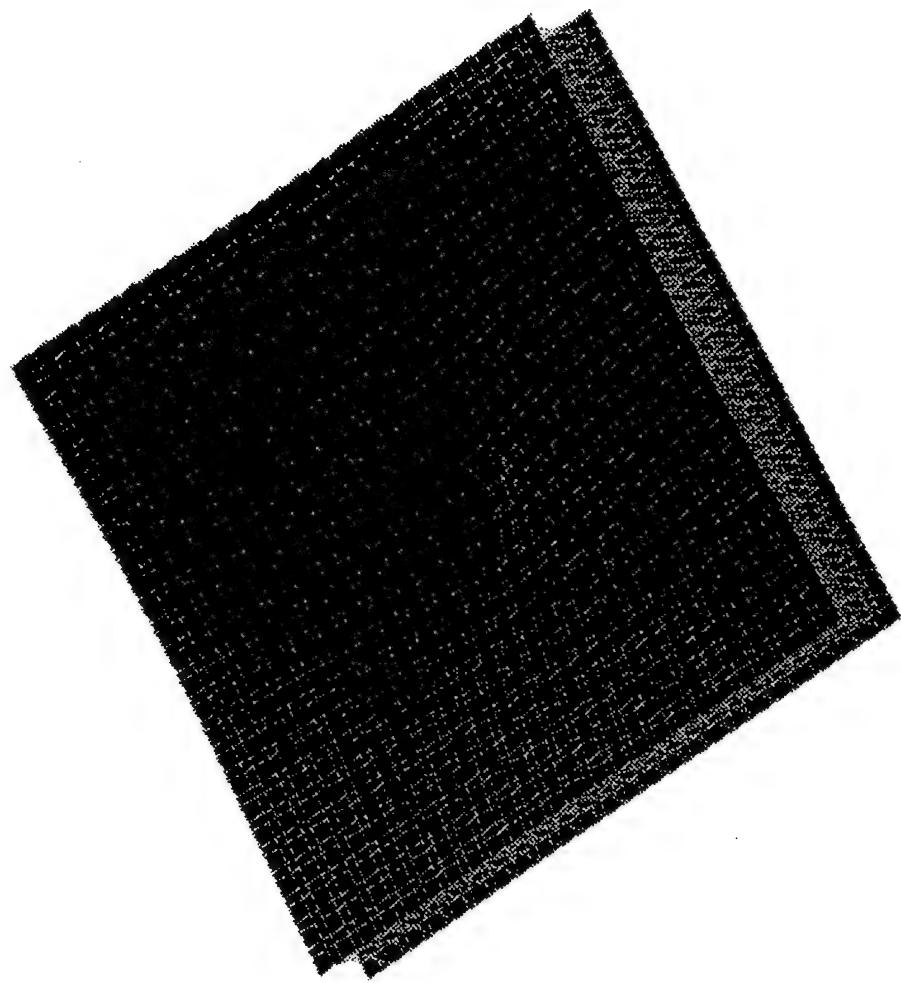
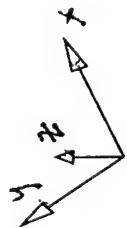


Figure 4.4 Load position



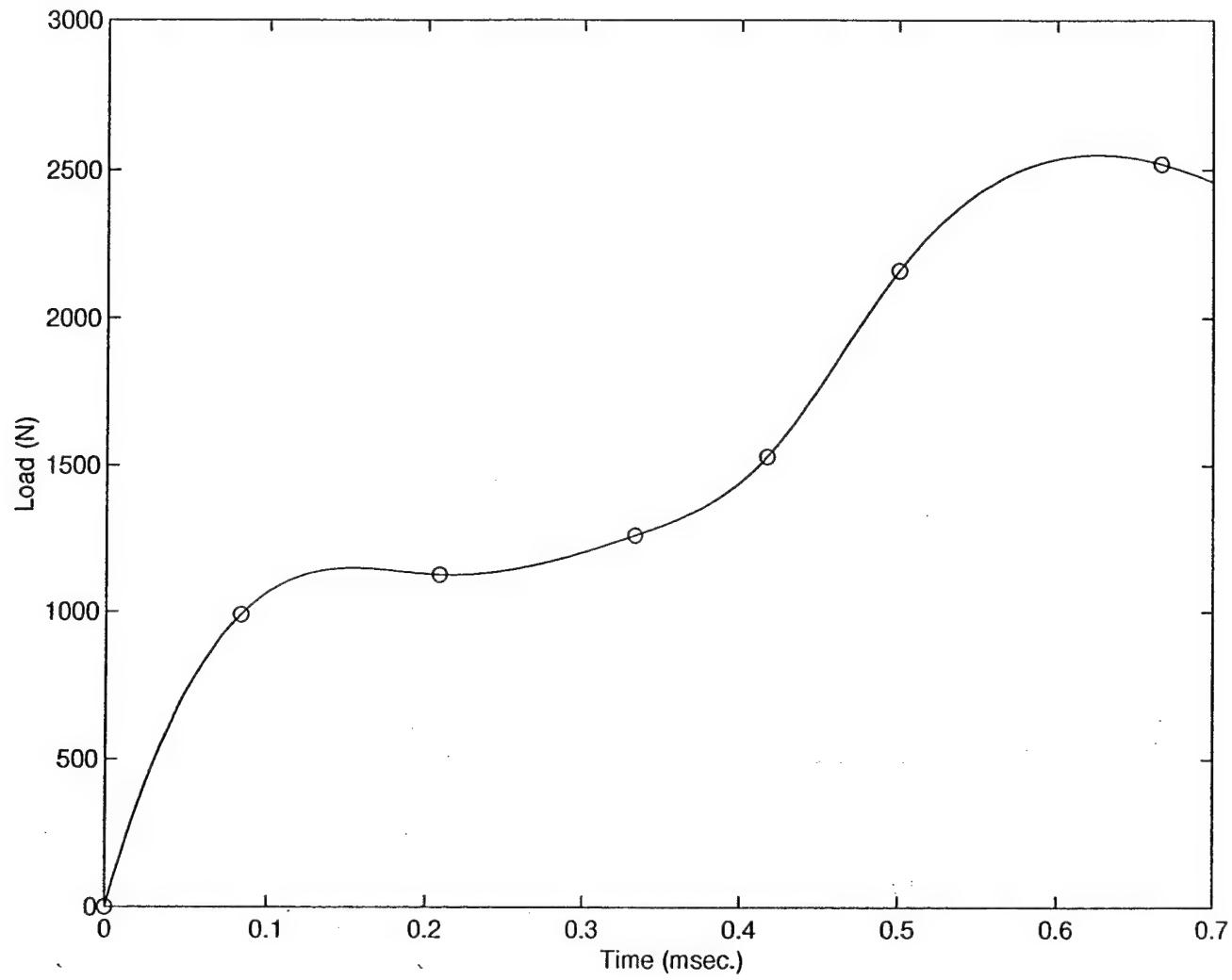


Figure 4.5 Load-time function

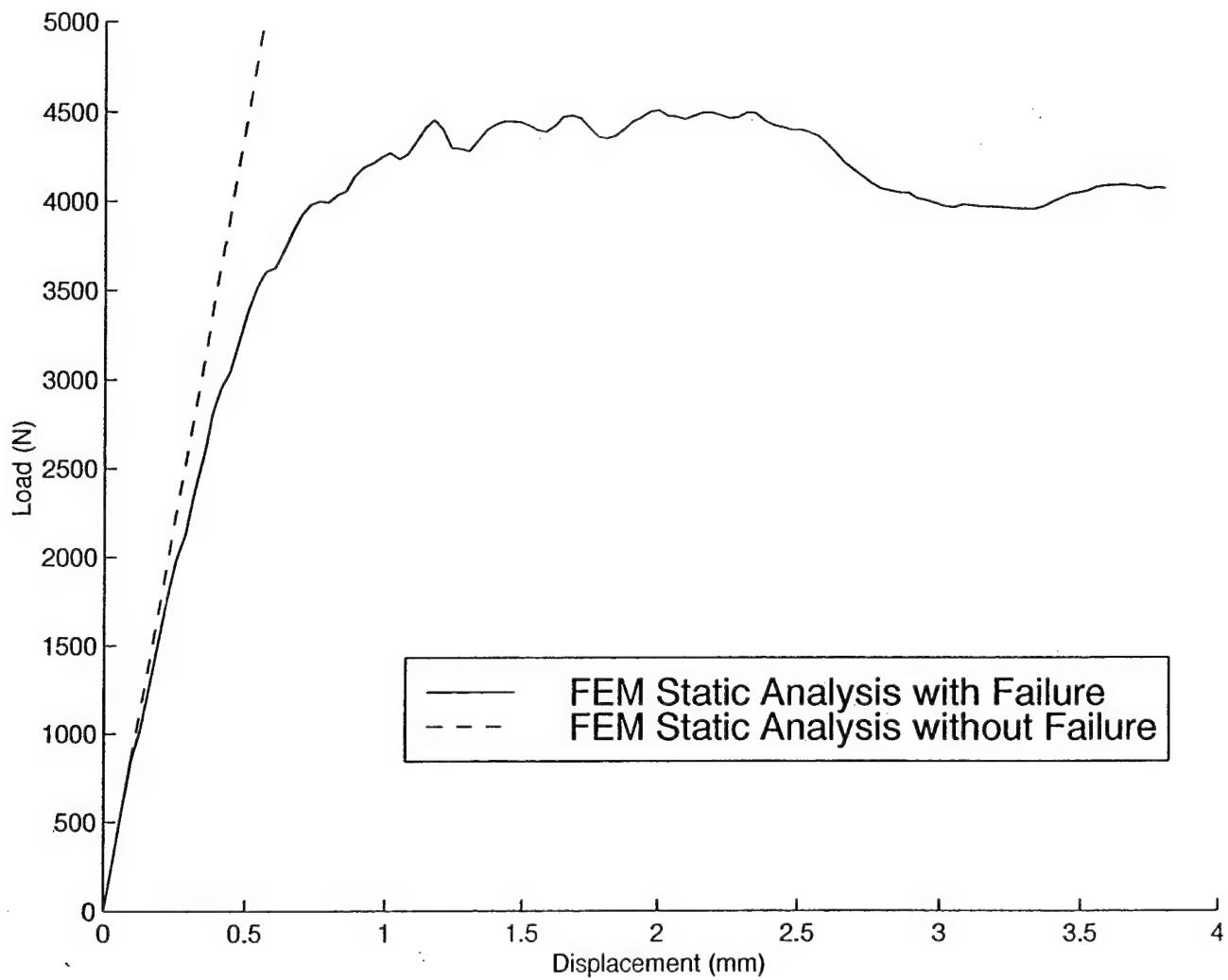


Figure 4.6 Finite element static analysis

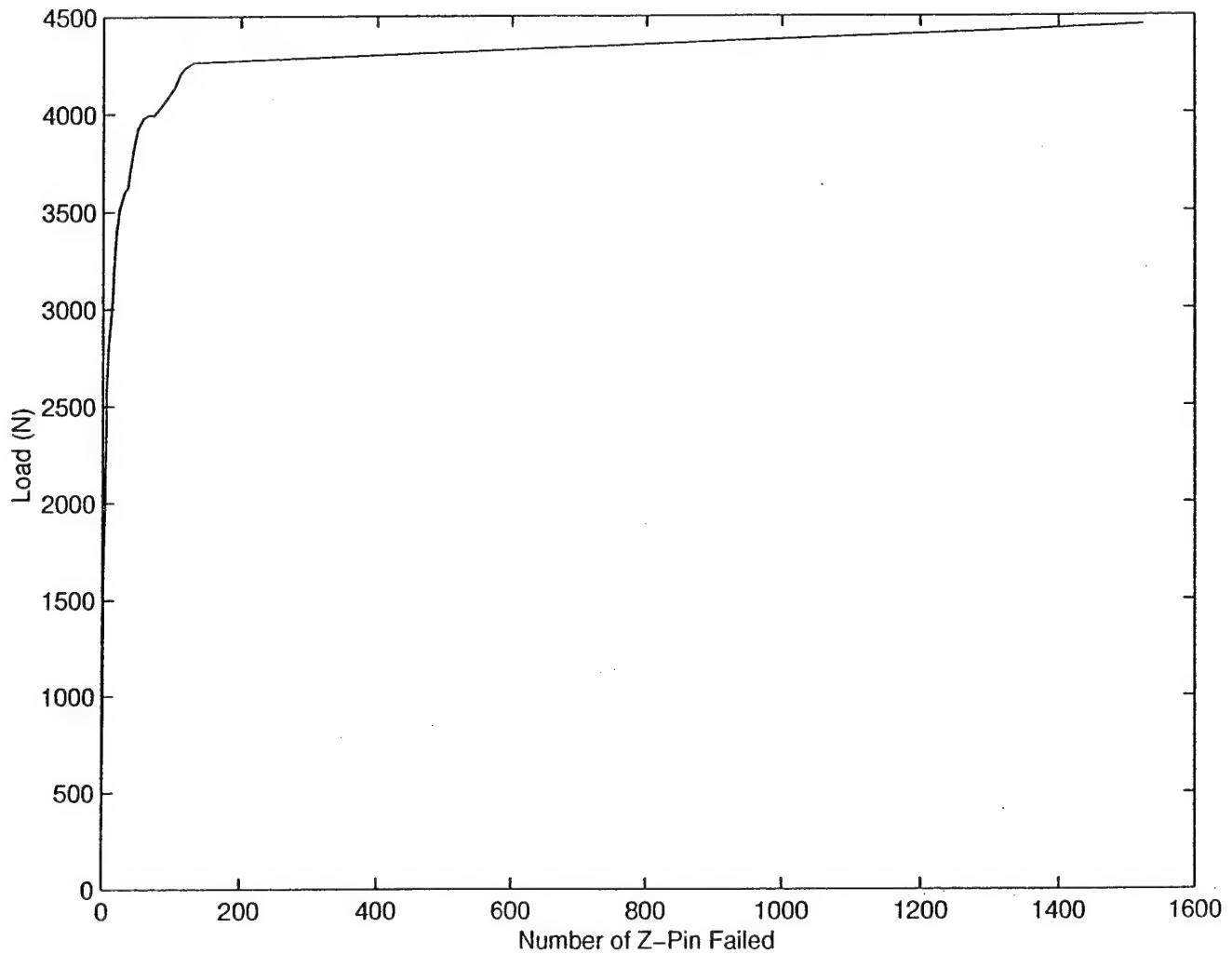


Figure 4.7 Load vs. Pin failures

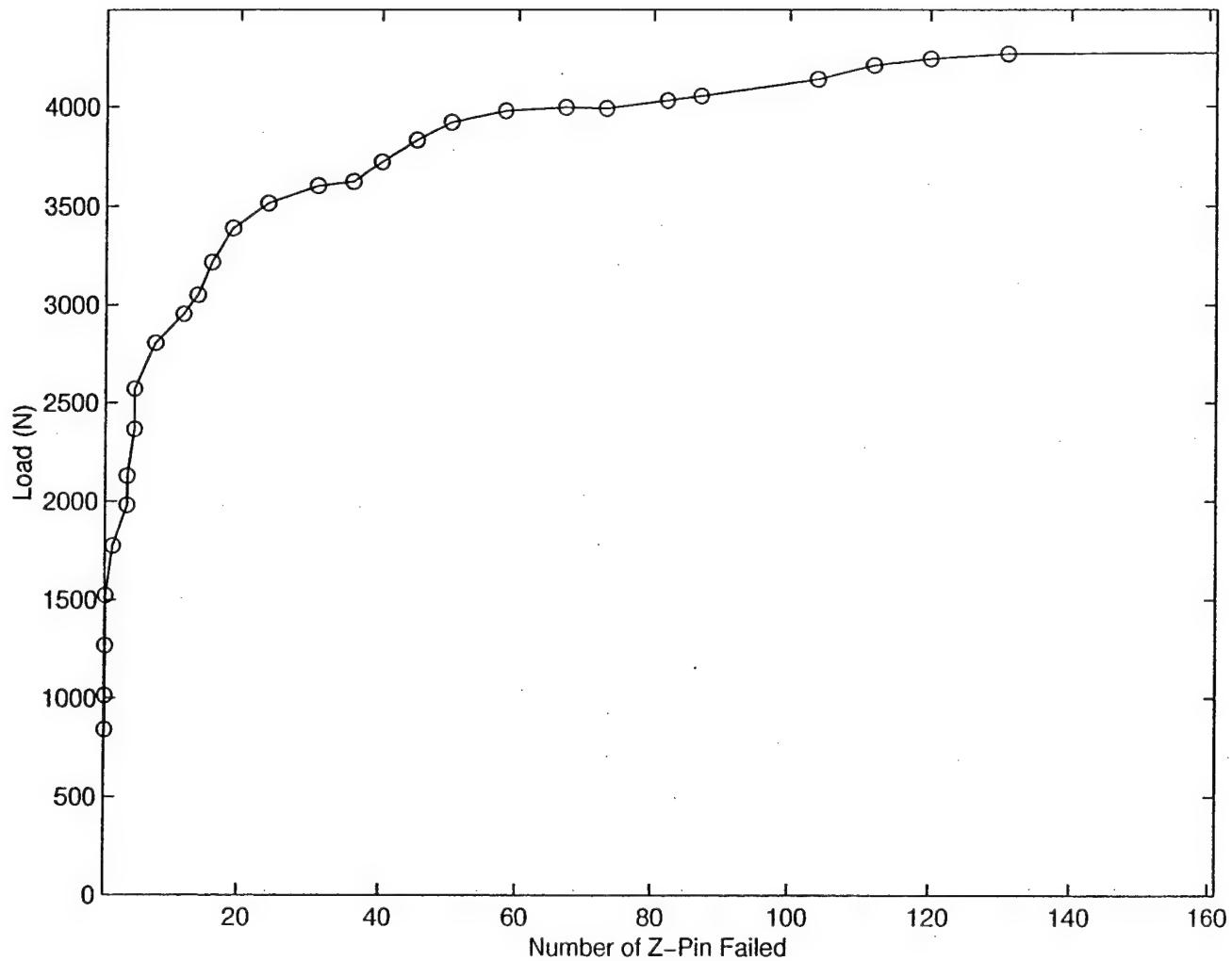


Figure 4.8 Load vs. Pin failures (up to 160 pins)

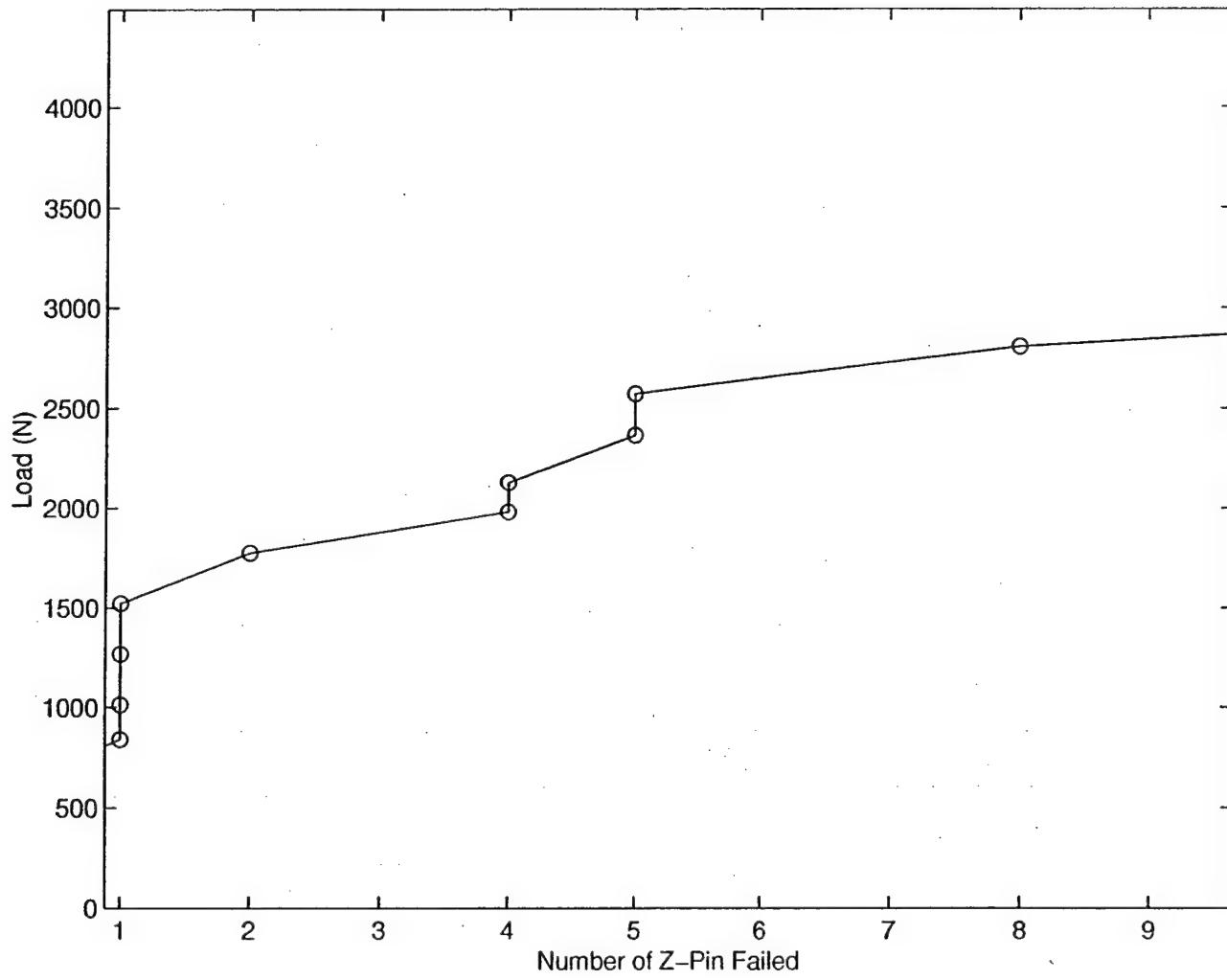
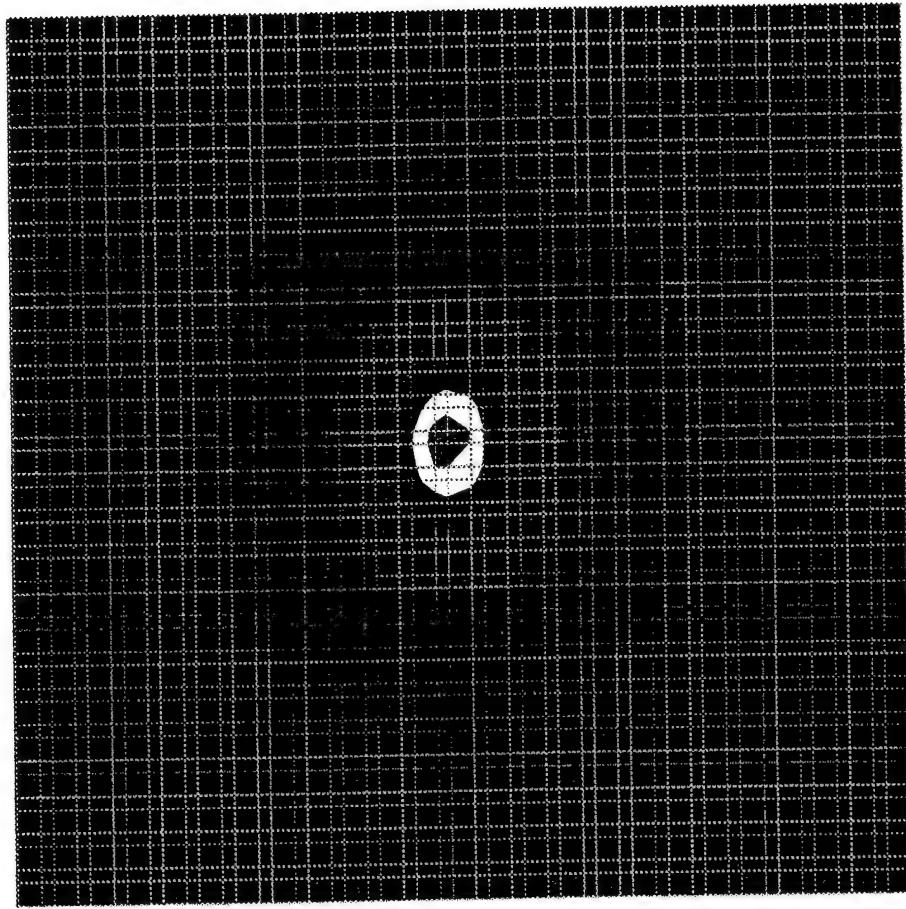
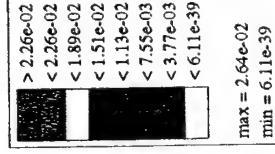


Figure 4.9 Load vs. Pin failures (up to 10 pins)

step1 inc:20, t=1.88e-01
Displacements



A - 45

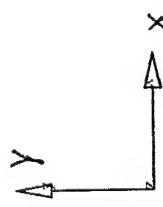


Figure 4.10 Vertical displacement of top face sheets, force equals 4.39 kN

This Page Left Blank

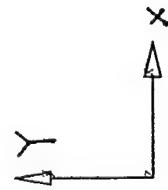
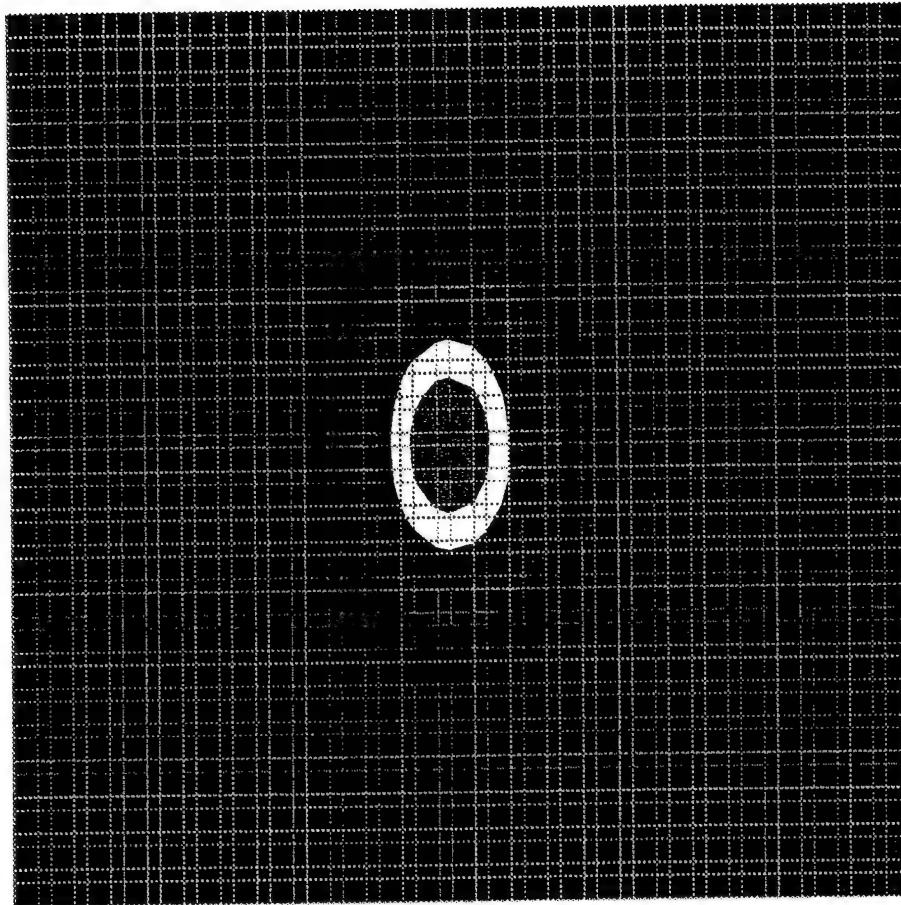
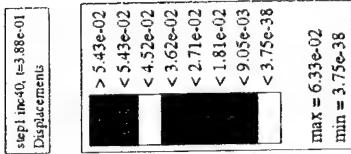


Figure 4.11 Vertical displacement of top face sheets, force equals 4.41 kN

Figure 4.12 Vertical displacement of top face sheets, force equals 4.08 kN

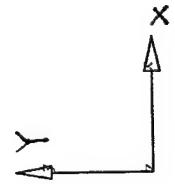
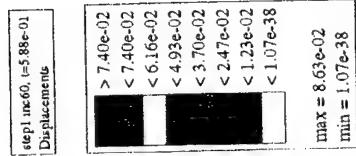
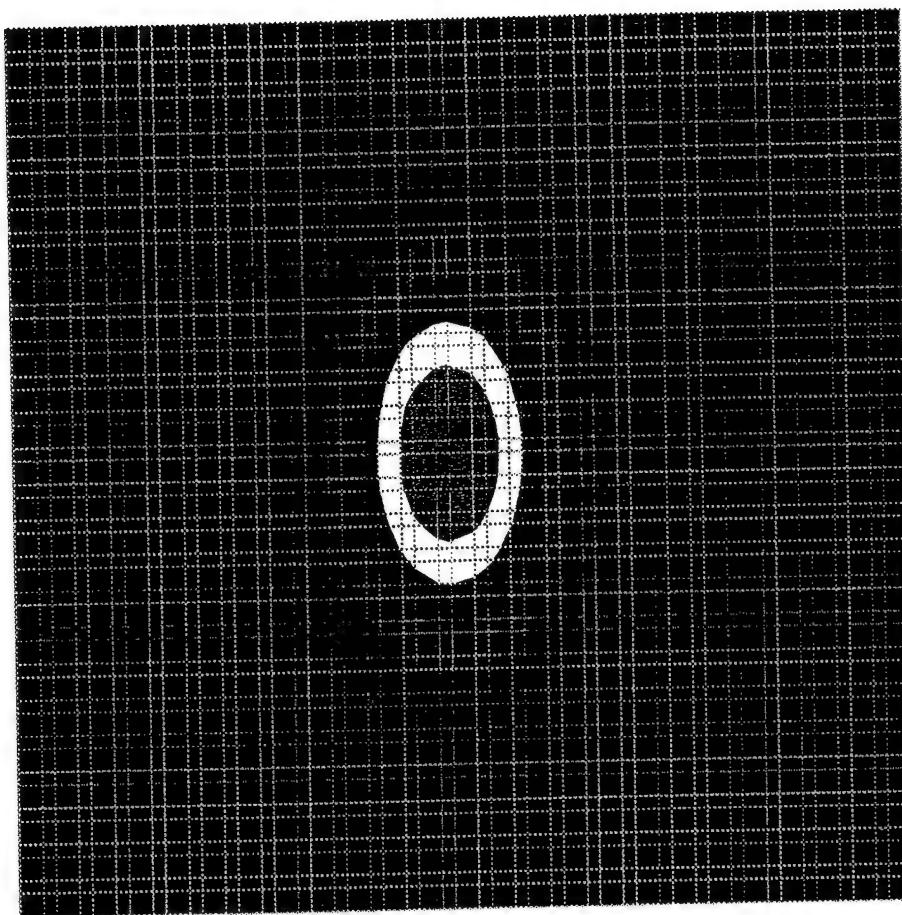
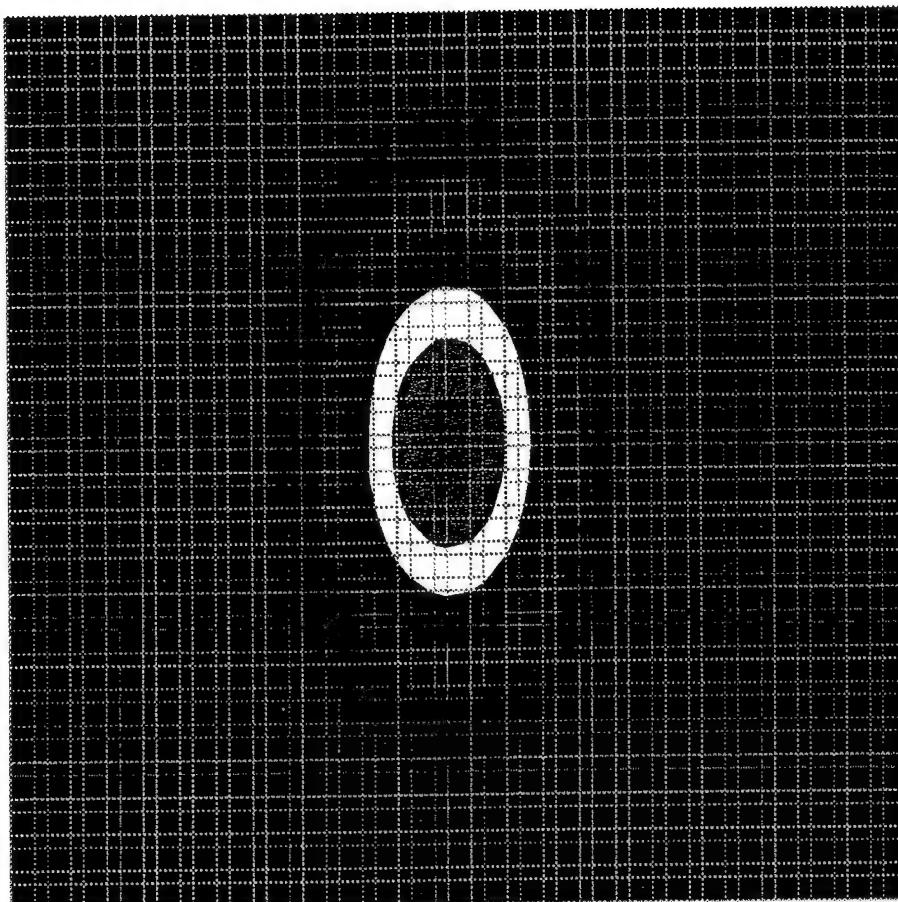
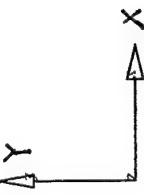


Figure 4.13 Vertical displacement of top face sheets, force equals 4.05 kN



step inc80 t=7.38e-01
Displacements

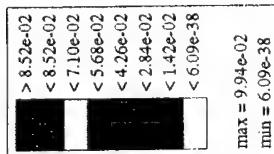
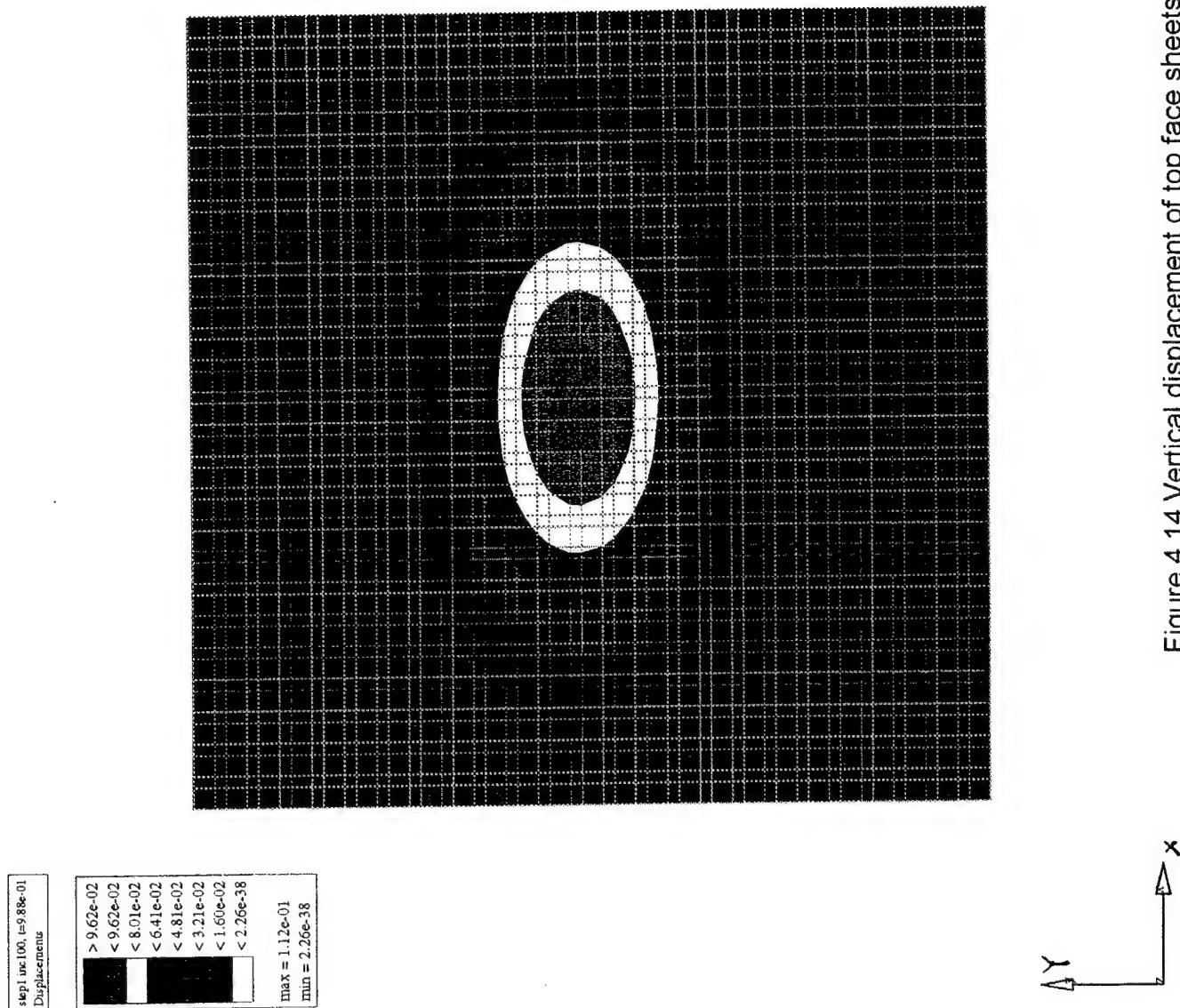


Figure 4.14 Vertical displacement of top face sheets, force equals 4.14 kN



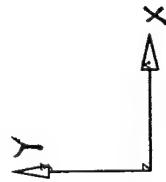
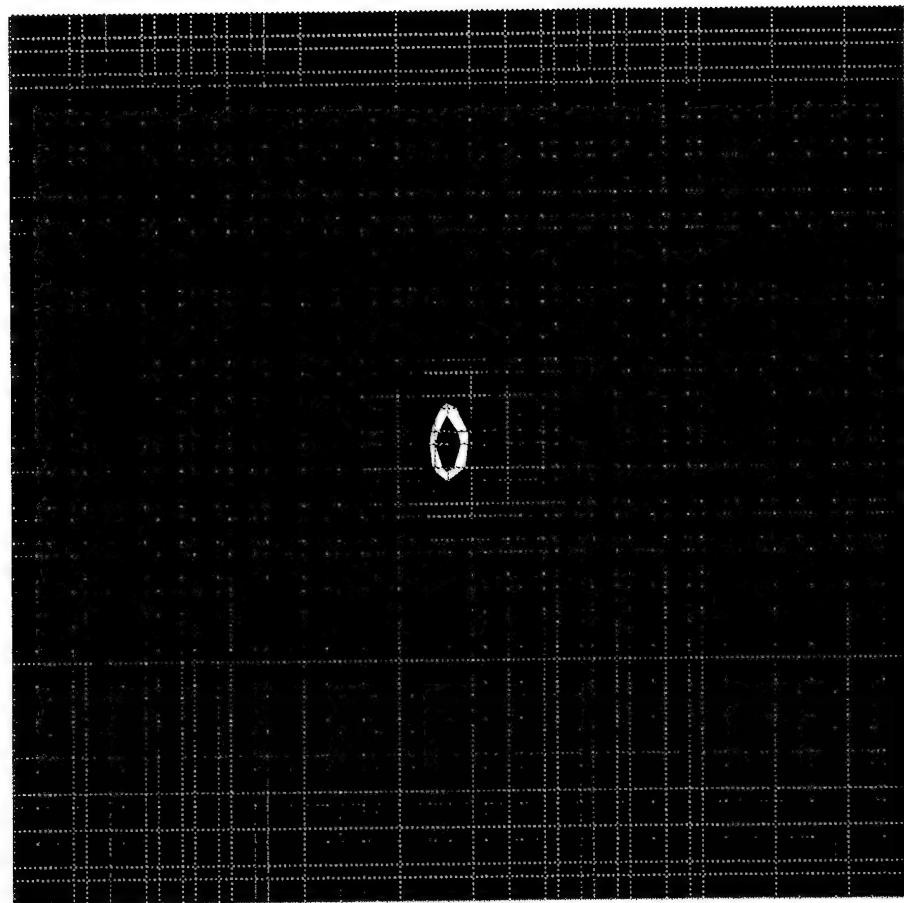
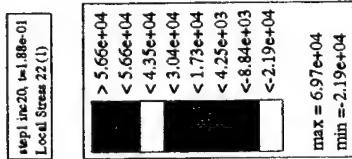
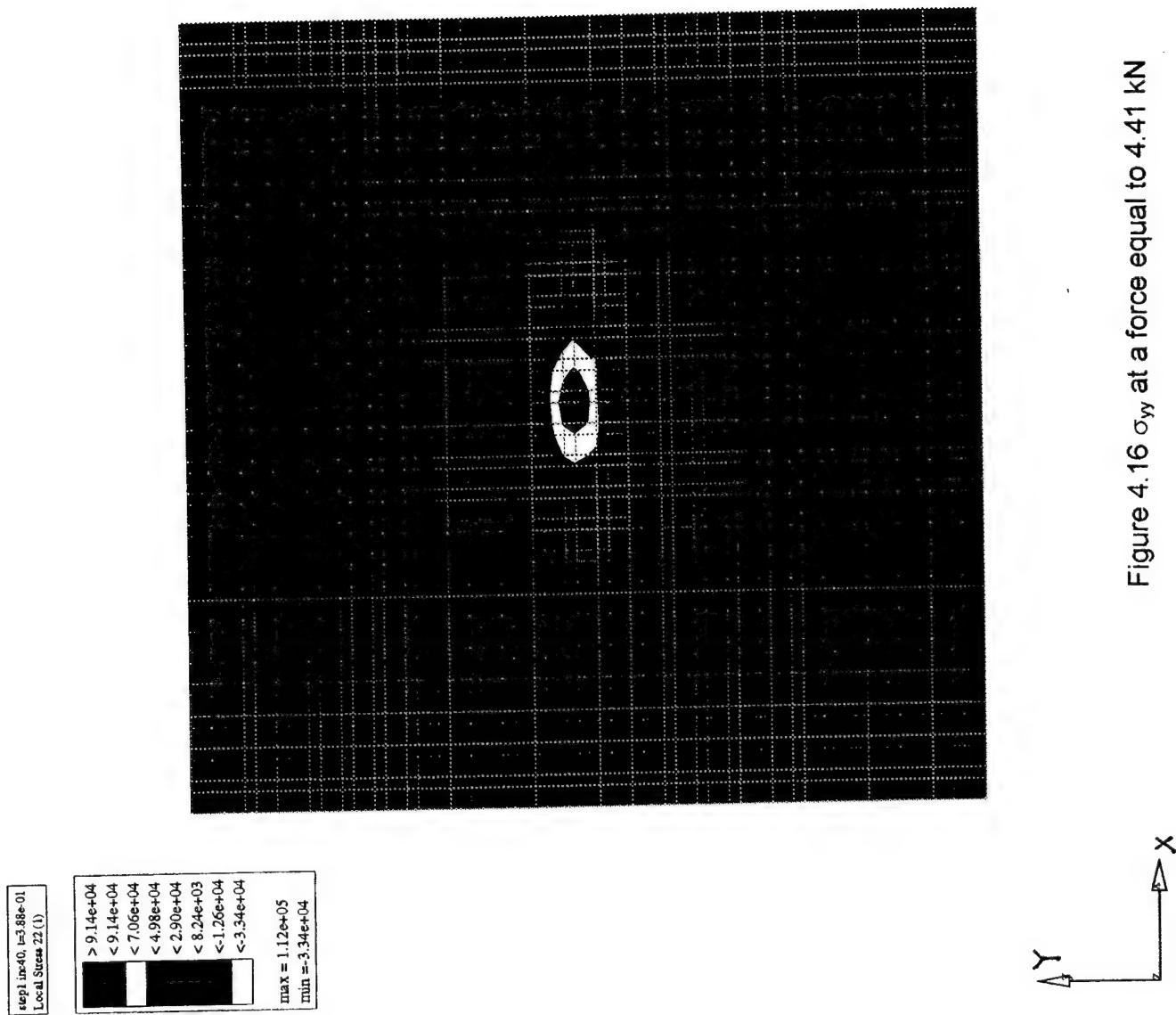


Figure 4.15 σ_y at a force equal to 4.39 kN

Figure 4.16 σ_y at a force equal to 4.41 kN



step in 0, val 7.98e-01
Local Stress 22 (1)

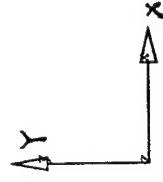
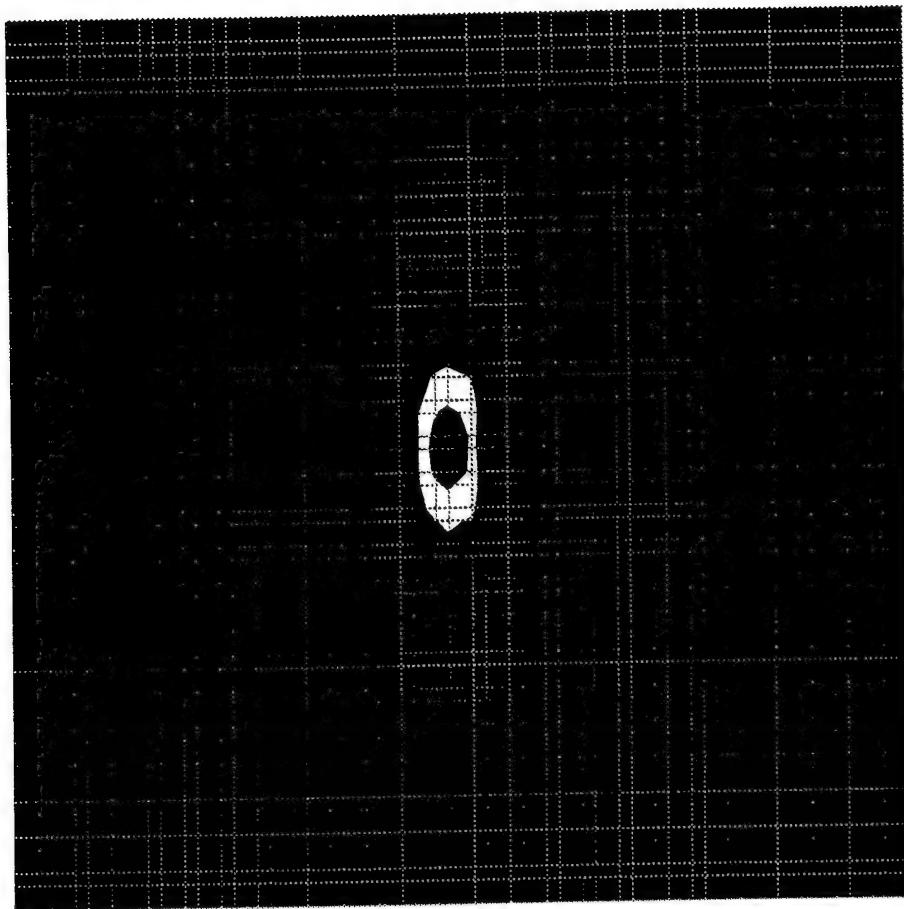
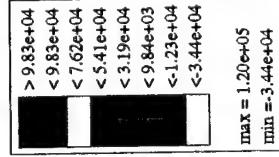


Figure 4.18 σ_y at a force equal to 4.05 kN

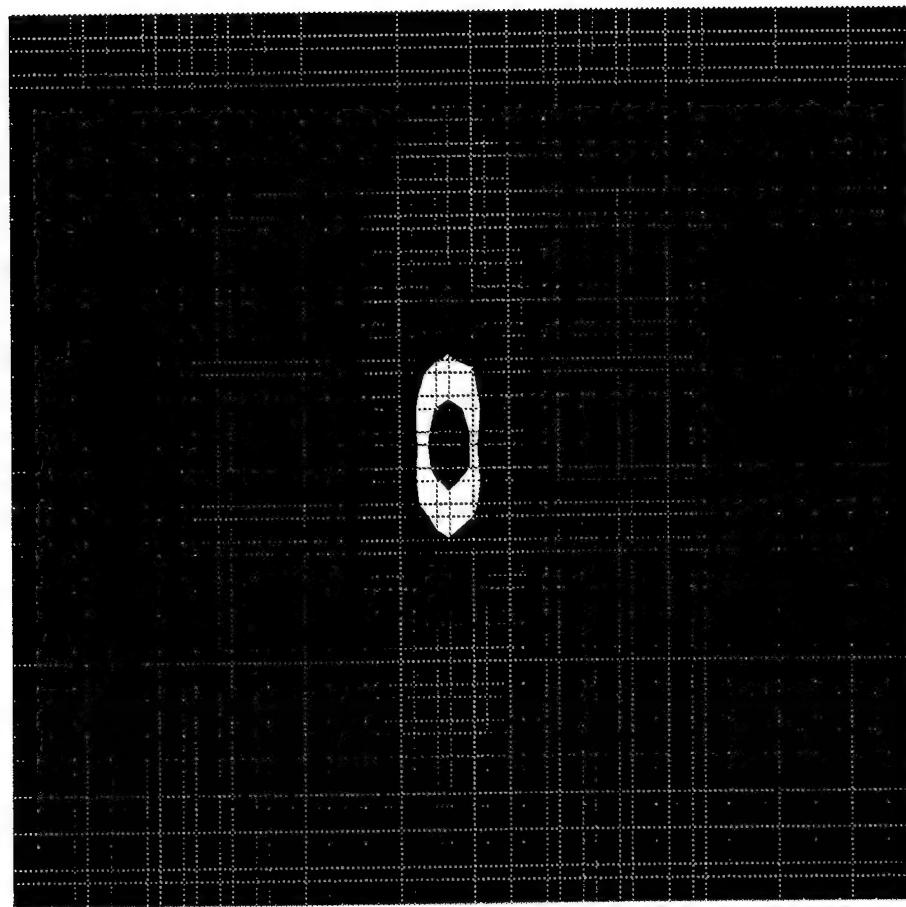
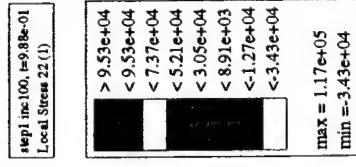
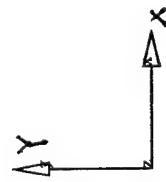


Figure 4.19 σ_{yy} at a force equal to 4.41 kN



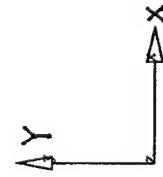
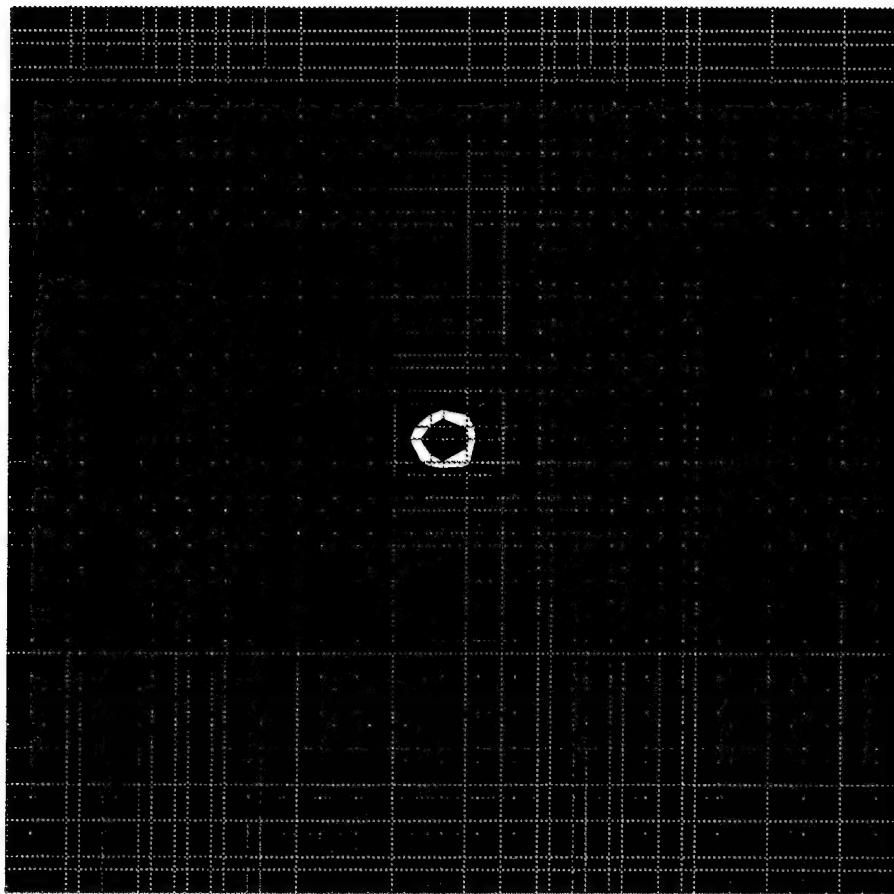
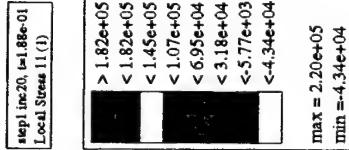


Figure 4.20 σ_{xx} at a force equal to 4.39 kN

step11x40, t=1.81e-01
Local Stress 11(1)

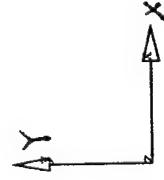
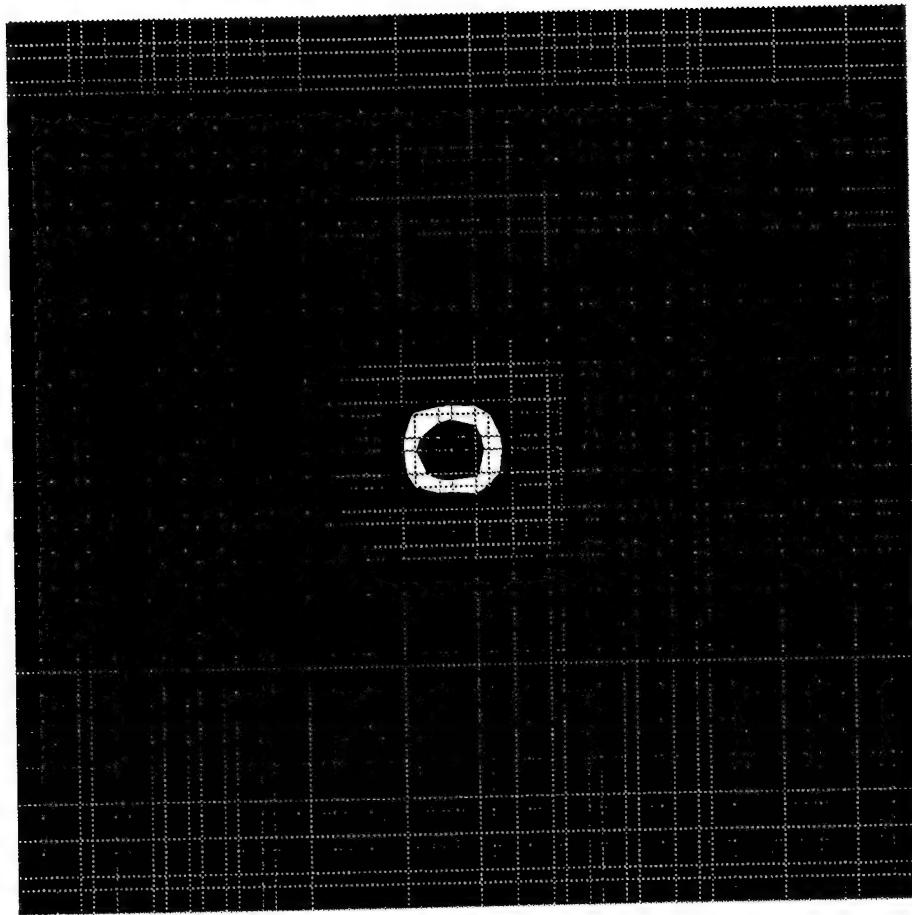
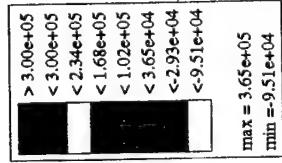


Figure 4.21 σ_{xx} at a force equal to 4.41 kN

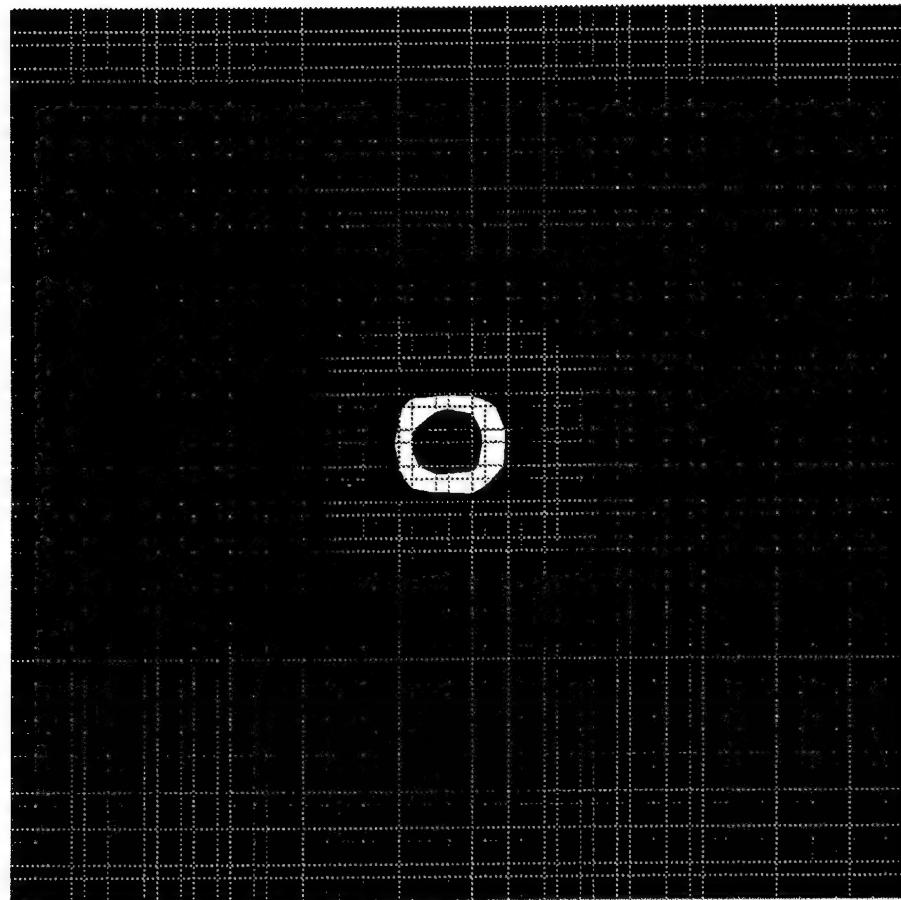
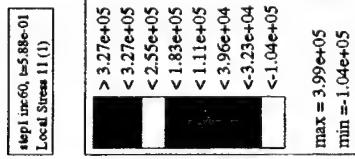
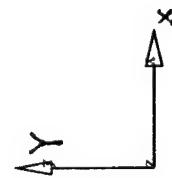


Figure 4.22 σ_{xx} at a force equal to 4.05 kN



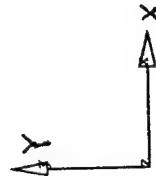
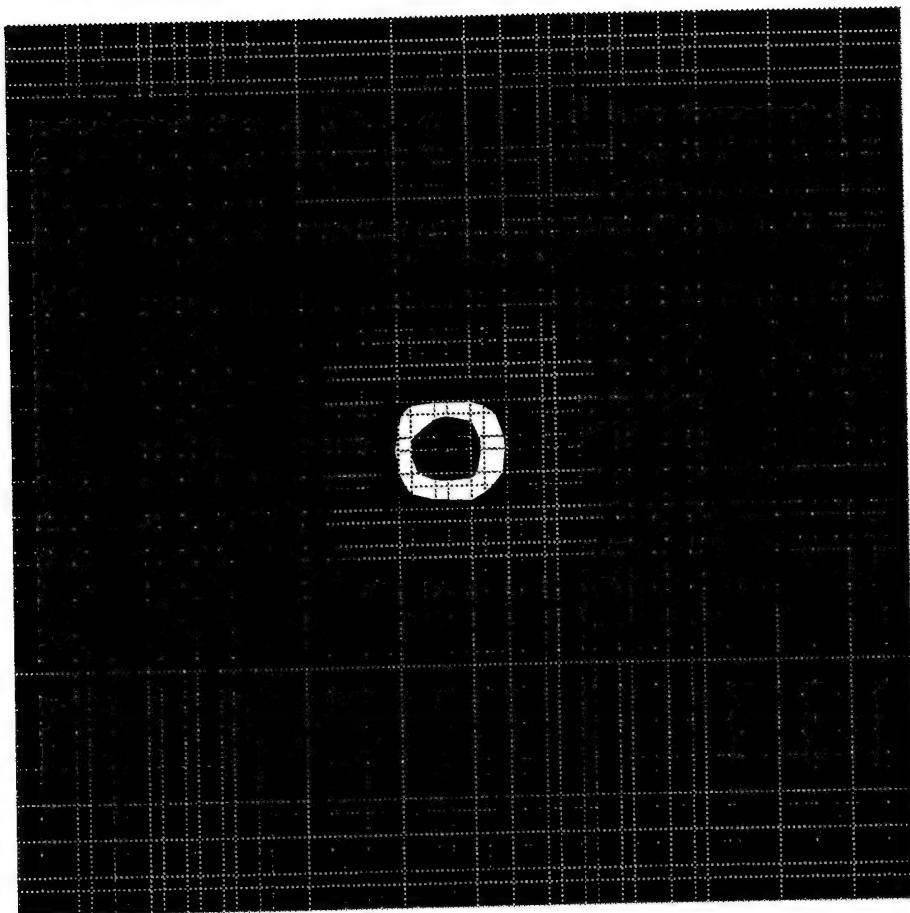
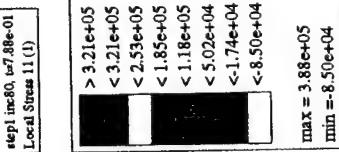


Figure 4.23 σ_{xx} at a force equal to 4.05 kN

Step Inc [0.0, 1e-9.85e-01]
Local Stress II (1)

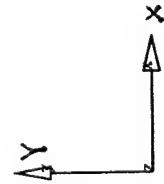
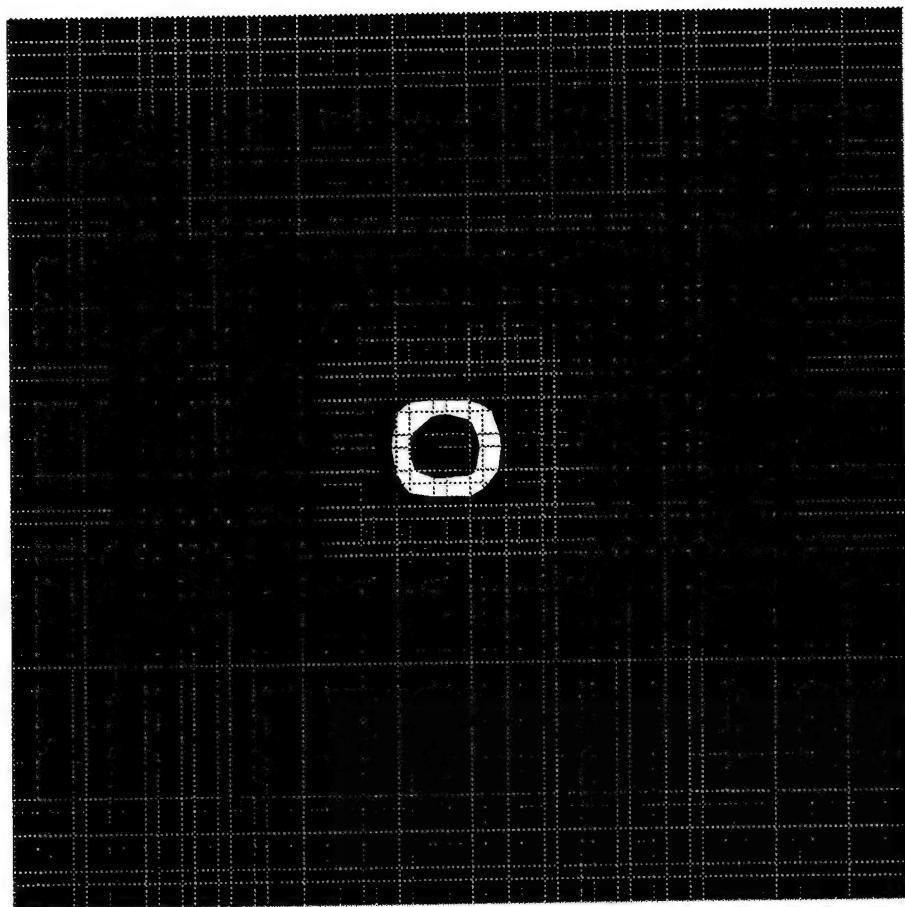
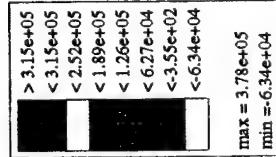


Figure 4.24 σ_{xx} at a force equal to 4.41 kN

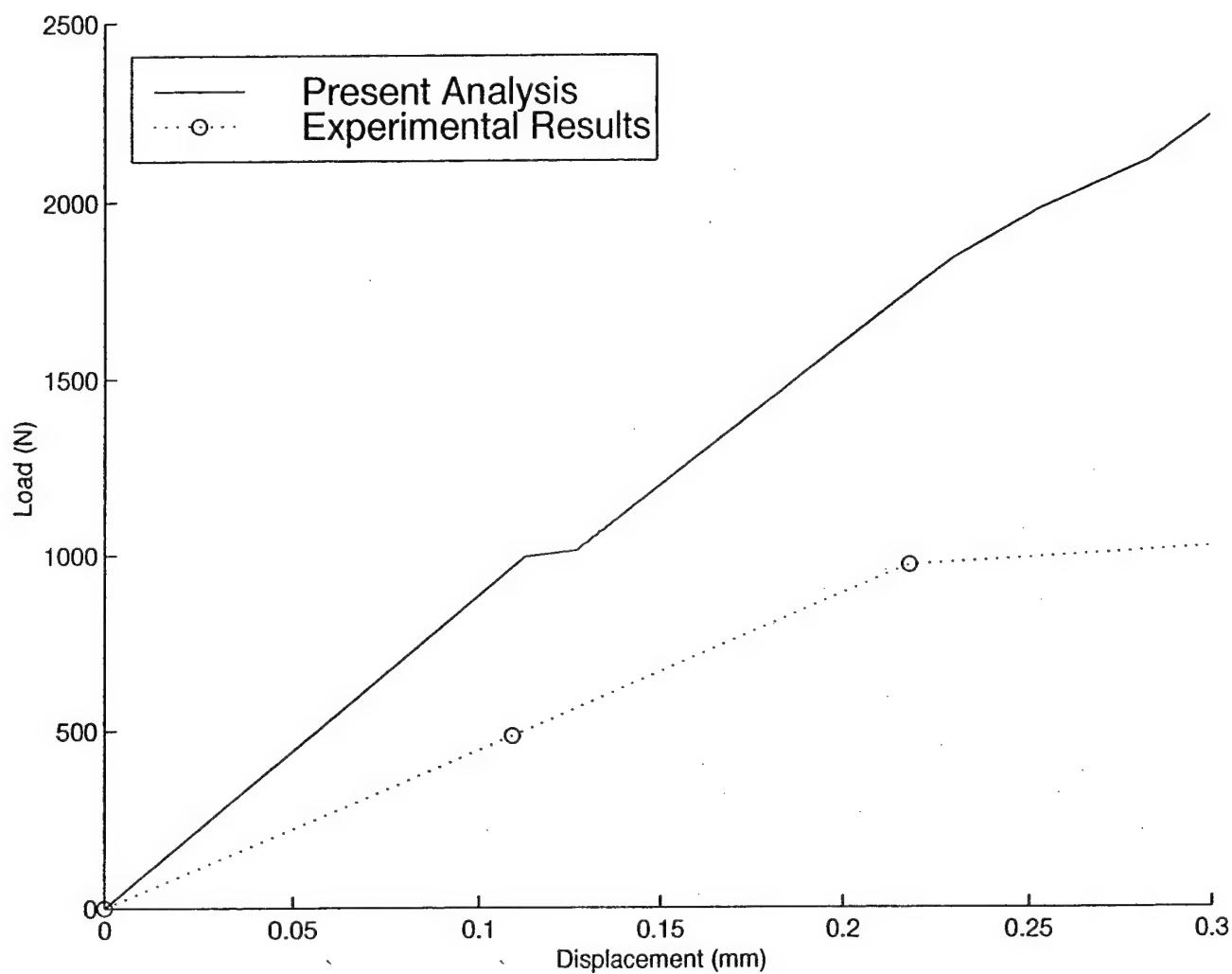


Figure 4.25 Dynamic analysis results

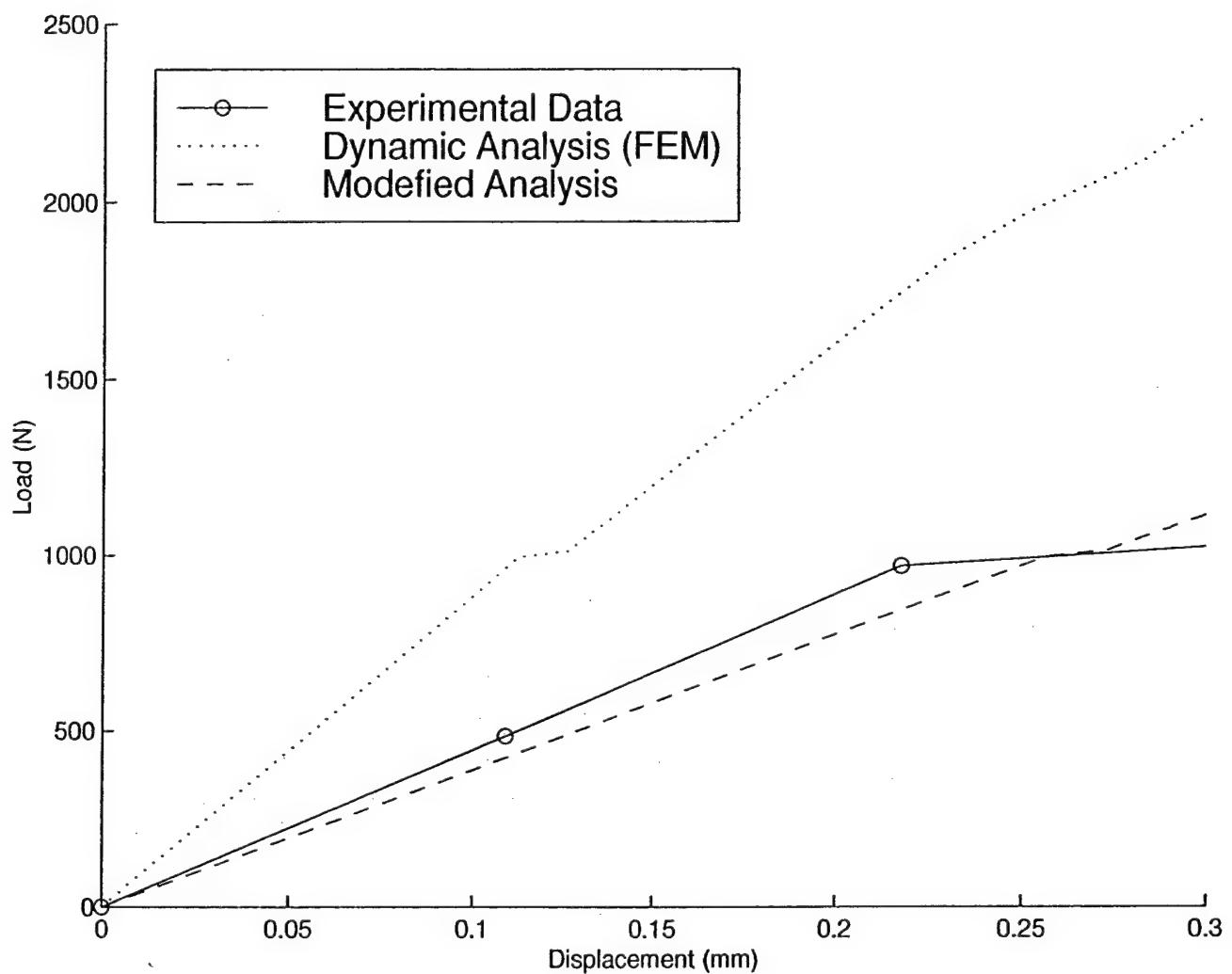
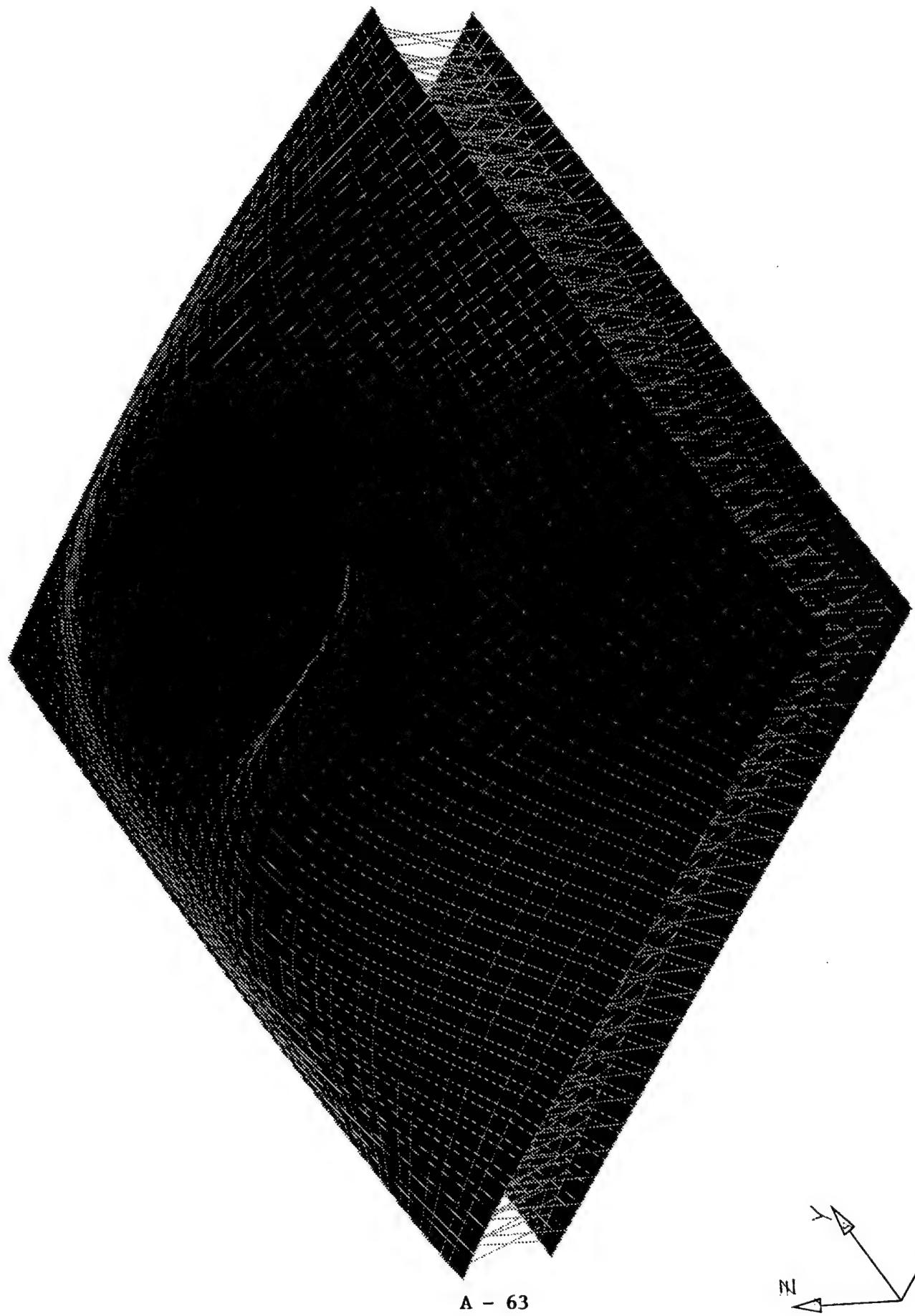
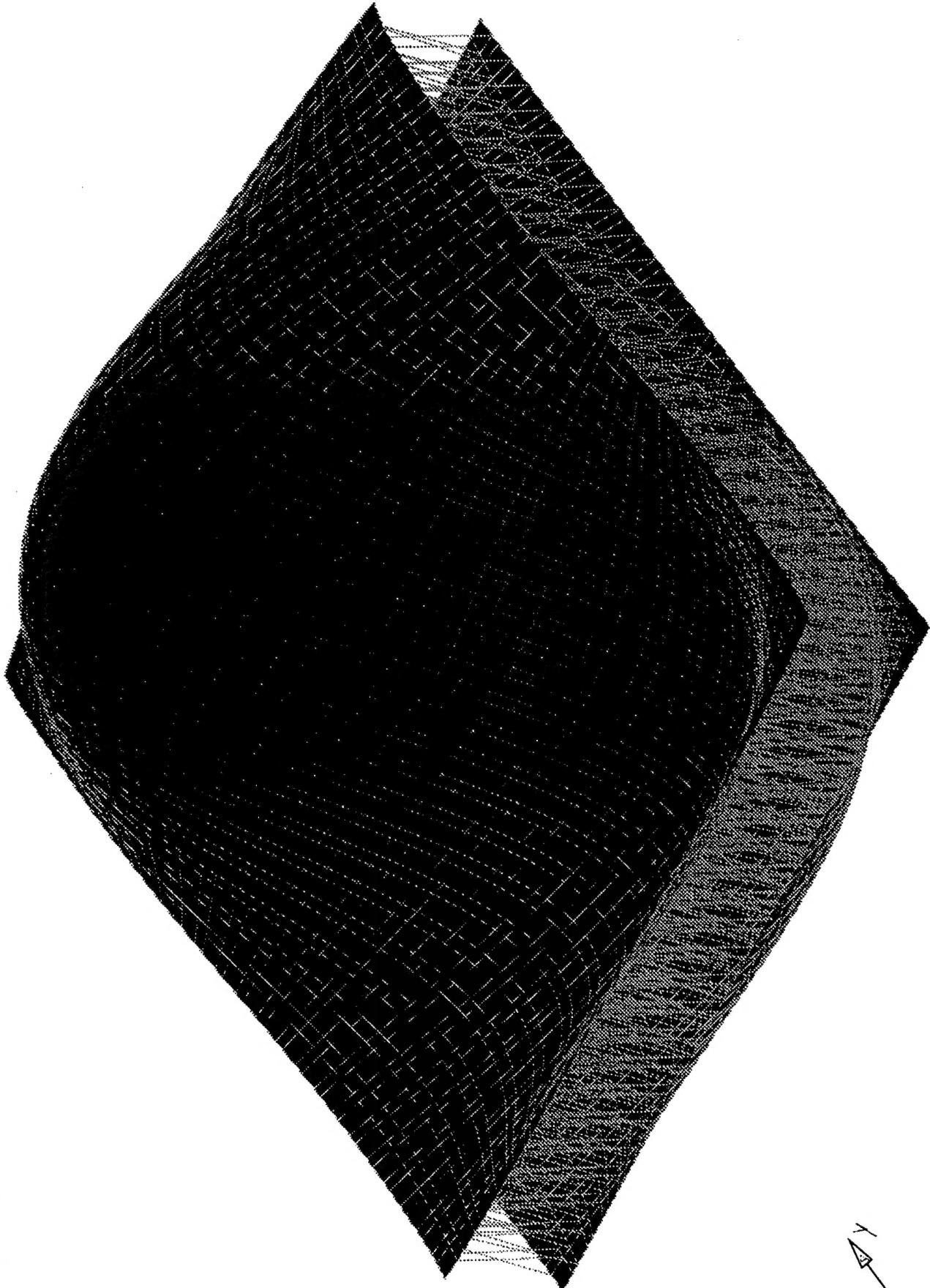


Figure 4.26 Dynamic analysis results with face sheet failure

Figure 4.27 First mode shape



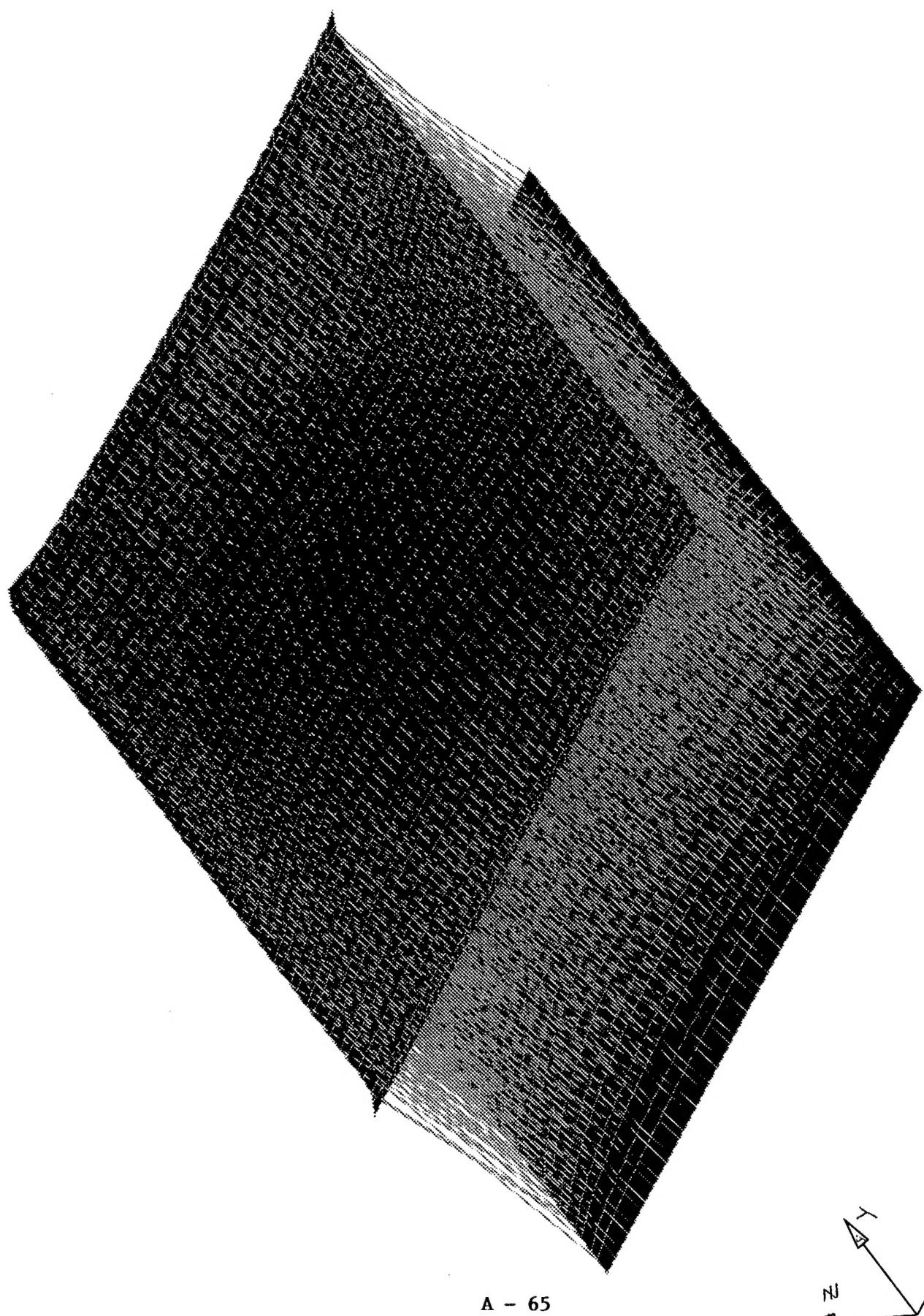


A - 64

Mode# 2, $f_m = 3.008e+03$ Hz
Displacements

Figure 4.28 Second mode shape

Figure 4.29 Third mode shape



Mode# 3, f= 3.677e+03 Hz
Displacements

Chapter 5 Conclusion

This report has considered a Z-pin reinforced composite sandwich plate acting under low velocity impact. Certain conclusions can be stated for a hollow core made from circular titanium Z-pins. The face plate was modeled as a composite unidirectional zero oriented material. The finite element analysis was compared with experimentation where at all possible. These conclusions are:

1. The optimized pin orientation is 30° with the vertical axis.
2. The static analysis can be used to characterize initial significant failure by considering pin buckling.
3. The dynamic analysis must be used to depict the continuous failure features.
4. In order for the overall analytical failure to compare well with experimentation, the face sheet damage must be included. A phenomenological technique was developed within this report.
5. The impact event was very local when displacement and stress were considered. In fact, the nature of the event deformed the upper face sheet differently than the lower face sheet. This therefore negated the usual sandwich plate bending normally associated with plate solutions.
6. The natural frequencies for the first three modes decreased with Z-pin failure.

7. Analytical results compared favorable with experimentation.

Thus, the initial stages of low velocity impact can be

represented using the finite element approach considered in
this study.